EVOLVING VIRTUAL AND COMPUTATIONAL PALEONTOLOGY

EDITED BY: Luca Pandolfi, Lorenzo Rook, Pasquale Raia and Josep Fortuny
PUBLISHED IN: Frontiers in Earth Science and Frontiers in Ecology and Evolution

frontiers Research Topics

frontiers

ISSN 1664-8714
ISBN 978-2-88966-258-6
DOI 10.3389/978-2-88966-258-6

About Frontiers

Frontiers is more than just an open-access publisher of scholarly articles: it is a pioneering approach to the world of academia, radically improving the way scholarly research is managed. The grand vision of Frontiers is a world where all people have an equal opportunity to seek, share and generate knowledge. Frontiers provides immediate and permanent online open access to all its publications, but this alone is not enough to realize our grand goals.

Frontiers Journal Series

The Frontiers Journal Series is a multi-tier and interdisciplinary set of open-access, online journals, promising a paradigm shift from the current review, selection and dissemination processes in academic publishing. All Frontiers journals are driven by researchers for researchers; therefore, they constitute a service to the scholarly community. At the same time, the Frontiers Journal Series operates on a revolutionary invention, the tiered publishing system, initially addressing specific communities of scholars, and gradually climbing up to broader public understanding, thus serving the interests of the lay society, too.

Dedication to Quality

Each Frontiers article is a landmark of the highest quality, thanks to genuinely collaborative interactions between authors and review editors, who include some of the world's best academicians. Research must be certified by peers before entering a stream of knowledge that may eventually reach the public - and shape society; therefore, Frontiers only applies the most rigorous and unbiased reviews.
Frontiers revolutionizes research publishing by freely delivering the most outstanding research, evaluated with no bias from both the academic and social point of view. By applying the most advanced information technologies, Frontiers is catapulting scholarly publishing into a new generation.

What are Frontiers Research Topics?

Frontiers Research Topics are very popular trademarks of the Frontiers Journals Series: they are collections of at least ten articles, all centered on a particular subject. With their unique mix of varied contributions from Original Research to Review Articles, Frontiers Research Topics unify the most influential researchers, the latest key findings and historical advances in a hot research area! Find out more on how to host your own Frontiers Research Topic or contribute to one as an author by contacting the Frontiers Editorial Office: researchtopics@frontiersin.org

EVOLVING VIRTUAL AND COMPUTATIONAL PALEONTOLOGY

Topic Editors:
Luca Pandolfi, University of Florence, Italy
Lorenzo Rook, University of Florence, Italy
Pasquale Raia, University of Naples Federico II, Italy
Josep Fortuny, Institut Català de Paleontologia Miquel Crusafont Cerdanyola del Vallès, Spain

Citation: Pandolfi, L., Rook, L., Raia, P., Fortuny, J., eds. (2020). Evolving Virtual and Computational Paleontology. Lausanne: Frontiers Media SA.
doi: 10.3389/978-2-88966-258-6

Table of Contents

frontiers in Earth Science

EDITORIAL
published: 15 October 2020
doi: 10.3389/feart.2020.591813

Editorial: Evolving Virtual and Computational Paleontology

Luca Pandolfi[1*†], *Pasquale Raia*[2†], *Josep Fortuny*[3†] *and Lorenzo Rook*[1†]

[1] *Department of Earth Sciences, University of Florence, Florence, Italy,* [2] *Department of Earth Sciences, Environmental and Resources, University of Naples "Federico II," Naples, Italy,* [3] *Institut Català de Paleontologia Miquel Crusafont, Cerdanyola del Vallès, Spain*

Keywords: digital models, surface scanning, photogrammetry, computed tomography, computational analyses

Editorial on the Research Topic

Evolving Virtual and Computational Paleontology

During the last few decades, the development of new technologies and methods, and increases in computational power, are widening Paleontology's research frontiers, moving this discipline—situated halfway between Biology and Geology—toward increasing use of (paleo) biological and (paleo)ecological approaches, and providing the opportunity to fully explore quantitative aspects of phenotypic evolution as well as new clues to the history of life. The ever-increasing availability of 3D models obtained by CT, surface scanning (SC) and/or photogrammetry (PT) is increasing the visibility and accessibility of rare, difficult to handle, remains, and therefore the number of virtual fossil representations that feature in scientific papers, contributing to this "revolution" and leading to the dawn of the "Virtual and Computational Paleontology" era. The pioneering steps toward this new era were taken in the early 1980s, when Tate and Cann (1982) and Conroy and Vannier (1984) became the first research teams to apply CT to Vertebrate Paleontology. Almost two decades later, the first applications of SC and PT to Vertebrate Paleontology opened the door to many new ideas and approaches (Lyons et al., 2000; Breithaupt and Matthews, 2001). Since the beginning of this digital paleontological era, the number of scientists merging traditional techniques with virtualization and computational advances has greatly increased, a process that still continues (and the first comprehensive reviews were published a few years later - see Zollikofer and Ponce de Leon, 2005; Cardini and Loy, 2013; Sutton et al., 2014).

Virtual (digital) representations have a great variety of non-invasive applications, including but not limited to digital curation (based on 3D models libraries), virtual restoration of specimens, and anatomical studies of both external and internal morphological structures, and open up the opportunities for development of new analytical tools. Thanks to virtualization, many Computational analyses and techniques (including geometric morphometrics, finite element analysis, multibody dynamic analysis, computational fluid dynamics, machine-learning, etc.) have been widely applied in Vertebrate Paleontology. Furthermore, their use is currently rapidly increasing thanks to continuing efforts to create more and better 3D virtual models, which are the basis for new computational approaches. Despite these many benefits, Virtual and Computational Paleontology is still not prevalent as it might be. Virtual data are therefore not broadly shared and new methodologies and techniques usually do not easily reach the widest audience, in particular younger researchers who usually show an insatiable hunger for learning and acquiring new skills.

This Research Topic was conceived with the principal goal of spreading this technological knowledge and, by taking advantage of the Open Access format of Frontiers, was intended to reach the widest possible number of researchers. The volume includes 15 different papers on the use and analysis of virtual representations and new computational methods, applied to several vertebrate taxa.

OPEN ACCESS

Edited and reviewed by:
Corwin Sullivan,
University of Alberta, Canada

****Correspondence:***
Luca Pandolfi
luca.pandolfi@unifi.it

†ORCID:
Luca Pandolfi
orcid.org/0000-0002-4186-4126
Pasquale Raia
orcid.org/0000-0002-4593-8006
Josep Fortuny
orcid.org/0000-0003-4282-1619
Lorenzo Rook
orcid.org/0000-0001-8923-5428.

Specialty section:
This article was submitted to Paleontology, a section of the journal Frontiers in Earth Science

Received: *05 August 2020*
Accepted: *25 September 2020*
Published: *15 October 2020*

Citation:
Pandolfi L, Raia P, Fortuny J and Rook L (2020) Editorial: Evolving Virtual and Computational Paleontology. Front. Earth Sci. 8:591813. doi: 10.3389/feart.2020.591813

3D models of external structures, obtained by means of SC and PT were the study subjects of several papers. Bartolini Lucenti et al. used a 3D visualization and digital imaging technique to study a new fossil canid from Georgia. They applied for the first time augmented reality to a few specimens through a simple web app. A new virtual reconstruction protocol, called Target Deformation, was applied by Cirilli et al., to 3D models of fossil horse skulls. This method allowed to virtually restore the strongly deformed holotype of *Equus stenonis* by using undeformed skull fragments of the same species found elsewhere. A caudal series of the dinosaur *Giraffatitan* was digitalized by Díez Díaz et al. *via* PT. The authors presented the first detailed 3D volumetric reconstruction of the caudal epaxial and hypaxial musculature of this sauropod. PT was at the core of Mujal et al.'s study, applied to Permian and Triassic tetrapod footprints. They used their 3D data to not only describe footprints but also to offer an initial qualitative interpretation of relative depth patterns within the tracks and their functional implications. Serio et al. combined PT and geometric morphometrics to study morphological convergence in the humerus of Xenarthra. The authors suggested that the highly specialized morphologies seen in digging taxa and tree sloths reflect major deviations from the plesiomorphic xenarthran body plan which occurred several times during the history of the group. Morphological convergence was the issue with Sansalone et al. who investigated the humeri of fossorial mammals by means of CT scans. They showed that fossorial mammals evolved multiple strategies to exploit the subterranean ecotope, characterized by different functional trade-offs rather than by convergence toward a single adaptive optimum.

Data on internal structures were obtained by means of CT scans of several fossil taxa, and 3D models and images were analyzed using several techniques. In Boscaini et al. endocranial features of giant sloths revealed by CT, helps elucidating the evolutionary history of sloths, whereas Iurino et al. described the first brain endocast of a juvenile fossil rhinoceros obtained *via* the CT method. Melchionna et al. used information on brain size and asymmetry in *Homo* species to argue that the emergence of handedness and early manifestations of cultural modernity nicely coincided with the emergence of the three species with the largest and most rapidly evolving brains among hominoids, namely *Homo heidelbergensis*, *Homo neanderthalensis* and *Homo sapiens*.

The variations in shape of stapes of Ruminantia was explored by Mennecart et al. on 3D tomographic data, whereas Pusch et al. reported endocranial data from Permo-Triassic therapsids, redescribing the skull of the therocephalian *Lycosuchus* on the basis of CT reconstruction. Püschel et al. studied a fossil primate from Cuba, *Paralouatta*, using 3D talar models and geometric morphometrics combined with machine-learning classification algorithms to argue for some degree of terrestriality in this extinct platyrrhine.

In addition, the Research Topic covers several other aspects of Virtual and Computational Paleontology, including methodological approaches and problems. Pérez Ramos and Figueirido focused on using virtual approaches to solve technical issues commonly encountered by paleontologists and evolutionary biologists. The authors proposed various solutions and used fossil skulls of the cave bears to test them. Piras et al. investigated visualization of local deformation in modern shape analysis, considering paleontological case studies and proposing new computational methods for evaluating and visualizing local deformations. Neutron microtomography was successfully used by Zanolli et al. to extract, three-dimensionally render and quantitatively assess the internal morphological details of fossil hominid material from different localities and strata; This Research Topic represents a new step in the development of methods for use of virtual representations of specimens by the scientific community. The Topic also explores how these models provide the basis for numerous applications, techniques and methodologies, providing new insights into vertebrate paleobiology. Finally, the Topic serves as both a meeting point for the new generation of paleontologists and evolutionary biologists, and an updated overview of Virtual and Computational Paleontology, a discipline that is rapidly evolving thanks to a never-ending stream of technological improvements.

AUTHOR CONTRIBUTIONS

All authors listed have made a substantial, direct, and intellectual contribution to the work, and approved it for publication.

ACKNOWLEDGMENTS

We would like to thank all reviewers for their contributions, and all authors of the submitted manuscripts. We also would like to thank the editor Corwin Sullivan and the Frontiers Team for their support and suggestions.

REFERENCES

Breithaupt, B. H., and Matthews, N. A. (2001). "Preserving paleontological resources using photogrammetry and geographic information systems," in Crossing boundaries in park management: proceedings of the 11th conference on research and resource management in parks and public lands, Denver, CO, April 16–20, 2001. Editor D. Harmon (Hancock, MI: The George Wright Society, Inc.), 62–70.

Cardini, A., and Loy, A. (2013). Virtual morphology and evolutionary morphometrics in the new millenium. *Hystrix* 24 (1), 1–5. doi:10.4404/hystrix-24.1-8749

Conroy, G. C., and Vannier, M. W. (1984). Noninvasive three-dimensional computer imaging of matrix-filled fossil skulls by high-resolution computed tomography. *Science* 226 (4673), 456–458. doi:10.1126/science.226.4673.456

Lyons, P. D., Rioux, M., and Patterson, R. T. (2000). Application of a three-dimensional color laser scanner to paleontology: an interactive model of a juvenile *Tylosaurus* sp. basisphenoid-basioccipital. *Palaeontol. Electron.* 3 (2), 4A.

Sutton, M. D., Rahman, I. A., and Garwood, R. J. (2014). *Techniques for virtual palaeontology*. London, UK: Wiley Blackwell, 208.

Tate, J. R., and Cann, C. E. (1982). High-resolution computed tomography for the comparative study of fossil and extant bone. *Am. J. Phys. Anthropol.* 58 (1), 67–73. doi:10.1002/ajpa.1330580108

Zollikofer, C. P., and Ponce de Leon, M. (2005). *Virtual reconstruction: a primer in computer-assisted paleontology and biomedicine*. Hoboken, NJ: John Wiley and Sons, 333.

Conflict of Interest: The authors declare that the research was conducted in the absence of any commercial or financial relationships that could be construed as a potential conflict of interest.

frontiers in Ecology and Evolution

ORIGINAL RESEARCH
published: 23 January 2020
doi: 10.3389/fevo.2019.00464

Novel Endocranial Data on the Early Therocephalian *Lycosuchus vanderrieti* Underpin High Character Variability in Early Theriodont Evolution

Luisa C. Pusch[1,2]*, *Jasper Ponstein*[1,2], *Christian F. Kammerer*[3,4] and *Jörg Fröbisch*[1,2,4]

[1] Museum für Naturkunde, Leibniz-Institut für Evolutions- und Biodiversitätsforschung, Berlin, Germany, [2] Institut für Biologie, Humboldt-Universität zu Berlin, Berlin, Germany, [3] North Carolina Museum of Natural Sciences, Raleigh, NC, United States, [4] Evolutionary Studies Institute, University of the Witwatersrand, Johannesburg, South Africa

Therocephalia is one of the major therapsid clades and ranges from the middle Permian to Middle Triassic. The earliest therocephalians were large-bodied predators whose fossils are common in middle Permian rocks of South Africa, but have received little study. Here we present a redescription of the skull of the early therocephalian *Lycosuchus* based on a specimen from the middle Permian *Tapinocephalus* Assemblage Zone of the South African Karoo Basin. By using a computed tomographic (CT) reconstruction of this specimen, we describe for the first time several endocranial characters of this taxon including a highly ramified maxillary canal and the inner ear, which is characterized by a lengthened lateral semicircular canal, a feature previously only known from the anomodont *Kawingasaurus* among non-mammalian therapsids, and the presence of a cochlear recess, so far only known within Therocephalia from the highly specialized Triassic taxon *Microgomphodon*. We also provide new insights into patterns of tooth replacement in lycosuchids, which have proven controversial for this taxon. Craniodental characters generally support the placement of *Lycosuchus* as the most basal taxon in therocephalian phylogeny. The morphology of the maxillary canal and inner ear reveal a mosaic of features indicating a complex history of character acquisition and loss in Therocephalia, comparable to that of cynodonts.

Keywords: therapsida, computed tomography, endocranial anatomy, maxillary canal, bony labyrinth, mosaic evolution, mandible

OPEN ACCESS

Edited by:
Josep Fortuny, Institut Català de Paleontologia Miquel Crusafont, Spain

Reviewed by:
Fernando Abdala, Unidad Ejecutora Lillo, Argentina
Julien Benoit, University of the Witwatersrand, South Africa

***Correspondence:**
Luisa C. Pusch
luisa.pusch@mfn.berlin

Specialty section:
This article was submitted to Paleontology, a section of the journal Frontiers in Ecology and Evolution

Received: *23 August 2019*
Accepted: *18 November 2019*
Published: *23 January 2020*

Citation:
Pusch LC, Ponstein J, Kammerer CF and Fröbisch J (2020) Novel Endocranial Data on the Early Therocephalian Lycosuchus vanderrieti Underpin High Character Variability in Early Theriodont Evolution. Front. Ecol. Evol. 7:464. doi: 10.3389/fevo.2019.00464

INTRODUCTION

The advent of widely-used computed tomographic (CT) imaging on fossil specimens has allowed paleontologists unprecedented access to the once-obscure internal features of vertebrate crania. In the context of mammalian origins, these novel endocranial data have been instrumental in elucidating patterns of brain and ear evolution, facial innervation, and the evolution of endothermy in non-mammalian therapsids (e.g., Rodrigues et al., 2013, 2014; Crompton et al., 2015, 2017; Laaß, 2015a,b, 2016; Benoit et al., 2016a,b, 2017a,b,c, 2018, 2019; Araújo et al., 2017, 2018; Bendel et al., 2018; Pusch et al., 2019). As the therapsid clade ancestral to (and including) modern

mammals, Cynodontia has been the primary focus for CT-assisted morphological studies in Synapsida (e.g., Rowe et al., 1993; Rodrigues et al., 2013, 2014; Crompton et al., 2015, 2017; Benoit et al., 2016a, 2019; Pavanatto et al., 2019; Pusch et al., 2019). By contrast, Therocephalia, generally considered the sister-group of Cynodontia (e.g., Hopson and Barghusen, 1986; Hopson, 1991; Huttenlocker, 2009; Huttenlocker and Sidor, 2016; Huttenlocker and Smith, 2017; but see Abdala, 2007; Botha et al., 2007), has received little study.

Therocephalia is a species-rich and ecomorphologically varied group ranging from the middle Permian to the Middle Triassic, with highest diversity in the late Permian (Abdala et al., 2008; Huttenlocker et al., 2011; Huttenlocker, 2014; Huttenlocker and Smith, 2017).The earliest known representatives of this group have been reported from the middle Permian *Eodicynodon* Assemblage Zone (AZ) in the Karoo Basin of South Africa (Abdala et al., 2008), and they are the most abundant group of predatory therapsids in the subsequent, middle–earliest late Permian *Tapinocephalus* and *Pristerognathus* AZs, with hundreds of known specimens (Smith et al., 2012). Despite their abundance, these early therocephalian taxa have received little study relative to their later Permo-Triassic relatives. Two families of early therocephalians are current recognized (Scylacosauridae and Lycosuchidae), both consisting of large-bodied (1–3 m body length) predators (van den Heever, 1994; Abdala et al., 2014a). Scylacosaurids exhibit long, comparably narrow snouts and include the oldest known therocephalians (both taxa reported from the *Eodicynodon* AZ are scylacosaurids; Abdala et al., 2008). By contrast, lycosuchids are characterized by relatively short, broad snouts and reduction of the postcanine dentition (van den Heever, 1994; Abdala et al., 2008, 2014a).

Abdala et al. (2014a) recently described new lycosuchid specimens and reviewed the family's taxonomy, recognizing only two valid species: *Lycosuchus vanderrieti* and *Simorhinella baini*. *Simorhinella* is restricted to the *Tapinocephalus* AZ, whereas *Lycosuchus* ranges from the uppermost *Tapinocephalus* AZ through the *Pristerognathus* AZ. Cladistic analyses have found that *Lycosuchus* occupies the most basal position in therocephalian phylogeny (e.g., van den Heever, 1994; Abdala, 2007; Botha et al., 2007; Huttenlocker, 2009; Huttenlocker et al., 2011; Huttenlocker and Sidor, 2016; Huttenlocker and Smith, 2017; Kammerer and Masyutin, 2018). The position of *Simorhinella* is less certain, and it has generally been excluded from phylogenetic analyses of Therocephalia. Abdala et al. (2014a) noted that *Simorhinella* shares some features with scylacosaurids to the exclusion of *Lycosuchus* (e.g., presence of a median vomerine crest, ventral extension of ridges from the transverse processes of the pterygoid), suggesting that Lycosuchidae may be paraphyletic. More recently, Liu and Abdala (2019) recovered *Gorynychus masyutinae*, a Russian taxon originally found to be the sister-taxon of Eutherocephalia (Kammerer and Masyutin, 2018), as the sister taxon of *Lycosuchus*. These variable results indicate substantial instability in basal (i.e., non-eutherocephalian) therocephalian phylogeny, probably associated with extensive homoplasy in this group (Kammerer and Masyutin, 2018) and necessitating a more detailed understanding of the anatomy of basal therocephalians.

Although the holotype of *Lycosuchus vanderrieti* consists of a complete, well-preserved skull and jaws (US D173, **Figure 1**), only superficial accounts of its anatomy have been published in the literature. Broom (1903) initially described the taxon, but discussed its anatomy only briefly. Boonstra (1964) described additional lycosuchid specimens, but primarily dealt with their postcranial anatomy. Not until the work of van den Heever (1980, 1987, 1994) was there extensive description of cranial morphology in the group. Because van den Heever (1994) based his description on semi-disarticulated lycosuchid crania (CGS C60 and CGS M793), he was even able to discuss portions of the anatomy rarely visible in therocephalian specimens (e.g., the medial surface of the snout wall). Nevertheless, he was unable to address many aspects of the endocranial anatomy in *Lycosuchus* due to technological limitations of the time (and rarity of the study taxon making serial sectioning inadvisable).

Olson (1944) first described internal skull anatomy in several purported basal therocephalians based on serial sections, but more recent research has demonstrated that some of these specimens instead represent gorgonopsians (van den Heever and Hopson, 1982). Hillenius (1994) described ridges on the internal ventral margin of the nasal bones in the basal therocephalian *Glanosuchus*, which he argued supported maxilloturbinals, though this has been disputed (Sigurdsen, 2006). Sigurdsen (2006) provided the first detailed description of many therocephalian endocranial characters on the basis of serial sections of an indeterminate akidnognathid. More recent, CT-based investigations by Sigurdsen et al. (2012) and Benoit et al. (2016a,b, 2017a,b) have shed additional light on therocephalian endocranial anatomy, providing new information on facial innervation and brain and inner ear morphology. Among this new data, Benoit et al. (2017b) presented the first instance of a cochlear recess in the inner ear of a therocephalian, in the highly specialized Triassic taxon *Microgomphodon*.

Here, we present new information on the skull of *Lycosuchus vanderrieti* based on MB.R.995 from the *Tapinocephalus* AZ, which consists of a partial snout, braincase and mandible. This specimen was initially described by Janensch (1952), but his description focused only on surface details of the lower jaw. By using a computed tomographic (CT) reconstruction of this specimen, we describe for the first time several endocranial characters of this taxon and also provide new insights into patterns of tooth replacement in lycosuchids, which have historically been controversial (Broom, 1903; Boonstra, 1969; van den Heever, 1980). MB.R.995 includes a complete, well-preserved lower jaw, an element rarely discussed in previous accounts of lycosuchid anatomy (van den Heever, 1994 provided a thorough generalized description of the jaw in early therocephalians, but not *Lycosuchus* specifically). Although the jaw of MB.R.995 has been discussed in the literature before, the brief description by Janensch (1952) provided little information beyond the shape of the reflected lamina of the angular. Our redescription of this element provides substantial new data on its anatomy and permits broader comparisons with other therocephalians. CT-reconstruction of the jaw and cranium of *Lycosuchus* allows us

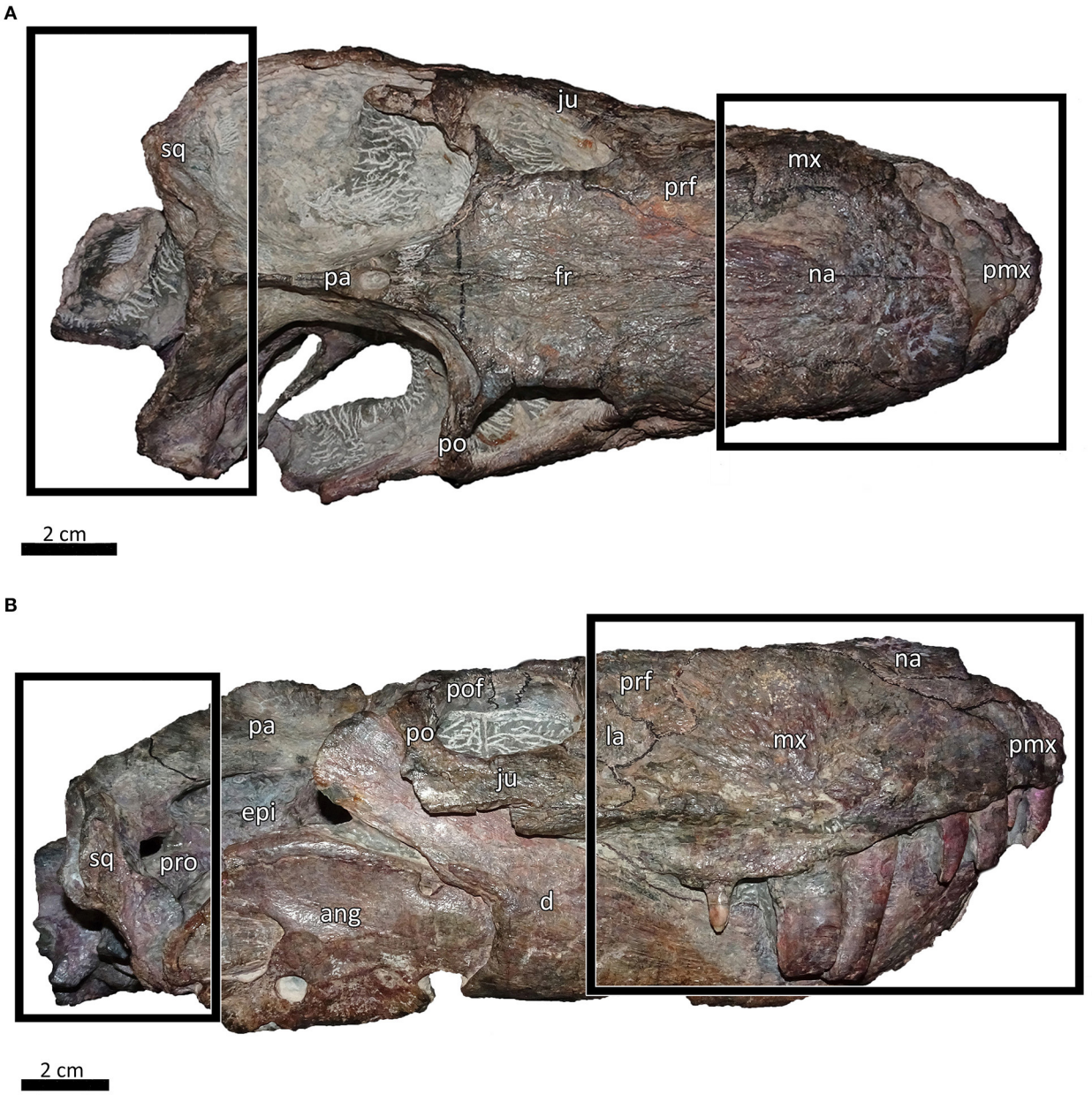

FIGURE 1 | Type specimen of *Lycosuchus vanderrieti* (US D173) in **(A)** dorsal and **(B)** right lateral view. Black boxes highlighting the portions of the cranium preserved in MB.R.995. ang, angular; d, dentary; epi, epipterygoid; fr, frontal; ju, jugal; la, lacrimal; mx, maxilla; na, nasal; pa, parietal; pmx, premaxilla; po, postorbital; pof, postfrontal; prf, prefrontal; pro, prootic, sq, squamosal.

to evaluate the character support for *Lycosuchus* as the most basal taxon in therocephalian phylogeny and discuss character evolution in Therocephalia.

MATERIALS AND METHODS

The incomplete cranium and associated mandible of the specimen of *Lycosuchus vanderrieti* described herein (MB.R.995, **Figures 2**–**4**, **10**, **12**) are part of the collection of the Museum für Naturkunde Berlin. This specimen was collected by W. Janensch in the *Tapinocephalus* AZ of Letjesbosch near Beaufort West, South Africa in 1929, and later prepared by E. Siegert and J. Schrober (Janensch, 1952). Although fragmented, the existing parts of the skull of MB.R.995 are in relatively good condition. The bones forming the snout and parts of the palate are preserved up to the level of the pterygoid, of which only the anterior part is preserved. The total length of the partial snout is ∼19.5 cm and

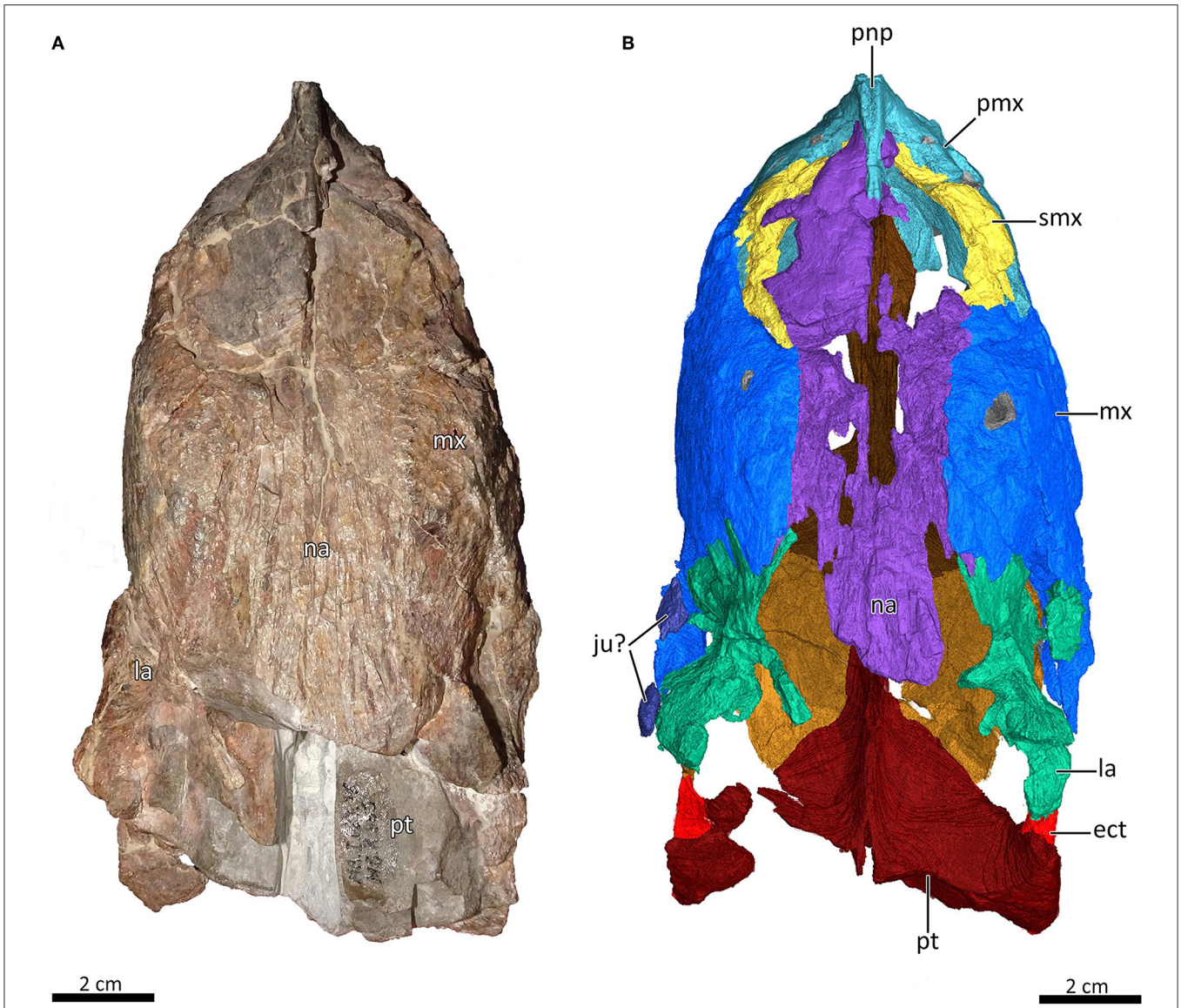

FIGURE 2 | Snout of MB.R.995 in dorsal view. **(A)** Photograph and **(B)** 3D reconstruction of the snout. ect, ectopterygoid; ju?, jugal?; la, lacrimal; mx, maxilla; na, nasal; pmx, premaxilla; pnp, prenasal process of the premaxilla; pt, pterygoid; smx, septomaxilla.

its maximum width is 9.4 cm. The partially preserved braincase primarily consists of bones forming the occiput and is about 7.9 cm high and 12 cm wide. Both lower jaw rami are preserved, but the left one is more complete, with the postdentary bones missing on the right. We scanned only the left mandibular ramus, which is ∼21.5 cm long.

MB.R.995 was CT scanned in the CT-Laboratory of the Museum für Naturkunde Berlin using an YXLON FF35 X-ray CT scanner. The complete scan sets consist of 3,154 (for the snout), 3,147 (for the braincase), and 2,354 (for the left mandible) slices. The slices were generated in coronal planes with a voxel size of 0.0486 mm (for the snout), 0.0366 mm (for the braincase), and 0.0323 mm (for the left mandible). Tube voltage ranged from 130 to 200 kV, and tube current from 40 to 172 μA. The visualization of the slices, virtual 3D rendering, and segmentation of selected structures were performed using VGStudio Max 3.2 (Volume Graphics GmbH, Heidelberg, Germany) in the 3D Visualization Laboratory at the Museum für Naturkunde Berlin. The inner ear endocast was segmented from the sediment infilling the right bony labyrinth of the skull. Its measurements were taken using VGStudio Max and follow the protocol of Benoit et al. (2017b, **Figure 2**).

INSTITUTIONAL ABBREVIATIONS

CGS, Council for Geosciences, Pretoria, South Africa; MB.R., Museum für Naturkunde, Fossil Reptile Collection, Berlin, Germany; US, University of Stellenbosch, Stellenbosch, South Africa.

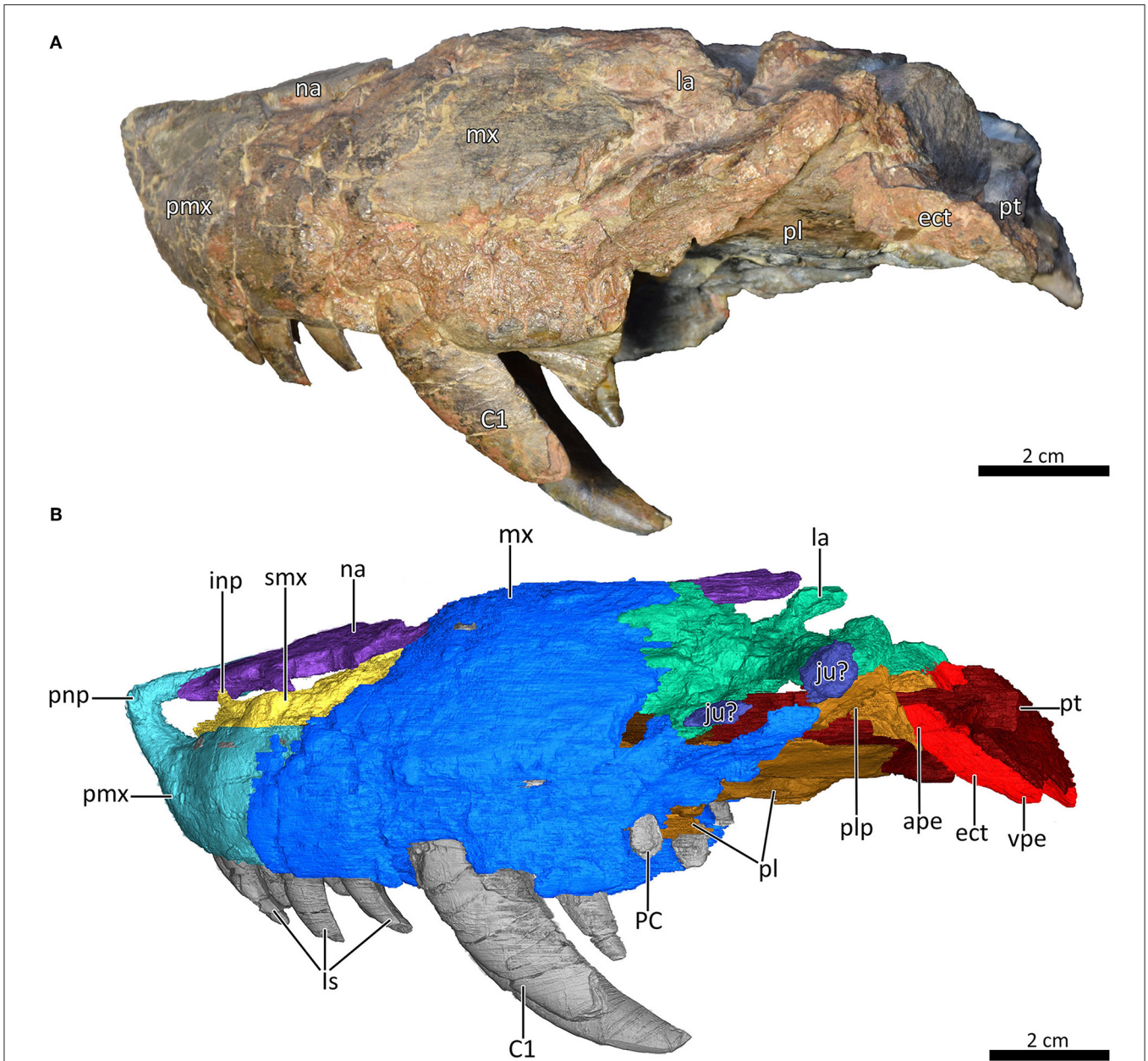

FIGURE 3 | Snout of MB.R.995 in left lateral view. **(A)** Photograph and **(B)** 3D reconstruction of the snout. ape, anterior process of the ectopterygoid; C1, first canine; ect, ectopterygoid; inp, intranarial process; ls, upper incisors; ju?, jugal?; la, lacrimal; mx, maxilla; na, nasal; PC, upper postcanine; pl, palatine; plp, posterolateral process of the palatine; pmx, premaxilla; pnp, prenasal process of the premaxilla; pt, pterygoid; smx, septomaxilla; vpe, ventral process of the ectopterygoid.

RESULTS

General Preservation

The left side of the snout of MB.R.995 is generally better preserved than the right one, with only the posterior portion of the snout better preserved on the right side. The portion of the palate consisting of the vomer and the palatine is well-prepared and its bone surface is in relatively good condition. The nasals are badly damaged, with the anterior portion of the right nasal bone almost completely missing. Both lacrimals are badly crushed, with only the anteromedial portions being relatively well-preserved (**Figures 2–4**, **5A**, **7**, **8**, **9A**). MB.R.995 is missing the prefrontals, frontals, postorbitals, postfrontals, zygomatic arches, most of the pterygoid and parabasisphenoid, the orbitosphenoid, epipterygoids, stapes, and the quadrate-quadratojugal complex. However, there seems to be at least a part of the posterior region of the parietal preserved in the damaged dorsal portion of the occiput. In addition, there are two small pieces of bone lateral to the left maxilla and lacrimal that may be parts of the jugal (**Figures 2–4**, **8**, **10**). Despite damage to the

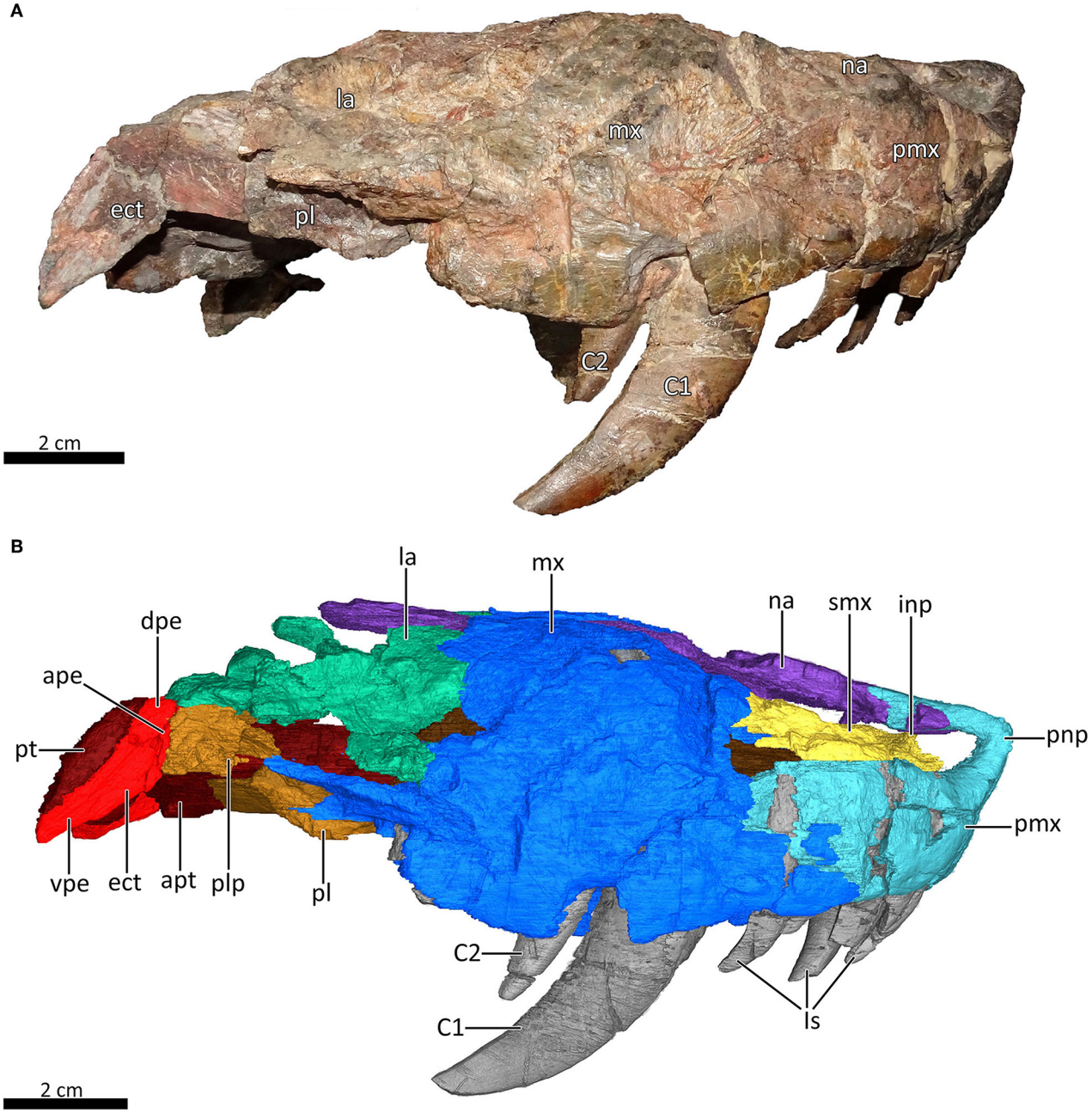

FIGURE 4 | Snout of MB.R.995 in right lateral view. **(A)** Photograph and **(B)** 3D reconstruction of the snout. ape, anterior process of the ectopterygoid; apt, anterior process of the pterygoid; C1, first canine; C2, second canine; dpe, dorsal process of the ectopterygoid; ect, ectopterygoid; inp, intranarial process; ls, upper incisors; la, lacrimal; mx, maxilla; na, nasal; pl, palatine; plp, posterolateral process of the palatine; pmx, premaxilla; pnp, prenasal process of the premaxilla; pt, pterygoid; smx, septomaxilla; vpe, ventral process of the ectopterygoid.

dorsal and anterior portion of the braincase, the occiput is generally in relatively good condition, but preserves only part of the left squamosal, with the right squamosal absent entirely (**Figure 10**). The reader is therefore directed to the descriptions of Broom (1903) and van den Heever (1987, 1994) for additional information on the exterior morphology of these elements, based on complete crania of *Lycosuchus*. The left mandible is long and fairly robust, as is typical of early therocephalians (van den Heever, 1987, 1994; Suchkova and Golubev, 2019). It is relatively well-preserved, with only the posterodorsal end of the coronoid process missing, broken above the dorsal margin of the surangular. However, enough of the coronoid process is

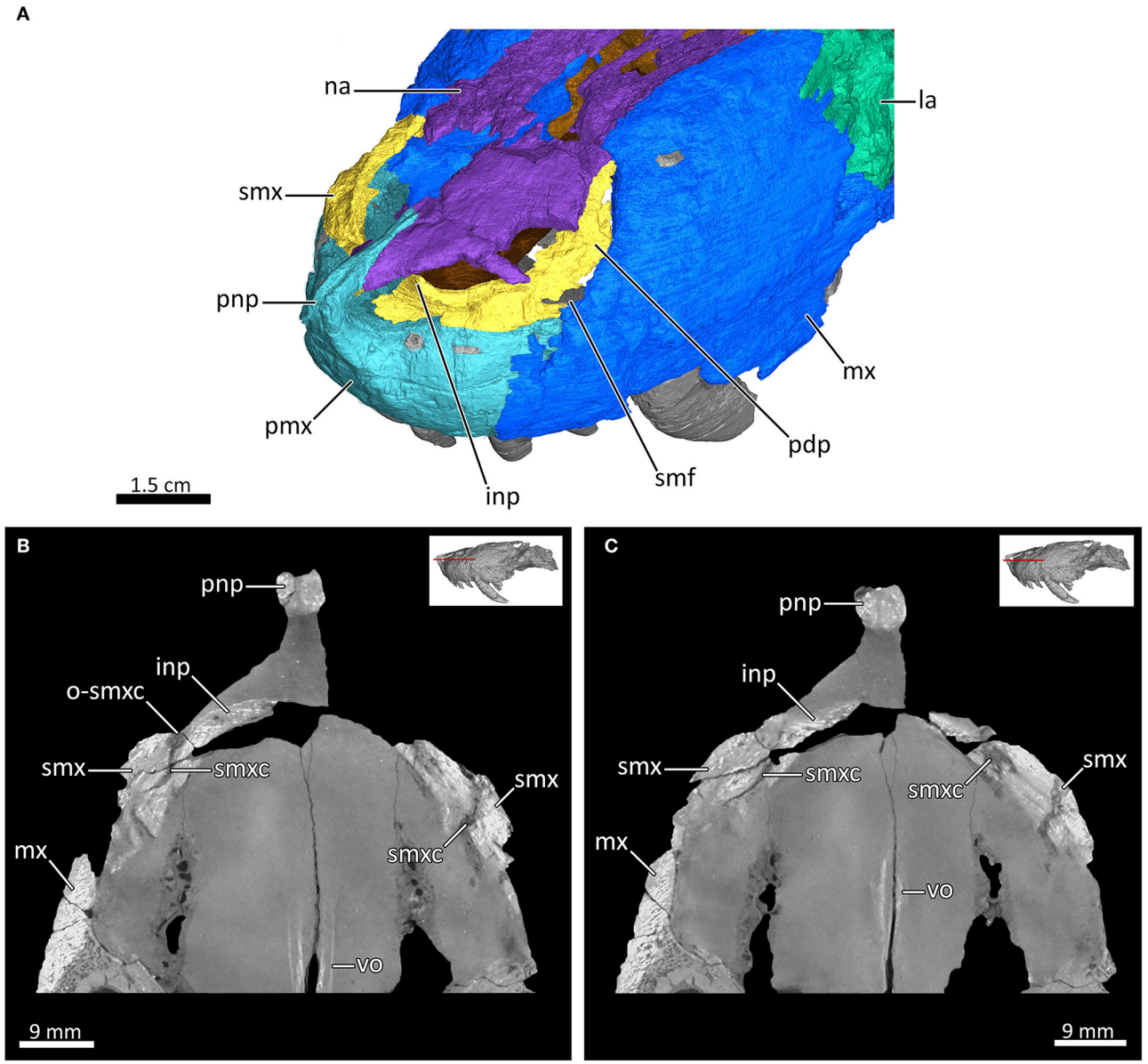

FIGURE 5 | The rostral nasal cavity of MB.R.995. **(A)** 3D reconstruction of the anterior portion of the snout left anterodorsolateral view. **(B,C)** Transverse CT sections through the rostral part of the nasal cavity. inp, intranarial process; la, lacrimal; mx, maxilla; na, nasal; o-smxc, opening of the septomaxillary canal; pdp, posterodorsal process of the septomaxilla; pmx, premaxilla; pnp, prenasal process of the premaxilla; smf, septomaxillary foramen; smx, septomaxilla; smxc, septomaxillary canal; vo, vomer.

preserved to show that it was free standing above the postdentary bones (**Figure 12**).

Snout

The premaxilla forms the anterior portion of the snout and is characterized by a tall, strongly arched prenasal (intranarial) process projecting beyond the anterior margin of main body of the premaxilla (**Figures 3**, **4**). The prenasal process continues posterodorsally as an elongate, narrow process extending between the nasals and the external naris (**Figures 2–4**, **5A**, **7**, **8A**). This morphology is similar to that of the whaitsiid therocephalian *Theriognathus microps* (Huttenlocker and Abdala, 2015), although the posterior portion of the prenasal process of MB.R.995 is even longer than in *Theriognathus*. The facial surface of the premaxilla is broadly overlapped by the maxilla posteriorly, up to the level of I4 (**Figures 3B**, **4B**, **5A**, **8B**). Each premaxilla bears five incisors (damaged to varying degrees), which are enclosed in a broad ventral alveolar plate. The alveolus of the left I1 is almost completely empty, with only a fragment of the root present;

otherwise at least part of the crown is preserved for all other incisors (**Figures 3**, **4**, **7**, **8B**, **12**). Posteromedially, the premaxilla forms a short, posteriorly-located vomerine process, which underlies the anterior portion of the vomer (**Figures 7A,C**, **8**, **13D**). van den Heever (1987, 1994) questioned the presence of a vomerine process in *Lycosuchus,* because of the apparent absence of this feature in the specimen CGS M793. However, our results clearly show the presence of a vomerine process in MB.R.995, indicating that its absence in CGS M793 was a preservational artifact.

The septomaxilla is large and forms the posteroventral border of the external naris. Its footplate broadly contacts the premaxilla ventrally, making up the external narial floor (**Figures 2B**, **3B**, **4B**, **5**, **7**, **8A**). The anterior portion of the footplate curves inward, resting on a medial platform of the premaxilla. It bears a well-developed, transversely-oriented intranarial process (only preserved on the left side) (**Figures 3B**, **4B**, **5A**, **7A,B**). The dorsal tip of this process is just lateral to the anteriormost part of the nasal, nearly contacting it, though this extreme proximity is probably due to post mortem distortion, as it is broadly separated from the nasal in uncrushed skulls (see, e.g., van den Heever, 1994). The septomaxillary canal is clearly visible in section in the scan (**Figures 5B,C**). It enters the bone from the inside of the nasal cavity in the posterior region of the septomaxilla at the septomaxillary foramen. The latter is large and located on the lateral surface of the snout, bordered by the septomaxilla anteriorly and the maxilla posteriorly. The anterior opening of the septomaxillary canal is near the base of the intranarial process (**Figure 4**). Posterodorsal to the septomaxillary foramen, the septomaxilla has a facial (posterodorsal) process extending between the nasal and the maxilla (**Figures 2B**, **3B**, **4B**, **5A**, **7A,B**).

The nasal is a large bone forming the dorsal roof of the snout and the nasal cavity. Anteriorly, the nasal becomes wider and flatter in the region where it forms the dorsal margin of the external naris, but tapers at its anteriormost portion where it contacts the prenasal process of the premaxilla and nearly contacts the intranarial process of the left septomaxilla (**Figure 2**). The external naris appears unusually narrow in MB.R.995 (**Figures 3**, **4**, **5A**, **7A,B**) as a result of dorsoventral crushing in this specimen. Laterally, the nasal is overlapped by the dorsal lamina of the maxilla. Posterolaterally, the nasal would usually contact the prefrontal and the anterior margin of the frontal (missing in this specimen). In this area the posterior margin of the nasals, which is V-shaped in better preserved skulls of *Lycosuchus* (e.g., Broom, 1903; van den Heever, 1987, 1994), is also slightly crushed and incompletely preserved (**Figures 2B**, **3B**, **4B**, **5A**, **7A,B**). Internally, the ventral margin of the nasal is posteriorly overlain by the anterior process of the lacrimal, which is in turn overlapped by the maxilla (**Figures 7**, **9C**). Although badly damaged, the ventral surface of the nasal bones seems to be transversely concave, becoming flatter in the region where they usually contact the frontals and prefrontals. In this region, a pair of weakly preserved ridges occurs along the ventral surface of the nasal, parallel to the midline suture, which probably extended from the ventral surface of the frontals. These ridges probably would have stretched along the entire ventral surface of the nasals, although this cannot be seen in this specimen due to damage (**Figure 9**). These ridges may have served as attachment points for cartilaginous nasal turbinals, as has been described for several therapsids in recent years (e.g., Kemp, 1979; Hillenius, 1994; Crompton et al., 2015, 2017; Bendel et al., 2018; Pusch et al., 2019). In therocephalians in particular, cartilaginous turbinals attaching to the nasals have been proposed for the basal taxon *Glanosuchus macrops* (Hillenius, 1994; van den Heever, 1994), akidnognathids (Sigurdsen, 2006), and for the baurioid *Tetracynodon darti* (Sigurdsen et al., 2012). A median ridge on the midline suture of the nasals, as has been inferred to support the dorsal edges of a cartilaginous internasal septum in cynodonts (Crompton et al., 2017), could not be observed. However, given the incompleteness of the nasals, its absence in *Lycosuchus* should not be taken as definite.

The maxilla is a large element, which forms most of the lateral surface of the snout and much of the side wall of the nasal cavity. It has a very high and broad facial lamina that largely excludes the nasal from sight in lateral view (which probably is not just an artifact of crushing, as the same is true in the relatively undistorted holotype, **Figure 1B**), and a posterolateral process that tapers gradually beneath the orbit, where it usually underlies the jugal. However, both maxillae are damaged in that area, and other than two possible fragments, the jugals are not preserved. Posteriorly and posterodorsally, the maxilla contacts the lacrimal (**Figures 2–4**, **8**). The external surface of the maxilla is finely rugose, especially in the dorsal region of the first canine where its root is exposed on the dorsal lamina of the maxilla. This rugosity is most clearly visible on the left maxilla, since the outer surface of the right maxilla is largely damaged. The internal surface of the facial portion of the maxilla is generally smooth and flat, but becomes substantially thicker anteriorly due to the large boss around the alveolus of the first canine. Immediately anterior to the canine boss and medioventral to the suture with the septomaxilla, the maxilla bears a small depression, the anterior maxillary fossa (**Figure 7**). This feature is also present in *Glanosuchus* (van den Heever, 1994) and the akidnognathid *Shiguaignathus wangi* (Liu and Abdala, 2017). By contrast, an anterior maxillary fossa is not known in the baurioid *Tetracynodon darti* (Sigurdsen et al., 2012). Posterior to the canine boss, there is a second depression, called the posterior maxillary fossa by van den Heever (1994) and the anterior maxillary sinus by Sigurdsen (2006). The anterior and posterior maxillary fossae seem to be simple artifacts of the extensive medial development of the canine boss. Along the majority of its ventral margin the maxilla contacts the palatine, starting anteromedial to the canine boss and ending posteriorly where the posterolateral process of the maxilla contacts the lateral margin of the posterolateral process of the palatine, which in turn contacts the anterior process of the ectopterygoid (**Figures 3B**, **4B**, **7**, **8**). However, due to damage to the maxilla, there is a small gap between it and the palatine here (**Figure 8**). According to van den Heever (1987, 1994), the posterolateral process of the maxilla overlies the lateral margin of the contact between the palatal process of the palatine and the anterior process of the ectopterygoid in that area.

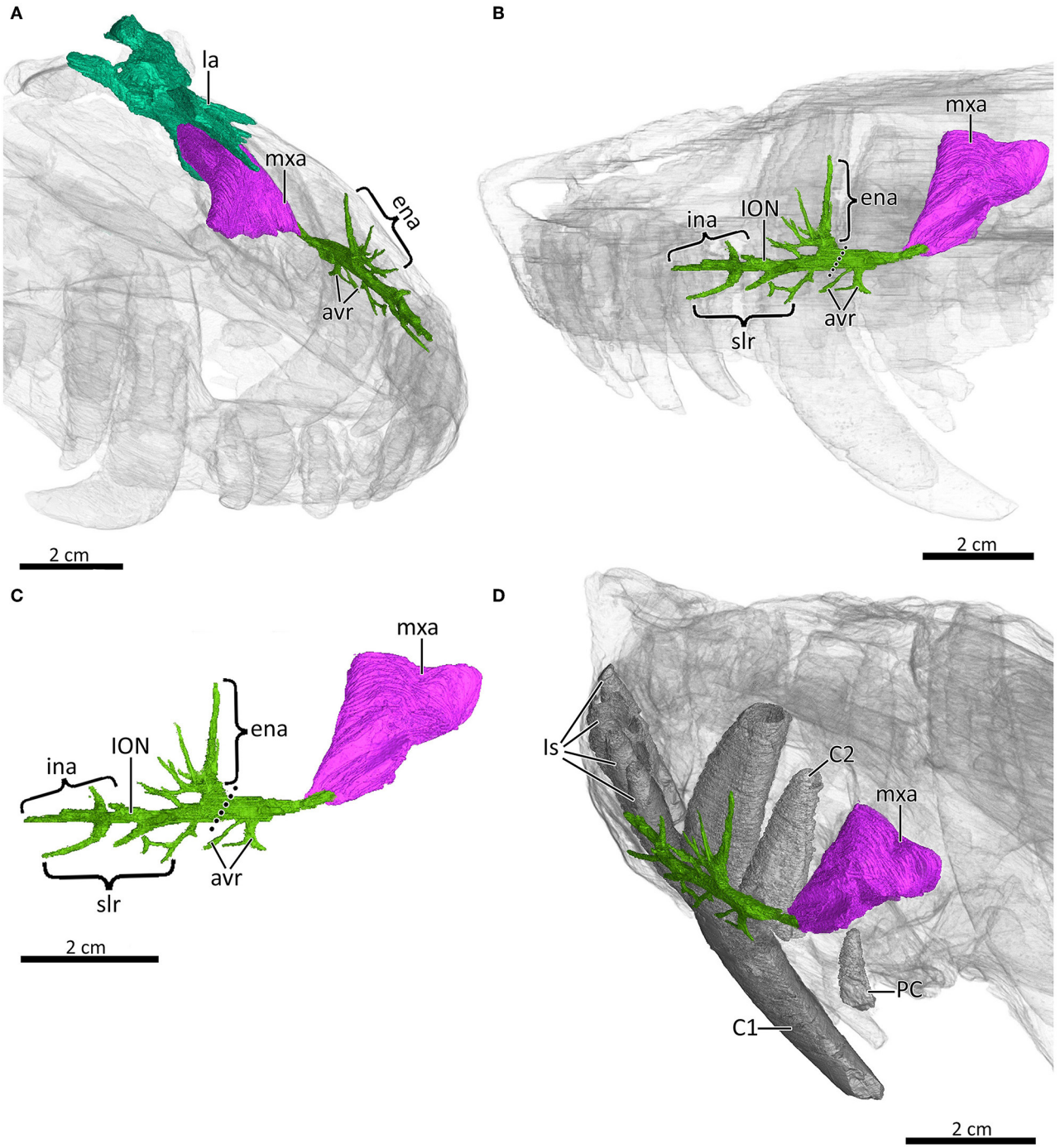

FIGURE 6 | 3D reconstructions of the maxillary canal (in green), maxillary antrum (in pink), and the lacrimal (in turquoise) of MB.R.995 in **(A)** right anterodorsolateral view with the snout transparent, **(B)** left lateral view with the snout transparent, **(C)** left lateral view, and **(D)** right posterodorsolateral view with the snout transparent. Dotted line illustrates the caudal extremity of the infraorbital nerve. avr, alveolar rami of the CNV_2; C1, first canine; C2, second canine; ena, external nasal rami of the ION; ina; internal nasal rami of the ION; ION, infraorbital nerve; Is, upper incisors; la, lacrimal; mxa, maxillary antrum; PC, upper postcanine; slr, superior labial rami of the ION.

Posterior to the posterior maxillary fossa, in the region where the maxilla underlies the anterior margin of the lacrimal, the former appears slightly convex medially. A large, internal facial recess is present in this area of the maxilla, extending onto the medial surface of the anterior portion of the lacrimal (**Figures 6A**, **7**, **9C**, **13D**). This recess corresponds to the

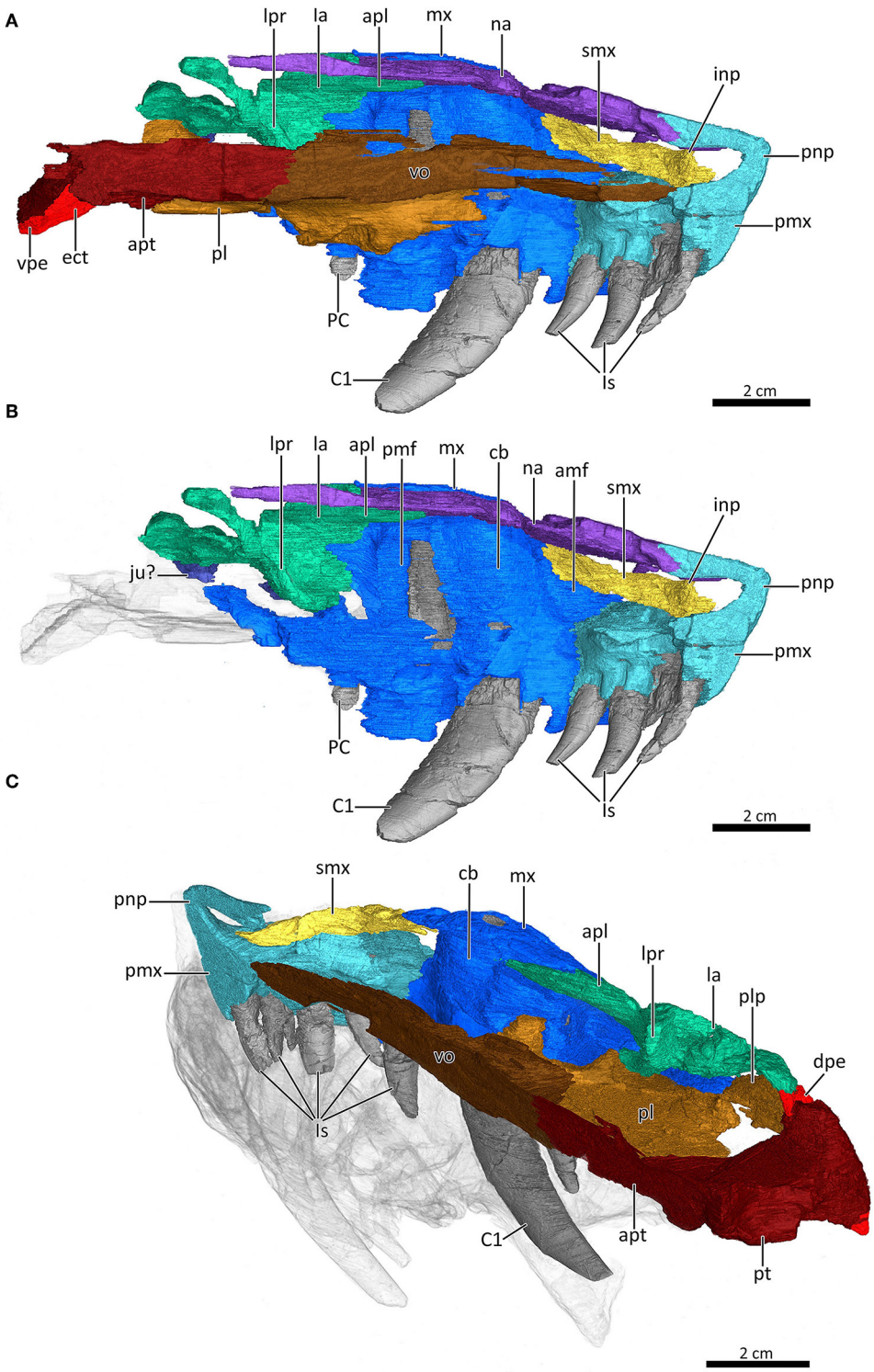

FIGURE 7 | Mid-sagittal section through the reconstructed snout of MB.R.995 to show its internal morphology. **(A,B)** Internal view of the left nasal region with the vomer, palatine, and ectopterygoid digitally removed in **(B)** to expose the internal structure. **(C)** Internal morphology of the right nasal region in posterodorsolateral view with the nasal digitally removed to expose the internal structure. amf, anterior maxillary fossa; apl, anterior process of the lacrimal; apt, anterior process of the pterygoid; C1, first canine; cb, canine boss; dpe, dorsal process of the ectopterygoid; ect, ectopterygoid; inp, intranarial process; ls, upper incisors; ju?, jugal?; la, lacrimal; lpr, lacrimo-palatine ridge; mx, maxilla; na, nasal; PC, upper postcanine; pl, palatine; plp, posterolateral process of the palatine; pmf, posterior maxillary fossa; pmx, premaxilla; pnp, prenasal process of the premaxilla; pt, pterygoid; smx, septomaxilla; vo, vomer; vpe, ventral process of the ectopterygoid.

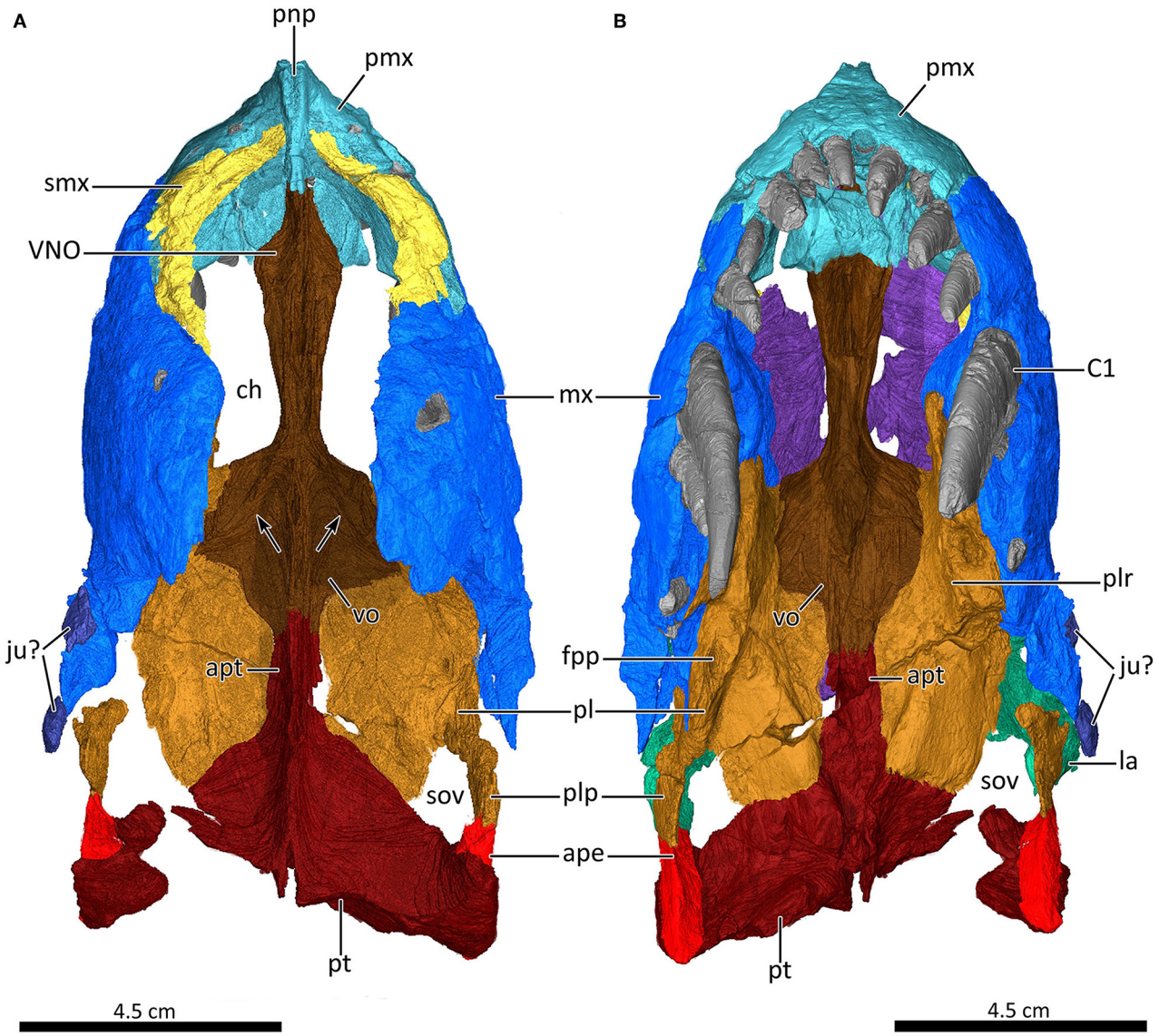

FIGURE 8 | 3D reconstruction of the snout of MB.R.995. **(A)** Snout in dorsal view with the nasals and lacrimals digitally removed to expose the internal structure. Arrows indicate the weakly-developed ridges on the posterior portion of the vomer. **(B)** Ventral view of the palate. ape, anterior process of the ectopterygoid; apt, anterior process of the pterygoid; C1, first canine; ch, choane; fpp, foramen palatine posterior; ju?, jugal?; la, lacrimal; mx, maxilla; pl, palatine; plp, posterolateral process of the palatine; plr, palatine ridge; pmx, premaxilla; pnp, prenasal process of the premaxilla; pt, pterygoid; smx, septomaxilla; sov, suborbital vacuity; VNO, channel housing the vomeronasal organ; vo, vomer.

posterior maxillary sinus of van den Heever (1994) and Sigurdsen (2006). Based on our examination of this feature in *Lycosuchus* and other theriodonts, we agree with van den Heever (1994) that the posterior maxillary sinus in therocephalians is homologous with the maxillary antrum in cynodonts (e.g., Fourie, 1974; Crompton et al., 2017; Pusch et al., 2019). At the anteroventral tip of the maxillary antrum, a branching maxillary canal extends forwards, starting at the level of the root of the second canine and ending at the posterior margin of the premaxilla at the level of the root of the fifth incisor (**Figures 6**, **13C**). This maxillary canal would have housed the maxillary branch of the trigeminal nerve (CNV_2), a branch of the facial nerve, and blood vessels (Benoit et al., 2016a). The caudal part of the maxillary canal, which is connected to the maxillary antrum, ramifies into two of the three branches for the alveolar rami of the CNV_2 (probably the caudal and medial alveolar rami), as in the baurioid *Choerosaurus dejageri* (Benoit et al., 2016b). Both rami radiate from the same point within the maxillary canal. As in *Choerosaurus*, the caudal part of the maxillary canal appears relatively long (Benoit et al., 2016a,b). Its diameter is generally larger than that of the rostral part of the canal, but narrows posteriorly where it disappears into the maxillary antrum (**Figure 6**). The rostral part of the maxillary

canal, which is the homolog of the tube for the infraorbital ramus (ION) (Benoit et al., 2016a) begins immediately anterior to the bifurcation of the alveolar rami. It is highly ramified in MB.R.995 with three main ramifications: the external nasal rami, internal nasal rami, and superior labial rami. At the posterior portion of the rostral part, a complex of canals for the external nasal rami of the ION diverge dorsally at the level of the root of the large C1, consisting of a long, nearly vertically-directed major ramus, which has a robust base within the maxillary canal and further smaller, strongly ramified anterodorsally-directed ramifications diverging ventrally near its base. Anterior to this complex there is a further small, anteriorly-directed canal for the external nasal ramus diverging from the main branch of the maxillary canal (**Figure 6**). Just anterior to the complex of external nasal rami, a narrow ramus diverges ventrally from the maxillary canal, which bears a small anteriorly-directed ventral ramification. This ramus might have housed the superior labial ramus of the ION. There are two further ventral ramifications for the superior labial rami diverging anterior to the ramified ventral ramus, consisting of a small anteroventrally-directed ramus and a long anteriorly-curved ramus near the anterior tip of the maxillary canal (**Figure 6**). The latter terminates anteriorly as an internal nasal ramus lateral to I5. Two further canals that probably housed internal nasal rami of the ION diverge dorsally from the maxillary canal toward the superior labial rami. The posterior one is small and anteriorly directed, whereas the anterior one curves anterodorsally (**Figures 6B,C**). A definite rostral alveolar canal cannot be discerned in this specimen. Benoit et al. (2019) recently discussed whether the posteriormost branch of the superior labial canal is homologous with the rostral alveolar canal of the CNV_2 in cynodonts; we consider this possible, but uncertain pending additional data on facial innervation in eutheriodonts.

The plate-like lacrimal is positioned at the anterior wall of the orbit. Both lacrimals are badly damaged. They show unusually expansive lateral exposure for a therocephalian, due to external wear to the snout surface exposing portions that normally would have been covered by the maxilla, prefrontal, and jugal (**Figures 2–4**, **7**, **9B**). In more intact skulls of *Lycosuchus*, the dorsal portion of the maxilla and the prefrontal exclude the lacrimal from contacting the nasal externally (Broom, 1903; van den Heever, 1987, 1994), as is the case in almost all therocephalians except lycideopids (e.g., Sigurdsen et al., 2012). However, since the prefrontal is not preserved in MB.R.995, the anterodorsal part of the lacrimal is exposed where it contacts the nasal internally. In this area, the lacrimal has a slender anterior process extending out from its anterodorsal portion onto the medial surface of the posteroventral margin of the nasal, which is overlapped by the maxilla laterally (**Figure 7**). An anterior process of the lacrimal contacting the nasal internally has also been described for akidnognathids (Sigurdsen, 2006), *Tetracynodon* (which has a relatively short anterior process; Sigurdsen et al., 2012), and is also observed in *Glanosuchus* (van den Heever, 1987, 1994; Hillenius, 1994). van den Heever (1987) questioned the presence of an anterior process of the lacrimal in Lycosuchidae, since this feature appeared absent in the specimen CGS C60. Later, van den Heever (1994) countered that interpretation, stating that both scylacosaurids and lycosaurids possess an anterior process of the lacrimal, although still basing his conclusions on CGS C60, in which the lacrimal is damaged. Our reconstruction of MB.R.995 confirms van den Heever's (1994) inference that this feature is present in lycosuchids. On its medial surface, the lacrimal exhibits a distinct ridge, the lacrimo-palatine ridge, which contacts the dorsolateral margin of the palatine and forms the posterior border of the maxillary antrum (**Figures 6A**, **7**). The lacrimal has a further ridge, the lacrimo-ectopterygoidal ridge, which is posteroventrally oriented (van den Heever, 1987, 1994). This ridge is poorly preserved on the right lacrimal, which is more completely preserved posteriorly than the left, and contacts the dorsal process of the ectopterygoid and the posterolateral process of the palatine ventrally on the floor of the orbit (**Figures 2B**, **4B**, **7C**). Broom (1903) and van den Heever (1987, 1994) described a single lacrimal foramen in the anterior edge of the orbit in *Lycosuchus*. However, our CT-scans of MB.R.995 show that two foramina are present in the anterior region of the orbit (**Figure 9B**). Although the exact point where the canal opens anteriorly cannot be determined with certainty, it probably opened below the base of the anterior process of the lacrimal, above the maxillary antrum (**Figures 6A**, **7**, **9C**), as suggested by Sigurdsen (2006), rather than at the anteriormost tip of the anterior process as described by Hillenius (1994) for *Glanosuchus*. Hillenius (1994) described a further ridge in *Glanosuchus*, immediately anterior to the anterior process of the lacrimal and below the nasoturbinal ridge, that may have supported maxilloturbinals. In contrast, Sigurdsen (2006) proposed that maxilloturbinals were absent in therocephalians. No internal snout ridges other than those on the nasals (described above) can be observed in MB.R.995 (**Figure 7**), indicating that cartilaginous maxilloturbinals were probably not present in *Lycosuchus*.

Palate

The paired vomer is a broad, elongated element with a long interchoanal process (**Figures 7A,C**, **8**). This process expands anteriorly and becomes widest where it contacts the vomerine process of the premaxilla. In ventral view, the anterior process of the vomer is deeply vaulted. An equally long but much narrower trough is present on the dorsal surface of the interchoanal process. Anterior to this trough, the vomer tapers toward its tip, which overlies the vomerine process of the premaxilla (**Figure 8**). A slight median ridge separating two shallow grooves is present on this attenuate anteriormost part of the vomer (**Figure 8A**). Similar grooves on the dorsal surface of the vomer have been described for several therapsids and are interpreted as the location for a pair of vomeronasal organs (e.g., Hillenius, 2000; Crompton et al., 2017; Kammerer, 2017; Liu and Abdala, 2017; Bendel et al., 2018; Pusch et al., 2019). Posteriorly, where the vomer contributes to the posterior margin of the choana, the vomer becomes a broad plate-like element, which is bordered laterally by the palatine. At its posteriormost end, the vomer constricts in transverse width and terminates in a contact with the anterior process of the pterygoid. In dorsal view, the broadened posterior portion of the vomer appears to form two short "wings" that project laterally, overlying the

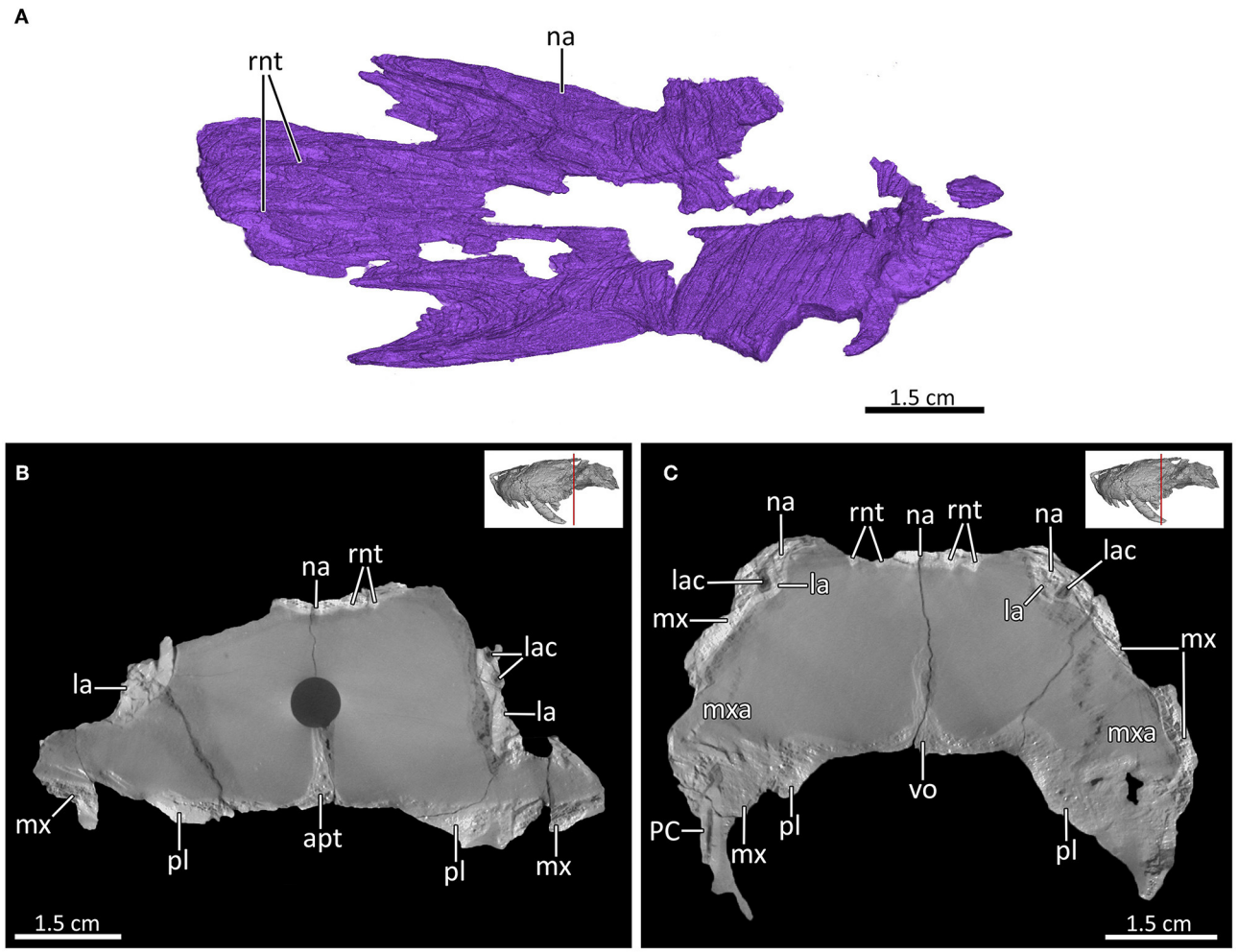

FIGURE 9 | (A) 3D reconstruction of the nasals in ventrolateral view. **(B,C)** Transverse CT sections through posterior nasal region. apt, anterior process of the pterygoid; la, lacrimal; lac, lacrimal canal; maxilla; mxa, maxillary antrum; na, nasal; PC, upper postcanine; pl, palatine; rnt, ridges for cartilaginous nasal turbinals; vo, vomer.

palatines (**Figures 7C**, **8A**). This winged structure of the posterior portion of the vomer slightly resembles the condition described for cynodonts, in which the laterally directed wings form a transverse lamina with the transverse processes of the palatine (e.g., Crompton et al., 2015, 2017; Pusch et al., 2019). The dorsal surface of the posterior portion of the vomer has a median ridge that continues onto the anterior process of the pterygoid. Our reconstruction of the position of the vomerine-pterygoid suture is based on examination of the external surface of the specimen and comparisons with other lycosuchids, as this suture is indeterminable in our scans. The dorsal margin of this ridge bears a slight groove medially and might have supported the ventral edge of the cartilaginous nasal septum as suggested by van den Heever (1987, 1994), similar to the condition in cynodonts (Fourie, 1974; Crompton et al., 2015, 2017; Pusch et al., 2019). Lateral to the median ridge, there are a pair of more weakly-developed ridges, running anteromedially to posterolaterally on the wings of the vomer and slightly extending onto the dorsal surface of the palatines, which are covered by the dorsal laminae of the maxillae in this area (**Figure 8A**, arrows).

The palatine is a large bone that forms much of the palate and consists of two portions, an anterior process and a raised posteromedial boss. The anterior process is narrow, contacting the canine boss of the maxilla laterally and the vomer medially. It forms the posterolateral margin of the choana (anteromedially) and the lateral borders of the maxillary sinus (posteriorly) and the maxillary antrum (further posteriorly). Close to its contact with the maxilla, its lateral portion is rugose and bordered by a distinct, medially-situated ridge, the palatine ridge, which stretches posteriorly until it contacts the dorsal margin of the suborbital vacuity. Anterior to the latter, the palatine is pierced by a pronounced posterior palatine foramen (**Figures 7A,C**, **8B**). At the level of the posterior border of the maxillary antrum, the palatine contacts the lacrimo-palatine ridge of the lacrimal and widens to form the posteromedial boss, an elongated element that contacts the narrow posterior portion of the vomer and the

anterior process of the pterygoid medially, the anterior margin of the pterygoid posteromedially, and forms the anteromedial margin of the suborbital vacuity. The posteromedial bosses of the palatines and the anterior process of the pterygoid are slightly damaged in MB.R.995 due to a large crack starting anterolaterally on the left palatine and ending posterolaterally near the anteromedial margin of the right suborbital vacuity (**Figures 8**). The ventral surface of the posteromedial boss bears the anterior portion of the pterygo-palatine ridge, which extends onto the anteromedial portion of the pterygoid (**Figure 8B**). Posterolaterally, the palatine bears a posterolateral process (damaged on the left side), which contacts the anterior process of the ectopterygoid posteriorly, the posterior process of the lacrimal dorsally, and forms the anterolateral margin of the suborbital vacuity (**Figures 3B**, **4B**, **7A,C**, **8**). The dorsal surface of the palatine is generally flat and smooth (**Figure 8A**), but seems to be slightly concave medially.

The ectopterygoid is a narrow, vertically oriented strut situated at the lateral margin of the transverse flange of the pterygoid and forming the posterolateral margin of the suborbital vacuity. It bears three processes: a ventral process at the edge of the transverse flange of the pterygoid, an anterior process contacting the lateral process of the palatine, and a dorsal process contacting the poorly-preserved lacrimo-ectopterygoidal ridge of the right lacrimal (**Figures 2B**, **3B**, **4B**, **7A,C**, **8**). In dorsal view, the ectopterygoid only has a small, triangular exposure, since its dorsal surface is mostly covered by the lateral margin of the transverse flange of the pterygoid (**Figures 2B**, **8A**).

Only the anterior part of the pterygoid is preserved, consisting of a relatively long and slender anterior process and parts of the pterygoid transverse flanges. The anterior process extends between the posteromedial bosses of the palatines and contacts the narrow posterior end of the vomer (**Figures 2B**, **7A,C**, **8**). The dorsal surface of the anterior process exhibits a distinct median ridge, which extends from the posterior portion of the vomer and continues along the anterior portion of the pterygoid until it reaches a slight narrow slit posteriorly, separating the transverse processes (**Figures 8A**, **9B**). This slit probably represents the anterior opening of the interpterygoid vacuity, which extends posteriorly to the base of the processus cultrifomis of the parasphenoid (van den Heever, 1987, 1994). Such a median ridge on the dorsal surface of the anterior part of the pterygoid, which is continuous with that of the vomer, has also been described by van den Heever (1987, 1994) for basal therocephalians, Liu and Abdala (2017) for *Shiguaignathus*, and Sigurdsen (2006) for an indeterminate South African akidnognathid. The pterygoids form the posterior margin of the suborbital vacuity and define the posterior portion of the transverse process (**Figure 8**). This transverse process is usually dentigerous in *Lycosuchus*, bearing a row of teeth erupting directly from its ventral margin (van den Heever, 1987, 1994; Kammerer and Masyutin, 2018). However, these teeth are not preserved in MB.R.995.

Braincase

The prootic lies in front of the ear region and contributes to the anterior border of the inner ear and the sidewall of the braincase. It is bounded dorsally by the supraoccipital, posterodorsally by the tabular, posteroventrally by the opisthotic, and anteroventrally by the basioccipital and the parabasisphenoid (**Figures 10B,C,E,F**, **11D,E**). Anteriorly and anterodorsally it would usually contact the epipterygoid (missing in this specimen) and posterolaterally the squamosal, which is only partly preserved in MB.R.995 (**Figures 10B,C,E**) (van den Heever, 1987, 1994). The anterior portions of the prootics, which broadly contact the posterodorsal part of the basisphenoid and the anterolateral portion of the dorsal surface of the basioccipital, curve medially and near (but do not contact) one another. The medial processes of the prootics form the lateral border of the small dorsum sellae of the basisphenoid, which occupies the narrow space between them (**Figures 10C,E**, asterisk). Lateral to the medial process, the prootic usually bears an elongated pila antotica, which extends anterodorsally (van den Heever, 1987, 1994). However, the pila antotica is not preserved in MB.R.995, since the anterior part of both prootics is slightly crushed and not completely preserved. The dorsal surface of the prootic is characterized by a distinct lateral flange, which curves posterolaterally toward the supraoccipital and tabular and contacts them (**Figures 10B,C,E**). In scylacosaurids and eutherocephalians, the lateral flange of the prootic encloses, together with the prootic process of the squamosal, the pterygo-paroccipital foramen. This foramen and a prootic process of the squamosal are absent in lycosuchids (e.g., van den Heever, 1987, 1994; Huttenlocker et al., 2011; Huttenlocker and Abdala, 2015; Huttenlocker and Sidor, 2016).

Only parts of the posterior portion of the fused parabasisphenoid complex are preserved. The dorsal surface of this portion is almost completely covered by the anterior portion of the prootics. At its posteriormost part, the small dorsum sellae is situated at the suture with the basioccipital, immediately in front of a narrow unossified space, the unossified zone (**Figures 10E**, **11E**) mentioned by Olson (1944). The dorsum sellae is laterally bordered by the medial processes of the anterior part of the prootics and forms the posterior border of a shallow depression, the sella turcica, which housed the hypophysis. However, the sella turcica is only poorly preserved in MB.R.995 (**Figures 10C,E**). In ventral view, the parabasisphenoid meets the basioccipital posteriorly in a jagged suture and simultaneously overlaps much of its anterior part. In addition, the parabasisphenoid contributes to the anterior margin of the cochlear recess (**Figure 10F**).

The basioccipital is a short, stout bone, which forms the floor of the braincase posterior to the parabasisphenoid and part of the occipital condyle. Its dorsal surface is anterolaterally almost completely covered by the medial processes of the anterior portions of the prootics, which leave only a narrow space posterior to the dorsum sellae. Posterior to the medial processes of the prootics, the dorsal surface of the basioccipital is marked by a slight depression, which contributes to the floor of the hindbrain region. Laterally, it contacts the opisthotic and posterolaterally the exoccipital, which covers much of its dorsal surface in that area, so that the basioccipital just appears as a narrow strip of bone posteriorly (**Figures 10B–F**, **11D,E**). Only a small portion of the basioccipital is visible in occipital

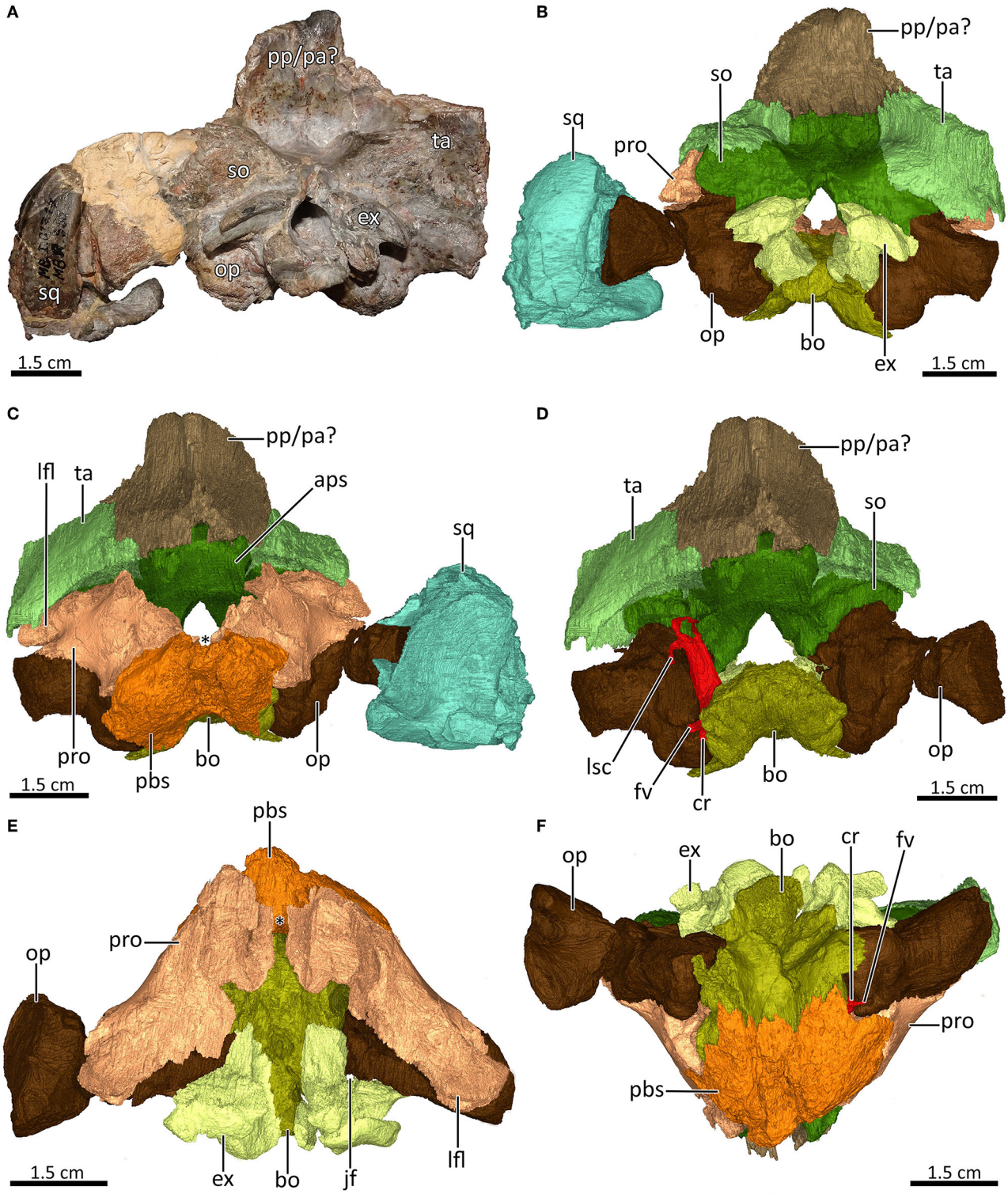

FIGURE 10 | Braincase of MB.R.995. **(A)** Photograph of the partial braincase in posterior view. **(B)** Posterior view of the reconstructed occiput. **(C)** 3D reconstruction of the braincase in anterior view. Asterisk indicates the location of the dorsum sellae. **(D)** Anterior view of the reconstructed occiput to illustrate the position of the inner ear within its bony housing with the parabasisphenoid, prootic and squamosal digitally removed. **(E)** Reconstructed braincase in dorsal and **(F)** ventral aspect, with the squamosal, tabular, supraoccipital, postparietal and parietal digitally removed in **(E)** and the squamosal digitally removed in **(F)**. Asterisk indicates the location of the dorsum sellae in **(E)**. aps, anterodorsal process of the supraoccipital; bo, basioccipital; cr, cochlea recess; ex, exoccipital; fv, fenestra vestibuli; jf, jugular foramen; lfl, lateral flange of the prootic; lsc, lateral semicircular canal; op, opisthotic; pa, parietal; pbs, parabasisphenoid; pp, postparietal; pro, prootic; so, supraoccipital; sq, squamosal; ta, tabular.

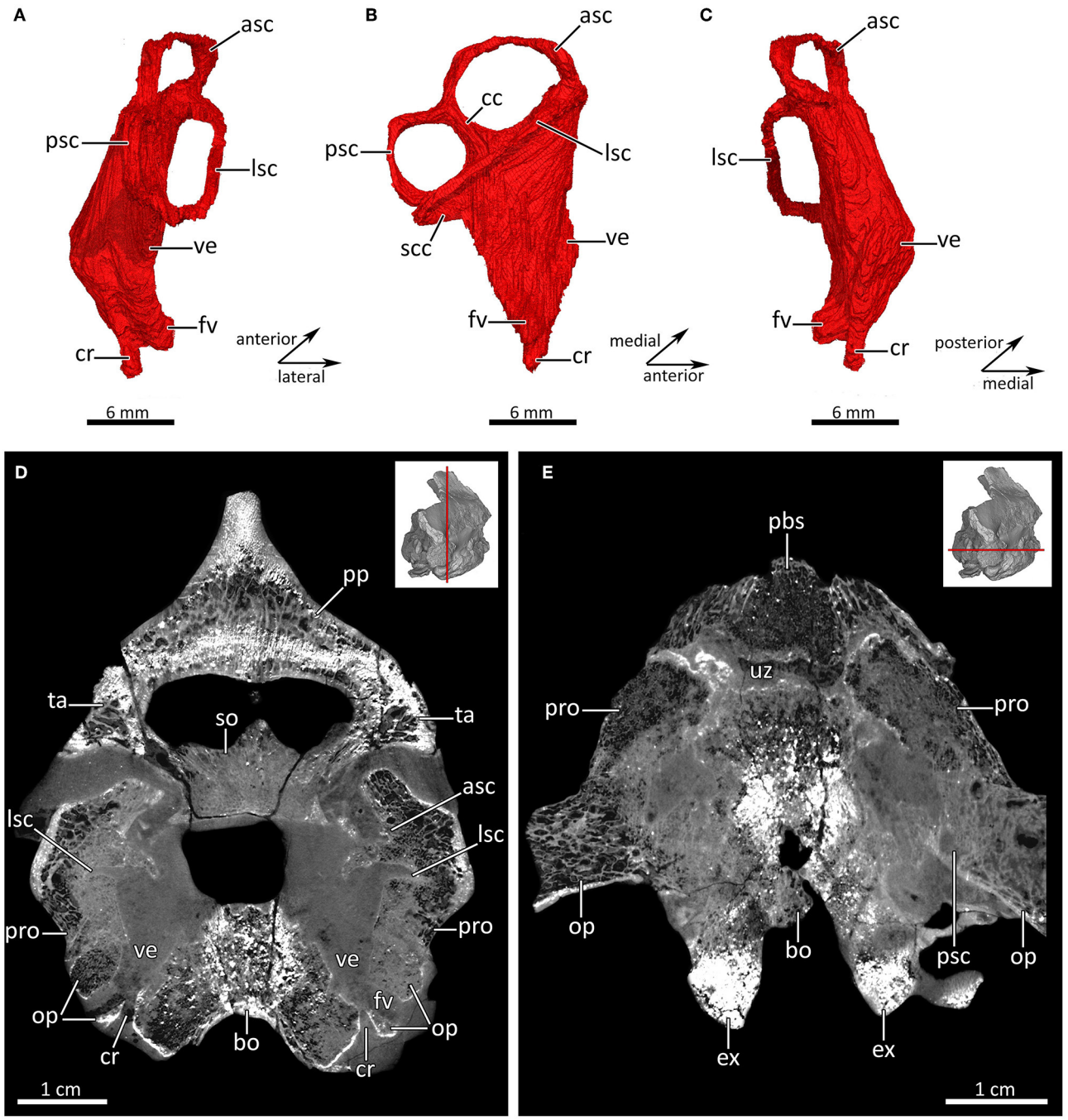

FIGURE 11 | The inner ear labyrinth of MB.R.995. Virtual cast of the right inner ear labyrinth in **(A)** posterior, **(B)** lateral, and **(C)** anterior views. **(D)** Transverse and **(E)** horizontal CT section through the otic region. asc, anterior semicircular canal; bo, basioccipital; cc, crus commune; cr, cochlear recess; ex, exoccipital; fv, fenestra vestibuli; lsc, lateral semicircular canal; op, opisthotic; pbs, parabasisphenoid; pp, postparietal; pro, prootic; psc, posterior semicircular canal; scc, secondary crus commune; so, supraoccipital; ta, tabular; uz, unossified zone; ve, vestibule.

view, forming the ventral border of the foramen magnum (**Figures 10B–D**). The ventral surface of the basioccipital is slightly damaged. It is concave medially but becomes convex laterally, with a process that slightly curves around the ventromedial margin of the opisthotic and contributes to the medial border of the cochlear recess (**Figures 10B–D,F**, **11D**).

The opisthotic consists of a robust paroccipital process, which is crushed on both sides. The right paroccipital process lacks much of its lateral portion, while the left one is more complete but is marked by a large crack and lacks part of its ventral portion. The lateral margin of the left opisthotic is concave and lies in a medially facing fossa of the squamosal.

Anterodorsally, the opistothic broadly contacts the prootic, and posteromedially it has a sutural contact with the exoccipital above the jugular foramen housing cranial nerves IX, X, and XI, of which it forms the lateral margin. Its medial portion contacts the basioccipital, where its ventral margin is slightly overlapped by the lateral process of the latter. The opisthotic also forms the posterior and lateral border of the inner ear and cochlear recess and encompasses the fenestra vestibuli (**Figures 10**, **11D,E**).

The supraoccipital appears as a broad element in occipital view, which forms the dorsal border of the foramen magnum. Ventrolaterally, it contacts the dorsal process of the opisthotic, ventrally the exoccipital, dorsolaterally the tabular, and dorsally the postparietal. However, the dorsal surface of the occiput is badly damaged and incomplete, leaving some uncertainties concerning the sutures between the supraoccipital, tabular, and postparietal (**Figures 10A,B**, **11D**). The tabular usually covers part of the supraoccipital, but is damaged on the left side such that much of the underlying supraoccipital is visible. In anterior view, the supraoccipital contacts the dorsal portion and part of the lateral flange of the prootic. The internal surface of the supraoccipital is generally smooth, forming the roof of the posterior region of the brain cavity and the foramen magnum. It bears an anterodorsal process that contributes to the side wall of the braincase and contacts the parietal, prootic, and usually also the squamosal and the epipterygoid (van den Heever, 1994) (**Figures 10C,D**).

The paired exoccipitals form the lateral portion of the foramen magnum and the occipital condyle. The exoccipital has an expanded dorsal process forming sutures with the supraoccipital dorsally and the paroccipital process of the opisthotic laterally. Ventrally, it has a long lateral process that meets the posterolateral margin of the basioccipital laterally and the posterior part of the paroccipital process dorsomedially, forming the dorsal and medial margins of the jugular foramen (**Figures 10A,B,E,F**, **11E**).

The paired tabulars are flat bones forming the dorsolateral portion of the occiput. Both tabulars are damaged, but the right one is better preserved, while the left tabular lacks portions that would otherwise cover the underlying supraoccipital. Dorsally and dorsolaterally, the tabular contacts the postparietal and the parietal, and medially the supraoccipital. Laterally, the tabular usually supports the squamosal in better preserved skulls, and between the foramen magnum and the posterodorsal margin of the post-temporal fenestra, the tabular usually exhibits a ridge (van den Heever, 1987, 1994). However, the tabular ridge is not preserved in MB.R.995 due to poor preservation. In anterior view, the tabular has a process that extends ventrolaterally and contacts the lateral flange of the prootic (**Figure 10C**).

The dorsal portion of the occiput is badly damaged, but the large complex of bones at its top probably consists of both postparietal and parts of the parietal (**Figures 9A–D**, **10D**). The postparietal is a median element, which is situated within a large depression where it is bounded between the parietal dorsally, the tabulars laterally and the supraoccipital ventrally. There seems to be a weakly preserved median ridge on the posterior surface of the bone, which divides the depression into two nuchal fossae (**Figures 10A–D**).

The left squamosal is only partially preserved, where it forms the posterolateral portion of the temporal region. It lacks several parts: e.g., the dorsal process that overlies the parietal dorsolaterally, the quadrate process, and the anterolaterally located zygomatic process, which overlies the posterior portion of the jugal (**Figures 10B,C**) (van den Heever, 1987, 1994). The squamosal bears a medially-located fossa for the paroccipital process of the opisthotic. On its posterior surface the dorsoventrally directed squamosal sulcus seems to be preserved, which is medially bordered by the squamosal ridge lateral to its contact with the opisthotic (**Figures 10B,C**).

Inner Ear

As in other therapsids, multiple bones of the basicranium contribute to the formation of the inner ear housing in MB.R.995, consisting of the opisthotic, prootic, supraoccipital, exoccipital and basioccipital (**Figures 10C,D,F**, **11C,D**) (e.g., Olson, 1944; Fourie, 1974; Sigogneau, 1974; Luo et al., 1995; Luo, 2001; Kielan-Jaworowska et al., 2004; Pusch et al., 2019). At greatest height, the inner ear of MB.R.995 is 22.95 mm tall. Its semicircular canals are surrounded by the exoccipital, supraoccipital, opisthotic, and prootic. Medially, both anterior and posterior semicircular canals derive from the crus commune, where they emerge dorsally at the same level from its posterior apex and curve downward to join the anterior and posterior ampullar recess, respectively. The posterior semicircular canal is smaller than the anterior with a height of 6.20 mm and a width of 5.52 mm, while the anterior canal is 7.21 mm tall and 7.69 mm wide. The lateral (horizontal) semicircular canal appears to be the longest of the three semicircular canals, with a height of 3.81 mm and a width of 10.88 mm (**Figures 10C,D**, **11**). This situation is unusual, because in most non-mammalian therapsids and mammals the anterior semicircular canal is the longest (e.g., Olson, 1944; Sigogneau, 1974; Luo, 2001; Kielan-Jaworowska et al., 2004; Rodrigues et al., 2013; Laaß, 2016; Araújo et al., 2017, 2018; Benoit et al., 2017b,c; Bendel et al., 2018; Pusch et al., 2019). Among therapsids, a lateral semicircular canal larger than the anterior and posterior one has only previously been reported for the fossorial anomodont *Kawingasaurus fossilis* (Laaß, 2015a). The lateral and posterior canal share a secondary crus commune (**Figure 11B**), as in most non-mammalian therapsids (e.g., Olson, 1944; Sigogneau, 1974; Castanhinha et al., 2013; Rodrigues et al., 2013; Laaß, 2015a, 2016; Araújo et al., 2017, 2018; Benoit et al., 2017b,c; Bendel et al., 2018; Pusch et al., 2019). The curved vestibule has a length of 13.59 mm and is surrounded by the opisthotic and the prootic, of which the opisthotic constitutes its posterior and lateral border and the prootic its anterior border. The fenestra vestibuli faces ventrolaterally and is exclusively bordered by the opisthotic. Of particular note is the presence of a small, globular cochlear recess, which is ventrally differentiated from the main part of the vestibule and located medial to the fenestra vestibuli. It is posteriorly bordered by the opisthotic and medially bordered by the basioccipital (**Figures 10C,D,F**, **11A–D**). The parabasisphenoid also indirectly contributes to the anterior margin of the cochlear

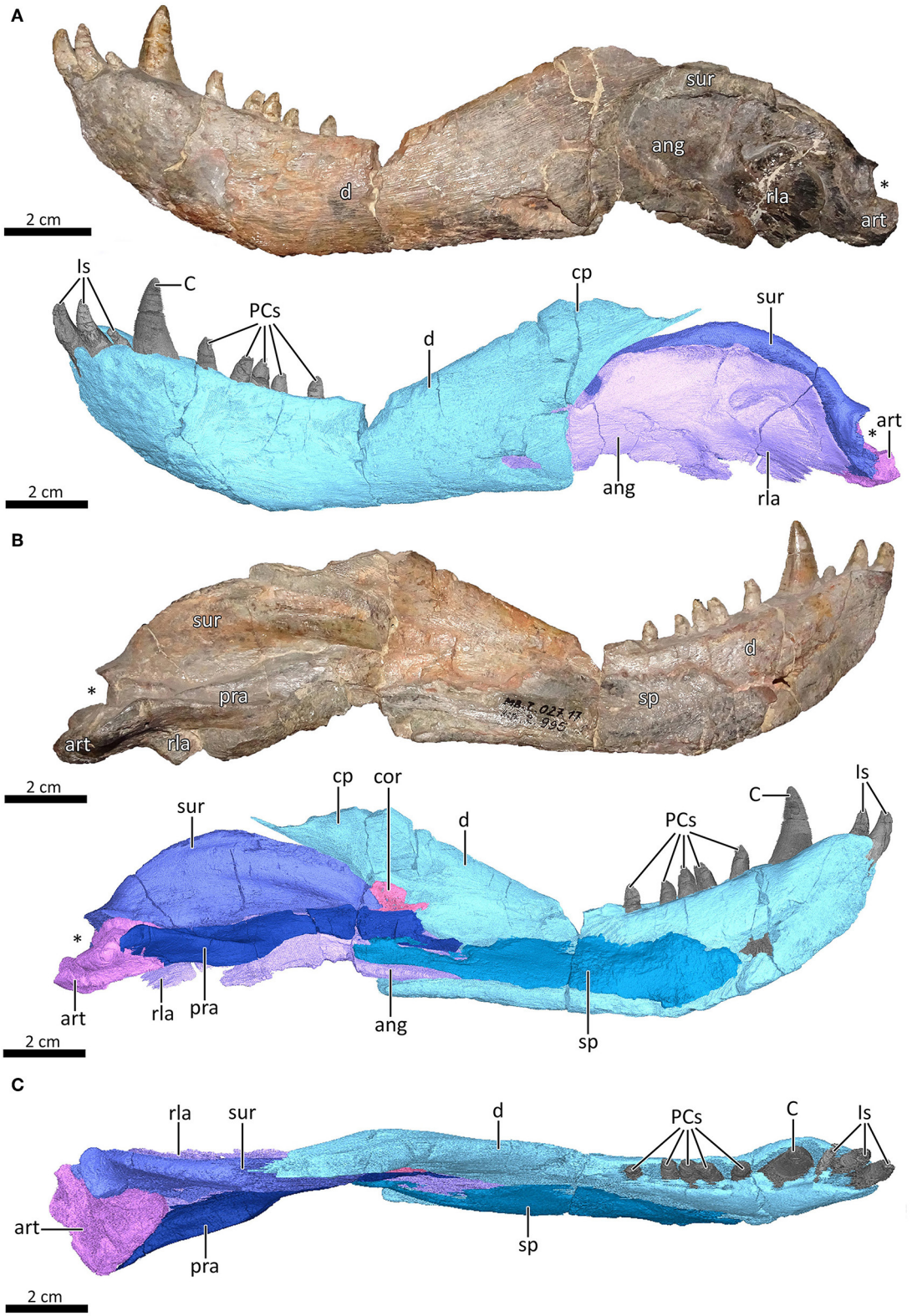

FIGURE 12 | Left mandible of MB.R.995. **(A)** Photograph (top) and 3D reconstruction (bottom) of the left mandible in lateral view. **(B)** Photograph (top) and 3D reconstruction (bottom) of the left mandible in medial view. **(C)** Dorsal view of the reconstructed left mandible. Asterisk indicates the location of the glenoid fossa. ang, angular; art, articular; C, lower canine; cor, coronoid; cp, coronoid process; d, dentary; ls, lower incisors; PCs, lower postcanines; pra, prearticular; rla, reflected lamina of the angular; sp, splenial; sur, surangular.

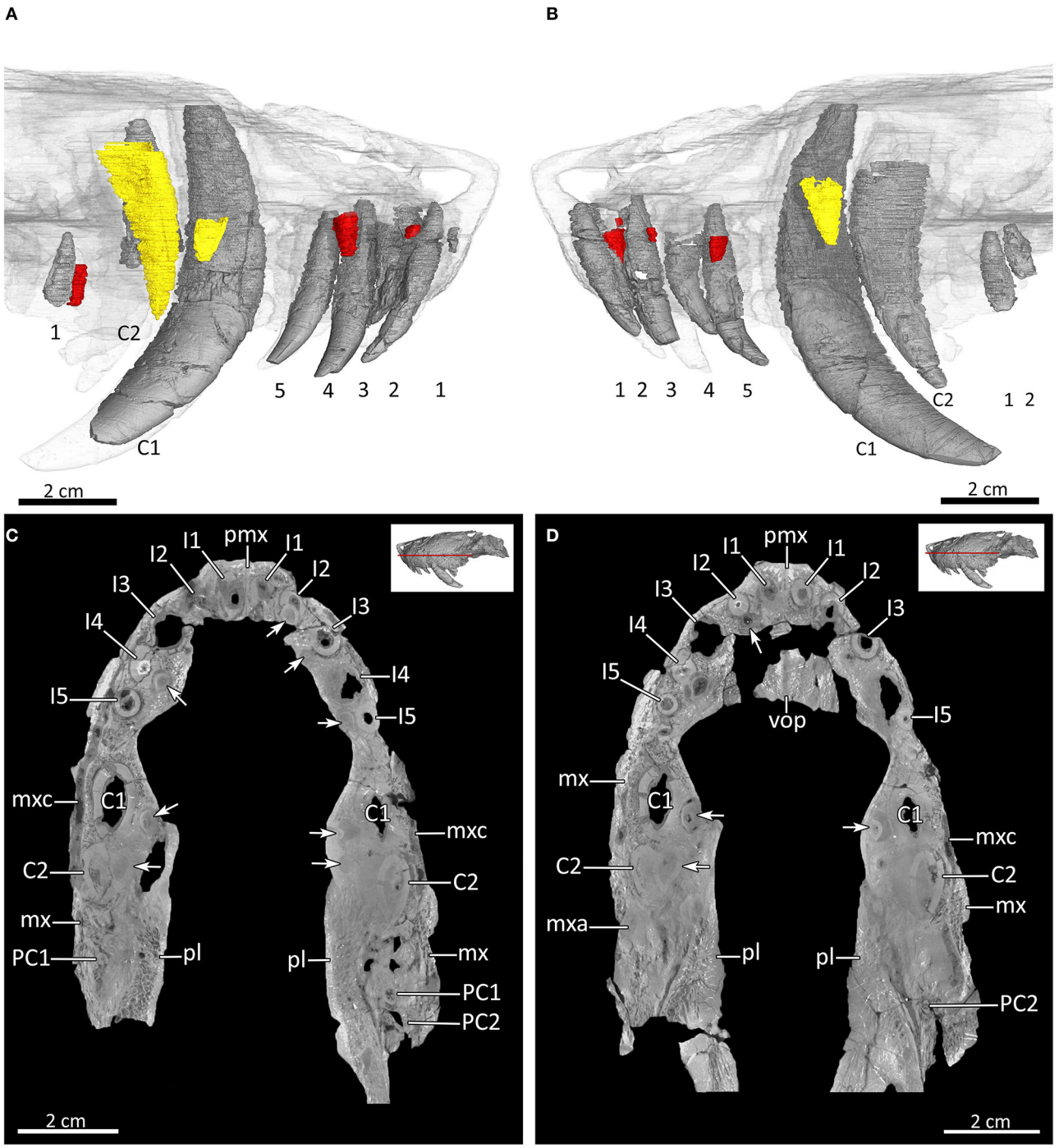

FIGURE 13 | Dentition and tooth replacement in the upper jaw of MB.R.995. **(A)** Three-dimensional rendering of the left and **(B)** right upper tooth rows in medial view. **(C,D)** Virtual horizontal CT sections through the upper jaw. Replacement canines in yellow; replacement incisors and postcanines in red. Arabic numerals indicate the teeth positions. Arrows mark the positions of the replacement teeth. C1, first canine; C2, second canine; I, upper incisor; mx, maxilla; mxa, maxillary antrum; mxc, maxillary canal; PC, upper postcanine; pl, palatine; pmx, premaxilla; vop, vomerine process of the premaxilla.

recess by overlapping the basioccipital (**Figure 10F**). Among therocephalians, a distinctive cochlear recess has so far only been described in the specialized baurioid *Microgomphodon oligocynus* (Benoit et al., 2017b).

Lower Jaw

The left mandible of MB.R.995 consists of seven bones: the dentary, splenial, angular, surangular, one coronoid (likely homologous to the posterior coronoid in early tetrapods

[*sensu* Ahlberg and Clack, 1998]), prearticular and articular. The dentary represents its largest element, composing roughly two-thirds of the anteroposterior jaw length (**Figure 12**). The lateral surface of the dentary is smooth up until the region below the canine, then becomes rugose on the symphysis. The mandibular symphysis was interpreted by van den Heever (1987, 1994) as a relatively loose contact—a feature that sets apart therocephalians from gorgonopsians and cynodonts. In eucynodonts the dentaries are fused at the symphysis (Hopson and Kitching, 2001), but even in earlier cynodonts where the dentaries remain separate elements they are tightly sutured. Anteriorly, the dentary is swollen laterally, with the greatest expansion positioned at the level of the canine (**Figure 12C**). A pronounced shelf runs medially along the tooth row. The ventral margin of the dentary is generally flat, in contrast to the gradually sloping ventral margin in Gorgonopsia and later Therocephalia (van den Heever, 1987, 1994). At the symphysis, it curves gently upwards anteriorly, unlike the sharply-sloping symphysis in Gorgonopsia. Posteriorly, the dentary terminates at a near-perpendicular angle to the vertical posterior margin, which curves smoothly posterodorsally to form the free-standing edge of the coronoid process (**Figure 12A**). A substantial portion of the medial dentary surface is covered by the splenial, resting on an anteroposteriorly directed gutter (**Figure 12B**), which together cover the Meckelian canal (van den Heever, 1987, 1994). Posteriorly, the dentary articulates with the angular and the surangular at the same point. Part of the anterior portion of the angular is visible through a crack at the dentary angle. The base of the coronoid process is posteromedially covered by the anteriormost part of the prearticular and the coronoid.

The splenial is present as an anteroposteriorly elongate element positioned medial to the dentary, extending from the root of the canine to a level in line with the apex of the coronoid process (**Figures 12B,C**). It has no lateral exposure. The dorsoventral height of the splenial is roughly conserved through its length, but does decrease slightly posteriorly, similar to what has been described for *Gorynychus* (Kammerer and Masyutin, 2018). According to van den Heever (1987, 1994), the splenial contributes to the symphysis in early therocephalians. As only the splenial of the left hemimandible is well-preserved in MB.R.995 and the posterior symphyseal region is slightly damaged, this condition can neither be confirmed nor disputed for this specimen. At its posterior end, the splenial medially overlies the anteriormost portion of the angular and the anteroventral part of the prearticular (**Figure 12B**).

The angular is a transversely thin, dorsoventrally tall bone positioned posterior to the dentary and is mostly exposed laterally (**Figures 12A,B**). Its ventral margin is somewhat damaged, but the lateral surface is intact. In lateral view, the angular obscures most of the surangular. The reflected lamina covers the posterior half of the angular. It is smooth and well-developed, forming a roughly circular, thin sheet of bone that, as a result of diagenesis, is closely pressed against the main body of the angular (**Figure 12B**). The ridges on the lateral surface of the reflected lamina could not be discerned in our reconstruction, but have been described in MB.R.995 by Janensch (1952). The angular is embedded in and supported anteriorly by a trough in the posteroventral margin of the dentary, where it is further covered medially by the splenial and the prearticular. Posteriorly, it supports the ventral part of the articular.

The surangular forms the posterodorsal region of the mandible, curving smoothly toward the glenoid fossa and forming a strongly convex dorsal surface (**Figures 12A,B**). It is a fairly robust bone, equal in width to the dentary that lies against the medial side of the angular. The angular covers most of the surangular in lateral view, leaving only a thin, sickle-shaped strip visible (**Figure 12A**). In MB.R.995, the ventral margin of the surangular is slightly damaged. A postdentary foramen between the surangular and prearticular has been described in US D173 (van den Heever, 1987), but could not be confirmed for MB.R.995. Anteriorly, the bone narrows dorsoventrally until it touches the dentary, where it is also covered medially by the coronoid and prearticular. At the posterior end, it overlies the dorsal part of the articular. At this contact, the surangular widens mediolaterally to form the dorsal roof of the glenoid fossa (**Figures 12A,B**, asterisk).

A small, flat and roughly triangular-shaped bone that sits medially to the base of the coronoid process of the dentary is interpreted as representing the coronoid bone (**Figure 12B**). The coronoid has not been described in US D173 (Broom, 1903), and is typically damaged, obscured or missing in other therocephalians. The coronoid cannot be seen in the ventral view of the jaw, unlike the condition in *Microgomphodon* (Abdala et al., 2014b). The coronoid borders the anterodorsal part of the prearticular and covers the anterior portion of the surangular and the posteroventral portion of the coronoid process of the dentary medially (**Figure 12B**).

The prearticular is an elongated strut, extending from the posterior part of the dentary to meet the anteromedial side of the articular (**Figure 12B**). It lies medially to the angular and ventral part of the surangular. Anteriorly, it defines the ventral margin of the coronoid, and it is overlain medially by the posterodorsal portion of the splenial. A small process extends anteriorly to contact the base of the coronoid process of dentary. Posteriorly, at the level of the apex of the surangular, a medial expansion is present (**Figures 12B,C**), ultimately terminating at a posteromedially oriented suture with the articular. An anteroposteriorly-oriented fossa on the dorsal surface of the prearticular is located anterior to this suture (**Figure 12C**).

The articular is the posteriormost element of the mandible, and bears the ventral and anterior boundaries of the glenoid fossa (**Figures 12A,B**). In MB.R.995, a fragment of the quadrate seems to be preserved inside the left glenoid. The articular is a robust bone, extending significantly beyond the dentary medially in an extended contact with the prearticular (**Figure 12C**). Anterolaterally, it contacts the posterior portions of the surangular and angular.

Dentition and Tooth Replacement

The teeth in the left dentary are generally well-preserved, while those in the upper jaw are mostly damaged, albeit slightly better preserved on the right side than on the left. All teeth in both the

upper jaw and the left dentary are preserved in place, except for the first incisor of the left premaxilla, which has fallen out with only a fragment of its root preserved in its alveolus (**Figures 3**, **4**, **7**, **8B**, **12–14**). Serrations are probably present on both the mesial and distal margins of all teeth (**Figures 13A,B**, **14A**) (see also van den Heever, 1987, 1994), although damaged on much of the upper dentition in MB.R.995.

MB.R.995 has five upper and three lower incisors. They have a simple conical shape and are slightly recurved, except for the third lower incisor, which is markedly smaller than all other incisors (**Figures 3**, **4**, **6D**, **7**, **8B**, **12–14**). The upper incisors are located in a broad ventral plate of the premaxilla (**Figures 7**, **8B**). van den Heever (1987, 1994) related incisor size in *Lycosuchus* to the height of the premaxilla at each tooth position, noting an increase in size from the first to the fourth upper incisor, which lies at a point where the bone is deepest, then a decrease in size to the fifth tooth, which is the smallest. In MB.R.995, there is indeed an increase in upper incisor size from the first to the fourth, but this is probably not related to the height of the premaxilla, as the premaxilla is not appreciably deeper at the position of the fourth incisor than anteriorly (**Figures 7**, **8B**). There are replacement teeth for upper incisors two and four on both sides, and for the upper third and fifth incisors on the right side. The replacement teeth are located either posterior (I2) or medial (I3, I4, I5) to the functional tooth. There is a coalescence between the alveoli of the functional and replacement teeth of the right I2 and the left I4, with the new incisor for I2 penetrating the root, and the new tooth for I4 eroding the root of the functional incisor. No evidence of replacement teeth or replacement pits can be observed for the first incisors on both sides and the third and fifth incisor on the left side (**Figure 13**). In the left dentary there are replacement teeth for all three lower incisors, which are positioned posterior to the functional teeth. The replacement teeth of I1 and I3 are still incipient, while that of I2 is much better developed. There is also a marked coalescence between the alveoli of the functional and replacement teeth, with the big replacement tooth behind I2 eroding the root of the functional tooth (**Figures 14A–C**).

Each maxilla bears an anterior and posterior canine alveolus. The anterior canines are fully erupted on both sides of the skull and are very large and nearly crescent-shaped. The right anterior canine is well-preserved; the left is broken at several places along its length and lacks the tip. A posterior canine is located immediately behind and slightly lateral to the anterior one in the right maxilla. The right posterior canine is not fully developed (the root has not fully formed) and its crown is only partially erupted (**Figures 3**, **4**, **6D**, **7**, **8B**, **13**). The root of a posterior canine is also present in the left maxilla, but its crown is missing entirely. Two unerupted developing canines are present in the left maxilla: a small, poorly-developed canine tip is present medial to the anterior canine and a large, well-developed tooth (consisting of most of the crown) is present medial to the broken posterior canine root. The incipient left anterior replacement canine has not yet eroded the root of the erupted canine. By contrast, the incipient left posterior replacement canine has penetrated the root of the old posterior canine tooth and is almost erupted. The anterior canine in the right maxilla has a medially located replacement tooth as well, which is comparable in proportions and state of development to its counterpart on the left. The posterior canine alveolus in the right maxilla is not fully occupied by the erupting tooth, indicating that the previous tooth was shed and the erupted canine is the replacing tooth in the process of development (**Figure 13**). The lower canine has a broader base than the upper canines and is only weakly recurved (**Figures 12**, **14**). There is no replacement tooth visible for the lower canine, only the remnant of an older canine root is present anterior to the functional one, which nearly contacts the root of the lower i2 (**Figure 14**).

MB.R.995 has two upper postcanines in the right maxilla but only one postcanine in the left maxilla. By contrast, in the dentary there are five postcanines present. The postcanines are simple, conical teeth (Broom, 1903), with the uppers smaller than the lowers (**Figures 2**, **6D**, **7A,B**, **8B**, **13**). Only the single upper postcanine in the left maxilla is paired with a replacement tooth, which is anteromedially situated to the functional tooth. In the dentary there are incipient replacement teeth for lower postcanines one, three, and four, which are located either medial (PC1, PC3) or posteromedial (PC4) to the functional tooth. There is a coalescence between the alveolus of the replacement tooth of PC3 and the functional one. However, the replacement tooth does not erode the root of the functional PC3 (**Figures 13**, **14A,C,D**).

DISCUSSION

Maxillary Canal Evolution

The morphology of the maxillary canal of *Lycosuchus vanderrieti* reinforces the idea that homoplasy and mosaic evolution are major features of the evolutionary history of this structure in therapsids, as previously suggested based on the condition in the basal cynodont *Galesaurus planiceps* (Pusch et al., 2019). In comparison to eutherocephalians such as the akidnognathid *Olivierosuchus* and the bauriid *Bauria,* in which the maxillary antrum is anteroposteriorly extensive (Benoit et al., 2016a, 2018), the maxillary antrum of *Lycosuchus* is relatively small and restricted to a region anteroventral to the orbit. Comparable variation in maxillary antrum size is observed in cynodonts, where this structure is substantially greater in relative volume and anteroposterior extent in gomphodonts than in stemward cynodonts and probainognathians (Crompton et al., 2015, 2017; Benoit et al., 2016a, 2019; Pusch et al., 2019). Within-clade variation in maxillary antrum size seems to reflect differing degrees of ossification of the snout rather than differences in length of the nerves and vessels within—a shorter caudal portion of the maxillary canal appears to be present in cynodonts compared to therocephalians and gorgonopsians regardless of antrum dimensions. As in other non-cynodont therapsids (Benoit et al., 2016a,b, 2017a,c, 2018, 2019), the alveolar rami ramify directly from the maxillary canal and not from the maxillary antrum in *Lycosuchus*. Like the baurioid therocephalian *Choerosaurus*, only two of the three branches for the alveolar rami are present, which probably represent the caudal and medial alveolar rami. However, unlike in *Choerosaurus*, these rami in *Lycosuchus* radiate from the same point within the caudal part of the maxillary canal. This also occurs in *Olivierosuchus*, but in that

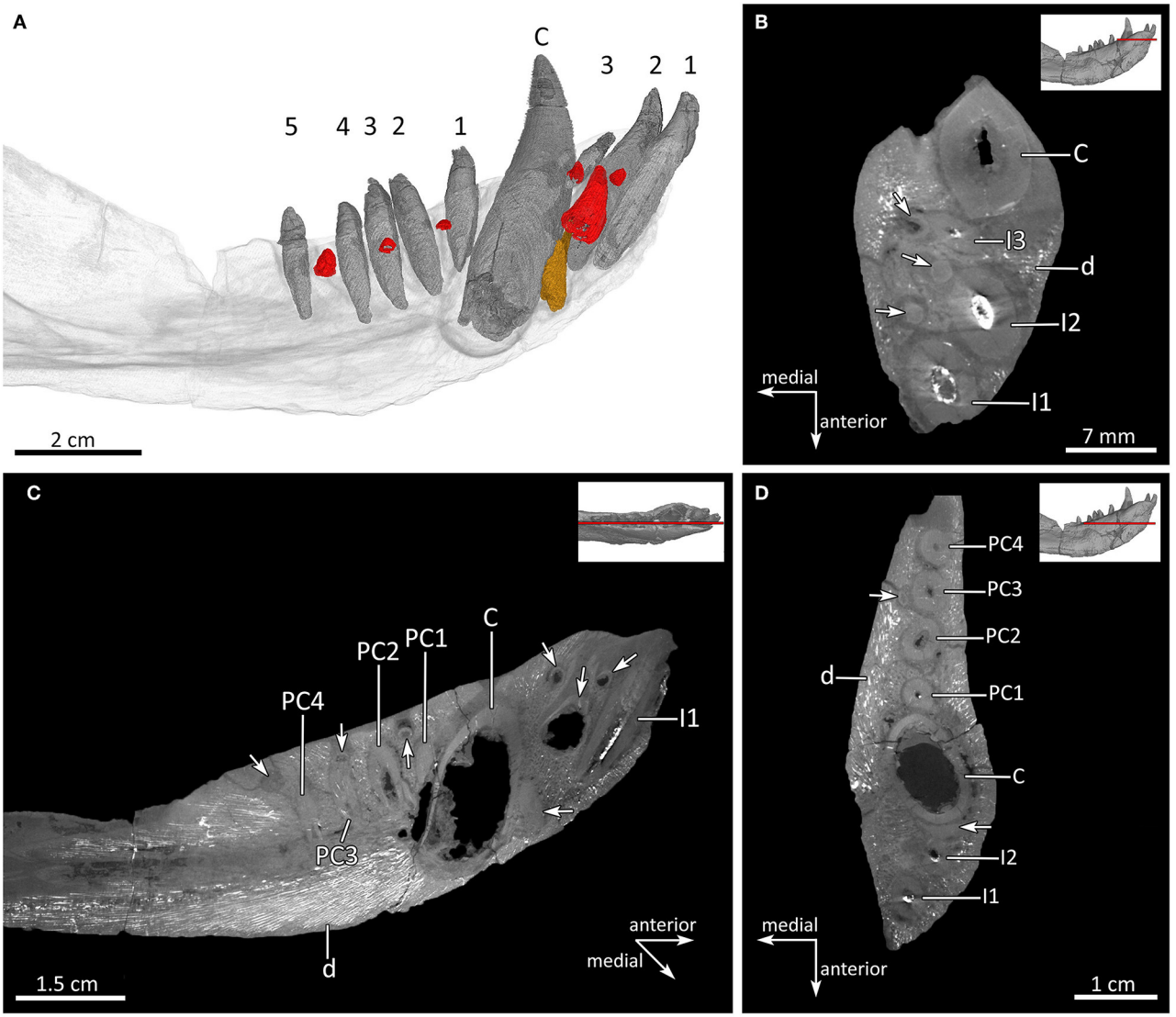

FIGURE 14 | Dentition and tooth replacement in the left mandible of MB.R.995. **(A)** Three-dimensional rendering of the left lower tooth row in medial view. **(B,D)** Virtual horizontal CT sections through the left mandible. **(C)** Sagittal CT section through the left mandible to show the positions of the replacement teeth as seen in **(A)**. Replacement incisors and postcanines in red; old remnant root of the canine in brown. Arabic numerals indicate the teeth positions. Arrows mark the positions of the replacement teeth and the remnant root of the old canine. C, lower canine; I, lower incisor; d, dentary; PC, lower postcanine.

taxon there is also a rostral alveolar ramus diverging just anterior to the caudal and medial alveolar rami (Benoit et al., 2016a,b, 2018).

The morphology of the external nasal ramus in *Lycosuchus* differs from that known in later-diverging therocephalians. In *Lycosuchus*, the external nasal ramus is highly ramified and forms a complex at the posterior part of the ION. Of particular note is the morphology of the lengthened major ramus, which resembles that of the external nasal ramus in the dinocephalian *Moschops* (Benoit et al., 2017c) and the anomodont *Patranomodon* (Benoit et al., 2018). However, in those taxa the ramus extends far posterodorsally toward the orbit, unlike in *Lycosuchus* in which the ramus is nearly vertical. In the eutherocephalians *Choerosaurus*, *Euchambersia*, *Olivierosuchus*, and *Bauria*, the external nasal rami ramify into three or more branches, but they do not form the pronounced lengthened ramification of *Lycosuchus* (Benoit et al., 2016a,b, 2017a, 2018). Based on its shared presence in the earliest therocephalians and cynodonts, the highly ramified complex of canals for the external nasal rami in *Lycosuchus* likely represents the primitive condition. A more derived condition is present in some derived therocephalians such as *Olivierosuchus* and non-probainognathian cynodonts, in which the external nasal ramus is shorter and less ramified than in *Lycosuchus*. A further reduction of the external nasal ramus, associated with a reduction of the canals for the internal nasal

and superior labial rami, is only present in Probainognathia (Benoit et al., 2016a, 2018, 2019; Pusch et al., 2019).

Benoit et al. (2019) recently reinterpreted the short canal directed toward the base of the canine in the probainognathian *Ecteninion* as the canal for the rostral alveolar ramus, based on the fact that in mammals this ramus is consistently oriented toward the upper canine. A similar morphology is also observed in the maxillary canal of the basal cynodont *Galesaurus,* in which there is a slender ramus directed toward the upper canine, just anterior to the external nasal rami, which has also been interpreted as the rostral alveolar ramus (Pusch et al., 2019). This is similar to what is seen in *Lycosuchus*, but the narrow ramus just anterior to the complex of external nasal rami, diverging ventrally from the maxillary canal, is here interpreted as part of a complex superior labial ramus that has several origins from the main branch of the maxillary canal. The course of the maxillary canal in *Lycosuchus* differs from that described in most other therocephalians and therapsids (Fourie, 1974; Benoit et al., 2016a,b, 2017a,c, 2018, 2019; Pusch et al., 2019). The maxillary canal in *Lycosuchus* extends from the maxillary antrum anterior to the first postcanine along the roots of the two canines, and terminates lateral to the level of the root of the fourth incisor. Accordingly, both the canals for the alveolar rami and the canal just anterior to the external nasal rami are directed toward the canines. The morphology of the ventral ramifications of the maxillary canal is similar to that of *Olivierosuchus*, in which all three alveolar rami appear to be oriented toward the canine, but *Lycosuchus* lacks the canal for the rostral alveolar ramus just anterior to the medial and caudal alveolar rami, and the canals just anterior to the external nasal rami are here interpreted as the ones for the superior labial rami (Benoit et al., 2016a, 2018). Accordingly, the homologies of the alveolar rami do not seem to be as clear-cut as reported by (Benoit et al., 2019) in cynodonts, as they did not consider therocephalians or other therapsid outgroups in their analysis, and there is extensive variation and homoplasy in maxillary canal in general. Denser sampling of maxillary canal morphology in basal cynodonts, therocephalians and gorgonopsians is needed to see whether this variation is consistent and possibly autapomorphic for lower-level clades within these groups.

Variation in Bony Labyrinth Morphology in Therapsids

The inner ear of *Lycosuchus* generally shows the primitive condition visible in non-cynodont therapsids. As in several other non-cynodont therapsids (e.g., Castanhinha et al., 2013; Laaß, 2016; Benoit et al., 2017b), the fenestra vestibuli is positioned at the ventrolateral part of the vestibule, which is exclusively bordered by the opisthotic in *Lycosuchus*. This situation is different from what has been described for basal cynodonts such as *Galesaurus* and *Thrinaxodon*, in which the laterally facing fenestra vestibuli is located further dorsally and bordered by the opisthotic, prootic, basioccipital, and also partly by the basisphenoid wing (Fourie, 1974; Luo, 2001; Benoit et al., 2017b; Pusch et al., 2019). However, as in these and other basal cynodonts (e.g., Fourie, 1974; Luo, 2001; Kielan-Jaworowska et al., 2004; Benoit et al., 2017b; Pusch et al., 2019), a small, globular cochlear recess is ventrally differentiated from the main part of the vestibule. Outside of Cynodontia, a cochlear recess is also present in the anomodonts *Niassodon mfumukasi* (Castanhinha et al., 2013) and *Pristerodon mackayi* (Laaß, 2016), the biarmosuchian *Lemurosaurus pricei,* and the specialized baurioid *Microgomphodon oligocynus* (Benoit et al., 2017b). The latter taxon is the only therocephalian so far for which a distinct cochlear recess has been described. However, given the limited sampling in this clade, it is currently uncertain whether the absence of a cochlear recess is typical of therocephalians. The conclusion of Benoit et al. (2017b) that a distinct cochlear recess likely evolved multiple times among therapsids requires additional sampling—it appears to be present ancestrally in therocephlians (based on the condition in *Lycosuchus*), and it is at present uncertain whether multiple origins or multiple losses of this structure characterize therapsid evolution.

Different from what is usually the case in non-mammalian therapsids and mammals, in which the anterior semicircular is the longest (e.g., Olson, 1944; Sigogneau, 1974; Luo, 2001; Kielan-Jaworowska et al., 2004; Rodrigues et al., 2013; Laaß, 2016; Araújo et al., 2017, 2018; Benoit et al., 2017b,c; Bendel et al., 2018; Pusch et al., 2019), the lateral semicircular canal appears to be the longest of the three semicircular canals in *Lycosuchus*. Several studies have shown that the elongated morphology of the semicircular canals can be linked to the animals' lifestyle (e.g., Spoor, 2003; Spoor et al., 2007; Walsh et al., 2009; Wittmer and Ridgely, 2009; Cox and Jeffery, 2010; Laaß, 2015a; Araújo et al., 2018). The anomodont *Kawingasaurus* is the only other non-mammalian therapsid described with a lateral semicircular canal larger than the anterior and posterior one, but it was suggested that its elongated morphology is related to the inflated geometry of the vestibule rather than its locomotory behavior (Laaß, 2015a). In *Lycosuchus*, the inner ear is posteriorly tilted and the curved vestibule has the typical subtriangular shape common in non-mammalian therapsids. The anterior and posterior semicircular canals are ellipsoidal, while the lateral canal is rather linear and not as curved as the other canals. This is reflected in its lower height (3.81 mm) relative to the anterior (7.21 mm) and posterior (6.20 mm) canals, but much greater width (10.88 mm) than the anterior (7.69 mm) and posterior (5.52 mm) one. In modern mammals, an elongated lateral semicircular canal is usually associated with an agile or fossorial behavior (e.g., Lindenlaub et al., 1995; Spoor et al., 2007; Cox and Jeffery, 2010; Olori, 2010). An enlarged lateral semicircular canal is also known in many aquatic non-mammalian tetrapod taxa (e.g., Benoit et al., 2013; Neenan et al., 2017; Yi and Norell, 2018; Evers et al., 2019). Based on appendicular morphology (Boonstra, 1964), *Lycosuchus* is very unlikely to represent a fossorial or aquatic animal. Nevertheless, the lengthened morphology of the lateral semicircular canal could be related to its lifestyle as an active predator, showing more adaptations for agility and cursoriality than coeval potential prey taxa (e.g., dicynodonts, dinocephalians, pareiasaurs). Other coeval therocephalians (i.e., scylacosaurids) had similar inferred

behaviors, and further sampling of bony labyrinth morphology in scylacosaurids would be useful to test whether an elongated lateral semicircular canal is related to lifestyle, or if this feature is unique to *Lycosuchus* within the clade.

Canine Replacement in Lycosuchids

The pattern of tooth replacement has long been controversial in Lycosuchidae. Originally, the family was diagnosed by the presence of two functional canines in each maxilla (Broom, 1903; Haughton and Brink, 1954; Kermack, 1956; Boonstra, 1969). However, van den Heever (1980) considered this feature to be invalid, and suggested that lycosuchids instead have one functional and one replacement canine in alternation, as in other early theriodonts. Abdala et al. (2014a) recently concurred with this interpretation and suggested a rapid rate of canine replacement in lycosuchids based on the occurrence of canine replacement in most of the specimens they investigated.

Based on our CT data for MB.R.995, we would argue that both the historical (e.g., Kermack, 1956) and more modern interpretations (e.g., van den Heever, 1980) of lycosuchid tooth replacement have merit, but hinge on the definition of what constitutes a "functional" canine. Two erupted canine crowns are definitely present in the right maxilla of MB.R.995, and both anterior and posterior would presumably be in use during prey capture. Abdala et al. (2014a: Table 6) showed that the majority of lycosuchid specimens have both the anterior and posterior canines erupted in each maxilla, in contrast to the condition in gorgonopsians and scylacosaurids in which there is usually only a single erupted canine per maxilla. In terms of positional homology, we do not think that lycosuchids are any different from gorgonopsians or scylacosaurids (i.e., they had alternating replacement of C1 in anterior and posterior alveoli, not multiple canine tooth positions homologous with those of non-therapsid sphenacodonts), but that their tooth developmental rates are different and distinctive for the family. We suggest that canine development in lycosuchids was protracted rather than rapid, such that old canines were retained for much of the development of their alternates, allowing direct replacement teeth in their own alveolus to begin forming before their loss (as visible in **Figures 12A,B**). Rather than having a worn canine fall out and be functionally replaced by its alternate, as appears to be the case in gorgonopsians and scylacosaurids, in lycosuchids both anterior and posterior maxillary canines seem to be erupted concurrently (and to some degree being functional concurrently) for much of the animal's life. In this context, it is worth noting that *Gorynychus*, recently recovered as a possible lycosuchid (Liu and Abdala, 2019), has only a single erupted canine in each maxilla and appears to show the typical scylacosaurid pattern of replacement (Kammerer and Masyutin, 2018). It is also worth noting that this delay in canine replacement, if accurate, seems to be limited to the upper dentition, as only a single lower canine per side is erupted.

Evaluating the Systematic Position of *Lycosuchus*

Our CT reconstruction of MB.R.995 provides additional information relevant to evaluating the phylogenetic position of *Lycosuchus vanderrieti*. Despite damage to and loss of some cranial elements, the craniodental characters visible in the scan and described herein confirm many characters used to position *Lycosuchus* as a basal taxon in the analysis of Huttenlocker (2009) (and subsequent variants of this analysis, e.g., Huttenlocker and Sidor, 2016; Huttenlocker and Smith, 2017). These characters include, e.g., a long septomaxilla that is well-exposed on the facial surface, a high dorsal lamina of the maxilla, the presence of large upper and lower canines, and the absence of palatal processes of the maxilla and a crista choanalis. The paired vomer of MB.R.995 also demonstrates the primitive condition, based on the deeply vaulted and expanded morphology of the anterior process at its contact with the premaxilla and the absence of a ventromedian crest between the palatines.

In addition, MB.R.995 provides further information on the presence of cranial features that have previously been questioned for *Lycosuchus*, such as the presence of a vomerine process of the premaxilla (van den Heever, 1987, 1994; Huttenlocker, 2009). In the most recent phylogenetic analysis by Huttenlocker and Smith (2017), this character is listed to be present in *Lycosuchus*, in which there is a short contact between the vomerine process of the premaxilla and the anterior part of the vomer. We agree with this interpretation based on our description of this feature in MB.R.995. The presence of a lateral process of the prootic and the structure and orientation of the dorsal surface of the paroccipital process of the opisthotic have also been questioned in previous analyses (e.g., Huttenlocker, 2009; Huttenlocker and Sidor, 2016; Huttenlocker and Smith, 2017). In MB.R.995 we are able to recognize a lateral process of the prootic, but it is differently angled than in scylacosaurids and eutherocephalians, in which the lateral process of the prootic participates in the formation of the pterygoparoccipital foramen, which is absent in *Lycosuchus* (e.g., van den Heever, 1987, 1994; Huttenlocker et al., 2011; Huttenlocker and Abdala, 2015; Huttenlocker and Sidor, 2016). Despite damage, we suggest that the dorsal surface of the paroccipital process of the opisthotic was relatively straight. This character is shared with *Glanosuchus* and *Pristerognathus* to the exclusion of eutherocephalians, in which the dorsal surface of the paroccipital process of the opisthotic is deeply hollowed in the floor of the posttemporal fenestra (Huttenlocker, 2009; Huttenlocker and Sidor, 2016; Huttenlocker and Smith, 2017). Also similar to *Glanosuchus* and *Pristerognathus*, the orientation of the paroccipital process is transverse relative to horizontal in *Lycosuchus*. But this character is also present in eutherocephalians (Huttenlocker, 2009; Huttenlocker and Sidor, 2016; Huttenlocker and Smith, 2017).

The 3D reconstruction of MB.R.995 also provides new information on several internal cranial characters that have rarely been described for therocephalians and largely ignored in phylogenetic analyses of non-mammalian therapsids in general. Absence of a naso-lacrimal contact on the external snout surface is a key synapomorphy of Therocephalia (Huttenlocker, 2009), present in all known therocephalians (e.g., van den Heever, 1987, 1994; Sigurdsen, 2006; Huttenlocker et al., 2011; Huttenlocker and Abdala, 2015; Huttenlocker and Sidor, 2016; Huttenlocker and Smith, 2017; Kammerer and Masyutin, 2018) except lycideopids (Sigurdsen et al., 2012). On the internal snout

surface, however, basal therocephalians such as *Lycosuchus* and *Glanosuchus* (van den Heever, 1987, 1994; Hillenius, 1994) and akidnognathids (Sigurdsen, 2006; Sigurdsen et al., 2012) have a lacrimal bearing an anterior process that contacts the nasal. Similar to other therocephalians (van den Heever, 1987, 1994; Sigurdsen, 2006; Liu and Abdala, 2017), the dorsal surface of the posterior part of the vomer in *Lycosuchus* is characterized by a median ridge, which continues along the anterior portion of the pterygoid. In addition to the median ridge, the dorsal surface of the posterior portion of the vomer in *Lycosuchus* is characterized by two weakly-developed, transversely oriented ridges running parallel to the median one. The median ridge on the dorsal surface of the posterior part of the vomer and the ridges on the ventral surface of the nasals likely served as attachment points for cartilaginous nasal turbinals, and correspond to those described for therocephalians and several other therapsids (e.g., Fourie, 1974; van den Heever, 1987, 1994; Hillenius, 1994; Crompton et al., 2015, 2017; Bendel et al., 2018; Pusch et al., 2019). As in akidnognathids (Sigurdsen, 2006), no ridges for cartilaginous maxilloturbinals are observed in *Lycosuchus*, suggesting that they might have first evolved within cynodonts.

CONCLUSION

Our redescription of *Lycosuchus vanderrieti* based on a computed tomographic reconstruction of the skull of the specimen MB.R.995 provides new insights into the internal cranial morphology of this taxon. Most of the craniodental characters described herein support previous reports based on external characters that *Lycosuchus* represents the most basal taxon in therocephalian phylogeny. The maxillary canal and inner ear are newly described anatomical features of *Lycosuchus*, and their morphologies support the idea of extensive homoplasy in these structures, with a combination of apparent primitive and derived features among therocephalians. The maxillary canal is highly ramified (interpreted as a primitive character), and the maxillary antrum is relatively small compared to eutherocephalians. For the inner ear, notable is the presence of seemingly derived features such as a cochlear recess and the lengthened morphology of the lateral semicircular canal. A cochlear recess is otherwise only known in the Triassic baurioid *Microgomphodon* among therocephalians, but more thorough sampling of this character in the clade is needed, while the lengthened morphology of the lateral semicircular canal could be a taxonomically-variable feature related to lifestyle. The pattern of tooth replacement in lycosuchids follows the standard pattern described in theriodonts, but teeth were likely replaced more slowly in contrast to scylacosaurids, resulting in the unusual condition of multiple erupted canines in each maxilla at most times.

DATA AVAILABILITY STATEMENT

The raw CT data supporting the conclusions of this manuscript are available in the Data Repository of the Museum für Naturkunde Berlin, https://doi.org/10.7479/hwt8-c010.

AUTHOR CONTRIBUTIONS

LP analyzed, interpreted and drafted the manuscript, and prepared all figures. JP contributed to the analysis and interpretation of the manuscript. CK was involved in the data acquisition, contributed to conceptualization, analysis and interpretation, and critical revision of the manuscript. JF was involved in the data acquisition and contributed to the conceptualization and critical revision of manuscript.

FUNDING

This study was financially supported by the Humboldt-Universität zu Berlin within the Excellence Initiative of the states and federal government to JP and by the German Research Foundation (DFG) with the grant numbers KA 4133/1-1 and FR 2457/8-1.

ACKNOWLEDGMENTS

We would like to thank Kristin Mahlow and Martin Kirchner from the CT-Laboratory of the Museum für Naturkunde Berlin for scanning MB.R.995. Furthermore, we thank Fernando Abdala and Julien Benoit for their thorough and constructive reviews of this manuscript, and Josep Fortuny for editing.

REFERENCES

Abdala, F. (2007). Redescription of *Platycraniellus elegans* (Therapsida, Cynodontia) from the Lower Triassic of South Africa, and the cladistic relationships of eutheriodonts. *Palaeontology* 50, 591–618. doi: 10.1111/j.1475-4983.2007.00646.x

Abdala, F., Jashashvili, T., Rubidge, B. S., and van den Heever, J. (2014b). "New material of *Microgomphodon oligocynus* (Eutherapsida, Therocephalia) and the taxonomy of southern African Bauriidae," in *Early Evolutionary History of the Synapsida*, eds C. F. Kammerer, K. D. Angielczyk, and J. Fröbisch (Dordrecht: Springer), 209–231.

Abdala, F., Kammerer, C. F., Day, M. O., Jirah, S., and Rubidge, B. S. (2014a). Adult morphology of the therocephalian *Simorhinella baini* from the middle Permian of South Africa and the taxonomy, paleobiogeography, and temporal distribution of the *Lycosuchidae*. *J. Paleontol.* 88, 1139–1153. doi: 10.1666/13-186

Abdala, F., Rubidge, B., and van den Heever, J. (2008). The oldest therocephalians (Therapsida, Eutheriodonta) and the early diversification of *Therapsida*. *Palaeontology* 51, 1011–1024. doi: 10.1111/j.1475-4983.2008.00784.x

Ahlberg, P., and Clack, J. A. (1998). Lower jaws, lower tetrapods – a review based on the Devonian genus *Acanthostega*. *Earth Environ. Sci. Trans. R. Soc.* 89, 11–46. doi: 10.1017/S0263593300002340

Araújo, R. M., Fernandez, V., Polcyn, M. J., Fröbisch, J., and Martins, R. M. S. (2017). Aspects of gorgonopsian paleobiology and evolution: insights from the basicranium, occiput, osseous labyrinth, vasculature, and neuroanatomy. *PeerJ* 5:e3119. doi: 10.7717/peerj.3119

Araújo, R. M., Fernandez, V., Rabbitt, R. D., Ekdale, E. G., Antunes, M. T., Castanhinha, R., et al. (2018). Endothiodon cf. bathystoma

(Synapsida: Dicynodontia) bony labyrinth anatomy, variation and body mass estimates. *PLoS ONE* 13:e0189883. doi: 10.1371/journal.pone.0189883

Bendel, E.-M., Kammerer, C. F., Kardjilov, N., Fernandez, V., and Fröbisch, J. (2018). Cranial anatomy of the gorgonopsian *Cynariops robustus* based on CT-reconstruction. *PLoS ONE* 13:e0207367. doi: 10.1371/journal.pone.0207367

Benoit, J., Adnet, S., El Mabrouk, E., Khayati, H., Ben Haj Ali, M., Marivaux, L., et al. (2013). Cranial remain from Tunisia provides new clues for the origin and evolution of Sirenia (Mammalia, Afrotheria) in Africa. *PLoS ONE* 8:e54307. doi: 10.1371/journal.pone.0054307

Benoit, J., Angielczyk, K. D., Miyamae, J. A., Manger, P., Fernandez, V., and Rubidge, B. (2018). Evolution of facial innervation in anomodont therapsids (Synapsida): insights from X-ray computerized microtomography. *J. Morphol.* 279, 673–701. doi: 10.1002/jmor.20804

Benoit, J., Manger, P. R., Fernandez, V., and Rubidge, B. S. (2016b). Cranial bosses of *Choerosaurus dejageri* (Therapsida, Therocephalia): earliest evidence of cranial display structures in eutheriodonts. *PLoS ONE* 11:e0161457. doi: 10.1371/journal.pone.0161457

Benoit, J., Manger, P. R., Fernandez, V., and Rubidge, B. S. (2017b). The bony labyrinth of the late Permian Biarmosuchia: palaeobiology and diversity in non-mammalian *Therapsida*. *Palaeontology* 52, 58–77. Available online at: http://wiredspace.wits.ac.za/handle/10539/23023

Benoit, J., Manger, P. R., Norton, L., Fernandez, V., and Rubidge, B. S. (2017c). Synchrotron scanning reveals the paleoneurology of the head-butting *Moschops capensis* (Therapsida, Dinocephalia). *PeerJ* 5:e3496. doi: 10.7717/peerj.3496

Benoit, J., Manger, P. R., and Rubidge, B. S. (2016a). Palaeoneurological clues to the evolution of defining mammalian soft tissue traits. *Sci. Rep.* 6:25604. doi: 10.1038/srep25604

Benoit, J., Norton, L. A., Manger, P. R., and Rubidge, B. S. (2017a). Reappraisal of the envenoming capacity of *Euchambersia mirabilis* (Therapsida, Therocephalia) using μCT-scanning techniques. *PLoS ONE* 12:e0172047. doi: 10.1371/journal.pone.0172047

Benoit, J., Ruf, I., Miyamae, J. A., Fernandez, V., Rodrigues, P. G., Rubidge, B. S., et al. (2019). The evolution of the maxillary canal in probainognathia (Cynodontia, Synapsida): reassessment of the homology of the infraorbital foramen in mammalian ancestors. *J. Mamm. Evol.* 1–20. doi: 10.1007/s10914-019-09467-8

Boonstra, L. D. (1964). The girdles and limbs of the pristerognathid *Therocephalia*. *Ann. S. Afr. Mus.* 48, 121–165.

Boonstra, L. D. (1969). The fauna of the *Tapinocephalus* Zone (Beaufort beds of the Karoo). *Ann. S. Afr. Mus.* 56, 1–73.

Botha, J., Abdala, F., and Smith, R. M. H. (2007). The oldest cynodont: new clues on the origin and diversification of the *Cynodontia*. *Zool. J. Linn. Soc.* 149, 477–492. doi: 10.1111/j.1096-3642.2007.00268.x

Broom, R. (1903). On an almost perfect skull of a new primitive theriodont (*Lycosuchus vanderrieti*). *Trans. S. Afr. Phil. Soc.* 14, 197–205. doi: 10.1080/21560382.1903.9526025

Castanhinha, R., Araújo, R., Júnior, L. C., Angielczyk, K. D., Martins, G. G., Martins, R. M. S., et al. (2013). Bringing dicynodonts back to life: paleobiology and anatomy of a new emydopoid genus from the Upper Permian of Mozambique. *PLoS ONE* 8:e80974. doi: 10.1371/journal.pone.0080974

Cox, P. G., and Jeffery, N. (2010). Semicircular canals and agility: the influence of size and shape measures. *J. Anat.* 216, 37–47. doi: 10.1111/j.1469-7580.2009.01172.x

Crompton, A. W., Musinsky, C., and Owerkowicz, T. (2015). "Evolution of the mammalian nose," in *Great Transformations in Vertebrate Evolution*, eds K. Dial, N. Shubin, and E. Brainerd (Chicago, IL: Chicago Press), 189–203.

Crompton, A. W., Owerkowicz, T., Bhullar, B.-A. S., and Musinsky, C. (2017). Structure of the nasal region of non- mammalian cynodonts and mammaliaforms: speculations on the evolution of mammalian edothermy. *J. Vertebr. Paleontol.* 37:e1269116. doi: 10.1080/02724634.2017.1269116

Evers, S., Neenan, J., Ferreira, G. S., Werneburg, I., Barrett, P. M., and Benson, R. B. J. (2019). Neurovascular anatomy of the protostegid turtle *Rhinochelys pulchriceps* and comparisons of membranous and endosseous labyrinth shape in an extant turtle. *Zool. J. Linn. Soc.* 187, 800–828. doi: 10.1093/zoolinnean/zlz063

Fourie, S. (1974). The cranial morphology of *Thrinaxodon liorhinus* Seeley. *Ann. S. Afr. Mus.* 65, 337–400.

Haughton, A. A., and Brink, S. (1954). A bibliographical list of Reptilia from the Karoo beds of Africa. *Paleontology* 2, 1–187.

Hillenius, W. J. (1994). Turbinates in therapsids: evidence for Late Permian origins of mammalian endothermy. *Evolution* 48, 207–229.

Hillenius, W. J. (2000). Septomaxilla of nonmammalian synapsids: soft-tissue correlates and a new functional interpretation. *J. Morphol.* 245, 29–50.

Hopson, J. A. (1991). "Systematics on the nonmammalian synapsida and implications for patterns of evolution in synapsids," in *Origins of the Higher Groups of Tetrapods: Controversy and Consensus*, eds H. P. Schultze and L. Trueb (Ithaca: Comstock Publishing Associates), 635–693.

Hopson, J. A., and Barghusen, H. (1986). "An analysis of therapsid relationships," in *The Ecology and Biology of the Mammal-Like Reptiles*, eds N. Hotton, P. D. Maclean, J. J. Roth, and E. C. Roth (Washington, DC: Smithsonian Institution Press), 83–106.

Hopson, J. A., and Kitching, J. W. (2001). A probainognathian cynodont from South Africa and the phylogeny of nonmammalian cynodonts. *Bull. Mus. Comp. Zool.* 156, 5–35.

Huttenlocker, A. (2009). An investigation into the cladistic relationships and monophyly of therocephalian therapsids (Amniota: Synapsida). *Zool. J. Linn. Soc.* 157, 865–891. doi: 10.1111/j.1096-3642.2009.00538.x

Huttenlocker, A. K. (2014). Body size reductions in nonmammalian eutheriodont therapsid (Synapsida) during the end-Permian mass extinction. *PLoS ONE* 9:e87553. doi: 10.1371/journal.pone.0087553

Huttenlocker, A. K., and Abdala, F. (2015). Revision of the first therocephalian, *Theriognathus* Owen (Therapsida: Whaitsiidae), and implications for cranial ontogeny and allometry in nonmammaliaform eutheriodonts. *J. Paleontol.* 89, 645–664. doi: 10.1017/jpa.2015.32

Huttenlocker, A. K., and Sidor, C. A. (2016). The first karenitid (Therapsida, Therocephalia) from the upper Permian of Gondwana and the biogeography of Permo-Triassic therocephalians. *J. Vertebr. Paleontol.* 36:e1111897. doi: 10.1080/02724634.2016.1111897

Huttenlocker, A. K., Sidor, C. A., and Smith, R. M. H. (2011). A new specimen of *Promoschorhynchus* (Therapsida: Therocephalia: Akidnognathidae) from the Lower Triassic of South Africa and its implications for theriodont survivorship across the Permo-Triassic boundary. *J. Vertebr. Paleontol.* 31, 405–421. doi: 10.1080/02724634.2011.546720

Huttenlocker, A. K., and Smith, R. M. H. (2017). New whaitsioids (Therapsida: Therocephalia) from the Teekloof Formation of South Africa and therocephalian diversity during the end-Guadalupian extinction. *Peer J* 5:e3868. doi: 10.7717/peerj.3868

Janensch, W. (1952). Über den Unterkiefer der Therapsiden. *Paläont. Z.* 26, 229–247.

Kammerer, C. F. (2017). Anatomy and relationships of the South African gorgonopsian *Arctops* (Therapsida, Theriodontia). *Pap Paleontol.* 3, 583–611. doi: 10.1002/spp2.1094

Kammerer, C. F., and Masyutin, V. (2018). A new therocephalian (*Gorynychus masyutinae* gen. *et*. Sp. nov*)* from the Permian Kotelnich locality, Kirov Region, Russia. *PeerJ* 6:e4933. doi: 10.7717/peerj.4933

Kemp, T. S. (1979). The primitive cynodont *Procynosuchus*: functional anatomy of the skull and relationships. *Philos. Trans. Royal Soc. B* 285, 73–122. doi: 10.1098/rstb.1979.0001

Kermack, K. (1956). Tooth replacement in mammal-like reptiles of the suborders Gorgonopsia and Therocephalia. *Philos. Trans. Royal Soc.* 240, 95–133. doi: 10.1098/rstb.1956.0013

Kielan-Jaworowska, Z., Cifelli, R. L., and Luo, Z.-X. (2004). *Mammals From the Age of Dinosaurs: Origin, Evolution, and Structure*. New York, NY: Columbia University Press.

Laaß, M. (2015a). Bone-conduction hearing and seismic sensitivity of the late Permian anomodont *Kawingasaurus fossilis*. *J. Morphol.* 276, 121–143. doi: 10.1002/jmor.20325

Laaß, M. (2015b). Virtual reconstruction and description of the cranial endocast of *Pristerodon mackayi* (Therapsida, Anomodontia). *J. Morphol.* 276, 1089–1099. doi: 10.1002/jmor.20397

Laaß, M. (2016). The origins of the cochlea and impedance matching hearing in synapsids. *Acta Palaeontol. Pol.* 61, 267–280. doi: 10.4202/app.00140.2014

Lindenlaub, T., Burda, H., and Nevo, E. (1995). Convergent evolution of the vestibular organ in the subterranean mole-rats, *Cryptomys* and *Spalax*, as

compared with the aboveground rat, *Rattus*. *J. Morphol.* 224, 303–311. doi: 10.1002/jmor.1052240305

Liu, J., and Abdala, F. (2017). The tetrapod fauna of the upper Permian naobaogou formation of China: 1. *Shiguaignathus wangi* gen. et sp. nov., the first akidnognathid therocephalian from China. *Peer J* 5:e4150. doi: 10.7717/peerj.4150

Liu, J., and Abdala, F. (2019). The tetrapod fauna of the upper Permian Naobaogou Formation of China: 3. *Jiufengia jiaj* gen. et sp. nov., a large akidnognathid therocephalian. *PeerJ* 7:e6463. doi: 10.7717/peerj.6463

Luo, Z.-X. (2001). The inner ear and its bony housing in tritylodontids and implications for evolution of the mammalian ear. *Bull. Mus. Comp. Zool.* 156, 81–97.

Luo, Z.-X., Crompton, A. W., and Lucas, S. G. (1995). Evolutionary origins of the mammalian promontorium and cochlea. *J. Vertebr. Paleontol.* 15, 113–121. doi: 10.1080/02724634.1995.10011211

Neenan, J. M., Reich, T., Evers, S. W., Druckenmiller, P. S., Voeten, D. F. A. E., Choiniere, J. N., et al. (2017). Evolution of the sauropterygian labyrinth with increasingly pelagic lifestyle. *Curr. Biol.* 27, 3852–3858. doi: 10.1016/j.cub.2017.10.069

Olori, J. C. (2010). Digital endocasts of the cranial cavity and osseous labyrinth of the burrowing snake *Uropeltis woodmasoni* (Alethinophidia: Uropeltidae). *Copeia* 2010, 14–26. doi: 10.1643/CH-09-082

Olson, E. C. (1944). Origin of mammals based upon cranial morphology of the therapsid suborders. *Geol. Soc. Am. Spec. Pap.* 55, 1–130. doi: 10.1130/SPE55-p1

Pavanatto, A. E. B., Kerber, L., and Dias-da-Silva, S. (2019). Virtual reconstruction of cranial endocasts of traversodontid cynodonts (Eucynodotia: Gomphodontia) from the upper Triassic of Southern Brazil. *J. Morphol.* 280, 1267–1281. doi: 10.1002/jmor.21029

Pusch, L. C., Kammerer, C. F., and Fröbisch, J. (2019). Cranial anatomy of the early cynodont *Galesaurus planiceps* and the origin of mammalian endocranial characters. *J. Anat.* 234, 592–621. doi: 10.1111/joa.12958

Rodrigues, P. G., Ruf, I., and Schultz, C. L. (2014). Study of a digital cranial endocast of the nonmammaliaform cynodont *Brasilitherium riograndensis* (Later Triassic, Brazil) and its relevance to the evolution of the mammalian brain. *Paläont. Z* 88, 329–352. doi: 10.1007/s12542-013-0200-6

Rodrigues, P. G., Ruf,.I., and Schultz, C. L. (2013). Digital reconstruction of the otic region and inner ear of the non-mammalian cynodont *Brasilitherium riograndensis* (Late Triassic, Brazil) and its relevance to the evolution of the mammalian ear. *J. Mamm. Evol.* 20, 291–307. doi: 10.1007/s10914-012-9221-2

Rowe, T., Carlson, W., and Bottorff, W. (1993). *Thrinaxodon: Digital Atlas of the Skull (CD-ROM)*. Austin, TX: University of Texas Press.

Sigogneau, D. (1974). The inner ear of *Gorgonops* (Reptilia, Therapsida, Gorgonopsia). *Ann. S. Afr. Mus.* 64, 53–69.

Sigurdsen, T. (2006). New features of the snout and orbit of a therocephalian therapsid from South Africa. *Acta Palaeontol. Pol.*51, 63–75.

Sigurdsen, T., Huttenlocker, A. K., Modesto, S. P., Rowe, T. B., and Damiani, R. (2012). Reassessment of the morphology and paleobiology of the therocephalian *Tetracynodon darti* (Therapsida), and the phylogenetic relationships of Baurioidea. *J. Vertebr. Paleontol.* 32, 1113–1134. doi: 10.1080/02724634.2012.688693

Smith, R. M. H., Rubidge, B. S., and van der Walt, M. (2012). "Therapsid biodiversity patterns and palaeoenvironments of the Karoo Basin, South Africa," in *Forerunners of Mammals. Radiation, Histology, Biology*, ed A. Chinsamy-Turan (Bloomington, IN: Indiana University Press), 31–62.

Spoor, F. (2003). The semicircular canal system and locomotor behaviour, with special reference to hominin evolution. *Courier Forschungsinstitut Senckenberg* 243, 93–104.

Spoor, F., Garland, T., Krovitz, G., Ryan, T. M., Silcox, M. T., and Walker, A. (2007). The primate semicircular canal system and locomotion. *PNAS* 104, 10808–10812. doi: 10.1073/pnas.0704250104

Suchkova, Y. A., and Golubev, V. K. (2019). A new primitive therocephalian (Theromorpha) from the middle Permian of Eastern Europe. *Paleontol. J.* 53, 305–314. doi: 10.1134/S0031030119030158

van den Heever, J. A. (1980). On the validity of the therocephalian family Lycosuchidae (Reptilia, Therapsida. *Ann. S. Afr. Mus.* 81, 111–125.

van den Heever, J. A. (1987). *The comparative and functional cranial morphology of the early Therocephalia (Amniota: Therapsida)* [Unpublished dissertation]. University of Stellenbosch, Stellenbosch, South Africa.

van den Heever, J. A. (1994). The cranial anatomy of the early Therocephalia (Amniota: Therapsida). *Ann. Univ. Stellenbosch* 1, 1–59.

van den Heever, J. A., and Hopson, J. A. (1982). The systematic position of "Therocephalia B" (Reptilia, Therapsida). *S. Afr. J. Sci.* 78, 424–425.

Walsh, S. A., Barrett, P. M., Milner, A. C., Manley, G., and Witmer, L. M. (2009). Inner ear anatomy is a proxy for deducing auditory capability and behaviour in reptiles and birds. *Proc. R. Soc. Lond. B Biol.* 276, 1355–1360. doi: 10.1098/rspb.2008.1390

Wittmer, L. M., and Ridgely, R. C. (2009). New insights into the brain, braincase, and ear region of tyrannosaurs (Dinosauria, Theropoda), with implications for sensory organization and behavior. *Anat. Rec.* 292, 1266–1296. doi: 10.1002/ar.20983

Yi, H., and Norell, N. (2018). The bony labyrinth of *Platecarpus* (Squamata: Mosasauria) and aquatic adaptations in squamate reptiles. *Paleoworld*. doi: 10.1016/j.palwor.2018.12.001

Conflict of Interest: The reviewer, JB, declared to the editor a permanent affiliation to the University of the Witwatersrand in which two of the authors, CK and JF, have an honorary affiliation, and declared no collaboration with the authors at the time of the review.

The remaining authors declare that the research was conducted in the absence of any commercial or financial relationships that could be construed as a potential conflict of interest.

frontiers in Ecology and Evolution

ORIGINAL RESEARCH
published: 27 February 2020
doi: 10.3389/fevo.2020.00042

When X-Rays Do Not Work. Characterizing the Internal Structure of Fossil Hominid Dentognathic Remains Using High-Resolution Neutron Microtomographic Imaging

Clément Zanolli[1], Burkhard Schillinger[2], Ottmar Kullmer[3,4], Friedemann Schrenk[3,4], Jay Kelley[5,6,7], Gertrud E. Rössner[8,9] and Roberto Macchiarelli[10,11]*

[1] Laboratoire PACEA, UMR 5199 CNRS, Université de Bordeaux, Pessac, France, [2] Heinz Maier-Leibnitz Center (FRM-II), Technische Universität München, Garching, Germany, [3] Department of Paleoanthropology, Senckenberg Research Institute and Natural History Museum Frankfurt, Frankfurt, Germany, [4] Department of Paleobiology and Environment, Institute of Ecology, Evolution, and Diversity, Goethe University Frankfurt, Frankfurt, Germany, [5] Institute of Human Origins, School of Human Evolution and Social Change, Arizona State University, Tempe, AZ, United States, [6] Department of Paleobiology, National Museum of Natural History, Smithsonian Institution, Washington, DC, United States, [7] Department of Human Evolutionary Biology, Harvard University, Cambridge, MA, United States, [8] SNSB-Bayerische Staatssammlung für Paläontologie und Geologie, Munich, Germany, [9] Department of Earth and Environmental Sciences, Palaeontology & Geobiology, Ludwig–Maximilians–Universität München, Munich, Germany, [10] UMR 7194 CNRS, Muséum National d'Histoire Naturelle, Musée de l'Homme, Paris, France, [11] Unité de Formation Géosciences, Université de Poitiers, Poitiers, France

OPEN ACCESS

Edited by:
Luca Pandolfi, University of Florence, Italy

Reviewed by:
Masato Nakatsukasa, Kyoto University, Japan
Amélie Beaudet, University of the Witwatersrand, South Africa

***Correspondence:**
Clément Zanolli
clement.zanolli@gmail.com

Specialty section:
This article was submitted to Chemical Ecology, a section of the journal Frontiers in Ecology and Evolution

Received: *13 January 2020*
Accepted: *11 February 2020*
Published: *27 February 2020*

Citation:
Zanolli C, Schillinger B, Kullmer O, Schrenk F, Kelley J, Rössner GE and Macchiarelli R (2020) When X-Rays Do Not Work. Characterizing the Internal Structure of Fossil Hominid Dentognathic Remains Using High-Resolution Neutron Microtomographic Imaging. Front. Ecol. Evol. 8:42. doi: 10.3389/fevo.2020.00042

The internal structure of the bones and teeth of extinct primates holds a significant amount of valuable paleobiological information for assessing taxonomy, phylogenetic relationships, functional, dietary and ecological adaptive strategies, and reconstructing overall evolutionary history. Technologies based on X-ray microfocus (X-μCT) and synchrotron radiation (SR-μCT) microtomography are increasingly used to non-invasively and non-destructively investigate the endostructural properties of fossil mineralized tissues. However, depending on the taphonomic dynamics that affected the specimens following deposition, and on the nature of diagenetic processes, X-μCT and even SR-μCT may provide only faint or no contrast between the mineralized tissues, thus complicating or inhibiting the study of structural features. Using a diverse sample of dentognathic hominid specimens from continental Asia, East Africa and Indonesia, chronologically ranging from the Late Miocene to the Early Middle Pleistocene, we present examples of the successful application of another imaging technology, neutron microtomography (n-μCT), for the extraction, 3D rendering and quantitative assessment of internal morphological detail. The specimens were scanned at the ANTARES Imaging facility (SR4a beamline) at the FRM II reactor of the Technical University of Munich, Germany, at energies ranging from 3 to 25 meV. The datasets were reconstructed with a voxel size from 20 to 27 μm, i.e., at resolutions directly comparable to the X-ray-based microtomographic records commonly used in paleobiological studies of fossil primate remains. Our analyses focused on a mandible, SNSB-BSPG 1939 X 4, representing the Late Miocene hominid *Sivapithecus* from the Siwaliks of Pakistan; the early Pleistocene

(Gelasian) partial mandible HCRP-U18-501 from Malawi, among the earliest specimens attributed to the genus *Homo*; and an assemblage of hominid dentognathic specimens from the Early Middle Pleistocene deposits of the Sangiran Dome, Indonesia. While X-ray-based imaging revealed from low to moderate internal contrasts for the specimen of *Sivapithecus*, or from extremely poor to virtually no contrast for the Pleistocene remains from East Africa and Indonesia, the application of n-μCT produced sufficient differences in contrast to distinguish between tooth tissues on the one hand, and between cortical and trabecular bone on the other, thus enabling reliable qualitative and quantitative assessments of their characteristics.

Keywords: neutron microtomography, micromorphology, mineralized tissues, taphonomy, diagenesis, paleoanthropology

INTRODUCTION

Before radiation-based analytical methods were made available for paleobiological research, the only way to extract information from the internal structure of fossils was to either study naturally broken remains, or to physically section specimens. Shortly after the discovery of X-rays by Röntgen (1895), plain radiography was first used in paleoanthropology to image some Neanderthal and Upper Paleolithic human dentognathic remains from Belgium (La Naulette, Goyet), Croatia (Krapina), Germany (Mauer), and Moravia (Pøedmostí) (Walkhof, 1902; Gorjanović-Kramberger, 1906; Schoetensack, 1908). Among other anatomical details, radiography revealed that the Neanderthal cheek teeth commonly bear an enlarged pulp cavity associated with pyramidal (or prismatic) roots (Gorjanović-Kramberger, 1906, 1907), a distinctive Neanderthal feature subsequently termed "taurodontism" (Keith, 1913).

Since these pioneering studies that revealed previously unreported dental and bony features, X-ray imaging has increasingly been used in paleobiological and paleoanthropological research, sometimes through the application of derivative techniques such as xeroradiography and multiple projection (stereo) X-rays (e.g., Meschan et al., 1979). However, plain film radiography generates two-dimensional (2D) synthetic images of the hidden anatomy resulting from the superimposition of overlying three-dimensional (3D) structures, which, depending on the volume of the investigated specimen, are limited in the extraction of subtle information from complex architectures, especially in fossils (Skinner and Sperber, 1982). The invention of X-ray computed tomography (CT; Hounsfield, 1973, 1975) provided for the first time the possibility to derive from the same object, and to treat separately and/or cumulatively, a series of cross-sectional images each taken on a distinct plane, thus avoiding the superimposition effect.

Medical CT scanning techniques led to new and exciting perspectives in paleontology and paleoanthropology, with the first applications of 3D imaging to fossil hominin remains dating to the 1980s (e.g., Tate and Cann, 1982; Wind, 1984; Conroy and Vannier, 1985, 1987; Zonneveld and Wind, 1985; Wind and Zonneveld, 1989). Often complemented by stereolithographic solid reconstructions, CT constituted the most effective technology to render inner structural variation at millimetric scale (rev. in Ulhaas, 2007; Macchiarelli et al., 2008; Braga, 2016). This remarkable methodological advance in 3D imaging enabled virtual access to previously infrequently investigated structures, such as the complete morphology of the bony labyrinth, which provided original information about locomotor behaviors and phylogenetic relationships (Spoor et al., 1994), and also allowed quantitative assessment of many other functionally related cranial and postcranial features (e.g., Jungers and Minns, 1979; Trinkaus, 1984; Ruff and Leo, 1986; Daegling, 1989). CT imaging also allows virtual reconstruction of broken and/or distorted areas through techniques of mirroring and interpolation, as well as by shape retro-deformation using morphometric approaches (e.g., Zollikofer and Ponce de León, 2005; Weber and Bookstein, 2011).

Nonetheless, even CT imaging has certain intractable limitations when analyzing highly mineralized specimens and/or specimens filled/surrounded by a dense sedimentary matrix, resulting from insufficient contrast among various structural components (e.g., mineralized tissues, infill, "empty" spaces/air) (Spoor et al., 2000). Overflow artifacts may also appear when the density of a specimen is greater than the scale maximum of the CT scan (i.e., when the signal received exceeds the dynamic range of the detector). Additionally, beam hardening – due to the absorption of low−energy X−rays leaving mostly high−energy photons – may result in overflow artifacts with saturated contrasts on the borders or in the densest areas (Spoor et al., 2000; Ulhaas, 2007). Depending on taphonomic history, fossils that have incorporated high-density elements (like iron) show streak artifacts on the CT images (Spoor et al., 2000). If the CT number scale is not fully adapted, as frequently occurs, or if no recalibration is applied, the resulting images have no contrast and altered thresholds. However, by using *ad hoc* filters, software and algorithm calibration, in most cases these kinds of problems can be minimized, if not fully overcome (Spoor et al., 2000; Ulhaas, 2007).

While CT scanning is still used to image relatively large fossil specimens and blocks of sedimentary breccia (e.g., Wu and Schepartz, 2009; Smilg and Berger, 2015), for smaller anatomical elements, like teeth and dentognathic fragments, the level of detail in digital reconstructions based on CT data is limited by the spatial resolution in the scan plane, slice thickness, and slice increment (for recent applications, see Beaudet et al., 2015;

Zanolli et al., 2017a). Indeed, with conventional CT scans it is possible to attain a final voxel size of only a few hundred micrometers (μm), while cone beam CT instruments (CBCT) reach resolutions near 100 μm but generate noisy images (Maret et al., 2014).

In the hominid fossil record, dentognathic remains are the most commonly preserved elements (Wood, 2011). Recent advances in the genetics and development of mineralized tissues demonstrate that the internal morphological structure of tooth crowns and roots bears a wealth of valuable taxon-specific biological information stored at a micrometric scale (Hillson, 2014; Guatelli-Steinberg, 2016; Scott et al., 2018; see also Smith and Tafforeau, 2008). Thus, given the conflicting requirements of preservation versus scientific exploitation of the fossil record, higher resolution non-invasive investigative techniques other than medical CT scanning are needed to safely but satisfactorily access the endostructural record (rev. in Macchiarelli et al., 2008).

X-ray microtomography (X-μCT) enabling the study of 3D features at micrometer scale was invented in the 1980s (Elliott and Dover, 1982). The results of the first applications of industrial X-μCT equipment to image the 3D endostructure of fossil hominoid (the Late Miocene ape *Oreopithecus*) and hominin (*Australopithecus*) teeth were published in 2004 (Macchiarelli et al., 2004; Rossi et al., 2004, respectively). These were quickly followed by the development of synchrotron radiation microtomography (SR-μCT), a highly effective analytical tool to detail meso/microscopic features (see Tafforeau et al., 2012), including dental endostructural morphology in extinct hominids (e.g., Macchiarelli et al., 2006, 2007, 2008; Mazurier et al., 2006; Tafforeau et al., 2006; Smith and Tafforeau, 2008; Tafforeau and Smith, 2008; Smith et al., 2009; Le Cabec et al., 2015). High-resolution X-μCT and SR-μCT have now become indispensable tools for the virtual exploration, extraction, cleaning, 2-3D rendering and quantitative assessment of the paleobiological information stored in fossilized remains (among the very many studies, see Rook et al., 2004; Olejniczak and Grine, 2005, 2006; Olejniczak et al., 2008; Skinner et al., 2008, 2015, 2016; Bayle et al., 2009, 2011; Macchiarelli et al., 2009, 2013; Braga et al., 2010; Kupczik and Hublin, 2010; Benazzi et al., 2011a,b; Jaeger et al., 2011; DeSilva and Devlin, 2012; Puymerail et al., 2012a,b; Zanolli et al., 2012, 2014, 2015, 2018a,b; Barak et al., 2013; Le Cabec et al., 2013; Zanolli and Mazurier, 2013; Spoor et al., 2015; Zanolli, 2015; Kappelman et al., 2016; Kivell, 2016; Macchiarelli and Zanolli, 2017; Martínez de Pinillos et al., 2017; Pan et al., 2017; Beaudet et al., 2018; Martín-Francés et al., 2018; Ryan et al., 2018; Beaudet, 2019; Cazenave et al., 2019a,b; Genochio et al., 2019; Grine et al., 2019; Haile-Selassie et al., 2019; Kupczik et al., 2019; Martinón-Torres et al., 2019; Pan and Zanolli, 2019).

Nevertheless, depending on the degree of alteration affecting specimens during fossilization, especially the impact of diagenesis, X-ray analyses of dental tissues do not always provide a distinct structural signal, thus sometimes limiting access to and extraction of information, or resulting in the recovery of no information whatsoever (Zanolli et al., 2017b). While X-μCT or SR-μCT usually make it possible to focus on local regions of interest (ROIs), or to use selected individual virtual slices to assess certain internal features (e.g., Smith et al., 2009, 2018; Skinner et al., 2013, 2015; Zanolli et al., 2015), there are also instances in which there is insufficient tissue contrast to allow reliable measurement, thus inhibiting the analysis of volumes of interest (VOIs).

Recently, a new investigative tool has become available to successfully detail the internal structure of fossil remains, neutron microtomography (n-μCT). Although neutrons were discovered in the 1930s and neutron radiography was applied for the first time to investigate fossil hominin remains already in the late 1990s (Le Roux et al., 1997), the exploitation of their physical characteristics in 3D imaging developed only when high quality neutron sources and detector systems became available (Tremsin et al., 2011). Neutrons have an absorption profile (interaction mechanism with matter) that differs from that of X-rays (Kardjilov et al., 2003; Winkler, 2006; Sutton, 2008; Tremsin et al., 2015). Because of a unique capacity of neutrons to penetrate materials opaque to X-rays, neutron-based analytical techniques such as neutron radiography and n-μCT represent highly effective tools for imaging fossil remains, often times providing adequate contrast resolution when other methods fail to do so (Zanolli et al., 2017b).

Following on the pioneering application of n-μCT to the analysis of fossil primate cranial and dental remains (Beaudet et al., 2016; Urciuoli et al., 2017; Zanolli et al., 2017b, 2019a), here we detail a series of cases illustrating the formidable potential of this analytical tool in the study of densely mineralized hominid dentognathic remains from different time periods and geographic contexts.

MATERIALS AND METHODS

Specimens

To illustrate different examples where X-ray-based imaging does not deliver a satisfying structural signal whereas n-μCT does, we selected an *ad hoc* assemblage of six hominid dentognathic remains chronologically ranging from the Late Miocene to the Early Middle Pleistocene, all from open-air sites in continental Asia, Africa and Indonesia.

The first specimen is a partial mandible of the late Miocene hominid *Sivapithecus*, from the Siwaliks of Pakistan. This genus exhibits a number of craniofacial similarities with extant orangutans and is considered to be related to *Pongo* (Pilbeam, 1982; Ward and Brown, 1986). However, *Sivapithecus* also displays features that are unlike those of *Pongo*, including dentognathic morphology (Kelley, 2002). We examined the left mandibular corpus, bearing two premolars and two molars, of the adult specimen SNSB-BSPG 1939 X 4, the holotype of *S. parvada*, from c. 10 million years (Ma) old levels of the Potwar Plateau (Dehm, 1983; Kelley, 1988, 2002). *S. parvada* is nearly twice the size of the two other common species of *Sivapithecus*, *S. indicus* and *S. sivalensis* (Dehm, 1983; Kelley, 1988, 2002). Resolving its relationships with the other *Sivapithecus* species, as well as clarifying its phylogenetic position with respect to *Pongo*, remain open research topics for which the extraction of additional dentognathic endostructural features could add

potentially relevant information. The specimen SNSB-BSPG 1939 X 4 is stored at the Bavarian Natural History Collections – Bavarian State Collection of Palaeontology and Geology, Munich, Germany.

We also examined the Early Pleistocene (Gelasian) partial mandible of an adult individual, HCRP-U18-501 (hereafter UR 501), found in 1991/92 at the Uraha site, Malawi (Schrenk et al., 1993). It comes from the stratigraphic Unit 3A of the Chiwondo Beds, Karonga Basin, biochronologically dated to 2.3–2.5 Ma (Kullmer, 2008). This is an especially relevant time period in hominin evolution as it corresponds to the emergence and initial diversification of the genus *Homo* (Villmoare, 2018). UR 501 consists of two joined parts of the corpus broken on both sides behind the m2s, but preserving the p3-m2 tooth sequence. We analyzed the X-μCT and n-μCT records of the right portion. The size and proportions of this specimen, the symphyseal shape, the anteroposteriorly elongated dental arcade, and details of external tooth morphology show remarkable similarities with the specimen KNM-ER 1802 from Koobi Fora, Kenya, regarded as representing *Homo* cf. *habilis*, as well as with OH 7 from Olduvai Gorge, Tanzania, the holotype of *H. habilis* (Spoor et al., 2015). However, it also possesses some *Australopithecus*-like as well as unique features, a mosaic which makes the taxonomic placement of this fossil challenging. Thus, any diagnostic information deriving from the analysis of its endostructure has the potential of contributing to a more definitive taxonomic assignment, and therefore better assessment of its likely affinities (Zanolli et al., 2019b). The mandible UR 501 is stored at the Senckenberg Museum of Frankfurt am Main, Germany.

We also selected an assemblage of four hominid dentognathic remains from the Early Middle Pleistocene deposits of the Sangiran Dome, Java, Indonesia. These include the right mandibular portion of Sangiran 6a, the holotype of *Meganthropus palaeojavanicus* (Weidenreich, 1945; von Koenigswald, 1950), as well as the isolated hominid permanent lower molars Sangiran 7–20, Sangiran 7–65, and SMF-8888, all of whose taxonomic attribution to *H. erectus*, *Meganthropus* or even *Pongo* remain uncertain. Indeed, Indonesian hominid diversity across the Pleistocene has been a matter of contention for over a century (rev. in Zanolli et al., 2019a). Due to the marked morphological and metric variation characterizing the larger fossil assemblage from which these specimens derive, some robust specimens from Sangiran have been alternatively allocated to various hominid taxa (e.g., *Pithecanthropus dubius*, *Meganthropus palaeojavanicus*, *Pongo* sp.) (von Koenigswald, 1950; Tyler, 2004). More recently, the variation displayed by the Indonesian assemblage has also been regarded as being compatible with a single taxon, *Homo erectus* (e.g., Kaifu et al., 2005). In contrast, new analyses of the endostructural signature virtually extracted from some of the Sangiran specimens using a combination of X-μCT, SR-μCT, and n-μCT have revealed a higher level of taxonomic diversity than previously recognized, thus supporting the validity of the taxon *Meganthropus*, an ape that coexisted during the Early to Middle Pleistocene in the region with *H. erectus*, *Pongo* and, perhaps, also *Gigantopithecus* (Zanolli et al., 2019a). All fossils from the Sangiran Dome formations considered in this study are stored at the Senckenberg Research Institute and Natural History Frankfurt in Frankfurt am Main, Germany.

Methods of Analysis

The left portion of the mandible SNSB-BSPG 1939 X 4, the right portion of the mandible UR 501 and the four dentognathic specimens from Sangiran (Sangiran 6a, Sangiran 7–20, Sangiran 7–65, and SMF-8888) were scanned between 2016 and 2018 at the ANTARES imaging facility located at the FRM II reactor of the Technical University of Munich, Germany. The facility operates on one channel (of two) of the cold neutron beamline SR4, being the only cold neutron imaging facility at a reactor with direct sight to the cold source with neutron flight tubes instead of neutron guides. Due to this architecture, neutrons travel on a straight flight path and do not lose collimation and spectral homogeneity by reflection on neutron guides. There are two chambers containing sample and detector positions, one for samples up to 15 cm in size, and another one for larger samples up to 30 cm (Schillinger et al., 2018).

The neutron beam originates from the cold source of the FRM II reactor with an energy range mostly from 3 to 25 meV, a collimation ratio of L/D = 500 (the ratio between the sample-detector distance and collimator aperture), and an intensity of 6.4×10^7 n/cm^{2}s. A 20 μm Gadox screen was used to detect neutrons. Both a cooled, charge-coupled device camera (ikon-L 936; Andor) and a cooled complementary metal-oxide semiconductor camera (Neo 5.5 sCMOS; Andor) were used as detectors. The final virtual volume of the analyzed specimens was reconstructed with an isotropic voxel size of 20–27 μm, i.e., at resolutions directly comparable to the X-ray-based microtomographic records commonly used in studies of fossil primate teeth.

All specimens were also preliminarily imaged by X-μCT at comparable resolutions (**Table 1**). For two of them, Sangiran 7–20 and Sangiran 7–65, a SR-μCT record was produced at the European Synchrotron Radiation Facility of Grenoble, France, within the context of another independent study (Smith et al., 2018) and made available online[1].

Because in both X-μCT and n-μCT the detection of the tissue interfaces is based on attenuation at the boundary of the target, we performed a threshold-based segmentation as usually applied for X-ray acquisitions (Beaudet et al., 2016; Zanolli et al., 2017b; Schillinger et al., 2018). Due to parallel beam geometry and much lower source intensity with respect to X-ray-based analyses (the neutron beam contains about three to five orders of magnitude fewer particles than an X-ray or synchrotron beam contains photons), the reconstructed n-μCT images are generally noisier than those obtained at comparable spatial resolutions by X-μCT or SR-μCT (**Figure 1**) with much higher counting statistics. Thus, a median filter with a kernel size of 2–3 was applied to the n-μCT records both prior to and during the segmentation process, and manual corrections were also locally applied to eliminate the remaining artifacts (Zanolli et al., 2017b, 2019a; Schillinger et al., 2018). A previous test performed on a fossil hominid tooth on

[1]http://paleo.esrf.fr

TABLE 1 | Acquisition parameters of the X-μCT and n-μCT records of the specimens used in this study.

Specimen	Chronology	Origin	X-μCT					n-μCT			
			Instrument	Voltage	Current	Filter	Projections	Voxel size	Energy range	L/D collimation ratio	Intensity	Voxel size
SNSB-BSPG 1939 X 4	Tortonian	Pakistan	Nanotom m	140 kv	0.02 mA	0.2 mm Cu	1400	51.9 μm	3–25 meV	500	6.4 × 10^7 n/cm^2s	27.1 μm
HCRP-U18-501	Gelasian	Malawi	BIR SN001	150 kV	0.11 mA	0.5 mm brass	5000	32.8 μm	3–25 meV	500	6.4 × 10^7 n/cm^2s	26.0 μm
Sangiran 6a	Early Middle Pleistocene	Java	BIR SN001	150 kV	0.11 mA	0.5 mm brass	5000	39.3 μm	3–25 meV	500	6.4 × 10^7 n/cm^2s	20.5 μm
Sangiran 7–20	Early Middle Pleistocene	Java	Skyscan 1172	100 kV	0.10 mA	Al + Cu	3000	13.7 μm	3–25 meV	500	6.4 × 10^7 n/cm^2s	19.5 μm
Sangiran 7–65	Early Middle Pleistocene	Java	Skyscan 1172	100 kV	0.10 mA	Al + Cu	1800	27.5 μm	3–25 meV	500	6.4 × 10^7 n/cm^2s	22.0 μm
SMF-8888	Early Middle Pleistocene	Java	Nanotom	100 kV	0.07 mA	none	1800	25.8 μm	3–25 meV	500	6.4 × 10^7 n/cm^2s	21.7 μm

*Acquisition parameters of the SR-μCT data are detailed below the table (see asterisk). *The SR-μCT records of Sangiran 7–20 and Sangiran 7–65 were downloaded from the European Synchrotron Radiation Facility Paleontological Microtomographic Database (see text footnote 1). These specific data were acquired on beamline ID 19 at the European Synchrotron Radiation Facility (ESRF, Grenoble, France), with an average energy of 68.3 keV filtering the white beam of the ID19 W150 wiggler set at a gap of 35 mm by 3 mm of aluminum, 0.25 mm of copper and 0.06 mm of tungsten, using a FReLoN 2K14 CCD camera in frame transfer mode, a 24 μm thick GGG:eu scintillator, and 5000 projections of 0.3 s each in half-acquisition mode (Smith et al., 2018). The final dataset was generated with a voxel size of 4.96 μm, then downsampled to 20 μm for comparison with the n-μCT data.*

FIGURE 1 | Comparison between the X-μCT- **(A)** and n-μCT-based **(B)** virtual sections through the mesial cusps of a modern human maxillary M3. The enamel (light gray) – dentine (dark gray) boundary is distinctly traceable in both cases. The total acquisition times to scan the specimen were of 120′ (X-μCT) and 22 h (n-μCT).

the degree of coherence between the X-μCT and n-μCT data sets showed average volume differences <5% (Zanolli et al., 2019a).

RESULTS

Both the X-μCT and n-μCT records of the *Sivapithecus parvada* mandible SNSB-BSPG 1939 X 4 provided relatively good contrast between enamel and dentine tissues (**Figure 2**). For example, in both records the linear measure of the maximal cuspal enamel thickness assessed here at the protoconid cusp of the m2 (**Figure 2**) ranges from 1.68 to 1.75 mm. However, X-ray- and neutron-based imaging do not systematically render the same structural information. As imaged by X-rays, the internal structure of the mandibular corpus appears as nearly uniform gray, while relevant details are revealed by the neutron record (**Figures 2C,D**). In the latter case the endosteal perimeter can be confidently traced and the distinction among cortical shell, trabecular bone and matrix infill can be discerned, thus allowing assessment of topographic variation in cortical bone thickness and, at least at some site-specific ROIs and limited VOIs, assessment of 2-3D local textural properties of the cancellous

FIGURE 2 | 3D virtual rendering of the *Sivapithecus parvada* left mandibular corpus, SNSB-BSPG 1939 X 4, in lingual **(A)** and occlusal **(B)** views. The longitudinal virtual sections through the corpus [orange line, in **(B)**] were extracted from the X-μCT **(C)** and n-μCT **(D)** records, respectively. The dotted white line in **(D)** shows the endosteal margin of the cortical bone, not visible in **(C)**.

network, such as strut thickness and orientation. The neutron record also much more clearly reveals the multiple breaks affecting the molar roots, especially those of the m2, evidence hardly appreciable on the entire set of related X-μCT-based slices. In paleobiological research, qualifying and quantifying the degree of internal taphonomic alteration is critical, particularly when planning for potentially invasive sampling.

Additional differences between the two records of SNSB-BSPG 1939 X 4 are evident by comparing the virtual sections through the mesial m2 cusps (**Figure 3**). While both imaging types show similar contrasts between enamel and dentine, the X-μCT reveals poor contrast between bone and radicular dentine and, in addition to failing to render root cracking, also masks the extent of bone micro-fragmentation between the roots, a feature distinctly unveiled by n-μCT (**Figures 3A,B**). It is noteworthy that, besides more easily penetrating denser materials generally opaque to X-rays, neutrons also actively interact with light chemical elements, such as hydrogen or lithium (Tremsin et al., 2015), occurring in the glues commonly used to fix broken specimens, or in the varnishes formerly employed to coat the fossils. In the case of SNSB-BSPG 1939 X 4, the interaction of neutrons with these light elements is revealed by brighter areas such as those occurring along the breakages present at the base of the m2 crown, originally consolidated by glue (**Figure 3B**); this information is missing in the corresponding X-μCT image (**Figure 3A**).

The partial mandible UR 501 from Malawi and virtual sections through its right m1 are shown in **Figure 4**. In this densely mineralized specimen, X-μCT reveals only faint contrasts between bone and dentine, while the endosteal contour of the cortical bone is distinguishable from the homogenized inner cancellous network and sedimentary matrix (**Figure 4C**). However, no distinction is discernable between enamel and dentine. This is likely due to a combination of factors, including remineralization of the dental tissues during fossilization and the taphonomic inclusion of heavy elements absorbing part of the X radiation, a phenomenon visible as saturation overflow in the X-μCT images (**Figure 4C**). Using the X-μCT record, a recent study tentatively segmented and imaged the m2 pulp chamber, but the result is incomplete (Kupczik et al., 2019: **Figure 4B**). In contrast, n-μCT distinctly distinguishes cortical bone from the sedimentary matrix and also reveals some details of the porous cancellous network (**Figure 4D**). The conformation of the enamel-dentine junction (EDJ) of the p4 and first two molars, useful in taxonomic comparisons among extinct hominids (Skinner et al., 2008, 2016; Zanolli et al., 2012, 2014, 2019a; Macchiarelli et al., 2013; Pan et al., 2017), can also be visualized and confidently assessed (**Figure 5**).

Both X-μCT and n-μCT of Sangiran 6a from Early Pleistocene Java revealed good contrast between the m1 enamel and dentine (**Figures 6A,B**). This permitted two independent segmentations of this specimen to compare measurements of 3D virtual EDJ surfaces. Our repeated tests show that, when superimposing the X-μCT- and n-μCT-based surfaces, the differences do not exceed the 240 μm distance between the faces of each surface, with an average of 65.7 μm (Zanolli et al., 2019a). Considering the difference in voxel size between the original records (39.3 and

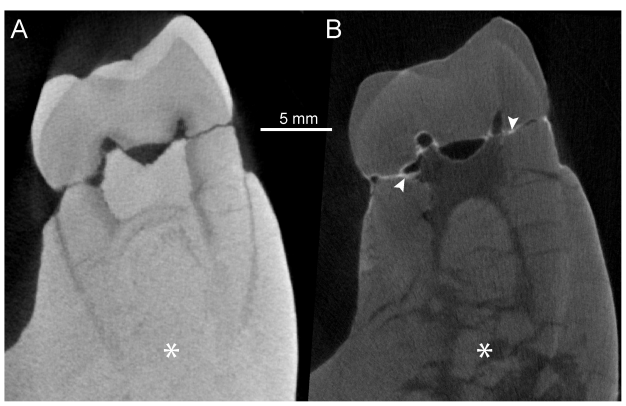

FIGURE 3 | X-μCT- **(A)** and n-μCT-based **(B)** virtual sections through the mesial cusps of the left m2 of SNSB-BSPG 1939 X 4 (*S. parvada*). The white arrows in **(B)** highlight areas where lighter elements contained in the glue originally used to consolidate the specimen absorbed more neutrons, thus generating a whiter fringe along the fractures. The asterisks, respectively, indicate **(A)** the lack of structural signal in the X-μCT section and **(B)** the actual degree of bone and radicular micro-fragmentation uniquely revealed by n-μCT imaging.

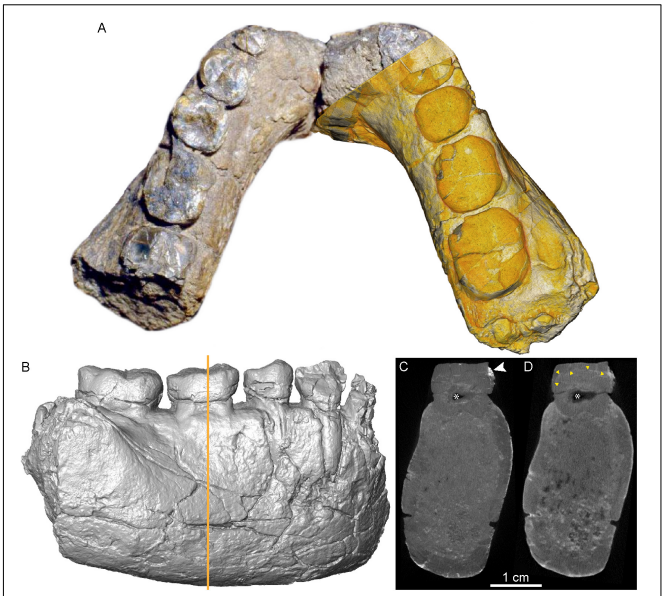

FIGURE 4 | Photomontage of the UR 501 hominin mandible, with the n-μCT-based 3D rendering virtually superimposed over the right portion **(A)**. The X-μCT-based rendering of the same portion in buccal view is shown in **(B)**. The coronal virtual sections through the corpus [orange line in **(B)**] were respectively, extracted from the X-μCT **(C)** and the n-μCT **(D)** records. The white arrow in **(C)** highlights a denser area that absorbed more X-rays, creating a local saturation overflow that overwhelms the rest of the contrast range, thus reducing contrasts between enamel and dentine. The yellow arrow heads in **(D)** indicate the enamel-dentine boundary, not visible in **(C)**. The asterisks in **(C)** and **(D)** show differences in imaging of the pulp chamber, which is partially infilled with sediment (nearly transparent in the neutron analysis).

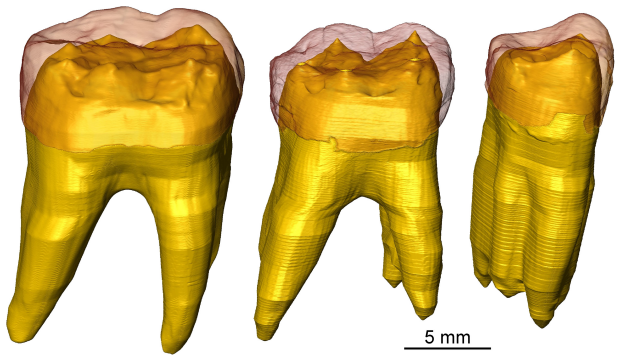

FIGURE 5 | n-μCT-based 3D surfaces of the virtually extracted right p4, m1, and m2 of the UR 501 mandible, with the reddish enamel in semi-transparency revealing details of the EDJ and the crown and radicular dentine rendered in yellow.

20.5 μm for, respectively, X-μCT and n-μCT), such differences can be considered as negligible. In fact, measurements of the enamel and crown dentine volumes (the latter including the crown pulp), show differences of <3 μm^3, which represents less than 1% of the respective volumes (Zanolli et al., 2019a). This demonstrates a high level of concordance between the X-ray- and neutron-based records, even in the rendering of micro-features such as details of the EDJ morphology (**Figures 6C–F**).

However, due to diagenetic changes, only a fraction of dentognathic fossil specimens imaged by industrial X-μCTs provide results as satisfactory as those obtained on Sangiran 6 (e.g., Olejniczak and Grine, 2006; Zanolli et al., 2015, 2019a). This is true for a large majority of the Early Middle Pleistocene isolated hominid teeth from Java, for which X-μCT records of endostructural features are largely unsatisfactory (Smith et al., 2009; Zanolli et al., 2017b, 2019a; Schillinger et al., 2018), and for which interfaces among enamel, dentine, bone and sediment are sometimes difficult to distinguish. The same is true even using SR-μCT (Smith et al., 2009, 2018). This was also found to be the case with the three isolated lower molars from the Sangiran Dome considered in this study.

The X-μCT scan of the lower molar crown SMF-8888 resulted in a rather homogeneous gray signal, with no contrasts among the subocclusal structures (**Figure 7A**). Conversely, the n-μCT record of this specimen unambiguously distinguishes between enamel and dentine, and also reveals the shape of the pulp horns, barely perceptible on the X-ray images (**Figure 7B**). Similarly, the original X-μCT record of the lower molar Sangiran 7–20 showed no internal contrasts, whereas the SR-μCT scan revealed some tissue-related density differences (**Figure 8A**). However, the contrasts are moderate and there are a number of marginal bright areas resulting from phase contrast imaging that make the segmentation of dental tissues arduous (Smith et al., 2018; see SR-μCT data available at http://paleo.esrf.eu/picture.php?/3229/category/2223). Despite the presence of some noise in the

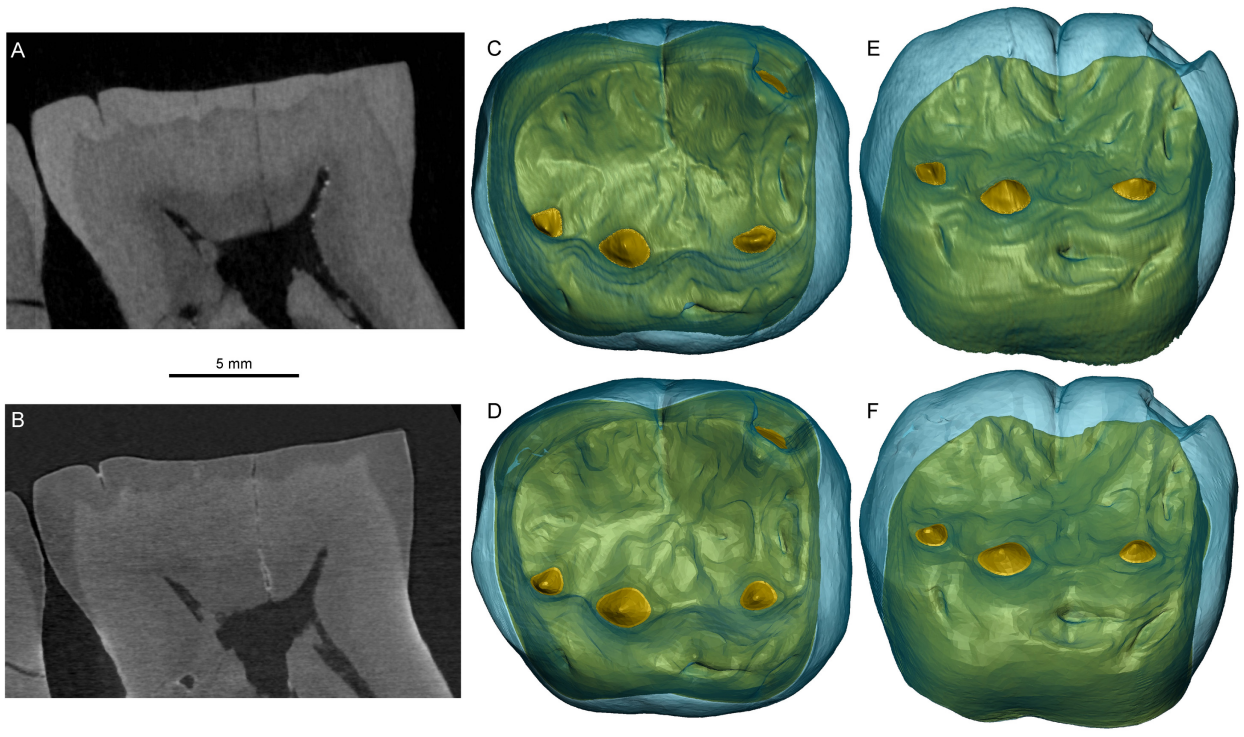

FIGURE 6 | X-μCT- **(A)** and n-μCT-based **(B)** mesiodistal virtual sections through the middle of the right m1 of the Sangiran 6a mandible (*Meganthropus palaeojavanicus*). The 3D renderings of the crown, respectively, generated by the X-ray-based **(C,E)** and neutron-based **(D,F)** records are shown in occlusal **(C,D)**, and occlusobuccal **(E,F)** views.

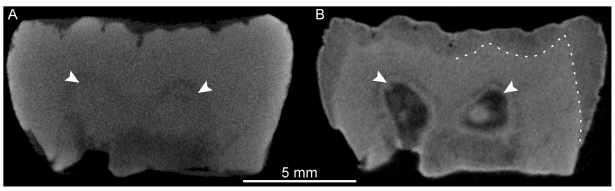

FIGURE 7 | X-μCT- **(A)** and n-μCT-based **(B)** mesiodistal virtual sections through the buccal cusps of the lower molar SMF-8888. The white arrows indicate the positions of two pulp horns barely discernible on the X-ray image **(A)** but clearly rendered by the neutron-based record **(B)**. The dotted line in **(B)** highlights the enamel-dentine boundary, not visible in **(A)**.

record, neutron imaging separates the darker gray enamel from the lighter gray dentine (**Figure 8B**). In contrast to the model generated from the original X-μCT record, the 3D surfaces, respectively, derived from SR-μCT (**Figure 8C**) and n-μCT (**Figure 8D**) are compatible in rendering subtle features of the EDJ, notably the five low but well-expressed dentine horns and the faint crests emanating from them. Finally, in the case of the lower molar Sangiran 7–65, neither the X-μCT nor SR-μCT records produced contrasts sufficient to distinguish enamel and dentine across the whole crown (**Figures 9A,B**). In some SR-μCT virtual slices the phase contrast fringes appearing along some fractures may even be confounded with the contour of the EDJ interface (**Figure 9B**). Misinterpreting these features would lead to the false assessment of extremely thick enamel in this specimen, reaching an apparent thickness of 2.08 mm at the level of the orange arrow in **Figure 9B**. Instead, as revealed by the neutron analysis, the EDJ contour (**Figure 9C**) is much nearer the enamel occlusal surface (**Figure 9D**), with actual enamel thickness at the same point being at most 1.15 mm.

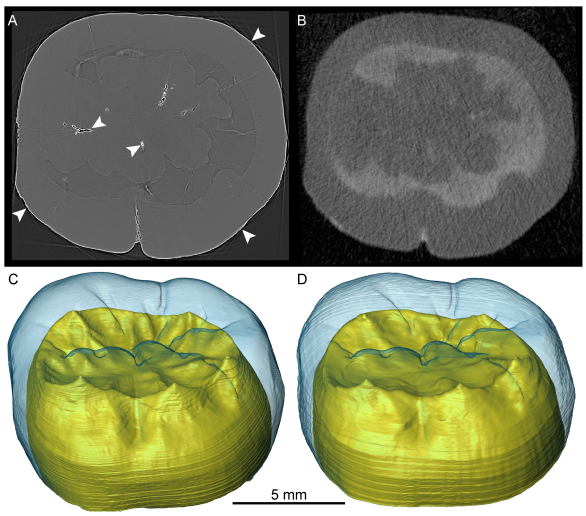

FIGURE 8 | SR-μCT- **(A)** and n-μCT-based **(B)** transverse virtual cross-sections of the crown of the lower molar Sangiran 7–20. The corresponding 3D surfaces are shown in **(C,D)**, respectively, where the blue enamel in semi-transparency reveals details of the EDJ and the crown dentine is rendered in yellow. The white arrows in **(A)** show the bright fringes produced by the phase contrast effect.

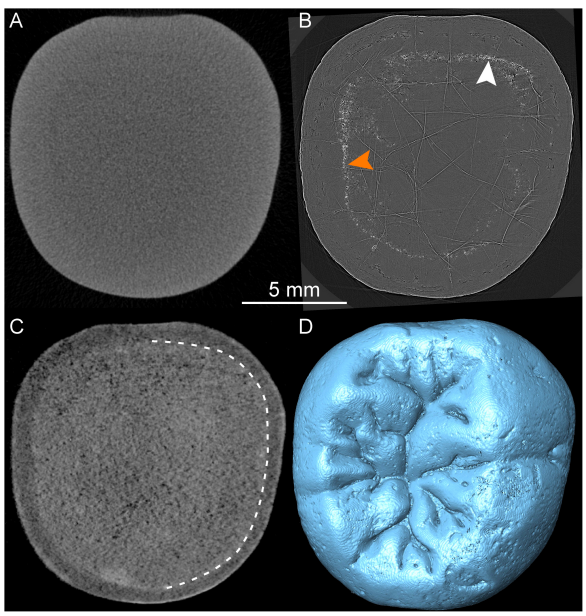

FIGURE 9 | X-μCT- **(A)**, SR-μCT- **(B)**, and n-μCT-based **(C)** transverse virtual cross-sections of the crown of the lower molar Sangiran 7–65. The SR-μCT-based 3D rendering of the crown occlusal morphology is shown in **(D)**. The white and orange arrows in **(B)** show the bright fringes produced by the phase contrast effect. The dotted line in **(C)** indicates the enamel-dentine boundary, not visible in **(A)** (X-μCT) or **(B)** (SR-μCT).

DISCUSSION

Industrial X-μCT instruments are now increasingly available for routine analyses in national museums and research institutions and are generally regarded as the best-suited tool for the non-invasive and non-destructive examination, and virtual "immortalization," of cultural heritage and fossil remains (Macchiarelli and Weniger, 2011). However, as commonly experienced by researchers investigating highly re-mineralized specimens, SR-μCT phase-contrast imaging may be a much more effective analytical tool (Paganin and Pellicia, 2019), capable of rendering subtle details even at infra-micrometric scale (e.g., Le Cabec et al., 2015, 2017; Smith et al., 2015, 2018; Xing et al., 2019). The recent use of n-μCT in paleoanthropology is revealing new and exciting opportunities for examining fossil specimens of higher density whose inner structural organization cannot be satisfactorily rendered by X-ray-based equipment (Beaudet et al., 2016; Urciuoli et al., 2017; Zanolli et al., 2017b, 2019a; Schillinger et al., 2018).

With X-μCT and SR-μCT, imaging contrasts among different materials result from the interactions of the X-rays with the electrons of the target (i.e., photoelectric and Compton effects), which depend on the atomic number of its elements. The contrasts obtained by X-rays are due to different natural absorption and scattering properties of the analyzed materials,

and to the different electron cloud densities surrounding the atoms within them (Winkler, 2006; Sutton, 2008). Thus, in the case of densely re-mineralized specimens, X-rays might be highly absorbed and thus deliver weak contrast signals (e.g., Skinner et al., 2013, 2015; Zanolli et al., 2015). Since neutrons, as neutral particles, are only absorbed or scattered by the nucleus of the atom, this does not apply to neutron-based analyses. n-μCT's imaging contrast depends only on the composition of the nuclei in the sample, often showing high attenuation (absorption and scattering) differences between neighboring elements, and even between isotopes of the same element (Kardjilov et al., 2003; Winkler, 2006; Tremsin et al., 2015). While enamel and dentine are originally mainly composed of hydroxyapatite $[Ca_{10}(PO_4)_6(OH)_2]$, they also integrate different proportions of organic matter and water that are almost always eliminated in fossil specimens and eventually replaced by various elements during diagenesis. Therefore, it is likely the differences in composition of hydroxyapatite in the mineralized dental tissues that are mostly responsible for the different contrasts in the virtual images. Hydrogen is a special case, as it attenuates neutron beams by equal-mass scattering. This is why glues and coatings that contain a high level of hydrogen (and other light elements) appear well-visible in neutron analyses (see **Figure 3**). For this reason, and because they could also affect future biomolecular analyses, chemical products should be used sparingly when preparing and restoring fossils (Le Cabec and Toussaint, 2017).

Compared with X-rays, neutrons also have the ability to penetrate materials with minimal attenuation (Tremsin et al., 2015) and are thus well-suited to analyze the internal structure of geological and paleontological samples, especially to distinguish between mineralized tissues and matrix (Schwarz et al., 2005; Sutton, 2008; Beaudet et al., 2016; Zanolli et al., 2017b; Schillinger et al., 2018). With recent advances in hardware and beamline settings, n-μCT can now reach a resolution of <5 μm, closing the gap with X-μCT instruments. In any case, neutron analyses deliver high imaging contrasts different from those of X-rays, and are therefore complementary (Sutton, 2008). In addition, the very low energies of cold neutrons and consequent weak interactions with matter make them penetrative and non-destructive, including for organic matter like DNA and proteins (Lakey, 2009). Thus, compared with SR-μCT, which can affect DNA preservation in fossil samples (Immel et al., 2016), n-μCT represents a very safe approach to investigate the internal structure of biological and fossilized materials without damaging the potentially preserved organic molecules.

Even if neutron analyses represent a viable complement or alternative to X-ray investigations, they also have limitations and downsides. First, compared with availability of synchrotrons in many countries worldwide, there are only a handful of neutron facilities that can perform high-resolution n-μCT scans. These include ANTARES at the Technical University of Munich in Germany, ICON at the Paul Scherrer Institute in Switzerland, NEXT at the Institut Laue-Langevin in France, NIST at the National Institute of Standards and Technology in the United States, and DINGO at the Australian Nuclear Science and Technology Organisation in Australia (Lehmann, 2017; Schillinger et al., 2018), plus a few more emerging facilities. As is the case with synchrotrons, access to these n-μCT facilities is based on the acceptance of *ad hoc* scientific proposals following a solicitation, and beamtime is generally limited to a few days per year. A further limitation is that n-μCT acquisition for fossil material takes several hours, as the exposure time needs to be long-enough to record sufficient signal (on average, each scan performed in this study required 20 h with exposure times between 30 and 90 s/projection) and the number of needed projections to get a high resolution is quite large (877 projections in total for each analysis performed in this study). However, in contrast to X-rays, which are strongly absorbed by materials such as fossil mineralized tissues, with n-μCT several isolated specimens can be scanned simultaneously without losing contrast quality. For example, 10–20 isolated hominid teeth were scanned in each acquisition at ANTARES, including the three specimens from Sangiran illustrated here. Another important aspect to consider is the temporary increase of radioactivity of the material induced by the neutron radiation absorbed during n-μCT scanning. As proscribed by national and international radioprotection legislation, irradiated samples have to be kept on-site in radiation-proof safes until they return to the natural background level of radioactivity and are authorized to leave the facility. However, the level of radioactivity of the specimens just after an acquisition is low (a few tens to hundreds of μSv) and generally decreases quickly. In the last 5 years, some hundreds of fossils from various time periods, locations and geological contexts have been analyzed at ANTARES, and all came back to their natural radioactivity level after some days or a few weeks (on average, after 12–15 days) to then be returned to the institutions where they are permanently stored.

As demonstrated in this study, neutron imaging reveals structural information that is not always visible with X-rays. In the case of the Miocene specimen SNSB-BSPG 1939 X 4 attributed to *S. parvada*, enamel and dentine are well-distinguished on both X-μCT and n-μCT images, while the internal bone structure and its damages are only visible on the neutron record. Mandibular cortical bone thickness is partly linked with functionally related strains of mastication and feeding behaviors (see Genochio et al., 2019). Thanks to n-μCT, the assessment of cortical thickness is now possible in this specimen, and together with the study of teeth, its analysis will potentially reveal new information on the biomechanical adaptions and taxonomic-related features of this species.

Among the examples presented in this study illustrating the variable nature and quality of the endostructural signals comparatively rendered by X-ray- and neutron-based records, those of the partial mandibles UR 501 from Malawi, and Sangiran 6a from Java, deserve further comment because of the taxonomic implications of the results. As briefly mentioned, the 2.3–2.5 Ma specimen UR 501 shows outer morphological and dimensional affinities with both *Homo habilis* (e.g., OH 7 and KNM-ER 1802) and early *Homo* (e.g., KNM-ER 64060) remains (Spoor et al., 2015; Grine et al., 2019), while its plate-like premolar roots and some microanatomical features of the teeth resemble those of *Paranthropus* (Kullmer et al., 2011). Indeed, its taxonomic attribution (Schrenk et al., 1993) and that of the few other African earliest Pleistocene fossils regarded as potentially representing earliest members of the genus *Homo* is still debated (Wood and Boyle, 2016; Villmoare, 2018). As summarized in

Figures 4, **5**, the n-μCT imaging of UR 501 recently allowed the extraction of information from the postcanine dentition of this specimen previously unavailable on the basis of the X-μCT record. In particular, a comparative geometric morphometric (GM) analysis of the molar EDJ with representatives of the taxa *Australopithecus*, *Paranthropus*, and *Homo* now suggests that UR 501 may be more closely related to the australopiths than to *Homo* (Zanolli et al., 2019b). Combined with new paleoecological scenarios associated with the Malawian hominin fossil record (Lüdecke et al., 2018), these results highlight the complexities of the phylogenetic and biogeographic history of early *Homo* and stimulate the discussion about the emergence of our own genus.

Concerning Sangiran 6a, because of its especially large size and primitive morphology, it was originally attributed to the taxon *Meganthropus* (Weidenreich, 1945; von Koenigswald, 1950), but was shortly thereafter integrated into the growing *H. erectus s.s.* hypodigm (e.g., Kaifu et al., 2005). Indeed, following the discovery at Trinil in 1891 of *Pithecanthropus* (*Homo*) *erectus* by E. Dubois (1894), the taxonomic attribution of some of the most robust hominid specimens from Java became the object of intense debate for nearly a century, and the question of the hypothetical presence of a non-*Pongo* great ape penecontemporaneous with *H. erectus* in the region remained unanswered (Ciochon, 2009). In the case of Sangiran 6a, the combined use of X-μCT and n-μCT analyses unveiled details of internal structure demonstrating that, together with other robust Javanese remains, this specimen actually belongs to the non-hominin hominid *Meganthropus palaeojavanicus* (Zanolli et al., 2019a). However, for other isolated teeth from the Pleistocene of Indonesia, both X-μCT and even SR-μCT analyses failed to deliver sufficient contrast between tissues to confidently assess their characteristics (e.g., Smith et al., 2009, 2018). Conversely, as illustrated by the three specimens Sangiran 7–20, Sangiran 7–65, and SMF-8888, the n-μCT record illuminated critical qualitative and quantitative information invisible by X-ray imaging.

CONCLUSION

It is likely that the Miocene to Pleistocene available fossil record only samples a portion of actual hominid and hominin taxonomic paleodiversity (e.g., Haile-Selassie et al., 2016; Wood and Boyle, 2016). Thus, the importance of continually developing preferably non-destructive investigative methods capable of maximizing the information extracted from typically fragmentary and scattered remains. Recently developed advanced technologies now enable the high-resolution imaging and subtle characterization of both external and internal morphology of fossil specimens, assuring both a virtual repository of this fragile record and providing the capability of "virtual dissection" at unprecedented levels of detail. Thanks to progresses in hardware technologies, increases in computing power, the emergence of commercial and free software dedicated to the analysis of 3D data, and to the dissemination of universal formats and Internet facilities, it has become possible to store and share online databases and to easily exchange images and data from fossil specimens worldwide in real time, a genuine revolution in the traditionally parsed field of paleoanthropology (Rook et al., 2004; Macchiarelli et al., 2008, 2013; Macchiarelli and Weniger, 2011; Hublin, 2013; Skinner et al., 2013). In this realm, X-ray-based analytical tools remain the first choice for the study of fossil specimens, and their systematic use to build "digital archives" easily accessible to students and researchers worldwide should be encouraged and supported by *ad hoc* programs. However, whenever X-rays, given their limited penetration range, fail to render important endostructural details, neutron imaging represents a complementary and/or alternative analytical solution.

Following our ongoing examinations, we predict that the use of n-μCT will contribute in the near future to significantly increase the quality and amount of paleobiological information routinely extracted from the fossil record and, with special reference to dentognathic remains, will likely play a relevant role in answering questions about the taxonomic status of some still controversial specimens, including those potentially representing early *Homo*.

DATA AVAILABILITY STATEMENT

All data supporting the findings of this study are included in the article.

AUTHOR CONTRIBUTIONS

CZ, OK, FS, and RM designed the research. CZ, BS, OK, JK, and GR realized the *n*-μCT analyses of the fossil specimens. GR performed the X-μCT scan of SNSB-BSPG 1939 X 4. CZ performed the segmentation and extracted the data for this study. All authors contributed to the discussion and interpretation of the results. CZ and RM wrote the manuscript with contributions from all other authors.

FUNDING

FRM II measurements were supported by the European Commission under the 7th Framework Program through the "Research Infrastructures" action of the "Capacities" Program NMI3-II (grant number 283883). This project was produced with financial support from the French National Research Agency (ANR) under the Investments for the Future Scheme, within the LaScArBx Cluster (ANR-10-LABX-52).

ACKNOWLEDGMENTS

We thank the co-editors L. Pandolfi, L. Rook, P. Raia, and J. Fortuny for their kind invitation to contribute to this special volume "Evolving Virtual and Computational Palaeontology." We acknowledge the Bavarian Natural History Collections for access to its X-μCT instrument, and the Department of Human Evolution at the Max Planck Institute for Evolutionary Anthropology, Leipzig, for access to the comparative X-μCT records of the UR 501 mandible and Sangiran 7–20, Sangiran

7–65, and SMF-8888 isolated teeth. T. L. Kivell, C. B. Ruff, and E. Trinkaus kindly provided bibliographic information. We express our gratitude to the Werner Reimers Foundation in Bad Homburg, which provides the Gustav Heinrich Ralph von Koenigswald collection as a permanent loan for scientific research to the Senckenberg Research Institute and Natural History Museum Frankfurt. We also thank A. Beaudet for discussion. Finally, we gratefully acknowledge the financial support provided by FRM II to perform the neutron measurements at the Heinz Maier-Leibnitz Zentrum (MLZ), Garching, Germany.

REFERENCES

Barak, M. M., Lieberman, D. E., Raichlen, D., Pontzer, H., Warrener, A. G., and Hublin, J.-J. (2013). Trabecular evidence for a human-like gait in *Australopithecus africanus*. *PLoS One* 8:e77687. doi: 10.1371/journal.pone.0077687

Bayle, P., Bondioli, L., Macchiarelli, R., Mazurier, A., Puymerail, L., Volpato, V., et al. (2011). "Three-dimensional imaging and quantitative characterization of human fossil remains. Examples from the Nespos database," in *Pleistocene Databases: Acquisition Storing Sharing*, eds R. Macchiarelli, and G. C. Weniger (Mettmann: Wissenschaftliche Schriften des Neanderthal Museums 4), 29–46.

Bayle, P., Braga, J., Mazurier, A., and Macchiarelli, R. (2009). Dental developmental pattern of the Neanderthal child from Roc de Marsal: a high-resolution 3D analysis. *J. Hum. Evol.* 56, 66–75. doi: 10.1016/j.jhevol.2008.09.002

Beaudet, A. (2019). The inner ear of the *Paranthropus* specimen DNH 22 from Drimolen. *South Africa. Am. J. Phys. Anthropol.* 170, 439–446. doi: 10.1002/ajpa.23901

Beaudet, A., Braga, J., de Beer, F., Schillinger, B., Steininger, C., Vodopivec, V., et al. (2016). Neutron microtomography-based virtual extraction and analysis of a cercopithecoid partial cranium (STS 1039) embedded in a breccia fragment from Sterkfontein Member 4 (South Africa). *Am. J. Phys. Anthropol.* 159, 737–745. doi: 10.1002/ajpa.22916

Beaudet, A., Carlson, K. J., Clarke, R. J., de Beer, F., Dhaene, J., Heaton, J. L., et al. (2018). Cranial vault thickness variation and inner structural organization in the StW 578 hominin cranium from Jacovec Cavern. *South Africa. J. Hum. Evol.* 121, 204–220. doi: 10.1016/j.jhevol.2018.04.004

Beaudet, A., Zanolli, C., Engda Redae, B., Endalamaw, M., Braga, J., and Macchiarelli, R. (2015). A new cercopithecoid dentognathic specimen attributed to *Theropithecus* from the late Early Pleistocene (c. 1 Ma) deposits of Simbiro, at Melka Kunture. Ethiopian highlands. *C. R. Palevol.* 14, 657–669. doi: 10.1016/j.crpv.2015.07.003

Benazzi, S., Douka, K., Fornai, C., Bauer, C. C., Kullmer, O., Svoboda, J., et al. (2011a). Early dispersal of modern humans in Europe and implications for Neanderthal behaviour. *Nature* 479, 525–528. doi: 10.1038/nature10617

Benazzi, S., Viola, B., Kullmer, O., Fiorenza, L., Harvati, K., Paul, T., et al. (2011b). A reassessment of the Neanderthal teeth from Taddeo cave (southern Italy). *J. Hum. Evol.* 61, 377–387. doi: 10.1016/j.jhevol.2011.05.001

Braga, J. (2016). "Non-invasive imaging techniques," in *A Companion to Dental Anthropology*, eds J. D. Irish, and G. R. Scott (Chichester: John Wiley & Sons, Inc), 514–527.

Braga, J., Thackeray, F., Subsol, G., Kahn, J. L., Maret, D., Treil, J., et al. (2010). The enamel-dentine junction in the postcanine dentition of *Australopithecus africanus*: intra individual metameric and antimeric variation. *J. Anat.* 216, 62–79. doi: 10.1111/j.1469-7580.2009.01154.x

Cazenave, M., Braga, J., Oettlé, A., Pickering, T. R., Heaton, J. L., Nakatsukasa, M., et al. (2019a). Cortical bone distribution in the femoral neck of *Paranthropus robustus*. *J. Hum. Evol.* 135:102666. doi: 10.1016/j.jhevol.2019.102666

Cazenave, M., Oettlé, A., Thackeray, J. F., Nakatsukasa, M., de Beer, F., Hoffman, J., et al. (2019b). The SKX 1084 hominin patella from swartkrans member 2, South Africa: an integrated analysis of its outer morphology and inner structure. *C. R. Palevol.* 18, 223–235. doi: 10.1016/j.crpv.2018.06.002

Ciochon, R. (2009). The mystery ape of Pleistocene Asia. *Nature* 459, 910–911. doi: 10.1038/459910a

Conroy, G. C., and Vannier, M. W. (1985). "Endocranial volume determination of matrix-filled fossil skulls using high resolution computed tomography," in *Hominid Evolution: Past Present and Future*, ed. P. V. Tobias (New York, NY: Alan R. Liss, Inc), 419–426.

Conroy, G. C., and Vannier, M. W. (1987). Dental development of the Taung skull from computerized tomography. *Nature* 329, 625–627. doi: 10.1038/329625a0

Daegling, D. J. (1989). Biomechanics of cross-sectional size and shape in the hominoid mandibular corpus. *Am. J. Phys. Anthropol.* 80, 91–106. doi: 10.1002/ajpa.1330800111

Dehm, R. (1983). "Miocene hominoid primate dental remains from the Siwaliks of Pakistan," in *New Interpretations of Ape and Human Ancestry*, eds R. L. Ciochon, and R. S. Corruccini (New York, NY: Plenum Publishing Corporation), 527–537. doi: 10.1007/978-1-4684-8854-8_20

DeSilva, J. M., and Devlin, M. J. (2012). A comparative study of the trabecular bony architecture of the talus in humans, non-human primates, and Australopithecus. *J. Hum. Evol.* 63, 536–551. doi: 10.1016/j.jhevol.2012.06.006

Dubois, E. (1894). *Pithecanthropus erectus, Eine Menschenaehnliche Ubergangsform Aus Java*. Batavia: Landesdruckerei.

Elliott, J. C., and Dover, S. D. (1982). X-ray microtomography. *J. Microsc.* 126, 211–213.

Genochio, L., Mazurier, A., Dumoncel, J., Theye, C. E. G., and Zanolli, C. (2019). Inner structural organization of the mandibular corpus in the late Early Pleistocene human specimens Tighenif 1 and Tighenif 2. *C. R. Palevol.* 18, 1073–1082. doi: 10.1016/j.crpv.2019.09.002

Gorjanović-Kramberger, D. (1906). "Der diluviale mensch von krapina in kroatien: ein beitrag zur paläoanthropologie," in *Studien über die Entwicklungs-Mechanik des Primatenskeletes. Kreidel, Wiesbaden*, Vol. II, ed. O. Walkhoff (Wiesbaden: Kreidel), 59–277.

Gorjanović-Kramberger, D. (1907). Die kronen und wurzeln der mahlzähne des *Homo primigenius* und ihre genetische bedeutung. *Anat. Anz.* 31, 97–134.

Grine, F. E., Leakey, M. G., Gathago, P. N., Brown, F. H., Mongle, C. S., Yang, D., et al. (2019). Complete permanent mandibular dentition of early *Homo* from the upper burgi member of the koobi fora formation. *Ileret, Kenya. J. Hum. Evol.* 131, 152–175. doi: 10.1016/j.jhevol.2019.03.017

Guatelli-Steinberg, D. (2016). *What Teeth Reveal about Human Evolution*. Cambridge: Cambridge University Press.

Haile-Selassie, Y., Melillo, S. M., and Su, D. F. (2016). The Pliocene hominin diversity conundrum: do more fossils mean less clarity? *Proc. Nat. Acad. Sci. U.S.A.* 113, 6364–6371. doi: 10.1073/pnas.1521266113

Haile-Selassie, Y., Melillo, S. M., Vazzana, A., Benazzi, S., and Ryan, T. M. (2019). A 3.8-million-year-old hominin cranium from Woranso-Mille. *Ethiopia. Nature* 573, 214–219. doi: 10.1038/s41586-019-1513-8

Hillson, S. (2014). *Tooth Development in Human Evolution and Bioarchaeology*. Cambridge: Cambridge University Press.

Hounsfield, G. N. (1973). Computerized transverse axial scanning (tomography): i. description of system. *Brit. J. Radiol.* 46, 1016–1022. doi: 10.1259/0007-1285-46-552-1016

Hounsfield, G. N. (1975). *Method of and Apparatus for Examining a Body by Radiation such as X or Gamma Radiation*. Patent specification 1283915. Bangalore: The Patent Office.

Hublin, J.-J. (2013). Free digital scans of human fossils. *Nature* 497:183. doi: 10.1038/497183a

Immel, A., Le Cabec, A., Bonazzi, M., Herbig, A., Temming, H., Schuenemann, V. J., et al. (2016). Effect of X-ray irradiation on ancient DNA in sub-fossil bones – Guidelines for safe X-ray imaging. *Sci. Rep.* 6:32969. doi: 10.1038/srep32969

Jaeger, J.-J., Aung Naing Soe, A. N., Chavasseau, O., Coster, P., Emonet, E.-G., Guy, F., et al. (2011). First hominoid from the Late Miocene of the Irrawaddy Formation (Myanmar). *PLoS One* 6:e17065. doi: 10.1371/journal.pone.0017065

Jungers, W. L., and Minns, F. L. J. (1979). Computed tomography and biomechanical analysis of fossil long bones. *Am. J. Phys. Anthropol.* 50, 285–290. doi: 10.1002/ajpa.1330500219

Kaifu, Y., Baba, H., Aziz, F., Indriati, E., Schrenk, F., and Jacob, T. (2005). Taxonomic affinities and evolutionary history of the Early Pleistocene hominids of Java: dentognathic evidence. *Am. J. Phys. Anthropol.* 128, 709–726. doi: 10.1002/ajpa.10425

Kappelman, J., Ketcham, R. A., Pearce, S., Todd, L., Akins, W., Colbert, M. W., et al. (2016). Perimortem fractures in Lucy suggest mortality from fall out of tall tree. *Nature* 537, 503–507. doi: 10.1038/nature19332

Kardjilov, N., Baechler, S., Bastürk, M., Dierick, M., Jolie, J., Lehmann, E., et al. (2003). New features in cold neutron radiography and tomography. Part II: applied energy-selective neutron radiography and tomography. *Nucl. Instr. Meth. Phys. Res. A* 501, 536–546. doi: 10.1016/s0168-9002(03)00423-6

Keith, A. (1913). Problems relating to the teeth of the earlier forms of prehistorical man. *Proc. Roy. Soc. Med.* 6, 103–119.

Kelley, J. (1988). A new large species of *Sivapithecus* from the Siwaliks of Pakistan. *J. Hum. Evol.* 17, 305–324. doi: 10.1016/0047-2484(88)90073-5

Kelley, J. (2002). "The hominoid radiation in Asia," in *The Primate Fossil Record*, ed. W. Hartwig (Cambridge: Cambridge University Press), 369–384.

Kivell, T. L. (2016). A review of trabecular bone functional adaptation: what have we learned from trabecular analyses in extant hominoids and what can we apply to fossils? *J. Anat.* 228, 569–594. doi: 10.1111/joa.12446

Kullmer, O. (2008). The fossil suidae from the Plio-Pleistocene Chiwondo beds of northern Malawi, Africa. *J. Vert. Paleont.* 208, 208–216. doi: 10.1671/0272-4634(2008)28[208:TFSFTP]2.0.CO;2

Kullmer, O., Sandrock, O., Kupczik, K., Frost, S. R., Volpato, V., Bromage, T. G., et al. (2011). New primate remains from Mwenirondo, Chiwondo beds in northern Malawi. *J. Hum. Evol.* 61, 617–623. doi: 10.1016/j.jhevol.2011.07.003

Kupczik, K., Delezene, L. K., and Skinner, M. M. (2019). Mandibular molar root and pulp cavity morphology in *Homo naledi* and other Plio-Pleistocene hominins. *J. Hum. Evol.* 130, 83–95. doi: 10.1016/j.jhevol.2019.03.007

Kupczik, K., and Hublin, J.-J. (2010). Mandibular molar root morphology in Neanderthals and Late Pleistocene and recent *Homo sapiens*. *J. Hum. Evol.* 59, 525–541. doi: 10.1016/j.jhevol.2010.05.009

Lakey, J. H. (2009). Neutrons for biologists: a beginner's guide, or why you should consider using neutrons. *J. R. Soc. Interface* 6, S567–S573. doi: 10.1098/rsif.2009.0156.focus

Le Cabec, A., Dean, M. C., and Begun, D. (2017). Dental development and age at death of the holotype of *Anapithecus hernyaki* (RUD 9) using synchrotron virtual histology. *J. Hum. Evol.* 108, 161–175. doi: 10.1016/j.jhevol.2017.03.007

Le Cabec, A., Gunz, P., Kupczik, K., Braga, J., and Hublin, J.-J. (2013). Anterior tooth root morphology and size in Neanderthals: taxonomic and functional implications. *J. Hum. Evol.* 64, 169–193. doi: 10.1016/j.jhevol.2012.08.011

Le Cabec, A., Tang, N., and Tafforeau, P. (2015). Accessing developmental information of fossil hominin teeth using new synchrotron microtomography-based visualization techniques of dental surfaces and interfaces. *PLoS One* 10:e0123019. doi: 10.1371/journal.pone.0123019

Le Cabec, A., and Toussaint, M. (2017). Impacts of curatorial and research practices on the preservation of fossil hominid remains. *J. Anthropol. Sci.* 95, 7–34. doi: 10.4436/JASS.95002

Le Roux, S. D., de Beer, F., and Thackeray, J. F. (1997). Neutron radiography of cranial bone of Sts 5 (*Australopithecus africanus*) from Sterkfontein. *South Afr.. S. Afr. J. Sci.* 93:176.

Lehmann, E. H. (2017). Neutron imaging facilities in a global context. *J. Imaging* 3, 52. doi: 10.3390/jimaging3040052

Lüdecke, T., Kullmer, O., Wacker, U., Sandrock, O., Fiebig, J., Schrenk, F., et al. (2018). Dietary versatility of Early Pleistocene hominins. *Proc. Nat. Acad. Sci. U.S.A.* 115, 13330–13335. doi: 10.1073/pnas.1809439115

Macchiarelli, R., Bayle, P., Bondioli, L., Mazurier, A., and Zanolli, C. (2013). "From outer to inner structural morphology in dental anthropology. The integration of the third dimension in the visualization and quantitative analysis of fossil remains," in *Anthropological Perspectives on Tooth Morphology: Genetics, Evolution, Variation*, eds R. G. Scott, and J. D. Irish (Cambridge: Cambridge University Press), 250–277. doi: 10.1017/cbo9780511984464.011

Macchiarelli, R., Bondioli, L., Debénath, A., Mazurier, A., Tournepiche, J.-F., Birch, W., et al. (2006). How Neanderthal molar teeth grew. *Nature* 444, 748–751. doi: 10.1038/nature05314

Macchiarelli, R., Bondioli, L., Falk, D., Faupl, P., Illerhaus, B., Kullmer, O., et al. (2004). Early Pliocene hominid tooth from Galili, Somali Region, Ethiopia. *Coll. Antropol.* 28, 65–76.

Macchiarelli, R., Bondioli, L., and Mazurier, A. (2008). "Virtual dentitions: touching the hidden evidence," in *Technique and Application in Dental Anthropology*, eds J. D. Irish, and G. C. Nelson (Cambridge: Cambridge University Press), 426–448. doi: 10.1017/cbo9780511542442.018

Macchiarelli, R., Mazurier, A., Illerhaus, B., and Zanolli, C. (2009). *Ouranopithecus macedoniensis* (Mammalia, Primates, Hominoidea): virtual reconstruction and 3D analysis of a juvenile mandibular dentition (RPl-82 and RPl-83). *Geodiversitas* 31, 851–864.

Macchiarelli, R., Mazurier, A., and Volpato, V. (2007). "L'apport des nouvelles technologies à l'étude des Néandertaliens," in *Les Néandertaliens. Biologie et Cultures*, eds B. Vandermeersch, and B. Maureille (Paris: : Comité des Travaux Historiques et Scientifiques), 169–179.

Macchiarelli, R., and Weniger, G.-C. (eds) (2011). *Pleistocene Databases. Acquisition, Storing, Sharing*. Mettmann: Wissenschaftliche Schriften des Neanderthal Museums 4.

Macchiarelli, R., and Zanolli, C. (2017). Hominin Biomechanics, virtual anatomy and inner structural morphology: from head to toe. A tribute to laurent puymerail. *C. R. Palevol.* 16, 493–498. doi: 10.1016/j.crpv.2017.06.001

Maret, D., Ove, A. P., Galibourg, A., Dumoncel, J., Esclassan, R., Kahn, J. L., et al. (2014). Comparison of the accuracy of 3-dimensional cone-beam computed tomography and micro-computed tomography reconstructions by using different voxel sizes. *J. Endod.* 40, 1321–1326. doi: 10.1016/j.joen.2014.04.014

Martínez de Pinillos, M., Martinón-Torres, M., Martín-Francés, L., Arsuaga, J. L., and Bermúdez de Castro, J. M. (2017). Comparative analysis of the trigonid crests patterns in *Homo antecessor* molars at the enamel and dentine surfaces. *Quat. Int.* 433, 189–198. doi: 10.1016/j.quaint.2015.08.050

Martín-Francés, L., Martinón-Torres, M., Martínez de Pinillos, M., García-Campos, C., Modesto-Mata, M., Zanolli, C., et al. (2018). Tooth crown tissue proportions and enamel thickness in Early Pleistocene *Homo antecessor* molars (Atapuerca. Spain). *PLoS One* 13:e0203334. doi: 10.1371/journal.pone.0203334

Martinón-Torres, M., Bermúdez de Castro, J. M., Martínez de Pinillos, M., Modesto-Mata, M., Xing, S., Martín-Francés, L., et al. (2019). New permanent teeth from gran dolina-TD6 (Sierra de Atapuerca). The bearing of *Homo antecessor* on the evolutionary scenario of Early and Middle Pleistocene Europe. *J. Hum. Evol.* 127, 93–117. doi: 10.1016/j.jhevol.2018.12.001

Mazurier, A., Volpato, V., and Macchiarelli, R. (2006). Improved noninvasive microstructural analysis of fossil tissues by means of SR-microtomography. *Appl. Phys. A* 83, 229–233. doi: 10.1007/s00339-006-3511-6

Meschan, I., Bo, W. J., and Krueger, W. A. (1979). The utilization of xeroradiography for radiography of cross-section of thin cadaveric slices. *Invest. Radiol.* 14, 97–102. doi: 10.1097/00004424-197901000-00015

Olejniczak, A. J., and Grine, F. E. (2005). High-resolution measurement of Neanderthal tooth enamel thickness by micro-focal computed tomography. *South Afr. J. Sci.* 101, 219–220.

Olejniczak, A. J., and Grine, F. E. (2006). Assessment of the accuracy of dental enamel thickness measurements using microfocal X-ray computed tomography. *Anat. Rec.* 288, 263–275. doi: 10.1002/ar.a.20307

Olejniczak, A. J., Smith, T. M., Feeney, R. N. M., Macchiarelli, R., Mazurier, A., Bondioli, L., et al. (2008). Dental tissue proportions and enamel thickness in Neandertal and modern human molars. *J. Hum. Evol.* 55, 12–23. doi: 10.1016/j.jhevol.2007.11.004

Paganin, D. M., and Pellicia, D. (2019). Tutorials on X-ray phase contrast imaging: some fundamentals and some conjectures on future developments. *arXiv*. [preprint]. Avaliable at: https://arxiv.org/abs/1902.00364 (accessed January 29, 2020).

Pan, L., Thackeray, J. F., Dumoncel, J., Zanolli, C., Oettlé, A., de Beer, F., et al. (2017). Intra-individual metameric variation expressed at the enamel-dentine junction of lower post-canine dentition of South African fossil hominins and modern humans. *Am. J. Phys. Anthropol.* 163, 806–815. doi: 10.1002/ajpa.23240

Pan, L., and Zanolli, C. (2019). Comparative observations on the premolar root and pulp canal configurations of Middle Pleistocene *Homo* in China. *Am. J. Phys. Anthropol.* 168, 637–646. doi: 10.1002/ajpa.23777

Pilbeam, D. R. (1982). New hominoid skull material from the Miocene of Pakistan. *Nature* 295, 232–234. doi: 10.1038/295232a0

Puymerail, L., Ruff, C. B., Bondioli, L., Widianto, H., Trinkaus, E., and Macchiarelli, R. (2012a). Structural analysis of the Kresna 11 *Homo erectus* femoral shaft (Sangiran. Java). *J. Hum. Evol.* 63, 741–749. doi: 10.1016/j.jhevol.2012.08.003

Puymerail, L., Volpato, V., Debenath, A., Mazurier, A., Tournepiche, J.-F., and Macchiarelli, R. (2012b). A Neanderthal partial femoral diaphysis from the "grotte de la Tour", La Chaise-de-Vouthon (Charente, France): outer

morphology and endostructural organization. *C. R. Palevol.* 11, 581–593. doi: 10.1016/j.crpv.2012.07.001

Röntgen, W. (1895). "Ueber eine neue art von strahlen. *vorläufige mitteilung*," in *Aus den Sitzungsberichten der Würzburger Physik.-medic. Gesellschaft Würzburg* (Berlin: Springer-Verlag), 137–147.

Rook, L., Bondioli, L., Casali, F., Rossi, M., Köhler, M., Moyá Solá, S., et al. (2004). The bony labyrinth of *Oreopithecus bambolii*. *J. Hum. Evol.* 46, 345–352.

Rossi, M., Casali, F., Romani, D., Bondioli, L., Macchiarelli, R., and Rook, L. (2004). MicroCT scan in paleobiology: application to the study of dental tissues. *Nucl. Instr. Meth. Phys. Res. B* 213, 747–750. doi: 10.1016/s0168-583x(03)01697-5

Ruff, C. B., and Leo, F. P. (1986). Use of computed tomography in skeletal structure research. *Yearb. Phys. Anthropol.* 29, 181–196. doi: 10.1002/ajpa.1330290508

Ryan, T. M., Carlson, K. J., Gordon, A. D., Jablonski, N., Shaw, C. N., and Stock, J. T. (2018). Human-like hip joint loading in *Australopithecus africanus* and Paranthropus robustus. *J. Hum. Evol.* 121, 12–24. doi: 10.1016/j.jhevol.2018.03.008

Schillinger, B., Beaudet, A., Fedrigo, A., Grazzi, F., Kullmer, O., Laaβ, M., et al. (2018). Neutron imaging in cultural heritage research at the FRM II Reactor of the Heinz Maier-Leibnitz Center. *J. Imaging* 4:22. doi: 10.3390/jimaging4010022

Schoetensack, O. (1908). *Der Unterkiefer des Homo heidelbergensis aus den Sanden von Mauer bei Heidelberg*. Leipzig: Engelmann.

Schrenk, F., Bromage, T. G., Betzler, C. G., Ring, U., and Juwayeyi, Y. M. (1993). Oldest *Homo* and Pliocene biogeography of the malawi rift. *Nature* 365, 833–836. doi: 10.1038/365833a0

Schwarz, D., Vontobel, P., Lehmann, E. H., Meyer, C. A., and Bongartz, G. (2005). Neutron tomography of internal structures of vertebrate remains: a comparison with X-ray computed tomography. *Palaeontol. Electronica* 8:30A.

Scott, G. R., Turner, C. G. II, Townsend, G. C., and Martinón-Torres, M. (eds) (2018). *The Anthropology of Modern Human Teeth*. Cambridge: Cambridge University Press.

Skinner, M. F., and Sperber, G. H. (1982). *Atlas of Radiographs of Early Man*. New York, NY: A.R. Liss.

Skinner, M. M., Alemseged, Z., Gaunitz, C., and Hublin, J.-J. (2015). Enamel thickness trends in Plio-Pleistocene hominin mandibular molars. *J. Hum. Evol.* 85, 35–45. doi: 10.1016/j.jhevol.2015.03.012

Skinner, M. M., de Vries, D., Gunz, P., Kupczik, K., Klassen, R. P., Hublin, J.-J., et al. (2016). A dental perspective on the taxonomic affinity of the Balanica mandible (BH-1). *J. Hum. Evol.* 93, 63–81. doi: 10.1016/j.jhevol.2016.01.010

Skinner, M. M., Gunz, P., Wood, B. A., and Hublin, J.-J. (2008). Enamel-dentine junction (EDJ) morphology distinguishes the lower molars of *Australopithecus africanus* and *Paranthropus robustus*. *J. Hum. Evol.* 55, 979–988. doi: 10.1016/j.jhevol.2008.08.013

Skinner, M. M., Kivell, T. L., Potze, S., and Hublin, J.-J. (2013). Microtomographic archive of fossil hominin specimens from Kromdraai B. *South Afr. J. Hum. Evol.* 64, 434–447. doi: 10.1016/j.jhevol.2013.01.007

Smilg, J. S., and Berger, L. R. (2015). Discovering hominins - application of medical computed tomography (CT) to fossil-bearing rocks from the site of Malapa. South Africa. *PLoS One* 10:e0145340. doi: 10.1371/journal.pone.0145340

Smith, T. M., Houssaye, A., Kullmer, O., Le Cabec, A., Olejniczak, A. J., Schrenk, F., et al. (2018). Disentangling isolated dental remains of Asian Pleistocene hominins and pongines. *PLoS One* 13:e0204737. doi: 10.1371/journal.pone.0204737

Smith, T. M., Olejniczak, A. J., Kupczik, K., Lazzari, V., de Vos, J. C., Kullmer, O., et al. (2009). Taxonomic assessment of the Trinil molars using non-destructive 3D structural and development analysis. *Paleo Anthropol.* 2009, 117–129.

Smith, T. M., and Tafforeau, P. (2008). New visions of dental tissue research: tooth development, chemistry, and structure. *Evol. Anthropol.* 17, 213–226. doi: 10.1002/evan.20176

Smith, T. M., Tafforeau, P., Le Cabec, A., Bonnin, A., Houssaye, A., Pouech, J., et al. (2015). Dental ontogeny in Pliocene and Early Pleistocene hominins. *PLoS One* 10:e0118118. doi: 10.1371/journal.pone.0118118

Spoor, F., Gunz, P., Neubauer, S., Stelzer, S., Scott, N., Kwekason, A., et al. (2015). Reconstructed *Homo habilis* type OH 7 suggests deep-rooted species diversity in early Homo. *Nature* 519, 83–86. doi: 10.1038/nature14224

Spoor, F., Jeffery, N., and Zonneveld, F. (2000). "Imaging skeletal growth and evolution," in *Development, Growth and Evolution: Implications for the Study of the Hominid Skeleton*, eds P. O'Higgins, and M. Cohn (San Diego: Academic Press for the Linnean Society of London), 123–161.

Spoor, F., Wood, B., and Zonneveld, F. (1994). Implications of early hominid labyrinthine morphology for evolution of human bipedal locomotion. *Nature* 369, 645–648. doi: 10.1038/369645a0

Sutton, M. D. (2008). Tomographic techniques for the study of exceptionally preserved fossils. *Proc. R. Soc. B* 275, 1587–1593. doi: 10.1098/rspb.2008.0263

Tafforeau, P., Boistel, R., Boller, E., Bravin, A., Brunet, M., Chaimanee, Y., et al. (2006). Applications of X-ray synchrotron microtomography for non-destructive 3D studies of paleontological specimens. *Appl. Phys. A* 83, 195–202. doi: 10.1073/pnas.0807047106

Tafforeau, P., and Smith, T. M. (2008). Nondestructive imaging of hominoid dental microstructure using phase contrast X-ray synchrotron microtomography. *J. Hum. Evol.* 54, 272–278. doi: 10.1016/j.jhevol.2007.09.018

Tafforeau, P., Zermeno, J. P., and Smith, T. M. (2012). Tracking cellular-level enamel growth and structure in 4D with synchrotron imaging. *J. Hum. Evol.* 62, 424–428. doi: 10.1016/j.jhevol.2012.01.001

Tate, J. R., and Cann, C. E. (1982). High-resolution computed tomography for the comparative study of fossil and extant bone. *Am. J. Phys. Anthropol.* 58, 67–73. doi: 10.1002/ajpa.1330580108

Tremsin, A. S., McPhate, J. B., Vallerga, J. V., Siegmund, O. H. W., Feller, W. B., Lehman, E., et al. (2011). High-resolution neutron microtomography with noiseless neutron counting detector. *Nucl. Instr. Meth. Phys. Res. A* 652, 400–403. doi: 10.1016/j.nima.2010.08.009

Tremsin, A. S., Morgano, M., Panzner, T., Lehmann, E., Filgers, U., Vallerga, J. V., et al. (2015). High resolution neutron imaging capabilities at BOA beamline at Paul Scherrer Institut. *Nucl. Instr. Meth. Phys. Res. A* 784, 486–493. doi: 10.1016/j.nima.2014.09.026

Trinkaus, E. (1984). "Western Asia," in *in The Origins of Modern Humans: A World Survey of the Fossil Evidence*, eds F. H. Smith, and F. Spencer (New York, NY: Alan R. Liss, Inc), 251–293.

Tyler, D. E. (2004). An examination of the taxonomic status of the fragmentary mandible Sangiran 5, (*Pithecanthropus dubius*). *Homo erectus*, "*Meganthropus*", or *Pongo*? *Quat. Int.* 117, 125–130. doi: 10.1016/s1040-6182(03)00122-8

Ulhaas, L. (2007). "Computer-based reconstruction: technical aspects and application," in *Handbook of Palaeoanthopology*, eds W. Henke, and I. Tattersall (Berlin: Springer), 787–814.

Urciuoli, A., Zanolli, C., Fortun, J., Almécija, S., Schillinger, B., Moyà-Solà, S., et al. (2017). Neutron-based computed microtomography: *Pliobates cataloniae* and *Barberapithecus huerzeleri* as a test-case study. *Am. J. Phys. Anthropol.* 166, 987–993. doi: 10.1002/ajpa.23467

Villmoare, B. (2018). Early *Homo* and the role of the genus in palaeoanthropology. *Am. J. Phys. Anthropol.* 165, 72–89. doi: 10.1002/ajpa.23387

von Koenigswald, G. H. R. (1950). Fossil hominids of the lower Pleistocene of Java. 18th Intl. *Geol. Congr.* 9, 59–61.

Walkhof, O. (1902). *Der Unterkiefer der Anthropomorphen und des Menschen in Seiner Funktionellen Entwickelung und Gestalt*. Wiesbaden: C. W. Kreidel's Verlag.

Ward, S. C., and Brown, B. (1986). "The facial skeleton of *Sivapithecus indicus*," in *Comparative Primate Biology Systematics, Evolution and Anatomy*, Vol. 1, Chap. New York, NY, eds D. Swindler, and S. Erwin (Alan R. Liss), 413–452.

Weber, G. W., and Bookstein, F. L. (2011). *Virtual Anthropology. A Guide to a New Interdisciplinary Field*. Wien: Springer.

Weidenreich, F. (1945). Giant early man from Java and South China. *Anthropol. Pap. Am. Mus. Nat. Hist.* 40, 1–134.

Wind, J. (1984). Computerized x−ray tomography of fossil hominid skulls. *Am. J. Phys. Anthropol.* 63, 265–282. doi: 10.1002/ajpa.1330630303

Wind, J., and Zonneveld, F. W. (1989). Computed tomography of an *Australopithecus* skull (Mrs Ples): a new technique. *Naturwissenschaften* 76, 325–327. doi: 10.1007/bf00368433

Winkler, B. (2006). Applications of neutron radiography and neutron tomography. *Rev. Min. Geochem.* 63, 459–471. doi: 10.2138/rmg.2006.63.17

Wood, B. (2011). *Wiley-Blackwell Encyclopedia of Human Evolution*. Chichester: Blackwell Publishing Ltd.

Wood, B. A., and Boyle, E. K. (2016). Hominin taxic diversity: Fact or fantasy? *Yearb. Phys. Anthropol.* 159, S37–S78. doi: 10.1002/ajpa.22902

Wu, X., and Schepartz, L. A. (2009). Application of computed tomography in paleoanthropological research. *Progr. Nat. Sci.* 19, 913–921. doi: 10.1016/j.pnsc.2008.10.009

Xing, S., Tafforeau, P., O'Hara, M., Modesto-Mata, M., Martín-Francés, L., Martinón-Torres, M., et al. (2019). First systematic assessment of dental growth and development in an archaic hominin (genus, *Homo*) from East Asia. *Sci. Advances* 5:eaau0930. doi: 10.1126/sciadv.aau0930

Zanolli, C. (2015). Molar crown inner structural organization in Javanese *Homo erectus*. *Am. J. Phys. Anthropol.* 156, 148–157. doi: 10.1002/ajpa.22611

Zanolli, C., Bondioli, L., Coppa, A., Dean, M. C., Bayle, P., Candilio, F., et al. (2014). The late Early Pleistocene human dental remains from Uadi Aalad and Mulhuli-Amo (Buia), Eritrean Danakil: macromorphology and microstructure. *J. Hum. Evol.* 74, 96–113. doi: 10.1016/j.jhevol.2014.04.005

Zanolli, C., Bondioli, L., Mancini, L., Mazurier, A., Widianto, H., and Macchiarelli, R. (2012). Two human fossil deciduous molars from the Sangiran Dome (Java, Indonesia): outer and inner morphology. *Am. J. Phys. Anthropol.* 147, 472–481. doi: 10.1002/ajpa.21657

Zanolli, C., Dean, M. C., Assefa, Y., Bayle, P., Braga, J., Condemi, S., et al. (2017a). Structural organization and tooth development in a *Homo* aff. *erectus* juvenile mandible from the Early Pleistocene site of Garba IV at Melka Kunture, Ethiopian highlands. *Am. J. Phys. Anthropol.* 162, 533–549. doi: 10.1002/ajpa.23135

Zanolli, C., Grine, F. E., Kullmer, O., Schrenk, F., and Macchiarelli, R. (2015). The Early Pleistocene deciduous hominid molar FS-72 from the Sangiran Dome of Java, Indonesia: a taxonomic reappraisal based on its comparative endostructural characterization. *Am. J. Phys. Anthropol.* 157, 666–674. doi: 10.1002/ajpa.22748

Zanolli, C., Kullmer, O., Kelley, J., Bacon, A.-M., Demeter, F., Dumoncel, J., et al. (2019a). Evidence for increased hominid diversity in the Early-Middle Pleistocene of Indonesia. *Nature Ecol. Evol.* 3, 755–764. doi: 10.1038/s41559-019-0860-z

Zanolli, C., Martinón-Torres, M., Bernardini, F., Boschian, G., Coppa, A., Dreossi, D., et al. (2018a). The Middle Pleistocene (MIS 12) human dental remains from Fontana Ranuccio (Latium) and Visogliano (Friuli-Venezia Giulia), Italy. A comparative high resolution endostructural assessment. *PLoS One* 13:e0189773. doi: 10.1371/journal.pone.0189773

Zanolli, C., and Mazurier, A. (2013). Endostructural characterization of the *H. heidelbergensis* dental remains from the early Middle Pleistocene site of Tighenif, Algeria. *C. R. Palevol.* 12:293–304. doi: 10.1016/j.crpv.2013.06.004

Zanolli, C., Pan, L., Dumoncel, J., Kullmer, O., Kundrát, M., Liu, W., et al. (2018b). Inner tooth morphology of *Homo erectus* from Zhoukoudian. New evidence from an old collection housed at Uppsala University, Sweden. *J. Hum. Evol.* 116, 1–13. doi: 10.1016/j.jhevol.2017.11.002

Zanolli, C., Schillinger, B., Beaudet, A., Kullmer, O., Macchiarelli, R., Mancini, L., et al. (2017b). Exploring hominin and non-hominin primate dental fossil remains with neutron microtomography. *Phys. Procedia* 88, 109–115. doi: 10.1016/j.phpro.2017.06.014

Zanolli, C., Skinner, M. M., Schrenk, F., Bromage, T. G., Hublin, J.-J., Schillinger, B., et al. (2019b). Taxonomic revision of the initial Early Pleistocene HCRP-U18-501 hominin mandible from Malawi: a tooth internal structural perspective. *Proc. Eur. Soc. Hum. Evol.* 8:206.

Zollikofer, C. P. E., and Ponce de León, M. S. (2005). *Virtual Reconstruction: A Primer in Computer-Assisted Paleontology and Biomedicine*. Hoboken: J. Wiley & Sons, Inc.

Zonneveld, F. W., and Wind, J. (1985). "High resolution computed tomography of fossil hominid skulls: a new method and some results," in *Hominid Evolution: Past, Present and Future*, ed. P. V. Tobias (New York, NY: Alan R. Liss, Inc), 427–436.

Conflict of Interest: The authors declare that the research was conducted in the absence of any commercial or financial relationships that could be construed as a potential conflict of interest.

frontiers in Earth Science

ORIGINAL RESEARCH
published: 24 March 2020
doi: 10.3389/feart.2020.00066

Current Options for Visualization of Local Deformation in Modern Shape Analysis Applied to Paleobiological Case Studies

Paolo Piras[1†], *Antonio Profico*[2], *Luca Pandolfi*[3], *Pasquale Raia*[4*], *Fabio Di Vincenzo*[5,6], *Alessandro Mondanaro*[3,4], *Silvia Castiglione*[4] *and Valerio Varano*[7†]

[1] Department of Scienze Cardiovascolari, Respiratorie, Nefrologiche, Anestesiologiche e Geriatriche, Sapienza Università di Roma, Rome, Italy, [2] PalaeoHub, Department of Archaeology, University of York, York, United Kingdom, [3] Department of Earth Science, University of Florence, Florence, Italy, [4] Department of Earth Sciences, Environmental and Resources, University of Naples "Federico II", Naples, Italy, [5] Department of Environmental Biology, Sapienza University of Rome, Rome, Italy, [6] Italian Institute of Human Palaeontology (IsIPU), Anagni, Italy, [7] Department of Architecture, Roma Tre University, Rome, Italy

OPEN ACCESS

Edited by:
Paul Antony Selden,
University of Kansas, United States

Reviewed by:
David A. T. Harper,
Durham University, United Kingdom
Manuel F. G. Weinkauf,
Charles University, Czechia

***Correspondence:**
Pasquale Raia
pasquale.raia@unina.it

[†]These authors have contributed equally to this work

Specialty section:
This article was submitted to Paleontology, a section of the journal Frontiers in Earth Science

Received: 15 November 2019
Accepted: 20 February 2020
Published: 24 March 2020

Citation:
Piras P, Profico A, Pandolfi L, Raia P, Di Vincenzo F, Mondanaro A, Castiglione S and Varano V (2020) Current Options for Visualization of Local Deformation in Modern Shape Analysis Applied to Paleobiological Case Studies. Front. Earth Sci. 8:66. doi: 10.3389/feart.2020.00066

In modern shape analysis, deformation is quantified in different ways depending on the algorithms used and on the scale at which it is evaluated. While global affine and non-affine deformation components can be decoupled and computed using a variety of methods, the very local deformation can be considered, infinitesimally, as an affine deformation. The deformation gradient tensor $\mathbf{F}$ can be computed locally using a direct calculation by exploiting triangulation or tetrahedralization structures or by locally evaluating the first derivative of an appropriate interpolation function mapping the global deformation from the undeformed to the deformed state. A suitable function is represented by the thin plate spline (TPS) that separates affine from non-affine deformation components. $\mathbf{F}$, also known as Jacobian matrix, encodes both the locally affine deformation and local rotation. This implies that it should be used for visualizing primary strain directions (PSDs) and deformation ellipses and ellipsoids on the target configuration. Using $\mathbf{C} = \mathbf{F}^{\mathrm{T}}\mathbf{F}$ allows, instead, one to compute PSD and to visualize them on the source configuration. Moreover, $\mathbf{C}$ allows the computation of the strain energy that can be evaluated and mapped locally at any point of a body using an interpolation function. In addition, it is possible, by exploiting the second-order Jacobian, to calculate the amount of the non-affine deformation in the neighborhood of the evaluation point by computing the body bending energy density encoded in the deformation. In this contribution, we present (i) the main computational methods for evaluating local deformation metrics, (ii) a number of different strategies to visualize them on both undeformed and deformed configurations, and (iii) the potential pitfalls in ignoring the actual three-dimensional nature of $\mathbf{F}$ when it is evaluated along a surface identified by a triangulation in three dimensions.

Keywords: local deformation, tensor visualization, strain directions, thin plate spline, first derivative, second derivative

INTRODUCTION

Modern shape analysis exploits the potential of specific computational algorithms applied to phenomena where the deformation and/or the variation of shapes are under investigation. In geometrical terms, shapes are represented by vectors of point coordinates (=landmarks) that can be compared by means of different mathematical formalisms. In shape analysis, the term "shape" is referred to forms (intended as shape+size) that have been standardized at unit size that can be quantified in various ways (see below). Prior to computing any kind of shape distance or deformation estimation, two or more shapes are commonly "superimposed" to filter out information relative to position, rotation, and, optionally, size, which do not represent intrinsic shape variation. At this point, two principal cases must be distinguished:

i) Shapes are identified by clouds of points without any specific correspondence/homology.
ii) Shapes are defined by landmarks that are anatomically or topologically homologous across different configurations (=points correspondence).

As for the first case, while most applications, from biology (Adams et al., 2013) to paleontology (Piras et al., 2010) to medicine (Piras et al., 2019), usually analyze shapes and forms by using homologous anatomical landmarks, the use of continuous surfaces without points correspondence is faced by exploiting the potential of a plethora of diffeomorphic techniques not treated in detail here (see Trouvé, 1998; Durrleman et al., 2012). Briefly, when using these diffeomorphic techniques, shapes are considered as images (2D) or surfaces (3D) that are registered using different algorithms (Ceritoglu et al., 2013): diffeomorphic approaches are used for this purpose such as large diffeomorphic deformation metric mapping (LDDMM; Miller et al., 2014, 2015) that represents, today, one of the most used (among many others) approaches for estimating shape differences, surface matching, and Parallel Transport of deformations (Charlier et al., 2017). In this context, size is more frequently quantified using m-Volume.

In the second case, one of the most used approaches to align a shape onto another is ordinary Procrustes analysis (OPA; Gower, 1975). If multiple shapes are to be analyzed, their consensus landmark configuration (=grand mean) is computed by applying the generalized Procrustes analysis (GPA; Gower, 1975; Rohlf and Slice, 1990). OPA and GPA can be performed with or without scaling landmark configurations to unit size, the latter being usually represented by centroid size (CS, the square root of sum of squared distance between landmark's configuration and their centroid). Scaling or not scaling shapes at unit CS leads to different Riemannian manifolds (size- and shape-space or shape-space; Dryden and Mardia, 2016) described by different metrics and possessing different geometrical properties (Le, 1988). The Riemannian manifolds are curved spaces that can be considered as the multidimensional generalization of a curved surface. Shape-spaces are particular Riemannian spaces whose points represent shapes. In general, shape-spaces are not representable pictorially except for the shape-space case of three landmarks in two dimensions where the manifold is a sphere where shapes live under the same equivalence classes of rotation translation and size (defined as CS).

OPA and GPA translate all shapes imposing their centroids on the origin of axes and rotating them to minimize the Procrustes distance D as defined as in Equation (1):

$$D = 2arcsin\left\{\frac{\sqrt{\sum_{ij}^{km}\left(X_{ij}-Y_{ij}\right)^2}}{2}\right\} \quad (1)$$

where X and Y represent two centered, aligned, and scaled configurations; k is the number of landmarks; and m is the number of dimensions. D is a geodesic distance that is often linearized by orthogonally projecting it in the plane tangent to the consensus. After GPA, common ordination methods, such as principal component analysis (PCA), are frequently applied in order to find directions of variations. This workflow is routinely applied in Geometric Morphometrics (GM; Bookstein, 1991; Claude, 2008; Zelditch et al., 2012; Dryden and Mardia, 2016).

In this article, we focus on those applications where point homology/correspondence is assumed (i). In the case of two aligned shapes or of a PCA performed on a collection of shapes either, the notion of deformation always pertains to a pair of shapes, i.e., a source (X: the "undeformed" shape that can be a real shape or a sample's consensus) and a target (Y: representing the deformation of the source, i.e., a real shape or a shape predicted by an ordination axis). Recently, several contributions focused on the visualization of deformations by using different kinds of local measures from infinitesimal local area changes (Márquez et al., 2012, 2014) to velocity fields of local deformations (Kratz et al., 2013). Locally (see below), tensors are used to quantify local deformation. The choice to visualize a unique particular metric extracted from a tensor inevitably implies a certain loss of information even in the simplest case of local affine deformation of finite elements (FE) that are usually triangular in 2D or tetrahedral (less commonly cubic) in 3D (tetrahedral FE structures will be treated here). Márquez et al. (2012) showed the importance of the evaluation, quantification, and statistical assessment of local deformation in GM examples coming from evolutionary biology. GM is being routinely used to address a wide spectrum of hypotheses. In particular, the use of shape analysis has been fruitfully coupled with phylogenetic comparative methods in order to explore patterns of convergence/divergence (Stayton, 2015; Castiglione et al., 2019), morphospace occupation (Santos et al., 2019), morphological integration (Piras et al., 2014; Sansalone et al., 2019), functional hypothesis (Oxnard and O'Higgins, 2009), and developmental growth (Angulo-Bedoya et al., 2019; Colangelo et al., 2019). All these studies share the same basic source of phenomenological interpretation: the shape change studied via shape analysis (very often GM). The importance to evaluate more quantitatively the local deformation stems from the fact that it allows a statistical treatment of shape variation (Márquez et al., 2012).

In this paper, we aim to describe and discuss the principal strategies available for computation of local deformation and its visualization for paleontologists and evolutionary biologists that usually use shape analysis in their investigations. We also

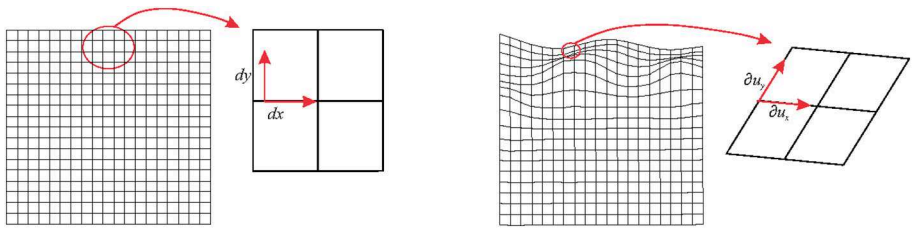

FIGURE 1 | Left panel: a non-affine deformation of a regular square. **Right panel**: a global non-affine deformation is shown. Infinitesimally, the deformation can be considered as linear.

present the very basic mathematical details underlying analytical machinery encoded in common shape analysis practice coupled with essential notions of continuum mechanics related to the estimation of local deformation. In particular we (i) describe the main analytical basis for the quantification of local deformation; (ii) illustrate and, in some cases, implement the main options and metrics for visualizing it on both 2D and 3D objects; (iii) illustrate an important feature of deformation in 3D when the shapes are represented by triangular surfaces having only a "shell" structure rather than a volumetric appearance; and (iv) present some applications in both 2D and 3D paleontological case studies.

We also provide (as **Supplementary Material**) fully reproducible codes in R with all necessary *ad hoc* built functions aimed at reproducing any figure and analysis presented in the paper.

COMPUTATION METHODS

Deformation Gradient Tensors at Local Scale

The main statement of the present paper is related to the concept of local deformation that is always considered, infinitesimally, as an affine transformation even when the global transformation affecting the source shape is not (**Figure 1**). For simplicity, we will use here the term affine as a synonym of uniform and linear deformation. In fact, one gets linear deformations by removing translations from affine deformations. Uniform means that the gradient of the deformation (the local strain, see below) is constant. At the same time, we will use non-uniform as a synonym of non-linear and non-affine. In the first example, we consider the non-affine deformation affecting a square grid in **Figure 1**. Infinitesimally, each square sub-element of the grid experiences an affine transformation that deforms it into a parallelogram. In $\mathbb{R}^2$ (i.e., in two-dimensions), the neighborhood around every point of a square can be mapped onto a different one by a linear transformation represented by a 2×2 matrix. We would deal with 3×3 matrix in $\mathbb{R}^3$ (i.e., in three dimensions). In particular, it is possible to transform a point of coordinates $\mathbf{p} \equiv (x, y)$ into an infinitesimally deformed one of coordinates $\mathbf{p} + \mathbf{u} \equiv (\mathbf{x},\mathbf{y}) + (\mathbf{u}_x,\mathbf{u}_y) = (\mathbf{x} + \mathbf{u}_x,\mathbf{y} + \mathbf{u}_y)$ with the displacement vector field $\mathbf{u} \equiv (\mathbf{u}_x, \mathbf{u}_y)$ through the displacement gradient tensor

$$\mathbf{H} = \begin{bmatrix} \frac{\partial u_x}{\partial x} & \frac{\partial u_x}{\partial y} \\ \frac{\partial u_y}{\partial x} & \frac{\partial u_y}{\partial y} \end{bmatrix} \quad (2)$$

If we add the identity matrix **I**, we obtain the deformation gradient tensor

$$\mathbf{F} = \mathbf{H} + \mathbf{I} = \begin{bmatrix} \frac{\partial u_x}{\partial x} + 1 & \frac{\partial u_x}{\partial y} \\ \frac{\partial u_y}{\partial x} & \frac{\partial u_y}{\partial y} + 1 \end{bmatrix} \quad (3)$$

Denoting **X** the $k \times m$ matrix, with k the number of landmarks and m the number of dimensions, of an undeformed configuration (here we refer to the small squared cell of the grid), we can obtain **Y** as linear transformation of **X** using

$$\mathbf{Y} = \mathbf{X}\mathbf{F}^{\mathrm{T}} \quad (4)$$

With "T" the transpose symbol.

The same holds in $\mathbb{R}^3$ by adding the z-coordinate to the system.

F encodes deformation + rotation, and these two aspects can be decoupled by computing a polar decomposition of **F**.

$$\mathbf{F} = \mathbf{R}\mathbf{U} \quad (5)$$

with **R** the $m \times m$ rotation matrix encoded in **F** and

$$\mathbf{U} = \sqrt{\mathbf{C}} \quad (6)$$

with

$$\mathbf{C} = \mathbf{F}^{\mathrm{T}}\mathbf{F} \quad (7)$$

C is symmetric and positive definite. The very nature of **C** is that it encodes exclusively the local deformation on the source *without* rotation. It can be used to perform an eigenvalue decomposition obtaining **v** and **λ**, i.e., the eigenvectors and the corresponding eigenvalues; **λ** is the collection of m eigenvalues usually returned in decreasing order, while **v** is its corresponding collection of m vectors each with m components. It must be noted that **R** resulting from the polar decomposition of **F** is not equal to the rotation found during OPA for the minimization of D. Varano et al. (2018, section 4.3) distinguish the two rotations by unifying OPA and modified OPA (MOPA) in one formalism. Moreover, **R** has a local meaning and can be different at any chosen evaluation point while when two configurations are superimposed, a global rotation is found.

It is not uncommon, in GM studies, to interpret the local deformation of a given target (w.r.t. a source) as the

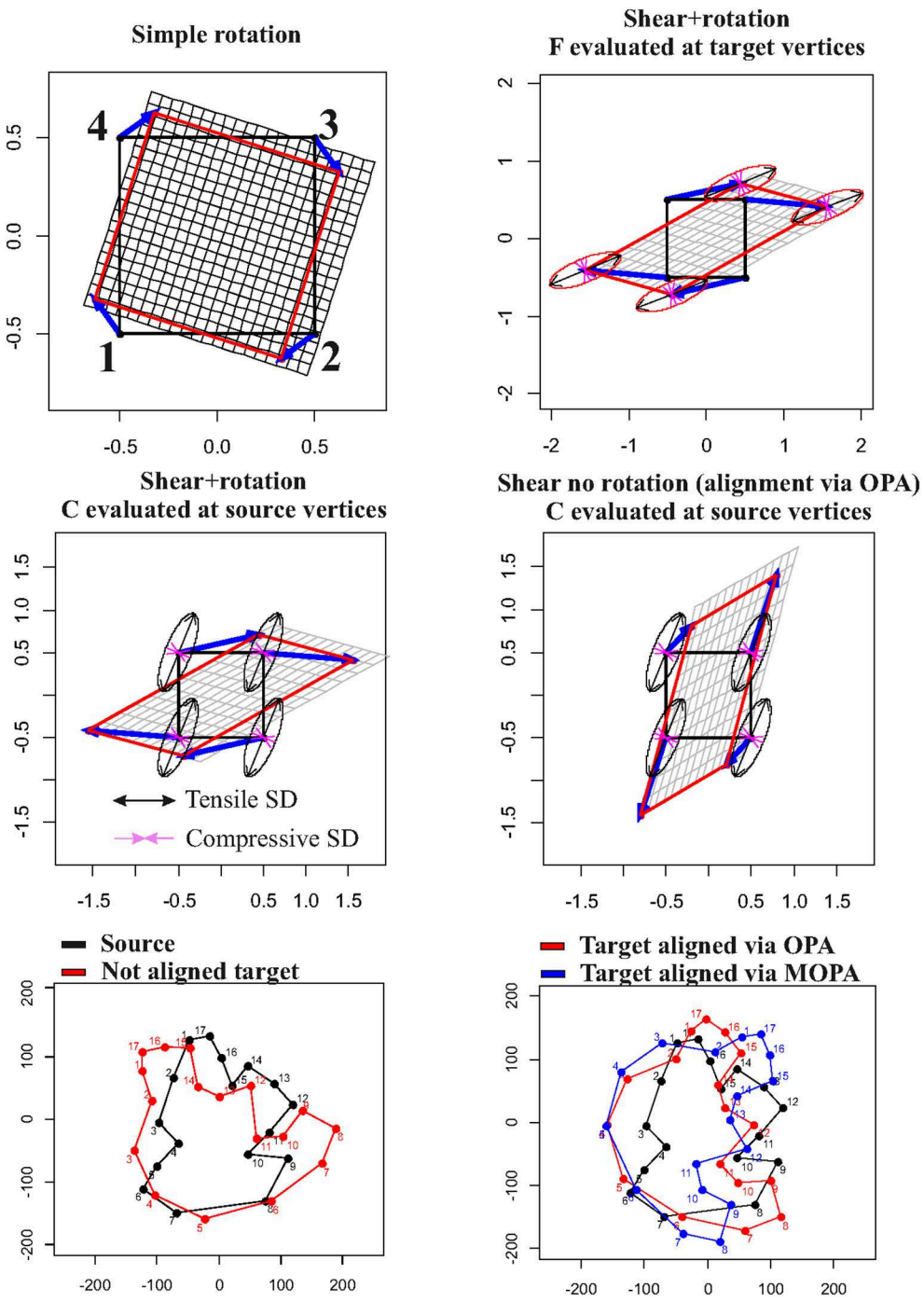

FIGURE 2 | Relationship between displacement vectors (in blue) and local deformations as depicted using $\sqrt{\mathbf{C}}$ (on the source) or **F** (on the target). First row, **left panel**: a simple rotation that produces displacements without deformation; first row, **right panel**: a shear+rotation with deformation ellipses evaluated at target vertices; second row, **left panel**: the same shear+rotation with deformation ellipses evaluated at source vertices; second row, **left panel**: the same shear without global rotation (filtered out via OPA) with deformation ellipses evaluated at source vertices; third row, **left panel**: a generic source (in black) and a non-aligned generic target (in red); third row, **right panel**: plot with source and the target aligned using OPA (in red) or MOPA (in blue). Principal strain directions (=ellipse's axes) are in black if tensile and in violet if compressive.

collection of displacement vectors of landmarks identifying the configurations. This practice inevitably leads to a misconception of what local deformation actually is and, consequently, to a misinterpretation of the process underlying observed shapes.

Figure 2 shows this point by starting with a simple rotation (first row, left panel) of a square **X** with coordinates $x_1(-0.5,0.5)$, $x_2(0.5,0.5)$, $x_3(0.5,0.5)$, $x_4(-0.5,0.5)$ that does not encode a shape deformation but that presents non-null displacements (blue

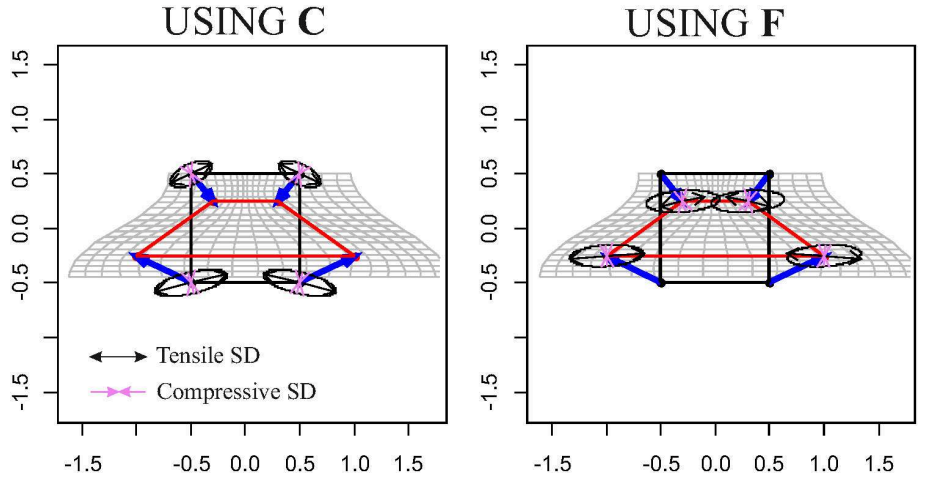

FIGURE 3 | Left panel: a bilinear transformation deforms the regular square into a trapezoid; $\sqrt{\mathbf{C}}$ was used to compute local deformations at source vertices with displacement vectors (in blue). **Right panel**: the same with deformation ellipses evaluated on the target using **F**. Principal strain directions (=ellipse's axes) are in black if tensile and in violet if compressive.

arrows). When applying a shear + rotation–deformation using $\mathbf{F} = \begin{bmatrix} 1.12 & 2 \\ 0.31 & 1.12 \end{bmatrix}$, we can show that **F** and **C** (which are constant in the case of affine transformations), evaluated at target and source vertices, respectively, do not follow displacements in any way (first row, right panel and second row, left panel). Even removing *global* rotation using OPA, displacements do not bear the same meaning of deformation ellipses. In this particular case, OPA and MOPA coincide: the two rotations, in fact, coincide if we found $\mathbf{UX}^{\mathrm{T}}\mathbf{X} = \mathbf{X}^{\mathrm{T}}\mathbf{XU}$ with **U** defined in Equation (6). This is the same as saying that the principal axes of X have the same directions as the principal strains of **F**. A square is also a particular case as the inertia tensor $\mathbf{X}^{\mathrm{T}}\mathbf{X}$ is spherical and does not have principal axes. In the case of two generic shapes, a source and a target linked by a non-affine transformation, OPA and MOPA lead to different global alignments (**Figure 2**, third row). The same effects are evident also in the case of non-affine transformations. **Figure 3** shows a simple bilinear transformation that deforms the same square as in **Figure 2** into a trapezoid with coordinates $x'_1(-1,0.25)$, $x'_2(1,0.25)$, $x'_3(0.3,0.25)$, $x'_4(-0.3,0.25)$. Rotation is not present in this transformation, and the two shapes are then intrinsically aligned. **C** and **F** were evaluated at source and target vertices, respectively. Displacements, again, cannot be considered as proxies of local deformation mainly for landmarks 1 and 2 (= at the square base). It is thus important to underline that during OPA, position and rotation (as well as optionally size) are removed globally. Locally, rotations are still present and the relationship between local deformation and displacements depends on the *infinitesimal differences* among displacements as encoded in the displacement gradient tensor **H**. When dealing with shapes more complex than the platonic ones shown here, things become more complex, and it is necessary to carefully look at local deformations and displacements in the correct way (see real examples below). **F** maps infinitesimal deformations between the reference and target configurations by measuring the rate of shape deformation at any point along all directions simultaneously. It is also known in literature as Jacobian matrix (Márquez et al., 2012). In this paper, we consider **F** as a synonym of Jacobian matrix and its determinant indicates the ratio between target and source *m*-Volumes, i.e., the infinitesimal change in *m*-Volume in the neighborhood of the point where **F** is evaluated.

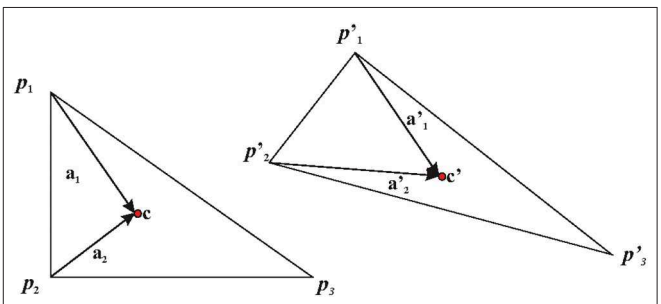

FIGURE 4 | Left panel: an undeformed triangle. **Right panel**: its deformed state. Axes used for deriving **F** are shown. c, centroid.

While the explanation above refers to the general continuous case, **F** and **C** can be obtained in the discrete case using alternative ways. In this paper, we propose two approaches:

a) Direct calculation: the simplest case to illustrate this is the case of two triangles **X** and **Y** as illustrated in **Figure 4**. Triangles are the most used basic geometries in 2D FE analysis, and they can experience only affine transformations. For this reason, they are used for mesh generation (as done in this paper) in order to evaluate **F** within a larger body (see below). We calculate the covariant basis $\mathbf{a_1}$ and $\mathbf{a_2}$ on **X** as the vector differences between two vertices $\boldsymbol{p_1}$ and $\boldsymbol{p_2}$ and **X** centroid (**c**) and their normal vector $\mathbf{a_3}$.

$$\begin{aligned} \mathbf{a_1} &= \boldsymbol{p_1} - \mathbf{c} \\ \mathbf{a_2} &= \boldsymbol{p_2} - \mathbf{c} \\ \mathbf{a_3} &= \mathbf{a_1} \times \mathbf{a_2} \end{aligned}$$

we can use $\mathbf{a_3}$ in order to obtain the contravariant basis

$$\begin{aligned}\mathbf{a^1} &= (\mathbf{a_2} \times \mathbf{a_3})/(\mathbf{a_1} \cdot (\mathbf{a_2} \times \mathbf{a_3}))\\ \mathbf{a^2} &= (\mathbf{a_3} \times \mathbf{a_1})/(\mathbf{a_1} \cdot (\mathbf{a_2} \times \mathbf{a_3}))\end{aligned}$$

The covariant basis in **Y** is as follows

$$\begin{aligned}\mathbf{a'_1} &= \boldsymbol{p}'_1 - \mathbf{c}'\\ \mathbf{a'_2} &= \boldsymbol{p}'_2 - \mathbf{c}'\end{aligned}$$

F is obtained as

$$\mathbf{F} = \left(\mathbf{a}'_1 \otimes \mathbf{a^1}\right) + \left(\mathbf{a}'_2 \otimes \mathbf{a^2}\right) \quad (8)$$

This workflow is valid for triangles in both $\mathbb{R}^2$ and $\mathbb{R}^3$. For tetrahedra in $\mathbb{R}^3$, the workflow is pretty similar with the inclusion of the calculation of a third axis corresponding to the tetrahedron's face not lying along the plane identified by three landmarks belonging to the tetrahedron.

b) Evaluation of the deformation gradient tensor **F** starting from a global interpolating function that models the deformation of **X** to obtain **Y**.

A convenient interpolant is represented by the thin plate spline (TPS), a special case of kriging (Kent and Mardia, 1994). TPS is the most used interpolation function in biological and paleobiological investigations that exploit modern shape analysis potential.

X and **Y** can be complex bodies constituted by homologous landmarks within which we evaluate **F** locally at any desired point (thus not by using the direct calculation on mesh triangle's centroids) starting from TPS coefficients.

The landmark-wise representation of TPS (Dryden and Mardia, 2016, Equation 12.8) is

$$\psi(\boldsymbol{x}) = \boldsymbol{c} + \boldsymbol{A}\boldsymbol{x} + W^T \boldsymbol{s}(\boldsymbol{x}), \boldsymbol{x} \in \varepsilon^m \quad (9)$$

with ε^m being the m-dimensional Euclidean space, c is a point of ε^m represented by an $m \times 1$ matrix, A is a linear transformation of ε^m represented by an $m \times m$ matrix, W is a $k \times m$ matrix representing the non-affine component (Dryden and Mardia, 2016; see below), and s is a $k \times 1$ matrix $s(\mathrm{x}) = (\sigma(\mathrm{x} - \mathrm{x}_1) \ldots \sigma(\mathrm{x} - \mathrm{x}_k))^T$ with:

$$\begin{aligned}\sigma(h) &= ||h||^2 \log\left(||h||^2\right) \text{ if } ||h|| > 0; \sigma(h)\\ &= 0 \text{ if } ||h|| = 0 \text{ for } m = 2.\\ \sigma(h) &= -||h|| \text{ if } ||h|| > 0; \sigma(h) = 0 \text{ if } ||h|| = 0\\ &\quad \text{for } m = 3.\end{aligned}$$

Using the shape-wise representation, where a configuration is defined in the C_m^k configuration space (with k the number of landmarks and m the number of dimensions), we have:

$$\psi(X) = l_k c^T + XA^T + SW, X \in C_m^k, S_{ij} = \sigma(x_i - x_j) \quad (10)$$

where l_k is a column vector of ones of length k.

TPS finds the best functions by minimizing the cost function *bending energy*

$$J(\psi) = \nu\pi \text{ trace } (\boldsymbol{W}^T \boldsymbol{S}\boldsymbol{W}) \quad (11)$$

where $\nu = 16$ for $m = 2$ and $\nu = 8$ for $m = 3$ (see Varano et al., 2017). This corresponds to the integral

$$J(\psi) = \sum_{i=1}^m \sum_{j=1}^m \sum_{l=1}^m \int_{\mathbb{R}^m} \left(\frac{\partial^2 \psi_i}{\partial x_j \partial x_l}\right)^2 \quad (12)$$

This represents a mean elastic energy evaluated on the *whole* $\mathbb{R}^m$ as the effect of the non-affine part of the deformation ψ (Bookstein, 1989).

The usefulness of TPS is that it separates the global affine part from the non-affine one. $\boldsymbol{X}\boldsymbol{A}^{\mathrm{T}}$ in Equation (10) represents the affine part of the transformation with A an $m \times m$ matrix that corresponds exactly to **F** in the special case of a uniform deformation applied to **X**. Varano et al. (2018) argued that while $\boldsymbol{X}\boldsymbol{A}^T \perp \boldsymbol{W}$, it is not orthogonal to $\boldsymbol{S}\boldsymbol{W}$ (i.e., the non-affine part of the deformation). $\boldsymbol{S}$ is the $k \times k$ matrix where the biharmonic function $\sigma(h)$ is evaluated on the source configuration and

$$\boldsymbol{W} = \boldsymbol{\Gamma}_{11} \boldsymbol{Y} \quad (13)$$

With $\boldsymbol{\Gamma}_{11}$ being the bending energy matrix (see Dryden and Mardia, 2016) estimated upon $\boldsymbol{X}$.

Varano et al. (2018) proposed different methods and strategies to calculate the affine component even while using the TPS by exploiting the so-called "TPS space" (Varano et al., 2017, 2018). For the same reason, Rohlf and Bookstein (2003) added to the existing method proposed in Bookstein (1996) two new methods for computing the affine component in a transformation: (i) the complement of the space of pure bending shape variation and (ii) the regression method. These two methods do not require the reference configuration to be aligned to its principal axes. While the former implies the computation of the bending energy matrix, the latter does not and can be easily implemented using the computation of the pseudoinverse matrix in a linear system relating the source and the target configurations. This solution is the same as the least squares estimator when the aim is the estimation of the affine transformation between a source and a target shape.

When evaluating infinitesimally the gradient of the deformation estimated by the TPS, namely, $\mathbf{F}_{\mathrm{tps}}$, we always obtain a linear transformation as, infinitesimally, all transformations become linear.

Figure 5 summarizes the main concept briefly exposed in this section.

Computationally, $\mathbf{F}_{\mathrm{tps}}$ can be derived as follows:

– Given a pair of shapes $\mathbf{X} \epsilon C_m^k$ (the undeformed) and $\mathbf{Y} \epsilon C_m^k$ (the deformed), one can compute A, W, and S using Equation (10), yielding the best interpolant ψ.

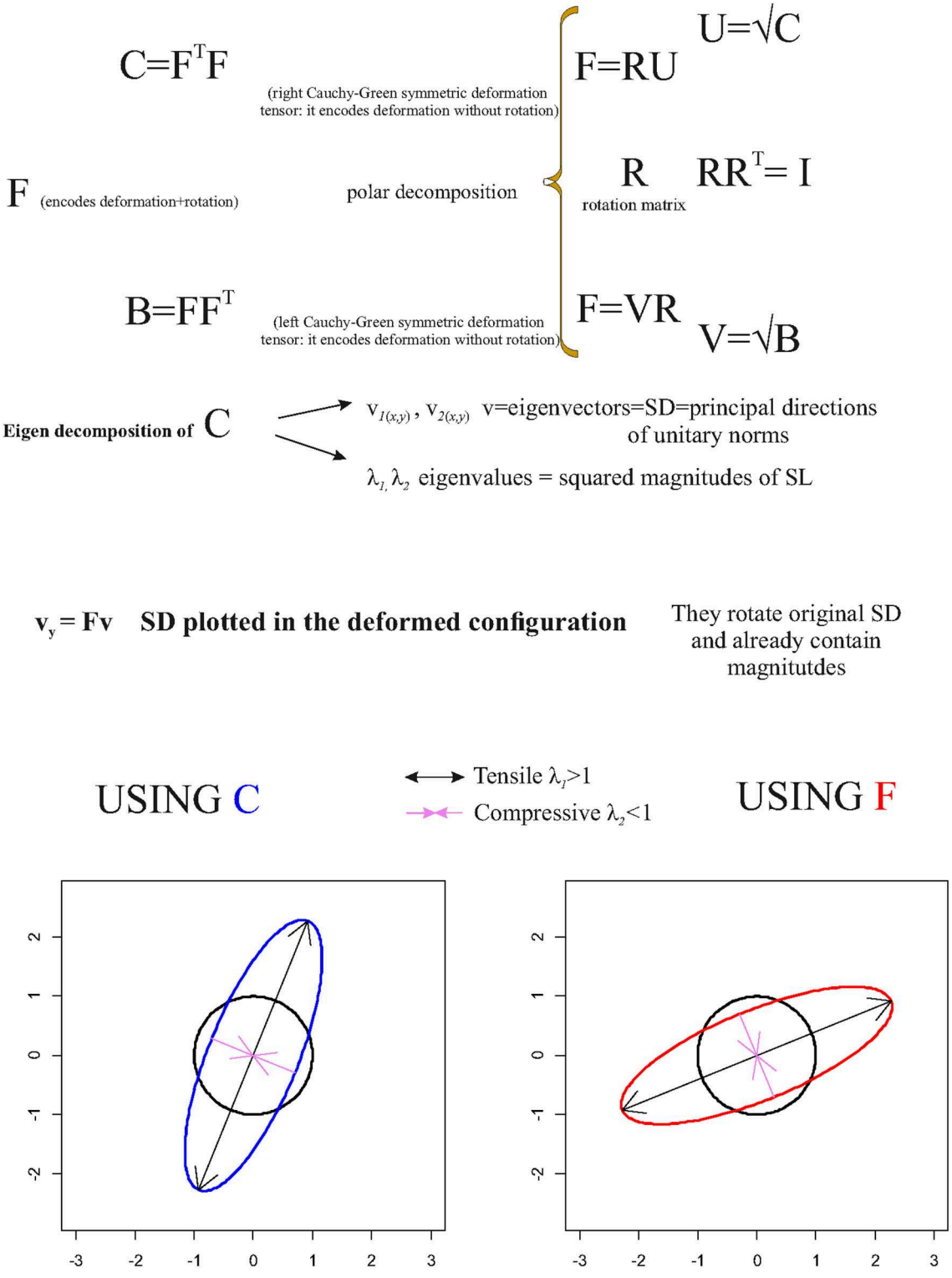

FIGURE 5 | Synthetic illustration showing the very basic mathematical relationship between **F**, **C**, and **R** as well as the geometrical meaning of **v** and $\mathbf{v}_y$.

– The gradient of the interpolant is the map: $\nabla\psi$: $\varepsilon^m \rightarrow M_{m\times m}$ associating to each point $n\epsilon\varepsilon^m$ the $M_{m\times m}$ matrix resulting from the sum of $\boldsymbol{A}$ in Equation (10) with the product between the $m \times k$ matrix $\boldsymbol{W}^T$ in Equation (10) and the $k \times m$ matrix $\nabla \boldsymbol{s}$ containing the first partial derivatives of the biharmonic function evaluated on each point n.

Specifically in 2D:

$$\nabla(\psi)_n = \begin{bmatrix} \frac{\partial \psi_1}{\partial x} & \frac{\partial \psi_1}{\partial y} \\ \frac{\partial \psi_2}{\partial x} & \frac{\partial \psi_2}{\partial y} \end{bmatrix} = \begin{bmatrix} A_{11} & A_{12} \\ A_{21} & A_{22} \end{bmatrix} + \begin{bmatrix} W_{11} & \dots & W_{1k} \\ W_{21} & \dots & W_{2k} \end{bmatrix} \begin{bmatrix} \frac{\partial \sigma_1}{\partial x} & \frac{\partial \sigma_1}{\partial y} \\ \dots & \dots \\ \frac{\partial \sigma_k}{\partial x} & \frac{\partial \sigma_k}{\partial y} \end{bmatrix} \quad (14)$$

With first partial derivatives:

$$\partial\sigma/\partial x = 2\delta x \log(\delta x^2 + \delta y^2) + 2\delta x \quad (15)$$

$$\partial\sigma/\partial y = 2\delta y \log(\delta x^2 + \delta y^2) + 2\delta y \quad (16)$$

$$\text{Where } \delta x = x_n - x_k \text{ and } \delta y = y_n - y_k \quad (17)$$

And in 3D

$$\nabla(\psi)_n = \begin{bmatrix} \frac{\partial \psi_1}{\partial x} & \frac{\partial \psi_1}{\partial y} & \frac{\partial \psi_1}{\partial z} \\ \frac{\partial \psi_2}{\partial x} & \frac{\partial \psi_2}{\partial y} & \frac{\partial \psi_2}{\partial z} \\ \frac{\partial \psi_3}{\partial x} & \frac{\partial \psi_3}{\partial y} & \frac{\partial \psi_3}{\partial z} \end{bmatrix} = \begin{bmatrix} A_{11} & A_{12} & A_{13} \\ A_{21} & A_{22} & A_{23} \\ A_{31} & A_{32} & A_{33} \end{bmatrix} + \begin{bmatrix} W_{11} & \dots & W_{1k} \\ W_{21} & \dots & W_{2k} \\ W_{31} & \dots & W_{3k} \end{bmatrix} \begin{bmatrix} \frac{\partial \sigma_1}{\partial x} & \frac{\partial \sigma_1}{\partial y} & \frac{\partial \sigma_1}{\partial z} \\ \dots & \dots & \dots \\ \frac{\partial \sigma_k}{\partial x} & \frac{\partial \sigma_k}{\partial y} & \frac{\partial \sigma_k}{\partial z} \end{bmatrix} \quad (18)$$

With first partial derivatives:

$$\partial\sigma/\partial x = -\frac{\delta x}{\sqrt{\delta x^2 + \delta y^2 + \delta z^2}} \quad (19)$$

$$\partial\sigma/\partial y = -\frac{\delta y}{\sqrt{\delta x^2 + \delta y^2 + \delta z^2}} \quad (20)$$

$$\partial\sigma/\partial z = -\frac{\delta z}{\sqrt{\delta x^2 + \delta y^2 + \delta z^2}} \quad (21)$$

Where

$$\delta x = x_n - x_k,\ \delta y = y_n - y_k, \text{ and } \delta z = z_n - z_k \quad (22)$$

While $\nabla(\psi)$ informs about the deformation directions and magnitudes at evaluation points, one could be interested in the local changes of these directions and magnitudes. This means computing the second-order gradient deformation tensor $\nabla\nabla(\psi)$ that allows to quantify the amount of local bending energy stored in the deformation. $\nabla\nabla(\psi)$ has $m \times (m \times m)$ components. It is convenient to represent these components in matrix format. In particular, we represent $\nabla\nabla(\psi)_n$ as the product of an $m \times k$ matrix with a $k \times (m \times m)$ matrix with n the point where $\nabla\nabla(\psi)$ is evaluated.

For 2D problems we have:

$$\nabla\nabla(\psi)_n = \begin{bmatrix} \frac{\partial^2 \psi_1}{\partial x^2} & \frac{\partial^2 \psi_1}{\partial x \partial y} & \frac{\partial^2 \psi_1}{\partial y \partial x} & \frac{\partial^2 \psi_1}{\partial y^2} \\ \frac{\partial^2 \psi_2}{\partial x^2} & \frac{\partial^2 \psi_2}{\partial x \partial y} & \frac{\partial^2 \psi_2}{\partial y \partial x} & \frac{\partial^2 \psi_2}{\partial y^2} \end{bmatrix} = \begin{bmatrix} W_{11} & \dots & W_{1k} \\ W_{21} & \dots & W_{2k} \end{bmatrix} \begin{bmatrix} \frac{\partial^2 \sigma_1}{\partial x^2} & \frac{\partial^2 \sigma_1}{\partial y \partial x} & \frac{\partial^2 \sigma_1}{\partial x \partial y} & \frac{\partial^2 \sigma_1}{\partial y^2} \\ \dots & \dots & \dots & \dots \\ \frac{\partial^2 \sigma_k}{\partial x^2} & \frac{\partial^2 \sigma_k}{\partial y \partial x} & \frac{\partial \sigma_k}{\partial x \partial y} & \frac{\partial^2 \sigma_k}{\partial y^2} \end{bmatrix} \quad (23)$$

With second partial derivatives:

$$\frac{\partial^2 \sigma}{\partial x^2} = 2 + (4\,\delta x^2)/(\delta x^2 + \delta y^2) + 2\,\log(\delta x^2 + \delta y^2) \quad (24)$$

$$\frac{\partial^2 \sigma}{\partial y^2} = 2 + (4\,\delta x^2)/(\delta x^2 + \delta y^2) + 2\,\log(\delta x^2 + \delta y^2) \quad (25)$$

$$\frac{\partial^2 \sigma}{\partial x \partial y} = \frac{4\delta x \delta y}{\delta x^2 + \delta y^2} \quad (26)$$

Where

$$\delta x = x_n - x_k \text{ and } \delta y = y_n - y_k \quad (27)$$

In 3D, we have:

$$\nabla\nabla(\psi)_n = \begin{bmatrix} \frac{\partial^2 \psi_1}{\partial x^2} & \frac{\partial^2 \psi_1}{\partial y^2} & \frac{\partial^2 \psi_1}{\partial z^2} & \frac{\partial^2 \psi_1}{\partial x \partial y} & \frac{\partial^2 \psi_1}{\partial y \partial x} & \frac{\partial^2 \psi_1}{\partial x \partial z} & \frac{\partial^2 \psi_1}{\partial z \partial x} & \frac{\partial^2 \psi_1}{\partial z \partial y} & \frac{\partial^2 \psi_1}{\partial y \partial z} \\ \frac{\partial^2 \psi_2}{\partial x^2} & \frac{\partial^2 \psi_2}{\partial y^2} & \frac{\partial^2 \psi_2}{\partial z^2} & \frac{\partial^2 \psi_2}{\partial x \partial y} & \frac{\partial^2 \psi_2}{\partial y \partial x} & \frac{\partial^2 \psi_2}{\partial x \partial z} & \frac{\partial^2 \psi_2}{\partial z \partial x} & \frac{\partial^2 \psi_2}{\partial z \partial y} & \frac{\partial^2 \psi_2}{\partial y \partial z} \\ \frac{\partial^2 \psi_3}{\partial x^2} & \frac{\partial^2 \psi_3}{\partial y^2} & \frac{\partial^2 \psi_3}{\partial z^2} & \frac{\partial^2 \psi_3}{\partial x \partial y} & \frac{\partial^2 \psi_3}{\partial y \partial x} & \frac{\partial^2 \psi_3}{\partial x \partial z} & \frac{\partial^2 \psi_3}{\partial z \partial x} & \frac{\partial^2 \psi_3}{\partial z \partial y} & \frac{\partial^2 \psi_3}{\partial y \partial z} \end{bmatrix} = \begin{bmatrix} W_{11} & \dots & W_{1k} \\ W_{21} & \dots & W_{2k} \\ W_{31} & \dots & W_{3k} \end{bmatrix} \begin{bmatrix} \frac{\partial^2 \sigma_1}{\partial x^2} & \frac{\partial^2 \sigma_1}{\partial y^2} & \frac{\partial^2 \sigma_1}{\partial z^2} & \frac{\partial^2 \sigma_1}{\partial x \partial y} & \frac{\partial^2 \sigma_1}{\partial y \partial x} & \frac{\partial^2 \sigma_1}{\partial x \partial z} & \frac{\partial^2 \sigma_1}{\partial z \partial x} & \frac{\partial^2 \sigma_1}{\partial z \partial y} & \frac{\partial^2 \sigma_1}{\partial y \partial z} \\ \dots & \dots & \dots & \dots & \dots & \dots & \dots & \dots & \dots \\ \frac{\partial^2 \sigma_k}{\partial x^2} & \frac{\partial^2 \sigma_k}{\partial y^2} & \frac{\partial^2 \sigma_k}{\partial z^2} & \frac{\partial^2 \sigma_k}{\partial x \partial y} & \frac{\partial^2 \sigma_k}{\partial y \partial x} & \frac{\partial^2 \sigma_k}{\partial x \partial z} & \frac{\partial^2 \sigma_k}{\partial z \partial x} & \frac{\partial^2 \sigma_k}{\partial z \partial y} & \frac{\partial^2 \sigma_k}{\partial y \partial z} \end{bmatrix} \quad (28)$$

With second partial derivatives:

$$\frac{\partial^2 \sigma}{\partial x^2} = (-\delta y^2 \delta z^2)/\left(\delta x^2 + \delta y^2 + \delta z^2\right)^{3/2} \quad (29)$$

$$\frac{\partial^2 \sigma}{\partial x \partial y} = (\delta x \delta y)/\left(\delta x^2 + \delta y^2 + z^2\right)^{3/2} \quad (30)$$

$$\frac{\partial^2 \sigma}{\partial z^2} = -(\delta x^2 - \delta y^2)/\left(\delta x^2 + \delta y^2 + \delta z^2\right)^{3/2} \quad (31)$$

$$\frac{\partial^2 \sigma}{\partial x \partial z} = (\delta x \delta z)/\left(\delta x^2 + \delta y^2 + \delta z^2\right)^{3/2} \quad (32)$$

$$\frac{\partial^2 \sigma}{\partial y^2} = (\delta y \delta z)/\left(\delta x^2 + \delta y^2 + \delta z^2\right)^{3/2} \quad (33)$$

$$\frac{\partial^2 \sigma}{\partial y \partial z} = (-\delta x^2 \delta z^2)/\left(\delta x^2 + \delta y^2 + \delta z^2\right)^{3/2} \quad (34)$$

Where

$$\delta x = x_n - x_k, \delta y = y_n - y_k, \text{and } \delta z = z_n - z_k \quad (35)$$

$||\nabla\nabla(\psi)||^2$ represents just $J(\psi)$ presented in Equation (12) when it is evaluated on whole $\mathbb{R}^m$. Locally, $||\nabla\nabla(\psi)_n||^2$ can be interpreted as the *bending energy density*, i.e., how much is non-affine (=non constant) local deformation in the neighborhood of n where it has been evaluated. Moreover, in the presence of an FE mesh, it can be evaluated at centroids of each element and multiplied by the element's m-Volume to compute, in a discrete way, the body bending energy J_Ω that has an important mechanical meaning in the decomposition

of deformation and for its relationship with the strain energy φ (see below). Varano et al. (2018) provided a detailed description of the relationship between J, J_Ω, and ϕ and their importance in computing the direct transport, i.e., the parallel transport the TPS space (Varano et al., 2017, 2018).

In particular,

$$\rho = J/J_\Omega$$

gives the *decay* index Varano et al. (2018), i.e., the ratio between bending energy computed on whole R^m and on the body only. Recently, Varano et al. (2019) proposed the construction of the body bending energy matrix B_Ω in order to restrict it exclusively within the physical boundaries of objects involved in the deformation analysis.

The bending energy can be considered as a pseudo-distance as it vanishes for globally affine transformations. A more physical distance, used in continuum mechanics, that vanishes on the rotational part of the local deformation, is the complete strain energy:

$$\varphi_s = \frac{1}{2}\int_\Omega 2\mu \boldsymbol{E}\cdot\boldsymbol{E} + \boldsymbol{\lambda}(tr\boldsymbol{E})^2 \tag{36}$$

where μ and $\boldsymbol{\lambda}$ are the Lamé elastic moduli, related to the material properties of the body, and

$$\boldsymbol{E} = \frac{\nabla \boldsymbol{u} + \nabla \boldsymbol{u}^T}{2} \tag{37}$$

is the strain tensor (for small displacement). In the case of pure geometrical structures, μ and $\boldsymbol{\lambda}$ are immaterial and we could adopt a simplified expression for the strain energy:

$$\varphi = \frac{1}{2}\int_\Omega \boldsymbol{E}\cdot\boldsymbol{E} \tag{38}$$

As already stated for body bending energy, this strain energy becomes an energy density when evaluated infinitesimally at specific locations.

Principal Strain Directions, Deformation Ellipses, and Ellipsoids

One can use $\mathbf{v}$ and $\boldsymbol{\lambda}$ in order to depict deformation directions of a unitary circumference (in 2D) or a sphere (in 3D) as shown in **Figure 5**, conveniently rescaled if necessary, and the principal axes of the resulting ellipses (or ellipsoids in $\mathbb{R}^3$).

The principal axes identify the (reciprocally) orthogonal principal strain direction (SD) given by $\mathbf{v}$ while $\boldsymbol{\lambda}$ gives their squared magnitudes.

As stated above, $\mathbf{C}$ does not encode rotation; thus, $\sqrt{\mathbf{C}}$, $\mathbf{v}$, and $\boldsymbol{\lambda}$ must be used in order to map SD, and to depict deformation ellipses or ellipsoids, on the *source* shape; in order to depict this information on the target shape using SD encoded in $\mathbf{v}$, $\mathbf{v}$ must be pre-multiplied by $\mathbf{F}$ in order to depict SD on the target configuration such as

$$\mathbf{v_y} = \mathbf{F}\mathbf{v} \tag{39}$$

$\mathbf{v}_y$ already encodes SD magnitudes. This procedure rotates $\mathbf{v}$ within the target according to $\mathbf{R}$ encoded in $\mathbf{F}$.

SD possesses an important deformational and mechanical meaning when computed on deformed shapes that are the result of specific forces such as in the left ventricle contraction (Evangelista et al., 2015; Gabriele et al., 2016; Piras et al., 2017; Varano et al., 2018). $\boldsymbol{\lambda}_i = 1$ indicates no deformation, $\boldsymbol{\lambda}_i > 1$ indicates a deformation that produces an expansion (=tensile SD) along the direction of the corresponding SD, while $\boldsymbol{\lambda}_i < 1$ indicates a deformation that produces a compression (=compressive SD). The closer the $\boldsymbol{\lambda}_i$ to 1, the smaller is the deformation. This means that in case of $\boldsymbol{\lambda}_i > 1$ or $\boldsymbol{\lambda}_i < 1$, the direction of maximal deformation $\hat{\boldsymbol{\lambda}}$ is dictated by the $\mathbf{v}$ corresponding to the $\boldsymbol{\lambda}_i$ most distant from 1:

$$\hat{\boldsymbol{\lambda}} = argmax\,(|1 - \boldsymbol{\lambda}|) \tag{40}$$

The corresponding direction of maximal deformation (either tensile or compressive) $\hat{\mathbf{v}}$, on the source, or $\hat{\mathbf{v}}_\mathbf{y}$ on the target, is often called primary strain direction (PSD).

We recall here that we are dealing with locally affine transformations. In case of direct calculation (see above) made on single triangular (or tetrahedral) FE of a Delaunay triangulation computed within two general X and Y shapes, these FEs should not be re-aligned via OPA. Accordingly, if using $\mathbf{F}_{tps}$, one should use $\mathbf{C}_{tps} = \mathbf{F}_{tps}^T\mathbf{F}_{tps}$ and $\sqrt{\mathbf{C}_{tps}}$ for deforming unitary circumference or sphere on the source and $\mathbf{v}_{ytps} = \mathbf{F}_{tps}\mathbf{v}_{tps}$ and $\mathbf{F}_{tps}$ for plotting them on the target. **Figure 6** illustrates a square that is deformed in a parallelogram using the tensor $= \begin{bmatrix} 1.12 & 2 \\ -0.31 & 1.12 \end{bmatrix}$. Using either the direct calculation or TPS interpolation in $\mathbb{R}^2$, $\mathbf{F}$ is fully recovered. One can use $\mathbf{F}$ or $\sqrt{\mathbf{C}}$ in order to depict the deformation ellipse and corresponding SD on target or source configuration, respectively.

Choosing Evaluation Points and Their Visualization

The concept of "localness" inevitably implies the choice of a series of evaluation points within the geometry subjected to a deformation. One of the most effective approaches, widely applied over a large spectrum of applications, is the Delaunay triangulation (Márquez et al., 2014; Dryden and Mardia, 2016). The construction of the triangulation proceeds iteratively by choosing the centroids of the initial sets of defined triangles as a new set of triangle's vertices. In this manner, an unlimited number of triangles can be assembled. Specifically, the *constrained* Delaunay triangulation allows limiting the construction of the triangulation itself exclusively within the body of interest by providing proper contour information in 2D and surface in 3D. Once a criterion to choose deformation gradient evaluation points is established (i.e., constrained Delaunay), it is essential to have also a criterion to locate them in both source and target configurations as homologous points. While this could be of lesser importance in non-biological applications, it is instead mandatory to have them as much as possible anatomically homologous when dealing

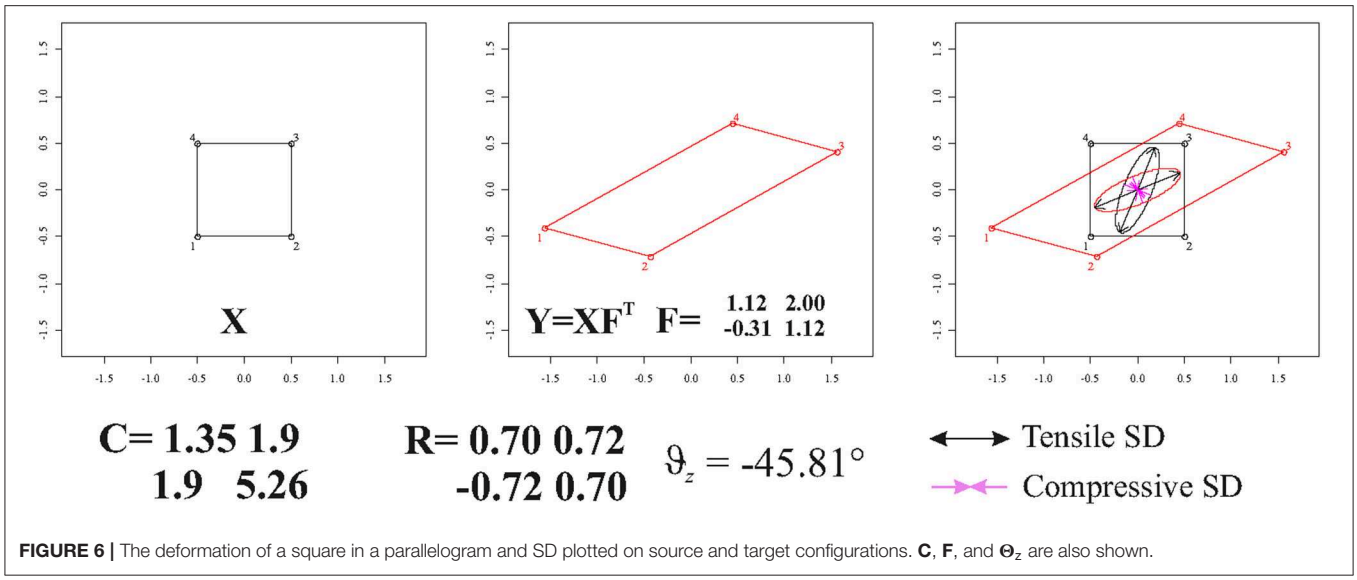

FIGURE 6 | The deformation of a square in a parallelogram and SD plotted on source and target configurations. **C**, **F**, and Θ_z are also shown.

with biological structures. Whereas, the homology of a point, in a biological structure, is an elusive concept (as a point is dimensionless; Bookstein, 1991; Dryden and Mardia, 2016), it is nevertheless approached in those cases where histological delimitations are visible, for example, at the meeting point between cranial sutures ("Type I" landmarks). A less strict homology occurs if landmarks are digitized on curves or surfaces ("Type II" and "Type III" landmarks). Of course, centroids of a triangulation cannot be manually re-digitized on the target once estimated on the source. For this reason, we suggest to use the same TPS computed centroids to estimate evaluation points within the target configuration. TPS coefficients are then used to deform the set of centroids coordinates of constrained Delaunay triangulation built on the source to predict a new set of points to be used for visualization within the target configuration body. This new set could be considered reasonably (though with a certain approximation) "continuously homologous" between source and target configuration. Besides TPS, many other spline functions can be used for this purpose (Márquez et al., 2012).

Surfaces in 3D

We dedicate a special attention to surfaces in 3D. These particular shapes are dealt with, in classic GM studies, using TPS as formulated in $\mathbb{R}^3$. Shapes are often represented, however, using triangulation that mimics a shell structure. Frequently, once TPS deformation coefficients have been estimated, the morphological interpretation is made by looking at the deformation of the surface triangles. In this case, the appropriate way to visualize local deformation is to compute energies, and to depict deformation ellipses and PSD on the surface of triangles. A triangle in $\mathbb{R}^3$ is a particular type of 3D shape: its landmarks are always coplanar and, as for any other coplanar shape, if we compute **F** in a discrete way using Equation (8) between two generic triangles in $\mathbb{R}^3$, this leads to **F** and **C** that are 3×3 matrices but that are also singular: this means that performing an eigenvalue decomposition on **C** returns only two non-zero eigenvalues and that deforming a sphere results in a flat ellipsoid, in practice an ellipse in $\mathbb{R}^3$. Instead, using TPS to estimate $\mathbf{F}_{tps}$ and $\mathbf{C}_{tps}$ leads to an ambiguous reading of the morphological change experienced by the source's triangle. In fact, TPS in $\mathbb{R}^3$ deforms the ambient space in all directions. In the case of two non-coplanar triangles in $\mathbb{R}^3$, TPS looks for the function whose A in Equation (10) corresponds just to the deformation gradient **F**, being the transformation uniform. However, it can be easily verified that $\mathbf{F}_{tps}$ and $\mathbf{C}_{tps}$ are non-singular and $\mathbf{F}_{tps} \neq \mathbf{F}$ and $\mathbf{C}_{tps} \neq \mathbf{C}$: if a sphere is deformed according to $\mathbf{F}_{tps}$ or $\mathbf{C}_{tps}$, it transforms into an ellipsoid. Nevertheless, if we deform the source triangle using $\mathbf{F}_{tps}$, we obtain exactly the target triangle. This happens because $\mathbf{F}_{tps}$ produces a deformation that acts on the entire ambient space in $\mathbb{R}^3$, but this deformation vanishes in those points not belonging to the plane identified by target triangle. It follows that given two generic triangles in $\mathbb{R}^3$, a source **X** and a target **Y**, the deformed state **Y** can be obtained using either **F** or $\mathbf{F}_{tps}$.

$$\mathbf{Y} = \mathbf{X}\mathbf{F}^{\mathbf{T}} = X\mathbf{F}_{\mathbf{tps}}^{\mathbf{T}}$$

Interestingly, if we deform a cube, thus a non-planar shape, using **F** or $\mathbf{F}_{tps}$, we obtain different deformed states. Only **F** flattens the cube in a planar shape, while $\mathbf{F}_{tps}$ confers an affine three-dimensional transformation. **Figure 7** shows the effect of **F** and $\mathbf{F}_{tps}$ on triangles and cubes in $\mathbb{R}^3$.

It is worth noticing that if **X** and **Y** are two coplanar triangles w.r.t. each other but still in $\mathbb{R}^3$, the direct calculation still returns **F** and **C** while TPS cannot find a solution as the L matrix (Bookstein, 1989) becomes singular; it happens as in the absence of any displacement, between **X** and **Y**, along the dimension perpendicular to the plane containing them, no interpolation is possible in $\mathbb{R}^3$.

The abovementioned example therefore suggests that, when looking at a surface's elements, deformation estimated by TPS could not be adequate to interpret what happens on them.

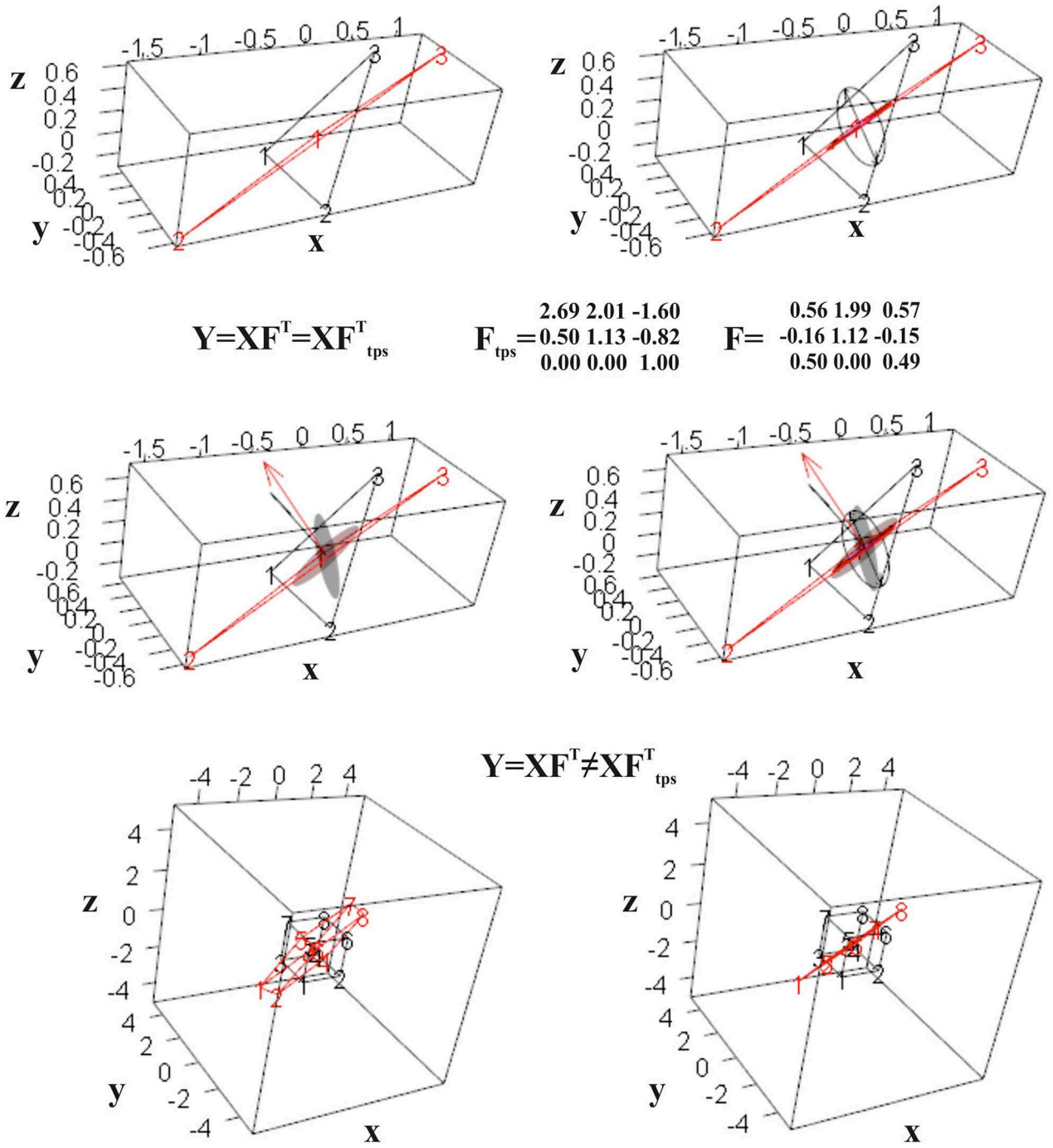

FIGURE 7 | Computation of **F** for two triangles in $\mathbb{R}^3$. **Top row**: the undeformed black triangle is deformed into the red one; the direct computation leads to a tensor that flattens a unitary sphere in an ellipse in $\mathbb{R}^3$. **Mid row**: $\mathbf{F}_{tps}$ deforms a unitary sphere into an ellipsoid. Both **F** and $\mathbf{F}_{tps}$ return the deformed state if used to deform the source triangle. **Bottom row**: when applied to a regular cube, only **F** deforms it into a flat shape, while it does not hold for $\mathbf{F}_{tps}$.

Another simple example is to deform a cube with a known **F** and looking what happens to a single cube's faces. **Figure 8** synthetically depicts this simple experiment. The ellipsoids at the cubes' centroids (source and target) were generated using $\sqrt{\mathbf{C}}$ and **F**, respectively. Using the direct discrete computation explained above, $\overline{\mathbf{F}}$ and $\overline{\mathbf{C}}$, e.g., the projections of **F** and **C** on the faces, were calculated for any face and corresponding deformation ellipses were drawn. As it can be seen, these ellipses are very different descriptors w.r.t. the deformation encoded in the ellipsoid. $\overline{\mathbf{F}}$ on a specific face is just the

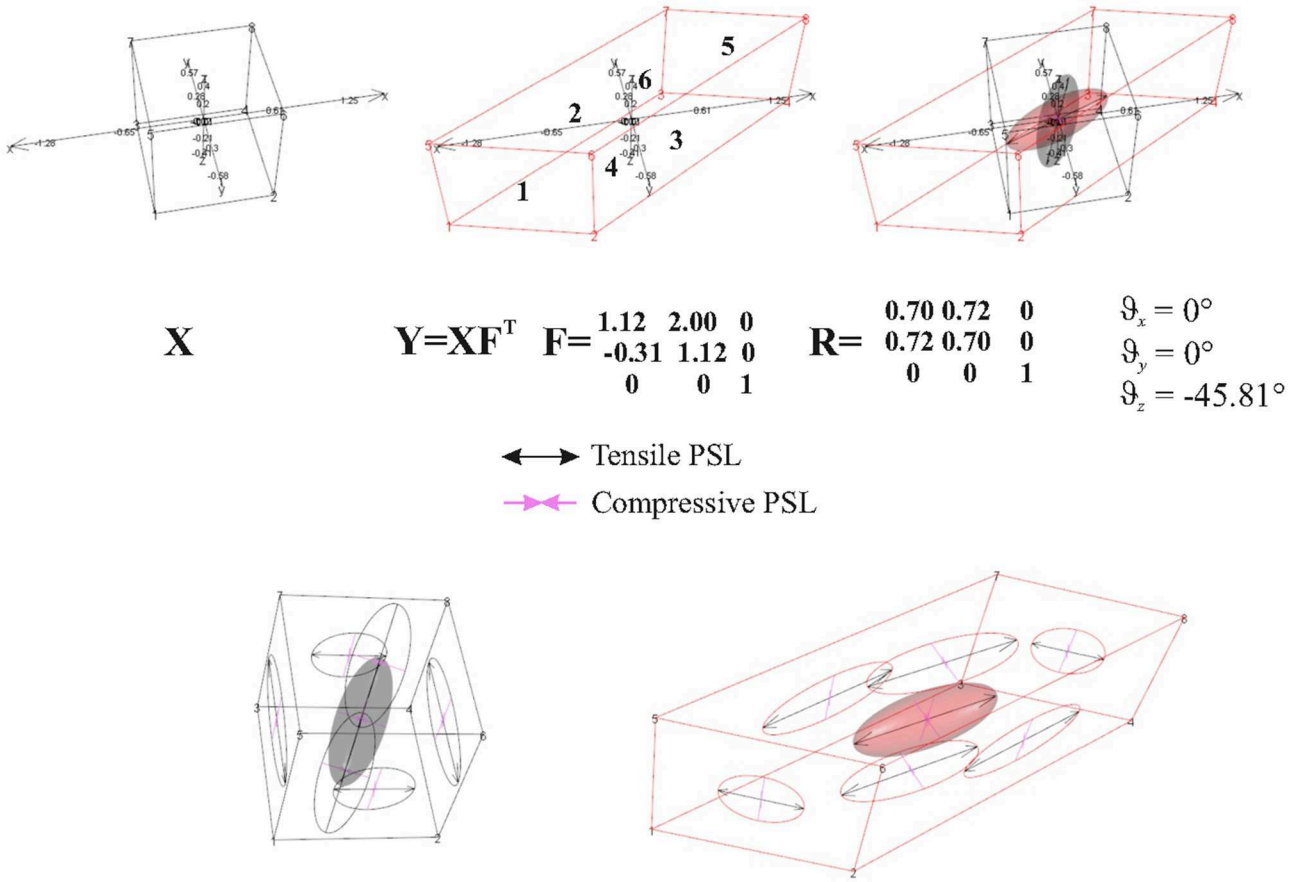

FIGURE 8 | Top row: a regular black cube is deformed onto the red parallelepiped. **Bottom row**: **F** is then projected onto single faces using the procedure exposed in the text. Six projected tensors are then obtained.

projection of **F** on the plane containing the face. To project **C**, we calculate $\mathbf{a}_{1s}$ and $\mathbf{a}_{2s}$ on a face on the source shape **X**, as the vector differences between two vertices $\boldsymbol{p}_{1s}$ and $\boldsymbol{p}_{2s}$ and **X** centroid x_c and their normal vector

$$\mathbf{a_{1s}} = \boldsymbol{p}_{1s} - \mathbf{x_c}$$
$$\mathbf{a_{2s}} = \boldsymbol{p}_{2s} - \mathbf{x_c}$$

The normalized axis $\hat{\mathbf{a}}_{3s}$ perpendicular to $\mathbf{a}_{1s}$ and $\mathbf{a}_{2s}$ is found as

$$\mathbf{a_{3s}} = \mathbf{a_{1s}} \times \mathbf{a_{2s}}; \hat{\mathbf{a}}_{3s} = \frac{\mathbf{a_{3s}}}{|\mathbf{a_{3s}}|} - \mathbf{x_c} \tag{41}$$

The projector on the source $\boldsymbol{P}_s$ is derived as

$$\boldsymbol{P}_s = \mathbf{I} - \hat{\mathbf{a}}_{3s}\hat{\mathbf{a}}_{3s}^{\mathrm{T}} \tag{42}$$

$\overline{\mathbf{C}}$ is then found as

$$\overline{\mathbf{C}} = \boldsymbol{P_s}^T \mathbf{C} \boldsymbol{P_s} \tag{43}$$

In order to find $\overline{\mathbf{F}}$, we derived $\mathbf{P_t}$ (in the same way used for deriving $\mathbf{P_s}$); then, $\overline{\mathbf{F}}$ can be found using

$$\overline{\mathbf{F}} = \boldsymbol{P_t}^T \mathbf{F} \boldsymbol{P_s} \tag{44}$$

This procedure can be done for any face for which $\overline{\mathbf{F}}$ or $\overline{\mathbf{C}}$ need to be calculated.

EXAMPLES

Simulated Example

Figure 9 shows a regular square grid composed of 49 landmarks that is deformed in an irregular shape that is stretched and compressed in two different landmark columns, respectively. The procedure for estimating an approximately homologous triangulation as explained above on both source and target is also shown. The deformed shape is rotated onto the undeformed one via OPA without scaling. **Figure 10** shows the first options we present for the visualization of local deformation. 2×2 local tensors ($\mathbf{F}$ for the target and $\sqrt{\mathbf{C}}$ for the source) have been used to deform unitary circumferences appropriately rescaled (magnification: 0.07). The color of each ellipse corresponds to the $\log(\det(\mathbf{F}))$, thus indicating the local infinitesimal area ratio between target and source. Values < 0 indicate a reduction in local areas, values > 0 denote an enlargement, while 0 indicates no area change. The change in area alone does not inform about the direction of the deformation given by SD. Here, they are black if tensile and violet if compressive. In this example, all SD1 are tensile and they are larger in correspondence of the two columns of landmarks that undergo a compression and an expansion, respectively. We also depicted SD without ellipses; this gives a more clear perception of the direction and magnitude of local deformation only. The effect of rotation encoded in $\mathbf{F}$ is highly visible when using $\mathbf{F}$ on target or $\sqrt{\mathbf{C}}$ on source shape.

Figure 11 shows in the upper left panel the interpolation (via TPS) within the entire body of $\log\left(\det(\mathbf{F})\right)$, while in the upper right panel, $\log(\varphi)$ density interpolated in the same manner. Larger values, as expected, can be found around regions corresponding to the two landmark's columns subjected to stretching and compression. In the lower left panel, we show the distribution of $\log(\left\|\nabla\nabla(\psi)_n\right\|^2)$ density: here, we can appreciate the "non-affinity" of deformation around points where $\nabla\nabla(\psi)$ was evaluated; $\log(\left\|\nabla\nabla(\psi)_n\right\|^2)$ density is distributed on alternate bands of large and small values with largest values in correspondence of the two landmark's columns that were stretched and compressed.

Real Examples

2D Paleontological Case Study

The 2D real example is related to the deformation occurring between two configurations in lateral view of two Hippopotamidae species: the extinct species *Archaeopotamus harvardi* from the Late Miocene of Eastern Africa (Coryndon, 1977; Harrison, 1997; Boisserie, 2005), here considered as the undeformed shape, and the extant species *Hippopotamus amphibius* distributed on the sub-Saharan African continent (Lewison and Pluháček, 2017) treated as the target shape. *A. harvardi* is one of the most primitive species within Hippopotamidae and displays some peculiar plesiomorphic traits including the low orbits whose rim flushes not beyond the profile of cranial roof. Moreover, the skull is shorter and less massive than in the extant hippo, with lower orbits and a slender zygomatic arch. The latter features are also present in the pigmy-insular Madagascan hippos (Pandolfi et al., 2020), which are characterized by reduction of size with respect to their continental ancestors, by a general decrease of the height of the orbits (Caloi and Palombo, 1994), and by brain size reduction (Weston and Lister, 2009). The opposite condition can be found in more derived *Hexaprotodon* (*H. palaeindicus*) and in *H. amphibius* (Boisserie, 2005, 2007; Boisserie et al., 2011; Pandolfi et al., 2020): in these species, orbits are elevated beyond the cranial roof. Elevated orbits, a long facial region, and a short postorbital part of the skull in Hippopotamidae are related to specialization for a semiaquatic lifestyle.

The adaptation to a semiaquatic lifestyle evolved independently in *Hippopotamus* and *Hexaprotodon*, suggesting a convergence between the two lineages (Boisserie, 2005, 2007; Boisserie et al., 2011 and references therein).

The morphological information encoded in Hippopotamidae skull lateral view is thus very important to depict evolutionary patterns during clade diversification, morphological convergences, and adaptations to different lifestyles including terrestrialization of some species (e.g., *H. madagascariensis*).

Figure 12 shows results relative to this 2D example.

We digitized 15 landmarks and 32 semi-landmarks from photographs in lateral view on each specimen using the tpsDig2 v. 2.17 software (Rohlf, 2013). Semi-landmarks were used to capture the morphology of complex outlines where anatomical homology is difficult to recognize. See **Figure 1** in Pandolfi et al. (2020) for landmarks definition. Semi-landmarks assume that curves or contours are homologous among specimens (Adams et al., 2004; Perez et al., 2006). First, a GPA implemented in the procSym() function from the R-package "Morpho" (Schlager, 2014) was used to rotate, translate, and scale landmark configurations to unit CS; here, we used the minimization of bending energy during the sliding of semi-landmarks as an alignment method. Second, OPA was used to align the two configurations. During OPA, the semi-landmarks previously used to align shapes with their consensus were treated as fixed landmarks, an approximation here considered not relevant for the purposes of the present article. The second row in **Figure 12** shows the direction of SD and deformed ellipses (left side) colored according to $\log(\det(\mathbf{F}))$, while on the right side, $\log(\det(\mathbf{F}))$ has been continuously interpolated (using TPS) on the body domain of the target shape. The third row shows on the left side $\log(\varphi)$ and $\log(\left|\left|\nabla\nabla(\psi)_n\right|\right|^2)$ densities (right side), respectively. The fourth row shows SD on the left side and PSD on the right side. SD and PSD are colored according to $\sqrt{\boldsymbol{\lambda}}$ and $\sqrt{\hat{\boldsymbol{\lambda}}}$, respectively.

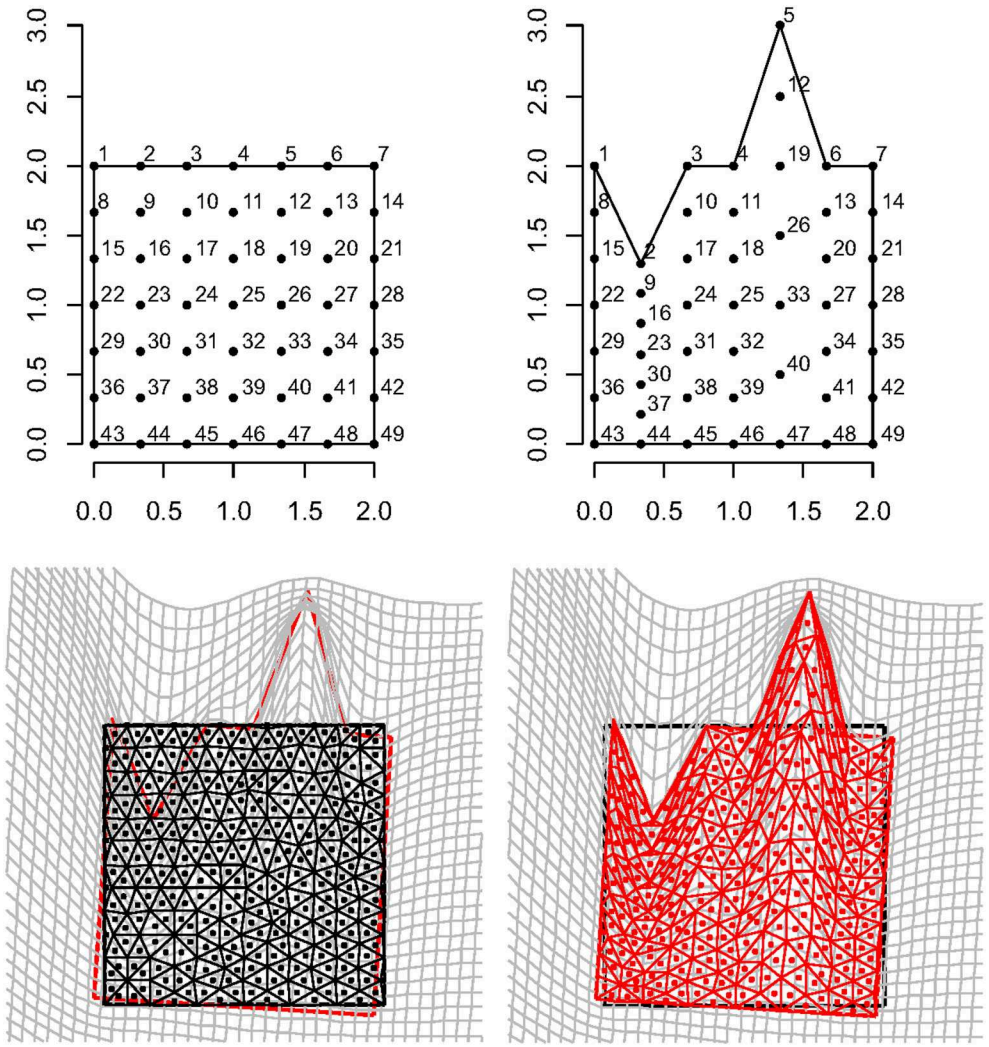

FIGURE 9 | Top row: a regular square grid **(left)** is deformed onto an irregular polygon **(right)**. Bottom row: a constrained Delaunay triangulation derived on the source shape **(left)** is estimated on the target using TPS; source and target shapes were aligned via OPA. Triangle's centroids will be used as evaluation points for estimating **F**, $\nabla\nabla\,(\psi)$, and other metrics.

From all these panels, an interesting pattern emerges: the elevated orbit of *H. amphibius* has, on its upper borders, approximately horizontal PSD as also visible by oblique/horizontal ellipses in the second row (left) of **Figure 12**. This means that the "elevation" of the orbit and related structures takes place on the ventral side of the skull in lateral view; in fact, this is observable on the PSD panel where it appears evident that PSDs are oriented vertically with $\sqrt{\hat{\boldsymbol{\lambda}}} > 1$ in particular in the jugal area. Closely outside the orbit, instead, we find oblique/vertical PSD with $\sqrt{\hat{\boldsymbol{\lambda}}} < 1$ indicating that, there, the target bones (the frontal and parietal in particular) experience a local dorso-ventral contraction.

Without the help of PSD, one could still look at the usual deformation grid, but it does not furnish equally clear details and, more importantly, cannot quantify locally the amount and direction of local deformation.

3D Paleontological Case Study

The first 3D example considers the deformation occurring between the humeral morphology of two Talpoidea species: the extinct *Mesoscalops montanensis* (Barnosky, 1981) from the Early Miocene of North America and the extant *Neurotrichus gibbsii* Baird 1858 distributed in northwestern United States and southwestern British Columbia. These two species belong to a clade (Talpoidea) well-known for including several fossorial moles (Piras et al., 2012, 2015). Among these species, different degrees of fossoriality can be found from complex tunnel diggers to more ambulatorial species. Fossoriality degree is linked mainly to the adaptation shown by humeral morphology. While slender humeri are less adapted to borrowing activity, the humeral morphology of subterranean species experienced several shape changes in both distal and proximal regions with evident enlargements in medio-lateral direction. Proscalopidae,

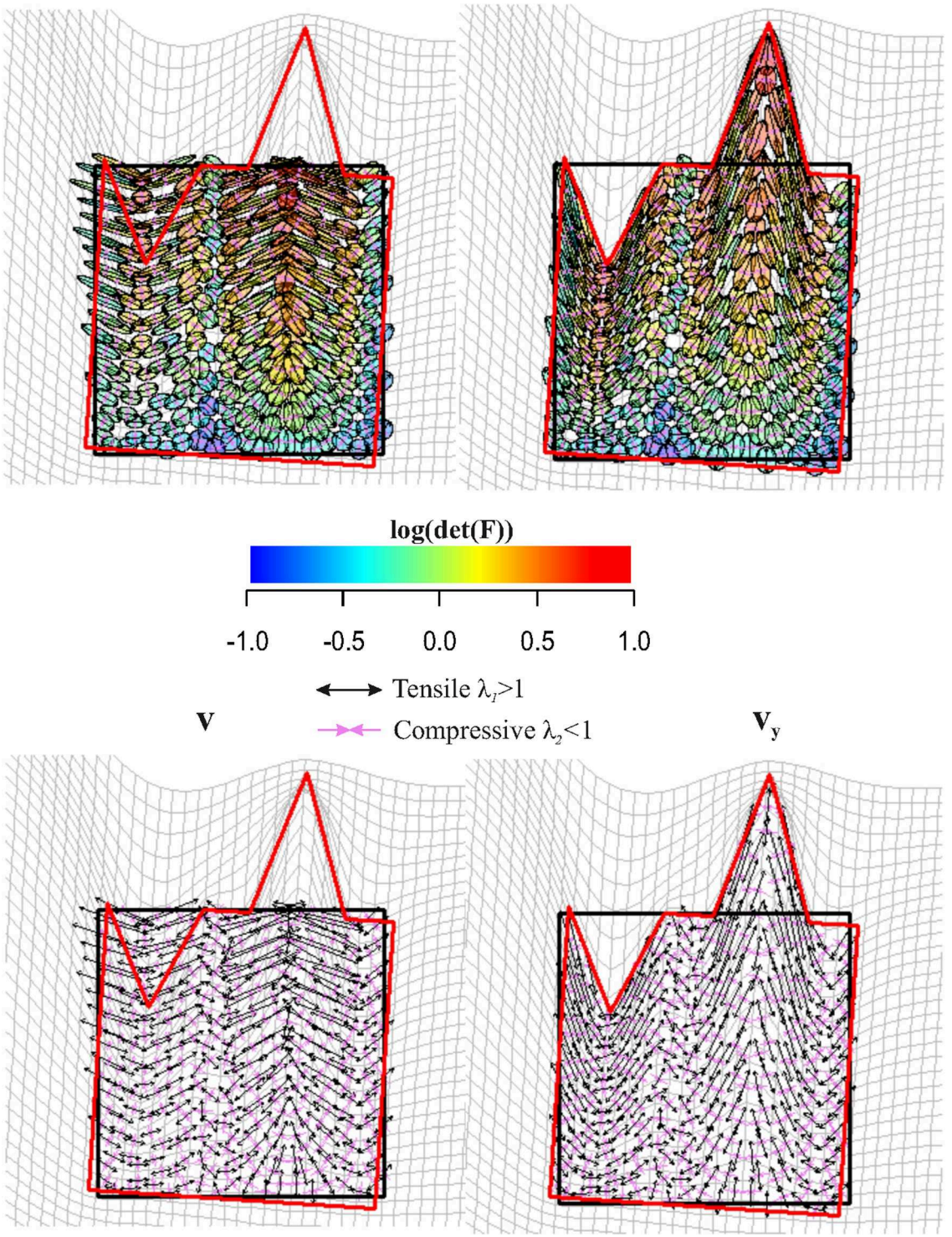

FIGURE 10 | Top row: **C** (left) is used to deform unitary spheres appropriately rescaled for sake of visualization; **F** (right) was used for the same purpose on the target configuration. Ellipse's color is proportional to log(det(**F**)). Values < 0 indicate a reduction in local area, values > 0 indicate an expansion. **Bottom row**: the direction of deformation is dictated by $\mathbf{v}_y$ and $\hat{\mathbf{v}}_\mathbf{y}$ (i.e., SD = ellipse's axes). Tensile and compressive SD actions are indicated. Source and target shapes were aligned via OPA.

the clade to which *Mesoscalops* belongs, shows one of the most peculiar humeral morphologies among mammals, with unique shape and mechanical stress in the context of burrowing species (Barnosky, 1981, 1982; Piras et al., 2015). For our experiment here, we used CT scan data from Piras et al. (2015) for *M. montanensis* and for the non-complex tunnel digger *N.*

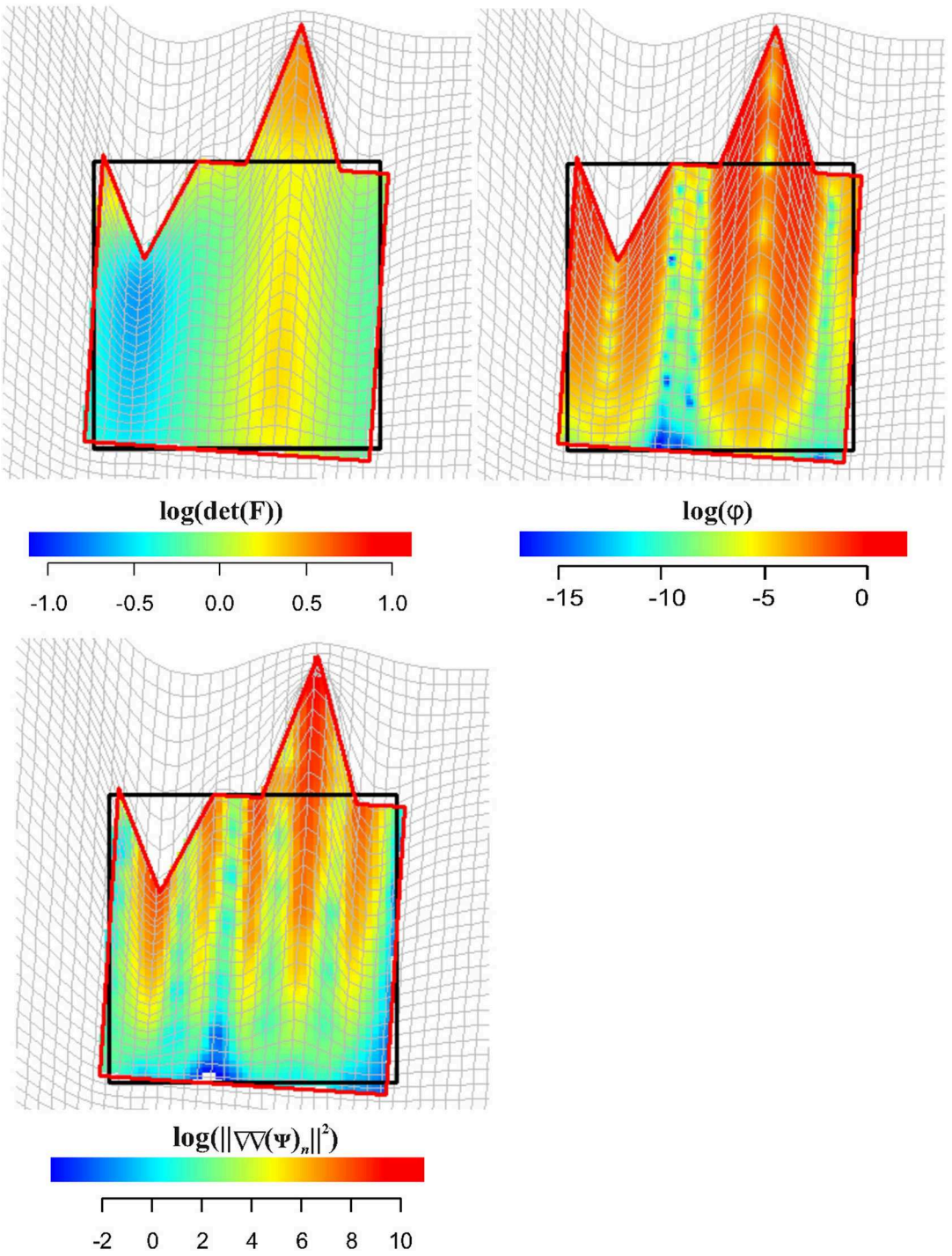

FIGURE 11 | Visualization of local deformation via interpolation (using TPS) of log(det(**F**)), log(ϕ), and $\log(||\nabla\nabla(\psi)_n||^2)$. Source and target shapes were aligned via OPA.

gibbsii. As our procedure requires homologous triangulation, we used the TPS coefficients found when applying TPS to the 32 landmarks set used in Piras et al. (2015) belonging to *M. montanensis* (as source) and to *N. gibbsii* (as target) to deform *M. montanensis* mesh; this allows dealing with meshes constituted by homologous landmarks and triangulations. In this example, when aligning source and target via OPA, we did not scale shapes at unit size in order to show the effect of size and shape variation when evaluated on a local triangle's surfaces on the whole $\mathbb{R}^3$.

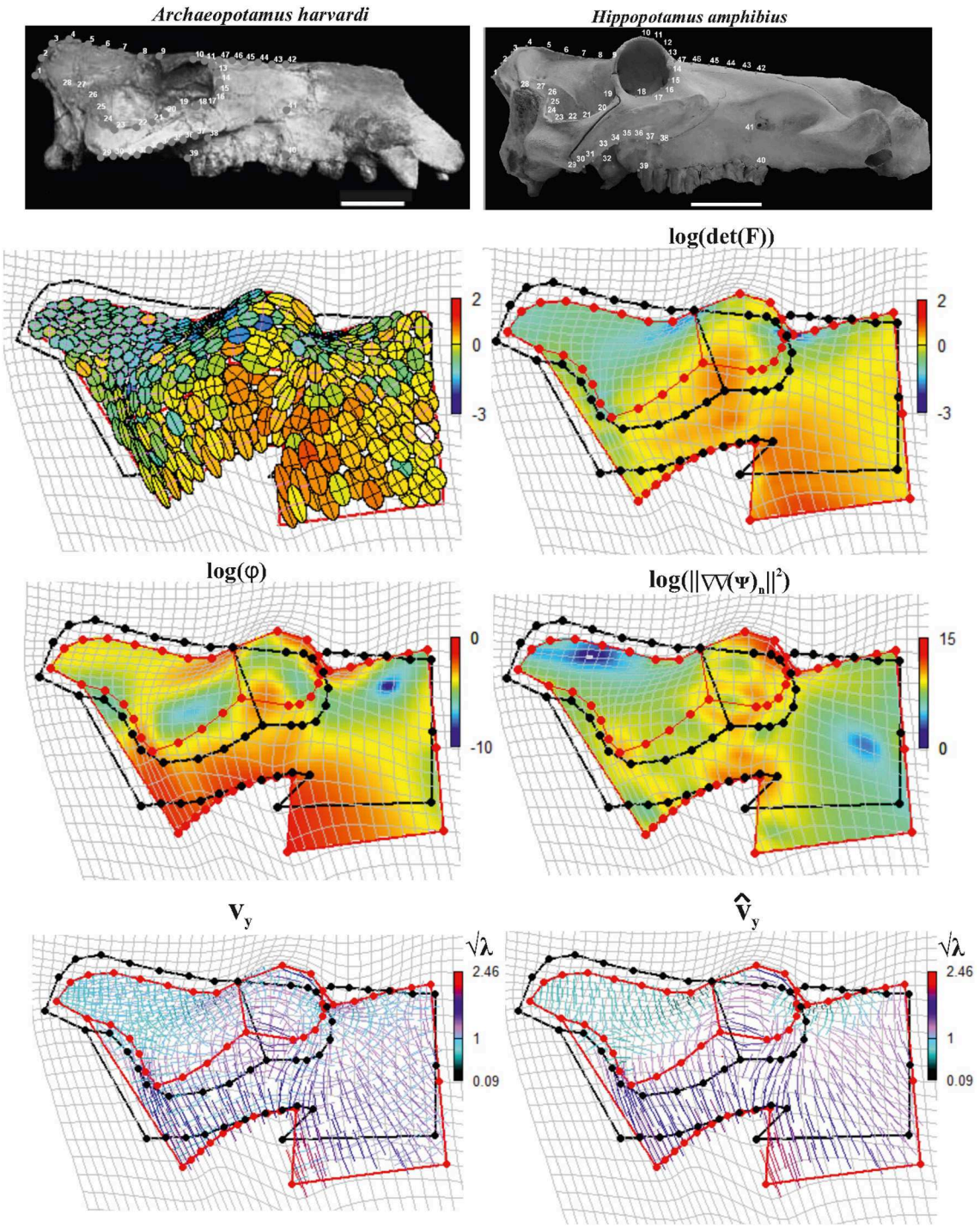

FIGURE 12 | Local deformations observable between *Archaeopotamus harvardi* KNM-LT 4 (as source) and *Hippopotamus amphibius* MSNF 1135 (as target). We show both deformation ellipses obtained using **F** as well as main metrics derived using approaches explained in the text. In particular, we show log(det(**F**)), log(ϕ), and log($\|\nabla\nabla(\psi)_n\|^2$). $\mathbf{v}_y$ and $\hat{\mathbf{v}}_\mathbf{y}$ are also shown colored according to corresponding values in the interval [$\sqrt{\lambda}$, $\sqrt{\tilde{\lambda}}$]; values < 1 indicate compressive $\mathbf{v}_y$ and $\hat{\mathbf{v}}_\mathbf{y}$, values > 1 indicate tensile actions. Source and target shapes were aligned via OPA. Scales equal 10 cm. KNM, Kenya National Museum; MSNFS, Museo di Storia Naturale di Firenze, sezione di Zoologia La Specola.

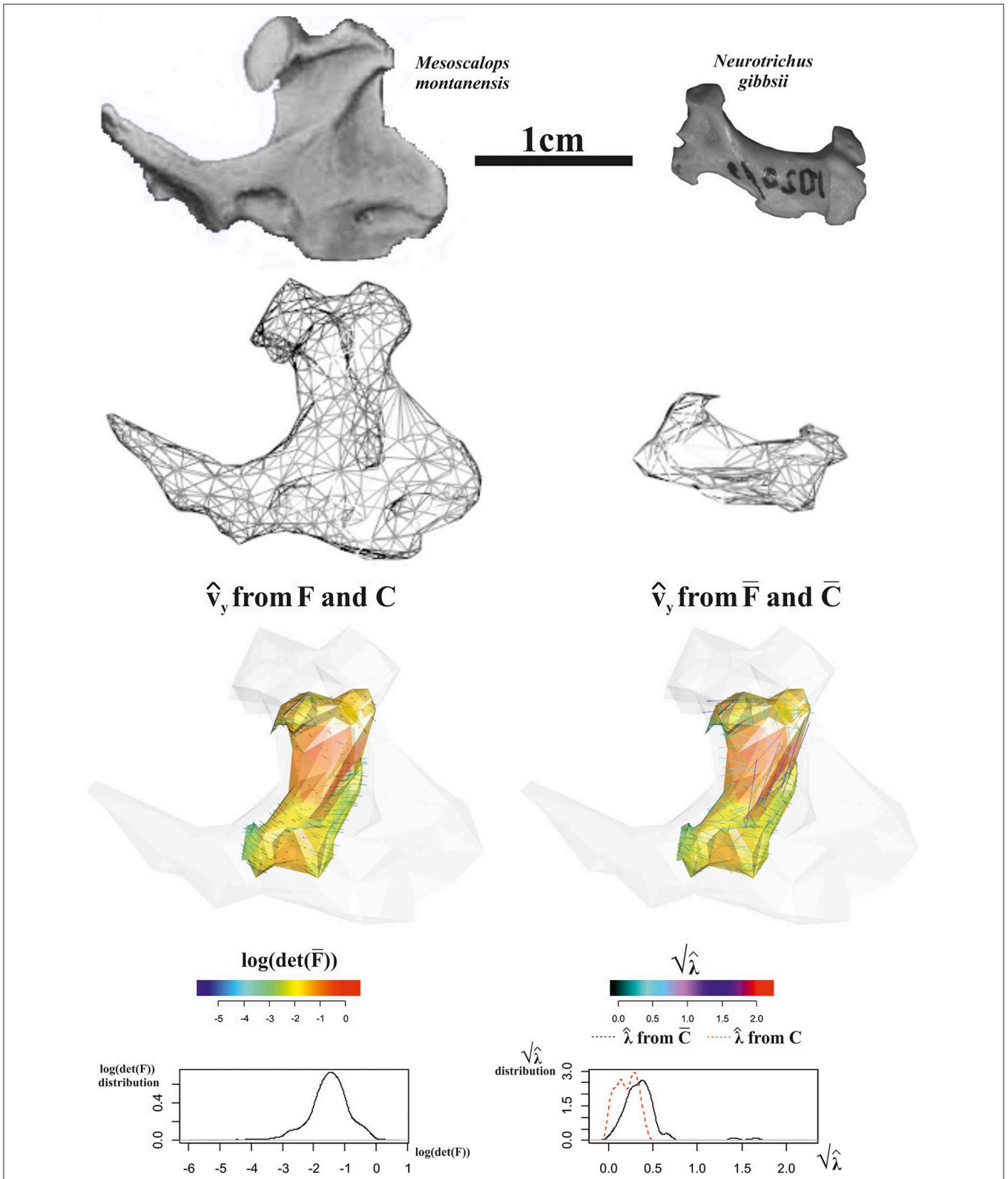

FIGURE 13 | Local deformations observable between *Mesoscalops montanensis* UWBM 54708 (as source) and *Neurotrichus gibbsii* LACM 093944 (as target). 3D meshes are also shown. $\hat{\mathbf{v}}_\mathbf{y}$ calculated upon **F** or $\overline{\mathbf{F}}$ are shown and colored according to the corresponding $\sqrt{\hat{\lambda}}$. Meshes' triangular faces are colored according to log(det($\overline{\mathbf{F}}$)). Densities of relevant metrics are also illustrated. Source and target shapes were aligned via OPA without scaling. UWBM, University of Washington, Burke Memorial Washington State Museum, Seattle; LACM, Los Angeles County Museum.

Figure 13 shows data and results relative to this analysis. Triangle face colors correspond to $\log(\det(\overline{\mathbf{F}}))$, while $\hat{\mathbf{v}}_\mathbf{y}$ (i.e., PSD plotted on the target) color is proportional to $\sqrt{\hat{\boldsymbol{\lambda}}}$ computed either on $\mathbf{C}$ *or* on $\overline{\mathbf{C}}$, i.e., on tensors evaluated at the triangle's centroids on the whole $\mathbb{R}^3$ (**Figure 13**, third row, right) or successively projected on the triangle's surfaces (**Figure 13**, third row, left). Corresponding distributions of these metrics are also illustrated. $\log(\det(\overline{\mathbf{F}}))$ presents all values < 0, thus indicating a considerably smaller size of target shape as exemplified by source shaded silhouette. $\sqrt{\hat{\boldsymbol{\lambda}}}$ and $\hat{\mathbf{v}}_\mathbf{y}$ computed upon $\mathbf{C}$ or $\overline{\mathbf{C}}$ and $\mathbf{F}$ or $\overline{\mathbf{F}}$, respectively, give different information: in fact when using $\mathbf{C}$ and $\mathbf{F}$, we obtain centripetal PSD dictated by size change with $\sqrt{\hat{\boldsymbol{\lambda}}}$ constantly < 0, while using $\overline{\mathbf{C}}$ and $\overline{\mathbf{F}}$, we observe PSDs that are formally tangent to the body surface but with $\sqrt{\hat{\boldsymbol{\lambda}}}$ that in some cases have values >1, thus indicating an expansion. We note here that it is not inherently better looking at $\overline{\mathbf{F}}$ or $\mathbf{F}$. We highlight that, in most cases, this distinction is not considered and very often only deformation on meshes' surface is described and interpreted in functional, morphological, or biomechanical terms. This could lead to an incomplete or partial appreciation of the actual deformative phenomenon under study. This ineffectiveness could be partially mitigated by performing analyses in the shape-space. We used here the size-and shape-space with a purely didactic aim as it makes more evident the fact that PSDs of the *whole body* (thus *not* the body surface) when the target is considerably smaller than the source are very different from those on its surface.

Surfaces in 3D

The 3D surface example observes the occipital scale (exocranial surface) of two *Homo erectus* skulls from Java: Trinil 2 skull (belonging to the original Dubois collection from 1891's excavation) is of uncertain age, the estimate spanning from about 1 Ma and 0.5 Ma, and Ngandong 12 from Ngandong site (discovered in 1933 by von Koenigswald) about 50 km north from Trinil dated between 550 and 143 ka by Indriati et al. (2011) and recently re-placed between 110 and 120 ka by Rizal et al. (2020).

We digitized 133 landmarks distributed over the entire bone surface between the superior nuchal lines and the lambda on Ngandong 12 CT scans kindly provided by Dominique Grimaud-Hervé (GE medical systems/high speed RP; voxel size: 512 × 512 pixels; pixel size: 0.48; slice increment: 1 mm) and on Trinil 2 acquired with NextEngine laser scanner at the Department of Environmental Biology (Sapienza University of Rome). The configurations of points were digitized through the 3D software EVAN Toolbox v. 1.0 (www.evan-society.org). The same software was used for the 3D sliding procedure. In this way, 129 semi-landmarks were defined in relation to 4 fixed landmarks represented by the lambda, the inion and the two asterions (left and right). Spline relaxation (Bookstein, 1996, 1997) was carried out by sliding semi-landmarks on a plane tangent to the surface of each specimen (Gunz et al., 2005). This procedure involves the minimization of the bending energy with respect to the distribution of semi-landmarks on the surface of the three-dimensional object (not on a single curve) with reference to the position of the selected fixed landmarks and ensures the geometric homology (Gunz et al., 2005) of the points between the configurations. Configurations were then symmetrized w.r.t. sagittal plane.

The target was aligned to the source via OPA and both shapes were scaled at unit CS. For the sake of visualization, we decimated triangulation of meshes in order to better show deformation ellipsoids (see below). **Figure 14** shows data collection and results relative to computation of $\mathbf{F}$, $\overline{\mathbf{F}}$ and related metrics. Trinil 2 and Ngandong 12 are usually ascribed to the same species, i.e., *H. erectus*, albeit Trinil 2 is commonly considered a more primitive stage in *H. erectus* evolution, while Ngandong 12 constitutes, probably, a more derived form. Ngandong 12 shows a larger encephalization than Trinil 2 with a more elevated occipital scale relatively to the lambda. However, in both specimens, the opistocranion (the most distant point from the glabella) coincides with inion. A very marked difference is the morphology of occipital torus that is approximately straight in Trinil 2, while in Ngandong 12, it is a jutting structure laterally arching and with a noticeable thickness both medially and laterally. The orientation of $\hat{\mathbf{v}}_\mathbf{y}$ varies considerably if they are computed upon $\mathbf{F}$ or $\overline{\mathbf{F}}$. We depicted the ellipsoids circumscribed to $\hat{\mathbf{v}}_\mathbf{y}$ computed from $\mathbf{F}$: they clearly cross the body surface and are oriented in some regions nearly orthogonally to $\hat{\mathbf{v}}_\mathbf{y}$ computed upon $\overline{\mathbf{F}}$. This detail deserves particular attention as, looking at the surface only, one would underestimate the fact that the deformation acts primarily along a direction that, in some regions, is far from being tangent to the surface itself. In particular, the dorsal region of occipital scale, which includes the lambda, is more elevated dorso-ventrally in Ngandong 12 than in Trinil 2. This is related to the more pronounced dorso-ventral flattening of the latter w.r.t. the former that presents also a larger cranial capacity. Lack of cultural evidences, such as particular lithic industry, does not allow linking the larger encephalization of Ngandong 12 with an increased complexity of cultural behavior. Instead, the shape of occipital scales was probably more related to the development of neck muscles expansion and the antero-posterior deformation indicated by $\hat{\mathbf{v}}_\mathbf{y}$ computed from $\mathbf{F}$ (and much less clearly by $\overline{\mathbf{F}}$) can be interpreted just as the structural bone response to nuchal muscle hyper-development. We suggest that the use of $\mathbf{F}$ instead of $\overline{\mathbf{F}}$ leads to a very different morphological reading of the actual local deformation process than looking at surfaces only. The OPA (or GPA) alignment, in fact, superimposes centroid's shapes and globally rotates them in such a way that the target could appear less deformed locally than it does actually. Local strain analysis, instead, being locally rotation-independent, allows visualizing and quantifying PSDs and their magnitudes independently from initial position of source and target.

DISCUSSION AND CONCLUSIONS

In this study, we presented several strategies in order to quantify and visualize local deformation in the context of geometric morphometrics, a kind of shape analysis that exploits the concept of homologous landmarks digitization. Starting from corresponding points found on both the source and target

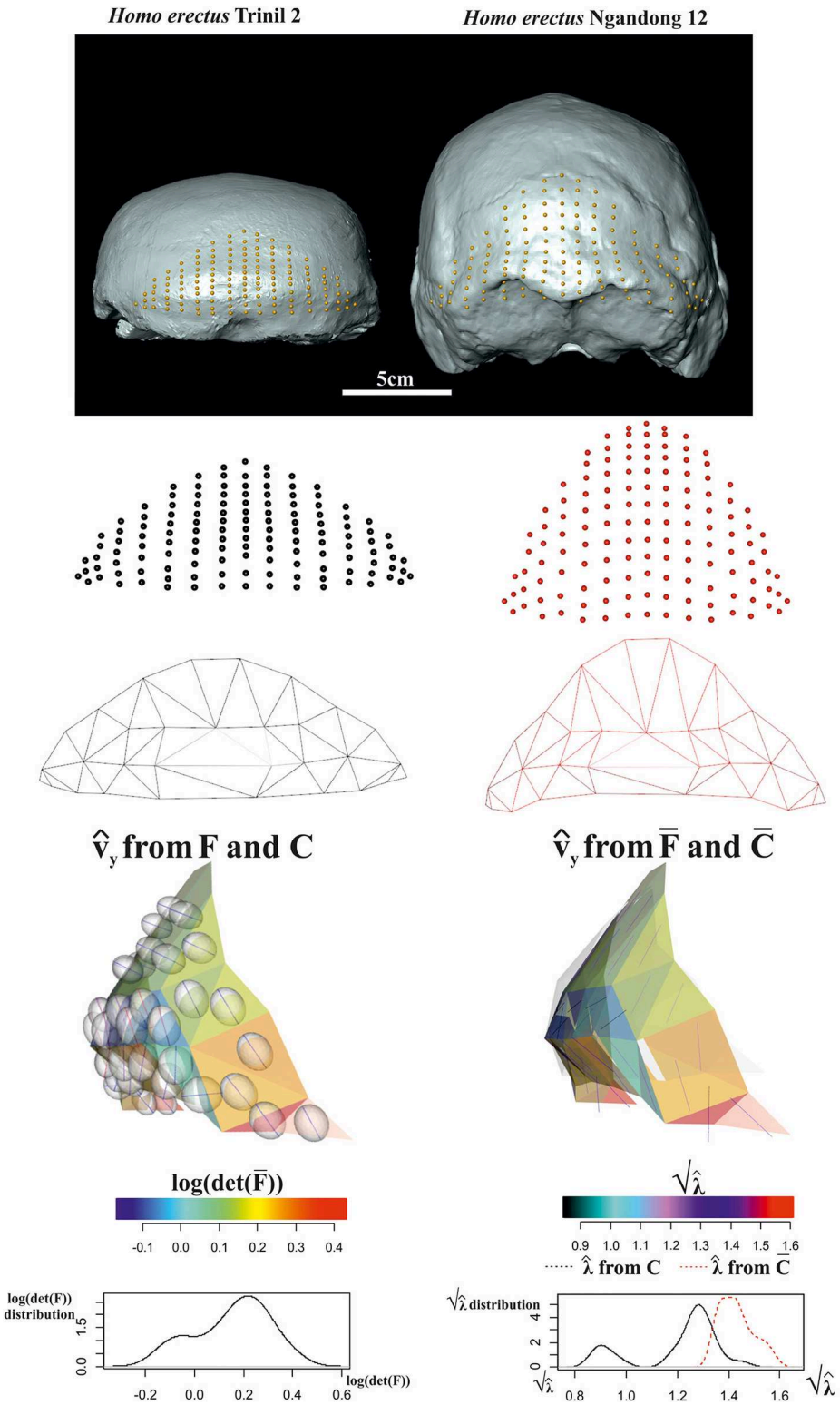

FIGURE 14 | Local deformations observable between *Homo erectus* Trinil 2 (as source) and *H. erectus* Ngandong 12 (as target). 3D meshes are also shown. $\hat{\mathbf{v}}_y$ calculated upon **F** or $\overline{\mathbf{F}}$ are shown and colored according to the corresponding $\sqrt{\hat{\lambda}}$. Meshes' triangular faces are colored according to log(det($\overline{\mathbf{F}}$)). Densities of relevant metrics are also illustrated. Source and target shapes were aligned via OPA. Trinil 2 is housed at the Nationaal Museum van Natuurlijke Historie, Leiden, The Netherlands; Ngandong 12 is housed at the Department of Physical Anthropology, Gadja Mada University College of Medicine, Yogyakarta, Indonesia.

TABLE 1 | Relevant objects used for visualization of local deformation.

Object	Notation	Equation or definition	Meaning
First-order gradient tensor	$\mathbf{F}$	In $\mathbb{R}^2$ $\mathbf{F}=\mathbf{H}+\mathbf{I}=\begin{bmatrix}\frac{\partial u_x}{\partial x}+1 & \frac{\partial u_x}{\partial y}\\ \frac{\partial u_y}{\partial x} & \frac{\partial u_y}{\partial y}+1\end{bmatrix}$ In $\mathbb{R}^3$ $\mathbf{F}=\mathbf{H}+\mathbf{I}=\begin{bmatrix}\frac{\partial u_x}{\partial x}+1 & \frac{\partial u_x}{\partial y} & \frac{\partial u_x}{\partial z}\\ \frac{\partial u_y}{\partial x} & \frac{\partial u_y}{\partial y}+1 & \frac{\partial u_y}{\partial z}\\ \frac{\partial u_z}{\partial x} & \frac{\partial u_z}{\partial y} & \frac{\partial u_z}{\partial z}+1\end{bmatrix}$	Compute local deformation of a unitary circumference in $\mathbb{R}^2$ or a sphere in $\mathbb{R}^3$ on the target shape
First-order gradient tensor computed upon TPS interpolation	$\mathbf{F}_{tps}$ or $\nabla(\psi)$	In $\mathbb{R}^2$ $\nabla(\psi)_n=\begin{bmatrix}\frac{\partial \psi_1}{\partial x} & \frac{\partial \psi_1}{\partial y}\\ \frac{\partial \psi_2}{\partial x} & \frac{\partial \psi_2}{\partial y}\end{bmatrix}=\begin{bmatrix}A_{11} & A_{12}\\ A_{21} & A_{22}\end{bmatrix}+\begin{bmatrix}W_{11} & \dots & W_{1k}\\ W_{21} & \dots & W_{2k}\end{bmatrix}\begin{bmatrix}\frac{\partial \sigma_1}{\partial x} & \frac{\partial \sigma_1}{\partial y}\\ \dots & \dots\\ \frac{\partial \sigma_k}{\partial x} & \frac{\partial \sigma_k}{\partial y}\end{bmatrix}$ In $\mathbb{R}^3$ $\nabla(\psi)_n=\begin{bmatrix}\frac{\partial \psi_1}{\partial x} & \frac{\partial \psi_1}{\partial y} & \frac{\partial \psi_1}{\partial z}\\ \frac{\partial \psi_2}{\partial x} & \frac{\partial \psi_2}{\partial y} & \frac{\partial \psi_2}{\partial z}\\ \frac{\partial \psi_3}{\partial x} & \frac{\partial \psi_3}{\partial y} & \frac{\partial \psi_3}{\partial z}\end{bmatrix}$ $=\begin{bmatrix}A_{11} & A_{12} & A_{13}\\ A_{21} & A_{22} & A_{23}\\ A_{31} & A_{32} & A_{33}\end{bmatrix}+\begin{bmatrix}W_{11} & \dots & W_{1k}\\ W_{21} & \dots & W_{2k}\\ W_{31} & \dots & W_{3k}\end{bmatrix}\begin{bmatrix}\frac{\partial \sigma_1}{\partial x} & \frac{\partial \sigma_1}{\partial y} & \frac{\partial \sigma_1}{\partial z}\\ \dots & \dots & \dots\\ \frac{\partial \sigma_k}{\partial x} & \frac{\partial \sigma_k}{\partial y} & \frac{\partial \sigma_k}{\partial z}\end{bmatrix}$	Compute local deformation of a unitary circumference in $\mathbb{R}^2$ or a sphere in $\mathbb{R}^3$ on the target shape according to TPS first partial derivatives
Projected first-order gradient tensor	$\overline{\mathbf{F}}$	$\overline{\mathbf{F}}=\boldsymbol{P_t}^{\mathsf{T}}\mathbf{F}\boldsymbol{P_s}$	Project $\mathbf{F}$ on a plane in $\mathbb{R}^3$
Right Cauchy–Green symmetric deformation tensor	$\mathbf{C}$	$\mathbf{C}=\mathbf{F}^{\mathsf{T}}\mathbf{F}$	Compute local deformation of a unitary circumference in $\mathbb{R}^2$ or a sphere in $\mathbb{R}^3$ on the source shape
Projected right Cauchy–Green symmetric deformation tensor	$\overline{\mathbf{C}}$	$\overline{\mathbf{C}}=\boldsymbol{P_s}^{\boldsymbol{T}}\boldsymbol{C}\boldsymbol{P_s}$	Project $\mathbf{C}$ on a plane in $\mathbb{R}^3$
Eigenvalues of $\mathbf{C}$	$\boldsymbol{\lambda}$	Eigenvalues of $\mathbf{C}$	Squared magnitudes of $\mathbf{v}$
Eigenvalue of largest deformation	$\hat{\boldsymbol{\lambda}}$	$\hat{\boldsymbol{\lambda}}=argmax(\lvert 1-\boldsymbol{\lambda}\rvert)$	Largest deformation' (the most distant from 1) squared magnitude
Strain directions (on source configuration)	$\mathbf{v}$	Eigenvectors of $\mathbf{C}$	Strain directions on the source at unitary norm
Strain directions on target configuration	$\mathbf{v}_y$	$\mathbf{v}_y=\mathbf{F}\mathbf{v}$	Strain directions on the target; they contain magnitudes
Primary strain direction	$\hat{\mathbf{v}}_\mathbf{y}$	Eigenvectors corresponding to $\hat{\boldsymbol{\lambda}}$	Strain directions corresponding to the largest deformation
Second-order gradient tensor computed upon TPS interpolation	$\nabla\nabla(\psi)$	In $\mathbb{R}^2$ $\nabla\nabla(\psi)_n=\begin{bmatrix}\frac{\partial^2 \psi_1}{\partial x^2} & \frac{\partial^2 \psi_1}{\partial x\partial y} & \frac{\partial^2 \psi_1}{\partial y\partial x} & \frac{\partial^2 \psi_1}{\partial y^2}\\ \frac{\partial^2 \psi_2}{\partial x^2} & \frac{\partial^2 \psi_2}{\partial x\partial y} & \frac{\partial^2 \psi_2}{\partial y\partial x} & \frac{\partial^2 \psi_2}{\partial y^2}\end{bmatrix}$ $=\begin{bmatrix}W_{11} & \dots & W_{1k}\\ W_{21} & \dots & W_{2k}\end{bmatrix}\begin{bmatrix}\frac{\partial^2 \sigma_1}{\partial x^2} & \frac{\partial^2 \sigma_1}{\partial y\partial x} & \frac{\partial^2 \sigma_1}{\partial x\partial y} & \frac{\partial^2 \sigma_1}{\partial y^2}\\ \dots & \dots & \dots & \dots\\ \frac{\partial^2 \sigma_k}{\partial x^2} & \frac{\partial^2 \sigma_k}{\partial y\partial x} & \frac{\partial \sigma_k}{\partial x\partial y} & \frac{\partial^2 \sigma_k}{\partial y^2}\end{bmatrix}$ In $\mathbb{R}^3$ $\nabla\nabla(\psi)_n=\begin{bmatrix}\frac{\partial^2 \psi_1}{\partial x^2} & \frac{\partial^2 \psi_1}{\partial y^2} & \frac{\partial^2 \psi_1}{\partial z^2} & \frac{\partial^2 \psi_1}{\partial x\partial y} & \frac{\partial^2 \psi_1}{\partial y\partial x} & \frac{\partial^2 \psi_1}{\partial x\partial z} & \frac{\partial^2 \psi_1}{\partial z\partial x} & \frac{\partial^2 \psi_1}{\partial z\partial y} & \frac{\partial^2 \psi_1}{\partial y\partial z}\\ \frac{\partial^2 \psi_2}{\partial x^2} & \frac{\partial^2 \psi_2}{\partial y^2} & \frac{\partial^2 \psi_2}{\partial z^2} & \frac{\partial^2 \psi_2}{\partial x\partial y} & \frac{\partial^2 \psi_2}{\partial y\partial x} & \frac{\partial^2 \psi_2}{\partial x\partial z} & \frac{\partial^2 \psi_2}{\partial z\partial x} & \frac{\partial \psi_2}{\partial z\partial y} & \frac{\partial^2 \psi_2}{\partial y\partial z}\\ \frac{\partial^2 \psi_3}{\partial x^2} & \frac{\partial^2 \psi_3}{\partial y^2} & \frac{\partial^2 \psi_3}{\partial z^2} & \frac{\partial^2 \psi_3}{\partial x\partial y} & \frac{\partial^2 \psi_3}{\partial y\partial x} & \frac{\partial^2 \psi_3}{\partial x\partial z} & \frac{\partial^2 \psi_3}{\partial z\partial x} & \frac{\partial \psi_3}{\partial z\partial y} & \frac{\partial^2 \psi_3}{\partial y\partial z}\end{bmatrix}$ $=\begin{bmatrix}W_{11} & \dots & W_{1k}\\ W_{21} & \dots & W_{2k}\\ W_{31} & \dots & W_{3k}\end{bmatrix}\begin{bmatrix}\frac{\partial^2 \sigma_1}{\partial x^2} & \frac{\partial^2 \sigma_1}{\partial y^2} & \frac{\partial^2 \sigma_1}{\partial z^2} & \frac{\partial^2 \sigma_1}{\partial x\partial y} & \frac{\partial^2 \sigma_1}{\partial y\partial x} & \frac{\partial^2 \sigma_1}{\partial x\partial z} & \frac{\partial^2 \sigma_1}{\partial z\partial x} & \frac{\partial^2 \sigma_1}{\partial z\partial y} & \frac{\partial^2 \sigma_1}{\partial y\partial z}\\ \dots & \dots & \dots & \dots & \dots & \dots & \dots & \dots & \dots\\ \frac{\partial^2 \sigma_k}{\partial x^2} & \frac{\partial^2 \sigma_k}{\partial y^2} & \frac{\partial^2 \sigma_k}{\partial z^2} & \frac{\partial^2 \sigma_k}{\partial x\partial y} & \frac{\partial^2 \sigma_k}{\partial y\partial x} & \frac{\partial^2 \sigma_k}{\partial x\partial z} & \frac{\partial^2 \sigma_k}{\partial z\partial x} & \frac{\partial^2 \sigma_k}{\partial z\partial y} & \frac{\partial^2 \sigma_k}{\partial y\partial z}\end{bmatrix}$	It notifies how much is non-constant $\nabla(\psi)$ in the neighborhood where $\nabla\nabla(\psi)$ is evaluated according to TPS second partial derivatives
Strain energy	ϕ	$\varphi=\frac{1}{2}\int_\Omega E\cdot E$	Strain energy associated to a deformation

shapes, reasonably homologous triangulations can be assembled using constrained Delaunay triangulation (or similar strategies) on both two and three dimensions. **Table 1** presents the main objects, together with their definitions, presented in the text. The use of direct calculation on triangles (or tetrahedra if available) or of the evaluation of $\nabla(\psi)$ at appropriate evaluation points

leads to the identification of the deformation gradient tensor **F** that is the base to derive the necessary objects needed for the quantification of local deformation and for its visualization on source or target shape: $\mathbf{C} = \mathbf{F}^T\mathbf{F}$, **v**, and **λ**, i.e., the eigenvectors and eigenvalues of **C**; log(det(**F**)) has been used in the past (Márquez et al., 2012) to illustrate the infinitesimal area change around the evaluation points. However, this does not inform about the direction of deformation. SDs, e.g., **v** and $\mathbf{v}_y$, are proper objects for this purpose: they notify the (locally affine) directions of deformation dictated by **C** and **F** and can be further investigated by selecting PSDs, i.e., the primary direction of local shape change corresponding to those eigenvalues most distant from 1 (that indicates no deformation). We have shown that depicting SD could be very effective for interpreting the shape change and allows identifying particular regions characterized by deformations whose effects take place in different parts of the target shape as illustrated in the 2D example regarding orbit elevation in *Archaeopotamus* and *Hippopotamus*. In three dimensions we distinguished the two cases of "full volume" shapes, such as in Talpoidea example, and "shell-like" configurations such as in *H. erectus* occipital scale example. In these cases, we highlighted the importance of interpreting **F** or $\overline{\mathbf{F}}$: in fact, looking at what happens to a triangle's surface cannot account for the deformation of the entire ambient space that also embraces the landmarks belonging to the surface itself. **F**, in fact, models deformation in every space direction and allows the appreciation of actual PSD representing the full shape change between source and target. Of course, both **F** and $\overline{\mathbf{F}}$ can be used to interpret the phenomenon. It is important, however, to be aware of what $\overline{\mathbf{F}}$ really means, i.e., a projection of the local actual deformation in three dimensions. While, in most GM applications related to paleontological and biological studies, the evaluation of local deformation in a quasi-continuous way is not very common, it could be of great help in inferring the deformational phenomenon when referred to bone's growth and development: for example, appreciating concomitantly $\nabla(\psi)$ and $\nabla\nabla(\psi)$ would permit the evaluation of the direction at specific locations of developmental process as well as its local variation possibly related to specific growth factors: in fact, as the growth is not an isotropic process (i.e., not homothetic), observing the eigendecomposition and spatial variation of the gradient tensor would inform about differential forces involved in the whole system. These forces could be related to muscle insertions such as in long bones of sauropod dinosaurs (Bonnan, 2007) or to mechanical pressures exerted in the complex reciprocal relationships existing between brain and its braincase abundantly investigated in paleoanthropology (Bruner, 2018). The range of use of the methods presented here is as wide as the range of shape analysis applications; their implementation is now available in R language using a set of specific *ad hoc* functions available in the online **Supplementary Material** together with scripts to reproduce each figure of the present paper. Each script is intended to work "stand alone" after loading the source file with ancillary functions and necessary R packages indicated therein. No workspace loading is necessary and landmark coordinates are furnished in individual scripts. More indications can be found in the "read me" file.

DATA AVAILABILITY STATEMENT

All the data used in this study can be generated by running the R scripts associated to the article.

AUTHOR CONTRIBUTIONS

PP and VV conceived the paper. PP, PR, AM, and LP wrote the paper. AP, LP, and FD acquired experimental data. PP, VV, and SC implemented necessary R functions.

ACKNOWLEDGMENTS

We thank Luciano Teresi for useful advice during manuscript preparation. LP developed part of this paper within the research project Ecomorphology of fossil and extant Hippopotamids and Rhinocerotids granted by the University of Florence (Progetto Giovani Ricercatori Protagonisti initiative). We also thank two reviewers for useful suggestions during manuscript preparation.

SUPPLEMENTARY MATERIAL

The Supplementary Material for this article can be found online at: https://www.frontiersin.org/articles/10.3389/feart.2020.00066/full#supplementary-material

REFERENCES

Adams, D. C., Rohlf, F. J., and Slice, D. E. (2004). Geometric morphometrics: ten years of progress following the 'revolution'. *It. J. Zool.* 71, 5–16. doi: 10.1080/11250000409356545

Adams, D. C., Rohlf, F. J., and Slice, D. E. (2013). A field comes of age: geometric morphometrics in the 21st century. Hystrix, *Ital. J. Mammal.* 24, 7–14.

Angulo-Bedoya, M., Correa, S., and Benítez, H. A. (2019). Unveiling the cryptic morphology and ontogeny of the Colombian *Caiman crocodilus*: a geometric morphometric approach. *Zoomorphology* 138, 387–397. doi: 10.1007/s00435-019-00448-2

Barnosky, A. D. (1981). A skeleton of *Mesoscalops* (Mammalia, Insectivora) from the Miocene deep river formation, montana, and a review of the proscalopid moles: evolutionary, functional, and stratigraphic relationships. *J. Vert. Pal.* 1, 285–339. doi: 10.1080/02724634.1981.10011904

Barnosky, A. D. (1982). Locomotion in moles (Insectivora, Proscalopidae) from the middle Tertiary of North America. *Science* 216, 183–185. doi: 10.1126/science.216.4542.183

Boisserie, J. R. (2005). The phylogeny and taxonomy of Hippopotamidae (Mammalia: Artiodactyla): a review based on morphology and cladistic analysis. *Zool. J. Linn. Soc.* 143, 1–26. doi: 10.1111/j.1096-3642.2004.00138.x

Boisserie, J. R. (2007). "Family hippopotamidae," in *The Evolution of Artiodactyls*, eds D. R. Prothero and S. E. Foss (Baltimore, MD: JHU Press), 106–119.

Boisserie, J. R., Fisher, R. E., Lihoreau, F., and Weston, E. M. (2011). Evolving between land and water: key questions on the emergence and history of the Hippopotamidae (Hippopotamoidea, Cetancodonta, Cetartiodactyla). *Biol. Rev.* 86, 601–625. doi: 10.1111/j.1469-185X.2010.00162.x

Bonnan, M. F. (2007). Linear and geometric morphometric analysis of long bone scaling patterns in Jurassic neosauropod dinosaurs: their functional and paleobiological implications. *Anat. Rec.* 290, 1089–1111. doi: 10.1002/ar.20578

Bookstein, F. L. (1989). Principal warps: thin-plate splines and the decomposition of deformations. *IEEE Trans. Pattern Anal. Mach. Intell.* 11, 567–585. doi: 10.1109/34.24792

Bookstein, F. L. (1991). *Morphometric Tools for Landmark Data: Geometry and Biology*. Cambridge: Cambridge University Press.

Bookstein, F. L. (1996). "Standard formula for the uniform shape component in landmark data," in *Advances in Morphometrics*, eds L. F. Marcus, M. Corti, A. Loy, G. J. P. Naylor, and D. E. Slice (Boston, MA: NATO ASI Series; Series A; Life Sciences; Springer), 153–168.

Bookstein, F. L. (1997). Landmark methods for forms without landmarks: morphometrics of group differences in outline shape. *Med. Im. An.*1, 225–243. doi: 10.1016/s1361-8415(97)85012-8

Bruner, E. (2018). "The brain, the braincase, and the morphospace," in *Digital Endocasts*, eds E. Bruner, N. Ogihara, and H. C. Tanabe (Tokio: Springer), 93–114.

Caloi, L., and Palombo, M. R. (1994). Le faune a grandi mammiferi del Pleistocene superiore dell'Italia centrale: biostratigrafia e paleoambiente. *Boll. Serv. Geol. Ital.* 111, 503–514.

Castiglione, S., Serio, C., Tamagnini, D., Melchionna, M., Mondanaro, A., Di Febbraro, M., et al. (2019). A new, fast method to search for morphological convergence with shape data. *PLoS ONE* 14:e0226949. doi: 10.1371/journal.pone.0226949

Ceritoglu, C., Tang, X., Chow, M., Hadjiabadi, D., Shah, D., Brown, T., et al. (2013). Computational analysis of LDDMM for brain mapping. *Front. Neurosci.* 7:151. doi: 10.3389/fnins.2013.00151

Charlier, B., Charon, N., and Trouvé, A. (2017). The fshape framework for the variability analysis of functional shapes. *Found. Comput. Math.* 17, 287–357. doi: 10.1007/s10208-015-9288-2

Claude, J. (2008). *Morphometrics With R*. New York, NY: Springer.

Colangelo, P., Ventura, D., Piras, P., Pagani Guazzugli Bonaiuti, J., and Ardizzone, G. (2019). Are developmental shifts the main driver of phenotypic evolution in *Diplodus* spp. (Perciformes: Sparidae)? *BMC Evol. Biol.* 19:106. doi: 10.1186/s12862-019-1424-1

Coryndon, S. C. (1977). The taxonomy and nomenclature of the Hippopotamidae (Mammalia, Artiodactyla) and a description of two new fossils species. *Proc. Kon. Ned. Akad. Wetensch. B.* 80, 61–88.

Dryden, I. L., and Mardia, K. V. (2016). *Statistical Shape Analysis, With Applications in R*, 2nd Edn. Chichester: John Wiley and Sons.

Durrleman, S., Pennec, X., Trouvé, A., Ayache, N., and Braga, J. (2012). Comparison of the endocranial ontogenies between chimpanzees and bonobos via temporal regression and spatiotemporal registration. *J. Hum. Evol.* 62, 74–88.

Evangelista, A., Gabriele, S., Nardinocchi, P., Piras, P., Puddu, P. E., Teresi, L., et al. (2015). "Continuum mechanics meets echocardiographic imaging: investigation on the principal strain lines in human left ventricle," in *Developments in Medical Image Processing and Computational Vision*, eds J. Tavares and J. R. M. Natal (Cham: Springer), 41–54.

Gabriele, S., Teresi, L., Varano, V., Nardinocchi, P., Piras, P., Esposito, G., et al. (2016). "Mechanics-based analysis of the left atrium via echocardiographic imaging," in *Proceedings of the 5th Eccomas Thematic Conference on Computational Vision and Medical Image Processing*, eds J. Tavares and J. R. M. Natal (Boca Raton, FL: VipIMAGE 2015, CRC press), 267–271.

Gower, J. C. (1975). Generalized procrustes analysis. *Psychometrika* 40, 33–51. doi: 10.1007/BF02291478

Gunz, P., Mitteroecker, P., and Bookstein, F. L. (2005). "Semilandmarks in three dimensions," in *Modern Morphometrics in Physical Anthropology,* ed D. E. Slice (Boston, MA: Springer), 73–98.

Harrison, T. (1997). "The anatomy, paleobiology, and phylogenetic relationships of the Hippopotamidae (Mammalia, Artiodactyla) from the Manonga Valley, Tanzania," in *Neogene Paleontology of the Manonga Valley, Tanzania*, ed T. Harrison (Boston, MA: Springer), 137–190.

Indriati, E., Swisher, C. C., Lepre, C., Quinn, R. L., Suriyanto, R. A., Hascaryo, A. T., et al. (2011). The age of the 20 meter Solo River terrace, Java, Indonesia and the survival of *Homo erectus* in Asia. *PLoS ONE* 6:e21562. doi: 10.1371/journal.pone.0021562

Kent, J. T., and Mardia, K. V. (1994). "The link between kriging and thin-plate splines," in *Probability, Statistics and Optimization: A Tribute to Peter Whittle*, ed F. P. Kelly (New York, NY: Wiley), 325–39.

Kratz, A., Auer, C., Stommel, M., and Hotz, I. (2013) Visualization and analysis of second-order tensors: moving beyond the symmetric positive-definite case. *Comp. Graph. For.* 32, 49–74. doi: 10.1111/j.1467-8659.2012.03231.x

Le, H.-L. (1988). *Shape theory in flat and curved spaces and shape densities with uniform generators* (Ph.D. dissertation). University Cambridge, Cambridge, United Kingdom.

Lewison, R., and Pluháček, J. (2017). *Hippopotamus amphibius*. *IUCN Red List Threat. Species* 2017:e.T10103A18567364. doi: 10.2305/IUCN.UK.2017-2.RLTS.T10103A18567364.en

Márquez, A., Moreno-González, A., Plaza, Á., and Suárez, J. P. (2014). There are simple and robust refinements (almost) as good as Delaunay. *Math. Comp. Sim.* 106, 84–94. doi: 10.1016/j.matcom.2012.06.001

Márquez, E. J., Cabeen, R., Woods, R. P., and Houle, D. (2012). The measurement of local variation in shape. *Evol. Biol.* 39, 419–439. doi: 10.1007/s11692-012-9159-6

Miller, M. I., Trouvé, A., and Younes, L. (2015). Hamiltonian systems and optimal control in computational anatomy: 100 years since D'Arcy Thompson. *Annu. Rev. Biomed. Eng.* 17, 447–509. doi: 10.1146/annurev-bioeng-071114-040601

Miller, M. I., Younes, L., and Trouvé, A. (2014). Diffeomorphometry and geodesic positioning systems for human anatomy. *Technology* 2, 36–43. doi: 10.1142/S2339547814500010

Oxnard, C., and O'Higgins, P. (2009). Biology clearly needs morphometrics. Does morphometrics need biology? *Biol. Theory* 4, 84–97. doi: 10.1162/biot.2009.4.1.84

Pandolfi, L., Martino, R., Rook, L., and Piras, P. (2020). Investigating ecological and phylogenetic constraints in Hippopotamidae skull shape. *Riv. It. Paleont. Strat.* 126, 37–49. doi: 10.13130/2039-4942/12730

Perez, S. I., Bernal, V., and Gonzalez, P. N. (2006). Differences between sliding semi-landmark methods in geometric morphometrics, with an application to human craniofacial and dental variation. *J. Anat.* 208, 769–784. doi: 10.1111/j.1469-7580.2006.00576.x

Piras, P., Buscalioni, A. D., Teresi, L., Raia, P., Sansalone, G., Kotsakis, T., et al. (2014). Morphological integration and functional modularity in the crocodilian skull. *Int. Zool.* 9, 498–516. doi: 10.1111/1749-4877.12062

Piras, P., Maiorino, L., Raia, P., Marcolini, F., Salvi, D., Vignoli, L., et al. (2010). Functional and phylogenetic constraints in Rhinocerotinae craniodental morphology. *Evol. Ecol. Res.* 12, 897–928.

Piras, P., Sansalone, G., Teresi, L., Kotsakis, T., Colangelo, P., and Loy, A. (2012). Testing convergent and parallel adaptations in talpids humeral mechanical performance by means of geometric morphometrics and finite element analysis. *J. Morphol.* 273, 696–711. doi: 10.1002/jmor.20015

Piras, P., Sansalone, G., Teresi, L., Moscato, M., Profico, A., Eng, R., et al. (2015). Digging adaptation in insectivorous subterranean eutherians. The enigma of Mesoscalops montanensis unveiled by geometric morphometrics and finite element analysis. *J. Morphol.* 276, 1157–1171. doi: 10.1002/jmor.20405

Piras, P., Torromeo, C., Evangelista, A., Esposito, G., Nardinocchi, P., Teresi, L., et al. (2019). Non-invasive prediction of genotype positive–phenotype negative in hypertrophic cardiomyopathy by 3D modern shape analysis. *Exp. Physiol.* 104, 1688–1700.

Piras, P., Torromeo, C., Evangelista, A., Gabriele, S., Esposito, G., Nardinocchi, P., et al. (2017). Homeostatic left heart integration and disintegration links atrio-ventricular covariation's dyshomeostasis in hypertrophic cardiomyopathy. *Sci. Rep.* 7, 1–12.

Rizal, Y., Westaway, K. E., Zaim, Y., van den Bergh, G. D., Bettis, E. A. III., Morwood, M. J., et al. (2020). Last appearance of Homo erectus at Ngandong, Java, 117,000–108,000 years ago. *Nature* 577, 381–385. doi: 10.1038/s41586-019-1863-2

Rohlf, F. J. (2013). *TpsDIG. Version 2.17*. SUNY Stonybrook.

Rohlf, F. J., and Bookstein, F. L. (2003). Computing the uniform component of shape variation. *Syst. Biol.* 52, 66–69. doi: 10.1080/10635150390132759

Rohlf, F. J., and Slice, D. (1990). Extensions of the Procrustes method for the optimal superimposition of landmarks. *Syst. Biol.* 39, 40–59. doi: 10.2307/2992207

Sansalone, G., Colangelo, P., Loy, A., Raia, P., Wroe, S., and Piras, P. (2019). Impact of transition to a subterranean lifestyle on morphological disparity and integration in talpid moles (Mammalia, Talpidae). *BMC Evol. Biol.* 19:179. doi: 10.1186/s12862-019-1506-0

Santos, B. F., Perrard, A., and Brady, S. G. (2019). Running in circles in phylomorphospace: host environment constrains morphological diversification in parasitic wasps. *Proc. Royal Soc. B* 286:20182352. doi: 10.1098/rspb.2018.2352

Schlager, S. (2014). *Morpho: Calculations and Visualizations Related to Geometric Morphometrics*. R-package version 2.0. 3–1.

Stayton, C. T. (2015). The definition, recognition, and interpretation of convergent evolution, and two new measures for quantifying and assessing the significance of convergence. *Evolution* 69, 2140–2153. doi: 10.1111/evo.12729

Trouvé, A. (1998). Diffeomorphisms groups and pattern matching in image analysis. *Int. J. Comput. Vis.* 28, 213–221.

Varano, V., Gabriele, S., Teresi, L., Dryden, I., Puddu, P. E., Torromeo, C., et al. (2017). The TPS direct transport: a new method for transporting deformations in the size-and-shape space. *Int. J. Comp. Vis.* 124, 384–408, doi: 10.1007/s11263-017-1031-9

Varano, V., Piras, P., Gabriele, S., Teresi, L., Nardinocchi, P., Dryden, I. L., et al. (2018). The decomposition of deformation: new metrics to enhance shape analysis in medical imaging. *Med. Im. An.* 46, 35–56. doi: 10.1016/j.media.2018.02.005

Varano, V., Piras, P., Gabriele, S., Teresi, L., Nardinocchi, P., Dryden, I. L., et al. (2019). Local and global energies for shape analysis in medical imaging. *Int. J. Num. Meth. Biomed. Engin. 36:e*3252. doi: 10.1002/cnm.3252

Weston, E. M., and Lister, A. (2009). Insular dwarfism in hippos and a model for brain size reduction in *Homo floresiensis*. *Nature* 459, 85–88. doi: 10.1038/nature07922

Zelditch, M. L., Swiderski, D. L., and Sheets, H. D. (2012). *Geometric Morphometrics for Biologists: A Primer*. San Diego, CA: Academic Press.

Conflict of Interest: The authors declare that the research was conducted in the absence of any commercial or financial relationships that could be construed as a potential conflict of interest.

frontiers in Earth Science

ORIGINAL RESEARCH
published: 25 March 2020
doi: 10.3389/feart.2020.00079

Getting Its Feet on the Ground: Elucidating *Paralouatta*'s Semi-Terrestriality Using the Virtual Morpho-Functional Toolbox

Thomas A. Püschel[1], Jordi Marcé-Nogué[2,3,4], Justin Gladman[5], Biren A. Patel[6,7], Sergio Almécija[8,9,4] and William I. Sellers[10]*

[1] Primate Models for Behavioural Evolution Lab, Institute of Cognitive and Evolutionary Anthropology, School of Anthropology, University of Oxford, Oxford, United Kingdom, [2] Department of Pathology and Anatomical Sciences, Jacobs School of Medicine and Biomedical Sciences, University of Buffalo, State University of New York, NY, United States, [3] Department of Mechanical Engineering, Universitat Rovira i Virgili, Tarragona, Spain, [4] Institut Català de Paleontologia Miquel Crusafont, Universitat Autònoma de Barcelona, Barcelona, Spain, [5] Shared Materials Instrumentation Facility (SMIF), School of Engineering, Duke University, Durham, NC, United States, [6] Department of Integrative Anatomical Sciences, Keck School of Medicine, University of Southern California, Los Angeles, CA, United States, [7] Human and Evolutionary Biology Section, Department of Biological Sciences, University of Southern California, Los Angeles, CA, United States, [8] Division of Anthropology, American Museum of Natural History, New York, NY, United States, [9] New York Consortium in Evolutionary Primatology, New York, NY, United States, [10] Department of Earth and Environmental Sciences, University of Manchester, Manchester, United Kingdom

Currently, there are no living platyrrhine primates inhabiting the main Caribbean islands. Nevertheless, the fossil record of this area has provided outstanding findings of different New World monkeys that were part of a diverse radiation exhibiting remarkably unusual morphologies. Among these, the Cuban genus *Paralouatta* corresponds to one of the most enigmatic primates ever found in the Greater Antilles. Some researchers have argued that *Paralouatta*'s post-cranium shows evidence of semi-terrestriality, a locomotor adaptation that is unusual, if not unique, in platyrrhine evolutionary history. Whether or not *Paralouatta* was truly semi-terrestrial remains uncertain, however, due to a lack of more sophisticated functional analyses on its morphology. Using novel virtual morpho-functional techniques on a comparative sample of 3D talar models belonging to diverse primate species representing three substrate preferences, this study aims to further evaluate whether *Paralouatta* was a semi-terrestrial genus or not. Geometric morphometrics and finite element analysis were used to empirically assess shape and biomechanical performance, respectively, and then several machine-learning (ML) classification algorithms were trained using both morphometric and biomechanical data to elucidate the substrate preference of the fossils. The ML algorithms categorized the *Paralouatta* specimens as either arboreal or as species commonly active on both ground and in trees. These mixed results are suggestive of some level of semi-terrestriality, thus representing the only known example of this locomotor behavior in platyrrhine evolutionary history.

Keywords: platyrrhine, semi-terrestriality, machine-learning, geometric morphometrics, finite element analysis, *Paralouatta*, talus

OPEN ACCESS

Edited by:
Lorenzo Rook,
University of Florence, Italy

Reviewed by:
Carmela Serio,
Liverpool John Moores University, United Kingdom
Sergio Furtado Dos Reis,
State University of Campinas, Brazil

****Correspondence:***
Thomas A. Püschel
thomas.puschelrouliez@anthro.ox.ac.uk

Specialty section:
This article was submitted to Paleontology, a section of the journal Frontiers in Earth Science

Received: *26 December 2019*
Accepted: *09 March 2020*
Published: *25 March 2020*

Citation:
Püschel TA, Marcé-Nogué J, Gladman J, Patel BA, Almécija S and Sellers WI (2020) Getting Its Feet on the Ground: Elucidating Paralouatta's Semi-Terrestriality Using the Virtual Morpho-Functional Toolbox. Front. Earth Sci. 8:79. doi: 10.3389/feart.2020.00079

INTRODUCTION

No extant platyrrhine primates are known in any of the Greater Antilles (i.e., Jamaica, Hispaniola, Cuba; Fleagle, 2013). However, during the Quaternary these Caribbean islands were home of some the most mysterious neotropical primates (Cooke et al., 2011), different from all extant species currently found in the New World (Cachel, 2015). At least four different genera belonging to this endemic radiation of unique platyrrhines have been described, including the following species: *Antillothrix bernensis* from the Dominican Republic (Rímoli, 1977; MacPhee and Iturralde-Vinent, 1995; Kay et al., 2011; Rosenberger et al., 2011); *Xenothrix mcgregori* from Jamaica (Williams and Koopman, 1952; Rosenberger, 1977; MacPhee and Fleagle, 1991; MacPhee and Meldrum, 2006); *Insulacebus toussaintiana* from Haiti (Cooke et al., 2011); and *Paralouatta varonai* and *Paralouatta marianae* from Cuba (Rivero and Arredondo, 1991; Horovitz and MacPhee, 1999; MacPhee and Meldrum, 2006). Most of these Antillean fossil primates are from the Quaternary, with some even surviving until the human settlement of these islands or even the time of the European conquest of the Caribbean (MacPhee and Fleagle, 1991; Turvey, 2009; Cooke et al., 2017a,b), at which time they went extinct along with most Quaternary non-volant mammal species, most likely due to anthropic pressures (Morgan and Woods, 1986; Cooke et al., 2017a,b).

These Caribbean primates represent a diverse radiation that displayed particularly unusual morphologies comprising several autapomorphies and seemingly derived conditions which exist across different platyrrhine groups. Even though clearly platyrrhines, they also display traits and feature combinations that are atypical or absent in any extant species (e.g., *Xenothrix* lacks third molars, and its first molars are much larger than the second ones). This morphological distinctiveness coupled with their noticeable differences when compared to extant continental taxa and the paucity of their remains has fueled an intense debate regarding the phylobiogeographic models that could explain the origin and adaptive radiation of this group. In fact, it has been challenging to determine the phylogenetic relationships of the Caribbean platyrrhine genera, and until recently they were not particularly clear. At different times, they have been associated with nearly all known platyrrhine sub-families (e.g., Williams and Koopman, 1952; Rosenberger, 1977; Rímoli, 1977; Ford and Morgan, 1986; Rivero and Arredondo, 1991; Woods and Ottenwalder, 1992; Horovitz, 1999; Rosenberger et al., 2011), classified as a sister group of living platyrrhines (Kay et al., 2011), or as stem platyrrhines that had established in the Greater Antilles in the Early Miocene (i.e., prior to the origin of modern New World monkey families; Kay, 2015). Several authors consider that the Caribbean endemic primates correspond to a monophyletic group, sister to *Callicebus sensu lato* (MacPhee and Horovitz, 2004), or to all crown platyrrhines (Kay, 2015), whereas others regard the striking morphological variation between the different species as evidence of multiple colonization events by different mainland lineages, or alternatively one multilineage colonization episode (Rosenberger, 2002). Fortunately, Woods et al. (2018) were able to retrieve DNA from a *Xenothrix* sample, providing several insights concerning this issue. They found that instead of being remotely related to living platyrrhines, *Xenothrix* corresponds to an extremely derived titi monkey (i.e., a member of the sub-family Callicebinae) that experienced significant morphological changes after arriving to Jamaica. Furthermore, they also found that based on the estimated splitting date between titi monkeys and *Xenothrix* (∼11 Ma), platyrrhines colonized the Greater Antilles more than once (Woods et al., 2018), since the oldest known Caribbean primate, *P. marianae*, was found in Miocene sediments dated to 17.5–18.5 Ma (MacPhee et al., 2003). This indicates that the Caribbean primates cannot be monophyletic and that there were at least two platyrrhine colonization events of the Greater Antilles at different times during the Neogene.

Among their many unique array of traits, Caribbean primates exhibit some of their most unusual in their post-cranial skeletons. For example, MacPhee and Fleagle (1991) considered that some aspects of the post-cranial morphology of *Xenothrix* (e.g., the adductor process of the femur) were so peculiarly dissimilar when compared to the post-crania of other platyrrhines, that they proposed that this species could have been a slow arboreal quadruped, thus representing a unique locomotion among platyrrhines. However, even more strikingly different are the set of post-cranial features of *P. varonai* which are thought to be related to a semi-terrestrial lifestyle (MacPhee and Meldrum, 2006). If correct, this interpretation would not only imply a locomotor convergence between some Old and a New World monkey species, but could also represent the first case of a locomotor behavior that does not exist in New World monkeys (among which all modern species are habitually arboreal) and that has no known analog in the platyrrhine fossil record. The amount of time that *P. varonai* may have spent on the ground, as well as to what degree it might have been similar to cercopithecids in postural and locomotor behaviors is yet to be resolved (MacPhee and Meldrum, 2006). Additionally, it remains unclear whether the older *P. marianae* exhibited any semi-terrestrial adaptations. Recently, Püschel et al. (2017, 2018) inferred the main locomotor behavior of *P. marianae* as one comparable to alouattines (i.e., exhibiting different levels of arboreal quadrupedalism, clambering and climbing), but it is important to bear in mind that they were not able to rule out possible semi-terrestrial adaptations, since they had not consider this category in their analyses.

Paralouatta marianae was originally described based on a single talus (MacPhee et al., 2003). It was described as only slightly different in morphology from that of *P. varonai*, in spite of the 17–18 Ma that allegedly separates them; the primary difference noted was that *P. marianae*'s talus is noticeably smaller (MacPhee and Meldrum, 2006). It has been argued that there is no appropriate morphological analog for the talus of *Paralouatta* amongst living platyrrhines (MacPhee and Iturralde-Vinent, 1995; MacPhee and Meldrum, 2006). MacPhee and Iturralde-Vinent (1995) described that atelid tali are different from *Paralouatta* in showing a "wedged" trochlea with a low trochlear relief (i.e., a trait associated with an increased mobility at the talocrural articulation), whereas *Paralouatta* displays a talus associated with increased stability. Additionally, the talus of *Paralouatta* has an evident cotylar

fossa, hence providing a stable articulation for the medial malleolus (MacPhee and Iturralde-Vinent, 1995). This feature, that usually does not exist in large New World monkeys, is commonly seen in highly terrestrial cercopithecines e.g., *Theropithecus* (MacPhee and Meldrum, 2006). MacPhee and Meldrum (2006) used twelve linear measurements to compute a principal component analysis (PCA) of different tali. They found that *Paralouatta*'s talus is particularly distinct from the tali of other New World monkeys, especially because the absence of trochlear "wedging" distinguishes *Paralouatta* from all other large New World monkeys. In contrast, Püschel et al. (2017) performed a PCA of landmark data using geometric morphometrics (GM) and found that *Paralouatta* occupied a position in the resulting morphospace near *Alouatta*, as well as to some of the oldest platyrrhines from Patagonia (i.e., *Dolichocebus, Soriacebus*, and *Carlocebus*). Similarly, they applied a hierarchical clustering analysis that placed this fossil near *Cebus/Sapajus* and *Dolichocebus*, *Soriacebus*, and *Carlocebus*, hence showing that, at least from a morphological perspective, the talus of *Paralouatta* is not as unusual as initially thought (Püschel et al., 2017).

Paralouatta varonai was discovered in association with Late Quaternary fauna in Western Cuba, whilst *P. marianae* was discovered in Early Miocene (17.5–18.5 Ma) deposits, hence representing the oldest Caribbean platyrrhine known and establishing an early date for the arrival of platyrrhines to the Greater Antilles. *P. varonai* was originally considered to be similar to *Alouatta* (hence the genus name), since its estimated size was close to that of an extant alouattine, and the cranium was somewhat similar to that of a howler monkey (Rivero and Arredondo, 1991; Rosenberger et al., 2011). Further phylogenetic studies have either confirmed a possible alouattine connection (Rosenberger, 2002; Rosenberger et al., 2015), or have classified *Paralouatta* as related to the Callicebinae from South America (Horovitz and MacPhee, 1999; MacPhee and Horovitz, 2002, 2004). Meanwhile and as mentioned above, classical morpho-functional analyses (i.e., simple observations, linear measurements, ratio computations, etc.) of the post-cranial remains of *Paralouatta* suggested a semi-terrestrial locomotor mode for the genus, based on traits such as its short digits for its size, combination of deep olecranon, narrow trochlea, fossa and retroflexed medial epicondyle, among other traits. However, it is important to stress that MacPhee and Meldrum (2006) admit that *Paralouatta* exhibits an unforeseen mix of traits that when taken together differentiate this genus from all other known extant and extinct New World monkeys. Among these distinguishing features there are some that can be interpreted as evidence of some degree of terrestriality (i.e., based on the morphology of ground dwelling cercopithecoids), whereas other traits do not show this behavioral signal. Whether the traits that seem adaptive to terrestriality are actually indicative of this locomotor behavior, or rather represent another form of locomotor adaption not observed in extant platyrrhines or even anthropoids is currently not clear. Certainly, a more complete post-cranial fossil record of *Paralouatta* would contribute to our understanding of this issue. In the absence of more fossils, it is also possible to utilize virtual morpho-functional toolkits (i.e., "engineering toolbox"), which are increasingly being used to analyze both living and fossil functional morphology (Rayfield, 2019). Accordingly, the primary goal of the present study is to perform a battery of different computational analyses in order to test the hypothesis that *Paralouatta* was habitually semi-terrestrial. This is of importance because if semi-terrestriality is confirmed, this would represent the first case of such behavior among both extant and extinct New World monkeys.

This study specifically focused on the talus as it is the only post-cranial element representing both *P. marianae* and *P. varonai*. Additionally, the talus plays an informative arthrodial connection between the foot and the leg (i.e., ankle joint), because of its important role in joint mobility and stability, as well as weight support (Püschel et al., 2018). In fact, it has been demonstrated that there is a strong and significant covariation between locomotor behaviors and talar shape (Püschel et al., 2017). As a result, we decided to apply a set of different techniques to elucidate whether or not *Paralouatta* represents the first known semi-terrestrial platyrrhine species. First, GM was applied to characterize the talar morphology of *Paralouatta* among a large and diverse anthropoid sample (Püschel et al., 2017). Second, we analyzed the mechanical strength of the extant anthropoid talar sample by applying finite-element analysis (FEA), as well as carrying out the simulation in the two *Paraloutta* tali available, since it has been shown that talar biomechanical performance can also be used as locomotor proxy (Püschel et al., 2018). Finally, given that the main aim of the present work is to classify the fossil tali within a substrate preference, several machine-learning (ML) algorithms were trained using the morphometric and biomechanical data from the extant species.

MATERIALS AND METHODS

Sample

The extant anthropoid sample included 3D surface renderings of tali from 109 individuals of 85 species representing all anthropoid sub-families; a large portion of the 3D data are available at https://www.morphosource.org/ (Boyer et al., 2016; Copes et al., 2016). Further details about the sample, including the Morphosource projects where the specimens can be found are provided in **Supplementary Table S1**. The fossil sample includes tali belonging to both *Paralouatta* species (**Figure 1** and **Supplementary Table S2**). The extant sample was classified according to their main substrate preference based on the database of Galán-Acedo et al. (2019). This database provides some important ecological traits, including substrate preference (i.e., locomotion type in the database) for 497 primate species. This information was compiled through a meticulous review of 1,216 studies published between 1941 and 2018 (Galán-Acedo et al., 2019). The substrate preference categorization scheme is provided in **Supplementary Table S1** and classifies each taxon as arboreal, terrestrial or as both substrate preferences (i.e., semi-terrestrial). This classification scheme refers to primary substrate preferences which reflects preferred or habitual environmental niche. The arboreal substrate preference comprises primate species that are strictly arboreal, which in undisturbed environments would seldom go to the

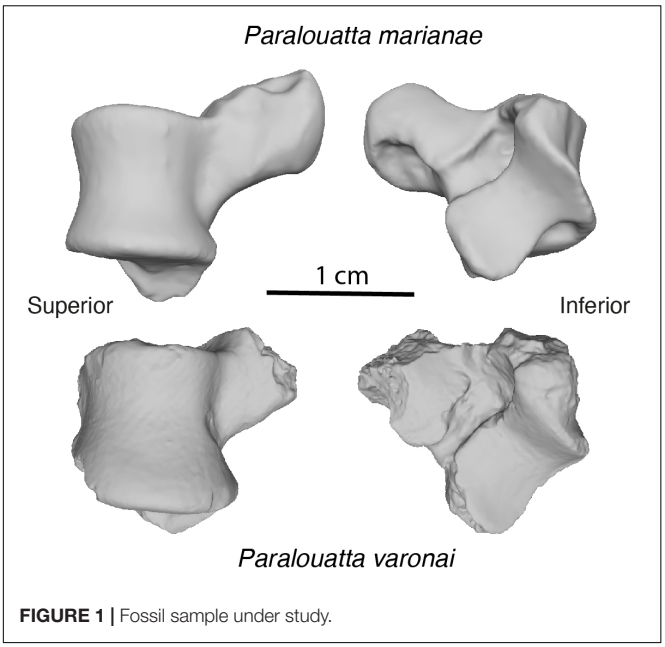

FIGURE 1 | Fossil sample under study.

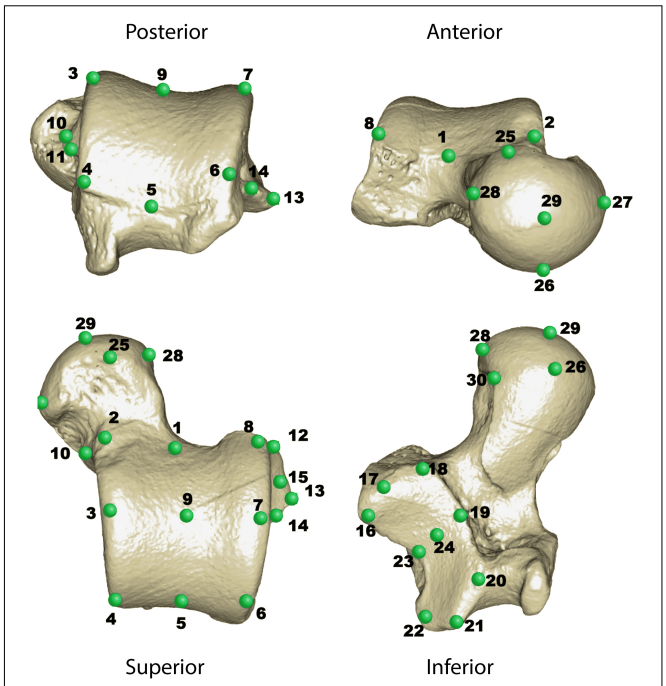

FIGURE 2 | A *Chiropotes satanas* talus (AMNH 95760) showing the 30 landmarks used in this study.

ground; the terrestrial category considers primates that are mostly terrestrial (i.e., they carry out most of their daily activity on the ground), whilst the category "both" involves species that are regularly active on both substrates (i.e., ground and trees). Although rather simplistic, this classification system can be considered as a first approximation to locomotor behavior that can be easily applied to the fossil record without making further assumptions. In addition, this classification scheme primarily deals with our main goal which is to elucidate the possible nature of *Paralouatta's* terrestriality.

3D Model Rendering

The refinement and smoothing tools available in Geomagic Studio® (3D Systems, v. 2014.3.0), Rock Hill, SC, United States) were used to repair the irregularities observed in some of the 3D models. All the tali were aligned with respect to the same reference position (further details about the alignment are available in **Supplementary Material S3**). The talus of *Paralouatta varonai* is relatively incomplete (i.e., the talar head is missing, and other areas exhibit minor damage), whereas the one for *Paralouatta marianae* is fairly complete (only the talar head exhibits some minimal erosion). Therefore, different reconstruction procedures were applied to generate models suitable for both GM and FEA analyses (these reconstruction procedures are described in **Supplementary Material S4**).

Geometric Morphometrics

Thirty 3D landmarks were collected using Landmark editor v. 3.6 (Wiley et al., 2005) on the surface of the virtual tali in order to represent their morphological variation (**Figure 2**; Harcourt-Smith, 2002; Turley and Frost, 2013). These raw coordinates are available in **Supplementary Material S5**. These landmarks were analyzed using the "geomorph" R package (Adams et al., 2018), where a generalized Procrustes analysis (GPA) was performed (Rohlf and Slice, 1990). The GPA translates the landmark configurations to the origin, scales them to a standard size (i.e., unit-centroid size), and rotates them (by employing a least-squares criterion) against each other until a best-fit of corresponding landmarks to each other is achieved. The aim of the GPA is to remove non-shape information from anatomical objects. Hence, the resulting aligned Procrustes coordinates correspond to the shape variables of each specimen under analysis. These shape variables were used to carry out a PCA to decompose shape variation into orthogonal axes of maximum variation. In addition, a multivariate phylogenetic generalized least square regression (PGLS) was used to assess the association between shape and the logarithm of centroid size for the extant dataset (centroid size corresponds to the square root of the sum of squared distances of a set of landmarks from their centroid) (Bookstein, 1997). The PGLS was performed using the procD.pgls() function of the "geomorph" R package, which performs ANOVA and regression models in a phylogenetic context assuming Brownian motion, in such a way that can cope with high-dimensional data (Adams, 2014). This allowed us to evaluate the influence of size on shape when taking into account phylogenetic non-independence. Since the PGLS requires a phylogeny, we downloaded a consensus phylogeny from https://10ktrees.nunn-lab.org/Primates/ that was computed from 10,000 Bayesian trees that included most of the species present in our dataset (Arnold et al., 2010). This phylogeny was slightly adjusted to incorporate some species that were originally not present. The resulting phylogeny is available in **Supplementary Material S6**.

All statistical analyses in this work were performed in R v. 3.6.0 (R Core Team, 2019).

Finite Element Analysis

The virtual talar models were imported into ANSYS® (Ansys, Inc., v. 17.1, Canonsburg, PA, United States)[1] to perform FEA. This engineering method reconstructs deformation, strain and stress in a digital structure after simulating a loading scenario (Richmond et al., 2005), and it is routinely used in vertebrate paleontology to tackle questions of organismal form, function, and evolution (Rayfield, 2007). In the present work we applied FEA to analyze talar mechanical strength, as it has been previously shown that talar biomechanical behavior can serve as locomotor proxy (Püschel et al., 2018). Each talus was modeled as a surface exclusively made of cortical bone; hence this required the use of shell elements in the finite element mesh. Homogeneous, linear and elastic material properties were used. Cortical bone values from a *Homo sapiens* talus were applied (Young's modulus: 20.7 GPa; Poisson's ratio: 0.3; Parr et al., 2013). The models were meshed using an adaptive mesh where the thickness of the shell elements representing the cortical bone was assumed to be constant. These values and further information about the FE models can be found in **Supplementary Table S3**. Cortical thickness values were obtained by measuring CT-data in some specimens and then, via a linear extrapolation of this data (see details of this procedure in **Supplementary Material S8**).

Loading Scenario and Boundary Conditions

Following the approach taken in Püschel et al. (2018), we applied a load on the trochlear surface of each talus in order to simulate a basic quadrupedal scenario. We decided to only model a generalized standing posture for all taxa since talar arthrokinematics are unknown in nearly all primates. The load was directed in the *z*-axis on the aligned talar models to simulate gravity and distributed on the trochlea to simulate a compressive force. The talus was constrained as indicated in **Figure 3**.

In this study, the values of the compressive force of each model were calculated using a quasi-homothetic transformation for planar models (Marcé Nogué et al., 2013). This methodology is also appropriate for shell models because the scaling of the forces is a function of the difference between the surface and overall thickness of the model. We used the talus of *Alouatta caraya* as a reference and applied a force of $F = 15.8186$ N. These values were obtained following Püschel et al. (2018) which computed the applied force as the 30% of the average body mass of the species multiplied by standard acceleration due to gravity $g = 9.81\ \mathrm{ms}^{-2}$. The scaled values of the force for the other species can be found in **Supplementary Table S3**.

Stress Values and Intervals' Method

We computed the von Mises stress because it combines all Cartesian components of the stress tensor into a single value (equivalent stress; Zienkiewicz et al., 2005). This enables easier and more understandable comparisons when assessing different models, and it has been used successfully as a proxy to compare the strength of bony structures (Marcé-Nogué et al., 2017b), where species with lower values of stress represented the stronger structures. Furthermore, it has been demonstrated that if the bone is modeled using isotropic material properties, then the von Mises criterion is the most suitable one when comparing of stress in bones (Doblaré et al., 2004).

New variables corresponding to different intervals of stress values were computed following the Intervals' Method proposed by Marcé-Nogué et al. (2017a). These interval variables were then used to analyze the FEA results. The Intervals' Method generates a set of variables, each one defined by an interval of stress values. Once all the stress values of a single specimen were obtained, all elements of the model are sorted according to their von Mises stress values. These are then grouped into a finite number of intervals, defined by their range of stress values. Each one of the intervals represents the amount of the volume of the original model (as a percentage value) exhibiting a specific range of stress values. This method allowed us to analyze the data from finite element models in a comparative multivariate framework. The method of Marcé-Nogué et al. (2017a) needs the definition of a Fixed Upper Threshold (i.e., FTupper = 12 MPa) and a number of intervals (i.e., $N = 100$). This value is obtained based on a convergence procedure based on a PCA that was performed to define the minimum number of intervals (Marcé-Nogué et al., 2017a). We considered that convergence has been achieved when the correlation values of the PCs of the intervals were higher than 0.99. The values of each vector for stress interval when $N = 100$ can be found in **Supplementary Table S4**. These newly generated variables were analyzed using a PCA performed on the correlation matrix.

Fossil Substrate Preference Classification

Previous studies have indicated that it was possible to distinguish between different locomotor modes using talar shape or stress information (Püschel et al., 2017, 2018). Consequently, we applied the same approach here but using different substrate preferences (i.e., arboreal, terrestrial, or both substrate preferences). Two different datasets were analyzed and used to elucidate the main substrate preference of *Paralouatta*: (a) morphometric and (b) biomechanical data. Each one of these datasets corresponded to the PCs that accounted for 90% of the variance of the sample using the shape and interval variables, respectively. Two pairwise PERMANOVA tests with a Holm correction for multiple comparisons were performed to assess for differences between the three substrate preferences using both the morphometric and biomechanical datasets. In both cases, Euclidean distances were selected as similarity index.

Six well-known supervised algorithms were chosen as they correspond to a diverse range of different classification techniques: (a) linear discriminant analysis (LDA); (b) classification and regression tree (CART); (c) k-nearest neighbors (KNN); (d) naïve Bayes (NB); (e) support vector machine (SVM); and (f) random forest (RF) (further details about this models can be found in Püschel et al., 2018). All the models were run using the "caret" package for R (Kuhn, 2008, 2015). Performance was

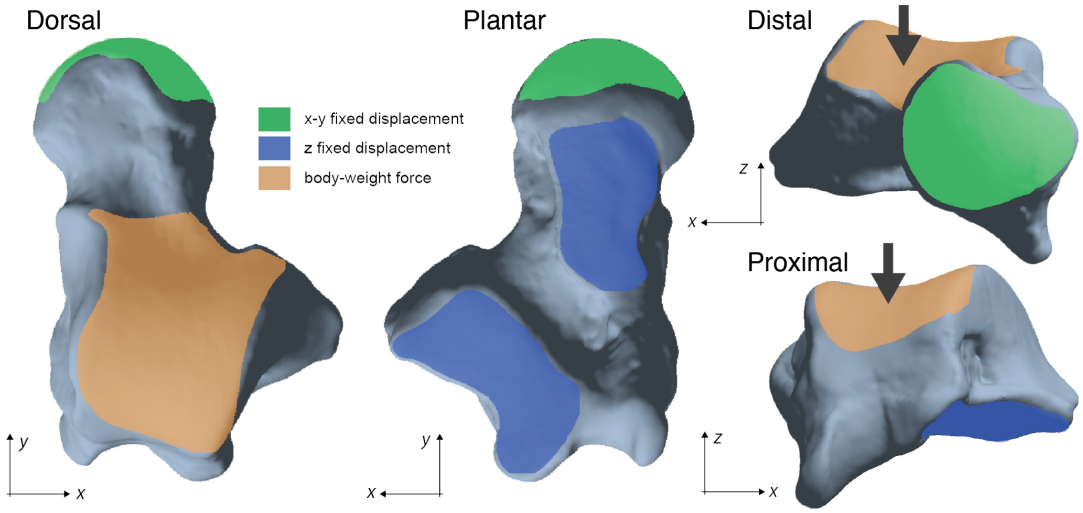

FIGURE 3 | Loading scenario tested in the FEA illustrated using a talus of *Alouatta caraya* (AMNH 211513). The large arrows represent the applied load on the trochlear surface.

calculated using the confusion matrix from which the overall classification accuracy was computed, as well as Cohen's Kappa (Kuhn and Johnson, 2013a). The complete dataset was resampled using a "leave-group-out" cross-validation (Kuhn and Johnson, 2013b), as a way to asses classification performance. This cross-validation strategy generates multiple splits of the data into modeling and prediction sets. This process was carried out 200 times and the data were split into a modeling sub-set comprising 75% of randomly assigned observations, whereas the testing sub-set considered the remaining 25%. The number of repeats was chosen to get a consistent classification performance and to minimize uncertainty. The models with the best classification performance for the morphometric and biomechanical data were then applied to deduce the principal substrate preference of both *Paralouatta* specimens by calculating their category probabilities.

Finally, the Euclidean distances obtained for the morphometric and biomechanical datasets were used to visualize morphological and biomechanical affinities between the extant species and the *Paralouatta* fossils. An unweighted pair-group average (UPGMA) algorithm for agglomerative hierarchical cluster analysis was used to generate two dendrograms (i.e., biomechanical and morphometric affinity dendrograms) that allowed us to assess general affinities (Sokal and Rohlf, 1962). Cophenetic correlation coefficients (CPCC) were computed as a way of measuring how closely the obtained dendrograms preserved the pairwise distances between the specimens (Sokal and Rohlf, 1962).

RESULTS

Geometric Morphometrics Results

The PCA performed using the shape variables obtained through a GPA returned 90 PCs. The first 24 PCs accounted for 90% of the total variance of the sample, hence offering a reasonable estimate of the total amount of talar shape variation, which were then used in the classification analyses (i.e., morphometric dataset). The PCA shows the main regions of occupied shape space (**Figure 4A**). Platyrrhines (which are almost exclusively arboreal; only *Cebus albifrons* is considered into the "both" category) are located on the extreme positive side of PC1 (i.e., lower right and extreme right of the upper right quadrants), whilst most cercopithecid monkeys occupy the upper left quadrant showing mixed substrate preferences. Apes are located on the lower left quadrant, with gorilla and chimpanzees displaying the lowest scores on PC2. PC1 seems to mostly distinguish apes from platyrrhines, with cercopithecids occupying an intermediate position. Knuckle-walking terrestrial African apes (i.e., chimpanzees and gorillas) show the minimum values along PC2, followed by habitually suspensory genera including *Pongo*, *Ateles, Lagothrix*, and *Hoolock*. The most positive PC2 values are shown by cercopithecines and colobines. Interestingly, *Paralouatta* fossils are located in an intermediate position between cercopithecids and platyrrhines, with *P. varonai* being closer to the former rather than to the latter. The variation on the negative side of PC1 can be related to a shorter anterior and a longer posterior calcaneal facet, and a broader and shorter talar head. The morphological variation on the positive side of PC1 can be associated with an increased anterior calcaneal facet and an antero-posteriorly shorter trochlea.

The PGLS regression showed that there is no association between talar shape and the logarithm of talar centroid size (R^2: 0.015; F: 1.325; Z: 1.027; p-value: 0.151; 9,999 permutations). This means that talar shape variation cannot be attributed to evolutionary allometric effects.

Finite-Element Analysis Results

Figure 5 displays stress maps for all the tali under analysis. By representing stress in a visual manner, it is possible to make qualitative inferences about biomechanical behavior, since the

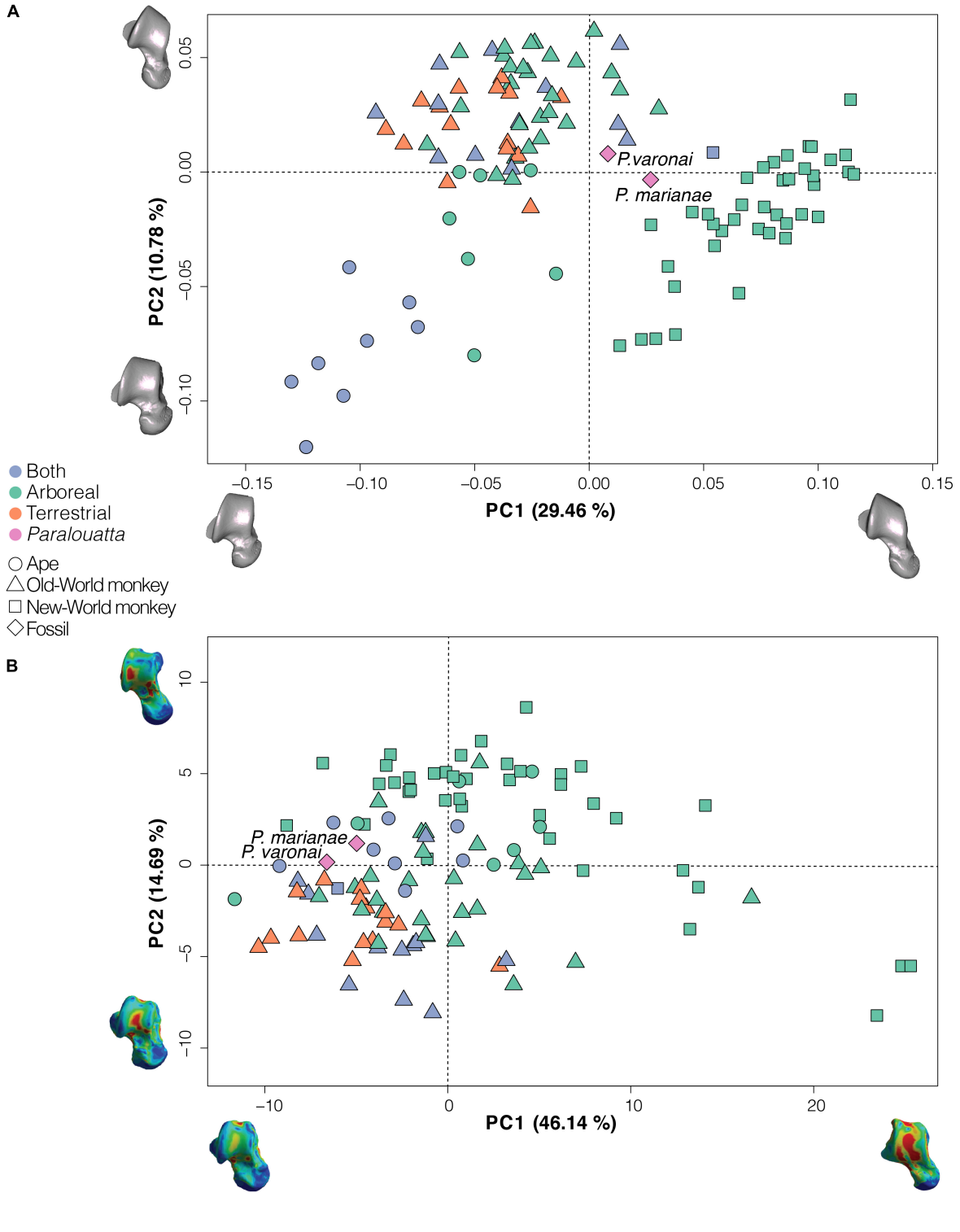

FIGURE 4 | (A) Principal component analysis (PCA) of the talar shape variables (only the two first PCs are shown). The models closest to the mean shape (i.e., *Cercopithecus mitis*) was warped to match the multivariate mean using the thin plate spline method. The obtained average model was then warped to represent the variation along the two plotted PC axes in both analyses (mag = 2); **(B)** Principal component analysis (PCA) of the stress data (i.e., intervals) obtained from the finite element simulations. The models located at the extremes of the PC axes correspond to the individuals showing the maximum or minimum values along the two first PCs.

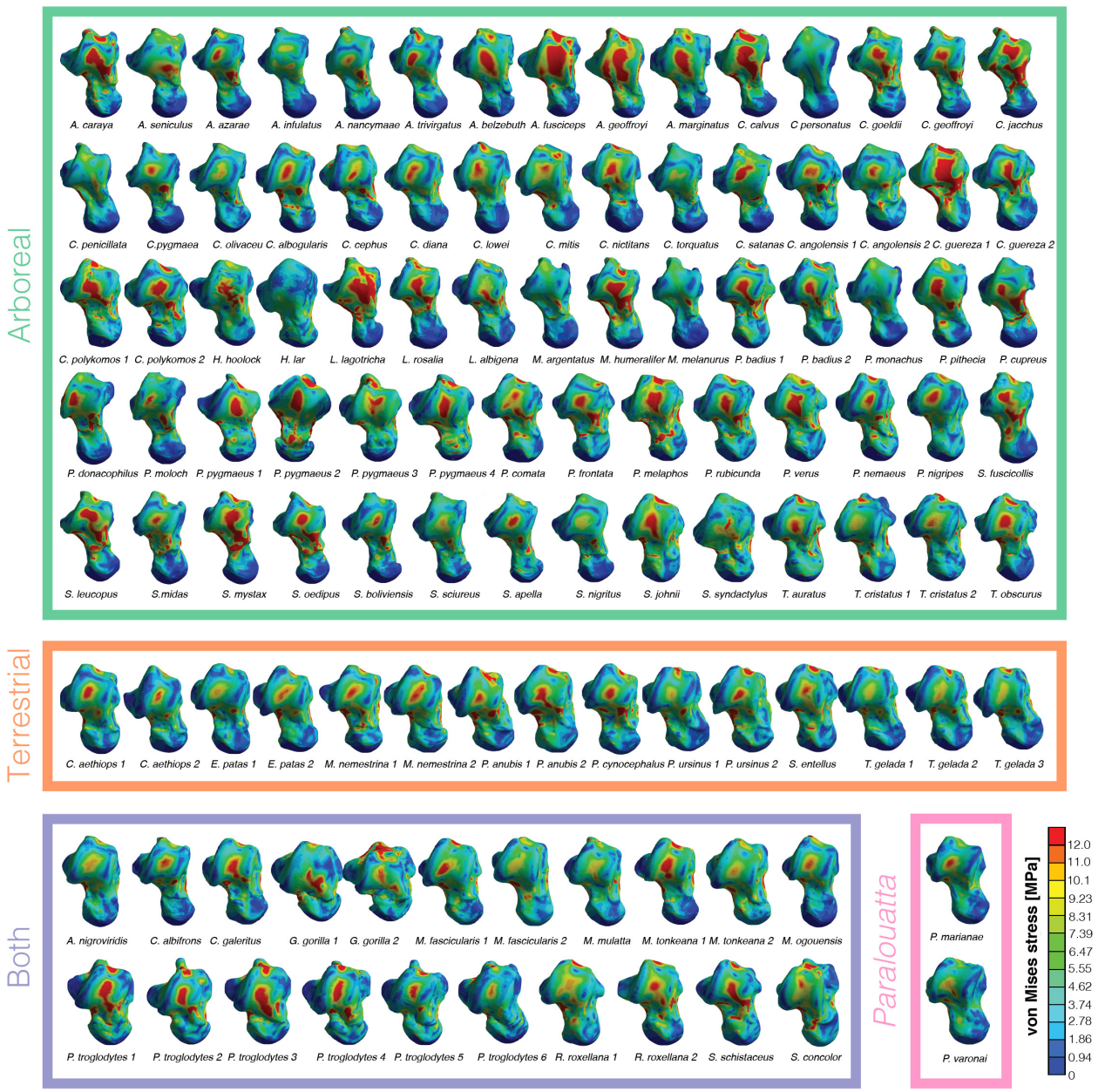

FIGURE 5 | von Mises stress distribution for all the analyzed specimens.

observed stress patterns can be read in terms of relative strength (i.e., individuals showing higher stress levels are weaker under the applied load). The correlation based PCA carried out using the 100 variables generated using the Intervals' method returned 100 PCs. The first nine PCs that accounted for 90% of the total variance of the sample were used in the classification analyses (i.e., biomechanical dataset) as a way to avoid collinearity and to reduce the dimensionality of our data. **Figure 4B** shows the first two PCs of this correlation based PCA.

When comparing locomotor behaviors in extant species, most specimens display moderate values, which makes it difficult to stablish a clear pattern with this proxy. However, the weakest tali -with high average values of stress- correspond to some of the arboreal species. **Figure 4B** shows the PCA of the stress data (i.e., intervals) obtained from the FE simulations. Mostly terrestrial and arboreal/terrestrial (i.e., "both" category) occupy the lower left quadrant of the PCA, whereas exclusively arboreal species are spread over the three remaining quadrants. This is probably because the "arboreal" category comprises several different locomotor styles (e.g., climbing/clambering, leaping, arboreal quadrupedalism, etc.). On the positive side of PC1 are located those individuals with intervals corresponding to

higher stress values, whilst those exhibiting intervals with lower stress values are located at the opposite extreme of the axis. In general, suspensory species tend to show higher stress values than terrestrial and arboreal/terrestrial (i.e., "both" category) specimens. The two *Paralouatta* specimens present low average values of stress in coincidence with both arboreal and terrestrial species and are located in the PCA close to the limit between the upper and the lower left quadrant, exhibiting lower stress values in an area occupied by many species using both ground and arboreal substrates.

Fossil Substrate Classification Results

There were significant differences between all substrate preferences when using the morphometric dataset (i.e., 24 PCs from the PCA carried out using the shape variables) (**Table 1a**.). When the same categories are compared but using the biomechanical dataset (nine PCs from the PCA performed using the stress intervals), there were no significant differences between "both" and "terrestrial" categories. Nonetheless, there were significant differences between the arboreal group and the other two categories (**Table 1b**).

Figure 6 displays the accuracy and Cohen's Kappa results for all the applied models, for both the morphometric and biomechanical data after carrying out the "leave-group-out" cross-validation procedure and after applying an automatic grid search. The morphometric data slightly outperformed the biomechanical data when classifying substrate preferences in both accuracy and Cohen's Kappa metrics. The best model for the morphometric data was a simple LDA model (**Table 2a**), whilst in the case of the biomechanical data, the best model was the KNN (**Table 2b**), although other models (i.e., LDA and NB) showed similar performance levels.

There are no extra parameters in the morphometric LDA, so no further tuning was required (average accuracy: 0.824; average Cohen's Kappa: 0.623; **Figure 7A**). The variables that contributed the most to the separation between categories were PC1 and PC5, followed by PC10 and PC13 (**Figure 7B**). Then, this model was used to classify the *Paralouatta* sample into the analyzed substrate preferences (i.e., arboreal, terrestrial and both). Using morphometric data, *P. marianae* was classified as an arboreal individual, whereas *P. varonai* was classified as "both" (i.e., arboreal/terrestrial species; **Table 3**). The obtained KNN model for the biomechanical data achieved its best performance with $k = 7$ (number of neighbors ranging from 5 to 23 were tested; average accuracy: 0.74; average Cohen's Kappa: 0.42; **Figure 7C**). The variables that contributed the most to the separation between categories were PC1 and PC2, followed by PC4 and PC7 (**Figure 7D**). By applying the final KNN model, both *Paralouatta* specimens were classified into the "both" category (**Table 3**). This likely indicates that they engaged in activities both in the ground as in trees.

The agglomerative-hierarchical cluster analysis of the PCs using the UPGMA algorithm displayed the affinities between living species and *Paralouatta* fossils for both the morphometric and biomechanical data (**Figures 8A,B**, respectively). The CPCCs of both datasets indicate a reasonable agreement between the cophenetic distances obtained from the trees, and the original Euclidean distances (morphometric CPCC: 0.78; biomechanical CPCC: 0.79) (Farris, 1969; Saraçli et al., 2013). In the case of the morphometric data, the clusters seem to predominantly reflect phylogenetic relatedness (i.e., platyrrhines, cercopithecids, and apes). In fact, the two *Paralouatta* fossils are located within the platyrrhine cluster next to *Chiropotes satanas*. The biomechanical data seems to mostly reflect a combination of substrate preference categories (i.e., most terrestrial and "both" species are located closer to each other), as well as phylogenetic relatedness. Interestingly, the *Paralouatta* fossils clustered next terrestrial (e.g., *Papio* and *Theropithecus*) or arboreal/terrestrial (e.g., *Macaca*) individuals.

TABLE 1 | Pairwise PERMANOVA results.

	F-model	R^2	adjusted *p*-value
(a) Morphometric data			
Arboreal vs. Both	11.200	0.109	0.003
Arboreal vs. Terrestrial	9.001	0.095	0.003
Both vs. Terrestrial	2.349	0.065	0.023
(b) Biomechanical data (intervals' method)			
Arboreal vs. Both	8.651	0.086	0.003
Arboreal vs. Terrestrial	11.491	0.118	0.003
Both vs. Terrestrial	1.582	0.044	0.169

DISCUSSION

The diverse post-cranial adaptations exhibited by extinct platyrrhine primates demonstrates that they occupied a wide variety of habitats and environments in the Americas (MacPhee and Horovitz, 2002). Among the different fossil New World monkeys, the origin and relationships of the endemic Caribbean primates are possibly one of the least understood aspects of platyrrhine evolution. These Antillean monkeys are of special interest for different reasons, including their intricate phylogenetic relationships to mainland forms, as well as due to their mysterious biogeographic history (Halenar et al., 2017). Nonetheless, the fact that they display a variety of features that are rare or absent in platyrrhines from the mainland is perhaps one of the most intriguing and enigmatic ones. It is likely that these traits appeared as a response to selective pressures that are particular to island environments, since insular species tend to significantly differentiate from mainland forms (e.g., non-volant small mammal species tend to evolve larger bodies whereas non-volant large mammal species tend to evolve smaller bodies as has been summarized by Foster's rule) (Foster, 1964; Case, 1978; Lomolino, 2005; Whittaker and Fernández-Palacios, 2007). Among the features distinguishing the extinct Caribbean species are several post-cranial traits that seem to indicate locomotor adaptations not seen in extant mainland taxa. The original morphological description provided by MacPhee and Meldrum (2006) suggested that *Paralouatta* was a primate adapted to semi-terrestrial locomotion, perhaps similar to some Old World monkeys. This is particularly striking since no extant platyrrhine species within this adaptive radiation is known to

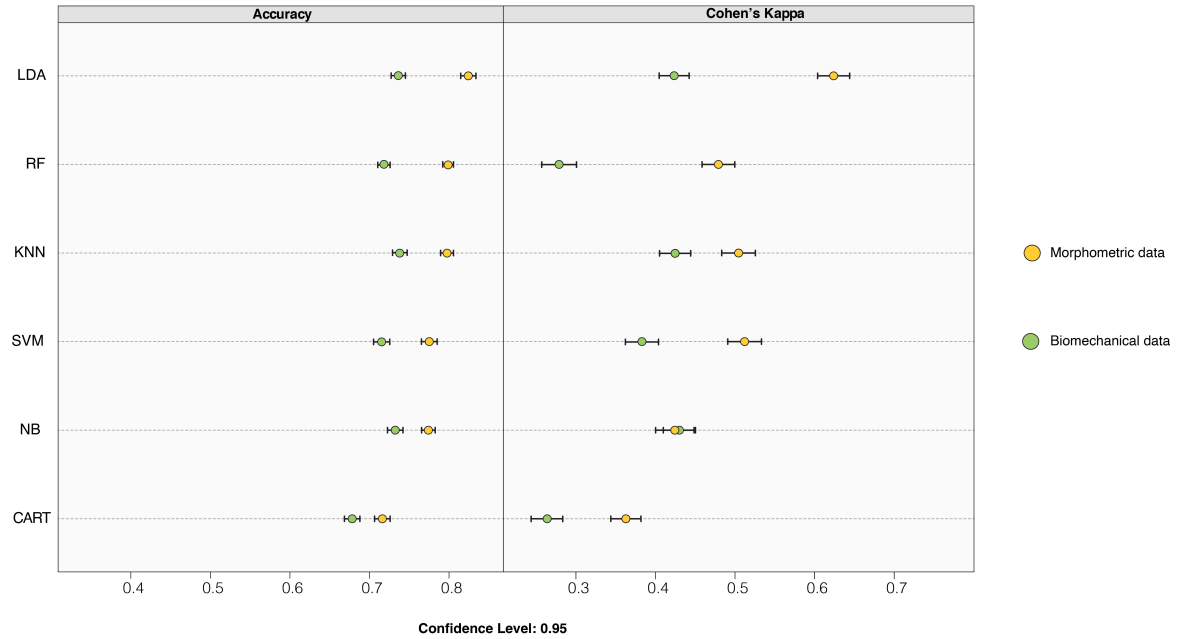

FIGURE 6 | Dot-plot comparing the accuracy and Cohen's Kappa values of the different classification models applied to morphometric and biomechanical data. The dots represent the average accuracy and Cohen's Kappa values after performing the "leave-group-out" cross-validation (200 repeats), while the whiskers display their respective 0.95 confidence level. Model acronyms: linear discriminant analysis (LDA); classification and regression tree (CART); k-nearest neighbors (KNN); naïve Bayes (NB); support vector machine (SVM) and random forest (RF).

exhibit frequent terrestrial behaviors as part of their locomotor repertoire. Nonetheless, MacPhee and Meldrum (2006) also mentioned that some of these terrestrial features observed in *Paralouatta* could be merely plesiomorphic traits shared with other anthropoid ancestors. In order to elucidate this issue, we applied a combined approach from the virtual morpho-functional toolkit (i.e., "engineering toolbox"), analyzing both morphometric and biomechanical data. We have arranged what is, to our knowledge, the largest number of 3D FE models to carry out meaningful comparisons that can contribute to a better understanding of the problem. Nevertheless, to properly address the polarity of changes in *Paralouatta* (e.g., to establish whether the talar traits are plesiomorphic or not) phylogenetically informed methods need to be applied (Almécija et al., 2019).

From a morphometric perspective our results indicate mixed locomotor behaviors. The morphometric PCA located the two *Paralouatta* specimens between the cercopithecids and the platyrrhines. This indicates that at least for the main axes of morphological variation (i.e., PC1 and PC2) *Paralouatta*'s talus seems quite distinctive, occupying an area of the morphospace almost vacated by other species. The classification algorithm (i.e., LDA) using the morphometric data classified *P. marianae* as an arboreal species, while *P. varonai* was categorized into the "both" category signifying a preference for a semi-terrestrial lifestyle. This is in agreement with Püschel et al. (2018), where it was found that *P. marianae* was most likely a clamber/suspensory species. Nevertheless, from the observation of **Figure 7A**, which displays the two variables that contribute the most to the classification models, it is evident that both *Paralouatta* specimens are located quite closely to the boundary between the arboreal and terrestrial categories. In general, it can be concluded that for *P. varonai* the traits that indicate semi-terrestriality are more pronounced when compared to *P. marianae*. If we take into account the millions of years separating these two species, one can speculate that the terrestrial behaviors which were more incipient (less frequent) in *P. marianae* became more ubiquitous in the later species *P. varonai*. The clustering analysis of the morphometric data mostly showed broad phylogenetic relatedness. The two *Paralouatta* specimens where located close to *Chiropotes satanas* a species known for its usual above branch quadrupedal locomotion, as well as some suspensory postures (Fleagle and Meldrum, 1988). However, it is important to notice that when carrying out the same analysis but using fewer morphometric PCs (e.g., 14 PCs that account for 80% of the variance of the sample), the fossils are located within the predominantly cercopithecid cluster, close to terrestrial or arboreal/terrestrial (i.e., "both") specimens (results not shown), thus indicating that additional PCs provide additional phylogenetic (rather than "functional") information.

The biomechanical results also indicate some mixed locomotor behaviors. The biomechanical PCA using the intervals showed that the two *Paralouatta* species are close to the "both" and terrestrial categories. However, it is important to stress that the "arboreal" species occupy most of the biomechanical-space and that many "arboreal" species are also close to the fossil specimens, probably because this category encompasses several other locomotor categories (e.g., leaping, climbing/clambering, arboreal quadrupedalism, etc.). The KNN algorithm classified

TABLE 2 | Summary statistics of the "leave-group-out" cross-validation procedure for the accuracy and Cohen's kappa values for all the tested models (best models in bold).

	Minimum	1st Quartile	Median	Mean	3rd Quartile	Maximum
(a) Morphometric data (24 PCs)						
Accuracy						
LDA	**0.654**	**0.769**	**0.846**	**0.824**	**0.885**	**0.962**
NB	0.615	0.731	0.769	0.774	0.808	0.962
CART	0.500	0.692	0.731	0.716	0.769	0.846
KNN	0.654	0.769	0.808	0.798	0.846	0.962
SVM	0.615	0.731	0.769	0.775	0.808	0.923
RF	0.654	0.769	0.808	0.799	0.846	0.923
Kappa						
LDA	**0.265**	**0.513**	**0.638**	**0.623**	**0.735**	**0.922**
NB	0.059	0.316	0.409	0.423	0.529	0.919
CART	−0.102	0.277	0.368	0.362	0.441	0.667
KNN	0.017	0.408	0.494	0.504	0.606	0.914
SVM	0.116	0.399	0.513	0.511	0.614	0.844
RF	0.017	0.373	0.478	0.478	0.603	0.828
(b) Biomechanical data (9 PCs)						
Accuracy						
LDA	0.538	0.692	0.731	0.737	0.769	0.885
NB	0.500	0.692	0.731	0.733	0.769	0.885
CART	0.423	0.654	0.692	0.678	0.731	0.808
KNN	**0.500**	**0.692**	**0.731**	**0.738**	**0.769**	**0.923**
SVM	0.462	0.692	0.731	0.716	0.769	0.923
RF	0.538	0.692	0.731	0.718	0.769	0.846
Kappa						
LDA	0.068	0.339	0.434	0.422	0.513	0.744
NB	0.008	0.342	0.432	0.429	0.531	0.753
CART	−0.166	0.181	0.264	0.264	0.351	0.596
KNN	**0.116**	**0.337**	**0.431**	**0.423**	**0.513**	**0.831**
SVM	−0.145	0.293	0.380	0.383	0.482	0.836
RF	−0.135	0.170	0.276	0.279	0.378	0.661

both fossil species into the "both" category, hence indicating some levels of terrestriality. Interestingly, *P. marianae* also shows a high posterior probability for the "arboreal" category which suggests that the terrestrial traits observed in *Paralouatta* are more incipient in the early evolution of this genus (i.e., semi-terrestriality is certainly a derived character). The clustering analysis shows that the *Paralouatta* fossils grouped close to terrestrial or arboreal/terrestrial (i.e., "both") individuals, which again shows some level of terrestriality.

Although the obtained results shown here are highly informative, there is certainly room for improvement. One limitation of our approach is the classification scheme applied. In fact, it is evident from both morphometric and biomechanical analyses that the arboreal category encompasses several locomotor styles that can vary greatly. Further studies could refine this classification scheme to provide a finer perspective when carrying out locomotor classifications. An alternative option, which would not require to force any species into discrete categories, would be to establish major patterns of covariation between a given shape data matrix (e.g., talar shape) and a locomotor behavior data matrix (see for e.g., Table 3 in Hunt, 2016). This approach has been successfully applied using two-block partial least squares analysis in a few studies (e.g., Almécija et al., 2015; Püschel et al., 2017) and it is certainly worth further exploration. Another limitation in our study arises from the fact that we only simulated one simple loading scenario (i.e., quadrupedal standing), which may not reflect the most realistic loading scenarios of the talus in order to distinguish between habitual substrate preferences adopted by primates. Hence, further works could simulate different loading scenarios and test their different discriminatory capabilities when elucidating locomotor behaviors.

Paralouatta was probably an island-adapted large-bodied genus that most likely diverged from other platyrrhines during the early Miocene. This would certainly explain the similarities of *Paralouatta* to the other platyrrhines, as well as many traits that are evidently unique to this genus and that seem to be exaggerated in the later species *P. varonai*. The talar morphology of *Paralouatta* combines some more primitive morphological aspects (both anthropoid and platyrrhine) with

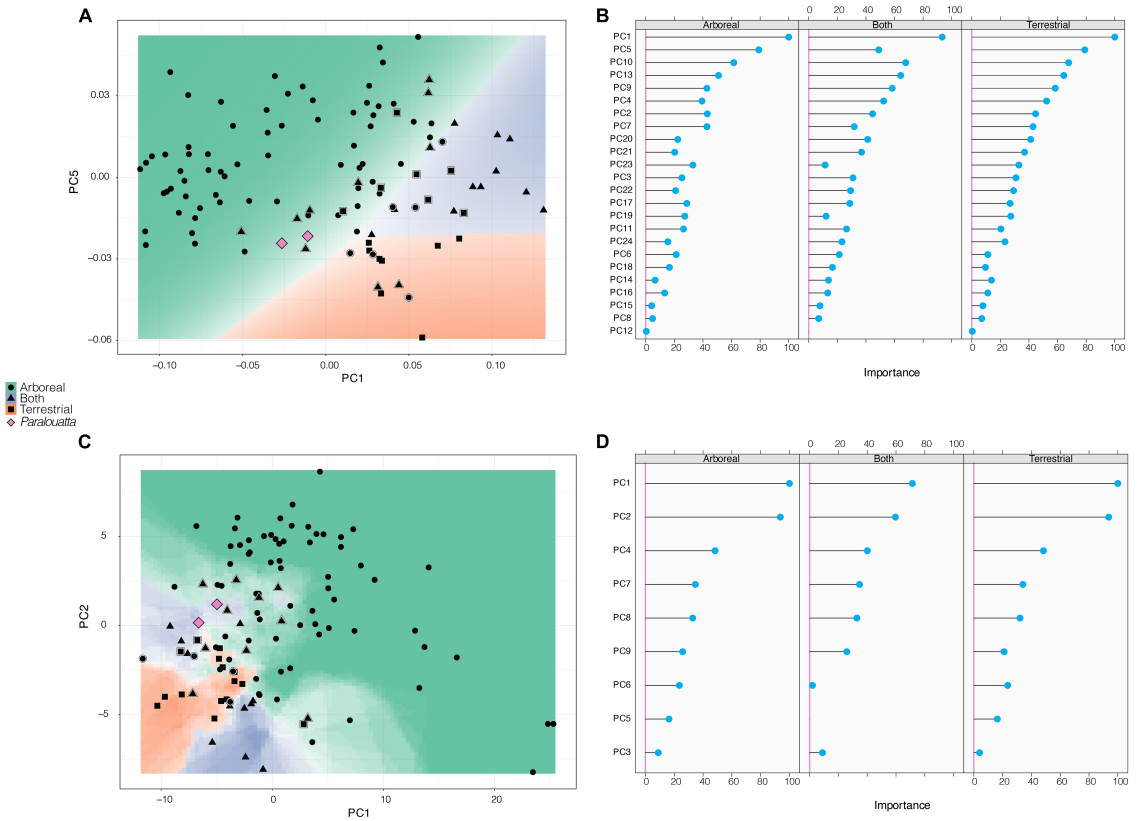

FIGURE 7 | Decision boundary plots for **(A)** morphometric and **(C)** biomechanical data. The two variables that contributed the most to each one of the models are displayed. The space is colored depending on what substrate preference the **(A)** LDA or the **(B)** KNN algorithm predict that region belongs to, whereas the lines between colored areas represent the decision boundaries. Color intensity indicates the certainty of the prediction in a particular graph area (i.e., darker colors mean a higher probability of belonging to a certain category). Symbols surrounded by a white rim correspond to misclassified specimens. In addition, variable importance scores for the predictors used are provided for the **(B)** morphometric (only the top 20 variables are shown) and **(D)** biomechanical models.

TABLE 3 | Prediction results for the fossil sample.

	LDA morphometric model			KNN biomechanical model		
	Posterior probabilities			Posterior probabilities		
Species	**Arboreal**	**Both**	**Terrestrial**	**Arboreal**	**Both**	**Terrestrial**
Paralouatta marianae	0.99	0.01	0.00	0.43	0.43	0.14
Paralouatta varonai	0.27	0.73	0.00	0.00	0.71	0.29

derived features associated to some terrestriality levels, as initially though by MacPhee and Meldrum (2006). Given that selection pressures and ecologies can vary significantly between islands and the mainland, different adaptations associated with species that are endemic to islands are to be expected. *Paralouatta* adapted to a different environment and probably employed a different locomotion, which based on our results it is highly likely to have involved a significant level of terrestrial activity, while still retaining arboreal behaviors as shown by Püschel et al. (2017, 2018). By the island rule (i.e., Foster's rule) small sized species are expected to become larger, whilst large species tend to become smaller (Foster, 1964). It is surely suggestive to think that when *Paralouatta* arrived in Cuba it might have become larger due to a more relaxed predation pressure, and therefore able to shift from an arboreal lifestyle to a more terrestrial one. However, this interpretation should be treated with caution, since more refined phylogenetically informed analyses are required to better establish the polarity of changes. Further trait-evolution phylogenetic comparative analyses could certainly contribute toward settling this issue, but firstly the phylogenetic position of *Paralouatta* needs to be fully resolved.

Finally, this study has shown that a combined virtual morpho-functional approach can help to the understanding of locomotor behaviors in other fossil taxa. By combining morphometrics, biomechanics and ML methods it is possible

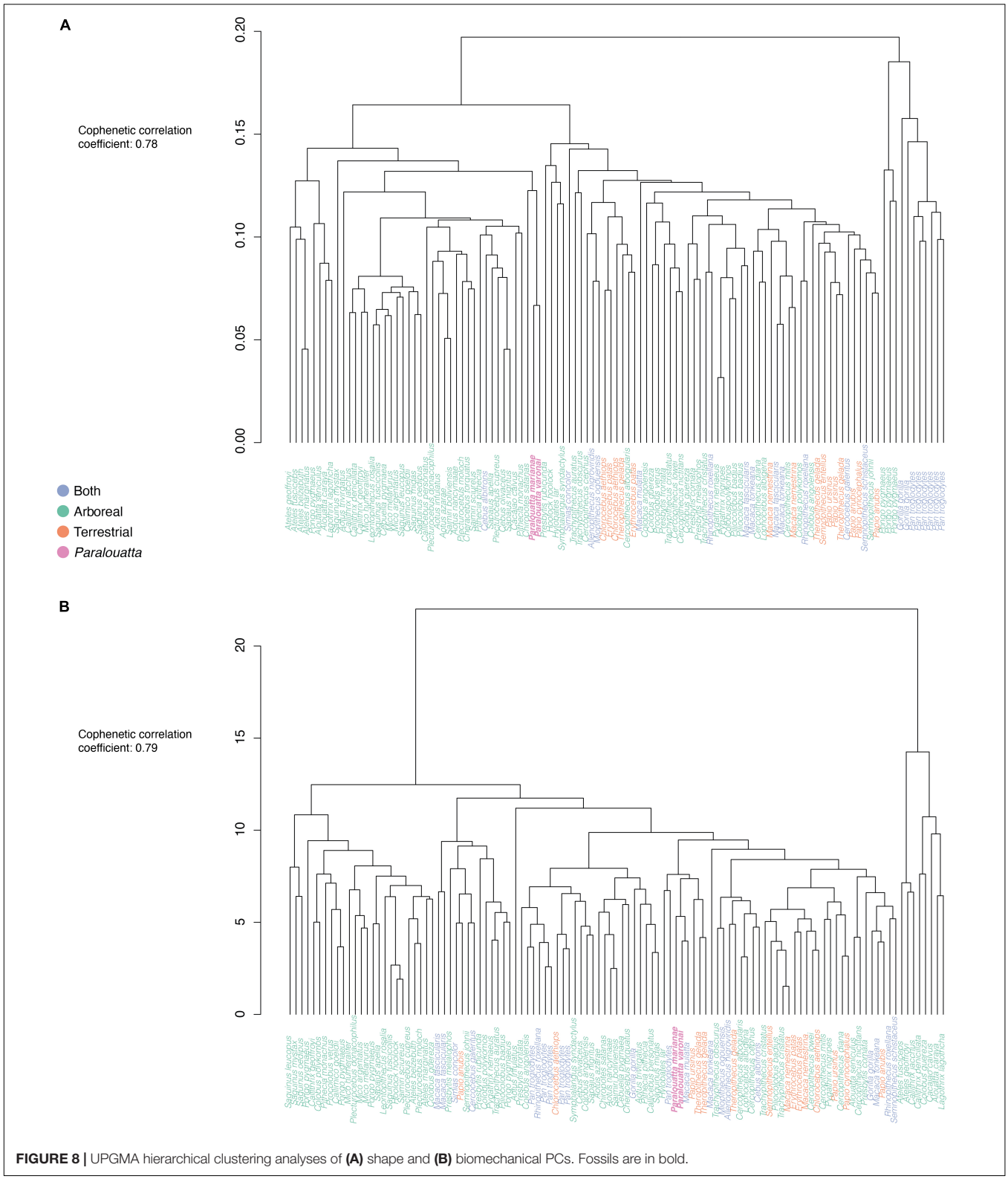

FIGURE 8 | UPGMA hierarchical clustering analyses of **(A)** shape and **(B)** biomechanical PCs. Fossils are in bold.

to provide a broader perspective regarding the locomotor behaviors of fossils species by analyzing different aspects of their functional morphology. The proposed methodological approach can certainly be beneficial when figuring out not only locomotion in fossil species, but also when assessing any other past behaviors that can be inferred from their morphology.

DATA AVAILABILITY STATEMENT

All datasets generated for this study are included in the article/**Supplementary Material**.

ETHICS STATEMENT

Ethical review and approval was not required for the animal study because we exclusively analyzed bones and fossils belonging to different museum collections. We did not perform any experiments on living animals.

AUTHOR CONTRIBUTIONS

TP and JM-N designed the study and carried out the different analyses. TP, SA, BP, and JG collected and analyzed data. All authors interpreted the data and wrote the manuscript.

FUNDING

This project was funded by the NERC (NE/R011168/1). TP was funded by the Leverhulme Trust Early Career Fellowship, ECF-2018-264, SA by the NSF-BCS 1316947, AEI/FEDER EU (CGL2017-82654-P), and BP by the National Science Foundation (BCS-1317047) and the Leakey Foundation. JM acknowledges Dr. Juan Liu and the Laboratory for the Evolution and Anatomy of Fish of the University at Buffalo. Both SA and JM-N acknowledge the CERCA Programe (Generalitat de Catalunya).

ACKNOWLEDGMENTS

We are grateful to the editors who invited us to take part of the "Evolving Virtual and Computational Palaeontology Research Topic" and to the two reviewers whose helpful comments improved this manuscript. A version of this work has been submitted as an abstract to the Program of the 89th Annual Meeting of the American Association of Physical Anthropologists (Püschel et al., 2020).

SUPPLEMENTARY MATERIAL

The Supplementary Material for this article can be found online at: https://www.frontiersin.org/articles/10.3389/feart.2020.00079/full#supplementary-material

REFERENCES

Adams, D. C. (2014). A method for assessing phylogenetic least squares models for shape and other high-dimensional multivariate data. *Evolution* 68, 2675–2688. doi: 10.1111/evo.12463

Adams, D. C., Collyer, M. L., and Kaliontzopoulou, A. (2018). *Geomorph: Software for Geometric Morphometric Analysis. R Package Version 3.0.6*. Available online at: http://CRAN.R-project.org/package=geomorph (accessed November 1, 2019).

Almécija, S., Orr, C. M., Tocheri, M. W., Patel, B. A., and Jungers, W. L. (2015). Exploring phylogenetic and functional signals in complex morphologies: the hamate of extant anthropoids as a test-case study. *Anat. Rec.* 298, 212–229. doi: 10.1002/ar.23079

Almécija, S., Tallman, M., Sallam, H. M., Fleagle, J. G., Hammond, A. S., and Seiffert, E. R. (2019). Early anthropoid femora reveal divergent adaptive trajectories in catarrhine hind-limb evolution. *Nat. Commun.* 10:4778. doi: 10.1038/s41467-019-12742-0

Arnold, C., Matthews, L. J., and Nunn, C. L. (2010). The 10kTrees website: a new online resource for primate phylogeny. *Evol. Anthropol. Issues News Rev.* 19, 114–118. doi: 10.1002/evan.20251

Bookstein, F. L. (1997). *Morphometric Tools for Landmark Data: Geometry and Biology*, 2nd edition. Cambridge: Cambridge University Press.

Boyer, D. M., Gunnell, G. F., Kaufman, S., and McGeary, T. M. (2016). Morphosource: archiving and sharing 3-D digital specimen data. *Paleontol. Soc. Pap.* 22, 157–181. doi: 10.1017/scs.2017.13

Cachel, S. (2015). *Fossil Primates*. Cambridge: Cambridge University Press.

Case, T. J. (1978). A general explanation for insular body size trends in terrestrial vertebrates. *Ecology* 59, 1–18. doi: 10.2307/1936628

Cooke, S. B., Dávalos, L. M., Mychajliw, A. M., Turvey, S. T., and Upham, N. S. (2017a). Anthropogenic extinction dominates Holocene declines of West Indian mammals. *Annu. Rev. Ecol. Evol. Syst.* 48, 301–327. doi: 10.1146/annurev-ecolsys-110316-022754

Cooke, S. B., Mychajliw, A. M., Southon, J., and MacPhee, R. D. E. (2017b). The extinction of Xenothrix mcgregori, Jamaica's last monkey. *J. Mammal.* 98, 937–949. doi: 10.1093/jmammal/gyw165

Cooke, S. B., Rosenberger, A. L., and Turvey, S. (2011). An extinct monkey from Haiti and the origins of the Greater Antillean primates. *Proc. Natl. Acad. Sci.U.S.A.* 108, 2699–2704. doi: 10.1073/pnas.1009161108

Copes, L. E., Lucas, L. M., Thostenson, J. O., Hoekstra, H. E., and Boyer, D. M. (2016). A collection of non-human primate computed tomography scans housed in MorphoSource, a repository for 3D data. *Sci. Data* 3:160011 doi: 10.1038/sdata.2016.1

Doblaré, M., Garcıa, J. M., and Gómez, M. J. (2004). Modelling bone tissue fracture and healing: a review. *Eng. Fract. Mech.* 71, 1809–1840. doi: 10.1016/j.engfracmech.2003.08.003

Farris, J. S. (1969). On the cophenetic correlation coefficient. *Syst. Biol.* 18, 279–285. doi: 10.2307/2412324

Fleagle, J. G. (2013). *Primate Adaptation and Evolution*, 3rd Edn. Boston, MA: Academic Press.

Fleagle, J. G., and Meldrum, D. J. (1988). Locomotor behavior and skeletal morphology of two sympatric pitheciine monkeys, Pithecia pithecia and Chiropotes satanas. *Am. J. Primatol.* 16, 227–249. doi: 10.1002/ajp.1350160305

Ford, S. M., and Morgan, G. S. (1986). A new ceboid femur from the late Pleistocene of Jamaica. *J. Vertebr. Paleontol.* 6, 281–289. doi: 10.1080/02724634.1986.10011623

Foster, J. B. (1964). Evolution of mammals on islands. *Nature* 202, 234–235.

Galán-Acedo, C., Arroyo-Rodríguez, V., Andresen, E., and Arasa-Gisbert, R. (2019). Ecological traits of the world's primates. *Sci. Data* 6:55. doi: 10.1038/s41597-019-0059-9

Halenar, L. B., Cooke, S. B., Rosenberger, A. L., and Rímoli, R. (2017). New cranium of the endemic Caribbean platyrrhine, Antillothrix bernensis, from La Altagracia Province, Dominican Republic. *J. Hum. Evol.* 106, 133–153. doi: 10.1016/j.jhevol.2017.02.002

Harcourt-Smith, W. (2002). *Form and Function in the Hominoid Tarsal Skeleton*. Ph.D. thesis, University College London, London.

Horovitz, I. (1999). A phylogenetic study of living and fossil platyrrhines. *Am. Mus. Novit.* 3269, 1–40

Horovitz, I., and MacPhee, R. D. E. (1999). The quaternary Cuban platyrrhine Paralouatta varonai and the origin of Antillean monkeys. *J. Hum. Evol.* 36, 33–68. doi: 10.1006/jhev.1998.0259

Hunt, K. D. (2016). Why are there apes? Evidence for the co-evolution of ape and monkey ecomorphology. *J. Anat.* 228, 630–685. doi: 10.1111/joa.12454

Kay, R. F. (2015). Biogeography in deep time – What do phylogenetics, geology, and paleoclimate tell us about early platyrrhine evolution? *Mol. Phylogenet. Evol.* 82, 358–374. doi: 10.1016/j.ympev.2013.12.002

Kay, R. F., Hunt, K. D., Beeker, C. D., Conrad, G. W., Johnson, C. C., and Keller, J. (2011). Preliminary notes on a newly discovered skull of the extinct monkey Antillothrix from Hispaniola and the origin of the Greater Antillean monkeys. *J. Hum. Evol.* 60, 124–128. doi: 10.1016/j.jhevol.2010.09.003

Kuhn, M. (2008). Caret package. *J. Stat. Softw.* 28, 1–26.

Kuhn, M. (2015). *Caret: Classification and Regression Training*. Available online at: http://topepo.github.io/caret/index.html (accessed November 12, 2019).

Kuhn, M., and Johnson, K. (2013a). "Measuring performance in classification models," in *Applied Predictive Modeling* (New York, NY: Springer), 247–273. doi: 10.1007/978-1-4614-6849-3_11

Kuhn, M., and Johnson, K. (2013b). "Over-fitting and model tuning," in *Applied Predictive Modeling*. New York, NY: Springer, 61–92.

Lomolino, M. V. (2005). Body size evolution in insular vertebrates: generality of the island rule. *J. Biogeogr.* 32, 1683–1699. doi: 10.1111/1749-4877.12055

MacPhee, R. D., and Horovitz, I. (2002). "Extinct quaternary platyrrhines of the Greater Antilles and Brazil," in *The Primate Fossil Record*, ed. W. C. Hartwig (Cambridge: Cambridge University Press), 189–200.

MacPhee, R. D., and Horovitz, I. (2004). New craniodental remains of the Quaternary Jamaican monkey *Xenothrix mcgregori* (Xenotrichini, Callicebinae, Pitheciidae), with a reconsideration of the Aotus hypothesis. *Am. Mus. Novit.* 2004, 1–52.

MacPhee, R. D. E., and Fleagle, J. G. (1991). Postcranial remains of Xenothrix-mcgregori (Primates, Xenotrichidae) and other late quaternary mammals from Long Mile cave, Jamaica. *Bull. Am. Mus. Nat. Hist.* 206, 287–321.

MacPhee, R. D. E., Iturralde-Vinent, M., and Gaffney, E. S. (2003). *Domo de Zaza, an Early Miocene Vertebrate Locality in South-Central Cuba: With Notes on the Tectonic Evolution of Puerto Rico and the Mona Passage*. New York, NY: American Museum of Natural History.

MacPhee, R. D. E., and Iturralde-Vinent, M. A. (1995). Earliest monkey from Greater Antilles. *J. Hum. Evol.* 28, 197–200. doi: 10.1006/jhev.1995.1014

MacPhee, R. D. E., and Meldrum, J. (2006). Postcranial remains of the extinct monkeys of the Greater Antilles, with evidence for semiterrestriality in Paralouatta. *Am. Mus. Novit.* 3516, 1–65.

Marcé Nogué, J., DeMiguel, D., Fortuny Terricabras, J., Trivigno, E., and Gil Espert, L. (2013). Quasi-homothetic transformation for comparing the mechanical performance of planar models in biological research. *Palaeontol. Electron.* 16, 1–15.

Marcé-Nogué, J., Esteban-Trivigno, S. D., Püschel, T. A., and Fortuny, J. (2017a). The intervals method: a new approach to analyse finite element outputs using multivariate statistics. *PeerJ* 5:e3793. doi: 10.7717/peerj.3793

Marcé-Nogué, J., Püschel, T. A., and Kaiser, T. M. (2017b). A biomechanical approach to understand the ecomorphological relationship between primate mandibles and diet. *Sci. Rep.* 7:8364. doi: 10.1038/s41598-017-08161-0

Morgan, G. S., and Woods, C. A. (1986). Extinction and the zoogeography of West Indian land mammals. *Biol. J. Linn. Soc.* 28, 167–203. doi: 10.1111/j.1095-8312.1986.tb01753.x

Parr, W. C. H., Chamoli, U., Jones, A., Walsh, W. R., and Wroe, S. (2013). Finite element micro-modelling of a human ankle bone reveals the importance of the trabecular network to mechanical performance: new methods for the generation and comparison of 3D models. *J. Biomech.* 46, 200–205. doi: 10.1016/j.jbiomech.2012.11.011

Püschel, T. A., Gladman, J. T., Bobe, R., and Sellers, W. I. (2017). The evolution of the platyrrhine talus: a comparative analysis of the phenetic affinities of the Miocene platyrrhines with their modern relatives. *J. Hum. Evol.* 111, 179–201. doi: 10.1016/j.jhevol.2017.07.015

Püschel, T. A., Marcé-Nogué, J., Gladman, J. T., Bobe, R., and Sellers, W. I. (2018). Inferring locomotor behaviours in Miocene New World monkeys using finite element analysis, geometric morphometrics and machine-learning classification techniques applied to talar morphology. *J. R. Soc. Interface* 15:20180520. doi: 10.1098/rsif.2018.0520

Püschel, T. A., Marcé-Nogué, J., Gladman, J. T., Patel, B. A., Almécija, S., and Sellers, W. I. (2020). "Elucidating Paralouatta's semi terrestriality using the virtual morpho-functional toolbox," in *Proceedings of the 89th Annual meeting of the American Association of Physical Anthropologists AAPA 2020* (Hoboken: Wiley), 225.

R Core Team (2019). *R: A Language and Environment for Statistical Computing*. Vienna: R Foundation for Statistical Computing. Available online at: http://www.R-project.org/

Rayfield, E. J. (2007). Finite element analysis and understanding the biomechanics and evolution of living and fossil organisms. *Annu. Rev. Earth Planet. Sci.* 35, 541–576. doi: 10.1146/annurev.earth.35.031306.140104

Rayfield, E. J. (2019). "What does musculoskeletal mechanics tell us about evolution of form and function in vertebrates?" in *Feeding in Vertebrates: Evolution, Morphology, Behavior, Biomechanics*, eds V. Bels, and I. Q. Whishaw (Cham: Springer), 45–70. doi: 10.1007/978-3-030-13739-7_3

Richmond, B. G., Wright, B. W., Grosse, I., Dechow, P. C., Ross, C. F., Spencer, M. A., et al. (2005). Finite element analysis in functional morphology. *Anat. Rec. A Discov. Mol. Cell. Evol. Biol.* 283A, 259–274. doi: 10.1002/ar.a.20169

Rímoli, R. O. (1977). *Una Nueva Especie de Monos (Cebidae: Saimirinae: Saimiri) de la Hispaniola*. Santo Domingo: Universidad Autónoma de Santo Domingo.

Rivero, M., and Arredondo, O. (1991). Paralouatta varonai, a new Quaternary platyrrhine from Cuba. *J. Hum. Evol.* 21, 1–11. doi: 10.1016/0047-2484(91)90032-Q

Rohlf, F. J., and Slice, D. (1990). Extensions of the procrustes method for the optimal superimposition of landmarks. *Syst. Zool.* 39, 40–59. doi: 10.2307/2992207

Rosenberger, A. L. (1977). Xenothrix and ceboid phylogeny. *J. Hum. Evol.* 6, 461–481. doi: 10.1016/s0047-2484(77)80058-4

Rosenberger, A. L. (2002). "Platyrrhine paleontology and systematics: the paradigm shifts," in *The Primate Fossil Record*, ed. W. C. Hartwig (Cambridge Cambridge University Press).

Rosenberger, A. L., Cooke, S. B., Rímoli, R., Ni, X., and Cardoso, L. (2011). First skull of Antillothrix bernensis, an extinct relict monkey from the Dominican Republic. *Proc. R. Soc. B Biol. Sci.* 278, 67–74. doi: 10.1098/rspb.2010.1249

Rosenberger, A. L., Pickering, R., Green, H., Cooke, S. B., Tallman, M., Morrow, A., et al. (2015). 1.32 ± 0.11 Ma age for underwater remains constrain antiquity and longevity of the Dominican primate Antillothrix bernensis. *J. Hum. Evol.* 88, 85–96. doi: 10.1016/j.jhevol.2015.05.015

Saraçli, S., Doğan, N., and Doğan, İ. (2013). Comparison of hierarchical cluster analysis methods by cophenetic correlation. *J. Inequalities Appl.* 2013:203. doi: 10.1186/1029-242X-2013-203

Sokal, R. R., and Rohlf, F. J. (1962). The comparison of dendrograms by objective methods. *Taxon* 11, 33–40. doi: 10.2307/1217208

Turley, K., and Frost, S. R. (2013). The shape and presentation of the catarrhine talus: a geometric morphometric analysis. *Anat. Rec.* 296, 877–890. doi: 10.1002/ar.22696

Turvey, S. T. (ed.) (2009). *Holocene Extinctions*, 1st Edn. Oxford?: OUP Oxford.

Whittaker, R. J., and Fernández-Palacios, J. M. (2007). *Island Biogeography: Ecology, Evolution, and Conservation*. Oxford: Oxford University Press.

Wiley, D. F., Amenta, N., Alcantara, D. A., Ghost, D., Kil, Y. J., Delson, E., et al. (2005). "Evolutionary morphing," in *Proceedings of the IEEE Visualization, 2005 VIS 05*, Piscataway, NJ.

Williams, E. E., and Koopman, K. F. (1952). West Indian fossil monkeys. *Am. Mus. Novit.* 1546, 1–16.

Woods, C. A., and Ottenwalder, J. A. (1992). *The Natural History of Southern Haiti*. Gainesville, FL: University of Florida.

Woods, R., Turvey, S. T., Brace, S., MacPhee, R. D. E., and Barnes, I. (2018). Ancient DNA of the extinct Jamaican monkey Xenothrix reveals extreme insular change within a morphologically conservative radiation. *Proc. Natl. Acad. Sci. U.S.A.* 115, 12769–12774. doi: 10.1073/pnas.1808603115

Zienkiewicz, O. C., Taylor, R. L., and Zhu, J. Z. (2005). *The Finite Element Method its Basis and Fundamentals*. Boston, MA: Elsevier Butterworth-Heinemann.

Conflict of Interest: The authors declare that the research was conducted in the absence of any commercial or financial relationships that could be construed as a potential conflict of interest.

The handling Editor declared a past co-authorship with one of the authors SA.

frontiers in Ecology and Evolution

ORIGINAL RESEARCH
published: 07 April 2020
doi: 10.3389/fevo.2020.00069

Cranial Anatomy and Paleoneurology of the Extinct Sloth *Catonyx tarijensis* (Xenarthra, Mylodontidae) From the Late Pleistocene of Oruro, Southwestern Bolivia

Alberto Boscaini[1]*, *Dawid A. Iurino*[2,3], *Bernardino Mamani Quispe*[4], *Rubén Andrade Flores*[4], *Raffaele Sardella*[2,3], *François Pujos*[1] and *Timothy J. Gaudin*[5]

[1] Instituto Argentino de Nivología, Glaciología y Ciencias Ambientales (IANIGLA), CCT-CONICET-Mendoza, Mendoza, Argentina, [2] Dipartimento di Scienze della Terra, Sapienza Università di Roma, Rome, Italy, [3] Paleo Factory, Sapienza Università di Roma, Rome, Italy, [4] Departamento de Paleontología, Museo Nacional de Historia Natural de Bolivia, La Paz, Bolivia, [5] Department of Biology, Geology, and Environmental Sciences, University of Tennessee at Chattanooga, Chattanooga, TN, United States

OPEN ACCESS

Edited by:
Lorenzo Rook,
University of Florence, Italy

Reviewed by:
Marina Melchionna,
University of Naples Federico II, Italy
Luciano Varela,
Universidad de la República, Uruguay
Gerardo De Iuliis,
University of Toronto, Canada

***Correspondence:**
Alberto Boscaini
aboscaini@mendoza-conicet.gob.ar;
alberto.boscaini@gmail.com

Specialty section:
This article was submitted to Paleontology, a section of the journal Frontiers in Ecology and Evolution

Received: 25 December 2019
Accepted: 04 March 2020
Published: 07 April 2020

Citation:
Boscaini A, Iurino DA, Mamani Quispe B, Andrade Flores R, Sardella R, Pujos F and Gaudin TJ (2020) Cranial Anatomy and Paleoneurology of the Extinct Sloth Catonyx tarijensis (Xenarthra, Mylodontidae) From the Late Pleistocene of Oruro, Southwestern Bolivia. Front. Ecol. Evol. 8:69. doi: 10.3389/fevo.2020.00069

Extinct scelidotheriine sloths are among the most peculiar fossil mammals from South America. In recent decades, the external cranial anatomy of Pleistocene scelidotheres such as *Scelidotherium*, *Catonyx*, and *Valgipes* has been the subject of numerous studies, but their endocranial anatomy remains almost completely unknown. Today, computed tomographic (CT) scanning methodologies permit the exploration of previously inaccessible anatomical areas through a completely non-destructive process. For this reason, we undertook an analysis of the external and internal cranial anatomy of *Catonyx tarijensis* from the late Pleistocene of the Department of Oruro, in southwestern Bolivia. One particularly well-preserved specimen allowed detailed observation of all the main cranial osteological features, including the ear region and an almost complete hyoid apparatus, previously unknown for this taxon. Moreover, CT-scanning and subsequent elaboration of digital models of this specimen allowed observation of the brain cavity and cranial sinuses, and reconstruction of the trajectory of the main cranial nerves for the first time in an extinct scelidotheriine sloth. Additionally, we recovered the first three-dimensional reconstructions of the nasal cavity and the turbinates of an extinct sloth. In contrast to the usual depiction, the combined information from the external and internal anatomy suggests reduced lingual protrusion in *Catonyx tarijensis*, or at least a consistently more limited protrusion of the tongue in comparison with other mylodontid sloths such as *Glossotherium robustum*. The new morphological information recovered from this extinct sloth is compared with the available information for both extant and extinct forms, providing insights in the paleobiology of the extinct species. The present study reveals the importance of applying these novel non-destructive techniques to elucidate the evolutionary history of sloths.

Keywords: Xenarthra, scelidotheriine sloth, *Catonyx tarijensis*, skull, anatomy, endocast, hyoid apparatus

INTRODUCTION

Sloths (Folivora) are today represented by only two genera, *Bradypus* and *Choloepus,* and constitute an endemic South and Central American mammalian clade restricted to Neotropical rain forests (Nowak, 1999). By contrast, their fossil record is extremely rich and diverse, spanning chronologically from the late Eocene to the early Holocene, and geographically covering nearly all of the American supercontinent (e.g., McNab, 1985; Steadman et al., 2005; Gaudin and Croft, 2015). Mylodontidae is one of the most important folivoran clades, representing a major subdivision of sloths' diversity (e.g., Gaudin, 2004; Boscaini et al., 2019a; Delsuc et al., 2019; Presslee et al., 2019). Its representatives were mainly quadrupedal and terrestrial, and in some cases developed digging capabilities (e.g., Vizcaíno et al., 2001; Pujos et al., 2012). Mylodontid sloths were particularly widespread and abundant in South America, but they also reached Central and North America in different migratory events (e.g., Robertson, 1976; Webb, 1989; McDonald and Pelikan, 2006).

Among mylodontids, Mylodontinae includes medium to large-sized herbivorous forms and, with a few exceptions (e.g., *Mylodon* and *Pseudoprepotherium*; see Hirschfeld, 1985 and Bargo et al., 2006), they show mediolaterally wide muzzles that are indicative of grazing diets (McDonald, 1997; Bargo et al., 2006; Pujos et al., 2012). A different morphology is observed in the sister group to Mylodontinae, Scelidotheriinae. The narrow muzzle of scelidotheriines have been associated with more selective diets (McDonald, 1997; Bargo et al., 2006). Indeed, scelidotheriine sloths have long been recognized as distinctive, based on their unusual dentition and skull morphology (e.g., Owen, 1839; Gervais and Ameghino, 1880; McDonald, 1987). McDonald (1987) noted that all scelidotheriine species possess elongated and narrow skulls. The dentition is also buccolingually compressed, so that every tooth has a long axis that is much longer than its orthogonal width, although the orientation of the long axis varies along the toothrow (Owen, 1839; Gervais and Ameghino, 1880; McDonald, 1987). Gaudin (2004) identified additional unique synapomorphies of Scelidotheriinae. For example, the maxilla is deeper in its midsection to accommodate the elongated tooth roots, and narrows anteriorly and posteriorly, in lateral view (Gaudin, 2004). This results in a ventrally convex profile of the palate in lateral view that is also unique to the group (Gaudin, 2004).

The scelidotheriine fossil record ranges chronologically from the middle Miocene to the Pleistocene/Holocene transition (Friasian to Bonaerian/Lujanian SALMAs; South American Land Mammal Age(s); McDonald, 1997; Scillato-Yané and Carlini, 1998; McDonald and De Iuliis, 2008; Miño-Boilini et al., 2019). In contrast to mylodontines, scelidotheriines were restricted to South America, and did not participate in the G.A.B.I. (Great American Biotic Interchange), as a probable consequence of their ecological restrictions due to specialized feeding habits (McDonald, 2005; Amson et al., 2016). During the Pleistocene, this clade was represented by three genera: (i) *Valgipes*, endemic to the intertropical region of Brazil (Cartelle et al., 2009, 2019), (ii) *Scelidotherium*, from the Pampas region of Argentina and Uruguay (McDonald and De Iuliis, 2008; Corona et al., 2013), and (iii) *Catonyx* (=*Scelidodon*) a more widespread taxon known from Argentina, Bolivia, Brazil, Chile, Ecuador, Peru, and Uruguay (Miño-Boilini, 2016).

According to Gaudin (2004), features that serve to differentiate the two scelidotheriine *Catonyx* and *Scelidotherium* include: the posterior extension of the temporal fossa, which is more pronounced in the former taxon (Gaudin, 2004: char. 97); in *Catonyx*, the orbital portion of the lacrimal is more expanded than the facial, whereas the two portions are equal in size in *Scelidotherium* (Gaudin, 2004: char. 140); a maxillo-lacrimal contact within the orbit is present in *Catonyx*, whereas it is absent in *Scelidotherium* (Gaudin, 2004: char. 109); the sphenorbital fissure is more posteriorly located in *Scelidotherium* than in *Catonyx* (Gaudin, 2004: char. 161), and *Scelidotherium* exhibits a smaller hypoglossal foramen than *Catonyx* (Gaudin, 2004: char. 187). Finally, *Catonyx* possesses distinct fossae for the rectus capitis muscles on the basioccipital that are lacking in *Scelidotherium* (Gaudin, 2004: char. 196).

Following the latest revisions of the group (i.e., McDonald and Perea, 2002; Corona et al., 2013; Miño-Boilini, 2016), *Catonyx* includes three species: (i) *C. chiliensis* from the Lujanian SALMA of Argentina, Bolivia, Chile, Ecuador, and Peru, (ii) *C. cuvieri* from the Lujanian SALMA of Brazil and Uruguay, and (iii) *C. tarijensis*, from the Ensenadan–Lujanian SALMAs of Argentina, Bolivia, and Uruguay. Only *C. chiliensis* and *C. tarijensis* have previously been recovered from Bolivia. The two species are easily recognizable by their general body size, the shape of the nasals, the development of the sagittal crest, and the morphology of the dentition in occlusal view (McDonald, 1987; McDonald and Perea, 2002; Corona et al., 2013; Miño-Boilini, 2016).

In the present contribution, based on an almost complete skull of *Catonyx tarijensis* from late Pleistocene deposits of the Department of Oruro, we provide a detailed description of its skull and mandible, with special emphasis on its poorly known ear region. We also provide a description of the almost complete hyoid apparatus of this species, together with the first digital reconstructions of the main endocranial structures of a scelidotherine sloth.

MATERIALS AND METHODS

The specimen of *Catonyx tarijensis* MNHN-Bol V 13364 analyzed in the present study was recovered in 2013 from late Pleistocene deposits at Chokxo Pata, Ayllu Yuruma locality (18° 43′ 28.5″ S; 67° 26′ 39.8″ W; altitude: 3.667 m a.s.l.). This locality is situated on the western side of Lake Poopó (Municipality of Santiago de Andamarca, Sud Carangas Province, Department of Oruro, southwestern Bolivia; **Figure 1**). The specimen was recovered in a friable non-laminated yellowish sandstone of lacustrine origin, without any other associated faunistic elements. However, the late Pleistocene age of the fossils is suggested by the unconsolidated nature of the sediments and low degree of

Abbreviations: MNHN, Muséum national d'Histoire naturelle, Paris, France; MNHN-Bol, Museo Nacional de Historia Natural de Bolivia, La Paz, Bolivia.

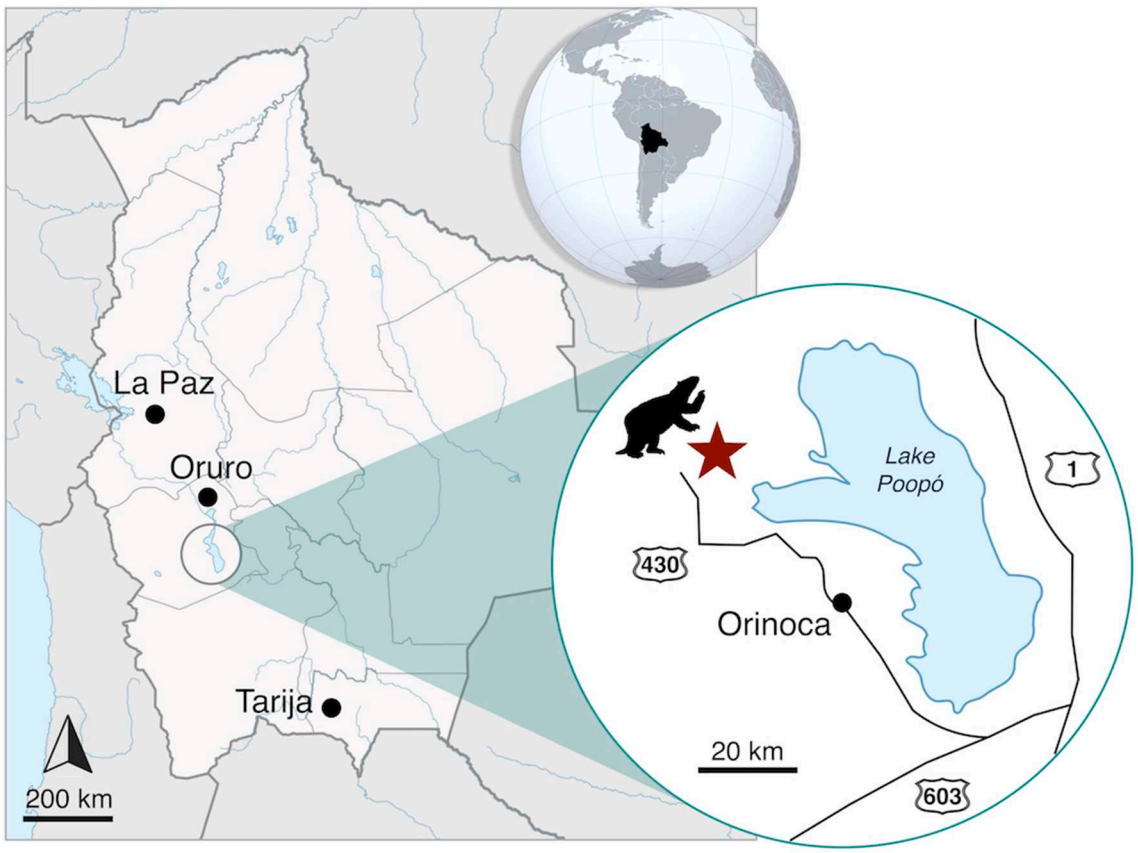

FIGURE 1 | Map of the locality in which the remains of *Catonyx tarijensis* MNHN-Bol V 13364 have been recovered. Circles: cities; Star: fossil locality.

petrification of the remains, together with absolute dates obtained in neighboring areas (Placzek et al., 2006). At the moment, a late Pleistocene age for these remains is the most plausible, given the wide distribution of *Catonyx* in other South American localities in this period (see Introduction). However, further paleontological surveys and detailed analyses at Chokxo Pata are necessary for a reliable chronological assessment of the recovered remains. The specimen labeled as MNHN-Bol V 13364 includes an almost complete skull, both mandibular rami, most of the hyoid apparatus, an incomplete left humerus and radius, and other postcranial fragments.

MNHN-Bol V 13364 is particularly well-preserved and exhibits only slight deformation, allowing detailed descriptions of the cranial and mandibular remains, with special emphasis on the ear region and the hyoid apparatus. Moreover, we report the first digital models of the endocranial cavities of a scelidotheriine sloth, based on scans of MNHN-Bol V 13364, taken with a Somatom Scope (Siemens) CT scanner at the "Clínica Alemana" Institute of La Paz (Bolivia). The scanning resulted in 1,032 slices with a slice thickness of 0.75 mm. The image segmentation process was performed using the digital tools provided by OsiriX v.5.6 32-bit and Materialize Mimics v.20. The 3D models of the nasal cavity, turbinates, brain cavity, and cranial sinuses were exported from Mimics as ".PLY" files, then converted to ".OBJ" format and imported into ZBrush 4R6 for the rendering process. Unfortunately, the resolution of the CT-scan did not allow for a detailed reconstruction of the bony labyrinth of MNHN-Bol V 13364, and for this reason this anatomical area is not treated in the present paper.

External craniodental measurements were taken with a digital caliper to the nearest 0.1 mm, whereas measurements of the digital models were obtained using the tools of the software Materialize Mimics v.20.

The comparative sample is largely based on the dataset assembled by Boscaini et al. (2020), which includes the two extant sloth species *Bradypus variegatus* and *Choloepus hoffmanni*, and the extinct giant mylodontine *Glossotherium robustum*. For the purposes of comparison, other non-digital endocranial information was obtained from Gervais (1869) and Dechaseaux (1958, 1962a,b, 1971).

RESULTS

Systematic Paleontology

XENARTHRA (Cope, 1889)
PILOSA (Flower, 1883)
FOLIVORA (Delsuc et al., 2001)
MYLODONTIDAE (Gill, 1872)

SCELIDOTHERIINAE (Ameghino, 1904)
Catonyx (Ameghino, 1891)
Catonyx tarijensis (Gervais and Ameghino, 1880)

Holotype MNHN.F.TAR1260, skull and mandible from the Pleistocene of Tarija Valley (southern Bolivia).

Referred material MNHN-Bol V 13364: complete skull, associated with both mandibular rami and most of the hyoid apparatus, incomplete left humerus and radius, and isolated postcranial fragments from late Pleistocene deposits at Chokxo Pata, Ayllu Yuruma locality (Sud Carangas Province, Department of Oruro, southwestern Bolivia).

Measurements see **Table 1**.

Type locality and age Department of Tarija (southern Bolivia), Tolomosa Formation, middle (0.76 ± 0.03 Ma; U–Th/Pb and U–Th/H; MacFadden et al., 2013) or late (44-21 ka; C^{14}; Coltorti et al., 2007) Pleistocene.

Distribution Pleistocene deposits of Bolivia, Argentina and Uruguay (McDonald and Perea, 2002; Corona et al., 2013; Miño-Boilini, 2016).

Comparative Description of the External Anatomy

Skull

The skull of *Catonyx tarijensis* MNHN-Bol V 13364 is tubular in section, anteroposteriorly elongated, and somewhat low dorsoventrally (**Figure 2**), all typical of scelidotheriine cranial morphology (e.g., McDonald, 1987; Gaudin, 2004; Miño-Boilini, 2012).

The medial and lateral anterior processes of the nasal are separated by a deep notch (**Figures 2A,C**), as is typical in scelidotheriines (Gaudin, 2004: char. 102). The anterior portion of the nasal is mediolaterally expanded and tapers posteriorly in a gradual and uniform fashion. The nasofrontal suture is almost transverse and straight (**Figure 2A**).

Only the posteriormost portion of the right premaxilla is present, preserving a minor portion of the lateral ramus (**Figure 2B**). The palatal portion of the maxilla exhibits a ventrally convex profile in lateral view (**Figure 2C**), a characteristic feature of scelidotheriines (Gaudin, 2004: char. 121; Cartelle et al., 2009). The palate itself is elongated and narrow, and extends well posterior to the last upper molariform as a broad postpalatal shelf that extends posteriorly along the medial surface of the pterygoid flange for almost half its anteroposterior length (**Figure 2B**). This shelf is pierced by at least one large postpalatal foramen (=minor palatine foramen of other mammals; Gaudin, 2011). The anterior palatal foramen is only preserved on the right side, where it forms a small opening emptying into a short, shallow anterior groove, roughly halfway between the lateral ramus of the premaxilla and the first molariform. The incisive foramina are largely hidden by the large medial palatal processes of the maxilla (as in *Scelidotherium*; Gaudin, 2004: char. 117) and are located within an elongate median groove at the anterior end of the palate (**Figure 2B**). The anterior end of the maxillopalatine suture lies medial to the third molariform, as it does in *Scelidotherium* (Gaudin, 2004: Figure 5B).

TABLE 1 | External and internal measurements of the craniodental remains of *Catonyx tarijensis* MNHN-Bol V 13364 from the Pleistocene of Oruro (Bolivian Altiplano).

Measurement	Value
Skull	
Basicranial width	200.8
Condyle external width	142.1
Condyle internal width	69.4
Foramen magnum height	49.7
Maxillary extension (anterior to Mf1)	91.8
Maxillo-condylar length	501.1
Maximum snout width	120
Minimum post-orbital width of the frontal	121.1
Minimum snout width	115.3
Occipital height	128.4
Palatal length (excluding the premaxilla)	232.7
Palatal width (at the level of Mf2)	58.4
Palatal width (at the level of Mf5)	48.8
Snout height	123.6
Snout length	104.6
Upper dental series length	120.8
Mandible	
Condyle-angle height	121.4
Coronoid process anteroposterior length	86.5
Height of ramus at the level of mf1	86.2
Height of ramus at the level of mf2	91.6
Height of ramus at the level of mf3	91.7
Height of ramus at the level of mf4	92.8
Lower dental series length	111.2
Mandibular condyle length	23.3
Mandibular condyle width	50.7
Symphyseal spout length	113.3
Symphyseal spout width	68.7
Total length of mandible	411.4
Upper dentition	
Mf1 mesiodistal length	23.6
Mf1 buccolingual width	11.2
Mf2 mesiodistal length	24.6
Mf2 buccolingual width	15.4
Mf3 mesiodistal length	24.1
Mf3 buccolingual width	15.3
Mf4 mesiodistal length	20.1
Mf4 buccolingual width	13.8
Mf5 mesiodistal length	13.9
Mf5 buccolingual width	13.4
Lower dentition	
mf1 mesiodistal length	29.7
mf1 buccolingual width	16.8
mf2 mesiodistal length	26.2
mf2 buccolingual width	10.6
mf3 mesiodistal length	26.1
mf3 buccolingual width	11.5
mf4 mesiodistal length	36.2
mf4 buccolingual width	20.9
Brain endocast	
Maximum anteroposterior length	155.6
Maximum mediolateral width	100.2
Volume (including nerves)	571.9

Mf, upper molariform tooth; mf, lower molariform tooth. Measurements are reported in mm, except for the brain endocast volume which is reported in cm^3.

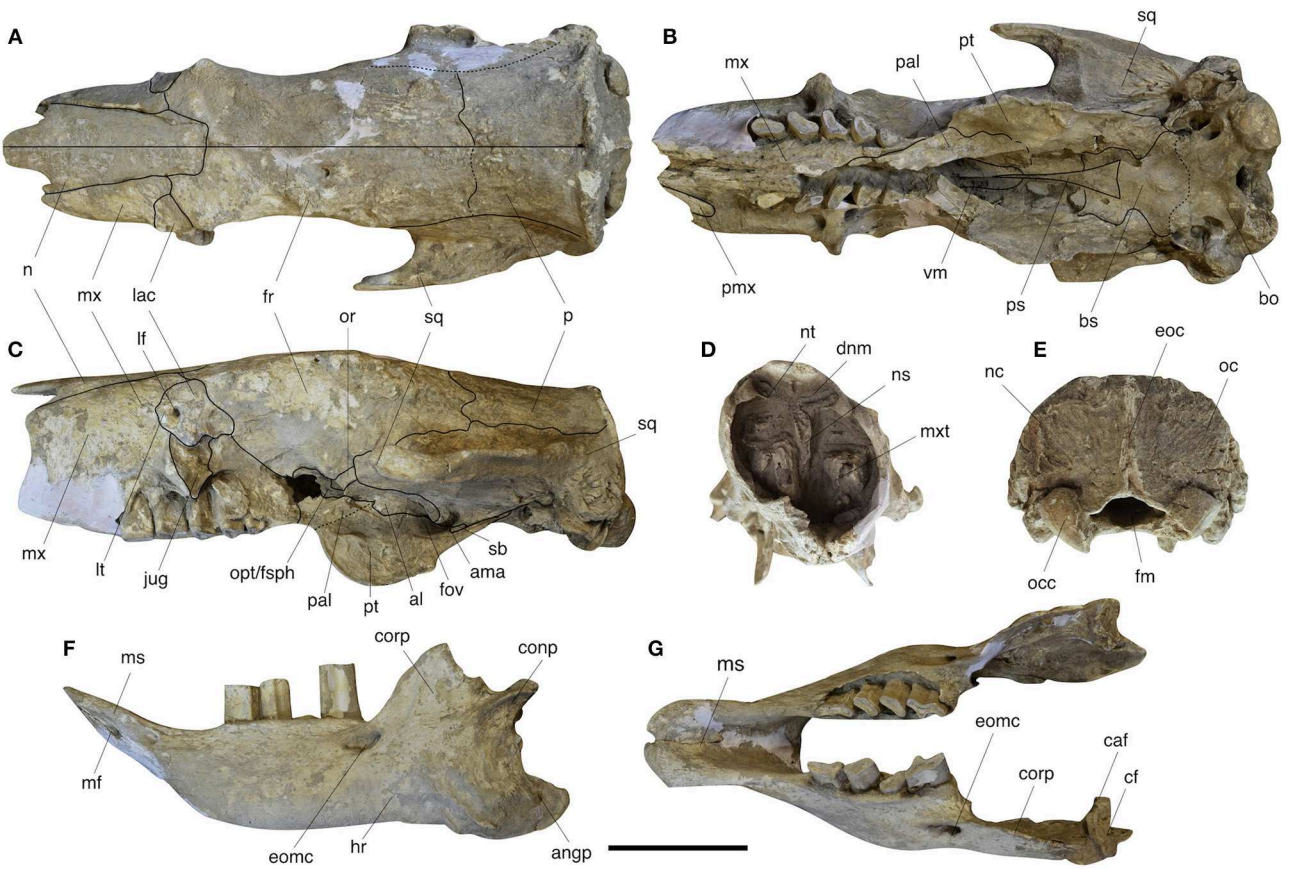

FIGURE 2 | Skull and mandible of *Catonyx tarijensis* MNHN-Bol V 13364 from the Pleistocene of Oruro (Bolivian Altiplano). Skull in dorsal **(A)**, ventral **(B)**, lateral **(C)**, anterior **(D)**, and posterior **(E)** views. Mandible in lateral **(F)** and occlusal **(G)** views. al, alisphenoid; ama, accessory mandibular articulation; angp, angular process; bo, basioccipital; bs, basisphenoid; caf, condylar accessory facet; cf, condylar facet; conp, condyloid process; corp, coronoid process; dnm, dorsal nasal meatus; eoc, external occipital crest; eomc, external opening of the mandibular canal; fm, foramen magnum; fov, foramen ovale; fr, frontal; hr, horizontal ramus of mandible; jug, jugal; lac, lacrimal; lf, lacrimal foramen; lt, lacrimal tubercle; mf, mental foramen; ms, mandibular spout; mx, maxilla; mxt, maxilloturbinate; n, nasal; nc, nuchal crest, ns, nasal septum; nt, nasoturbinate; oc, occipital; occ, occipital condyle; opt/fsph, common aperture for the optic foramen and sphenorbital fissure; or, orbitosphenoid; pal, palatine; p, parietal; pmx, premaxilla; ps, presphenoid; pt, pterygoid; sb, sutural bone; sq, squamosal; vm, vomer. Scale bar equals 10 cm.

The lacrimal is roughly quadrilateral in shape and has a relatively reduced facial exposure and an extensive orbital exposure (**Figure 2C**). In this respect, *Catonyx* differs from *Scelidotherium*, in which the orbital exposure is no larger than the facial (Gaudin, 2004: char. 140). There is a well-developed lacrimal tubercle just anterior to the single large and circular lacrimal foramen (**Figure 2C**). The latter is located on the facial portion of the lacrimal and just anterior to the orbital rim. The facial exposure of the lacrimal contacts the maxilla anteriorly and the frontal posteriorly. This contrasts with the information in Gaudin (2004: char. 107), in which a contact between the nasal and lacrimal is considered a synapomorphy of scelidotheres, suggesting that this feature may represent a variable feature at different taxonomic levels. The absence of contact between the nasal and the lacrimal in MNHN-Bol V 13364, differs from the arrangement depicted by McDonald (1987) for the same species. The variability of this feature was first mentioned by Kraglievich (1923) for *Scelidotherium* and is now also confirmed for *Catonyx*. In MNHN-Bol V 13364, the orbital exposure of the lacrimal contacts the jugal and the maxilla ventrally and the frontal posteriorly (**Figure 2C**). The contact between maxilla and lacrimal within the orbit is absent in *Scelidotherium* (Gaudin, 2004: char. 109).

Another distinctive feature of MNHN-Bol V 13364 is the exceptional preservation of the nasopharyngeal roof (**Figure 2B**). At the anterior end, both the alae and the median keel of the vomer are visible, the former well-outlined by sutures (**Figure 2B**). A typical triangular presphenoid is observable posterior to the vomer. The basisphenoid is irregular in shape but reminiscent of the butterfly shape commonly observed in some mylodontids, such as *Mylodon*, *Glossotherium*, and *Paramylodon* (Patterson et al., 1992) and other sloths, such as *Bradypus* and *Analcimorphus* (Gaudin, 2004: char. 198). The basisphenoid and basioccipital are completely fused. However, there are two strongly developed tubera which typically lie on the junction between the basisphenoid and the basioccipital, suggesting that

the suture occurs in this region (**Figure 2B**). The basioccipital is wide transversely and short anteroposteriorly, nearly flat but marked bilaterally by shallow depressions for the rectus capitis muscles (**Figure 2B**). As noted above, these fossae are absent in *Scelidotherium*.

As is common in mylodontids, there is a large ovate depression near the bottom of the medial orbital wall that houses most of the major orbital foramina (**Figure 2C**). The sphenopalatine/anterior palatal foramen, which is normally part of this complex, is not preserved on either side. However, the large opening, typical of sloths (Gaudin, 2004: char 160), that serves as a common aperture for the optic foramen and sphenorbital fissure, is well-preserved bilaterally (**Figure 2C**). *Scelidotherium* differs from *Catonyx* in the absence of a common depression for the orbital foramina, with the aperture of the optic foramen/sphenorbital fissure situated well posterior to the sphenopalatine/anterior palatal foramen (Gaudin, 2004: char. 161). The sutural relationships of the bones surrounding the aperture for the optic foramen/sphenorbital fissure are complex in MNHN-Bol V 13364 (**Figure 2C**). Indeed, four bones participate in the formation of the opening: frontal, orbitosphenoid, alisphenoid, and palatine. The frontal forms the anterior and dorsalmost portion of the aperture. The orbitosphenoid forms the roof and part of the lateral wall. The alisphenoid is the most complex, comprising a portion of the lateral wall, most of the medial wall, as well as a portion of the floor. The remaining part of the floor of the aperture is formed by the palatine (**Figure 2C**). The orbitosphenoid has a small lateral exposure lateral to the aperture of the sphenorbital fissure/optic foramen, extending posteriorly to contact the squamosal and largely separating the alisphenoid and frontal. A lateral exposure of the orbitosphenoid like this is quite unusual, not only in sloths, but for xenarthrans in general, but has been reported in a single juvenile specimen of the extant two-toed sloth *Choloepus hoffmanni* (Gaudin, 2011).

The foramen ovale of MNHN-Bol V 13364 is located between the alisphenoid, pterygoid, and squamosal. The last two elements form the bulk of the rim, with the alisphenoid contributing only a small portion of the anterior edge. In MNHN-Bol V 13364 there is also a rounded projection extending ventrally from the dorsolateral margin of the foramen ovale and partially shielding it in lateral view (**Figure 2C**). This small projection is comprised of alisphenoid anteriorly and squamosal posteriorly, and bears a slightly concave articular surface laterally (**Figure 2C**). This surface contacts a distinct medial facet on the mandibular condyle, and therefore we identify this as an accessory mandibular articulation (ama; **Figure 2C**), unknown in other sloths.

Behind the foramen ovale, an ovoid, reduced sutural bone is present, just at the junction between the pterygoid and the squamosal (**Figure 2C**). The pterygoid/squamosal suture extends posteriorly into the ear region (**Figures 2B,C**). The pterygoid of *C. tarijensis* appears less inflated basally than is the case in either *M. darwinii* or *G. robustum* (Patterson et al., 1992; Boscaini et al., 2018a). In the latter two taxa, a pair of inflated areas, lateral and medial, are observed at the base of the pterygoid, whereas in *C. tarijensis*, a single low pterygoid inflation is present (**Figure 2B**). The ventral portion of the pterygoid extends ventrally into a large pterygoid flange, as is typical for sloths (Gaudin, 2004). In *Catonyx,* the ventral margin of this flange is semicircular in shape, whereas in *Scelidotherium* it is more nearly triangular (Owen, 1857; Gaudin, 2004: Figure 5A).

In MNHN-Bol V 13364 many of the internal structures of the nasal cavity are visible in anterior view, including the nasal septum and the anteriormost portion of the nasoturbinates and maxilloturbinates (**Figure 2D**). The nasoturbinates terminate anteriorly on the underside of the long lateral process of the nasal and delimit the dorsal nasal meatus ventrally. The surface of the maxilloturbinates form a relatively smooth and conical mass at its anterior end (**Figure 2D**).

In dorsal view, the temporal lines are poorly developed and the sagittal crest is lacking (**Figure 2A**), two features that are probably related to the immaturity of the individual (Corona et al., 2013). In MNHN-Bol V 13364, the temporal lines are only observable at the level of the poorly developed postorbital processes, and posteriorly, where they merge with the nuchal crest (**Figure 2A**). Among Mylodontidae, the posterior convergence of the temporal lines and the nuchal crest is also observed in *Nematherium*, *Octodontotherium*, and Lestodontini (Gaudin, 2004: char. 97). In *Scelidotherium* and other mylodontines, the temporal lines turn ventrally, anterior to the nuchal crest. The frontoparietal suture is only partially detectable in MNHN-Bol V 13364 (**Figure 2A**), and shows an irregular and bilaterally asymmetric outline. The position of this suture, well posterior to the glenoid, represents a scelidotheriine + mylodontine synapomorphy according to Gaudin (2004: char. 172).

In posterior view (**Figure 2E**), the occipital is subrectangular in shape, as is typical for scelidotheriines (Brambilla and Ibarra, 2018), whereas the subtriangular occipital condyles are directed ventrally, as is typical for *Catonyx* (Corona et al., 2013; Miño-Boilini, 2016).

Ear Region

The ectotympanic and the middle ear ossicles are missing on both sides of MNHN-Bol V 13364, but the remainder of the auditory region is well-preserved.

Both entotympanics are present and complete. As is typical for sloths, they are located lateral to the basioccipital/basisphenoid tuber and ventral to the promontorium of the petrosal (**Figures 2B**, **3**). Again as in most sloths, the entotympanic is divided into medial and lateral plates by a deep sulcus for the internal carotid artery (**Figure 3**; Gaudin, 1995). At the anterior end of this sulcus, the entotympanic encloses a canal through which the artery passed (**Figure 3**); the presence of this canal is a variable feature in *Catonyx* and *Scelidotherium* (Gaudin, 1995). A carotid foramen/canal in the entotympanic is also present in *Nematherium* and *Pseudoprepotherium*, but is missing in other mylodontids (Patterson et al., 1992; Gaudin, 1995, 2004).

On the right side of MNHN-Bol V 13364, the lateral plate of the entotympanic has a small opening near its anterior end that likely accommodated the exit of the greater petrosal nerve (=vidian nerve) from the tympanic cavity. A short groove for the greater petrosal nerve extends from the opening toward the

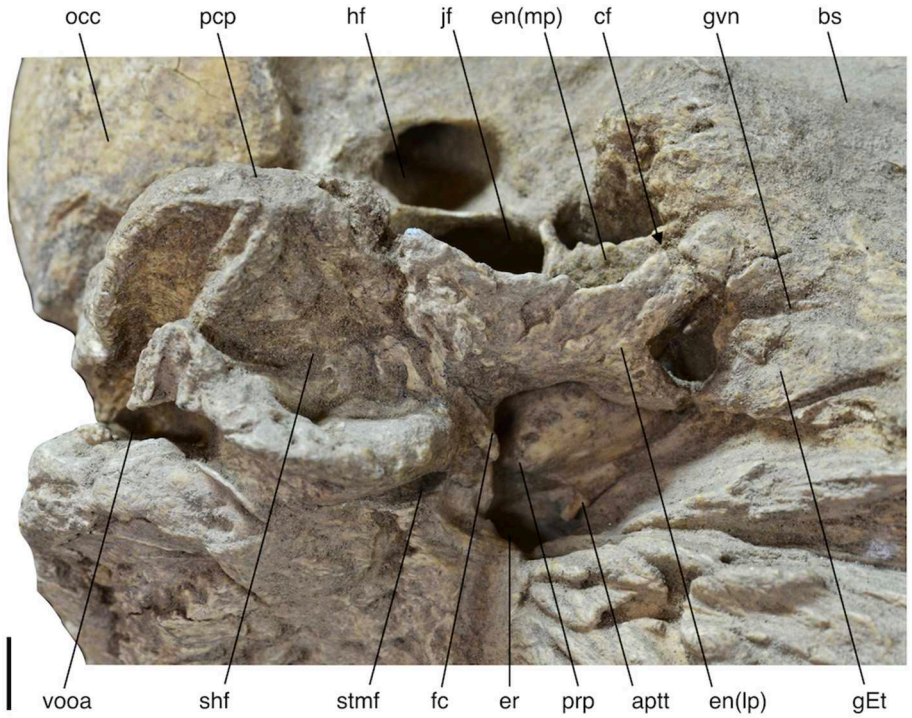

FIGURE 3 | Left ear region of *Catonyx tarijensis* MNHN-Bol V 13364 in ventrolateral view (anterior toward the right). aptt, anteroventral process of the tegmen tympani; bs, basisphenoid; cf, carotid foramen; en(lp), entotympanic (lateral plate); en(mp), entotympanic (medial plate); er, epitympanic recess; fc, fenestra cochleae; gEt, groove for the Eustachian tube; gvn, groove for the vidian nerve; hf, hypoglossal foramen; jf, jugular foramen; occ, occipital condyle; pcp, paracondylar process of exoccipital; prp, promontorium of petrosal; shf, stylohyal fossa; stmf, stylomastoid foramen; vooa, ventral opening for the occipital artery. Scale bar equals 1 cm.

nasopharynx. On the left side, there is a much larger aperture in roughly the same position (**Figure 3**), suggesting that this difference in size could be related to the immature development of this individual.

In fact, there are several additional features in the ear region which indicate the subadult status of MNHN-Bol V 13364 including: (i) a small gap between the medial entotympanic and the basioccipital/basisphenoid tuber (visible on the left side of the skull), (ii) an unusually deep stylohyal fossa, and (iii) the presence of an open groove for the occipital artery on the mastoid exposure of the petrosal (**Figure 3**). In all other mylodontids except *Nematherium*, the occipital artery is either partially or fully enclosed in a canal (Gaudin, 1995, 2004).

The petrosal morphology of MNHN-Bol V 13364 is typical for scelidotheres, and indeed for Mylodontidae as a whole (Patterson et al., 1992; Gaudin, 1995, 2004). One unusual aspect of this specimen is the small size of the anteroventral process of the tegmen tympani (aptt; **Figure 3**). The aptt is variable in size and shape among mylodontids, but was recorded as a "large, rugose bony mass" in prior observations of *Catonyx* (Gaudin, 1995, 2004). The small and triangular shape of the aptt in MNHN-Bol V 13364 (**Figure 3**) could also be related to its subadult status.

The large jugular foramen which marks the posteromedial boundary of the ear region is typical for mylodontids (**Figure 3**). However, the hypoglossal foramen is distinctive in a number of aspects. First, in MNHN-Bol V 13364 it is nearly identical in size to the jugular foramen (**Figure 3**), whereas in *Mylodon* and *Glossotherium* the hypoglossal foramen is larger than the jugular (Patterson et al., 1992; Boscaini et al., 2018a). Moreover, it nearly abuts the jugular foramen, the two being separated by a sharp ventral crest (**Figure 3**). In other mylodontids, the hypoglossal foramen is located farther posteriorly (Patterson et al., 1992; Boscaini et al., 2018a).

Mandible

The mandible of MNHN-Bol V 13364 shows an almost horizontal ventral border, as is typical for mylodontids (Gaudin, 2004; McDonald and De Iuliis, 2008). As in other scelidotheres, it has a very elongated and narrow mandibular spout with a rounded anterior edge (**Figures 2F,G**).

The very deep horizontal ramus of MNHN-Bol V 13364 (**Figure 2F**) is characteristic of *Catonyx tarijensis* and contrasts with the shallower ramus in *C. cuvieri* and *C. chiliensis* (Pujos, 2000; Miño-Boilini, 2016). The condyle is transversely extended as in other scelidotheres, but with a peculiar concave articular surface, which differs from the flat articular surface that is typical of the group (Gaudin, 2004: char. 55). The latter is bordered medially by a second articular surface for the accessory mandibular articulation, as discussed above.

Despite the apparent subadult status of the specimen, the grooves and ridges that mark the attachments of the masticatory muscles are very well-developed (**Figure 2F**). This is particularly

FIGURE 4 | Hyoid apparatus of *Catonyx tarijensis* MNHN-Bol V 13364 from the Pleistocene of Oruro (Bolivian Altiplano). Right stylohyal in medial view **(A)**; right epihyal in medial view **(B)**; V-bone in anterior view **(C)**; and ossified thyroid cartilage in anterior view **(D)**. Scale bar equals 5 cm.

evident along the ventrolateral margin of the angular process, where two strong grooves are present.

Hyoid Apparatus

A large part of the hyoid apparatus of MNHN-Bol V 13364 is preserved, the available elements including the right stylohyal and epihyal, the "V-bone" (fused basihyal and thyrohyals), and the ossified thyroid cartilage (**Figure 4**). Both ceratohyals, however, are missing. On the whole, the hyoid morphology of *Catonyx* reflects the general xenarthran pattern, which consists of three paired and unfused bones (representing the anterior cornua) and an unpaired V-bone (representing the posterior cornua) (Casali and Perini, 2017).

Stylohyal- The right stylohyal of MNHN-Bol V 13364 is almost complete, lacking only the articular facet for the basicranium (**Figure 4A**). The body of the stylohyal is cylindrical, with a slight enlargement toward the distal facet for the epihyal (**Figure 4A**), as is typical in Folivora (Gaudin, 2004: char. 79; Casali and Perini, 2017: char. 1). The shaft of the stylohyal is straight in *Catonyx* (**Figure 4A**), a condition that is observed in other scelidotheriines such as *Scelidotherium* and *Valgipes*, whereas the stylohyal shaft is curved in mylodontines such as *Mylodon*, *Paramylodon*, *Glossotherium*, and *Lestodon* (Gaudin, 2004; Pérez et al., 2010; Tambusso et al., 2015; Casali and Perini, 2017). However, the curved condition can be occasionally observed in some specimens of *Scelidotherium,* and the straight condition in some *Paramylodon* specimens (Casali and Perini, 2017). In *Paramylodon harlani*, Stock (1925) also identified an uncommon case of fusion between the stylohyal and the epihyal. This feature, commonly recovered among the extant sloths (Naples, 1986), is rarely observed in extinct taxa such as *Paramylodon harlani*, *Megatherium americanum*, and *Eremotherium laurillardi* (Casali and Perini, 2017). The stylohyal-epihyal contact is flat in lateral and medial views in MNHN-Bol V 13364 (**Figures 4A,B**). This feature is also typical of sclelidotheriines, in contrast to the more concavo-convex articulation of mylodontines (Pérez et al., 2010).

Epihyal- The epihyal of *Catonyx* MNHN-Bol V 13364 is shorter in length than the stylohyal (**Figures 4A,B**), a typical condition for pilosans (Gaudin, 2004: char 77; Casali and Perini, 2017: char. 2). The shaft of the epihyal is wide anteroposteriorly and compressed mediolaterally (**Figure 4B**), resembling the shape of the epihyal of *Scelidotherium* and in contrast to that observed in *Glossotherium* and *Paramylodon*, in which the epihyal decreases uniformly in width from its proximal to its distal end (Stock, 1925; Pérez et al., 2010). Both the facets for the stylohyal and the ceratohyal are flat (**Figure 4B**), again resembling the condition in *Scelidotherium* and contrasting with the morphology of *Paramylodon* and *Glossotherium*, in which they are concave and convex, respectively. Both ceratohyals are missing in MNHN-Bol V 13364. As in all extinct sloths, and in contrast to the living forms, they were unfused to the epihyals (Casali and Perini, 2017: char. 6).

V-bone and ossified thyroid cartilage- The fusion between the basihyal and the thyrohyals, forming the so-called V-bone, is a typical xenarthran feature (Pérez et al., 2010; Casali and Perini, 2017). The two anterior eminences that articulate with the ceratohyals are well-developed in *Catonyx* (**Figure 4C**) and similar in shape to those of *Glossotherium* and *Paramylodon* (Stock, 1925; Pérez et al., 2010). Posteriorly, the V-bone contacts the ossified thyroid cartilage through two roughly circular and flat facets (**Figure 4D**). In *Catonyx*, the V-bone and ossified thyroid cartilage are markedly V-shaped in anterior view (**Figures 4C,D**), similar to the morphology observed in *Scelidotherium* and distinct from the U-shaped homologous elements in *Glossotherium* and *Paramylodon* (Pérez et al., 2010).

Comparative Description of the Internal Anatomy

Nasal Cavity

The facial part of the respiratory tract is preserved, both externally (**Figure 2**) and internally (**Figure 5**). The main turbinates of this region, the nasoturbinate (an olfactory structure) and the maxilloturbinate (a respiratory structure), are observable in the anterior view of the nasal cavity (**Figure 2D**) and their morphology can be traced back posteriorly thanks to the digital endocranial reconstruction (**Figures 5A–D**).

The nasoturbinate of *Catonyx tarijensis* MNHN-Bol V 13364 is anteroposteriorly elongated and mediolaterally narrow. It is also inclined ventromedially in anterior view, facing the nasal septum. It constitutes the floor of the relatively large and undivided dorsal nasal meatus (**Figures 5A–D**). The nasoturbinate reaches the anterior edge of the nasal bone anteriorly (as noted above), and extends posteriorly to the level of the postorbital process of the frontal. Unfortunately, the ethmoidal crest and the ethmoturbinates are not preserved, preventing observation of the posterior attachment point for the nasoturbinates (**Figures 5A–C**). The nasoturbinates appear

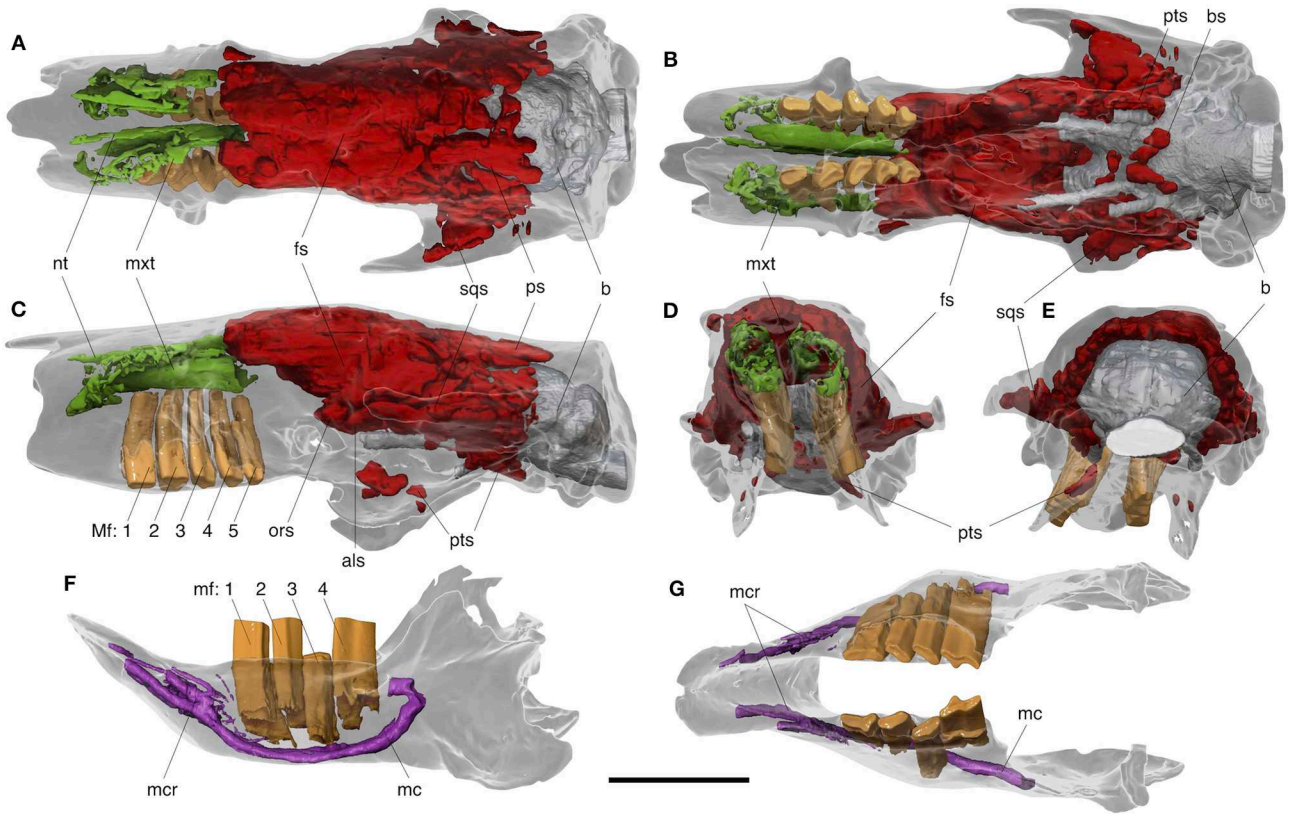

FIGURE 5 | Digital reconstructions of the skull and mandible of *Catonyx tarijensis* MNHN-Bol V 13364 from the Pleistocene of Oruro (Bolivian Altiplano), showing internal features. Skull in dorsal **(A)**, ventral **(B)**, lateral **(C)**, anterior **(D)**, and posterior **(E)** views. Mandible in lateral **(F)** and occlusal **(G)** views. als, alisphenoid sinus; b, brain endocast; fs, frontal sinus; mc, mandibular canal; mcr, mandibular canal ramifications; mf, lower molariform tooth; Mf, upper molariform tooth; mxt, maxilloturbinate; nt, nasoturbinate; ors, orbitosphenoid sinus; ps, parietal sinus; pts, pterygoid sinus; sqs, squamosal sinus. Colors indicate: green, turbinates; purple, mandibular canal and ramifications; orange, dentition; red, sinuses. Scale bar equals 10 cm.

to be somewhat shorter in Stock's (1925: Figure 60) illustration of *Paramylodon*.

The maxilloturbinates are also partially observable. They show the same anteroposterior elongation as the nasoturbinates, but their anatomical structure is more complex (**Figure 5A–D**). In fact, even if they are only partially preserved (broken in places and likely lacking the most delicate bony scrolls), they are clearly enrolled in a corkscrew fashion throughout most of their length (**Figure 5D**). The outermost scroll begins with a dorsolateral attachment to the inner wall of the nasal cavity, and then extends medially, curving ventrally as it approaches the nasal septum, then curving again medially, dorsally, and so on. Similarly scrolled maxilloturbinates are present in *Paramylodon harlani* (TJG, pers. observation). In ventral view, the maxilloturbinates of *Catonyx* appear thicker, forming a continuous surface, likely corresponding to the ventral concha (**Figures 5B,C**).

Cranial Sinuses

Cranial sinuses are well-developed in *Catonyx tarijensis* MNHN-Bol V 13364, extending for about two thirds of the entire skull length (**Figures 5A–C**). Pneumatization reaches its largest extent in the middle cranial area, where the sinuses mirror the external morphology of the cranium (**Figures 5A–C**). More posteriorly, at the level of the squamosal, parietal, and occipital bones, pneumatization is less dense or missing (**Figure 5**). This set of features is more similar to that of *Choloepus* (Boscaini et al., 2020) than that of other extinct giant sloths like *Glossotherium robustum* (Boscaini et al., 2020) and *Paramylodon harlani* (Stock, 1925), where the sinuses invade every bone all the way back to the occiput.

The frontal shows the highest level of pneumatization, with extensive sinuses extending from its anterior to posterior edges, in both dorsal and lateral views (**Figures 5A,C**). In lateral view, the extent of the sinuses reflects the anterior contact with both the lacrimal and the maxilla (**Figure 5C**). Frontal sinuses merge posteriorly with the orbitosphenoid and the alisphenoid sinuses. In fact, the latter bones are also largely pneumatized at the level of the common aperture for the optic foramen and sphenorbital fissure (**Figure 5C**), a common feature in extant and extinct sloths (Boscaini et al., 2020).

The squamosal of MNHN-Bol V 13364 is partially pneumatized, with large sinuses in its anteriormost portion, invading the tip of the zygomatic process (**Figures 5A–C**). However, the posterior half of the squamosal is not pneumatized

(**Figures 5A–C**), in contrast to *Glossotherium*, *Choloepus* and *Bradypus* (Boscaini et al., 2020). It should be noted that the squamosal pneumatization of the extant sloths is an epitympanic sinus continuous with the tympanic cavity ventrally, whereas that of *Catonyx* and *Glossotherium* is confined to the squamosal itself, as is typical for mylodontids (Gaudin, 1995). Parietal sinuses are observable in *Catonyx*, but only in proximity to the fronto-parietal suture (**Figures 5A–C**), as in *Choloepus* (Boscaini et al., 2020). In comparison to the frontal sinuses, the parietal sinuses are smaller in size, allowing observation of the underlying brain cavity in dorsal and lateral views (**Figures 5A–C**). In MNHN-Bol V 13364, sinuses at the level of the parietal represent the posteriormost extension of pneumatization, which is also lacking in most of the basicranium (**Figure 5**).

Ventrally, some sinuses were detected on the cranial base (**Figures 5B–E**). As already noted from the external aspect of MNHN-Bol V 13364, isolated sinuses are present in the pterygoid. They are placed in the middle of the descending lamina, but also posteriorly, at the posterior edge of the descending lamina (**Figures 5B–E**), as in *Glossotherium* and *Choloepus* (Boscaini et al., 2020). Moreover, some globose and individualized sinuses, similar to those of *Choloepus* (Boscaini et al., 2020), are visible in the basisphenoid, forming a "v-shaped" pneumatizatized area on the cranial base (**Figure 5B**). As in extant sloths (Boscaini et al., 2020), sinuses are lacking in the occipital (**Figure 5**).

Mandible and Dentition

The CT images of the mandible (**Figures 5F,G**) reveal the entire height of the lower teeth and the morphology of the mandibular canal. The left first, second, and fourth molariforms are pushed dorsally far out of their alveoli due to infilling sediment. The strongly hypselodont teeth once penetrated deeply in the mandible, reaching the mandibular canal.

The mandibular canal housed the mandibular division (V_3) of the trigeminal nerve, which exited the skull at the foramen ovale, entering the mandible through the internal aperture of the mandibular canal, located on the medial side of the coronoid process. As in all folivorans (Gaudin, 2004: char. 74), the mandibular canal also presents a posteroexternal opening on the lateral surface of the mandible.

The main branch of the mandibular canal is located ventrally in the dentary, extending medially to the lower dentition (**Figures 5F,G**). The most anterior portion of the mandibular canal diverges into several rami at the level of the mandibular spout, emerging from the numerous mental foramina (**Figures 5F,G**). The development of the mandibular canal and its rami reveal the many neurovascular terminations that occurred in this area.

Brain Endocast and Cranial Nerves

Brain endocast- The brain endocast of *Catonyx tarijensis* MNHN-Bol V 13364 (**Figure 6**) is generally similar to that of other mylodontid sloths and *Choloepus* (Gervais, 1869; Dechaseaux, 1958, 1962a,b, 1971; Boscaini et al., 2020), characterized by prominent olfactory bulbs, a globose telencephalon and mediolaterally expanded cerebellar hemispheres.

In dorsal view (**Figure 6A**), the olfactory bulbs of *Catonyx* are mediolaterally wide, as in *Glossotherium* and *Choloepus* (Boscaini et al., 2020). In MNHN-Bol V 13364, the olfactory bulbs are particularly protruded anteroposteriorly, and are connected to the telencephalon by two divergent olfactory peduncles (**Figure 6**). The olfactory bulbs are also dorsally directed in lateral view (**Figure 6C**) and appear elliptical in shape in anterior view (**Figure 6D**).

Compared to *Megatherium*, *Glossotherium*, and *Lestodon* (Dechaseaux, 1958, 1962a,b, 1971; Boscaini et al., 2020), the cerebrum of *Catonyx* is less domed in lateral view (**Figure 6C**). It is similar to *Choloepus* in this respect (Boscaini et al., 2020). In the same view, the telencephalon of *Catonyx* appears anteroposteriorly elongated, with prominent convolutions that are well-preserved on the left hemisphere. This convolution pattern consists of orbital, olfactory, suprasylvian, ectosylvian, and occipital gyri bordered by shallow furrows represented by the lateral, presylvian, suprasylvian, and pseudosylvian sulci, as well as by the rhinal and the transverse fissures (**Figure 6C**). The pyriform lobe is less developed than its homologue in *Glossotherium* (Boscaini et al., 2020), where it appears as a prominent bulge. In dorsal view (**Figure 6A**), the longitudinal fissure is barely visible on the anterior and posterior edges of the cerebrum, appreciable as slight surface inflections, whereas it is completely missing along its middle part. A weakly marked longitudinal fissure is also present in *Scelidotherium* (Gervais, 1869) and *Choloepus* (Boscaini et al., 2020) and differs from that in *Bradypus*, *Megatherium*, *Mylodon*, *Lestodon*, and *Glossotherium* (Gervais, 1869; Dechaseaux, 1958, 1962a,b, 1971; Boscaini et al., 2020), in which it is more marked and wider, particularly between the frontal lobes. Dorsally, both the frontal and temporal lobes are laterally expanded, crossed by wide gyri separated by slightly marked sulci. In dorsal view (**Figure 6A**), the lateral, suprasylvian, and occipital gyri, as well as the lateral and the entolateral sulci, are observable (**Figure 6A**). The general pattern of convolutions in *C. tarijensis* is comparable to that reported for *Glossotherium* and *Choloepus* (Dechaseaux, 1971; Boscaini et al., 2020).

More posteriorly, the cerebellum is mediolaterally expanded and separated from the cerebrum by a marked transverse fissure. As in *Lestodon*, *Mylodon*, *Scelidotherium*, *Megatherium*, *Choloepus* and *Glossotherium* (Gervais, 1869; Dechaseaux, 1958, 1962a,b, 1971; Boscaini et al., 2020), the cerebellar hemispheres are mediolaterally expanded and separated by a well-developed vermis (**Figure 6A**). In *Catonyx*, the strong development of the vermis and the marked transverse fissure are also particularly clear in lateral view (**Figure 6C**). As in *Glossotherium*, and in contrast to *Megatherium*, *Scelidotherium* and the extant sloths (Gervais, 1869; Dechaseaux, 1958, 1962a,b, 1971; Boscaini et al., 2020), the cerebellum appears wider mediolaterally in dorsal view than the posterior portion of the cerebrum (**Figure 6A**). However, when compared with *Glossotherium* (Boscaini et al., 2020), *Catonyx* shows a more anteroposteriorly compressed cerebellum (**Figure 6C**), similar to the condition observed in *Choloepus* (Boscaini et al., 2020).

Cranial nerves- Neither the ramifications of the olfactory nerves (I) nor the canals for the optic nerves (II) are preserved

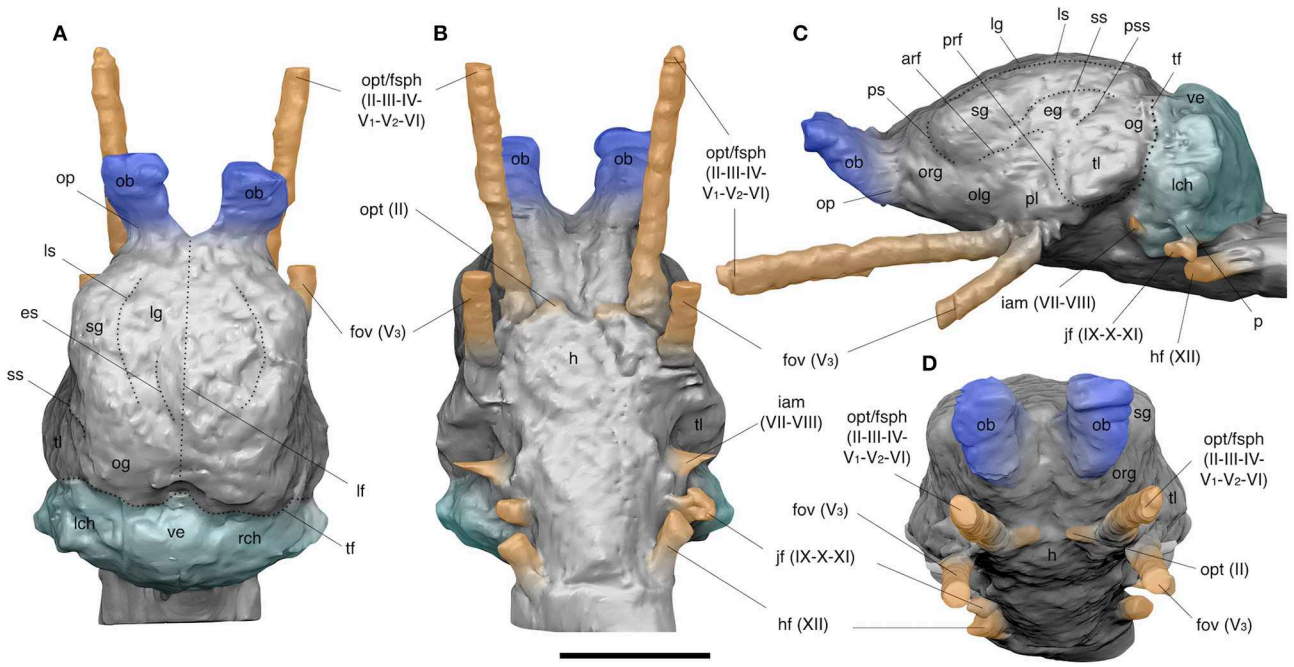

FIGURE 6 | Digital reconstructions of the brain cavity of *Catonyx tarijensis* MNHN-Bol V 13364 from the Pleistocene of Oruro (Bolivian Altiplano) in dorsal **(A)**, ventral **(B)**, lateral **(C)**, and anterior **(D)** views. arf, anterior rhinal fissure; eg, ectosylvian gyrus; es, entolateral sulcus; fov, foramen ovale groove; h, hypophysis; hf, hypoglossal foramen groove; iam, internal acoustic meatus; jf, jugular foramen groove; lch, left cerebellar hemisphere; lf, longitudinal fissure; lg, lateral gyrus; ls, lateral sulcus; ob, olfactory bulb; og, occipital gyrus; olg, olfactory gyrus; op, olfactory peduncle; opt, optic nerve; opt/fsph, common groove for the optic foramen and sphenorbital fissure; org, orbital gyrus; p, parafloccullus; pl, pyriform lobe; prf, posterior rhinal fissure; ps, presylvian sulcus; pss, pseudosylvian sulcus; rch, right cerebellar hemisphere; sg, suprasylvian gyrus; ss, suprasylvian sulcus; tf, transverse fissure; tl, temporal lobe; ve, vermis. Colors indicate: gray, cerebrum; blue, olfactory bulbs; turquoise, cerebellum; orange, neurovascular connections. Roman numeral designations indicate cranial nerves. Scale bar equals 5 cm.

in MNHN-Bol V 13364 (**Figure 6**). However, the impression of the optic chiasma itself is preserved, and it is likely that the optic nerve traveled some distance forward to merge with the sphenorbital fissure as in other mylodontids (Dechaseaux, 1971; Boscaini et al., 2020). In ventral view (**Figure 6B**), the common groove for the optic foramen and the sphenorbital fissure (accommodating cranial nerves II, III, IV, V_1, V_2, and VI), as well as that for the foramen ovale (housing V3, the mandibular branch of the trigeminal nerve), are the largest and most extended neurovascular canals in *Catonyx*. These openings are located at the level of the anteriormost portion of the brain (**Figures 6B–D**) and are more widely separated at their base than is the case in *Glossotherium*, in which the foramina converge at their origin (Boscaini et al., 2020). In lateral view, the sphenorbital fissure and the foramen ovale project forward strongly, forming an angle of about 30° to one another (**Figure 6C**). The internal acoustic meatus appears as a small bump located under the cerebellar hemispheres, close to the well-developed jugular and hypoglossal foramina (**Figure 6C**). The internal acoustic meatus is wider at its base and relatively larger than that of *Glossotherium* (Boscaini et al., 2020). In *Catonyx tarijensis* MNHN-Bol V 13364, the jugular and hypoglossal canals are similar in shape and close to each other (**Figures 6B–D**), whereas in *Glossotherium robustum* the hypoglossal is relatively larger and originates farther posteriorly (Boscaini et al., 2020). This is also reflected in the external cranial anatomy of *Catonyx* (see preceding section), and a similar condition was also observed in *Scelidotherium* (Gaudin, 2004; char. 187). In contrast, the hypoglossal foramen is larger than the jugular in *Mylodon* and *Glossotherium* (Patterson et al., 1992; Boscaini et al., 2018a).

DISCUSSION

The Pleistocene scelidotheriine sloth *Catonyx tarijensis* (Gervais and Ameghino, 1880) was first described on the basis of fossil remains recovered in the Tarija Valley (southern Bolivia). This locality is therefore the type locality of *C. tarijensis*, but it also represents the site that has provided the greatest number of skeletal remains for this species (Miño-Boilini, 2012). After the original description, many other remains referable to *C. tarijensis* were recovered in Argentina and Uruguay, extending its paleobiogeographic distribution to more southern latitudes in South America (McDonald and Perea, 2002; Corona et al., 2013; Miño-Boilini, 2016). The remains reported here represent the first record of this species from latitudes north of its type locality. They extend the geographic distribution of this taxon northward (**Figure 1**) and also expand the spectrum of paleoenvironments in which *C. tarijensis* could survive. Paleoenvironmental reconstructions of the Pleistocene of Tarija suggest the presence of open-county grasslands, with rivers and lakes surrounded by shrubs and scattered trees (Yoshida and Yamazaki, 1982; Coltorti et al., 2010; MacFadden et al., 2013).

The Bolivian Altiplano is distinguished by its higher altitude, but also its colder temperatures and dryer conditions relative to those recorded for the Tarija Valley. During the late Pleistocene, the Altiplano was characterized by periods of extreme dryness and shrinking bodies of water (Chepstow-Lusty et al., 2005; Coltorti et al., 2010). The recovery of *C. tarijensis* in the late Pleistocene of the Bolivian Altiplano suggests that this species could have been able to survive under a broad spectrum of paleoecological conditions.

The exceptional preservation of the skull of MNHN-Bol V 13364, together with its subadult ontogenetic stage, offer the opportunity for detailed observation of its external and internal anatomy, and to characterize some anatomical areas previously unknown for *Catonyx tarijensis*. The subadult age of MNHN-Bol V 13364 is indicated by the presence of many sutural contacts and the poorly developed temporal ridges and sagittal crest, as well as other features detected in the ear region, such as the narrow gap between the entotympanic and the basioccipital/basisphenoid tuber, the unusually deep stylohyal fossa, the presence of an open groove for the occipital artery on the paraoccipital process of the petrosal, and the reduced anteroventral process of the tegmen tympani (**Figures 2**, **3**). The presence of clear sutures in this skull has allowed us to observe the distinct outlines of many of the cranial bones for the first time, and have revealed at least one noteworthy, unusual feature, the small lateral exposure of the orbitosphenoid posterior to the aperture for the optic foramen/sphenorbital fissure (**Figure 2**). Another probable ontogeny-related feature is the occurrence of the lacrimal-nasal contact, which is absent in MNHN-Bol V 13364 (**Figure 2**), but figured as present in an adult *C. tarijensis* specimen by McDonald (1987). This feature was observed as variably present in *Scelidotherium leptocephalum* (Kraglievich, 1923) but its presence was later considered a synapomorphy of Scelidotheriinae by Gaudin (2004).

Other anatomical regions, such as the nasopharyngeal roof, the orbital foramina, and the hyoid apparatus are described in *Catonyx* for first time (**Figures 2**, **4**). Among these, the hyoid apparatus has been considered indicative of lingual anatomy and function, providing valuable information on the procurement and processing of dietary items in the oral cavity (Pérez et al., 2000, 2010). Although Pleistocene mylodontids were generally supposed to have had strong tongues, Pérez et al. (2010) suggested that *Scelidotherium* had significantly reduced lingual protrusion, when compared with the mylodontine *Glossotherium*. This was inferred mainly from the robust and barely mobile hyoid elements of *Scelidotherium*, which differ from the less rigidly articulated apparatus of *Glossotherium*. As a result, browsing species such as *S. leptocephalum* possessed long skulls and mandibular symphyses, and likely had strong prehensile lips but reduced lingual protrusion. In contrast, grazing species like *G. robustum* were characterized by shorter and broader skulls and mandibles, associated with reduced lips and increased lingual protrusion (Bargo et al., 2006; Bargo and Vizcaíno, 2008; Pérez et al., 2010). On the one hand, the hyoid apparatus of *Catonyx tarijensis* (**Figure 4**) bears a strong resemblance to that of *S. leptocephalum* (Pérez et al., 2010), further demonstrating that the morphology of the hyoid elements is phylogenetically informative (e.g., Gaudin, 2004; Casali and Perini, 2017; Zamorano, 2019). On the other hand, the strong similarity in the morphology of the hyoid apparatus among scelidotheriine sloths suggests similar feeding behaviors, characterized by limited lingual protrusion, with prehensile upper lips compensating for the less mobile tongue. Pérez et al. (2010) and Bargo et al. (2006) proposed that in narrow-muzzled sloths such as *Scelidotherium* and *Megatherium,* the upper lip was prehensile and used to select the plants. However, extinct sloths generally show a large mandibular canal, several foramina connected to the mandibular canal through multiple rami, including multiple mental foramina, as well as a wide posterior external opening of the mandibular canal, suggesting that the whole mandible was probably well-innervated and vascularized, especially in its anteriormost part (**Figure 5**). Accordingly, it is plausible that the lower lip also had greater mobility, contributing to better sensitivity and greater control of their grip on browse (**Figure 7**).

Strong bite movements concentrated in the mandible are also in accordance with the presence in MNHN-Bol V 13364 of two facets for the articulation of the mandible with cranial glenoid fossae (**Figure 2**). Moreover, the well-developed muscle scars in the ventral margin of the dentary are indicative of marked masticatory strength.

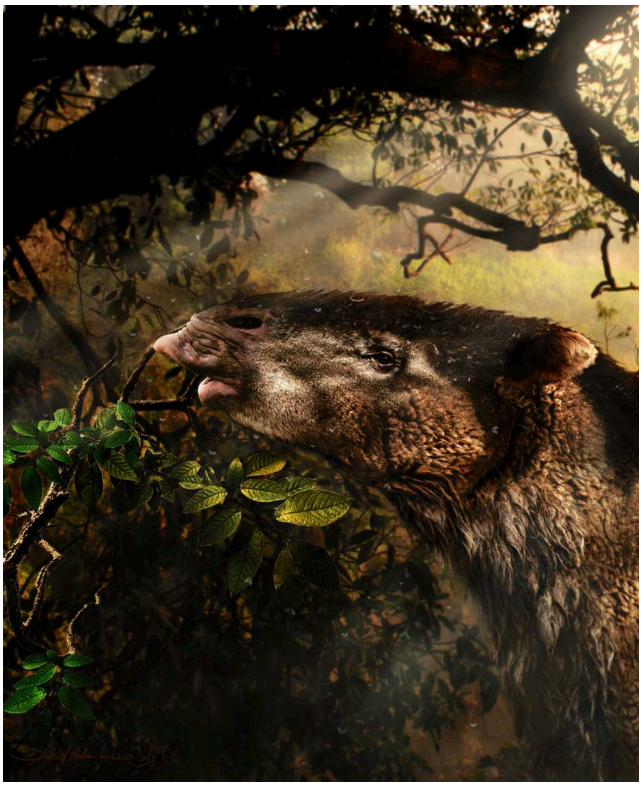

FIGURE 7 | Hypothetical life reconstruction of *Catonyx tarijensis* showing its inferred feeding behavior. The reconstruction is based on the skull MNHN-Bol V 13364 from the Pleistocene of Oruro (Bolivian Altiplano). Artwork by D. A. Iurino.

The digital model of the brain cavity of *Catonyx tarijensis* MNHN-Bol V 13364 (**Figure 6**) is extremely similar to that of *Glossotherium robustum* and *Choloepus hoffmanni* (Boscaini et al., 2020) and other giant extinct mylodontid sloths (Gervais, 1869; Dechaseaux, 1958, 1962a,b, 1971). In lateral view, only minor differences are observable between *C. tarijensis* and *G. robustum* in the shape of the olfactory bulbs, cerebral hemispheres, and cerebellum (Boscaini et al., 2020). Moreover, the pattern of sulci and gyri is extremely similar among extinct mylodontids sloths and the extant two-toed sloths (Boscaini et al., 2020). Although *Catonyx* and *Scelidotherium* show a weakly marked longitudinal fissure in comparison to other Mylodontidae, the general pattern of convolutions is similar to that in other members of the clade (Gervais, 1869; Dechaseaux, 1958, 1962a,b, 1971; Boscaini et al., 2018b, 2020). In general, the similar shape of the brain cavity and the shared pattern of convolutions among extinct mylodontid sloths and the living two-toed sloths, as well as the similar development of cranial sinuses in *Cholopeus* and the scelidotheriines (see below), is noteworthy. Indeed, recent molecular-based phylogenetic studies (i.e., Delsuc et al., 2019; Presslee et al., 2019) recovered the two-toed sloths as living representatives of Mylodontidae. Further CT-scanning data on other mylodontids and Antillean taxa is required to test this hypothesis, but the present study reveals the importance of accounting for novel morphological information from previously unexplored sources.

It should also be noted that there are also endocranial features which lack phylogenetic consistency among mylodontid sloths. Differences are evident in the pattern by which cranial nerves leave the brain cavity. As in *Glossotherium robustum*, but unlike extant sloths, *Catonyx tarijensis* possesses grooves for the optic foramen/sphenorbital fissure, the foramen ovale, and the hypoglossal foramen that are enlarged relative to other foramina transmitting cranial nerves (**Figure 6**; Boscaini et al., 2020). This suggests a greater development of the trigeminal and hypoglossal nerves, compared to other cranial nerves. However, in *C. tarijensis*, this relative difference in the size of cranial nerve grooves is not as marked as in *G. robustum*. This is particularly true for the groove for the hypoglossal nerve (XII), which is the only nerve leaving the skull from the hypoglossal foramen. In *Catonyx tarijensis* the hypoglossal foramen is roughly equivalent in size to the jugular foramen (**Figures 2**, **6**), whereas in *G. robustum* the hypoglossal foramen is larger (Boscaini et al., 2018a, 2020). The hypoglossal nerve, which innervates the glossal musculature, controls most of the intrinsic and extrinsic lingual musculature (Evans and de Lahunta, 2013). Together with evidence from the hyoid apparatus discussed above, this morphology can be viewed as further indirect evidence of more limited lingual protrusion of *C. tarijensis* in comparison to *G. robustum*.

Other differences between *Catonyx* and *Glossotherium* are noted in the morphology of their cranial sinuses. In general, cranial pneumatization is markedly reduced in the posteriormost portion of the skull of *C. tarijensis*, relative to that observed in *G. robustum* (Boscaini et al., 2020). As in *Choloepus* (Boscaini et al., 2020), the sinuses of *Catonyx* become smaller and more separate from one another at the frontoparietal suture, and are absent in the more posterior parts of the braincase (**Figure 5**). Preliminary observations suggest that this morphology is present in other Scelidotheriinae (Boscaini et al., 2018b), emphasizing the possible phylogenetic value of cranial pneumatization anatomy. In fact, for other large mammalian herbivores, the extent of cranial sinuses varies at the interspecific level according to both phylogeny and general body size (Farke, 2010). New body size estimations for mylodontid sloths (Boscaini et al., 2019b) predicted a larger body mass for *C. tarijensis* (∼1,640 kg) than *G. robustum* (∼1,480 kg), suggesting that among both xenarthrans and bovids (Farke, 2010), sinus organization could be driven primarily by phylogeny, and only secondarily related to general body mass.

However, the presence of functional or developmental constraints for explaining this alternative morphology cannot currently be refuted. Scelidotheriines have narrower heads than mylodontines and so may not have required as much pneumatization to reduce the weight of the head. However, it is also true that sinuses in sloths are more frequently present in the middle cranial region, extending posteriorly only in some cases (Boscaini et al., 2020), suggesting that this feature could be ontogeny-related. Thus, the question of the relative contributions of phylogeny and function to the pneumatic patterns observed in extinct sloths is clearly one that will require further study.

CONCLUSIONS

We report novel data on the external and internal cranial anatomy of the scelidotheriine sloth *Catonyx tarijensis*, further extending knowledge on the cranial morphology of South American extinct sloths. This discovery, from late Pleistocene deposits of the Department of Oruro (southwestern Bolivia), allowed us to extend the paleobiogeographic range of *C. tarijensis* to more northern latitudes, as well as to the high altitudes of the Bolivian Altiplano.

The specimen described in the present study, a particularly well-preserved skull with associated mandible and hyoid apparatus, corresponds to a subadult individual of *Catonyx tarijensis*. Combined information from the external and the internal anatomy, obtained through CT-scanning followed by digital modeling techniques, allowed us to analyze several anatomical regions that were unknown for this taxon.

Among these, the ear region, the nasopharyngeal area and the hyoid elements revealed several phylogenetically and functionally informative features. Digital models permitted observations of the brain cavity, neurovascular grooves and cranial sinuses, and comparisons of these features with other Pleistocene mylodontids.

The information presented in this report confirms previous hypotheses on inferred modes of food intake among extinct scelidotheriine sloths. According to the data now available, *C. tarijensis* was likely a browsing species, which tore vegetation mainly using its strong lips, rather than the tongue. This habit was probably common among Scelidotheriinae and contrasts with

that present in its sister clade, Mylodontinae, whose members were predominantly grazing species with smaller lips and more strongly protruding tongues.

The present study represents a further step in assembling broader morphological comparisons of digital endocranial models among extinct sloths, and emphasizes the importance of applying these new methodologies for understanding the evolution of this mammalian group.

DATA AVAILABILITY STATEMENT

All datasets generated for this study are included in the article/supplementary material.

AUTHOR CONTRIBUTIONS

AB, TG, DI, and FP conceived the paper. BM and RA collected and prepared the fossil specimen. DI and RS reconstructed the digital models. AB, TG, and DI wrote the paper with input from all authors. All authors contributed to the final version of the manuscript.

FUNDING

This research was funded by the National Geographic Society (projects NGS 9971-16 and EC-44712R-18). We are also particularly indebted to the MAECI (Ministry of Foreign Affairs and International Cooperation, Italy) for funding that greatly facilitated scientific collaboration between CONICET (Argentina) and Sapienza, Università di Roma (Italy), as well as funding from several sources at the University of Tennessee at Chattanooga.

ACKNOWLEDGMENTS

We are grateful to the Clínica Alemana Institute (La Paz, Bolivia) and the PaleoFactory Lab (Sapienza Università di Roma, Italy) for access to CT-scanning and digital modeling facilities. This research was made possible thanks to the cooperation agreement between the Bolivian institutions: GADOR (Gobernación Autónoma del Departamento de Oruro), GAM (Gobierno Autónomo Municipal) of Santiago de Andamarca, and MNHN-Bol. This paper greatly benefited from thoughtful comments and accurate revisions by three reviewers.

REFERENCES

Ameghino, F. (1891). Mamíferos y aves fósiles argentinas. Especies nuevas, adiciones y correcciones. *Rev. Argent. Hist. Nat.* 1, 240–259.

Ameghino, F. (1904). Nuevas especies de mamíferos cretáceos y terciarios de la república argentina. *An. Soc. Cient. Arg.* 58, 225–291.

Amson, E., Carrillo, J. D., and Jaramillo, C. (2016). Neogene sloth assemblages (Mammalia, *Pilosa*) of the cocinetas basin (La Guajira, Colombia): implications for the great American biotic interchange. *Palaeontology* 59, 563–582. doi: 10.1111/pala.12244

Bargo, M., Toledo, N., and Vizcaíno, S. F. (2006). Muzzle of South American Pleistocene ground sloths (*Xenarthra*, *Tardigrada*). *J. Morphol.* 267, 248–263. doi: 10.1002/jmor.10399

Bargo, M. S., and Vizcaíno, S. F. (2008). Paleobiology of pleistocene ground sloths (*Xenarthra*, *Tardigrada*): biomechanics, morphogeometry and ecomorphology applied to the masticatory apparatus. *Ameghiniana* 45, 175–196.

Boscaini, A., Iurino, D. A., Billet, G., Hautier, L., Sardella, R., Tirao, G., et al. (2018a). Phylogenetic and functional implications of the ear region anatomy of *Glossotherium robustum* (*Xenarthra*, *Mylodontidae*) from the Late Pleistocene of argentina. *Sci. Nat.* 105:28. doi: 10.1007/s00114-018-1548-y

Boscaini, A., Iurino, D. A., Cartelle, C., Strauss, A., De Iuliis, G., Sardella, R., et al. (2018b). "Digital endocranial reconstructions of the extinct scelidothere sloths (*Xenarthra*, *Mylodontidae*): emerging patterns in folivorans' evolution. IPC5," in *Abstract Book of the 5th International Palaeontological Congress* (Paris), 392.

Boscaini, A., Iurino, D. A., Sardella, R., Tirao, G., Gaudin, T. J., and Pujos, F. (2020). Digital cranial endocasts of the extinct sloth glossotherium robustum (*Xenarthra*, *Mylodontidae*) from the late pleistocene of argentina: description and comparison with the extant sloths. *J. Mammal. Evol.* 27, 55–71. doi: 10.1007/s10914-018-9441-1

Boscaini, A., Pujos, F., and Gaudin, T. J. (2019a). A reappraisal of the phylogeny of *Mylodontidae* (*Mammalia*, *Xenarthra*) and the divergence of mylodontine and lestodontine sloths. *Zool. Scr.* 48, 691–710. doi: 10.1111/zsc.12376

Boscaini, A., Toledo, N., Soto, I. M., Gaudin, T. J., and Pujos, F. (2019b). "Filogenia y evolución del tamaño corporal en perezosos milodóntidos (*Mammalia, Xenarthra, Folivora*)," in *RCAPA 2019. Abstract Book of the "Reunión de Comunicaciones de la Asociación Paleontológica Argentina"* (La Plata), 91.

Brambilla, L., and Ibarra, D. A. (2018). The occipital region of late pleistocene *Mylodontidae* of argentina. *Bol. Inst. Fis. Geol.* 88, 1–9.

Cartelle, C., De Iuliis, G., Boscaini, A., and Pujos, F. (2019). Anatomy, possible sexual dimorphism, and phylogenetic affinities of a new mylodontine sloth from the late Pleistocene of intertropical Brazil. *J. Syst. Palaeontol.* 17, 1957–1988. doi: 10.1080/14772019.2019.1574406

Cartelle, C., De Iuliis, G., and Lopes Ferreira, R. (2009). Systematic revision of tropical Brazilian scelidotheriine sloths (*Xenarthra*, *Mylodontoidea*). *J. Vertebr. Paleontol.* 29, 555–566. doi: 10.1671/039.029.0231

Casali, D. M., and Perini, F. A. (2017). The evolution of hyoid apparatus in *Xenarthra* (*Mammalia*: *Eutheria*). *Hist. Biol.* 29, 777–788. doi: 10.1080/08912963.2016.1241248

Chepstow-Lusty, A., Bush, M. B., Frogley, M. R., Baker, P. A., Fritz, S. C., and Aronson, J. (2005). Vegetation and climate change on the bolivian Altiplano between 108,000 and 18,000 years ago. *Quaternary Res.* 63, 90–98. doi: 10.1016/j.yqres.2004.09.008

Coltorti, M., Abbazzi, L., Ferretti, M. P., Iacumin, P., Ríos, F. P., Pellegrini, M., et al. (2007). Last glacial mammals in South America: a new scenario from the Tarija Basin (Bolivia). *Naturwissenschaften* 94, 288–299. doi: 10.1007/s00114-006-0196-9

Coltorti, M., Pieruccini, P., and Paredes, F. R. (2010). Late pleistocene stratigraphy, sedimentology and paleoenvironmental evolution of the Tarija-Padcaya basin (Bolivian Andes). *P. Geologist. Assoc.* 121, 162–179. doi: 10.1016/j.pgeola.2010.04.002

Cope, E. D. (1889). The edentata of North America. *Am. Nat.* 23, 657–664. doi: 10.1086/274985

Corona, A., Perea, D., and McDonald, H. G. (2013). *Catonyx cuvieri* (*Xenarthra*, *Mylodontidae*, *Scelidotheriinae*) from the late pleistocene of Uruguay, with comments regarding the systematics of the subfamily. *J. Vertebr. Paleontol.* 33, 1214–1225. doi: 10.1080/02724634.2013.764311

Dechaseaux, C. (1958). "Encéphales de xénarthres fossiles," in *Traité de Paléontologie*, ed J. Piveteau (Paris: Masson and Cie), 637–640.

Dechaseaux, C. (1962a). Encéfalos de notongulados y de desdentados xenarthros fósiles. *Ameghiniana* 2, 193–209.

Dechaseaux, C. (1962b). Singularités de l'encéphale de *Lestodon*, mammifère édenté géant du Pléistocène d'Amérique du Sud. *C. R. Acad. Sci.* 254, 1470–1471.

Dechaseaux, C. (1971). *Oreomylodon wegneri*, édenté gravigrade du Pléistocène de l'Équateur - Crâne et moulage endocrânien. *Ann. Paléontol.* 57, 243–285.

Delsuc, F., Catzeflis, F. M., Stanhope, M. J., and Douzery, E. J. (2001). The evolution of armadillos, anteaters and sloths depicted by nuclear and mitochondrial phylogenies: implications for the status of the enigmatic fossil *Eurotamandua*. *Proc. R. Soc. B* 268, 1605–1615. doi: 10.1098/rspb.2001.1702

Delsuc, F., Kuch, M., Gibb, G. C., Karpinski, E., Hackenberger, D., Szpak, P., et al. (2019). Ancient mitogenomes reveal the evolutionary history and biogeography of sloths. *Curr. Biol.* 29, 2031–2042.e6. doi: 10.1016/j.cub.2019.05.043

Evans, H. E., and de Lahunta, A. (2013). *Miller's Anatomy of the Dog*. St. Louis: Elsevier.

Farke, A. A. (2010). Evolution and functional morphology of the frontal sinuses in *Bovidae* (*Mammalia*: Artiodactyla), and implications for the evolution of cranial pneumaticity. *Zool. J. Linn. Soc.* 159, 988–1014. doi: 10.1111/j.1096-3642.2009.00586.x

Flower, W. (1883). On the arrangement of the orders and families of existing *Mammalia*. *Proc. Zool. Soc. Lond.* 1883, 178–186.

Gaudin, T. J. (1995). The ear region of edentates and the phylogeny of the *Tardigrada* (*Mammalia*, *Xenarthra*). *J. Vertebr. Paleontol.* 15, 672–705. doi: 10.1080/02724634.1995.10011255

Gaudin, T. J. (2004). Phylogenetic relationships among sloths (*Mammalia, Xenarthra, Tardigrada*): the craniodental evidence. *Zool. J. Linn. Soc.* 140, 255–305. doi: 10.1111/j.1096-3642.2003.00100.x

Gaudin, T. J. (2011). On the osteology of the auditory region and orbital wall in the extinct West Indian sloth genus *Neocnus* Arredondo, 1961 (*Placentalia*, *Xenarthra*, *Megalonychidae*). *Ann. Carnegie Mus.* 80, 5–28. doi: 10.2992/007.080.0102

Gaudin, T. J., and Croft, D. A. (2015). Paleogene *Xenarthra* and the evolution of South American mammals. *J. Mammal.* 96, 622–634. doi: 10.1093/jmammal/gyv073

Gervais, H., and Ameghino, F. (1880). *Los mamíferos fósiles de la América del Sud*. Paris: F. Savy and Buenos Aires: Hermanos Igon.

Gervais, P. (1869). Mémoire sur les formes cérébrales propres aux édentés vivants et fossiles. *Nouv. Arch. Mus. Hist. Nat. Paris* 5, 1–56.

Gill, T. (1872). Arrangement of the families of mammals, with analytical tables. *Smithson. Misc. Collect.* 11, 1–98.

Hirschfeld, S. E. (1985). Ground sloths form the friasian la venta fauna, with additions to the pre-friasian coyaima fauna of Colombia, South America. *Univ. Calif. Publ. Geol. Sci.* 128, 1–91.

Kraglievich, L. (1923). Descripción comparada de los cráneos de "*Scelidodon Rothi*" Amegh. y "*Scelidotherium Parodii*" n. sp. procedentes del horizonte "Chapadmalense." *Anales Mus. Nac. Hist. Nat. Buenos Aires* 33, 57–103.

MacFadden, B. J., Zeitler, P. K., Anaya, F., and Cottle, J. M. (2013). Middle pleistocene age of the fossiliferous sedimentary sequence from Tarija, Bolivia. *Quarter. Res.* 79, 268–273. doi: 10.1016/j.yqres.2012.12.009

McDonald, H. G. (1987). A systematic review of the plio-pleistocene scelidotherine ground sloth (*Mammalia: Xenarthra: Mylodontidae*) (Ph.D. Dissertation). University of Toronto, Toronto, ON, Canada.

McDonald, H. G. (1997). "Xenarthrans: pilosans," in *Vertebrate Paleontology in the Neotropics. The Miocene Fauna of La Venta, Colombia*, eds. R. F. Kay, R. H. Madden, R. L. Cifelli, and J. J. Flynn (Washington and London: Smithsonian Institution Press), 233–245.

McDonald, H. G. (2005). Paleoecology of extinct xenarthrans and the great biotic interchange. *Bull. Fla. Mus. Nat. Hist.* 45, 319–340.

McDonald, H. G., and De Iuliis, G. (2008). "Fossil history of sloths," in *The Biology of the Xenarthra*, eds *S. F. Vizcaíno and W. J. Loughry* (Gainesville, FL: University Press of Florida), 39–55.

McDonald, H. G., and Pelikan, S. (2006). Mammoths and mylodonts: exotic species from two different continents in North American pleistocene faunas. *Quatern. Int.* 142–143, 229–241. doi: 10.1016/j.quaint.2005.03.020

McDonald, H. G., and Perea, D. (2002). The large scelidothere *Catonyx tarijensis* (*Xenarthra, Mylodontidae*) from the Pleistocene of Uruguay. *J. Vertebr. Paleontol.* 22, 677–683. doi: 10.1671/0272-4634(2002)022<0677:TLSCTX>2.0.CO;2

McNab, B. K. (1985). "Energetics, population biology, and distribution of Xenarthrans, living and extinct," in *The Evolution and Ecology of Armadillos, Sloths and Vermilinguas,* ed G. G. Montgomery (Washington, DC: Smithsonian Institution Press), 219–232.

Miño-Boilini, Á. R. (2012). *Sistemática y Evolución de los Scelidotheriinae (Xenarthra, Mylodontidae) Cuaternarios de la Argentina. Importancia Bioestratigráfica, Paleobiogeográfica y Paleoambiental* (Ph.D. Dissertation), Universidad de La Plata, La Plata, Argentina.

Miño-Boilini, Á. R. (2016). Additions to the knowledge of the ground sloth *Catonyx tarijensis* (*Xenarthra*, *Pilosa*) in the pleistocene of argentina. *Paläontol. Z.* 90, 173–183. doi: 10.1007/s12542-015-0280-6

Miño-Boilini, Á. R., De Los Reyes, M., Zurita, A. E., Arrouy, M. J., and Poiré, D. G. (2019). Pliocene scelidotheriinae (*Xenarthra, Tardigrada*) from the pampean region of argentina: morphology, chronology, and comments on the diversity of the subfamily. *C. R. Palevol,* 18, 325–334. doi: 10.1016/j.crpv.2019.01.005

Naples, V. L. (1986). The morphology and function of the hyoid region in the tree sloths, *Bradypus* and *Choloepus*. *J. Mammal.* 67, 712–724. doi: 10.2307/1381132

Nowak, R. M. (1999). *Walker's Mammals of the World*. Baltimore; London: The John Hopkins University Press.

Owen, R. (1839). "Fossil Mammalia," in *The Zoology of the Voyage of H.M.S. Beagle, Under the Command of Captain Fitzroy, During the Years 1832 to 1836*, ed C. Darwin (London: Smith, Elder & Co.), 41–80.

Owen, R. (1857). On the scelidothere (*Scelidotherium leptocephalum*, Owen). *Philos. Trans. R. Soc. Lond.* 147, 101–110. doi: 10.1098/rstl.1857.0008

Patterson, B., Turnbull, W. D., Segall, W., and Gaudin, T. J. (1992). The ear region in xenarthrans (=Edentata: *Mammalia*). Part II. Pilosa (sloths, anteaters), palaeanodonts, and a miscellany. *Fieldiana Geol.* 24, 1–78. doi: 10.5962/bhl.title.3466

Pérez, L. M., Scillato-Yané, G. J., and Vizcaíno, C. F. (2000). Estudio morfofuncional del aparato hioideo de *Glyptodon* cf. *clavipes* Owen (*Cingulata*: *Glyptodontidae*). *Ameghiniana* 37, 293–300.

Pérez, L. M., Toledo, N., De Iuliis, G., Bargo, M. S., and Vizcaíno, S. F. (2010). Morphology and function of the hyoid apparatus of fossil xenarthrans (*Mammalia*). *J. Morphol.* 271, 1119–1133. doi: 10.1002/jmor.10859

Placzek, C., Quade, J., and Patchett, P. J. (2006). Geochronology and stratigraphy of late pleistocene lake cycles on the southern bolivian altiplano: implications for causes of tropical climate change. *GSA Bull.* 118, 515–532. doi: 10.1130/B25770.1

Presslee, S., Slater, G. J., Pujos, F., Forasiepi, A. M., Fischer, R., Molloy, K., et al. (2019). Palaeoproteomics resolves sloth relationships. *Nat. Ecol. Evol.* 3, 1121–1130. doi: 10.1038/s41559-019-0909-z

Pujos, F. (2000). *Scelidodon chiliensis* (*Xenarthra, Mammalia*) du Pléistocène terminal de "Pampa de los Fósiles". *Quaternaire* 11, 197–206. doi: 10.3406/quate.2000.1669

Pujos, F., Gaudin, T. J., De Iuliis, G., and Cartelle, C. (2012). Recent advances on variability, morpho-functional adaptations, dental terminology, and evolution of sloths. *J. Mammal. Evol.* 19, 159–169. doi: 10.1007/s10914-012-9189-y

Robertson, J. S. (1976). Latest Pliocene mammals from Haile XV A, Alachua County, Florida. *Bull. Fla. Mus. Nat. Hist.* 20, 111–186.

Scillato-Yané, G. J., and Carlini, A. A. (1998). Nuevos xenarthra del friasense (Mioceno medio) de Argentina. *Stvd. Geol. Salmant.* 34, 43–67.

Steadman, D. W., Martin, P. S., MacPhee, R. D. E., Jull, A. J. T., McDonald, H. G., Woods, C. A., et al. (2005). Asynchronous extinction of late quaternary sloths on continents and islands. *Proc. Natl. Acad. Sci. U.S.A.* 102, 11763–11768. doi: 10.1073/pnas.0502777102

Stock, C. (1925). Cenozoic gravigrade edentates of Western North America with special reference to the pleistocene megalonychinae and mylodontidae of Rancho La Brea. *Carnegie Inst. Wash. Publ.* 331, 1–206.

Tambusso, P. S., McDonald, H. G., and Fariña, R. A. (2015). Description of the stylohyal bone of a giant sloth (*Lestodon armatus*). *Palaeontol. Electron.* 18, 1–10. doi: 10.26879/506

Vizcaíno, S. F., Zárate, M., Bargo, M. S., and Dondas, A. (2001). Pleistocene burrows in the Mar del Plata area (Argentina) and their probable builders. *Acta Palaeontol. Pol.* 46, 289–301.

Webb, S. D. (1989). "Osteology and relationships of thinobadistes segnis, the first mylodont sloth in North America," in *Advances in Neotropical Mammalogy*, eds K. H. Redford and J.F. Eisenberg (Gainesville, FL: Sandhill Crane Press), 469–532.

Yoshida, A., and Yamazaki, E. (1982). "Micro-fossils," in *Tarija mammal-bearing formation in Bolivia*, ed F. *Takai* (Tokyo: Research Institute of Evolutionary Biology), 57–62.

Zamorano, M. (2019). Análisis filogenético de xenartros (*Mammalia*) basados en elementos óseos del aparato hioides: aspectos sobre la monofilia de gliptodóntidos. *Rev. Bras. Paleontolog.* 22, 53–66. doi: 10.4072/rbp.2019.1.05

Conflict of Interest: The authors declare that the research was conducted in the absence of any commercial or financial relationships that could be construed as a potential conflict of interest.

The reviewer GD, declared a past collaboration with the authors to the handling editor.

frontiers in Earth Science

ORIGINAL RESEARCH
published: 09 April 2020
doi: 10.3389/feart.2020.00094

Braincase With Natural Endocast of a Juvenile Rhinocerotinae From the Late Middle Pleistocene Site of Melpignano (Apulia, Southern Italy)

Dawid A. Iurino[1], Jacopo Conti[1], Beniamino Mecozzi[1,2] and Raffaele Sardella[1,2]*

[1] PaleoFactory, Laboratory, Department of Earth Sciences, Sapienza University of Rome, Rome, Italy, [2] Department of Earth Sciences, Sapienza University of Rome, Rome, Italy

Cranial remains of juvenile fossil rhinoceroses are rarely described in literature and very few is known about the ontogenetic development of their inner anatomy. In this study, we report the first CT based description of a juvenile braincase and its natural brain endocast of a late Middle Pleistocene Rhinocerotinae from Melpignano (Apulia, Italy). The specimen belongs to an individual about 12–18 months old, representing to date the youngest Pleistocene rhinoceros of Mediterranean Europe documented by neurocranial material. Through digital visualization methods the neurocranium has been restored and the anatomy of both the brain and the paranasal sinuses has been obtained and compared with those of juvenile and adult Pleistocene rhinoceroses. We evidence a different morphological development of the inner cranial anatomy in fossil and extant African species.

Keywords: perissodactyla, paleoneurology, computed tomography (CT), virtual paleontology, digital cranial endocasts, paranasal sinuses

OPEN ACCESS

Edited by:
Luca Pandolfi,
University of Florence, Italy

Reviewed by:
Esperanza Cerdeño,
CONICET Mendoza, Argentina
Maeva J. Orliac,
UMR5554 Institut des Sciences de l'Evolution de Montpellier (ISEM), France

****Correspondence:***
Dawid A. Iurino
dawid.iurino@uniroma1.it

Specialty section:
This article was submitted to Paleontology, a section of the journal Frontiers in Earth Science

Received: *10 December 2019*
Accepted: *17 March 2020*
Published: *09 April 2020*

Citation:
Iurino DA, Conti J, Mecozzi B and Sardella R (2020) Braincase With Natural Endocast of a Juvenile Rhinocerotinae From the Late Middle Pleistocene Site of Melpignano (Apulia, Southern Italy). Front. Earth Sci. 8:94. doi: 10.3389/feart.2020.00094

INTRODUCTION

During the Middle-Late Pleistocene, rhinoceroses were among the largest terrestrial mammals in European ecosystems together with proboscideans and hippopotamuses. They were represented by several taxa with different anatomical and ecological features, adapted to multiple environments from tropical scrublands and grasslands (Guérin, 1980) to cold glacial tundra (Deng et al., 2011; Boeskorov, 2012; Schreve et al., 2013). The finding in17th century at Klagenfurt (Austria) of a woolly rhino *Coelodonta antiquitatis* (Blumenbach, 1799) skull was interpreted as a dragon and a six-tone statue of this legendary animal became the symbol of the Austrian town (Witton, 2018). By the start of 1800, fossils rhinoceroses have been recovered in Eurasia, Africa and America (Stuart, 1991; Lacombat, 2006; Markova et al., 2013; Faith, 2014), their taxonomy and phylogeny has been studied by several authors (Prothero et al., 1986; Cerdeño, 1995; Tong and Moigne, 2000; Antoine, 2003; Antoine et al., 2003; Piras et al., 2010; Deng et al., 2011; Steiner and Ryder, 2011; Welker et al., 2017; Cappellini et al., 2019) and even direct evidence of human interactions with the Late Pleistocene woolly rhinoceroses have been documented by cut marks

and cave paintings (Bello et al., 2009; Boeskorov, 2012; Chen and Moigne, 2018). Although some exceptionally preserved specimens are known (Voorhies and Stover, 1978; Voorhies, 1985; Protopopov et al., 2015), the Pleistocene fossil record of the European rhinoceroses is less abundant compared to those of other megaherbivores, and especially juveniles are scarce and their skull remains are rarely described in literature (Prothero, 2005; Shpansky, 2014). Therefore, taxonomic and ontogenetic studies are mostly focused on teeth, being more frequently recorded and of high diagnostic value (Garutt, 1994; Shpansky and Billia, 2006; Álvarez-Lao and García, 2011; Böhmer et al., 2016). To date, the number of juvenile specimens documented by partial or complete skulls is very low and mostly represented by Miocene taxa (**Table 1**). The only CT based study on a fossil Rhinocerotinae has been performed on "Sasha," a mummified calf of *C. antiquitatis* from the Semyulyakh River in Abyi District of Yakutia Republic (Russia) (Protopopov et al., 2015). Surprisingly, also the skull anatomy of the extant species has been scarcely investigated and very few studies on this topic have been reported (Bordoloi and Kalita, 1996; Borthakur and Bordoloi, 1997), especially those with x-ray techniques (Hieronymus et al., 2006; Gerard et al., 2018). Probably due to technical difficulties in performing CT scans on bulk and large skulls with conventional medical equipment. Consequently, many developmental and morpho-functional aspects of the skull pneumatization and the brain morphology are still almost completely unknown in extinct and extant rhinoceroses (Garrod, 1878; Bhagwandin et al., 2017). The most comprehensive ontogenetic studies on fossil Rhinocerotinae, based on external craniodental features, were conducted on *Chilotherium wimani* with nine complete skulls from the Late Miocene of China (Deng, 2001b), on *Teleoceras major* represented by 27 skulls from the Miocene of Nebraska (Hagge, 2010) and probably the largest sample of 399 mandibular fragments and limb bones from a minimum of 42 individuals of *C. antiquitatis* was reported by Shpansky (2014) from two Late Pleistocene sites in the Tomsk Priob'e area (south-east Western Siberia). In Europe, isolated and fragmentary cranial remains of juvenile fossil Rhinocerotinae have been occasionally reported (van der Made, 2010; Diedrich, 2013; Pandolfi et al., 2017; Giaourtsakis et al., 2006, 2018).

In this scenario, the juvenile specimen from the late Middle Pleistocene area of Melpignano (Apulia, Italy), represented by a partial braincase (MPND1082) and its natural brain endocast (MPND1083), offers a rare opportunity to describe the internal and external neurocranial features of a Pleistocene rhinoceros in an early ontogenetic stage.

GEOLOGICAL AND PALEONTOLOGICAL FRAMEWORK

The fossiliferous area of Melpignano (Lecce, Italy 40°08′20″ N, 18°16′23″ E) (**Figure 1**) is located in a region where several quarries are open for the extraction of a Miocene calcarenite, known as Pietra Leccese. Since the Pliocene (Ciaranfi et al., 1983), the calcarenite was affected by an intense karst activity that formed an articulated fissured network (Selleri et al., 2003; Selleri, 2007). In the Melpignano area, these sub-vertical or funnel-shaped cavities exposed by the quarry activities and locally called "ventarole" are generally 1 m wide and up to 10 m high, filled with reddish clay-sands ("terre rosse") overlaid in some cases by brownish sediment ("terre brune") (Di Stefano et al., 1992; Bologna et al., 1994; Pandolfi et al., 2017). According to these authors, the chaotic arrangement of the bones in the sedimentary matrix, with any particular taphonomic pattern suggests that the origin of the deposit derived by the transport activity of the surface runoff waters and does not allow to define any stratigraphic succession. Moreover, based on faunal correlation of Melpignano assemblage with those from other paleontological sites of the Apulian area, the deposit has been initially assigned to the early Late Pleistocene (De Giuli, 1983; Bologna et al., 1994; Bedetti et al., 2004; Iurino et al., 2013; Pandolfi et al., 2017), although, a recent revision of the stratigraphic and fossil data suggests an older age of the site, referable to the late Middle Pleistocene (Mecozzi et al., 2019). A number of studies have focused on the rich vertebrate fauna of Melpignano, consisting of generally well preserved fossils with some articulated bones, attributed to: *Homo neanderthalensis*, *Palaeoloxodon antiquus*, *Equus ferus, Equus hydruntinus, Stephanorhinus hemitoechus, Hippopothamus amphibius, Dama dama, Cervus elaphus, Capreolus capreolus, Bos primigenius, Bison priscus, Sus scrofa, Canis lupus, Cuon alpinus, Vulpes vulpes, Panthera pardus, Felis silvestris, Lynx lynx, Crocuta crocuta, Meles meles, Mustela putorius, Lepus europaeus, Oryctolagus cuniculus, Erinaceus europaeus*, *Terricola savii, Apodemus sylvaticus*, and *Eliomys quercinus* (Mirigliano, 1941; De Giuli, 1980, 1983; Bologna et al., 1994; Bologna and Petronio, 1994; Pandolfi and Petronio, 2011; Bedetti et al., 2004; Iurino et al., 2013, 2015a; Vinuesa et al., 2016). The lack of signs of fluitation or long carrying on the surface of the fossil bones, suggests that the "ventarole" cavities have been probably filled in a short time span, collecting isolated bones and carcasses from the surrounding areas (Bologna et al., 1994). Furthermore, it is not excluded that these karst sinkholes worked as natural traps for living animals.

RHINOCEROTINAE FROM MELPIGNANO AREA

Starting from the second half of the last century, hundreds of fossil vertebrates, including rhinoceroses, have been collected from the fossiliferous area of Melpignano. Compared to other mammalian taxa, the fossil rhinoceroses are poorly documented and mostly represented by fragmented postcranial elements. The sample consists of about 25 specimens reported to date, excluding the material described herein. Considering the paucity, its taxonomic attribution has been problematic and has fueled a long debate among specialists. Indeed, the fossil rhinoceroses from Melpignano have been initially classified as *Rhinoceros* (= *Dicerorhinus*) *merckii* by Mirigliano (1941) and successively substituted as *nomen conservandum* with *Stephanorhinus kirchbergensis* (Jäger, 1835–1839) by Fortelius et al. (1993). This attribution was confirmed also by

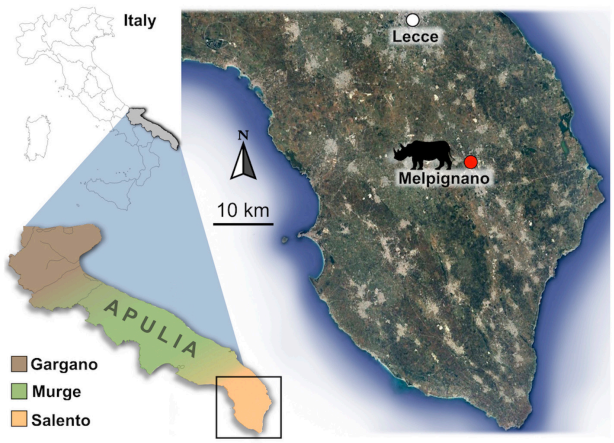

FIGURE 1 | Geographical location of the paleontological site of Melpignano (Lecce, Apulia, Italy).

Barbera et al. (2006). On the contrary, Petronio and Pandolfi (2008) attributed the material from Melpignano to a peculiar population of *Stephanorhinus hemitoechus* (Falconer, 1859), characterized by a reduced body-size compared to those reported from other European Middle Pleistocene sites. In the literature of the last decade, new fragmentary fossils have been reported from several Apulian sites as Avetrana, Grotta del Cavallo, Grotta del Sarcofago, Ingarano, Melpignano and Riparo l'Oscurusciuto, and all referred to *S. hemitoechus* (Pandolfi and Petronio, 2011; Pandolfi et al., 2017). Among the Apulian site, an exception is represented by the sample from Grotta Romanelli, which was attributed to three species: *Stephanorhinus hundsheimensis* and *Stephanorhinus* sp. from the level K and I respectively (Pandolfi et al., 2018); *Coelodonta antiquitatis* from the level I (Pandolfi and Tagliacozzo, 2013); *S. hemitoechus* from the level G (Pandolfi et al., 2018). New unpublished material (limb bones) have been unearthed during the 2019 field activity at Grotta Romanelli and still under study.

MATERIALS AND METHODS

Studied Material

In early 1990s, the braincase and its natural brain endocast (**Figure 2**) were collected together within the reddish clay-sands from a small karst fissure in the Melpignano area during a field survey carried out by a research team of the Earth Sciences Department of Sapienza University of Rome, where the material is currently housed in the PaleoFactory laboratory. At the moment of discovery, the braincase was split in eight disarticulated elements partially covered by the sediment and positioned with the dorsal surface facing upwards, while the natural endocast has been detected within the brain cavity during the recovery process. In addition to the braincase, no other large mammalian bones have been found. The sample was labeled with progressive catalog numbers: MPND1082 (cranium) and MPND1083 (brain endocast).

For comparative purposes, we used the available literature of juvenile crania of fossil Rhinocerotinae (**Table 1**) and adult skulls of extant species.

For the material of the extant species, a CT scan of a head of a 41-years-old male *Ceratotherium simum* (Burchell, 1817) OUVC:9754 and an adult skull of *Diceros bicornis* (Linnaeus, 1758) have been downloaded from morphosource[1,2] and segmented with Mimics 20.0.

[1]http://www.morphosource.org/Detail/MediaDetail/Show/media_id/14624
[2]http://www.morphosource.org/Detail/MediaDetail/Show/media_id/39879

TABLE 1 | List of the fossil and extant specimens of juvenile Rhinocerotine considered from literature.

Taxon	Age	Locality	References
Dicerorhinus cixianensis	middle Miocene	Jiulongkou, Cixian (China)	Tong, 2012
Alicornps simorrense	middle Miocene	El Lugarejo or Arévalo (Spain)	Cerdeño and Sánchez, 2000
Acerorhinus yuanmouensis	Late Miocene	Yuanmou Basin (china)	Lu, 2013
Diceros gansuensis	Late Miocene	Housan, Linxia basin (china)	Deng and Qiu, 2007
Chilotherium wimani	Late Miocene	Laogaochuan, Fugu (china)	Deng, 2001a,b
Ceratotherium primaevum	Late Miocene	Oued el Hammam (Algeria)	Geraads, 2010
Paradiceros mukirii	Late Miocene	Fort Ternan (Kenya)	Hooijer, 1968; Geraads, 2010
Acerorhinus neleus	Late Miocene	Pikermi (Greece)	Giaourtsakis et al., 2018
Teleoceras major	Miocene	Ashfall Fossil Beds, Nebraska (USA)	Voorhies and Stover, 1978; Voorhies, 1985; Hagge, 2010
Stephanorhinus etruscus	late Pliocene	Blassac-La-Girondie (France)	Heintz et al., 1974
Coelodonta nihowanensis	Early Pleistocene	Shanshenmiaozui (China)	Tong and Wang, 2014
Stephanorhinus kirchbergensis	Late Pleistocene	Shennongjia (China)	Tong and Wu, 2010
Coelodonta antiquitatis	Late Pleistocene	Yakutia Republic of Siberia (Russia)	Protopopov et al., 2015

CT-Scanning

Tomographic images of the specimens were taken using a Philips Brilliance CT 64-channel scanner at M.G. Vannini Hospital (Rome). Both the natural brain endocast and the cranial elements were scanned entirely in the coronal slice plane from front to back. The scanning resulted in 355 slices for the braincase, 437 for the disarticulated braincase fragments and 263 for the brain endocast, with standard dimensions of 512 × 512 pixels. The slice thickness is 0.8 mm with an interslice space of 0.4 mm. CT image processing was performed using Mimics 20.0, while the digital restoration process and bone coloring were made with ZBrush 4R6.

Virtual Restoration

Due to the fragility of the braincase, to avoid damaging the original material a digital restoration has been carried on. The virtual copies of all the fragments of the braincase have been manually reconnected matching the complementary margins of the bones (**Figures 3A–D**). The unavailability of skulls belonging to juvenile rhinoceroses prevented the digital acquisition of a 3D reference model for a restoration with geometric morphometric techniques. Despite this, the high correspondence of the fragments allowed obtaining a more complete version of the braincase. The basisphenoid (**Figures 3E–H**), obtained by the connection of three fragments is the only isolated bone due to the lack of connection edges with the restored braincase.

DESCRIPTION

Braincase

MPND1082 specimen (**Figures 2A–N** and **Supplementary Video S1**) is a partial juvenile braincase consisting of eight disarticulated elements in a good state of preservation. In dorsal view, the frontals are damaged and split in three portions, two isolated and one still articulated to the parietals. The dorsal surface of the largest isolated fragment is flat, and its anterior edge correspond to a quite damaged frontonasal suture. The parietals have a rounded and smooth surface, free of temporal lines and characterized by a butterfly-like outline (**Figure 2A**). Along the posterior margin of the parietals a marked notch receives a well-developed interparietal bone. The left side of the occipital is broken exposing the inner spongy bone tissue. The coronal, sagittal, and lambdoid sutures are clearly visible and unfused. In lateral view, the frontals are slightly projected upwards at the level of the coronal suture (**Figures 2C,D**). The parietals are dorsally quite flat with a small bulge crossed by the sagittal suture and located slightly in front of the interparietal bone. Anteriorly, the parietals are inflected forming a slight depression between the bulge and the coronal suture. On the left squamosal suture, a fragment of temporal is still connected to the parietal, whereas the right one is completely exposed and perfectly matches with the isolated fragment of the temporal. The caudal and basal portions of the right temporal are damaged, the zygomatic process is broken at the base, the external acoustic meatus is sub-elliptical in shape, the mastoid process is damaged, whereas the paraoccipital and postglenoid processes are missing (**Figure 2J**). Dorsally, the occipital crest follows the flat profile of the parietals and is slightly projected backwards. In ventral view, the frontals show a series of asymmetrical small pneumatic cavities corresponding to the frontal sinuses (**Figure 2G**). The vault of the brain cavity is free of convolutions traces, except for some small grooves left by the blood vessels on the parietal lobes (**Figure 2B**). In caudal view, the preserved portion of the occipital shows a trapezoidal profile crossed by a deep fracture which cuts the bone in to two parts. The plane of the occipital surface is sub-vertical with a marked recess just below the occipital crest (**Figure 2E**). The basisphenoid is divided in three fragments and both caudal alar foramina are partially preserved (**Figures 2L–N**). Moreover, thanks to the virtual restoration, all the bone fragments have been reconnected and a slight curvature between the frontals and parietals at the level of the coronal suture has been evidenced (**Figure 3C**).

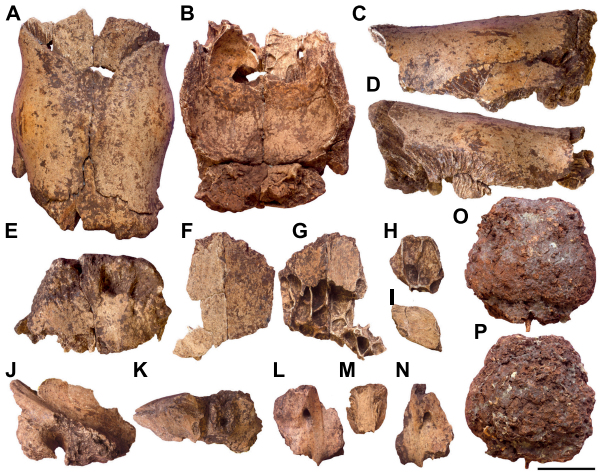

FIGURE 2 | Rhinocerotinae from Melpignano. Braincase MPND1082 in dorsal **(A)**, ventral **(B)**, left lateral **(C)**, right lateral **(D)**, and occipital **(E)** views; largest isolated fragment of the frontals in dorsal **(F)** and ventral **(G)** views; smallest isolated fragment of the frontals in ventral **(H)** view; fragment of the right parietal in dorsal **(I)** view; right temporal in right lateral **(J)** and ventral **(K)** views; fragmented basisphenoid in ventral **(L–N)** view. Natural brain endocast MPND1083 in dorsal **(O)** and ventral **(P)** views. Scale bar 5 cm.

By processing CT images of all the cranial fragments we observed their inner structure, as the bone porosity and the fusion of the sutures, to estimate the age of the specimen. The longitudinal sections of the braincase evidenced a reduced bone density at the innermost portions of the occipital and the parietals, consisting of spongy bone tissue with no evidence of well-developed pneumatic chambers (**Figure 4**). A bone thickening is observed at the level of the parietal bulge along the sagittal plane. The spongy bone structure of the parietals is dorso-ventrally expanded close to the lambdoid suture and it thins noticeably under the parietal inflection just before the coronal suture (**Figure 4**). The reduced fusion of all the neurocranial sutures have been also highlighted through the CT images. The lambdoid suture shows wide empty spaces between the occipital and the parietals with smooth bone walls, whereas on the coronal

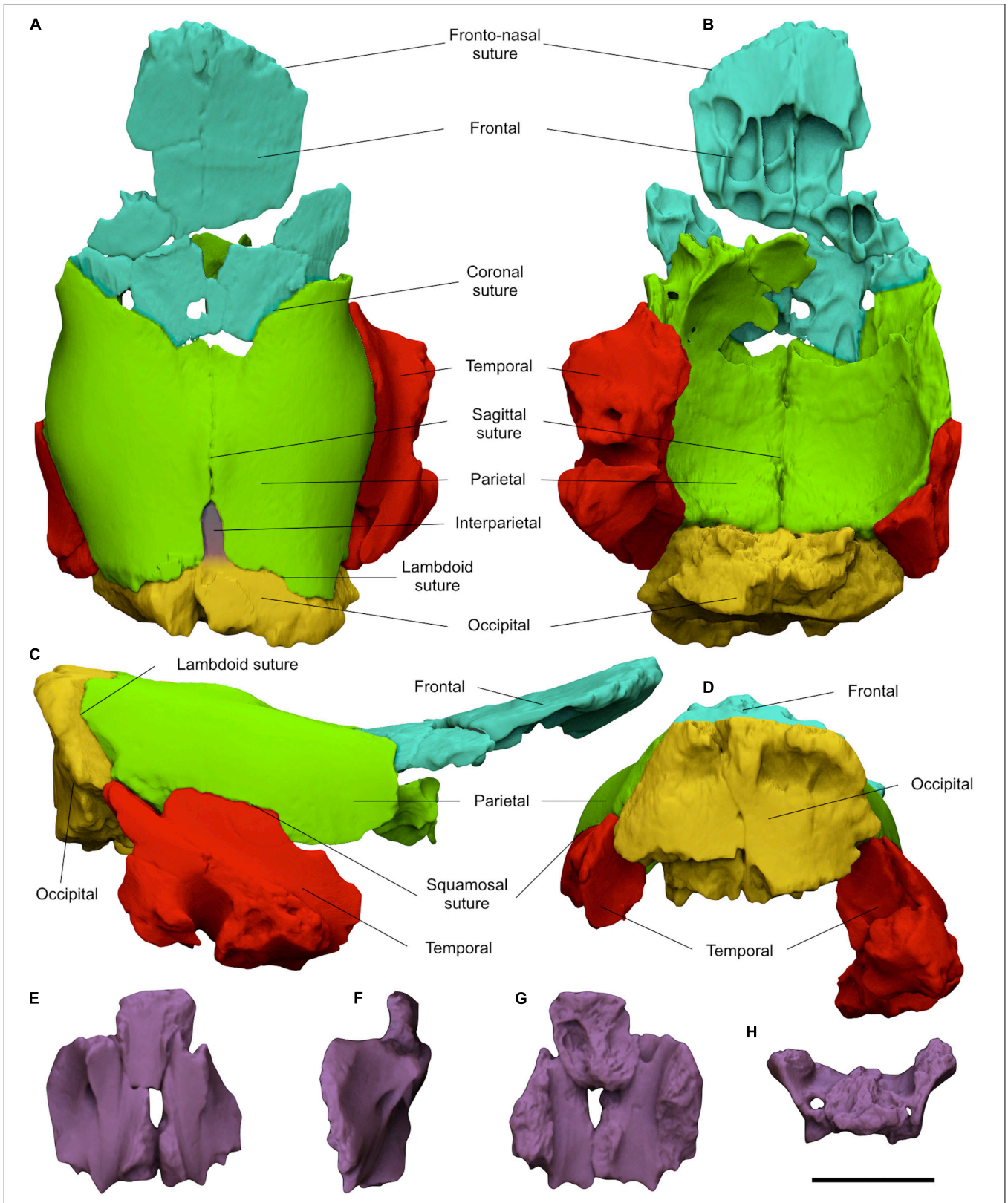

FIGURE 3 | Digitally restored braincase MPND1082 in dorsal **(A)**, ventral **(B)**, right lateral **(C)**, and occipital **(D)** views; reassembled basisphenoid in ventral **(E)**, right lateral **(F)**, dorsal **(G)**, and caudal **(H)** views. Scale bar 5 cm.

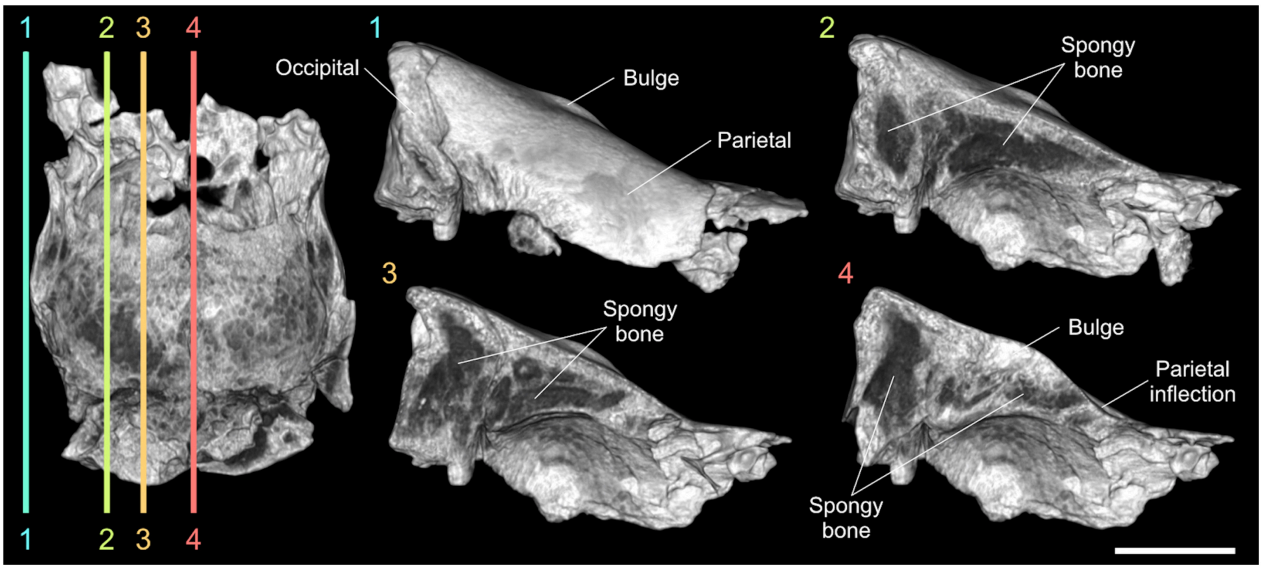

FIGURE 4 | Digital longitudinal sections of the braincase MPND1082 in right lateral view. The dark-gray areas indicate the spongy bone tissue. Sale bar 5 cm.

suture the bone tissue forms a hinge with very irregular and interdigitated bone margins. Concerning the paranasal sinuses, they are characteristic air-filled chambers developed in different cranial bones of placental mammals and are commonly divided into maxillary, frontal and sphenoidal sinuses (Falk, 2009; Boscaini et al., 2018). Processing the CT images of MPND1082, multiple chambers with a diameter just over 1 cm have been evidenced only in the frontal bones, thus corresponding to the frontal sinuses (**Figure 5C**). Such a pneumatization is missing inside the occipital, the parietals and the temporals, where instead, abundant spongy bone tissue is observed (**Figure 4**). In dorsal view, the frontal sinuses of MPND1082 are posteriorly delimited by the coronal suture with some terminal lobes that reach the anteriormost portion of the parietals, covering a large part of the frontal lobes of the brain (**Figure 5C**). Anteriorly, the air-filled chambers end 2 cm before the frontonasal suture in a completely different assessment compared to those of adult African rhinoceroses, where the frontal sinuses are part of a much extended and more complex system of cranial pneumatization (**Figures 5D–G**).

Natural Brain Endocast

A natural brain endocast is a brain replica obtained by the lithification of the sediment inside the brain cavity, a process that occurs only under specific sedimentary conditions (Hu et al., 2014; Ivanoff et al., 2014; Iurino et al., 2015b). The integrity of such a cast and the quality of its morphological details depend on multiple factors as the type and granulometry of the sediment, the amount of filling material and the presence of percolation waters depositing calcium. MPND1083 (**Figures 2O,P** and **Supplementary Video S2**) is a partial natural brain endocast mostly consisting of the telencephalon; olfactory bulbs are not preserved and the cerebellum seems almost completely missing. MPND1083 is globular in shape and is 97.3 mm long, 98.8 mm wide (maximum width) and 67.5 mm high with an approximate volume of 313 cm^3. The whole cast is formed by a poorly cemented sediment of fairly uniform granulometry and characterized by a reddish-brown color due to the iron oxides. Considering the fragility and the state of preservation of the specimen, only the general morphology of the telencephalon is appreciable. A gray-whitish patina partially enwraps some areas of the surface and corresponds to the residues of a consolidant agent applied in the early 1990s. In dorsal view (**Figure 2O**), the surface is irregular and affected by small cavities and fractures that prevent the identification of any morphological detail of the convolutions, blood vessels and nerves. Both cerebral hemispheres are preserved, but there is no evidence of the longitudinal fissure. The frontal lobes are less expanded than the parietal ones, which are divided from the cerebellum by a transverse fissure appreciable on the cast (**Figure 2O**). Unfortunately, the preserved portion of the cerebellum is too small and damaged to provide morphological and biometrical information. Along the broken portion of the cerebellum, a small coxal bone of a lagomorph partially protrudes from the sediment (**Figures 2O,P**). In ventral view, the brain cast is strongly damaged preventing any anatomical description (**Figure 2P**).

CT images (**Figure 6**) confirm the presence of several fracture lines of different thickness, ranging from 0.3 to 2.7 mm, which run irregularly within the natural endocast (**Figures 6E,F**). Some of these, especially the largest, are in continuity with the fractures visible on the surface with a pattern resembling those of the "mud cracks." A large number of empty sub-spherical holes ranging from 0.5 to 6.7 mm are arranged chaotically inside the specimen in partial overlap with the fractures (**Figures 6E,F**). Three small fragmented bones embedded and irregularly arranged in the sediment have been virtually extracted from the caudal portion of the endocast (**Figure 6G**). The size and morphology of these bones are compatible with those of a rabbit and consist of a left

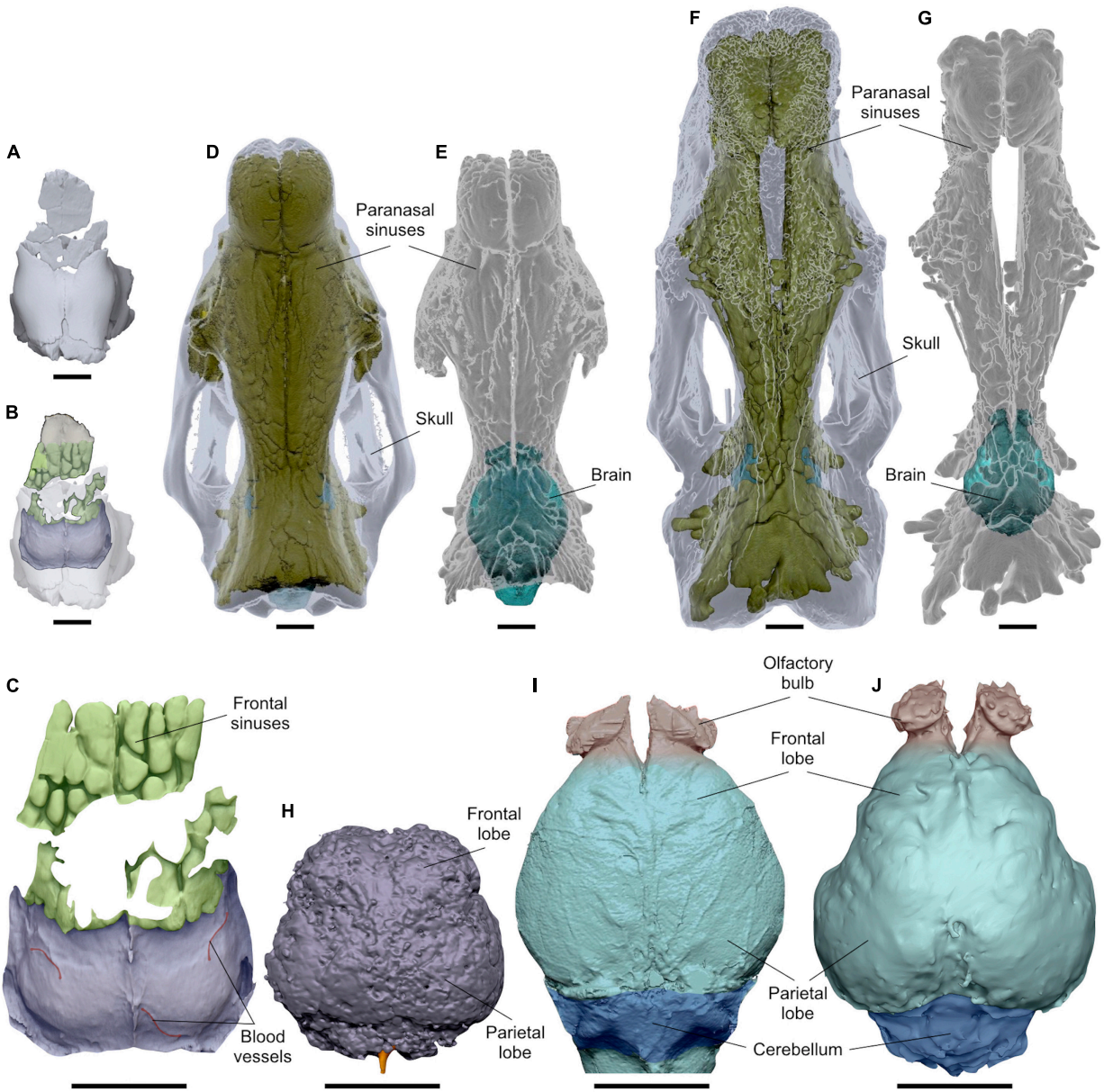

FIGURE 5 | Comparative CT images in dorsal view of the paranasal pneumatization and brain morphology of MPND1083 **(A–C)**, *Diceros bicornis* **(D,E)**, and *Ceratotherium simum* **(F,G)**. Digitalized natural endocast MPND1083 **(H)**; brain endocasts of *D. bicornis* **(I)**; and *C. simum* **(J)**. Sale bars 5 cm.

calcaneus, a proximal epiphysis of a third right metatarsal and a right coxal bone, the latter partially exposed on the surface (**Figures 6H–J**).

RESULTS

Virtual Endocasts

In addition to the digitalized natural endocast MPND1083, a second replica of the brain has been made using the braincase MPND1082 as a digital mold, which includes also a partial 3D model of the paranasal pneumatization (**Figures 5A–C**). On this second endocast the size and the anatomical details of the surface are better appreciable. The cerebrum is globular, divided in two hemispheres by a longitudinal fissure both with smooth surface and free of convolutions (**Figure 5C**). Some tubular marks interpreted as blood vessels are noticeable along the parietal lobes close to the transverse fissure (**Figure 5C**). As the consequence of the weak fusion of the sagittal suture, the longitudinal fissure impressed on the digital cast would seem to be projected upwards, but this effect is a graphic artifact originated during the segmentation process. Indeed, the two main protrusions of the longitudinal fissure correspond with the slits observed along the sagittal suture (**Figure 5C**).

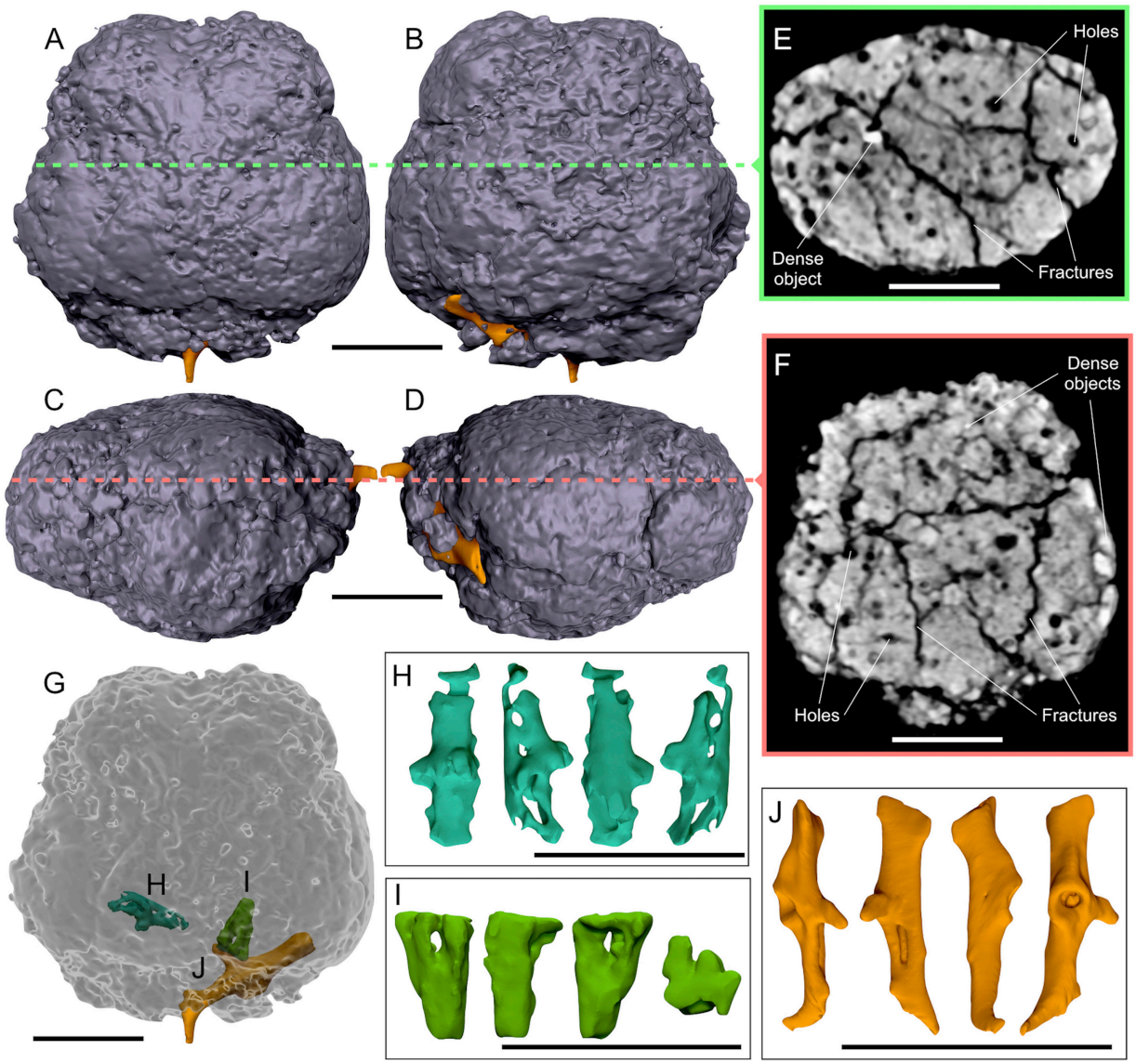

FIGURE 6 | CT images of the natural brain endocast MPND1083. 3D model of the brain in dorsal **(A)**, ventral **(B)**, left lateral **(C)**, and right lateral **(D)** views. Inner structure of the endocast in coronal **(E)** and longitudinal **(F)** sections. Arrangement of the bone fragments embedded within the endocast **(G)** corresponding to a left calcaneus **(H)**, a proximal epiphysis of a third right metatarsal **(I)**, and a right coxal bone **(J)** of a rabbit. Scale bar 3 cm.

Age Estimation

The unfused suture of the braincase and the volume of the natural endocast (313 cm^3), without the olfactory bulbs and cerebellum, of about half of those obtained for extant adult species (**Figures 5H–J**) indicate the early ontogenetic status of the fossil specimen. Considering the skull features, the development of the cranial sutures is similar in extinct and extant rhinoceroses species (Hagge, 2010). Therefore, we compared the Melpignano sample with extant and Miocene taxa, in order to better define the age of the individual (**Table 1**). The degree of fusion of the braincase sutures are compatible with those attributed to around 18-months-old specimen of *Coelodonta nihowanensis* (V 17616.1) from the early Pleistocene site of Shanshenmiaozui (China) (Tong and Wang, 2014). The development of adult morphological characters, as the occipital crest pronouncement and temporal lines appearance, is similar among extinct and extant rhinoceroses, which appear during the age class III–V (2–4 years; Hagge, 2010). In extant rhinoceroses the lengthening of the cranium and the development of adult morphological characters start from the class age V to X (4–9 years), in which the cranium become wider and more angular in adult morphologies (Hagge, 2010). The lack of both temporal lines and the occipital crest pronouncement on the Melpignano braincase also contributes to indicate that the age of the individual was <2–4 years. An age of 4–5 months has been attributed to the cub of *C. antiquitatis* from the Late Pleistocene of Yakutia

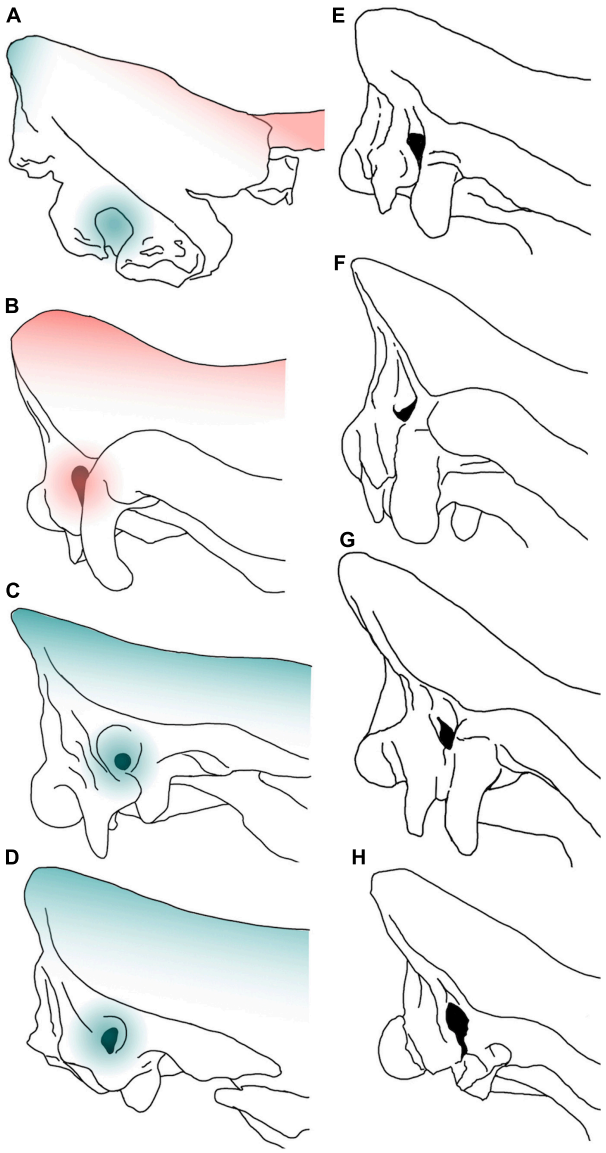

FIGURE 7 | Comparative images in right lateral view of selected braincases of juvenile **(A–D)** and adult **(E–H)** Pleistocene Rhinocerotinae from Eurasia. MPND1082 **(A)**, *Stephanorhinus kirchbergensis* No. H36 **(B)**, *Coelodonta antiquitatis* V 1453 **(C)**, *C. nihowanensis* V 17616.1 **(D)**, *S. etruscus* Mainz 1958/764 **(E)**, *S. kirchbergensis* from Spinadesco (Cremona, norther Italy) **(F)**, *S. hemitoechus* RGM 93302 **(G)**, and *C. antiquitatis* SfN **(H)**. The red-colored areas indicate the "*Stephanorhinus*" features, while the blue areas indicate the "*Coelodonta*" features evidenced on the juvenile specimens. The images are not to scale.

Republic (Russia) (Protopopov et al., 2015; Dirks et al., 2016), but unfortunately the exceptionally preserved fur partially cover the skull preventing the comparison. Finally, the juvenile cranium of the Late Pleistocene *Stephanorhinus kirchbergensis* (No. H36) from the Rhino Cave in Shennongjia (China), shows more fused sutures compared to the Melpignano braincase but the age was not estimated (Tong and Wu, 2010).

DISCUSSION

Age and Taxonomy

The specimen from Melpignano can be referred to a young individual, aged 12–18 months. In juvenile mammals, the process of bone development is intense and many of the diagnostic features used for taxonomic purposes, as well as for the sex determination, are not fully formed. The comparison with juvenile Pleistocene rhinoceroses (**Table 1** and **Figures 7A–D**) evidence how, in lateral view, the dorsal profile of MPND1082 shows a marked fronto-parietal angle compatible with that observed in *S. kirchbergensis* (No. H36) and noticeably different from *C. antiquitatis* (SJA 30, V 1453, "Sasha") and *C. nihowanensis* (IVPP V 17616.1), in which the fronto-parietal profile is almost flat. On the contrary, the lateral profile of the occipital crest is triangular with a narrow vertex in Melpignano and *Coelodonta* specimens, whereas it is more rounded and anteriorly projected in the juvenile *S. kirchbergensis* (**Figure 7B**). In caudal view, the latter (**Figure 7B**) shows a more marked dorso-ventral development of the occipital bone compared to MPND1082 and *Coelodonta* specimens (**Figures 7A,C,D**). The only comparative scheme of the auditory region in Rhinocerotinae was proposed by Loose (1975). The acoustic meatus of MPND1082 and wolly rhino specimens is quite broad and semicircular in shape, located in an advanced position with respect to the occipital plane. A different arrangement has been noticed in the juvenile and adult *S. kirchbergensis*, characterized by a drop-shaped meatus located in a more backward position close to the occipital plane (**Figures 7B,F**).

The combined set of *Coelodonta* – *Stephanorhinus* characters evidenced on the Melpignano specimen further complicates the taxonomic study and could be related to the young age of the individual. Being these two genera phylogenetically related (Piras et al., 2010; Deng et al., 2011; Welker et al., 2017; Cappellini et al., 2019) is likely that juveniles share similar morphological features.

Following the Hagge's (2010) scheme, the development of cranial features enables the identification of several age classes during the individual growth. Among these features, the occipital and temporal crests become more pronounced during the age classes X–XV (9–27 years) (Hagge, 2010).

This implies that the neurocranial portion in the juvenile rhinoceros offers a few information for taxonomy especially if compared with adult Pleistocene specimens (**Figures 7E–H**), being this region strongly involved during the ontogenetic development.

In the Melpignano area, fossil remains of adult *Stephanorhinus hemitoechus* have been reported by Petronio and Pandolfi (2008) and the young MPND1082 specimen could reasonably belong to this taxon. However, due to the lack of clear diagnostic features observable in the studied specimen, we refer the specimen to Rhinocerotinae to avoid circularity in the process of taxonomical attribution.

Nevertheless, the morphological differences detected in the auditory meatus rule out the attribution of MPND1082 to *S. kirchbergensis* and remarks the dubious presence of this taxon in southern Italy.

Brain

CT-scan devices have been largely used to obtain digital brain endocasts of a wide range of fossil vertebrates from different geological periods, including large mammals (e.g., Rowe et al., 2011; Knoll et al., 2012; Racicot and Colbert, 2013; Danilo et al., 2015; Forasiepi et al., 2016; Orihuela et al., 2019; Boscaini et al., 2018). Collecting and processing sensory information, the brain represents a fundamental organ for the interpretation of the sensory-perceptual ability in vertebrates, as well as its external morphology and volume can be addressed to anatomical and evolutionary studies (Dozo and Martínez, 2016; Vinuesa et al., 2016; Bertrand et al., 2017). Despite this, only few dated studies include paleoneurological aspects of fossil Rhinocerotinae (e.g., Gaudry and Boule, 1888), with the exception of the Late Pleistocene mummified cub of *C. antiquitatis* from the Yakutia Republic (Russia), whose CT images revealed the presence of several organs including brain tissue (Protopopov et al., 2015). Therefore, the MPND1083 represents one a few natural brain endocasts described in extinct Rhinocerotinae (**Figure 6**). MPND1083 consists of a globular telencephalon, free of convolutions with the frontal lobes less expanded than the parietal ones resembling in the general shape those reported on extant *Ceratotherium simum* and *Dicerorhinus sumatrensis* (Garrod, 1878; Bhagwandin et al., 2017), whereas it differs from that of *Diceros bicornis* (**Figure 5I**). In dorsal view, the brain of the black rhino shows a very rounded shape without the narrowing at the level of the lateral sulcus, which is evident in the other taxa. The different brain morphology of extant *D. bicornis* and *C. simum* (**Figures 5I,J**) has been studied with Magnetic Resonance Imaging by Bhagwandin et al. (2017) and related to diet. According to the authors, the shape of the brains reflects the overall architecture of the skulls, which in turn are related to the feeding habits of the two species, browsing for the black rhinoceros and grazing for the white rhinoceros. Such a relationship between brain morphology and feeding behavior in extant African rhinoceroses represent an interesting case study, which needs to be improved. Therefore, at the current status of knowledge we prefer to avoid any speculative morpho-functional inferences concerning the brain anatomy of the Melpignano specimen.

The lack of a detectable pattern of convolution observable on the Melpignano specimen as well as on both the adult African species (**Figures 5C,I,J**), seem not to be an age-related trait, since the brain endocasts of juvenile fossil mammals strongly resembles that of adults, indicating that the general brain morphology is almost completely formed in newborn individuals (Falk, 2009; Petrovič et al., 2018). Among gyrencephalic mammals, large herbivores have less complex and very prominent convolutions compared to carnivorans (Roth and Dicke, 2005; Macrini et al., 2007; Hu et al., 2014), consequently, their brain endocasts have fairly smooth appearance amplified by the covering effect of the meninges. This condition is noticeable also on our sample of Rhinocerotinae brain endocasts.

The Paranasal Sinuses

Several hypotheses have been proposed to explain different patterns of cranial pneumatization documented in some mammalian taxa, which involve multiple ecological, morpho-functional and developmental factors (Farke, 2010). Such studies on rhinoceroses are almost completely missing (Gerard et al., 2018) and the development of cranial pneumatization in fossil and extant taxa was poorly investigated. The paranasal sinuses of adult *C. simum* and *D. bicornis* form a complex asymmetrical system of breached pneumatization in almost all the cranial bones, including the parietals and the occipital (**Figures 5D–G**). In contrast, in the MPND1083 specimen the pneumatization concerns only the frontal bones (**Figure 5C**) whereas the occipital and the parietals are filled by spongy-bone tissue without pneumatic cavities (**Figure 4**). It is likely that the areas filled with spongy bones could be developing in paranasal sinuses. In adult specimens of white and black rhinoceroses, the chambers are very wide and of irregular shape compared to those of the Melpignano cub, characterized by sub-spherical shape, arranged more regularly and with a diameter just over 1 cm. The longitudinal sections of the skull reveal different developmental patterns of the paranasal pneumatization across the considered sample (**Figure 8**). The adult skulls of extant African rhinoceros, *C. simum* and *D. bicornis* (**Figures 8A,B**), share a very wide pneumatization involving almost all the neurocranial bones, as well as the splanchnocranial region, which is interested by large nasal sinuses. The pneumatization of the occipital bone is completely developed in adults (**Figures 8A–C**) and still full of spongy bone tissue in the 6-years-old *C. simum* (**Figure 8D**; Gerard et al., 2018). In adult *C. antiquitatis* the lack of nasoconcal sinus and the strong reduction of the cranial pneumatization is considered a peculiar trait of this species (**Figure 8C**) as indicated also by other authors (Garutt, 1997; García-Fernández and Vicente, 2008; Shidlovskiy et al., 2012). In fact, the cranial architecture of adult woolly rhinoceros differs considerably from that of other fossil and extant rhinoceroses for a larger thickness of the nasal bones, a completely ossified nasal septum, a flat nasal horn and the retracted back of the occipital (**Figure 8C**). This strengthening of the cranial architecture and the expansion of the insertion areas of the neck muscles have been interpreted as an adaptation to sweep away large volumes of snow to reach the forage in Arctic environments (Boeskorov, 2012; Shidlovskiy et al., 2012). Curiously, the CT images of the abovementioned mummified cub of woolly rhino (Protopopov et al., 2015) show a wide empty chamber inside the cranium just up to the brain cavity, which involves the occipital, the parietal and the frontal bones (**Figure 8E**). A similar set of the cranial sinuses has been briefly documented by García-Fernández and Vicente (2008) on another Late Pleistocene *C. antiquitatis* from the Bown Bank site of the North Sea. It is not clear how much the contrast of the CT images reported by Protopopov et al. (2015) has affected the visibility of the spongy bone tissue, which, however, appears evident in some areas of the figure. In addition, the section of the skull at the level of the coronal suture confirms the presence of two large frontal sinuses, suggesting that in a

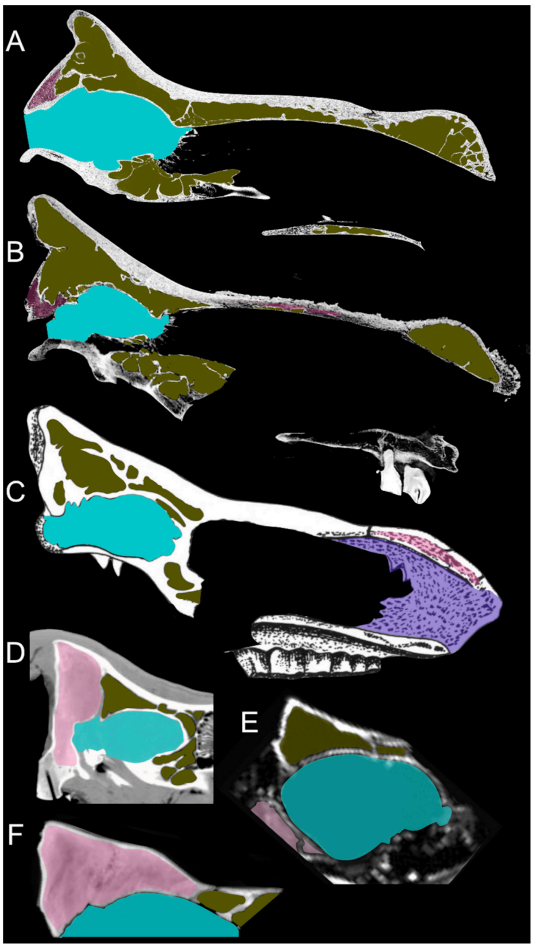

FIGURE 8 | Sagittal section of crania of an adult *Diceros bicornis* **(A)**, an adult *Ceratotherium simum* **(B)**, an adult *Coelodonta antiquitatis* **(C)** – modified from Garutt (1997), a 6-years-old *C. simum* **(D)** – modified from Gerard et al. (2018), a 4–5-months-old cub of *C. antiquitatis* **(E)** – modified from Protopopov et al. (2015), and the 12–18 months old specimen MPND1082 **(F)**. The images are not to scale.

4–5-months-old woolly rhino the cranial pneumatization was probably more developed than in the Melpignano braincase (**Figure 8F**), which is almost unpneumatized despite the older age of the individual. Wide neurocranial sinuses have been also documented in the 6-years-old white rhino mentioned above (Gerard et al., 2018), where the pneumatization is mostly represented by well-developed fronto-parietal sinuses with the occipital bone still completely filled by spongy tissue (**Figure 8D**). At the current state of knowledge, the reason of such an early and intense development of the skull pneumatization in juvenile woolly rhinoceroses and its paleoecological inferences are still unclear.

Taphonomy

The consistence of the Melpignano endocast is very friable and is crossed by several fracture lines, indicating a low degree of mineralization probably related to the low abundance of percolation water or its low mineral content. However, the overall size of the original specimen is comparable to the digital model obtained from the braincase MPND1082, with a reduction in thickness of about 5 mm in correspondence of the frontal and parietal lobes, indicating a weak erosive process that mainly affected the surface of the cast. Probably the presence of the braincase has performed a protective function against erosive agents, favoring the preservation of such a friable endocast.

CT analyses allowed to virtually extract three small bones embedded inside the natural cast (**Figures 6G–J**) represented by a left calcaneus, a third right metatarsal and a right coxal bone referred to *Oryctolagus cuniculus*. Both the heel and the metatarsal fragment, show a bad state of preservation. In particular, the external surface of the calcaneus is strongly altered and affected by several holes, whereas the inner portion is empty and the spongy bone tissue is missing. A similar deterioration could be due to weathering process or as a result of chemical aggression occurred during the digestion process of a medium-large predator (Horwitz, 1990).

The chaotic inner structure of the natural endocast and the presence of small mammal bones inside it, suggest a rapid burial and filling process of the skull with bone-rich sediments, whereas the lack of abrasions excludes a post-mortem transport of the braincase. The lack of signs of fluitation reported for other large fossil bones coming from the Melpignano area (Bologna et al., 1994) support the hypothesis that the karst sinkholes called "ventarole" probably worked more as natural traps rather than collectors of isolated bones and carcasses from the surrounding areas.

CONCLUSION

The study of juvenile specimens among mammals, relatively rare in the fossil record, is a promising topic, a source of information on the ontogeny and adaptations of extinct species. In particular, braincases and/or natural endocasts are of special interest and the use of CT scanning and digital analyses are a unique investigative tool. Nevertheless, the paucity of the available specimens of both extinct and extant taxa stresses as necessity of a larger set of information for this group, in order to better define the reconstruction of the ontogenetic development of different species of Rhinocerotidae and on their evolutionary framework.

However, for the juvenile Rhinocerothinae from the Middle Pleistocene of Melpignano tomographic images allowed to define the age of the individual and to analyze not only the hidden cranial anatomy, but also the inner structure of a natural endocast. The 3D models of the neurocranial cavities evidence the anatomical differences of the paranasal sinuses among the compared sample, including extinct and extant rhinoceroses. From the Melpignano area the occurrence of *Stephanorhinus hemithoechus* have been checked by different authors, but also other species have been described from other sites of the Italian Peninsula. The features of the Melpignano specimen cannot be considered fully diagnostic, therefore, to avoid circularity in the process of taxonomical attribution, we refer the specimen to Rhinocerotinae.

DATA AVAILABIITY STATEMENT

The datasets generated for this study are available on request to the corresponding author.

AUTHOR CONTRIBUTIONS

DI designed the research and wrote the manuscript with contribution of BM and RS. DI and JC processed and analyzed the CT images. All authors discussed the results and commented on the manuscript.

FUNDING

The study was funded by: Grandi Scavi 2018 (SA1181642D3B3C58), 2019 (SA11916B513E7C4B) of Sapienza, University of Rome (resp. RS).

ACKNOWLEDGMENTS

We wish to thank the editor LP and two referees for their valuable comments and suggestions. In addition, we gratefully thank Massimiliano Danti of "G. Vannini Hospital" in Rome, for providing access, assistance and facilities for making the CT scanning. Sincere appreciation is expressed to Federico Ciavatta for his help in the early stage of the work and to Luca Bellucci, Alessandro Iannucci, Antonio Profico, Flavia Strani, and Fabio Bona for fruitful discussions and constructive suggestions.

SUPPLEMENTARY MATERIAL

The Supplementary Material for this article can be found online at: https://www.frontiersin.org/articles/10.3389/feart.2020.00094/full#supplementary-material

VIDEO S1 | 3D model of the braincase MPND1082.

VIDEO S2 | 3D model of the natural brain endocast MPND1083.

REFERENCES

Álvarez-Lao, D. J., and García, N. (2011). Southern dispersal and Palaeoecological implications of woolly rhinoceros (*Coelodonta antiquitatis*): review of the Iberian occurrences. *Quat. Sci. Rev.* 30, 2002–2017. doi: 10.1016/j.quascirev.2011.05.005

Antoine, P. O. (2003). Middle Miocene elasmotheriine Rhinocerotidae from China and Mongolia: taxonomic revision and phylogenetic relationships. *Zool. Scr.* 32, 95–118. doi: 10.1046/j.1463-6409.2003.00106.x

Antoine, P. O., Duranthon, F., and Welcomme, J. L. (2003). *Alicornops* (Mammalia, Rhinocerotidae) dans le Miocčne supérieur des collines Bugti (Balouchistan, Pakistan): implications phylogénétiques. *Geodiversitas* 25, 575–603.

Barbera, C., Raia, P., and Meloro, C. (2006). I mammiferi di Melpignano conservati presso il Museo di Paleontologia di Napoli. *Thalassia Salentina* 29(Suppl. 2006), 237–243.

Bedetti, C., Pavia, M., and Sardella, R. (2004). Nuovi dati Sull'associazione a Vertebrati Fossili del Pleistocene Superiore di San Sidero, Maggio, (Puglia, SE Italia). IV Giornate di Paleontologia, Bolzano: Societá Paleontologica Italiana, 21–23.

Bello, S. M., Parfitt, S. A., and Stringer, C. (2009). Quantitative micromorphological analyses of cut marks produced by ancient and modern handaxes. *J. Archaeol. Sci.* 36, 1869–1880. doi: 10.1016/j.jas.2009.04.014

Bertrand, O. C., Amador-Mughal, F., and Silcox, M. T. (2017). Virtual endocast of the early Oligocene *Cedromus wilsoni* (Cedromurinae) and brain evolution in squirrels. *J. Anat.* 230, 128–151. doi: 10.1111/joa.12537

Bhagwandin, A., Haagensen, M., and Manger, P. R. (2017). The brain of the black (*Diceros bicornis*) and white (*Ceratotherium simum*) African rhinoceroses: morphology and volumetrics from magnetic resonance imaging. *Front. Neuroanat.* 11:74. doi: 10.3389/fnana.2017.00074

Blumenbach, J. F. (1799). *Handbuch der Naturgeschichte. Sechste Ausgabe*, 6th Edn. Göttingen: Johann Christian Dieterich.

Boeskorov, G. G. (2012). Some specific morphological and ecological features of the fossil woolly rhinoceros (*Coelodonta antiquitatis* Blumenbach, 1799). *Biol. Bull.* 39, 692–707. doi: 10.1134/s106235901208002x

Böhmer, C., Heissig, K., and Rössner, G. E. (2016). Dental eruption series and replacement pattern in Miocene *Prosantorhinus* (Rhinocerotidae) as revealed by macroscopy and X-ray: implications for ontogeny and mortality profile. *J. Mamm. Evol.* 23, 265–279. doi: 10.1007/s10914-015-9313-x

Bologna, P., Di Stefano, G., Manzi, G., Petronio, C., Sardella, R., and Squazzini, E. (1994). Late Pleistocene mammals from the Melpignano (LE) "Ventarole": preliminary analysis and correlations correlations. *Boll. Soc. Paleont. Ital.* 33, 265–274.

Bologna, P., and Petronio, C. (1994). The first occurrence of *Bison priscus* Bojanus in the Melpignano area (Lecce, southern Italy). *Boll. Soc. Paleont. Ital.* 33, 275–278.

Bordoloi, C. C., and Kalita, H. C. (1996). Gross anatomical studies of nasal cavity of rhino-calf (*Rhinoceros unicornis*). *Indian Vet. J.* 73, 470–472.

Borthakur, S., and Bordoloi, C. C. (1997). Gross anatomical study on the skull of adult rhino (*Rhinoceros unicornis*). *Indian Vet. J.* 74, 670–672.

Boscaini, A., Iurino, D. A., Sardella, R., Tirao, G., Gaudin, T. J., and Pujos, F. (2018). Digital Cranial Endocasts of the Extinct Sloth *Glossotherium robustum* (Xenarthra, Mylodontidae) from the Late Pleistocene of Argentina: Description and Comparison with the Extant Sloths. *J. Mamm. Evol.* 27, 55–71. doi: 10.1007/s10914-018-9441-1

Burchell, W. J. (1817). Note sur une nouvelle espèce de rhinocéros. *Bull. Soc. Philomath.* 1817, 96–97.

Cappellini, E., Welker, F., Pandolfi, L., Ramos-Madrigal, J., Samodova, D., Rüther, P. L., et al. (2019). Early Pleistocene enamel proteome from Dmanisi resolves *Stephanorhinus* phylogeny. *Nature* 574, 103–107. doi: 10.1038/s41586-019-1555-y

Cerdeño, E. (1995). Cladistic analysis of the family Rhinocerotidae (Perissodactyla). *Am. Mus. Novit.* 3143, 1–25.

Cerdeño, E., and Sánchez, B. (2000). Intraspecific variation and evolutionary trends of *Alicornops simorrense* (Rhinocerotidae) in Spain. *Zool. Scr.* 29, 275–305. doi: 10.1046/j.1463-6409.2000.00047.x

Chen, X., and Moigne, A. M. (2018). Rhinoceros (*Stephanorhinus hemitoechus*) exploitation in L evel F at the Caune de l'Arago (Tautavel, Pyrénéés-Orientales, France) during MIS 12. *Int. J. Osteoarchaeol.* 28, 669–680. doi: 10.1002/oa.2682

Ciaranfi, N., Ghisetti, F., Guida, M., Iaccarino, G., Lambiase, S., Pieri, P., et al. (1983). Carta neotettonica dell'Italia meridionale. *Prog. Fin. Geod. Pub.* 515, 1–62.

Danilo, L., Remy, J., Vianey-Liaud, M., Mérigeaud, S., and Lihoreau, F. (2015). Intraspecific variation of endocranial structures in extant *Equus*: a prelude to endocranial studies in fossil equoids. *J. Mamm. Evol.* 22, 561–582. doi: 10.1007/s10914-015-9293-x

De Giuli, C. (1980). *La fauna di Maglie (Lecce). I Vertebrati Fossili Italiani, Catalogo della Mostra*. Verona: Museo civico di storia Naturale, 241.

De Giuli, C. (1983). *Le faune pleistoceniche del Salento. 1. La fauna di San Sidero 3.1 Quaderni*. Maglie, LE: Museo di Paleontologia di Maglie, 45–84.

Deng, T. (2001a). New materials of *Chilotherium wimani* (Perrisodactyle, Rhinocerotidae) from the Late Miocene of Fugu, Shaanxi. *Vert. Pal Asiat.* 39, 129–138.

Deng, T. (2001b). "Cranial ontogenesis of *Chilotherium wimani* (Perissodactyla, Rhinocerotidae)," in *Proceedings of the Annual Meeting of the Chinese Society of Vertebrate Paleontology*, Vol. 8, Beijing, 101–112.

Deng, T., and Qiu, Z. X. (2007). First discovery of *Diceros* (Perissodactyla, Rhinocerotidae) in China. *Vert. Pal Asiat.* 45, 287–306.

Deng, T., Wang, X., Fortelius, M., Li, Q., Wang, Y., Tseng, Z. J., et al. (2011). Out of Tibet: Pliocene woolly rhino suggests high-plateau origin of Ice Age Megaherbivores. *Science* 333, 1285–1288. doi: 10.1126/science.1206594

Di Stefano, G., Petronio, C., Sardella, R., Savelloni, V., and Squazzini, E. (1992). - Nuove segnalazioni di brecce ossifere nella costa fra Castro Marina e Otranto (Lecce). *Il Quat. Ital. Quat. Sci.* 5, 3–10.

Diedrich, C. (2013). Recycling of badger/fox burrows in Late Pleistocene loess by hyenas at the den site Bad Wildungen-Biedensteg (NW, Germany): woolly rhinoceros killers and scavengers in a mammoth steppe environment of Europe. *J. Geol. Res.* 2013:190795.

Dirks, W., Potapova, O., Witzel, C., Kierdorf, U., Kierdorf, H., and Protopopov, A. (2016). "Preliminary Report on the Deciduous Premolars of "Sasha", the First Infant Woolly Rhino (*Coelodonta antiquitatis*) to be discovered," in *Proceedings of the XIV Annual Meeting of the European Association of Vertebrate Palaeontologists*, Haarlem.

Dozo, M. T., and Martínez, G. (2016). First digital cranial endocasts of late Oligocene Notohippidae (Notoungulata): implications for endemic South American ungulates brain evolution. *J. Mamm. Evol.* 23, 1–16. doi: 10.1007/s10914-015-9298-5

Faith, J. T. (2014). Late Pleistocene and Holocene mammal extinctions on continental Africa. *Earth Sci. Rev.* 128, 105–121. doi: 10.1016/j.earscirev.2013.10.009

Falconer, H. (1859). Modifications apportés par Mr. Falconer a la faune du Val d'Arno. *Bull. Soc. Vaudoise Sci. Nat.* 6, 130–131.

Falk, D. (2009). The natural endocast of Taung (*Australopithecus africanus*): insights from the unpublished papers of Raymond Arthur Dart. *Am. J. Phys. Anthropol.* 140, 49–65. doi: 10.1002/ajpa.21184

Farke, A. A. (2010). Evolution and functional morphology of the frontal sinuses in Bovidae (Mammalia: Artiodactyla), and implications for the evolution of cranial pneumaticity. *Zool. J. Linn. Soc.* 159, 988–1014. doi: 10.1111/j.1096-3642.2009.00586.x

Forasiepi, A. M., MacPhee, R. D., Del Pino, S. H., Schmidt, G. I., Amson, E., and Grohé, C. (2016). *Exceptional Skull of Huayqueriana (Mammalia, Litopterna, Macraucheniidae) from the Late Miocene of Argentina: Anatomy, Systematics, and Paleobiological Implications*. New York, NY: American Museum of Natural History, 1–76.

Fortelius, M., Mazza, P., and Sala, B. (1993). *Stephanorhinus* (Mammalia: Rhinocerotidae) of the Western European Pleistocene, with a revision of *S. etruscus* (Falconer, 1868). *Palaeontogr. Ital.* 80, 63–155.

García-Fernández, D., and Vicente, J. (2008). Nuevas aportaciones al conocimiento de *Coelodonta antiquitatis* (Blumenbach, 1799) de Brown Bank, mar del Norte. *Butll. Cent d'Estud. Nat. Barc. Nord* 7, 309–329.

Garrod, A. H. (1878). On the Brain of the Sumatran Rhinoceros (*Ceratorhinus sumatrensis*). *Trans. Zool. Soc. Lond.* 10, 411–414. doi: 10.1111/j.1096-3642.1878.tb00467.x

Garutt, N. V. (1994). Dental ontogeny of the "woolly rhinoceros" *Coelodonta antiquitatis* (Blumenbach, 1799). *Cranium* 11, 37–48.

Garutt, N. V. (1997). Traumatic skull damages in the woolly rhinoceros, *Coelodonta antiquitatis* Blumenbach, 1799. *Cranium* 14, 37–46.

Gaudry, A., and Boule, M. (1888). *Matériaux Pour l'histoire des Temps Quaternaires*. Paris: Librairie F. Savy.

Geraads, D. (2010). "Rhinocerotidae," in *Cenozoic Mammals of Africa*, eds L. Werdelin and W. J. Sanders (Berkeley, CA: University of California Press), 675–689.

Gerard, M. P., Glyphis, Z. G., Crawford, C., Blikslager, A. T., and Marais, J. (2018). Identification of a nasoconchal paranasal sinus in the white rhinoceros (*Ceratotherium simum*). *J. Zoo Wildl. Med.* 49, 444–449. doi: 10.1638/2017-0185.1

Giaourtsakis, I., Svorligkou, G., and Roussiakis, S. (2018). "A juvenile skull of the hornless rhinocerotid *Acerorhinus neleus* (Rhinocerotidae, Mammalia) from the late Miocene locality of Pikermi (Attica, Greece)," in *Proceedings of the 62nd Annual Meeting Palaeontological Association*, ed. G. G. Lash (Bristol: University of Bristol).

Giaourtsakis, I., Theodorou, G., Roussiakis, S., Athanassiou, A., and Iliopoulos, G. (2006). Late Miocene horned rhinoceroses (Rhinocerotinae, Mammlia) from Kerassia (Euboea, Greece). *Neues Jahrb. Geol. Paläontol. Abh.* 239, 367–398.

Guérin, C. (1980). Les rhinoceros (Mammalia, Perissodactyla) du Miocene terminal au Pleistocene superieur en Europe occidentale: comparison avec les especes actuelles. *Doc. Lab. Géol. Fac. Sci. Lyon* 79, 1–1182.

Hagge, M. D. (2010). *A Functional and Ontogenetic Skull Analysis of the Extant Rhinoceroses and Teleoceras Major, an Extinct Miocene North American rhinoceros*. Ph.D. dissertation, Louisiana State University, Baton Rouge, LA.

Heintz, E., Guérin, C., Martin, R., and Prat, F. (1974). Principaux gisements villafranchiens de France: listes fauniques et biostratigraphie. *Mém. Bur. Recherches Géol. Minières* 78, 169–182.

Hieronymus, T. L., Witmer, L. M., and Ridgely, R. C. (2006). Structure of white rhinoceros (*Ceratotherium simum*) horn investigated by X-ray computed tomography and histology with implications for growth and external form. *J. Morphol.* 267, 1172–1176. doi: 10.1002/jmor.10465

Hooijer, D. A. (1968). A rhinoceros from the late Miocene of Fort Ternan, Kenya. *Zool. Meded.* 43, 77–92.

Horwitz, K. L. (1990). The origin of partially digested bones recovered from archaeological contexts in Israel. *Paléorient* 97–106. doi: 10.3406/paleo.1990.4522

Hu, Y., Chen, Y., Wang, S., and Sun, Q. (2014). Pleistocene equid brain endocast from Shanxi Province, China. *Acta Palaeontol. Pol.* 59, 253–259.

Iurino, D. A., Fico, R., Petrucci, M., and Sardella, R. (2013). A pathological Late Pleistocene canid from San Sidero (Italy): implications for social-and feeding-behaviour. *Naturwissenschaften* 100, 235–243. doi: 10.1007/s00114-013-1018-5

Iurino, D. A., Fico, R., and Sardella, R. (2015a). A pathological Late Pleistocene badger from San Sidero (Apulia, Southern Italy): implications for developmental pathology and feeding behaviour. *Quat. Int.* 366, 96–101. doi: 10.1007/s00114-013-1018-5

Iurino, D. A., Profico, A., Cherin, M., Veneziano, A., Costeur, L., and Sardella, R. (2015b). A lynx natural brain endocast from Ingarano (Southern Italy; Late Pleistocene): Taphonomic, Morphometric and Phylogenetic approaches. *Hystrix* 26, 110–117. doi: 10.4404/hystrix-26.2-11465

Ivanoff, D. V., Wolsan, M., and Marciszak, A. (2014). Brainy stuff of long-gone dogs: a reappraisal of the supposed Canis endocranial cast from the Pliocene of Poland. *Naturwissenschaften* 101, 645–651. doi: 10.1007/s00114-014-1200-4

Jäger, G. F. (1835–1839). *Über die Fossilen Säugetiere welche in Württemberg in Verschiedenen Formationen Aufgefunden Worden Sind, Nebst Geognotischen Bemerkungen Über Diese Formtionen*. Stuttgart: Erhard Verlag.

Knoll, F., Witmer, L. M., Ortega, F., Ridgely, R. C., and Schwarz-Wings, D. (2012). The braincase of the basal sauropod dinosaur *Spinophorosaurus* and 3D reconstructions of the cranial endocast and inner ear. *PLoS One* 7:e30060. doi: 10.1371/journal.pone.0030060

Lacombat, F. (2006). Morphological and biometrical differentiation of the teeth from Pleistocene species of *Stephanorhinus* (Mammalia, Perissodactyla, Rhinocerotidae) in Mediterranean Europe and the Massif Central, France. *Palaeontogr. Abt. A Band* 274, 71–111.

Linnaeus, C. (1758). *Systema Naturae per Regna tria Naturae, Secundum Classes, Ordines, Genera, Species, cum Characteribus, Differentiis, Synonymis, locis Editio decima, Reformata*. Laurentii: Salvii Holmiae.

Loose, H. (1975). Pleistocene Rhinocerotidae of W. Europe with Reference to the Recent Two-Horned Species of Africa and SE Asia. *Scr. Geol.* 33, 1–59.

Lu, X. (2013). A juvenile skull of *Acerorhinus yuanmouensis* (Mammalia: Rhinocerotidae) from the Late Miocene hominoid fauna of the Yuanmou Basin (Yunnan, China). *Geobios* 46, 539–548. doi: 10.1016/j.geobios.2013.10.001

Macrini, T. E., Rougier, G. W., and Rowe, T. (2007). Description of a cranial endocast from the fossil mammal *Vincelestes neuquenianus* (Theriiformes) and its relevance to the evolution of endocranial characters in therians. *Anat. Rec.* 290, 875–892. doi: 10.1002/ar.20551

Markova, A. K., Puzachenko, A. Y., Van Kolfschoten, T., Van der Plicht, J., and Ponomarev, D. V. (2013). New data on changes in the European distribution of the mammoth and the woolly rhinoceros during the second half of the Late Pleistocene and the early Holocene. *Quat. Int.* 292, 4–14. doi: 10.1016/j.quaint.2012.11.033

Mecozzi, B., Bellucci, L., Giustini, F., Iurino, D. A., Mazzini, I., and Sardella, R. (2019). "Large mammal fauna from the late Middle Pleistocene sites of Melpignano and San Sidero (Lecce, Southern Italy)," in *Proceedings of the XIX Edizione delle Giornate di Paleontologia Paleodays 2019* (New York, NY: Springer), 24.

Mirigliano, G. (1941). Avanzi di vertebrati quaternari di Melpignano (Lecce). *Atti Acad. Sci. Napoli.* 2, 1–46.

Orihuela, J., Viñola López, L. W., and Macrini, T. E. (2019). First cranial endocasts of early Miocene sirenians (Dugongidae) from the West Indies. *J. Vert. Paleontol.* 39:e1584565. doi: 10.1080/02724634.2019.1584565

Pandolfi, L., Boscato, P., Crezzini, J., Gatta, M., Moroni, A., Rolfo, M., et al. (2017). Late Pleistocene last occurrences of the narrow-nosed rhinoceros *Stephanorhinus hemitoechus* (Mammalia, Perissodactyla) in Italy. *Riv. Ital. Paleontol. Stratigr.* 123, 177–192.

Pandolfi, L., Fiore, I., Gaeta, M., Szabó, P., Vennemann, T., and Tagliacozzo, A. (2018). Rhinocerotidae (Mammalia, Perissodactyla) from the middle Pleistocene levels of Grotta Romanelli (Lecce, southern Italy). *Geobios* 51, 453–468. doi: 10.1016/j.geobios.2018.08.008

Pandolfi, L., and Petronio, C. (2011). The small-sized rhinoceroses from the Late Pleistocene of Apulia (Southern Italy). *Riv. Ital. Paleontol. Stratigr.* 117, 509–520.

Pandolfi, L., and Tagliacozzo, A. (2013). Earliest occurrence of the woolly rhino (*Coelodonta antiquitatis*) in Italy (Late Pleistocene, Grotta Romanelli site). *Riv. Ital. Paleontol. Strat.* 119, 125–129. doi: 10.1016/j.quaint.2011.06.051

Petronio, C., and Pandolfi, L. (2008). Stephanorhinus hemitoechus (Falconer, 1868) del Pleistocene superiore dell'area di Melpignano-Cursi e S. *Sidero* (Lecce, Italia). *Geol. Rom.* 41, 1–12.

Petrovič, V., Sabol, M., Šurka, J., Pyszko, M., and Stehlík, L. (2018). External brain morphology of juvenile cave hyena (*Crocuta crocuta spelaea*) from the Jasovská jaskyňa Cave (Slovakia) revealed by X-ray computed tomography. *Acta Geol. Slovaca* 10, 133–142.

Piras, P., Maiorino, L., Raia, P., Marcolini, F., Salvi, D., Vignoli, L., et al. (2010). Functional and phylogenetic constraints in Rhinocerotinae craniodental morphology. *Evol. Ecol. Res.* 12, 897–928.

Prothero, D. R. (2005). *The evolution of North American rhinoceroses*. Cambridge: Cambridge University Press.

Prothero, D. R., Manning, E., and Hanson, C. B. (1986). The phylogeny of the Rhinocerotoidea (Mammalia, Perissodactyla). *Zool. J. Linn. Soc.* 87, 341–366. doi: 10.1111/j.1096-3642.1986.tb01340.x

Protopopov, A., Potapova, O., Plotnikov, V., Maschenko, E., Boeskorov, G., Klimovskii, A., et al. (2015). "The frozen mummy of the woolly rhinoceros, *Coelodonta antiquitatis* (Blum., 1799) calf: a new data on early ontogenesis of the extinct species," in *Proceedings of the 75th Annual SVP Meeting*, Dallas, TX, 199.

Racicot, R. A., and Colbert, M. W. (2013). Morphology and variation in porpoise (Cetacea: Phocoenidae) cranial endocasts. *Anat. Rec.* 296, 979–992. doi: 10.1002/ar.22704

Roth, G., and Dicke, U. (2005). Evolution of the brain and intelligence. *Trends Cogn. Sci.* 9, 250–257.

Rowe, T. B., Macrini, T. E., and Luo, Z. X. (2011). Fossil evidence on origin of the mammalian brain. *Science* 332, 955–957. doi: 10.1126/science.1203117

Schreve, D., Howard, A., Currant, A., Brooks, S., Buteux, S., Coope, R., et al. (2013). A Middle Devensian woolly rhinoceros (*Coelodonta antiquitatis*) from Whitemoor Haye Quarry, Staffordshire (UK): palaeoenvironmental context and significance. *J. Quat. Sci.* 28, 118–130. doi: 10.1002/jqs.2594

Selleri, G. (2007). Karstic landscape evolution of southern Apulia fore- land during the Pleistocene. *Geogr. Fis. Dinamica Quat.* 30, 77–86.

Selleri, G., Sanso, P., and Walsh, N. (2003). The karst of Salento region (Apulia, southern Italy): constraints for management. *Acta Carsol.* 32, 19–28.

Shidlovskiy, F. K., Kirillova, I. V., and Wood, J. (2012). Horns of the woolly rhinoceros *Coelodonta antiquitatis* (Blumenbach, 1799) in the Ice Age Museum collection (Moscow, Russia). *Quat. Int.* 255, 125–129. doi: 10.1016/j.quaint.2011.06.051

Shpansky, A. V. (2014). Juvenile remains of the "woolly rhinoceros" *Coelodonta antiquitatis* (Blumenbach, 1799)(Mammalia, Rhinocerotidae) from the Tomsk Priob'e area (southeast Western Siberia). *Quat. Int.* 333, 86–99. doi: 10.1016/j.quaint.2014.01.047

Shpansky, A. V., and Billia, E. (2006). *Remains of Juvenile "Woolly Rhinos" Coelodonta antiquitatis Blumenbach, 1799) (Mammalia, Rhinocerotidae) from the Tomsk Ob' Region (Western Siberia)//Modern Paleontology: Classical and New Methods*. (Moscow: Russian Academy of Sciences), 103–108.

Steiner, C. C., and Ryder, O. A. (2011). Molecular phylogeny and evolution of the Perissodactyla. *Zool. J. Linn. Soc.* 163, 1289–1303. doi: 10.1111/j.1096-3642.2011.00752.x

Stuart, A. J. (1991). Mammalian extinctions in the Late Pleistocene of northern Eurasia and North America. *Biol. Rev.* 66, 453–562. doi: 10.1111/j.1469-185x.1991.tb01149.x

Tong, H., and Moigne, A. M. (2000). Quaternary rhinoceros of China. *Acta Anthropol. Sin.* 19(Suppl.), 257–263.

Tong, H., and Wu, X. (2010). *Stephanorhinus kirchbergensis* (Rhinocerotidae, Mammalia) from the Rhino Cave in Shennongjia, Hubei. *Chin. Sci. Bull.* 55, 1157–1168. doi: 10.1038/s41586-019-1555-y

Tong, H. W. (2012). Evolution of the non-*Coelodonta* dicerorhine lineage in China. *C. R. Palevol* 11, 555–562. doi: 10.1016/j.crpv.2012.06.002

Tong, H. W., and Wang, X. M. (2014). Juvenile skulls and other postcranial bones of *Coelodonta nihowanensis* from Shanshenmiaozui, Nihewan Basin, China. *J. Vert. Paleontol.* 34, 710–724. doi: 10.1080/02724634.2013.814661

van der Made, J. (2010). The rhinos from the Middle Pleistocene of Neumark-Nord (Saxony-Anhalt). *Veröff. Landesam. Denkmalpflege Archäol.* 62, 433–500.

Vinuesa, V., Iurino, D. A., Madurell-Malapeira, J., Liu, J., Fortuny, J., Sardella, R., et al. (2016). Inferences of social behavior in bone-cracking hyaenids (Carnivora, Hyaenidae) based on digital paleoneurological techniques: implications for human–carnivoran interactions in the Pleistocene. *Quat. Int.* 413, 7–14. doi: 10.1016/j.quaint.2015.10.037

Voorhies, M. R. (1985). A Miocene rhinoceros herd buried in volcanic ash. *Natl. Geogr. Soc. Res. Rep.* 19, 671–688.

Voorhies, M. R., and Stover, S. G. (1978). An articulated fossil skeleton of a pregnant rhinoceros, *Teleoceras major* Hatcher. *Proc. Nebr. Acad. Sci.* 88, 47–48.

Welker, F., Smith, G. M., Hutson, J. M., Kindler, L., Garcia-Moreno, A., Villaluenga, A., et al. (2017). Middle Pleistocene protein sequences from the rhinoceros genus *Stephanorhinus* and the phylogeny of extant and extinct Middle/Late Pleistocene Rhinocerotidae. *PeerJ* 5:e3033. doi: 10.7717/peerj.3033

Witton, M. P. (2018). *Palaeoartist's Handbook: Recreating Prehistoric Animals in Art*. Ramsbury: The Crowood Press.

Conflict of Interest: The authors declare that the research was conducted in the absence of any commercial or financial relationships that could be construed as a potential conflict of interest.

frontiers in Earth Science

ORIGINAL RESEARCH
published: 21 April 2020
doi: 10.3389/feart.2020.00112

Decoupling Functional and Morphological Convergence, the Study Case of Fossorial Mammalia

Gabriele Sansalone[1], Silvia Castiglione[2], Pasquale Raia[2], Michael Archer[3], Blake Dickson[4], Suzanne Hand[3], Paolo Piras[5], Antonio Profico[6] and Stephen Wroe[1]*

[1] Function, Evolution & Anatomy Research Lab, Zoology Division, School of Environmental and Rural Science, University of New England, Armidale, NSW, Australia, [2] Department of Earth Sciences, Environment and Resources, University of Naples Federico II, Naples, Italy, [3] PANGEA Research Centre, School of Biological, Earth and Environmental Sciences, UNSW Sydney, Sydney, NSW, Australia, [4] Museum of Comparative Zoology Harvard University, Cambridge, MA, United States, [5] Dipartimento di Scienze Cardiovascolari, Respiratorie, Nefrologiche, e Geriatriche, Sapienza Università di Roma, Rome, Italy, [6] PaleoHub, Department of Archaeology, Hull York Medical School, University of York, Heslington, United Kingdom

Morphological similarity between biological structures in phylogenetically distant species is usually regarded as evidence of convergent evolution. Yet, phenotypic similarity is not always a sign of natural selection acting on a particular trait, therefore adaptation to similar conditions may fail to generate convergent lineages. Herein we tested whether convergent evolution occurred in the humerus of fossorial mammals, one of the most derived biological structures among mammals. Clades adapting to digging kinematics possess unusual, by mammalian standards, humeral shapes. The application of a new, computationally fast morphological test revealed a single significant instance of convergence pertaining to the Japanese fossorial moles (*Mogera*) and the North-American fossorial moles (Scalopini). Yet, the pattern only manifests when trade-off performance data (derived from finite element analysis) are added to shape data. This result indicates that fossorial mammals have found multiple solutions to the same adaptive challenge, independently moving around multiple adaptive peaks. This study suggests the importance of accounting for functional trade-off measures when studying morpho-functional convergence. We revealed that fossorial mammals, a classic example of convergent evolution, evolved multiple strategies to exploit the subterranean ecotope, characterized by different functional trade-offs rather than converging toward a single adaptive optimum.

Keywords: humerus, fossorial mammals, finite elements analysis, geometric morphometrics, convergence, RRphylo

OPEN ACCESS

Edited by:
Mary Teresa Silcox, University of Toronto Scarborough, Canada

Reviewed by:
Jürgen Kriwet, University of Vienna, Austria
Manuel F. G. Weinkauf, Charles University, Czechia

****Correspondence:***
Gabriele Sansalone
gsansalone@uniroma3.it

Specialty section:
This article was submitted to Paleontology, a section of the journal Frontiers in Earth Science

Received: *23 December 2019*
Accepted: *26 March 2020*
Published: *21 April 2020*

Citation:
Sansalone G, Castiglione S, Raia P, Archer M, Dickson B, Hand S, Piras P, Profico A and Wroe S (2020) Decoupling Functional and Morphological Convergence, the Study Case of Fossorial Mammalia. Front. Earth Sci. 8:112. doi: 10.3389/feart.2020.00112

INTRODUCTION

Independent evolution of similar morphological adaptations to similar environmental challenges is commonly regarded as evidence for convergence (Harmon et al., 2005; Losos, 2011) and convergent evolution underpins many hypotheses and processes that explain the repeated evolution of similar forms through time (Tseng and Flynn, 2018). However, species can adapt to similar environmental pressures in different ways (Wainwright et al., 2005; Losos, 2011). One-to-many mapping, and functional

trade-offs will drive the phenotypic evolution of a structure according to which traits affect fitness the most (Polly et al., 2016; Dickson and Pierce, 2019; Moen, 2019), and the evolution of a particular phenotype may result in the reduced fitness of other attributes (Alfaro et al., 2004; Moen, 2019). In addition, many different phenotypes can produce highly similar functional outputs, known as many-to-one mapping, and divergent morphologies may perform convergently in function (Alfaro et al., 2005; Wainwright et al., 2005; Losos, 2011; Renaud et al., 2018), meaning that functional convergence can be recognized even in the absence of morphological convergence. In this case, species distribute around different adaptive peaks, precluding a direct relationship between the traits and the environment. Overall, both trade-offs and many-to-one mapping can provide insights into how organisms evolve under similar environmental pressures and can necessitate reassessment of the way we measure or recognize convergent evolution (Moen, 2019).

Fossorial mammals have often been reported as a textbook example of convergent evolution (Nevo, 1979; Hildebrand et al., 1985). The subterranean environment is relatively predictable in time, and requires a high degree of specialization, which in turn can lead to comparable morphological forms (Nevo, 1979; Marcy et al., 2016; Sansalone et al., 2019). Moreover, locomotion underground requires extreme morphological specialization and digging kinematic is likely to have a strong impact on other functional traits (Piras et al., 2012, 2015; Sansalone et al., 2018). For instance, the overall anterior limb mobility of the forelimb is sacrificed in favor of maximizing the abduction moment (Gambaryan et al., 2002). Here we will measure the extent of functional and morphological convergence among ecologically convergent fossorial mammals ranging in degree of fossorial specialization (cursorial, semi-fossorial, fossorial) and from across Mammalia (monotremes, marsupials and placentals) including a number of extinct forms. When comparing distantly related groups, the presence of similar morphological features could be interpreted as the result of phylogenetic relatedness (e.g., parallelisms) rather than convergence. For this reason, it is highly recommended to consider the phylogenetic history of the species examined. Here, we have combined 3D geometric morphometrics (GMM), finite elements analysis (FEA) and novel phylogenetic comparative methods (Castiglione et al., 2019) to quantify the extent of functional and morphological convergence in the humeri of fossorial mammals.

MATERIALS AND METHODS

Material, CT-Scanning, Post-Processing and Finite Element Model Assembly

We have focused on a range of mammals exhibiting putative fossorial adaptations of the humerus. Among Talpidae we included highly fossorial taxa (Scalopini and Talpini), semi-aquatic (e.g., desmans) and semifossorial/ambulatory (e.g., shrew moles) species (Piras et al., 2015), including both extinct and living species (see **Supplementary Table S1**).

We managed to include four living species of Chrysochloridae, the well-preserved North-American proscalopid *Mesoscalops montanensis*, the extinct marsupial notoryctid *Naraboryctes philcreaseri* and the monotreme *Tachyglossus aculeatus*. **Supplementary Table S1** summarizes details about all the specimens included. All specimens, except for *N. philcreaseri, Chrysochloris sthulmanni*, *T. aculeatus* and were scanned at the "Studio dentistico Moscato", Rome, Italy using a Kodak 9000 3D-Cone Beam Computed Tomography (CBCT) scanner. *C. sthulmanni* CT are available from the digimorph database[1]. *M. montanensis* has been scanned using a Skyscan 1076 microCT at the Small ANimal Tomographic Analysis Facility (SANTA) at the Seattle Children's Research Institute, Seattle, Washington. The humeri of *N. philcreaseri* and *T. aculeatus* were scanned using a Siemens Inveon MicroPET-CT scanner at the University of New South Wales. Each specimen scan comprised 1000 slices and the images were processed and stacked using GE Phoenix proprietary software.

We reconstructed the 3D surface and volume meshes for FEA from each CT-scanned humerus using Mimics (v. 22.0) and 3-Matic (v. 8.0) (Materialize N. V.), following previously published protocols (Tsang et al., 2019).

The volume models possessed between 1.2 million and 1.4 million tetrahedral elements and between 317,549, and 401,341 nodes (i.e., tetrahedral vertices). The reconstructed volume meshes were then imported into Strand7 (v. 3.0) where finite element models were generated for each specimen. We used FEA in a comparative fashion, therefore we applied the same approximations to all the meshes. Material properties were assigned for cortical bone with a Young modulus of 10 GPa and Poisson ratio of 0.41 and homogeneously applied through the structure (Rayfield et al., 2001). According to published protocols (Stayton, 2009), simulations were conducted after scaling all models to a unit volume: 0.82 cm^3 (Piras et al., 2015).

Following Piras et al. (2015), we identified the different functional types occurring in our sample. For talpids, chrysochlorids and proscalopids we replicated the modeling approach presented in Piras et al. (2015) simulating the action of the main muscles involved in digging for each functional group. For notoryctids and tachyglossids, we utilized detailed anatomical descriptions of both myology and osteology in order to identify the main muscle groups involved in the digging kinematics (Jenkins, 1970; Warburton, 2003, 2006; Archer et al., 2010; Beck et al., 2016; Regnault and Pierce, 2018). Due to the comparative nature of this study, we applied the same resultant force to all the models. For this purpose, we used *Talpa europaea* as reference model since *in vivo* muscle force estimation is available for this species only (Gambaryan et al., 2002). We applied the same resultant force to the trochlear area for all the models following the methodology proposed by Piras et al. (2015).

Restraints

We applied on the models surface, over the selected restraint areas, an elastic solid mesh composed of beam elements (Structural Steel AS 4100–1998, Young's Modulus of 200,000 MPa). This strategy mitigates the impact of artifacts that

[1]http://www.digimorph.org/specimens/Chrysochloris_sp/whole/

can occur where single nodes are loaded (Attard et al., 2016; Tsang et al., 2019).

We applied the restraints on muscle insertion areas for each taxon. The restraints can perform along the axes of the reference system and were modeled as spring foundations. Talpids anatomical restraints were defined on the head of humerus and the clavicular articular facet. Chrysochlorids, proscalopids, notoryctids and tachyglossids restraints were identified only on the humeral head because these latter taxa either do not have a humerus clavicle articulation or it is extremely reduced (Jenkins, 1970; Puttick and Jarvis, 1977; Barnosky, 1981; Gasc et al., 1986; Warburton, 2006; Beck et al., 2016).

Loadings

As with restraints, the loadings have been applied on different selected areas according to the modeled muscles for the different taxa. For talpids, the loadings were defined on the areas of insertion of the m. teres major and m. pectoralis pars sternalis, two of the most important muscles used for burrowing (Dobson, 1882; Freeman, 1886; Edwards, 1937; Gambaryan et al., 2002). *M. montanensis* was loaded in the areas where m. teres major and either m. infraspinatus or m. spinodeltoideus insert (following Barnosky, 1981, Figure 28, p. 326; Piras et al., 2015; see also **Supplementary Figure S1**). For chrysochlorids, we marked the insertion areas of m. latissimus dorsi and m. triceps (Puttick and Jarvis, 1977; Gasc et al., 1986). For notoryctids we selected the areas corresponding to insertion of m. triceps, m. pectoralis and areas of the medial epicondyle corresponding to the attachment of muscles aimed at wrist and digit flexion (Warburton, 2006; Beck et al., 2016). For tachyglossids we selected the areas where m. latissimus dorsi and m. teres major insert (Regnault and Pierce, 2018). Orientation of muscles has been based on anatomical descriptions available (Jenkins, 1970; Puttick and Jarvis, 1977, Gasc et al., 1986; Gambaryan et al., 2002; Warburton, 2006; see **Figures 1C,D**).

Stress Evaluation

We integrated the results from FEA with GMM outputs to provide a more direct comparison of the results. At this purpose we followed the protocol published by Parr et al. (2012). The mean von Mises (VM) stress values were extracted from the four nearest tetrahedral elements (each tetrahedral element has four nodes) at the point were the 38 landmarks have been placed during the digitization process (see GMM section).

Forearm Mobility

In fossorial mammals, abduction of the humerus is instrumental to put the manus in the correct position to generate a laterally directed force on the substrate (Gambaryan et al., 2002). The movement of the scapula and the flexion of the shoulder and elbow joint are coordinated with humeral abduction. Among mammals, the range of movement available at the shoulder joint varies greatly (Luo, 2015), however, in fossorial species these movements are commonly limited by factors such as reduction of movement of the shoulder joint. Abduction can take place at the sterno-clavicular joint, and the humeral head can be entirely displaced in the transverse dimension within the scapula glenoid cavity (Gambaryan et al., 2002; Warburton, 2006; Archer et al., 2010; Regnault and Pierce, 2018). The result is that all abduction at the shoulder can be extremely constrained in its range of movement. In other mammals the longitudinal axes of the glenoid fossa is parallel to the plane of the costal surface of the scapula, whereas in fossorial mammals it may be directed at different angles. In this context a measure of this angle provides an appropriate proxy for the mobility of the shoulder joint, where higher angles suggest a reduction in the possible movements at the shoulder. Consequently, we measured the angle between the longitudinal axes of the glenoid fossa and the costal surface of the scapula for all the species included in our sample (see **Figures 1A,B**) to predict the limitations imposed by the digging kinematics.

Geometric Morphometric Shape Analysis

On each humerus, we digitized 38 homologous landmarks (**Supplementary Table S2** and **Supplementary Information**) to capture its shape in three dimensions (Piras et al., 2015; Neaux et al., 2018) using IDAV Landmark software (Wiley et al., 2005).

We then imported the landmark configurations into R version 3.5.3 (R Core Team, 2019) to further process the landmark coordinates. We rotated, translated, and scaled the landmark configurations to unit centroid size (CS, square root of the sum of squared distances of a set of landmarks from their centroid, Bookstein, 1991) performing a Generalized Procrustes Analysis (GPA, Rohlf and Slice, 1990; Goodall, 1991) on all landmark coordinates. The GPA is implemented in the ProcSym() function from the R package "Morpho" (Schlager, 2014). The multivariate ordination of the aligned Procrustes coordinates has been visualized through a principal component analysis (PCA).

Phylogeny

We built synthetic phylogenies, presented in **Supplementary Figure S2**, in Mesquite 3.02 (Maddison and Maddison, 2015). The stratigraphic range and phylogenetic position have been derived from the most updated literature (Piras et al., 2015; Sansalone et al., 2019). **Supplementary Table S1** includes the complete literature corpus employed to build the phylogenetic trees. We built two different phylogenies because of the lack of agreement between molecular and morphological data for talpids (see Sansalone et al., 2019, for an extensive discussion about the topic). For *Mesoscalops*, we used the data presented by Gunnel et al. (2008) and Barnosky (1981). The position of chrysochlorids has been based on the data provided by Piras et al. (2015) and O'Leary et al. (2013). The divergence between the echidna, *N. philcreaseri* and placental mammals has been set following Luo et al. (2007, 2011), Rowe et al. (2008); Phillips et al. (2009) and Bi et al. (2018).

RRphylo and Convergence Analysis

We employed a novel Phylogenetic Comparative Method specifically designed to deal with phylogenies including fossil taxa. The *RRphylo* method (Castiglione et al., 2018) performs a phylogenetic ridge regression on tree and data and returns branch-wise evolutionary rates and ancestral character estimates (ACEs) at nodes. In the case of multivariate data, such a

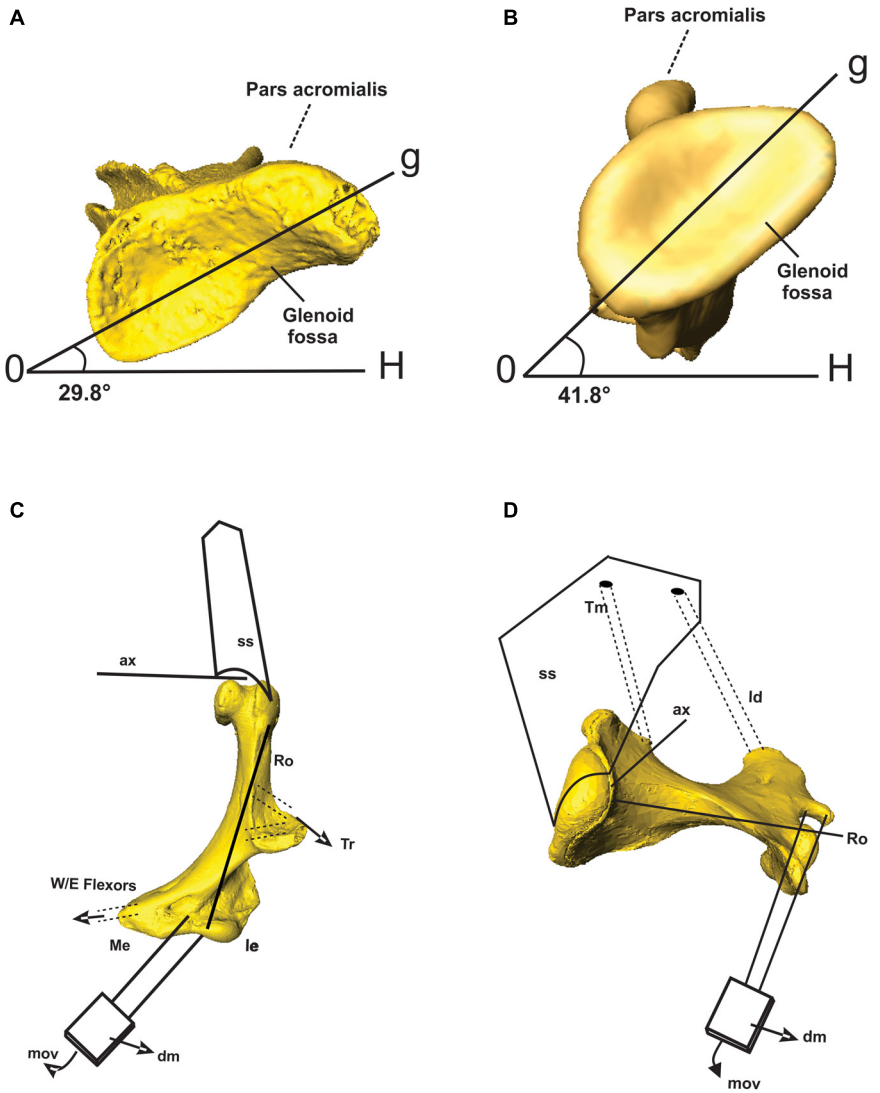

FIGURE 1 | Correlation between costal surface of the scapula and longitudinal axes of the glenoid fossa and functional context employed in the current study. **(A)** *Naraboryctes philcreaseri* **(B)** *Talpa romana* **(C)** *Naraboryctes philcreaseri* functional model **(D)** *Tachyglossus aculeatus* functional model. Abbreviation: H, costal surface; g, longitudinal axes of the glenoid fossa; ax, retraction axis; ss, scapula; ro: rotational axis; Tr, m. triceps; Me, medial epicondyle; Le, lateral epicondyle; W/E Flexors, wrist and elbow flexors muscles; dm, dorsal manus; mov, movement direction; ld, m. latissimus dorsi; Tm, m. teres major.

procedure is performed independently for each component of the phenotype, by applying a normalization factor essential to avoid extreme rate values and multicollinearity, under the hypothesis that rate variation is minimized within clades (Castiglione et al., 2018).

To identify instances of phenotypic convergence between either clades or between groups of species within specific categories (i.e., states) we used *search.conv*, a new method which has proven to be both fast and powerful in identifying morphological convergence (Castiglione et al., 2019). Under *search.conv* the phenotypic distance between species is quantified as the angle between their phenotypic vectors (i.e., multivariate phenotypes for each species). Under a Brownian Motion (BM) model of evolution, this angle should increase proportionally to the patristic distance between species. When morphological convergence is present, this assumption no longer applies as the angle (per unit time) become smaller than expected. The function *search.conv* is specifically designed to detect instances of convergence, as occurring either between entire clades ("clade case") or between selected species evolving according to specific states ("state case"). When comparing clades, the function computes the mean angle over all possible combinations of species pairs taking one species per clade, and divides this value by the patristic distance between the nodes subtending to the clades (i.e., the phylogenetic distance between the most recent common ancestors, MRCAs, of the clades). To assess significance, this value is contrasted to a random distribution of 1,000 angle-by-time values. The function randomly samples two species

within the tree, computes the angle between them and divides it by the patristic distance between their immediate ancestors.

Additionally, *search.conv* determines whether convergence occurred early in the clade (at divergence) or only applies at the level of terminal branches (i.e., species). Given two clades presumed to evolve under convergence, the function derives the ACEs for the MRCAs for both clades from the *RRphylo* results and computes the angle between them. Such angle is summed to the mean angle between species and divided by the patristic distance between the MRCAs. If the "summed" angle is smaller than expected by chance, it means the clades converged since their origin and subsequently followed parallel phenotypic evolutionary trajectories. The significance level is assessed as described above by randomizing phenotypes across the tree tips. Finally, if no specific hypothesis about converging clades is available, the function automatically scans the phylogeny to identify instances of convergence.

Under the "state case", *search.conv* computes the mean angle over all possible combinations of species pairs using one species per state. Each individual angle is divided by the patristic distance between the species. Significance is assessed by contrasting this value with a family of 1,000 random angles obtained by shuffling the state across the species.

Here, we applied *search.conv* under both "clade" and "state" cases on shape values (PC scores), by classifying species under fossorial/non-fossorial lifestyle. We repeated the analyses by collating the values of functional variables (i.e., angle and von Mises stress values) to PC values for each species and taking such "composite" vectors as the *search.conv* entry. All the functions used to compute rates, phenotypes and to test convergence are available as part of the R package RRphylo (Raia et al., 2019 available at[2]).

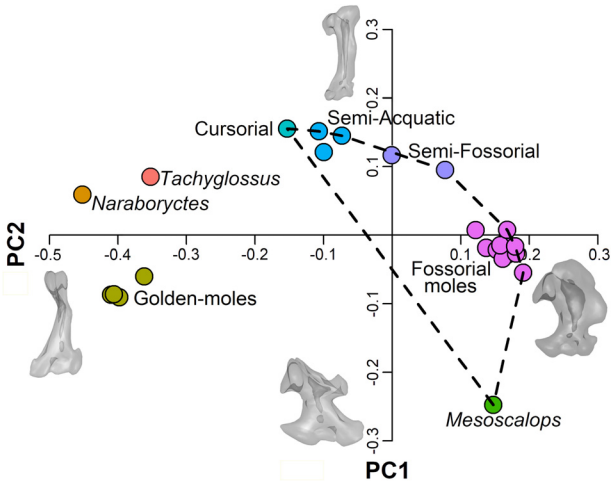

FIGURE 2 | Scatterplot of the first 2 PC scores. Convex hull indicates the Talpidae. Talpidae are colored according to their lifestyle. Other taxa are colored according to their specific status. Meshes are deformed according to PC axes extremes.

RESULTS

Shape Analysis

3D shape analysis evidences a clear phylogenetic signal with the different clades clustering in distinct regions of the morphospace (see **Figure 2**). Specifically, chrysochlorids grouped on the negative end of PC1 and PC2, whereas the echidna and *N. philcreaseri* separate along positive values of PC2. Highly fossorial talpids (i.e., Talpini and Scalopini) and *M. montanensis* cluster along positive values of PC1, but fossorial talpids separates between consensus and slightly negative values of PC2, whereas *M. montanensis* is placed at highly negative values. The remaining taxa (cursorial, semi-fossorial and semi-aquatic moles) are distributed from consensus to negative values of the PC1 and positive values of the PC2 (see **Figure 2**).

At positive values of PC1 the humerus shows a robust and rounded configuration characterized by a medially displaced and enlarged teres tubercle, the proximal region is relatively developed and the greater tuberosity is highly expanded. At negative values of the PC1 the humeri possess a relatively slender morphology characterized by a less developed teres tubercle, the proximal region is reduced and the articulation with clavicle is absent, features typical of chrysochlorids and *N. philcreaseri*. Slender, non-fossorial, talpids cluster at the positive values of PC2, whereas *M. montanensis* is positioned in a unique region of the morphospace at the negative extreme of the PC2. At positive values of this same axis the humerus presents a relatively slender configuration with an expanded proximal region, whereas the teres tubercle is poorly developed. At negative values of PC2, the teres tubercle is placed on the distal region of the humerus, the distal region broaden and bear an extremely elongated lateral epicondyle, peculiar of the proscalopid *M. montanensis*.

Finite Elements Analysis

The application of FEA to the humerus models, we revealed that the different functional groups were characterized by different VM stress magnitudes and distributions. The cursorial and semi-aquatic talpids showed the highest stress values, with a highly stressed humeral shaft. The semi-fossorial talpids display intermediate values with most of the stress again concentrated on the humeral shaft (see **Figure 3**). Fossorial talpids showed overall low stress values, with stress peaks mainly concentrated around the head of the humerus and the clavicular articular facet, whereas the areas of the muscles insertion showed lower VM stress values. The notoryctid showed averaged stress values lower than the cursorial and semi-aquatic talpids but higher than the semi-fossorial talpids and the chrysochlorids. *N. philcreaseri* displayed a highly stressed humeral shaft, in particular along the proximal half. The deltopectoral crest and the medial epicondyle showed remarkably lower stress values, reflecting the insertion of the main muscles involved during the power stroke (m. triceps longus, mm. pectorales, m. flexor carpi radialis, and m. flexor carpi ulnaris and m. flexor digitorum profundus). The echidna showed stress values

[2]https://github.com/pasraia/RRphylo

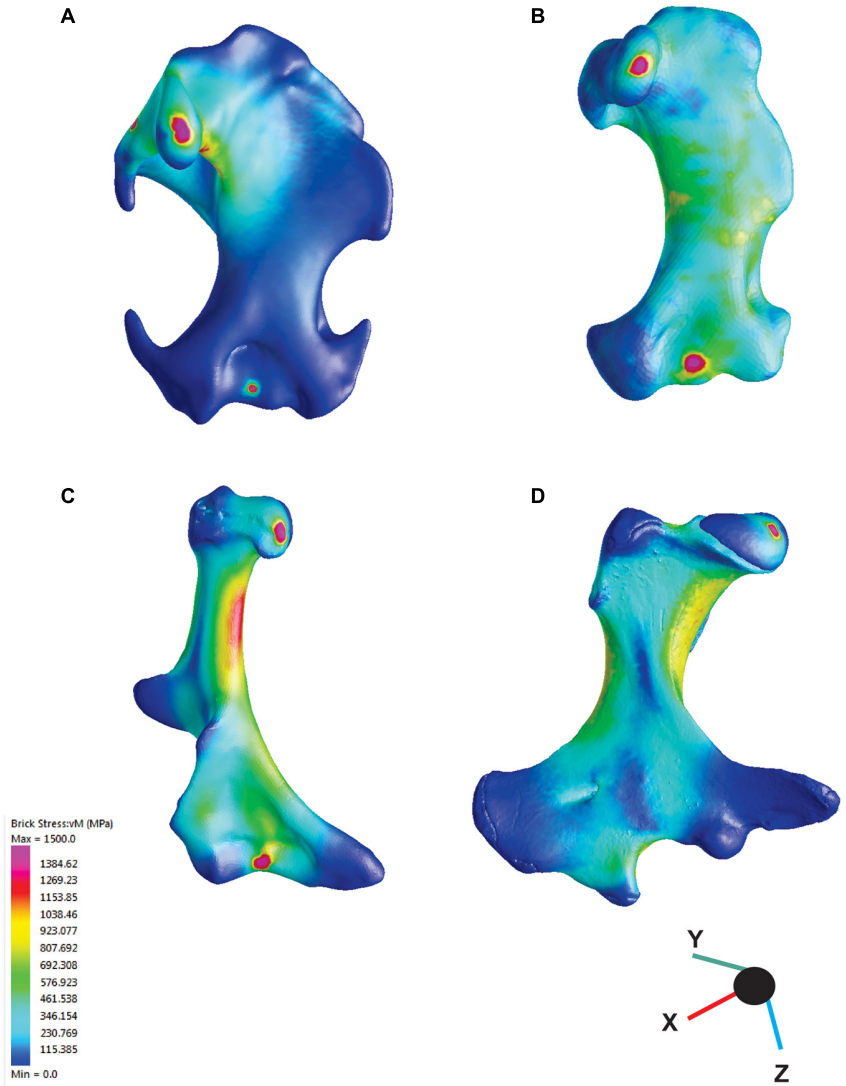

FIGURE 3 | Results from finite element analysis (FEA). Colors represent the intensity of the mechanical stress, warmer colors indicate high stress areas, cooler colous indicate low stress areas. **(A)** *Mogera wogura*, **(B)** *Neurotrichus gibbsii*, **(C)** *Naraboryctes philcreaseri*, **(D)** *Tachyglossus aculeatus*.

lower than *N. philcreaseri* but comparable with the semi-fossorial talpids. The highest stress values were located on the proximal half of the humeral shaft, in particular on the region below the humeral head. The area of insertion of the digging muscle and, overall, the greatly enlarged distal area of the humerus showed remarkably lower stress values. In chrysochlorids, high stress values were found on the distal region of the humerus, whereas the lateral and medial epicondyles, having the direct m. latissimus dorsi and m. triceps insertions were particularly stressed. In contrast, the proximal humeral region in chrysochlorids is less stressed compared to talpids because the muscles involved in digging do not insert in that region (Puttick and Jarvis, 1977; Barnosky, 1982; Gasc et al., 1986; Piras et al., 2015). The humerus of *M. montanensis* showed moderate stress values on the proximal region compared to talpids, though the teres tubercle was more stressed because of its distally shifted position (Piras et al., 2015). PC1 and PC2 scores, VM stress values, and angles for each species are reported in **Supplementary Table S3**.

RRphylo and Convergence Analysis

By applying *search.conv* on shape data (PC scores) alone we found no significant instance of convergence, neither under "clade" (angle per unit time = 1.051 degrees/myr, $p = 0.117$) or under "state" (angle per unit time = 1.240 degrees/myr, $p = 0.746$) case. When integrating functional variables, we found Japanese moles (i.e., *Mogera* species exclusive of *Mogera insularis*) to significantly converge on the clade including the north American moles within *Scapanus* plus *Scalopus* genera (i.e., Scalopini, **Figures 4A,B**), starting from their respective common ancestors (angle per unit time, tips plus ancestors = 0.199 degrees/myr, $p = 0.046$).

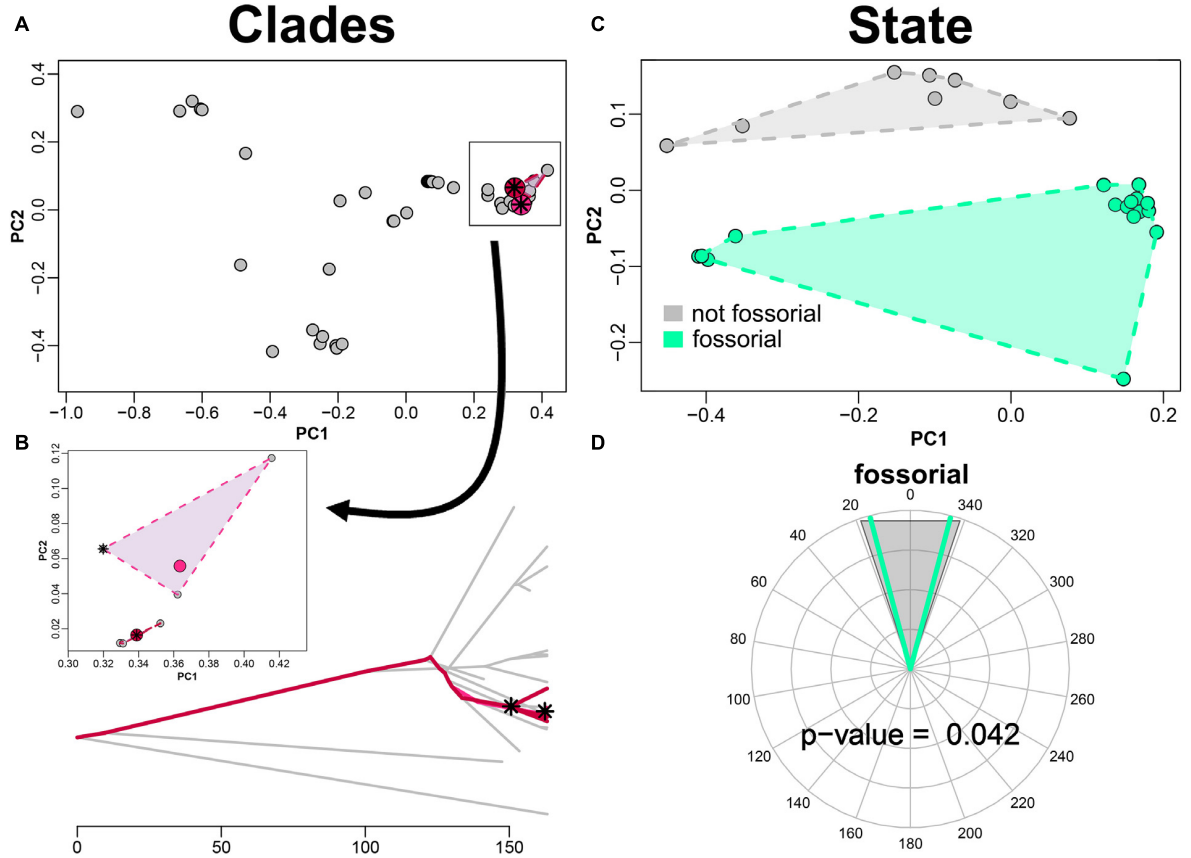

FIGURE 4 | Convergence test on fossorial mammals humeral shape. The convergence test is implemented for entire clades **(A,B)** and for fossorial species as they appear sparsely on the talpid tree **(C,D)**. PC plots appear in the upper row **(A,C)**. **(B)** phenogram describing the path of the convergent clades. **(D)** angle between the fossorial species as compared to the random distribution of angles obtained shuffling the states across species in the tree. The asterisks represent the ancestral states of the clades found to converge. The pink and purple dots represent the mean phenotype of the species within the respective clades found to converge.

As for the "state" case, the mean angle between species within the "fossorial" category becomes 0.404 degrees/myr by adding performance variables, which is significant ($p = 0.042$; **Figures 4C,D**).

DISCUSSION

Shape analysis showed the presence of a mixture of taxonomic and functional signals (see **Figure 2**). All the functional groups occupied different regions of the morphospace, suggesting the absence of a significant convergent signal in the humeral shape of fossorial mammals. This was confirmed by the *search.conv()* analysis which did not recover evidence of convergence across our morphological sample. This result suggests that fossorial mammals were able to find different solutions to a similar adaptive challenge: the exploitation of the underground. In this case natural selection has produced some of the most divergent and highly derived humeral morphologies among vertebrates (Luo and Wible, 2005; Piras et al., 2015).

Biological structures showing morphological similarity, despite phylogenetic distance, might be used for different purposes. A striking example is represented by the marsupial *N. philcreaseri* and the placental chrysochlorids, these two taxa share great expansion of the medial epicondyle and the deltopectoral process. In fact, both *N. philcreaseri* or the chrysochlorids heavily rely on the m. triceps and m. pectoralis action during the power stroke, as evidenced by the enlarged deltopectoral crest and by a similar orientation of these muscles in the these taxa (Jenkins, 1970; Warburton, 2006; Piras et al., 2015; Beck et al., 2016). However, on the medial epicondyle two different muscles groups insert. In the chrysochlorids the m. latissimus dorsi inserts on the medial epicondyle, whereas in the marsupial moles the m. latissimus dorsi inserts on the fascia of the elbow-forearm rather than on the medial epicondyle, where different flexor muscles insert (Warburton, 2006; Beck et al., 2016). This adaptation is unique to the marsupial moles and improves the mechanical advantage of the m. latissimus dorsi for flexion of the shoulder and the effect of the elbow flexion (Warburton, 2006). In this context, it is not surprising that *N. philcreaseri*, despite the morphological similarities displays different stress distributions to chrysochlorids. Furthermore, our analysis did not identify any morpho-functional convergence between these two clades,

suggesting that marsupial- and golden-moles are optimized for different trade-offs.

We found only one instance of morpho-functional convergence accounting for trade-off measures between the Japanese and North-American fossorial moles (*Mogera*, *Scalopus*, and *Scapanus* genera, see **Figure 4**). This result strongly suggests that fossorial mammals evolved around multiple different optima rather than around a single adaptive peak, as predicted by many-to-one mapping (Losos, 2011). It is likely that natural selection favored the evolution of humeral morphologies characterized by high performance (low stress) rather than promoting the optimization of humeral mobility. However, the trade-off between humeral strength and mobility resulted in different morphologies having similar fitness in the subterranean environment (Marks and Lechowicz, 2006; Losos, 2011).

For example, the lack of significant convergence between European (genus *Talpa*) and North-American moles may reflect the longstanding separation and phylogeographic histories of these two groups (Ziegler, 1999; Sánchez-Villagra et al., 2006; Schwermann et al., 2019). Scalopine moles went extinct in Europe during the Messinian salinity crisis (Krijgsman et al., 1999), whereas European mole (Talpini) diversity rose after the crisis ended, possibly exploiting the ecological niche left empty by the extinction of the Scalopini in Eurasia (Ziegler, 1999; van den Hoek Ostende and Fejfar, 2006). In this scenario, differences in the initial conditions for the two populations (Scalopini moles survived in North-America only, with one relict species in China; *Scapanulus oweni*), the phenotypes, genetic variation and the constraints acting on the ancestral populations, may have driven the evolution of trade-off values into different pathways for the two fossorial mole sub-clades (Sansalone et al., 2018).

Yet, the lack of convergent signals between clades evolving under similar selective conditions could be the result of phylogenetic history. In such a scenario, two species might be more similar to each than to their ancestors, but the magnitude of trait changes was not great enough to rule out pre-existing interclade differences (Losos, 2011). In these cases species do not reach "complete convergence" (Herrel et al., 2004) because natural selection might optimize their phenotypes within different selective contexts (environmental conditions might not be identical), or that developmental constraints might preclude two species to evolve around the same adaptive peak.

In the present study this is exemplified by the similar medial and proximal expansion of the humerus in both *T. aculeatus* and the fossorial talpids (Jenkins, 1970). However, in the former a wide humerus is an adaptation to rotation with the limitation of abduction, providing horizontal placement of the manus to sprawl the soil. On the other hand the expansion of the humerus in Talpidae is an adaptation to its abduction with limitation of rotation providing parasagittal positioning of the hands during burrowing. Hence, the wide humerus of the echidna and the similar humeral expansion in moles evolved pointing to opposite directions and opposite functions (Gambaryan, 2000).

Many examples of convergent evolution are based on simplistic descriptions of both function and phenotypes, but accounting for trade-off measures between different behaviors under similar selective contexts may reveal more complex scenarios. Here we have shown how, contrarily to expectations, fossorial mammals display only a very limited signal of morpho-functional convergence. We have detailed means by which different factors can play key roles in excluding species from evolving toward a single adaptive optimum, as predicted by the many-to-one mapping. On the contrary, our results show that fossorial mammal lineages have found different solutions to a similar adaptive regime evolving around multiple selective peaks defined by different biomechanical trade-offs. Our investigations highlight the fact that natural selection, even operating in similar selective conditions, may fail to produce convergent phenotypes in different evolutionary lineages. In this context, future investigations of morpho-functional convergence should expand on other skeletal elements participating in performing a particular function, this would allow a greater accuracy in defining the extent of convergence.

DATA AVAILABILITY STATEMENT

The data used in all the analyses are available in **Supplementary Material**. The raw data used to generate the results form this study have been made available at: doi: 10.25952/5e65995b36b6c.

ETHICS STATEMENT

The sample used in this study is entirely composed by specimens conserved in museums, including fossils for which no ethical approval is required.

AUTHOR CONTRIBUTIONS

GS and PR conceived the study. GS, PR, SC, AP, and PP analyzed the dataset. GS, SW, SH, AP, PP, and MA sampled and processed the dataset. GS, PR, SC, and BD wrote the manuscript with contribution form all the co-authors.

FUNDING

Australian Research Council Discovery and Linkage Project funding. ARC DP170101420 (Archer & Hand).

ACKNOWLEDGMENTS

We are grateful to Virginia Cristiani for her useful comments during the manuscript preparation. We thank Tzong Hung from the Biological Resources Imaging Laboratory and Marc Wainwright from Analytical Centre, UNSW, Sydney, Jessica A. Maisano from the High-Resolution X-ray CT Facility, University of Texas, Austin, and DigiMorph.org, Christiane Denys from Museum National d'Histoire Naturelle, Paris, Jim Dines from the Los Angeles County Museum, Shin-ichiro Kawada from Tokyo Natural History Museum, Emmanuel Robert from Lyon University, Lorenzo Quaglietta from Jardim

Botanico Tropical/IICT, Lisboa, Ursula Goelich from Wien Natural History Museum, Ugo Messana and Enrico Francucci from Studio Dentistico Messana. We are grateful to Ronald Eng and Timothy C. Cox from the Bourke Museum, Seattle, US. We are grateful to the two referees for their useful comments.

SUPPLEMENTARY MATERIAL

The Supplementary Material for this article can be found online at: https://www.frontiersin.org/articles/10.3389/feart.2020.00112/full#supplementary-material

REFERENCES

Alfaro, M. E., Bolnick, D. I., and Wainwright, P. C. (2004). Evolutionary dynamics of complex biomechanical systems: an example using the four-bar mechanism. *Evolution* 58, 495–503. doi: 10.1111/j.0014-3820.2004.tb01673.x

Alfaro, M. E., Bolnick, D. I., and Wainwright, P. C. (2005). Evolutionary consequences of many-to-one mapping of jaw morphology to mechanics in labrid fishes. *Am. Nat.* 165, E140–E154. doi: 10.1086/429564

Archer, M., Beck, R., Gott, M., Hand, S., Godthelp, H., and Black, K. (2010). Australia's first fossil marsupial mole (Notoryctemorphia) resolves controversies about their evolution and palaeoenvironmental origins. *Proc. R. Soc. B* 278, 1498–1506. doi: 10.1098/rspb.2010.1943

Attard, M. R., Wilson, L. A., Worthy, T. H., Scofield, P., Johnston, P., Parr, W. C., et al. (2016). Moa diet fits the bill: virtual reconstruction incorporating mummified remains and prediction of biomechanical performance in avian giants. *Proc. R. Soc. B* 283:20152043. doi: 10.1098/rspb.2015.2043

Barnosky, A. D. (1981). A skeleton of Mesoscalops (Mammalia, Insectivora) from the miocene deep river formation, Montana, and a review of the proscalopid moles: evolutionary, functional, and stratigraphic relationships. *J. Vertebr. Paleontol.* 1, 285–339. doi: 10.1080/02724634.1981.10011904

Barnosky, A. D. (1982). Locomotion in moles (Insectivora, Proscalopidae) from the middle Tertiary of North America. *Science* 216, 183–185. doi: 10.1126/science.216.4542.183

Beck, R. M., Warburton, N. M., Archer, M., Hand, S. J., and Aplin, K. P. (2016). Going underground: postcranial morphology of the early Miocene marsupial mole *Naraboryctes philcreaseri* and the evolution of fossoriality in notoryctemorphians. *Mem. Mus. Vic.* 74, 151–171. doi: 10.24199/j.mmv.2016.74.14

Bi, S., Zheng, X., Wang, X., Cignetti, N. E., Yang, S., and Wible, J. R. (2018). An Early Cretaceous eutherian and the placental–marsupial dichotomy. *Nature* 558:390. doi: 10.1038/s41586-018-0210-3

Bookstein, F. L. (1991). *Morphometrics Tools for Landmark Data*. Cambridge, MA: Cambridge University Press.

Castiglione, S., Serio, C., Tamagnini, D., Melchionna, M., Mondanaro, A., Di Febbraro, M., et al. (2019). A new, fast method to search for morphological convergence with shape data. *PLoS One* 14:e0226949. doi: 10.1371/journal.pone.0226949

Castiglione, S., Tesone, G., Piccolo, M., Melchionna, M., Mondanaro, A., Serio, C., et al. (2018). A new method for testing evolutionary rate variation and shifts in phenotypic evolution. *Met. Ecol. Evol.* 62, 181–110. doi: 10.1111/2041-210X.12954

Dickson, B. V., and Pierce, S. E. (2019). Functional performance of turtle humerus shape across an ecological adaptive landscape. *Evolution* 73, 1265–1277. doi: 10.1111/evo.13747

Dobson, G. E. (1882). A monograph of the Insectivora. Systematic and anatomical. *J. Van Voorst.* 12, 204–206. doi: 10.1080/00222938309459613

Edwards, L. F. (1937). Morphology of the forelimb of the mole (*Scalopus aquaticus*, L.) in relation to its fossorial habits. *Ohio J. Sci.* 37, 20–41.

Freeman, R. A. (1886). The anatomy of the shoulder and upper arm of the mole (talpa europaea). *J. Anat. Physiol.* 20, 201–219.

Gambaryan, P. P. (2000). A unique case of convergency in mammals. *Trudy Zoologicheskogo Instituta* 286, 41–44.

Gambaryan, P. P., Gasc, J. P., and Renous, S. (2002). Cinefluorographical study of the burrowing movements in the common mole, *Talpa europaea* (Lipotyphla, Talpidae). *Russ. J. Ther.* 1, 91–109. doi: 10.15298/rusjtheriol.1.2.03

Gasc, J. P., Jouffroy, F. K., Renous, S., and Blottnitz, F. V. (1986). Morphofunctional study of the digging system of the Namib Desert golden mole (Eremitalpa granti namibensis): cinefluorographical and anatomical analysis. *J. Zool.* 208, 9–35. doi: 10.1111/j.1469-7998.1986.tb04706.x

Goodall, C. (1991). Procrustes methods in the statistical analysis of shape. *J. R. Stat. Soc.* 53, 285–339. doi: 10.1111/j.2517-6161.1991.tb01825.x

Gunnel, G. F., Bown, T. M., Hutchinson, J. H., and Bloch, J. I. (2008). "Lipotyphla," in *Evolution of Tertiary Mammals of North America, Volume 2: Small Mammals, Xenarthrans, and Marine Mammals*, eds C. M. Janis, G. F. Gunnell, and M. D. Uhen (Cambridge, MA: Cambridge University Press), 89–125.

Harmon, L. J., Kolbe, J. J., Cheverud, J. M., and Losos, J. B. (2005). Convergence and the multidimensional niche. *Evolution* 59, 409–421. doi: 10.1111/j.0014-3820.2005.tb00999.x

Herrel, A., Vanhooydonck, B., and Van Damme, R. (2004). Omnivory in lacertid lizards: adaptive evolution or constraint? *J. Evol. Biol.* 17, 974–984. doi: 10.1111/j.1420-9101.2004.00758.x

Hildebrand, M., Bramble, D. M., Liem, K. F., and Wake, D. B. (1985). *Functional Vertebrate Morphology*. Cambridge, MA: Belknap Press of Harvard University Press.

Jenkins, F. A. (1970). Limb movements in a monotreme (*Tachyglossus aculeatus*): a cineradiographic analysis. *Science* 168, 1473–1475. doi: 10.1126/science.168.3938.1473

Krijgsman, W., Hilgen, F. J., Raffi, I., Sierro, F. J., and Wilson, D. S. (1999). Chronology, causes and progression of the Messinian salinity crisis. *Nature* 400:652. doi: 10.1038/23231

Losos, J. B. (2011). Convergence, adaptation, and constraint. *Evolution* 65, 1827–1840. doi: 10.1111/j.1558-5646.2011.01289.x

Luo, Z. X. (2015). "Origin of the mammalian shoulder," in *Great Transformations: Major Events in the History of Vertebrate Life*, eds K. P. Dial, N. Shubin, and E. L. Brainerd (Chicago, IL: The University of Chicago Press), 167–187.

Luo, Z. X., Chen, P., Li, G., and Chen, M. (2007). A new eutriconodont mammal and evolutionary development in early mammals. *Nature* 446:288. doi: 10.1038/nature05627

Luo, Z. X., and Wible, J. R. (2005). A late jurassic digging mammal and early mammalian diversification. *Science* 308, 103–107. doi: 10.1126/science.1108875

Luo, Z. X., Yuan, C. X., Meng, Q. J., and Ji, Q. (2011). A Jurassic eutherian mammal and divergence of marsupials and placentals. *Nature* 476:442. doi: 10.1038/nature10291

Maddison, W. P., and Maddison, D. R. (2015). *Mesquite: A Modular System for Evolutionary Analysis. Version 3.02*.

Marcy, A. E., Hadly, E. A., Sherratt, E., Garland, K., and Weisbecker, V. (2016). Getting a head in hard soils: convergent skull evolution and divergent allometric patterns explain shape variation in a highly diverse genus of pocket gophers (Thomomys). *BMC Evol. Biol.* 16:207. doi: 10.1186/s12862-016-0782-1

Marks, C. O., and Lechowicz, M. J. (2006). Alternative designs and the evolution of functional diversity. *Am. Nat.* 167, 55–66. doi: 10.1086/498276

Moen, D. S. (2019). What determines the distinct morphology of species with a particular ecology? The roles of many-to-one mapping and trade-offs in the evolution of frog ecomorphology and performance. *Am. Nat.* 194, E81–E95. doi: 10.1086/704736

Neaux, D., Sansalone, G., Ledogar, J. A., Heins-Ledogar, S., Luk, T., and Wroe, S. (2018). Basicranium and face: assessing the impact of morphological integration on primate evolution. *J. Hum. Evol.* 118, 43–55. doi: 10.1016/j.jhevol.2018.02.007

Nevo, E. (1979). Adaptive convergence and divergence of subterranean mammals. *Annu. Rev. Ecol. Syst.* 10, 269–308. doi: 10.1146/annurev.es.10.110179.001413

O'Leary, M. A., Bloch, J. I., Flynn, J. J., Gaudin, T. J., Giallombardo, A., Giannini, N. P., et al. (2013). The placental mammal ancestor and the post–K-Pg radiation of placentals. *Science* 339, 662–667. doi: 10.1126/science.1229237

Parr, W. C. H., Wroe, S., Chamoli, U., Richards, H. S., McCurry, M. R., Clausen, P. D., et al. (2012). Toward integration of geometric morphometrics and computational biomechanics: new methods for 3D virtual reconstruction and quantitative analysis of finite element models. *J. Theor. Biol.* 301, 1–14. doi: 10.1016/j.jtbi.2012.01.030

Phillips, M. J., Bennett, T. H., and Lee, M. S. (2009). Molecules, morphology, and ecology indicate a recent, amphibious ancestry for echidnas. *Proc. Natl. Acad. Sci. U.S.A.* 106, 17089–17094. doi: 10.1073/pnas.0904649106

Piras, P., Sansalone, G., Teresi, L., Kotsakis, T., Colangelo, P., and Loy, A. (2012). Testing convergent and parallel adaptations in talpids humeral mechanical performance by means of geometric morphometrics and finite element analysis. *J. Morphol.* 273, 696–711. doi: 10.1002/jmor.20015

Piras, P., Sansalone, G., Teresi, L., Moscato, M., Profico, A., Eng, R., et al. (2015). Digging adaptation in insectivorous subterranean eutherians. The enigma of M esoscalops montanensis unveiled by geometric morphometrics and finite element analysis. *J. Morphol.* 276, 1157–1171. doi: 10.1002/jmor.20405

Polly, P. D., Stayton, C. T., Dumont, E. R., Pierce, S. E., Rayfield, E. J., and Angielczyk, K. D. (2016). Combining geometric morphometrics and finite element analysis with evolutionary modeling: towards a synthesis. *J. Vertebr. Paleontol.* 36:e1111225. doi: 10.1080/02724634.2016.1111225

Puttick, G. M., and Jarvis, J. U. (1977). The functional anatomy of the neck and forelimbs of the Cape golden mole, *Chrysochloris asiatica* (Lipotyphla: Chrysochloridae). *Afr. Zool.* 12, 445–458. doi: 10.1080/00445096.1977.11447589

R Core Team (2019). *R: A Language and Environment for Statistical Computing, v. 3.5.3*.

Raia, P., Castiglione, S., Serio, C., Mondanaro, A., Melchionna, M., Di Febbraro, M., et al. (2019). *RRphylo: Phylogenetic Ridge Regression Methods for Comparative Studies. R package version 2.3.0*.

Rayfield, E., Norman, D. B., Horner, C. C., Horner, J. R., Smith, P. M., Thomason, J. J., et al. (2001). Cranial design and function in a large theropod dinosaur. *Nature* 408, 1033–1037. doi: 10.1038/35059070

Regnault, S., and Pierce, S. E. (2018). Pectoral girdle and forelimb musculoskeletal function in the echidna (*Tachyglossus aculeatus*): insights into mammalian locomotor evolution. *R. Soc. Open Sci.* 5:181400. doi: 10.1098/rsos.181400

Renaud, S., Ledevin, R., Pisanu, B., Chapuis, J. L., Quillfeldt, P., and Hardouin, E. A. (2018). Divergent in shape and convergent in function: adaptive evolution of the mandible in Sub-Antarctic mice. *Evolution* 72, 878–892. doi: 10.1111/evo.13467

Rohlf, F. J., and Slice, D. (1990). Extensions of the procrustes method for the optimal superimposition of landmarks. *Syst. Biol.* 39, 40–59. doi: 10.2307/2992207

Rowe, T., Rich, T. H., Vickers-Rich, P., Springer, M., and Woodburne, M. O. (2008). The oldest platypus and its bearing on divergence timing of the platypus and echidna clades. *Proc. Natl. Acad. Sci. U.S.A.* 105, 1238–1242. doi: 10.1073/pnas.0706385105

Sánchez-Villagra, M. R., Horovitz, I., and Motokawa, M. (2006). A comprehensive morphological analysis of talpid moles (Mammalia) phylogenetic relationship. *Cladistics* 22, 59–88. doi: 10.1111/j.1096-0031.2006.00087.x

Sansalone, G., Colangelo, P., Kotsakis, T., Loy, A., Castiglia, R., Bannikova, A. A., et al. (2018). Influence of evolutionary allometry on rates of morphological evolution and disparity in strictly subterranean moles (Talpinae, Talpidae, Lipotyphla, Mammalia). *J. Mamm. Evol.* 25, 1–14. doi: 10.1007/s10914-016-9370-9

Sansalone, G., Colangelo, P., Loy, A., Raia, P., Wroe, S., and Piras, P. (2019). Impact of transition to a subterranean lifestyle on morphological disparity and integration in talpid moles (Mammalia. Talpidae). *BMC Evol. Biol.* 19:179. doi: 10.1186/s12862-019-1506-0

Schlager, S. (2014). *Morpho: Calculations and visualisations related to Geometric Morphometrics. R-package version 2.0*.

Schwermann, A. H., He, K., Peters, B. J., Plogschties, T., and Sansalone, G. (2019). Systematics and macroevolution of extant and fossil scalopine moles (Mammalia, Talpidae). *Palaeontology* 62, 661–676. doi: 10.1111/pala.12422

Stayton, C. T. (2009). Application of thin-plate spline transformations to finite elements models, or, how to turn a bog turtle into a spotted turtle to analyze both. *Evolution* 63, 1348–1355. doi: 10.1111/j.1558-5646.2009.00655.x

Tsang, L. R., Wilson, L. A., Ledogar, J., Wroe, S., Attard, M., and Sansalone, G. (2019). Raptor talon shape and biomechanical performance are controlled by relative prey size but not by allometry. *Sci. Rep.* 9:7076. doi: 10.1038/s41598-019-43654-0

Tseng, Z. J., and Flynn, J. J. (2018). Structure-function covariation with nonfeeding ecological variables influences evolution of feeding specialization in Carnivora. *Sci. Adv.* 4:eaao5441. doi: 10.1126/sciadv.aao5441

van den Hoek Ostende, L. W., and Fejfar, O. (2006). Erinaceidae and Talpidae (Erinaceomorpha, Soricomorpha, Mammalia) from the lower miocene of merkur-nord (Czech Republic, MN 3). *Beiträge zur Paläontologie* 30, 175–203.

Wainwright, P. C., Alfaro, M. E., Bolnick, D. I., and Hulsey, C. D. (2005). Many-to-one mapping of form to function: a general principle in organismal design? *Integr. Comp. Biol.* 45, 256–262. doi: 10.1093/icb/45.2.256

Warburton, N. (2003). *Functional Morphology and Evolution of Marsupial Moles (Marsupialia: Notoryctemorphia)*. Doctoral Thesis, University of Western Australia, Perth.

Warburton, N. (2006). Functional morphology of marsupial moles (Marsupialia: Notoryctidae). *Verhandlungen Naturwissenschaftlichen Vereins Hamburg* 42, 39–149.

Wiley, D. F., Amenta, N., Alcantara, D. A., Ghosh, D., Kil, Y. J., Delson, E., et al. (2005). Evolutionary morphing. *Proc. IEEE Visual.* 5, 431–438. doi: 10.1109/VISUAL.2005.1532826

Ziegler, R. (1999). "Order insectivora," in *The Miocene Land Mammals of Europe*, eds G. E. Rössner, and K. Heissig (München: Verlag Dr. Friedrich Pfeil), 53–74.

Conflict of Interest: The authors declare that the research was conducted in the absence of any commercial or financial relationships that could be construed as a potential conflict of interest.

frontiers in Earth Science

ORIGINAL RESEARCH
published: 15 May 2020
doi: 10.3389/feart.2020.00131

The Wolf From Dmanisi and Augmented Reality: Review, Implications, and Opportunities

Saverio Bartolini Lucenti[1,2], Maia Bukhsianidze[3], Bienvenido Martínez-Navarro[4,5,6] and David Lordkipanidze[3]*

[1] Earth Science Department, Paleo[Fab]Lab, University of Florence, Firenze, Italy, [2] Natural History Museum, University of Florence, Firenze, Italy, [3] Georgian National Museum, Tbilisi, Georgia, [4] IPHES, Institut Català de Paleoecologia Humana i Evolució Social, Tarragona, Spain, [5] Area de Prehistoria, Universitat Rovira i Virgili (URV), Tarragona, Spain, [6] ICREA, Barcelona, Spain

In the complex scenario of Plio–Pleistocene mammalian faunal turnovers, recent research on canids has revealed an increasingly higher number of species than previously thought. In this framework, Georgia had a key role in the biogeographic dispersion of fauna from/to Asia, Africa, and Europe. Historically attributed to *Canis etruscus*, the rich *Canis* material recovered from Dmanisi possesses certain peculiar cranial and dentognathic features, which cannot be regarded only as intraspecific variability. We revealed closer similarities between the Dmanisi wolf and the younger European *Canis mosbachensis*, rather than with other Early Pleistocene canids as *C. etruscus* and *Canis arnensis*. The discovery of a *Canis borjgali* sp. nov. in Dmanisi, with characteristics close to those of *C. mosbachensis*, changes radically the idea of *Canis lupus* evolution as it is conveyed today, invalidating the paradigm *C. etruscus*–*C. mosbachensis*–*C. lupus* lineage. Furthermore, the geographic position of Dmanisi in the Caucasian area offers interesting insights regarding the Asian canids and their dispersion into Europe and Africa, an aspect still poorly investigated. The exquisite state of preservation of the fossil from Dmanisi combined with novel 3D visualization and a digital imaging technique gives us the opportunity to increase the outreach of the research thanks to user-friendly and free tools. Here, for the first time, we employed augmented reality on a few specimens of *C. borjgali* sp. nov. through a simple web app. The extraordinary chance offered by these technologies has yet to be implemented in scientific research and dissemination, particularly in paleontology.

Keywords: Canidae, Carnivora, Georgia, augmented reality, early Pleistocene, morphology

OPEN ACCESS

Edited by:
Pasquale Raia,
University of Naples Federico II, Italy

Reviewed by:
Francesco Carotenuto,
University of Naples Federico II, Italy
Gabriele Sansalone,
University of New England, Australia

****Correspondence:***
Saverio Bartolini Lucenti
saverio.bartolinilucenti@unifi.it

Specialty section:
This article was submitted to Paleontology, a section of the journal Frontiers in Earth Science

Received: *13 January 2020*
Accepted: *07 April 2020*
Published: *15 May 2020*

Citation:
Bartolini Lucenti S, Bukhsianidze M, Martínez-Navarro B and Lordkipanidze D (2020) The Wolf From Dmanisi and Augmented Reality: Review, Implications, and Opportunities. Front. Earth Sci. 8:131. doi: 10.3389/feart.2020.00131

INTRODUCTION

In the last decades, genetic and paleontological studies have revealed an intricate evolutionary history of the genus *Canis* (Tedford et al., 2009; Koepfli et al., 2015; Viranta et al., 2017; Zrzavý et al., 2018). The genus *Canis* Linnaeus, 1758, since its early appearance in North American Late Miocene and its dispersal and radiation throughout Asia, is known to have reached the western part of Europe around 3 Ma (Lacombat et al., 2008), where the first species described is *Canis etruscus* Forsyth-Major, 1877 from several sites of Europe (Cherin et al., 2014). There

is wide consensus considering the modern wolf as the final stage of an evolutionary line starting with the Early Pleistocene *C. etruscus* through the Early–Middle Pleistocene *Canis mosbachensis* Soergel, 1925 (see inter alios Brugal and Boudadi-Maligne, 2011). Morphologically modern wolves appear in the early Middle Pleistocene of North America (Tedford et al., 2009) and in several mid Middle Pleistocene Asian and European localities (Bonifay, 1971). In the framework of the Early and Middle Pleistocene radiation of Eurasian mammals, the site of Dmanisi is celebrated for its outstanding record of early Homo Linnaeus, 1758 (Lordkipanidze et al., 2007, 2013; Krijgsman et al., 2019; Rightmire et al., 2019), for the state of preservations of the fossils (allowing molecular analyses on its fossils, Cappellini et al., 2019), and for the pivotal documentation of the biogeographic faunal dispersals between the three continents, Asia, Africa, and Europe. Indeed, the Georgian site offers a unique glimpse on the turnovers that took place around 1.8 Ma (during the late Villafranchian Land Mammal Age) (Ferring et al., 2011; Bartolini Lucenti et al., 2019; Krijgsman et al., 2019). Among the large number of mammalian taxa recovered, carnivores are abundant. At least 13 different species of the five most common families of carnivorans are represented. Of these, *Canis* (referred to *C. etruscus* by Vekua, 1995) is by far the most abundant taxon with eight almost complete crania and more than 270 cranial specimens. This rich and remarkably well-preserved sample allowed us to assess its variability, compared to that of other Early and Middle Pleistocene canids. We here suggest an early origin of modern wolves and related species, redescribing the *Canis* from Dmanisi as a new species.

MATERIALS AND METHODS

The Comparative Sample

The present study is based on the comparative morphological analysis of the medium-sized *Canis* from Dmanisi and other wolf-like canids (tribe Canini) of the Early–Middle Pleistocene from Europe. The described fossils are housed at the S. Janashia Museum of Georgia, Georgian National Museum (Tbilisi). As comparative fossil material, the late Villafranchian canids from Eurasia housed at AMNH, AUT, ICP, and IGF (see abbreviation below) were studied. This fossil comparative sample includes specimens of *Canis arnensis* Del Campana, 1913 and *C. etruscus* from the Italian sites of Olivola, Upper Valdarno Basin, Coste San Giacomo, and Pantalla (Cherin et al., 2014); *Canis apolloniensis* Koufos and Kostopoulos (1997) from Apollonia-1 (Koufos, 2018); *Canis chihliensis* and *Canis palmidens* from Yushe Basin (Rook, 1993, 1994); remains of *C. mosbachensis* Soergel, 1925 from Cueva Victoria, Vallparadís (Bartolini Lucenti et al., 2017), Pirro Nord (Petrucci et al., 2013), 'Ubeidiya (Martínez-Navarro et al., 2009), Untermassfeld (Sotnikova, 2001), and Zhoukoudian (Jiangzuo et al., 2018). The relevant literature on the late Villafranchian canids was inspected (Del Campana, 1913; Crusafont Pairó, 1950; Thenius, 1954; Torre, 1967, 1974, 1979; Bonifay, 1971; Kurtén, 1974; Pons-Moyà and Moyà-Solà, 1978; Pons-Moyà, 1981; Koufos and Kostopoulos, 1997; Wang et al., 1999; Sotnikova, 2001; Garrido and Arribas, 2008; Lacombat et al., 2008; Tedford et al., 2009; Petrucci et al., 2013; Cherin et al., 2014; Koufos, 2014, 2018; Bartolini Lucenti and Rook, 2016; Amri et al., 2017; Mecozzi et al., 2017; Jiangzuo et al., 2018). Extant specimens housed at the AMNH, MZUF, ICP, and MG-GNM (see abbreviation below) were also used for morphological and morphometrical comparisons. We examined specimens of *Canis aureus* Linnaeus, 1758, *Canis latrans* Say, 1823, *Canis lupaster* Hemprich and Ehrenberg, 1828–1834, *Canis lupus* Linnaeus, 1758, *Lupulella adusta* (Sundevall, 1847), *Lupulella mesomelas* (Schreber, 1775), and *Lycaon pictus* (Temminck, 1820).

The 3D surface scan of the fossil and extant specimens was obtained with the Artec Space Spider high-resolution 3D blue light technology scan at the Museum of Georgia and at the Paleo[Fab]Lab, Earth Science Department of the University of Florence. The 3D surface scans were subsequently elaborated in Artec Studio 12 Professional. The 3D visualization of the cranium D64 and upper and lower teeth comparison models in Augmented Reality was created following the protocols described by several authors (e.g., Etienne, 2017; Carpignoli, 2019) in Visual Studio Code ver. 1.41, using AR.js and A-Frame v. 0.9.2 (www.aframe.io).

Morphometric and Statistical Analyses

Cranial and dental measurements were taken with a digital caliper to the nearest 0.1 mm following von den Driesch (1976) with minor modifications (see abbreviations below).

We performed a principal components analysis (PCA) on a dataset of selected $\log_{10}$-transformed cranial measurements, in order to establish the morphological similarities between various canid species, both extinct (*Canis* from Dmanisi, and *C. etruscus*) and extant (*C. aureus*, *C. lupus*, *C. lupaster*, *L. adusta*, *L. mesomelas*). We then used a permutational ANOVA on the most explicative principal components to test the statistical significancy of the differences resulting from the analysis.

We compared the material of *Canis* from Dmanisi with that of other European Late Villafranchian species by means of boxplots, to inspect differences in values distribution, and statistical tests. At this purpose, selected cranial ratios were used to test for statistical difference between the sample of Dmanisi, the other fossil taxa, and the extant species of the genera *Canis* and *Lupulella*. We tested these ratios by means of permutational ANOVA computed in R statistical environment (ver. 3.6.). The difference between the samples in dental measures were tested using a permutational multivariate ANOVA (MANOVA), using the pairwise Adonis package (Martinez Arbizu, 2019) computed in R.

Site and Institutional Abbreviations

AMNH, American Museum of Natural History, New York (United States); AUT, Earth Science Department of Aristotle University of Thessaloniki; D, Dmanisi site; ICP, Institut Català de Paleontologia Miquel Crusafont, Universitat Autònoma de Barcelona (Cerdanyola del Vallès, Barcelona, Spain); IGF, Museum of Natural History, Geological and Paleontological section, the University of Florence (Italy); MG-GNM, S. Janashia Museum of Georgia, Georgian National Museum (Tbilisi, Georgia); MZUF, Museum of Natural History, "La Specola" Zoology section, University of Florence (Italy); 0X/D,

P, provisional catalog number of unregistered specimens from Dmanisi housed in MG-GNM.

Anatomical Abbreviation

Cranium

AB, height of the cranium without the sagittal crest (inion–basion); BL, basal length of the cranium; CBL, condylobasal length of the cranium; Ect, width across the zygomatic processes of the frontals; ECW, width of the muzzle at level of the upper canine; Eu, greatest neurocranium width; FL, facial length; GPW, greatest palatal width; GWOC, greatest width of occipital condyles; NcL, neurocranial length; PL, palatal length; POCW, smallest width of postorbital constriction; SCL, splanchnocranial length; SH, skull height (with sagittal crest); TL, total length of the cranium (inion-prosthion); Zyg, zygomatic breadth.

Dentition

L, mesiodistal length; LCR, upper cheek toothrow length (P1–M2); LMR, upper molar row length (M1–M2); LPR, upper premolar row length (P1–P4); tdm1, talonid of m1; trm1, trigonid of m1; W, buccolingual width.

Mandible

HR, height of the mandible ramus; LLMR, length of the lower molar row (m1–m3); LLPR, length of the lower premolar row (p1–p4); Mm1B, mandibular corpus breadth below midpoint of m1; Mm1H, mandibular corpus height distal to m1 alveolus; Mp4H, mandibular corpus height distal to p4 alveolus; m1–m2

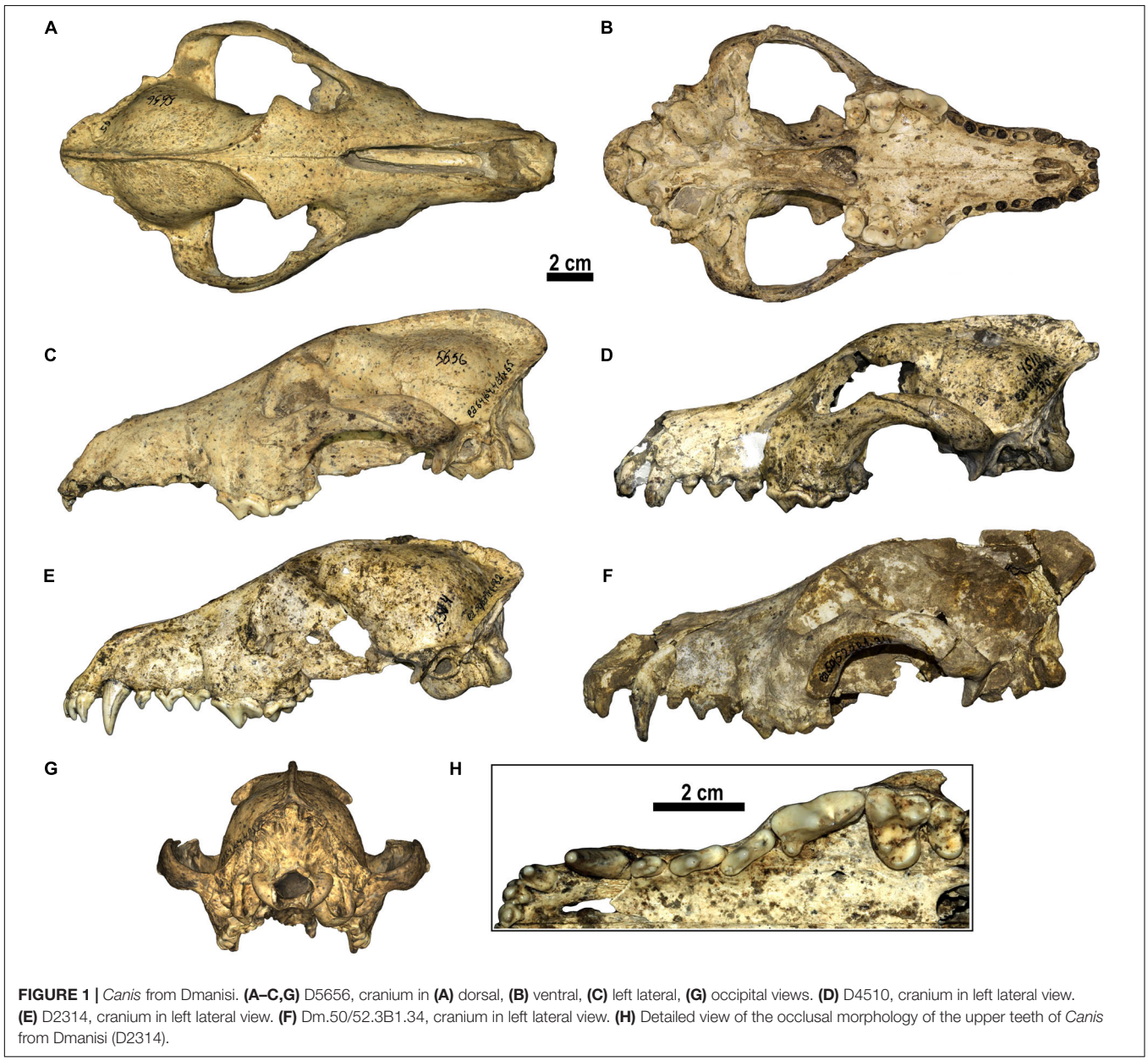

FIGURE 1 | *Canis* from Dmanisi. **(A–C,G)** D5656, cranium in **(A)** dorsal, **(B)** ventral, **(C)** left lateral, **(G)** occipital views. **(D)** D4510, cranium in left lateral view. **(E)** D2314, cranium in left lateral view. **(F)** Dm.50/52.3B1.34, cranium in left lateral view. **(H)** Detailed view of the occlusal morphology of the upper teeth of *Canis* from Dmanisi (D2314).

L, length of the first and second lower molars; p2–p4 L, length of premolar row between p2 and p4.

SYSTEMATIC PALEONTOLOGY

Order Carnivora Bowdich, 1821
Family Canidae Fischer, 1817
Subfamily Caninae Fischer, 1817
Tribe Canini Fischer, 1817
Genus *Canis* Linnaeus, 1758
Canis borjgali sp. nov.
Figures 1, **2**, **3**; **Supplementary Tables S1, S2, S3, S4**

Etymology. From the Georgian "ბორჯღალი," IPA: [bɔrdʒɣali], seven-rayed symbol of the sun and eternity typical of Georgia.

Holotype. D64, almost complete skull with I1-M2 and i1-m3.

Hypodigm. See **Supplementary Material**.

Type Locality and Age: Dmanisi, Georgia; ca 1.80 Ma.

Differential Diagnosis

A medium-sized canid, close or slightly smaller compared to *C. etruscus*, generally larger than other Villafranchian medium-sized canids. *Canis borjgali* differs from *C. arnensis* for the longer nasal bones, the well-developed frontal sinuses, the morphology of the upper molars, and the hypoconid on m1 larger than entoconid in the m1. It differs from *C. etruscus* for its overall cranial architecture, including the relatively higher cranium, the profile in lateral view, and shorter nasal bone and their morphology. It also differs in dental features, including the presence of accessory cuspulids on the lingual margin of m1 talonid. It is distinguished from *C. arnensis* and *C. etruscus* by the caudorostrally divergent medial walls of the tympanic bullae and few other dental features, including the deeper trigon basin compared to the talon basin on M1, the p3 that sets below the alveolar plane of p2 and p4. *C. borjgali* differs from *C. mosbachensis* for some less derived features, including the morphology of the second upper molar, the more arched lower toothrow, and larger metaconid on m1. *C. borjgali* possesses a marked apomorphy, i.e., the medial walls of tympanic bullae that diverge rostral direction.

Description and Comparison

The cranium is moderately elongated (**Figure 1**). Nasals are long, although not as long as in *C. etruscus* from Olivola and Pantalla. In lateral view, the profile of the cranium of *Canis* from Dmanisi is moderately arched, contrasting condition compared to the straight profile of *C. etruscus* from Olivola and Pantalla, but still less arched than in *C. mosbachensis* and *C. lupus*. The postorbital constriction is not marked for the considerable development of the frontal sinuses, which extend caudally toward the frontoparietal suture like in *C. chihliensis* from Yushe Basin, *C. etruscus* from Italy, *C. mosbachensis* from Eurasia, and *C. lupus*, although reduced compared to the latter (**Table 1**). The postorbital region is shorter compared to the elongated one of *C. lupus*, resembling other fossil species (e.g., *C. mosbachensis* from Cueva Victoria, Untermassfeld, and Zhoukoudian). The supraoccipital shield has the typical *Canis* triangular shape, although less sharp compared to that of *C. mosbachensis* from Eurasia (e.g., Cueva Victoria,ntermassfeld, and Zhoukoudian loc. 13) and extant *C. lupus* (**Table 1**). In ventral view, the tympanic bullae are oval shaped and moderately inflated. Their medial walls are not parallel, but tend to diverge in caudorostral direction, unlike *C. arnensis*, *C. etruscus*, and *C. chihliensis* from

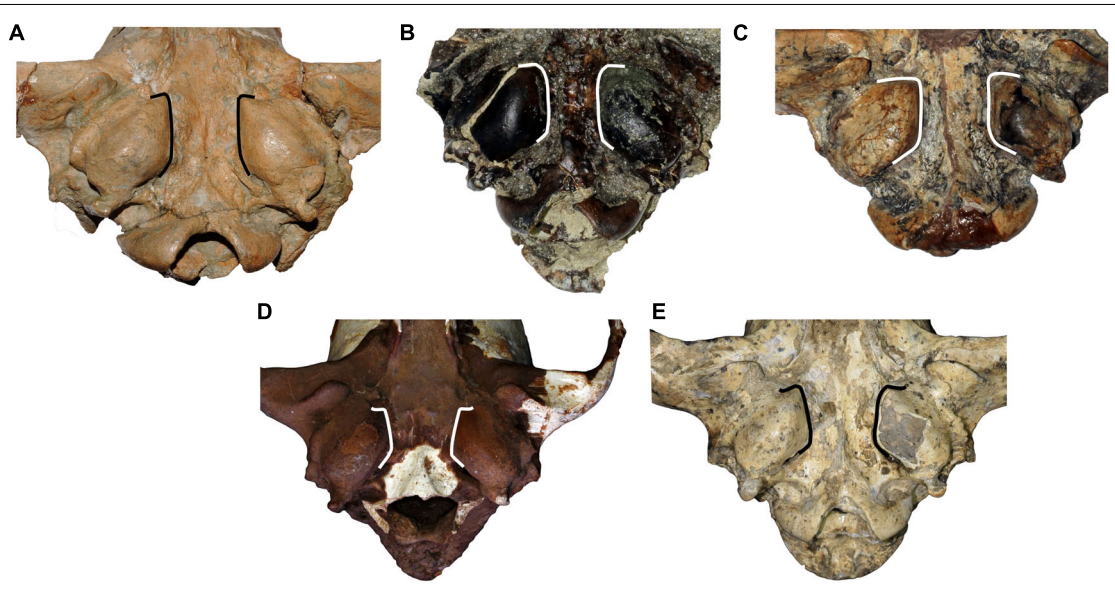

FIGURE 2 | Comparison of the tympanic region of **(A)** *C. etruscus* from Upper Valdarno, **(B)** *C. arnensis* from Poggio Rosso, **(C)** *C. chihliensis* from Yushe Basin, **(D)** *C. mosbachensis* from Cueva Victoria, and **(E)** *Canis* from Dmanisi. Note the marked divergence of the medial walls of the tympanic bullae of *C. mosbachensis* and of *Canis* from Dmanisi. This feature is not documented in the fossil taxa but present in extant wolf-related species (like *C. lupus*, *C. lupaster*, *C. aureus*, etc.).

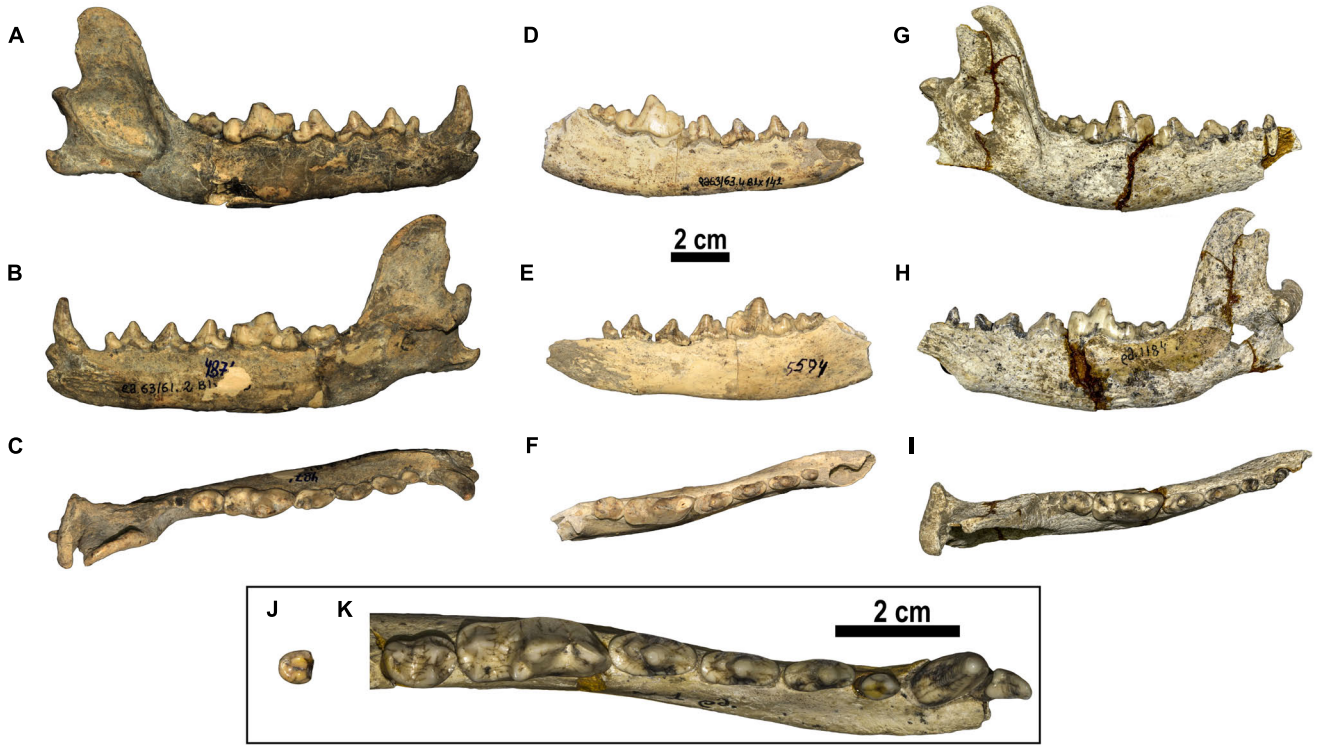

FIGURE 3 | *Canis* from Dmanisi. **(A–C)** D4871, right hemimandible in **(A)** buccal, **(B)** lingual, and **(C)** occlusal views. **(D–F)** D5594, right hemimandible in **(D)** buccal, **(E)** lingual, and **(F)** occlusal views. **(G–I)** D1184, right hemimandible in **(G)** buccal, **(H)** lingual, and **(I)** occlusal views. **(J,K)** Detailed occlusal morphology of the lower teeth of *Canis* from Dmanisi: **(J)** D372, left m3 ; and **(K)** D1, left hemimandible.

Yushe Basin (**Figure 2**). There are no diastemata between the upper teeth. The protocone of the upper carnassial is poorly individualized and relatively reduced, condition similar to that found in *C. lupus*, whereas in *C. etruscus* from Italy, the protocone is well separated from the rest of the tooth. The P4 also possesses a high and stout paracone, a sharp metastyle, and a strong mesiolingual cingulum. On the M1, the paracone is larger and higher than the metacone as in *C. apolloniensis*, *C. etruscus*, *C. mosbachensis*, and *C. lupus* (**Table 1**). As in these species, there is a well-developed metaconule, a high protocone, and a rather individualized protoconule. The protocone basin is deeper and larger than the hypocone basin, like in *C. apolloniensis*, *C. mosbachensis*, and *C. lupus*. The M1 shows a strong and well-developed buccal cingulum, expanded on both the mesial and distal sides, unlike *C. lupus* in which the cingulum is present but subdued. The morphology of the M2, in occlusal view, tends to be similar to that of *C. etruscus*, with a large buccal side. Some specimens share this more buccolingually elongated shape resembling the morphology of *C. apolloniensis* from Apollonia-1, *C. lupus*, and *C. mosbachensis* from Eurasia (**Table 1**).

The mandible of *Canis* from Dmanisi generally has a moderately deep horizontal ramus (**Figure 3**), similar in dorsoventral height and morphology to that of *C. etruscus* from Italy, unlike *C. arnensis* from Upper Valdarno, in which it is more slender. The postcanine toothrow is slightly arched (buccally convex at the p4–m1 commissure) as generally in *C. apolloniensis*, *C. etruscus*, *C. mosbachensis*, and *C. lupus*, whereas it is moderately arched in *C. arnensis* from Upper Valdarno (**Table 1**). Diastemata are absent between the lower premolars. In *Canis* from Dmanisi, the p3 generally sets in the mandible below the alveolar level of the p2 and p4, as in *C. mosbachensis* and *C. lupus* (**Figure 3** and **Table 1**). The p3 possesses a distal accessory cuspulid, generally absent in *C. apolloniensis* and *C. mosbachensis*. The p4 occlusal shape is wide and oval similar to *C. mosbachensis* from Eurasia compared the more slender shape of *C. apolloniensis* from Apollonia-1, *C. arnensis* from Upper Valdarno. The m1 paraconid is higher than the p4 protoconid, like in *C. apolloniensis* from Apollonia-1, C. *mosbachensis* from Eurasia, and *C. lupus*, in contrast to *C. arnensis* and *C. etruscus*. In the lower carnassial, the metaconid is large and individualized from the protoconid. It is larger compared to *C. apolloniensis* from Apollonia-1, *C. mosbachensis* from Eurasia, and *C. lupus*, which possess a reduced metaconid, closely attached to the large protoconid. Nevertheless, the lower carnassial is less developed compared to *C. arnensis* and *C. etruscus*. On the talonid, the hypoconid is larger than the entoconid, although the difference between them is reduced compared to that visible in *C. lupus* and *C. etruscus* (**Figure 3** and **Table 1**). The transverse cristid between the m1 hypoconid and entoconid is evident and generally sinuous, as in *C. mosbachensis* and *C. lupus*, unlike *C. arnensis* or *C. etruscus* from Italy. The m1 entoconid is more developed compared to

TABLE 1 | Summarizing table of the main craniodental features of *C. etruscus*, *C. arnensis*, *C. mosbachensis*, and *C. apolloniensis* compared to those of the *Canis* sp. from Dmanisi.

Character	*C. etruscus*	*C. arnensis*	*C. apolloniensis*	*C. mosbachensis*	*Canis* sp. from Dmanisi	References
Nasal bones, in dorsal view	very long, end well beyond maxillo-frontal suture	short, end slightly before the level of maxillo-frontal suture	–	long, end beyond maxillo-frontal suture	Long, end beyond maxillo-frontal suture	Sotnikova, 2001; Bartolini Lucenti et al., 2017
Nasal bones, in lateral view	straight profile in lateral view	gently dorsoventrally curved	–	dorsoventrally curved	slightly dorsoventrally curved	Bartolini Lucenti et al., 2017
Distal elongation of the postorbital constriction	modest	reduced	–	generally marked	modest	
Outline of nuchal crest	blunt dorsal outline	rounded outline	–	triangular, sharp-pointed	blunt dorsal outline	
Medial walls of the tympanic bullae	straight, parallel one another	straight, parallel one another	–	markedly rostrocaudally divergent	markedly rostrocaudally divergent	Bartolini Lucenti et al., 2017, here
GWOC/AB	>0.9	<0.9	–	<0.9	<0.9	Cherin et al., 2014
Axis of P3	inline with that of P4	inline with that of P4	generally deviates laterally from that of P4	generally deviates laterally from that of P4	may deviates laterally from that of P4	Koufos, 2018
M1 pararcone	larger than the metacone	slightly larger than the metacone	larger than the metacone	larger than the metacone	larger than the metacone	Sotnikova, 2001; Tedford et al., 2009
Trigon-talon basins on M1	same depth	same depth	trigon basin deeper	trigon basin deeper	trigon basin deeper	Sotnikova, 2001; Bartolini Lucenti et al., 2017
Occlusal shape of the M2	squared	short bean-like shape	generally buccolingually elongated bean-shaped	buccolingually elongated bean-shaped	generally triangular	Sotnikova, 2001
M2 metacone	smaller than the paracone	equal-sized with paracone	similar to the paracone	smaller than paracone	smaller than paracone	
Contact between M1-M2	reduced	broad	reduced	reduced	reduced	Cherin et al., 2014
Toothrow curvature	strong	slight	tend to be strong	tend to be strong	strong	Del Campana, 1913
Lower premolars protoconids	high	high	short	short	short	Bartolini Lucenti et al., 2017
p3 alveolus	at same level of p2-p4 alveoli	at same level of p2-p4 alveoli	at same level of p2-p4 alveoli	lower in the mandible, especially distally	lower in the mandible, especially distally	Sotnikova, 2001
p3 distal accessory cuspulid	developed	developed	generally reduced	generally reduced	present	
p4 secondary distal cuspulid and distal cingulid	separated	separated	fused	fused	fused	
Mesial margin of paraconid of m1	vertical and straight	vertical and straight	inclined distally and straight/slightly curved	inclined distally and straight/slightly curved	inclined distally and straight	Bartolini Lucenti et al., 2017
Hypoconid of m1	very large	similar size with entoconid	considerably larger than entoconid	larger than entoconid	larger than entoconid	Torre, 1967; Sotnikova, 2001
Transverse cristid	straight (rarely sinuous)	straight	straight (rarely sinuous)	generally sinuous	generally sinous	Sotnikova, 2001; Bartolini Lucenti et al., 2017
m1 accessory cuspids	absent	can be present	generally present	generally present	can be present	Martínez-Navarro et al., 2009; Bartolini Lucenti et al., 2017
m2 protoconid	larger than the metaconid	equal-sized with metaconid	larger than the metaconid	larger than the metaconid	larger than the metaconid	Tedford et al., 2009
m2 distolingual cuspids	absent	entoconid evident	generally absent	generally absent	absent	Martínez-Navarro et al., 2009; Tedford et al., 2009

"–" represents missing information in the literature or on the specimens.

C. apolloniensis and *C. mosbachensis*, similarly to *C. etruscus*. Accessory cuspulids may be present on the lingual side of the talonid, like in *C. apolloniensis* and *C. mosbachensis* from Eurasia. The m2 protoconid is larger compared to the metacone, unlike *C. arnensis* (**Table 1**). Distally on the m2, there is a hypoconid and a lingual cristid, generally with no accessory cuspulids, as in *C. apolloniensis* and *C. mosbachensis* (although in the latter, the m2 occlusal shape is generally more rectangular). The m3 has two cuspulids, with the buccal larger than the lingual one as in *C. etruscus* from Italy and *C. mosbachensis* from Europe, as opposed to *C. arnensis* (which has two equal-sized cuspids) and *C. lupus* (with a single and large cuspid).

RESULTS

Principal Component Analysis

The results of the PCA on cranial variables are reported in **Figure 4**. The PC1, which accounts for most of the variance (95.8%), has positive and similar loading for all the analyzed original variables (**Supplementary Table S5**), thus being positively influenced by cranial shape. Along the PC1, the modern wolves separate from other extant canids (jackals and golden wolves), the former on the positive end whereas the latter on the negative end. Extinct species (*Canis* from Dmanisi and *C. etruscus*) occupy an intermediate position, slightly overlapping with the modern wolf variation. *C. etruscus* variability on this axis is relatively limited, and its variance is included in that of *Canis* from Dmanisi. The PC2 only accounts for 1.5% of total variance, being dominated positively by greatest nasal length, splanchnocranial length, and facial length, whereas negatively by the skull height with the sagittal crest, the neurocranial length, and the width of the muzzle across the upper canines. On this axis, *C. etruscus* is considerably separated from the range of the other canids; therefore, it is visibly distinguished from *Canis* from Dmanisi. The results of the ANOVA on the PC1 is reported in **Supplementary Table S6**. The analysis confirms the significant difference between *C. lupus* and the other extant canids visible in **Figure 4**. Both *C. etruscus* and *Canis* from Dmanisi are different from the extant canids, yet there is no statistical difference between them on the PC1 (F = 0.2576, p = 0.99923), as visible from **Figure 4**.

Statistical Analyses

In both cranial and dental measures, *Canis* from Dmanisi is close to *C. etruscus* and other Early Pleistocene canids of Eurasia like *C. mosbachensis* and *C. apolloniensis*, and comparable to smaller subspecies of *C. lupus* (e.g., *Canis lupus arabs* or *Canis lupus pallipes*; **Supplementary Material**, **Supplementary Tables S1–S4**). Nevertheless, the cranial ratios (SCL/TL, GNL/TL, GWOC/AB, SH/TL) show significant difference between *C. etruscus* and *Canis* from Dmanisi (**Figure 5**). *C. etruscus* is considerably different in cranial proportions as opposed to the others species, fossil, and extant ones. The ratios of *Canis* from Dmanisi are more similar to *C. mosbachensis* and *C. lupus*. *C. arnensis* differs significantly from *C. etruscus* in three ratios (SCL/TL, GNL/TL, GWOC/AB) and cannot be distinguished from *Canis* from Dmanisi in these ratios. Nevertheless, the relative height of the skull is significantly different between *C. arnensis* and *Canis* from Dmanisi. The analysis of variance on the relative length of the nasals (**Supplementary Table S7**), the most numerous of the considered ratios, revealed to be statistically significant

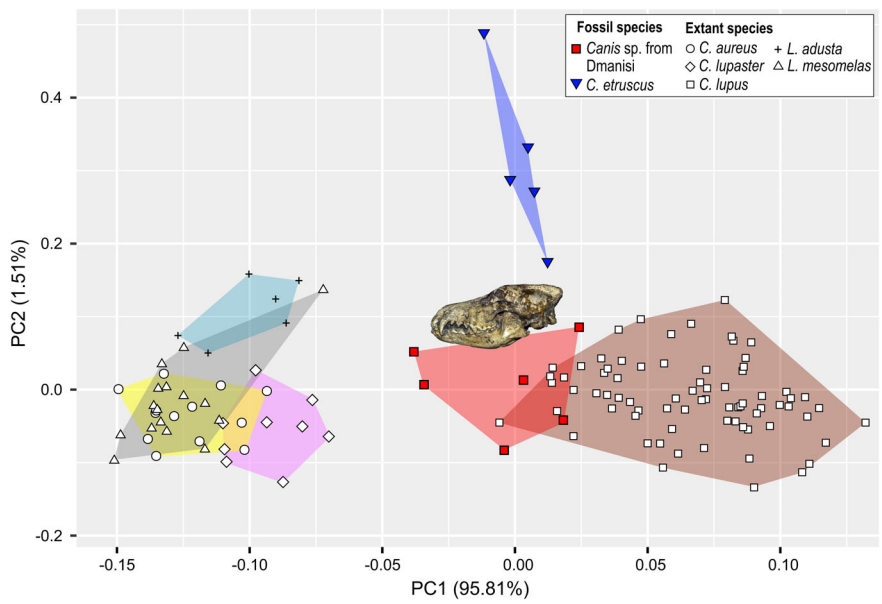

FIGURE 4 | Principal components analysis (PCA) based on selected log-transformed cranial measurements on extant and fossil species of the general *Canis* and *Lupulella*. Symbols are explained in the legend.

between *Canis* from Dmanisi and *C. etruscus* ($F = -0.102498$; $p << 0.01$; **Supplementary Table S7**). The MANOVA on dental measures (**Supplementary Tables S8, S9**) confirms the statistical difference between *Canis* from Dmanisi and *C. etruscus* (upper teeth: $F = 33.403$; $p = 0.04496$; lower teeth: $F = 19.4091$, $p = 0.04496$), on one side, and no difference between the former and *C. mosbachensis*, on the other. As for cranial ratios, the dental measures of *C. arnensis* are partially similar to *Canis* from Dmanisi, as the lower teeth values of the two species are significantly different ($F = 33.403$; $p = 0.04496$; **Supplementary Table S9**).

DISCUSSION

Taxonomic Attribution of *Canis* From Dmanisi and Implications for the Evolution of Canini

The results of the ANOVA on the PC1, the axis explaining the majority of the variability of the PCA (**Figure 4**), show no statistical distinction between *C. etruscus* and *Canis* sp. from Dmanisi (**Supplementary Table S6**). Nevertheless, the separation between these species in the plot of the principal component

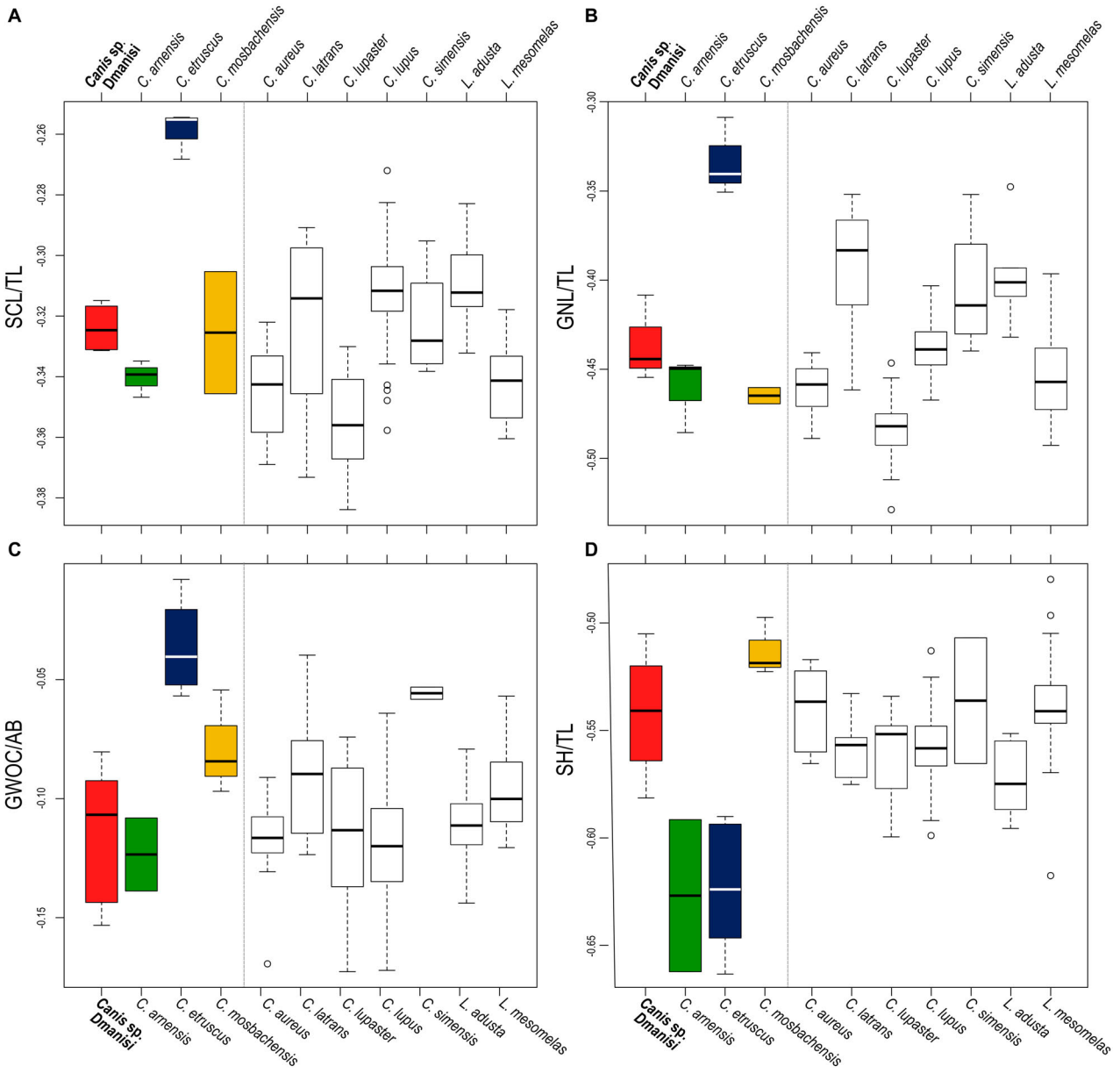

FIGURE 5 | Boxplots of selected cranial ratios: **(A)** relative length of the splanchnocranium, ScL/TL; **(B)** relative length of the nasals, GNL/TL; **(C)** width of the occipital condyles relative to the height of the cranium, GWOC/AB; **(D)** relative height of the cranium (including the sagittal crest), SH/TL. Gray dashed line separates the fossil species from the extant ones.

analysis is along the PC2 (as evident from **Figure 4**). The cranial ratios (SCL/TL, GNL/TL, GWOC/AB, and SH/TL) shown in **Figure 5** take into consideration those values that influence the dispersion of the specimens on this axis. A permutational ANOVA test on the GNL/TL, the most represented of the ratios and the most important parameter of PC2, clearly supports the distinction of *C. etruscus*. The result acknowledges the peculiarity of *C. etruscus* compared to other known fossil and extant species as noted by Cherin et al. (2014), including the sample from Dmanisi (**Supplementary Table S7**). The distinction between *Canis* sp. from Dmanisi and *C. etruscus* is confirmed also by the MANOVA on upper and lower teeth (**Supplementary Tables S8, S9**). Therefore, despite being considered as synonyms (Vekua, 1995), *C. etruscus* remarkably differs from the Georgian sample in both morphometrics and ratios measure (**Figure 5** and **Supplementary Tables S7–S9**). In this light, the material of *Canis* from Dmanisi cannot be ascribed to *C. etruscus*. Several of the morphometric and morphological results point out to a closer affinity of *Canis* from Dmanisi to the late Early Pleistocene *Canis* ex gr. *mosbachensis* (*C. mosbachensis*, e.g., from Untermassfeld, Sotnikova, 2001; Iberian Peninsula, Bartolini Lucenti et al., 2017; Pirro Nord, Petrucci et al., 2013; *C. mosbachensis variabilis* from Zhoukoudian localities, Jiangzuo et al., 2018; and *C. apolloniensis* from Apollonia-1, Koufos, 2018), rather than to *C. etruscus*. In addition to the affinity with these fossil taxa, *Canis* from Dmanisi shares also affinities with the group of wolf-related canids (see Lindblad-Toh et al., 2005), e.g., the caudorostrally divergent tympanic bullae; p3 alveolus at a lower level than p2–p4 (**Figures 1–3**). Indeed, the divergent walls of the bullae is shared by *C. lupus*, other wolf-related canids, and *C. mosbachensis* (see Bartolini Lucenti et al., 2017), as opposed to any other extinct species (**Figures 1–3**). Nevertheless, some other features of the sample from Dmanisi are more primitive, e.g., blunt or subrounded dorsal outline of the nuchal crest, reduced caudal elongation of the postorbital region; relatively developed crushing surface of the molars; and presence of an accessory cuspulid on p3. This combined pattern of features (similar to both primitive- and derived-like canids), unlike any other early Early Pleistocene canids, supports the ascription of the sample to a new species, *C. borjgali* sp. nov.

The new identity of *Canis* from Dmanisi casts some doubts on the current interpretation of the origin of modern wolf. The wide consensus in scientific literature supports that *C. lupus* and its lineage originates during the Early Pleistocene with the primitive *C. etruscus* (Torre, 1967; Kurtén, 1968; Musil, 1972; Sotnikova, 2001; Sotnikova and Rook, 2010), from which derived *C. mosbachensis* in the second half of the Early Pleistocene to first half of the Middle Pleistocene. Despite the taxonomical debate (Mecozzi et al., 2017), *C. mosbachensis* is widely considered the ancestor of *C. lupus* (in addition to the former: Brugal and Boudadi-Maligne, 2011; Sardella et al., 2014). Sotnikova and Rook (2010) were the first to suggest a possible alternative classification for the *Canis* of Dmanisi and the plausible ancestry of *C. lupus*. Here, such an interpretation is supported, as *C. etruscus* appears more primitive than *C. borjgali* and should probably be regarded as one of the earliest taxa to disperse into Europe (around the end of the Pliocene–early Pleistocene). On the contrary, *C. borjgali* might represent the ancestor or, in any case, a close-allied taxon of the clade of more derived species of Eurasian Canini (e.g., *C.* ex gr. *mosbachensis*, *C. lupus*). The morphological and morphometrical similarity between the *C. borjgali* and *C. mosbachensis* supports the idea of close relationship between the two species. Some authors (Bartolini Lucenti et al., 2017; Jiangzuo et al., 2018) reinterpreted the idea of direct ancestry between *C. mosbachensis* and *C. lupus*, putting

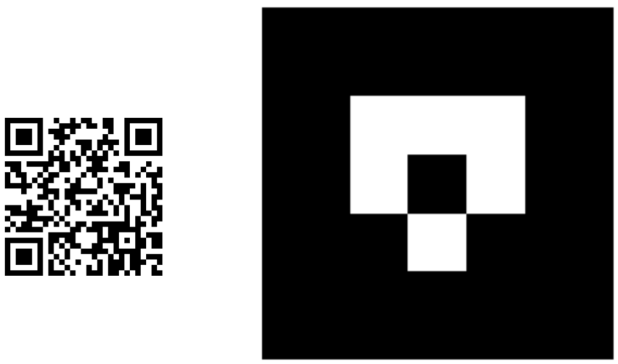

FIGURE 6 | QR code linking to the web app for Augmented Reality (AR) visualization of the 3D model of the skull D64. Instructions: Scan the QR code on the left; open the link; allow the browser to access the camera of your device; point the camera toward the marker (on the right); and wait for the model to load (up to 10 seconds). It is possible to turn the device around the marker (or to move the marker) to see different parts of the model. Best visualization performances can be achieved by printing the markers, rather pointing at them on screens. Refer to **Supplementary Material** for common issues.

FIGURE 7 | QR code and Augmented Reality (AR) marker showing 3D comparison between the upper teeth morphologies of *C. etruscus* from Upper Valdarno (blue), *Canis* from Dmanisi (red), and extant *C. lupus* (grayish). Instructions: Scan the QR code on the left; open the link; allow the browser to access the camera of your device; point the camera toward the marker (on the right); and wait for the model to load (up to 10 seconds). It is possible to turn the device around the marker (or to move the marker) to see different parts of the model. Best visualization performances can be achieved by printing the markers, rather pointing at them on screens. Refer to **Supplementary Material** for common issues.

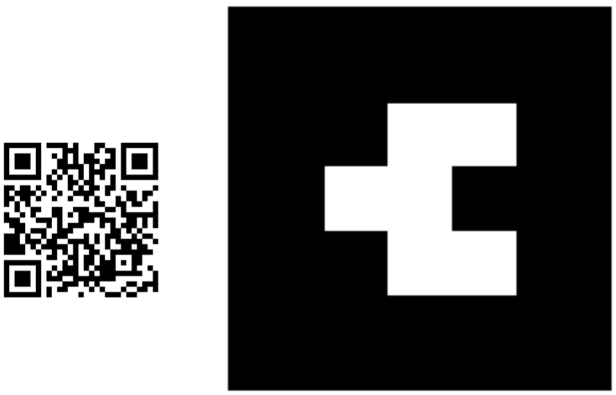

FIGURE 8 | QR code and Augmented Reality (AR) marker showing 3D comparison between the lower teeth morphologies of *C. etruscus* from Upper Valdarno (blue), *Canis* from Dmanisi (red), and extant *C. lupus* (grayish). Instructions: Scan the QR code on the left; open the link, allow the browser to access the camera of your device; point the camera toward the marker (on the right); and wait for the model to load (up to 10 seconds). It is possible to turn the device around the marker (or to move the marker) to see different parts of the model. Best visualization performances can be achieved by printing the markers, rather pointing at them on screens. Refer to **Supplementary Material** for common issues.

forward the idea that *C. mosbachensis*, as a large-ranged and time-spanned species, might actually be related to the crown species of the wolf clade (i.e., *C. latrans*, *C. lupaster*) rather than only to *C. lupus*. This might find support in recent molecular (e.g., Koepfli et al., 2015; Viranta et al., 2017) and paleontological evidence (Tedford et al., 2009). Koepfli et al. (2015) estimated the time of divergence between the *C. lupaster* and the *C. latrans*–*C. lupus* clade around 1.3 Ma and between *C. latrans* and *C. lupus* around 1.1 Ma. This suggests that the Early Pleistocene was a time of high diversification in modern canids, as is also confirmed by fossil record. Tedford et al. (2009) reported the early presence of *C. lupus* in the early Middle Pleistocene deposits of Alaska. In the broader and more intricate framework of the evolutionary history of crown-Canini, the privileged geographical position of the Caucasian region reveals its importance in canids' evolutionary history, as a noted by Sotnikova and Rook (2010). Indeed, the Caucasus sets as a crossroads between three continents, and its peculiar biotic evolution testifies to its role of key region in evolution of Old World faunas since Miocene times (Krijgsman et al., 2019). The discovery of a previously undescribed taxon in Dmanisi, with some modern features as opposed to *C. etruscus*, close but more primitive compared to *C. mosbachensis*, changes radically the idea of *C. lupus* evolution as it is conveyed today, invalidating the paradigm *C. etruscus*–*C. mosbachensis*–*C. lupus* lineage. As probable ancestor of *C.* ex gr. *mosbachensis*, *C. borjgali* sp. nov. might also represent one of the latest common ancestors of the crown clade of modern *Canis* species (*C. latrans*, *C. lupaster*, *C. lupus*).

Augmented Reality: Opportunities and Perspectives

The exquisite conservation of the fossil specimens of *C. borjgali* offers the perfect subject for the application of 3D and digital imaging techniques, like Augmented Reality (AR), thanks to the use of Artec Space Spider. AR allows interacting with

FIGURE 9 | Example of the visualization of the Augmented Reality web app in a comparison between a real cranium (that of an extant *C. lupus*) and the digital model D64 of *C. borjgali* (as visible from **Figure 6**). The digital specimen is not at the same scale of the real specimen.

computer-generated objects (*sensu lato*, from 2D pictures, videos to 3D objects) in the real world contexts in real time, allowing the users to perceive the real environment surrounding the digital rendering (Azuma, 1997; Zhou et al., 2008; Lee, 2012). Thus, differing from Virtual Reality (VR), in which users are immersed in a digital/computer-generated environment, AR can be considered a mixed-reality experience (Bower et al., 2014). It is not a brand-new technology, as its first applications date back to the 1990s. Currently, AR applications cover a diverse range of fields, from medicine to manufacturing, from aeronautics to entertainment and tourism (Bower et al., 2014). Particularly in educational sciences, AR has revealed its pedagogical potential, as much research documented (see Lee, 2012; Akçayır and Akçayır, 2017 and references therein). Nevertheless, no or little use has been made in scientific research, and its potentiality to paleontology and museology seems widely underestimated (at the very least, in Italian institutions). After the virtuous case of "Virtual Showcase" (Bimber et al., 2001, 2002), a multiuser AR display for museal exhibitions, no other use is reported in the literature. We propose here the first application of AR as support to paleontological research. Of the wide range of possible types of AR applications (see Bower et al., 2014's review), a marker-based one was chosen (for further discussion see Kan et al., 2011) to allow remote and independent use by any interested user. The application of easy-to-use, open-source, and marker-based tools like AR.js and A-Frame allows to expand the accessibility to superb fossil specimens like D64 (**Figure 6**). A smartphone, a tablet, or any device with a camera and internet connection would suffice to grant access to the actual 3D morphology of the specimens and their tiniest features, such as dental cuspules/cuspulids. The same tool can be used to perform digital comparisons between different species or specimens, like in **Figures 7**, **8**, where the upper and lower morphology of the teeth of *C. etruscus*, *C. borjgali*, and *C. lupus* can be compared as easily as would be with the three real specimens. Moreover, the use of a marker consent to even compare the 3D digital objects implemented in the app to real ones placed near the marker (for instance to a cranium of an extant canid, e.g., *C. lupus*, **Figure 9**), to directly see similarities and/or differences. In short, following the motto of the A-Frame team, "show, don't tell."

CONCLUSION AND PERSPECTIVES

The extensive record of *Canis* from Dmanisi is outstanding both for its state of preservation and abundance. Several morphological and morphometric patterns challenge the previous attribution to *C. etruscus* and favor the ascription of the taxon to a new species, *C. borjgali* sp. nov. The record of Dmanisi has already changed our understanding of evolutionary history of different species, like in the case of the rhino "*Stephanorhinus*" (Cappellini et al., 2019) or of the genus *Homo* (Rightmire et al., 2019 and reference therein) as the first discovery of the earliest Out-of-Africa hominids. The description of *C. borjgali* sp. nov. offers a new picture of the evolutionary history of modern wolves and wolf-like canids. Instead of considering the rather primitive species *C. etruscus* as the ancestor of *C. lupus*, the similarity between *C. borjgali* and *C. mosbachensis* suggests to acknowledge in the species from Dmanisi the ancestor of modern wolf-related canids. Furthermore, the present research reports the first application of Augmented Reality to a scientific paper in paleontology. Although especially used with pedagogical and educational purposes, scientific articles might benefit from the employment of AR contents thanks to its high interactivity and attractivity. Digital visualizations could be used to convey and communicate more easily the discoveries of a research, especially in life and physical sciences. In paleontology, the use of AR of digitalized fossil specimens in scientific articles might allow to increase the accessibility to superb fossils like D64 (**Figure 6**) without compromising the right and ownerships of institutions (museums or research ones) on these specimens. Undoubtedly, any 3D object, resulting from any different source (laser scan, CT scans, etc.), can be used. The implementation of web-based AR is valuable to other researchers, as it allows them to operate their observations of the 3D model better and more precisely than using 2D photos or even stereophotography. Relative height of cusps and cuspids, development of the crests, and depth of depressions are all features that become directly observable and other workers might make their own opinion and verify the finding of the paper. Digital comparisons between different species (**Figures 7**, **8**) and comparisons with real specimens placed near the marker (**Figure 9**). All of this can be achieved simply using a mobile device (smartphones, tablets, etc.). Digital technologies dealing with AR are constantly advancing while its potentials are already high; we just need to keep the pace.

DATA AVAILABILITY STATEMENT

The datasets generated for this study can be found in the ZooBank (urn:lsid:zoobank.org:pub:93965532-1069-44E1-9430-DCC5706EA312).

AUTHOR CONTRIBUTIONS

SB has studied the material together with the support of BM-N, MB, and DL. SB and MB digitalized the fossil specimens. SB designed the paper and wrote the manuscript with contributions from BM-N. DL and MB critically reviewed several parts and improved the first draft.

FUNDING

The Georgian-Italian collaborative project is supported by the Italian Ministry of Foreign Affairs (MAECI, DGSP-VI) and the Italian Embassy in Georgia. BM-N is supported by grant CGL2016-80975-P of the Spanish Ministry of Science, grant GENCAT 2017SGR 859 of the Generalitat de Catalunya, and MB by the grant FR-18-27262 of the Shota Rustaveli Georgian Science Foundation.

ACKNOWLEDGMENTS

The authors are indebted to the kindness and availability of the curators who granted access to the collections of their institutions and museum: P. Agnelli of MZUF; E. Cioppi of IGF; J. Galkin, and J. Meng of the AMNH, G. Koufos of AUT. The authors thank Prof. Rook for his constant help and support and for his advice and suggestions on the first draft of the manuscript; M. Nitti and B. Rossi of Bluefactor for their support on web developing; Paleo[Fab]Lab thanks TBNET SOLUZIONI 3D (Arezzo) for their support and kind availability; Dr. F. Carotenuto and Dr. G. Sansalone for their reviews, which greatly improved the first version of the manuscript.

SUPPLEMENTARY MATERIAL

The Supplementary Material for this article can be found online at: https://www.frontiersin.org/articles/10.3389/feart.2020.00131/full#supplementary-material

REFERENCES

Akçayır, M., and Akçayır, G. (2017). Advantages and challenges associated with augmented reality for education: a systematic review of the literature. *Edu. Res. Rev.* 20, 1–11.

Amri, L., Bartolini Lucenti, S., Mtimet, M. S., Karoui-Yaakoub, N., Ros-Montoya, S., Espigares, M. P., et al. (2017). *Canis othmanii* sp. nov. (Carnivora, Canidae) from the early Middle Pleistocene site of Wadi Sarrat (Tunisia). *CR Palevol.* 16, 774–782.

Azuma, R. T. (1997). A survey of augmented reality. *Presence* 6, 355–385.

Bartolini Lucenti, S., Alba, D. M., Rook, L., Moyà-Solà, S., and Madurell-Malapeira, J. (2017). Latest Early Pleistocene wolf-like canids from the Iberian Peninsula. *Quat. Sci. Rev.* 162, 12–25.

Bartolini Lucenti, S., Bukhsianidze, M., Lordkipanidze, D., Martínez-Navarro, B., and Rook, L. (2019). "The carnivorans guild from the Early Pleistocene site of Dmanisi (Georgia)," in *Proceedings of the XXXV Jornadas de Paleontología SEP, Baza*.

Bartolini Lucenti, S., and Rook, L. (2016). A review on the late Villafranchian medium-sized canid Canis arnensis based on the evidence from Poggio Rosso (Tuscany. Italy). *Quat. Sci. Rev.* 151, 58–71.

Bimber, O., Gatesy, S. M., Witmer, L. M., Raskar, R., and Encarnação, L. M. (2002). Merging fossil specimens with computer-generated information. *Computer* 35, 25–30.

Bimber, O., Fröhlich, B., Schmalstieg, B. D., and Encarnação, L. M. (2001). The virtual showcase. *IEEE Comput. Graph. Appl.* 21, 48–55.

Bonifay, M. F. (1971). *Carnivores quaternaires du Sud-Est de la France*. New York, NY: Éditions du Muséum.

Bowdich, T. E. (1821). *An Analysis of the Natural Classifications of Mammalia: For the Use of Students and Travellers*. Boston, MA: J. Smith.

Bower, M., Howe, C., McCredie, N., Robinson, A., and Grover, D. (2014). Augmented Reality in education–cases, places and potentials. *Edu. Media Int.* 51, 1–15.

Brugal, J. P., and Boudadi-Maligne, M. (2011). Quaternary small to large canids in Europe: taxonomic status and biochronological contribution. *Quat. Int.* 243, 171–182.

Cappellini, E., Welker, F., Pandolfi, L., Ramos-Madrigal, J., Samodova, D., Rüther, P. L., et al. (2019). Early Pleistocene enamel proteome from Dmanisi resolves Stephanorhinus phylogeny. *Nature* 574, 103–107. doi: 10.1038/s41586-019-1555-y

Carpignoli, N. (2019). *AR.js – The Simplest Way to get Cross-Browser Augmented Reality on the Web*. Available online at: https://medium.com/swlh/ar-js-the-simplest-way-to-get-cross-browser-augmented-reality-on-the-web-10cbc721debc (accessed May 11, 2019).

Cherin, M., Bertè, D. F., Rook, L., and Sardella, R. (2014). Re-defining Canis etruscus (Canidae, Mammalia): a new look into the evolutionary history of Early Pleistocene dogs resulting from the outstanding fossil record from Pantalla (Italy). *J. Mamm. Evol.* 21, 95–110.

Crusafont Pairó, M. (1950). El primer representante del género Canis en el Pontiense eurasiatico (*Canis cipio nova* sp.). *Bol. R. Soc. Esp. Hist. Nat.* 48, 43–51.

Del Campana, D. (1913). I cani pliocenici di Toscana. Tipografia successori fratelli Nistri. *Palaeont. It.* 19, 189–254.

Etienne, J. (2017). *AR-Code: a Fast Path to Augmented Reality*. Available at: https://medium.com/arjs/ar-code-a-fast-path-to-augmented-reality-60e51be3cbdf (accessed April 4, 2017).

Ferring, R., Oms, O., Agustí, J., Berna, F., Nioradze, M., Shelia, T., et al. (2011). Earliest human occupations at Dmanisi (Georgian Caucasus) dated to 1.85–1.78 Ma. *Proc. Natl. Acad. Sci. U.S.A.* 108, 10432–10436. doi: 10.1073/pnas.1106638108

Fischer, G. (1817). Adversaria zoologica. *Mem. Soc. Imp. Nat. Moscou* 5, 368–428.

Forsyth-Major, C. I. (1877). Considerazioni sulla fauna dei mammiferi pliocenici e post-pliocenici della Toscana. *Atti Soc. Tosc. Sci. Nat. Mem.* 3, 207–227.

Garrido, G., and Arribas, A. (2008). *Canis accitanus* nov. sp., a new small dog (Canidae, Carnivora, Mammalia) from the Fonelas P-1 Plio–Pleistocene site (Guadix basin, Granada, Spain). *Géobios* 41, 751–761. doi: 10.1093/mmy/myx007

Hemprich, F. G., and Ehrenberg, C. G. (1828–1834). *Symbolae Physicae, seu Icones et Descriptiones Corporum Naturalium Novorum aut Minus Cognitorum Quae ex Itineribus per Libyam, Aegyptium, Nubiam, Dongalam, Syriam, Arabiam et Habessiniam, Pars Zoologica II, Anima*. Berlin: Officina Academica.

Jiangzuo, Q., Liu, J., Wagner, J., Dong, W., and Chen, J. (2018). Taxonomical revision of fossil Canis in Middle Pleistocene sites of Zhoukoudian. Beijing, China and a review of fossil records of Canis mosbachensis variabilis in China. *Quat. Int.* 482, 93–108.

Kan, T. W., Teng, C. H., and Chen, M. Y. (2011). "QR code based augmented reality applications," in *Handbook of Augmented Reality*, ed. F. Borko (New York, NY: Springer), 339–354.

Koepfli, K. P., Pollinger, J., Godinho, R., Robinson, J., Lea, A., Hendricks, S., et al. (2015). Genome-wide evidence reveals that African and Eurasian golden jackals are distinct species. *Current Biol.* 25, 2158–2165. doi: 10.1016/j.cub.2015.06.060

Koufos, G. D. (2018). New Material and Revision of the Carnivora, Mammalia from the Lower Pleistocene Locality Apollonia 1, Greece. *Quaternary* 1:6.

Koufos, G. D. (2014). The Villafranchian carnivoran guild of Greece: implications for the fauna, biochronology and paleoecology. *Integr. Zool.* 9, 444–460. doi: 10.1111/1749-4877.12061

Koufos, G. D., and Kostopoulos, D. (1997). New carnivore material from the Plio-Pleistocene of Macedonia (Greece) with a description of a new canid. *Münchn. Geowiss. Abh.* 34, 33–63.

Krijgsman, W., Tesakov, A., Yanina, T., Lazarev, S., Danukalova, G., Van Baak, C. G. C., et al. (2019). Quaternary time scales for the Pontocaspian domain: Interbasinal connectivity and faunal evolution. *Earth Sci. Rev.* 188, 1–40.

Kurtén, B. (1968). *Pleistocene Mammals of Europe*. London: Weidenfeld and Nicolson.

Kurtén, B. (1974). A history of coyote-like dogs (Canidae, Mammalia). *Acta Zool Fenn.* 140, 1–38.

Lacombat, F., Abbazzi, L., Ferretti, M. P., Martínez-Navarro, B., Moullé, P. E., Palombo, M. R., et al. (2008). New data on the Early Villafranchian fauna from Vialette (Haute-Loire, France) based on the collection of the Crozatier Museum (Le Puy-en-Velay, Haute-Loire, France). *Quat. Int.* 179, 64–71.

Lee, K. (2012). Augmented reality in education and training. *TechTrends* 56, 13–21.

Lindblad-Toh, K., Wade, C. M., Mikkelsen, T. S., Karlsson, E. K., Jaffe, D. B., Kamal, M., et al. (2005). Genome sequence, comparative analysis and haplotype structure of the domestic dog. *Nature* 438:803. doi: 10.1038/nature04338

Linnaeus, C. (1758). *Systema Naturae per Regna Tria Naturae, Secundum Classes, Ordines, Genera, Species, Cum Characteribus, Differentiis. Synonymis, Locis. Tomus I. Editio Decima, Reformata*. Stockholm: Laurentius Salvius.

Lordkipanidze, D., de León, M. S. P., Margvelashvili, A., Rak, Y., Rightmire, G. P., Vekua, A., et al. (2013). A complete skull from Dmanisi, Georgia, and the evolutionary biology of early Homo. *Science* 342, 326–331. doi: 10.1126/science.1238484

Lordkipanidze, D., Jashashvili, T., Vekua, A., de León, M. S. P., Zollikofer, C. P., Rightmire, G. P., et al. (2007). Postcranial evidence from early Homo from Dmanisi. Georgia. *Nature* 449:305. doi: 10.1038/nature06134

Martinez Arbizu, P. (2019). *pairwiseAdonis: Pairwise Multilevel comparison using Adonis. R package version* 0.3.

Martínez-Navarro, B., Belmaker, M., and Bar-Yosef, O. (2009). The large carnivores from 'Ubeidiya (early Pleistocene, Israel): biochronological and biogeographical implications. *J. Hum. Evol.* 56, 514–524. doi: 10.1016/j.jhevol.2009.02.004

Mecozzi, B., Iurino, D. A., Berte, D. F., and Sardella, R. (2017). Canis mosbachensis (Canidae, Mammalia) from the Middle Pleistocene of Contrada Monticelli (Putignano, Apulia, southern Italy). *B. Soc. Paleontol. Ital.* 56:72.

Musil, R. (1972). Die Caniden der Stranská Skála. *Anthropos* 20, 107–112.

Petrucci, M., Cipullo, A., Martínez-Navarro, B., Rook, L., and Sardella, R. (2013). The late Villafranchian (Early Pleistocene) carnivores (Carnivora. Mammalia) from Pirro Nord (Italy). *Palaeontogr. A* 298, 113–145. doi: 10.1590/0001-3765201420140314

Pons-Moyà, J. (1981). El Canis etruscus Major (Carnivora, Mammalia) del Villafranquiense terminal de la Cueva Victoria. *Endins* 8, 43–46.

Pons-Moyà, J., and Moyà-Solà, S. (1978). La fauna de carnivoros del Pleistoceno medio (Mindel) de la Cueva Victoria (Cartagena, Murcia). *Acta Geol. Hisp.* 13, 54–58.

Rightmire, G. P., Margvelashvili, A., and Lordkipanidze, D. (2019). Variation among the Dmanisi hominins: multiple taxa or one species? *Am. J. Phys. Anthr.* 168, 481–495. doi: 10.1002/ajpa.23759

Rook, L. (1993). *I cani dell'Eurasia dal Miocene Superiore al Pleistocene Medio*. Ph.D. dissertation, Modena-Bologna-Firenze and Roma "La Sapienza" Universities, Italy.

Rook, L. (1994). The Plio-Pleistocene Old World Canis (*Xenocyon*) ex gr. *falconeri*. *Boll. Soc. Paleontol. It.* 33, 71–82.

Sardella, R., Bertè, D., Iurino, D. A., Cherin, M., and Tagliacozzo, A. (2014). The wolf from Grotta Romanelli (Apulia, Italy) and its implications in the evolutionary history of *Canis lupus* in the Late Pleistocene of Southern Italy. *Quat. Int.* 328, 179–195.

Say, T. (1823). *Account of an Expedition from Pittsburgh to the Rocky Mountains, Performed in the Years 1819 and '20, by Order of the Hon. J. C. Calhoun, Sec'y of War: under the Command of Major Stephen H. Long. From the Notes of Major Long, Mr. T. Say, and Other Gentlemen of the Exploring Party*, ed. E. James (Philadelphia, PA: H.C. Carey and I. Lea), 503.

Schreber, J. C. D. (1775). *Die Säugethiere in Abbildungen nach der Natur mit Beschreibungen*. Erlangen: Wolfgang Walther.

Soergel, W. (1925). Die Säugetierfauna des altdiluvialen Tonlages von Jockgrim in des Pfalz. *Zeits. Deut. Geol. Ges.* 77, 405–438.

Sotnikova, M., and Rook, L. (2010). Dispersal of the Canini (Mammalia, Canidae: Caninae) across Eurasia during the late Miocene to early Pleistocene. *Quat. Int.* 212, 86–97.

Sotnikova, M. V. (2001). "Remains of Canidae from the lower Pleistocene site of Untermassfeld," in *Das Pleistozän von Untermassfeld bei Meiningen (Thüringen) Teil. 2*, ed. R. D. Kahlke (Habelt Verlag: Bonn), 607–632.

Sundevall, C. J. (1847). Nya Mammalia från Sydafrika. *Ofv. K. Svenska Vet.-Akad. Forhandl. Stockholm* 3, 118–121.

Tedford, R. H., Wang, X., and Taylor, B. E. (2009). Phylogenetic systematics of the North American fossil caninae (Carnivora: Canidae). *Bull. Am. Mus. Nat. Hist.* 2009, 1–218.

Temminck, C. J. (1820). Sur le genre *Hyène*, et description d'une espèce nouvelle, découverte en Afrique. *Ann. Gen. Sci. Phys.* 3, 46–57.

Thenius, E. (1954). Die Caniden (Mammalia) aus dem Altquartär von Hundsheim (Niederösterreich) nebst Bemerkungen zur stammesgeschichte der Gattung Cuon. *N. Jb. Geol. Paläontol.* 99, 230–286.

Torre, D. (1967). I cani villafranchiani della Toscana. *Paleontogr. Ital.* 63, 113–138.

Torre, D. (1974). Affinità dentali del cane della grotta di l'Escale. *Riv. Ital. Paleontol.* 80, 147–156.

Torre, D. (1979). The Ruscinian and Villafranchian dogs of Europe. *Boll. Soc. Paleontol. Ital.* 18, 162–165.

Vekua, A. (1995). Die Wirbeltierfauna des Villafranchium von Dmanisi und Ihre biostratigraphishe bedeutung. *Jb. Röm.-Germ. Zentralmus. Mainz* 42, 77–180.

Viranta, S., Atickem, A., Werdelin, L., and Stenseth, N. C. (2017). Rediscovering a forgotten canid species. *BMC Zool.* 2:6. doi: 10.1186/s40850-017-0015-0

von den Driesch, A. (1976). A guide to the measurement of animal bones from archaeological sites. *Peabody Mus. Bull.* 1, 1–137.

Wang, X., Tedford, R. H., and Taylor, B. E. (1999). Phylogenetic systematics of the Borophaginae (Carnivora. Canidae). *Bull. Am. Mus. Nat. Hist.* 243, 1–391.

Zhou, F., Duh, H. B. L., and Billinghurst, M. (2008). "Trends in augmented reality tracking, interaction and display: a review of ten years of ISMAR," in *Proceedings of the 7th IEEE/ACM International Symposium on Mixed and Augmented Reality*, Cambridge, UK.

Zrzavý, J., Duda, P., Robovský, J., Okřinová, I., and Pavelková Řičánková, V. (2018). Phylogeny of the Caninae (Carnivora): combining morphology, behaviour, genes and fossils. *Zool. Scr.* 47, 373–389.

Conflict of Interest: The authors declare that the research was conducted in the absence of any commercial or financial relationships that could be construed as a potential conflict of interest.

frontiers in Ecology and Evolution

ORIGINAL RESEARCH
published: 27 May 2020
doi: 10.3389/fevo.2020.00139

Locomotory Adaptations in 3D Humerus Geometry of Xenarthra: Testing for Convergence

*Carmela Serio[1], Pasquale Raia[2] and Carlo Meloro[1]**

[1] Research Centre in Evolutionary Anthropology and Palaeoecology, School of Biological and Environmental Sciences, Liverpool John Moores University, Liverpool, United Kingdom, [2] Dipartimento Di Scienze Della Terra, Dell'Ambiente E Delle Risorse, Università degli Studi Di Napoli Federico II, Naples, Italy

Three-dimensional (3D) models of fossil bones are increasingly available, thus opening a novel frontier in the study of organismal size and shape evolution. We provide an example of how photogrammetry can be combined with Geometric Morphometrics (GMM) techniques to study patterns of morphological convergence in the mammalian group of Xenarthra. Xenarthrans are currently represented by armadillos, sloths, and anteaters. However, this clade shows an incredibly diverse array of species and ecomorphotypes in the fossil record, including gigantic ground sloths and glyptodonts. Since the humerus is a weight-bearing bone in quadrupedal mammals and its morphology correlates with locomotor behavior, it provides an ideal bone to gain insight into adaptations of fossil species. A 3D sample of humerii belonging to extant and fossil Xenarthra allowed us to identify a significant phylogenetic signal and a strong allometric component in the humerus shape. Although no rate shift in the evolution of the humerus shape was recorded for any clade, fossorial and arboreal species humerii did evolve at significantly slower and faster paces, respectively, than the rest of the Xenarthran species. Significant evidence for morphological convergence found among the fossorial species and between the two tree sloth genera explains these patterns. These results suggest that the highly specialized morphologies of digging taxa and tree sloths represent major deviations from the plesiomorphic Xenarthran body plan, evolved several times during the history of the group.

Keywords: photogrammetry, Xenarthra, morphological convergence, geometric morphometrics, RRphylo

OPEN ACCESS

Edited by:
Alexandra Houssaye, UMR7179 Mécanismes Adaptatifs et Evolution (MECADEV), France

Reviewed by:
Leo Botton-Divet, Humboldt University of Berlin, Germany
Sergio Fabián Vizcaíno, Consejo Nacional de Investigaciones Científicas y Técnicas (CONICET), Argentina

****Correspondence:***
Carlo Meloro
C.Meloro@ljmu.ac.uk

Specialty section:
This article was submitted to Paleontology, a section of the journal Frontiers in Ecology and Evolution

Received: *23 December 2019*
Accepted: *24 April 2020*
Published: *27 May 2020*

Citation:
Serio C, Raia P and Meloro C (2020) Locomotory Adaptations in 3D Humerus Geometry of Xenarthra: Testing for Convergence. Front. Ecol. Evol. 8:139. doi: 10.3389/fevo.2020.00139

INTRODUCTION

Species morphology varies in size and shape. These two components can be strongly correlated to each other (Shingleton et al., 2007; Figueirido et al., 2011; Voje et al., 2014; Klingenberg, 2016) and somewhat limited by the existence of evolutionary constraints (Gould, 1989; Brakefield, 2006; Arnold, 2015; Meloro et al., 2015a). In this regard, the vertebrate skeleton has been intensively investigated, because the shape of its components is greatly influenced by body size and by the constraints impinging on specific adaptations linked to body support and other essential organismal functions (e.g., locomotion, feeding). The skeleton also allows sampling ancient diversity that in many clades can greatly overcome variation of extant taxa. In fact, the appreciation of fossil diversity provides strong support for the existence of size-induced shape changes (allometry) across different taxonomic scales and several components of the skeleton (Speed and Arbuckle, 2016).

The combined effects of such size-related shape changes and the evolutionary pressure originated by adaptation might generate patterns of morphological convergence in distantly related clades (Harmon et al., 2005; Mahler et al., 2010; Losos, 2011; Meloro et al., 2015b). Convergence is more likely to take place when adaptation is at the most extreme, and it can be identified in both extant and fossil taxa (i.e., the skulls of marsupial and placental carnivores including sabertooth morphologies, Wroe and Milne, 2007; Goswami et al., 2011).

Extant Xenarthra are currently limited to 31 species falling within the two clades Cingulata (armadillos) and Pilosa (sloths and anteaters; Simpson, 1980; Engelmann, 1985; Springer et al., 2003; Delsuc et al., 2004). Yet, in the past they showed much greater phenotypic and taxonomic diversity, encompassing some 700 species overall, including the gigantic late Pleistocene ground sloths and armadillos (Prothero, 2016).[1] Although recent advances in proteomics and genomics provide new insights into Xenarthra phylogenetic history, their position within Placental mammals is still a matter of controversy (Gibb et al., 2016).

Previous morphological work provided insights into the ecology and behavior of fossil Xenathrans. Most of it was based on the study of body proportions (Bargo et al., 2000; Vizcaíno et al., 2006; Toledo et al., 2017), limb elements (Fariña et al., 2003; Milne et al., 2009; Toledo et al., 2015; Mielke et al., 2018), and the skull (Vizcaíno et al., 1998; De Iuliis et al., 2001; Bargo and Vizcaíno, 2008; Billet et al., 2011). For a full revision, see Bargo (2003); Vizcaíno et al. (2008), Amson and Nyakatura (2017), and Bargo and Nyakatura (2018).

Thanks to 3D modeling, it is currently possible to build precise replicas of fossil bones and investigate their size and shape variation with better accuracy than ever before. Applying such 3D modeling on Xenarthran limb elements is particularly welcome, given the great diversity of size and lifestyle the group experienced in its recent past (Amson and Nyakatura, 2017).

Here, we combine multiple methods for the 3D analysis and interpretation of Xenarthra humerus shape variation within a phylogenetic comparative framework. The humerus is a load-bearing postcranial element in quadrupedal mammals (Bertram and Biewener, 1992) and correlates quite strongly with body mass, locomotory, and habitat adaptations (Gingerich, 1990; Egi, 2001; Elton, 2002; Polly, 2007; Walmsley et al., 2012; Meloro et al., 2013; Elton et al., 2016; Botton-Divet et al., 2017). In Xenarthrans, the broad locomotory diversity well correlates with humerus functional morphology (Fariña and Vizcaíno, 1997; Toledo et al., 2012; de Oliveira and Santos, 2018).

We take advantage of the newly developed photogrammetry technique (Falkingham, 2012) to build a dataset of 51 Xenarthran humerus 3D models belonging to 29 species (16 extant plus 13 extinct). The advantage of photogrammetry is that it minimizes specimen handling (which is convenient for their fragile status) and allows a relatively quick data collection based on museum specimens (taking pictures for photogrammetry models might take between 5 and 10 min; Giacomini et al., 2019). On the other side, software post-processing time can still be quite long, although the development of professional software (e.g., Agisoft) and novel open access sources are making the process increasingly quicker.[2] There has been a lot of research focusing on the adequacy and the accuracy of photogrammetry method for GMM analyses (see Giacomini et al., 2019, for a recent overview). Particularly for long bones, Fau et al. (2016) demonstrated that photogrammetry provides a good level of accuracy compared to other laser scanners (e.g., structured light Artec laser or Breukmann) on relatively medium-sized vertebrate long bones.

We explored Xenarthran humerus 3D morphology using GMM within a comparative framework. This technique is now well established with a long record of research applications also on fossil mammals (Adams et al., 2004, 2013). The use of homologous points (landmarks) facilitates a comparison between species belonging to the same clade and additionally provides a powerful tool for separating and visualizing size and shape variations. GMM application to the study of Xenarthran functional morphology includes works from Monteiro and Abe (1999) focusing on the scapula or Milne et al. (2009, 2012) on humerus and femur shape.

Interestingly, the implementation of the comparative methods into GMM datasets is a relatively more recent phenomenon. Comparative methods were first introduced by Felsenstein in his seminal paper on the independent contrasts (Felsenstein, 1985). This method explores the assumption that interspecific data are not independent, since species might share a different degree of common ancestry in any macroevolutionary dataset. The effect of shared inheritance can be assessed by estimating the "phylogenetic signal" in the data. When fossil species are concerned, two major limitations occur: fossil phylogenies are morphology based, so that testing morphological hypotheses using these trees might generate a circular argument (in the majority of cases fossil dataset might exhibit higher phylogenetic signal); fossil phylogenies are generally incomplete with taxonomic confirmation generally scattered between different publications. In spite of this, early attempts demonstrated that fossil phylogenies can be incorporated to test macroevolutionary hypotheses, and their inclusion provides stronger statistical power (for early examples see: Finarelli and Flynn, 2006; Meloro et al., 2008). We provided on several occasions examples on how comparative methods can be implemented in macroevolutionary studies incorporating fossils and GMM (Meloro and Raia, 2010; Raia et al., 2010; Meloro and Slater, 2012; Piras et al., 2012). More recently, the development of new R packages (including geomorph Adams et al., 2019; and *RRphylo* Raia et al., 2020) allows to detect evolutionary rates with a high degree of accuracy (in spite of phylogenetic fossil uncertainty, e.g., Smaers et al., 2016; Castiglione et al., 2018).

We take advantage of the most recently published phylogenies for fossil sloths and armadillos in order to test hypotheses about the influence of size and locomotor behavior on humerus shape and rate of its morphological change in Xenarthra. Since behavioral and morphological convergence has been proposed for extant sloths, as well as fossil *Megatherium* and extant armadillos (Nyakatura, 2012; Billet et al., 2015), we explicitly tested convergence in humerus morphology using a

[1] https://paleobiodb.org/#/

[2] https://peterfalkingham.com/tag/photogrammetry/

novel approach that can well be applied to multivariate shape data and phylogenies inclusive of extant and fossil species (Castiglione et al., 2019).

MATERIALS AND METHODS

Studied Specimens

We built 3D models of Xenarthra humerii belonging to 29 species housed at the following museum institutions: the Natural History Museum (NHLM, London) and the Muséum National d'Histoire Naturelle (MNHN, Paris, see **Supplementary Table S1** for details).

For each specimen, we took about 200 photos based on dorsal, ventral, and lateral views using a dark background and a standard digital SLR (Nikon D5300, lens 18–140 mm). Most of the pictures were taken with the 55 mm lens setting on a fixed focus (see Giacomini et al., 2019). The software Agisoft Metashape was then employed to build 3D models, while MeshLab software (v1.3.3, 2014) was used for scaling them. The scaling was based on one single measurement (generally the maximum bone length), as recommended by Falkingham (2012). Sensitivity analyses testing relative bone proportion were performed on selected specimens of similar-sized mammalian humerii, generally providing a difference smaller than 5% when comparing measurements taken with digital caliper and those with the MeshLab software (v1.3.3, 2014).

Landmarking

The software Landmark (v. 3.0) was employed to identify on each specimen 28 landmarks (**Figure 1**). The landmarks were designed to cover main anatomical regions of the Xenarthran humerus including proximal and distal epiphyses as possible. The Landmark descriptions are in **Table 1** following anatomical nomenclature (**Figure 1**). Most of the landmarks were type 2, since humerus epiphyses do not allow to identify type 1 points. However, these were previously evaluated in Milne et al. (2009), which we followed as a baseline for our configuration (see **Table 1** and **Figure 1**). Landmarking was performed twice on a subsample of 20 specimens to detect the level of error in size and shape using Procrustes ANOVA, which in all cases turned out to be non-significant explaining less than 5% of inter-individual variation.

GMM and Comparative Methods

The 3D landmarked coordinates of the scaled models were subject to GPA (Generalized Procrustes Analysis, Rohlf and Slice, 1990). This technique removes the non-shape information related to size, position, and orientation of the specimens. GPA returns a new set of coordinates subsequently subjected to Principal Component Analysis (PCA, Rohlf and Slice, 1990). PCA decomposes the shape variation into orthogonal axes of maximum variation named PCs (Principal Components). PC vectors are used as variables in subsequent analyses. Species mean shapes were calculated before performing analyses so that our shape data represented inter-specific variation only. Humerus size was quantified using the natural logarithm (Ln) of the centroid size (=the square root of the sum of the squared distances from each landmark to the centroid of each configuration).

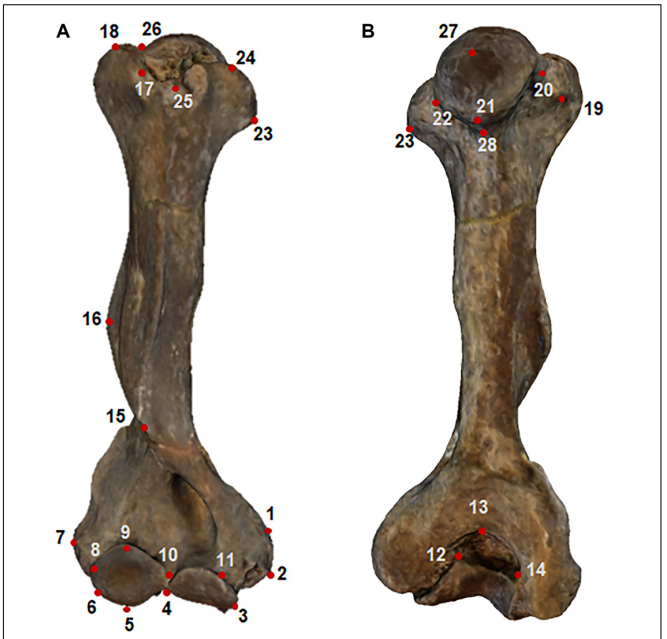

FIGURE 1 | Humerus model of Thallassocnus littoralis built using the photogrammetry method. Dots represent digitised anatomical landmarks. **(A)** frontal view, **(B)** posterior view.

We assembled two different phylogenetic trees. The first was based on molecular data following Presslee et al. (2019) and Raia et al. (2013; **Supplementary Data S1**). The second tree was based on purely morphological evidence and assembled on a backbone published in Delsuc et al. (2019); Varela et al. (2019), Boscaini et al. (2019); Fernicola et al. (2017), Herrera et al. (2017), and Gaudin and Wible (2006; **Supplementary Data S2**). We decided to use two different phylogenies because molecular vs. morphological trees may be conflicting (Cohen, 2018). For the phylogenetic position of species for both trees and references see **Supplementary Table S2**. The phylogenetic trees were calibrated by using the *scaleTree* function in the *RRphylo* package (Raia et al., 2020, species last appearance and internal node ages used for calibration are in **Supplementary Table S2**).

By using *plotGMPhyloMorphoSpace* function in the geomorph package (Adams et al., 2019), the trees were mapped into PCA in order to generate a phylomorphospace. Phylogenetic signals were quantified by using the K (for size) and the K_{multiv} (for shape) statistic (Adams, 2014).

Phylogenetic Generalized Least Squares (PGLS) regression was employed assuming Brownian motion as the mode of evolution to test for macroevolutionary allometry and differences among locomotory categories. We partitioned species into discrete stance categories as proposed by Amson et al. (2017) based on the main lifestyle of extant taxa. Tree sloths were considered as fully "arboreal." The anteaters, capable of both climbing and having a unique digging style, were classified as "intermediate" (Hildebrand, 1985; Kley and Kearney, 2007),

TABLE 1 | Landmark descriptions.

Landmark	Anatomical definitions
1	Point of maximum curvature of the medial epicondyle
2	Point of minimum curvature of the medial epicondyle
3	Trochlea bottom point
4	Point of maximum curvature in the trochlea, lower section
5	Most distal portion of the capitulum, lower section
6	Most proximal portion of the capitulum, lower section
7	Point of maximum projection of the lateral epicondyle
8	Most proximal portion of the capitulum, upper section
9	Most distal portion of the capitulum, upper section
10	Point of maximum curvature of trochlea, upper section
11	Highest point on the interior edge of the trochlea
12	Lateral point (sx) of olecranon fossa
13	Deepest point of olecranon fossa
14	Lateral point (dx) of olecranon fossa
15	Point of intersection between epicondylar ridge and deltoid crest
16	Point of maximum lateral projection of the deltoid crest
17	Proximal limit of the greater tubercle
18	Highest proximal point of the greater tubercle
19	Distal limit of the greater tubercle
20	Point of intersection between lesser tubercle and humeral head
21	Most proximal limit of the humerus head epiphyseal surface
22	Edge of the lesser tubercle intersecting the humerus head
23	Proximal limit of the lesser tubercle
24	Distal limit of the lesser tubercle
25	Bicipital sulcus
26	Point of intersection between greater tubercle and humeral head
27	Highest projection on the humerus head articular surface
28	Point of intersection between lesser tubercle and humeral neck

whereas armadillos were divided into fully "terrestrial" and "fossorial." For fossil species, we carried out an extensive revision of the literature (see **Supplementary Table S3**). Extant members of Cingulata are specialized diggers as inferred by their limb morphology (Vizcaíno and Milne, 2002; Milne et al., 2009; Marshall, 2018; Mielke et al., 2018). Other specialized diggers can be found also among Pilosa. *Glossotherium robustum* was demonstrated to be a specialized digger (Bargo et al., 2000; Vizcaíno et al., 2001; de Oliveira and Santos, 2018). On the contrary, other ground sloths were best adapted to a terrestrial lifestyle (Bargo et al., 2000; Vizcaíno et al., 2001; de Oliveira and Santos, 2018). Extant sloths (*Bradypus* and *Choloepus*) are known as tree sloths for their strictly arboreal lifestyle (Montgomery, 1985; Chiarello, 2008; Toledo et al., 2012), as well as the anteaters (White, 2010), but the latter are capable of above branch locomotion (Nyakatura, 2011). Locomotor categories were equally employed to test for convergence.

We assessed the rate of humerus size and shape evolution by using the *RRphylo* function (Castiglione et al., 2018). *RRphylo* returns a vector of evolutionary rates for all branches in the tree and a vector (or a matrix if the phenotype is multivariate, i.e., with the shape data) of ancestral states estimated for each node. We applied *RRphylo* on both size (log-transformed) and shape (as PC scores and by using size as covariate).

To search for possible shifts in the evolutionary rates between clades or locomotory categories we used the function *search.shift* (Castiglione et al., 2018). First, we applied *search.shift* on shape and size under the "clade" condition. In this case, the function compares the average absolute evolutionary rate of a specific clade with the rest of the tree. The significance level is assessed by randomizations. Then, we applied *search.shift* on shape and size under the "sparse" condition to test for differences in evolutionary rates among locomotor categories. Under this condition, the function tests if species having the same state evolve differently from the others.

Eventually, we applied the new function *search.conv* (Castiglione et al., 2019) to test for morphological convergence. This function tests morphological convergence by assessing the angle between phenotypic vectors (vectors of PC scores) between species and comparing this angle to a random expectation. Given two phenotypic vectors (here PC scores), the cosine of angle θ between them represents the correlation coefficient (Zelditch et al., 2012). Under the Brownian Motion, θ is expected to be proportionally related to phylogenetic distance. Yet, convergence violates this assumption. The new method *search.conv,* calculates the θ angles between entire clades ("automatic") or species under the same state ("state"). It tests whether the mean θ between the species evolving under a specific state or belonging to a single clade is smaller than expected by chance, and whether θ divided by the mean phylogenetic distance among convergent tips is smaller than expected. We applied *search.conv* to test for morphological convergence between fully arboreal sloths and the intermediate anteaters, and species evolving under fossorial lifestyles. Then, we tested convergence between the two tree sloths: *Bradypus* and *Choloepus*.

To test the robustness of our results to phylogenetic uncertainty and sampling effects, we applied the new implemented function *overfitRR* (Serio et al., 2019; Melchionna et al., 2020) in the *RRphylo* package (Raia et al., 2020). Under this function, the original tree is trimmed of a predetermined number of species (here 5%) and the position of tips is changed randomly by up to two nodes away from its original placement. For instance, a simple phylogenetic tree [(A, B), C], would be changed in [(C, B), A] or [(A, C), B] tree topology. In addition, the function changes the node age, randomly, within a range between the age of the focal node immediate ancestor node and the age of its older daughter node. We ran *overfitRR* with 100 iterations. At each iteration, the function swapped 5% of the tree size of tips and changed in age 5% of the tree size of tree nodes, then used a new phylogenetic tree to perform *search.conv* to either confirm or reject any instance of significant morphological convergence. All the analyses were performed both with the molecular and the morphological phylogenies.

RESULTS

Geometric Morphometric Results

GMM returned 28 PCs (**Supplementary Table S4**), of which the first 13 explained up to 95.80% of the shape variation. More in detail, PC1 and PC2 explained 53.58% and 15.72%, respectively,

and they show a degree of separation in humerus shape between Cingulata and Folivora, while Vermilingua clade overlap with the latter (**Figure 2**).

Deformations described by PC1 are related to the relative elongation of the humerus. Arboreal species occupy positive scores of PC1 and are characterized by a relatively longer and slender humerus morphology. Both proximal and distal epiphyses are reduced. This configuration is typical of the suspensory tree sloths (genera *Bradypus* and *Choloepus*). On the contrary, PC1 negative scores describe short and stocky humerus shape. The head and both the greater and lesser tuberosities are more expanded, as well as the trochlea, capitulum, and epicondyles (**Figure 2**).

Changes along PC2 axis described differences among Xenarthra clades. Folivora and Vermilingua occupy positive PC2 scores. In these clades, the humerus head is slender, the curvature between the deltoid crest and the distal part is wider and developed backward. On the negative scores of PC2, Cingulata shows distinct humerus head components with the distal part longer and slender (**Figure 2**).

Comparative Methods

When applying the molecular tree, the phylogenetic signal for both shape and size was statistically significant. The observed K (size) and K_{multiv} (shape) are 0.997 and 0.453 (p value = 0.001), respectively. Very similar results were obtained when the morphological tree was used (K size = 0.939; p value = 0.001, K_{multiv} shape = 0.497, p value = 0.001).

Differences in shape were explained by differences in size, as resulted by using Procrustes ANOVA without (**Table 2A**) and with the addition of the phylogenetic effect of the morphological tree (**Table 2C**). The allometric effect remained significant in Folivora and Cingulata when the phylogenetic relationship was accounted for (**Table 3** and **Figure 3**). Procrustes ANOVA showed a significant impact of locomotor categories on shape, either without considering phylogenetic effects or by using the molecular tree (**Table 2**). However, locomotion had no impact on humerus size variation (**Table 2**).

By applying *search.shift* to the humerus size, we found a significant increase in evolutionary rates in the clade, including Mylodontidae and *Choloepus* (average rate difference = 0.080, p = 0.001; **Figure 4A**), and a significant decrease in the clade, including *Panoctus*, *Doedicurus*, *Neosclerocalyptus*, and *Hoplophorus* (average rate difference = −0.025, p = 0.006; **Figure 4A**). This same negative shift applied when the morphological tree was considered (average rate difference = −0.020, $p < 0.001$; **Figure 4B**), whereas a positive rate shift was found for the clade including Euphractinae and

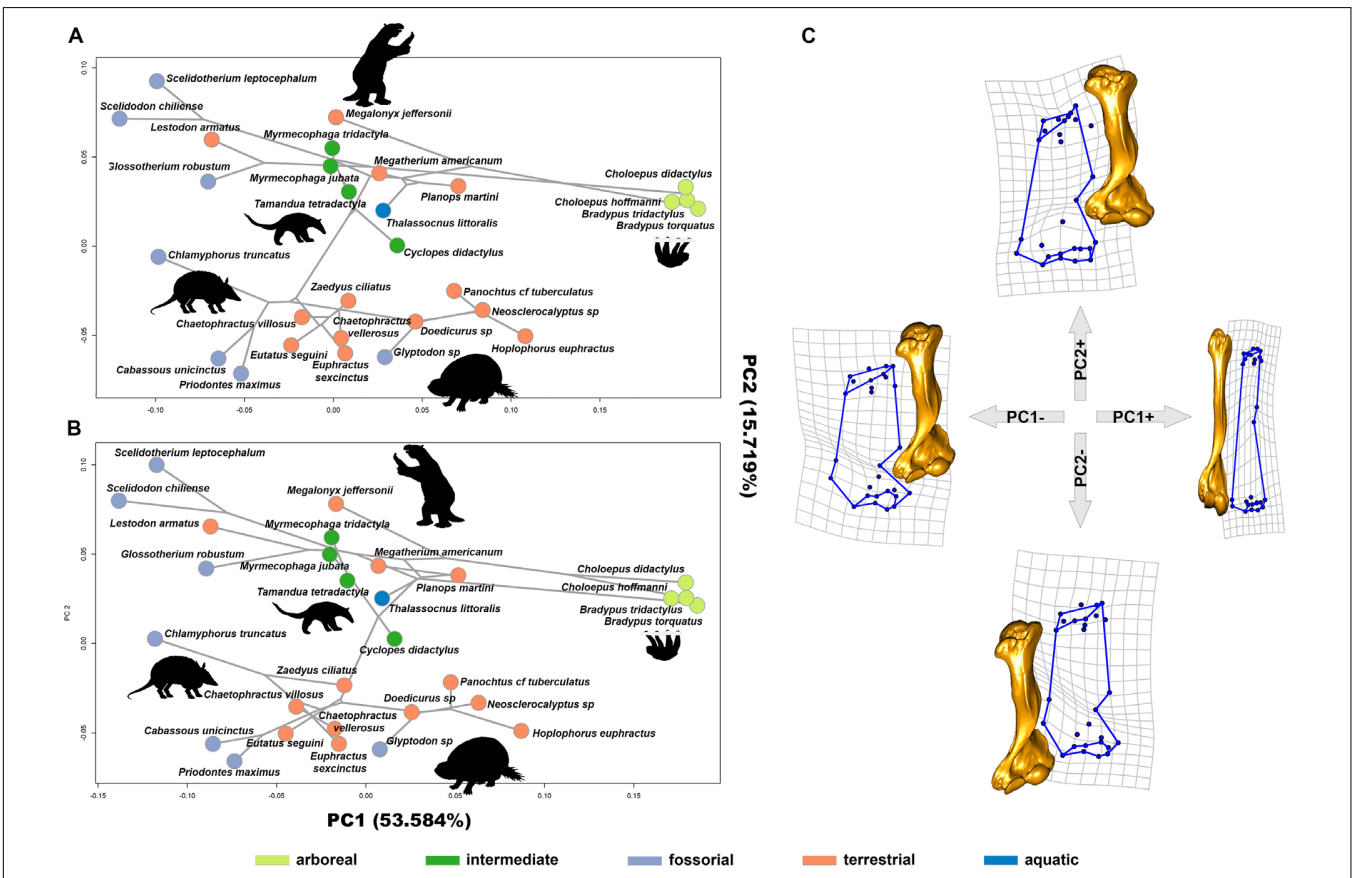

FIGURE 2 | Phylomorphospaces of PC1 vs. PC2 mapping molecular **(A)** and morphological tree **(B)**. Gray lines connect species with their reconstructed ancestral node. **(C)** Deformation grids and warping model (by using as reference *T. littoralis*).

TABLE 2 | Xenarthra summary statistics for different Procrustes ANOVA models without (A) and with (B, C) accounting for the phylogenetic effect.

Model	SS	MS	R^2	F	p values
(A) Proc ANOVA without phylogeny					
Shape∼size	0.069	0.069	0.160	5.156	**0.008**
Shape∼loc	0.102	0.026	0.238	1.870	**0.044**
Size∼loc	1.894	0.473	0.077	0.503	0.736
(B) Proc ANOVA with molecular tree					
Shape∼size + phy	0.001	0.001	0.068	1.960	0.097
Shape∼loc + phy	0.006	0.001	0.269	2.210	**0.016**
Size∼loc + phy	0.109	0.027	0.196	1.464	0.256
(C) Proc ANOVA with morphological tree					
Shape∼size + phy	0.002	0.002	0.104	3.146	**0.022**
Shape∼loc + phy	0.002	0.001	0.147	1.034	0.408
Size∼loc + phy	0.022	0.005	0.042	0.264	0.881

SS, the Sums of Squares; MS, Mean squares; R^2, the coefficient of determination for each model term; F, The F values for each model term; p values, probability computed for each model, significance (<0.05) is highlighted in bold; loc = locomotion.

TABLE 3 | Folivora and Cingulata summary statistics for different Procrustes ANOVA models without (A) and with (B, C) accounting for phylogenetic effect.

Group	Model	SS	MS	R^2	p values
(A) Proc ANOVA without phylogeny					
Folivora	shape∼size	0.125	0.125	0.562	**0.003**
Cingulata		0.037	0.037	0.345	**0.003**
(B) Proc ANOVA with molecular tree					
Folivora	shape∼size + phy	0.004	0.001	0.258	**0.008**
Cingulata		0.000	0.000	0.091	0.333
(C) Proc ANOVA with morphological tree					
Folivora	shape∼size + phy	0.004	0.004	0.439	**0.001**
Cingulata		0.002	0.002	0.342	**0.024**

SS, the Sums of Squares; MS, Mean squares; R^2, the coefficient of determination for each model term; F, The F values for each model term; p values, probability computed for each model, significance (<0.05) is highlighted in bold; loc = locomotion.

Chlamyphorus (average rate difference = 0.047, $p < 0.001$; **Figure 4B**) by using this tree. We did not find significant shifts in the rate of humerus shape evolution with either tree.

By testing for rate shifts in humerus size per locomotory state, we found a positive and significant difference in rates pertaining to strictly arboreal species (tree sloths) by using molecular trees (rate difference = 0.123, p value = 0.001, **Table 4**). Similarly, tree sloths showed significantly higher rates of shape evolution as compared to the rest of the taxa (rate difference = 11.259, p value <0.001, **Table 4**). With this same molecular tree, fossorial species had slower rates of humerus shape evolution as compared to the species falling in different locomotory states (rate difference = −2.040, $p = 0.002$, **Table 4**). When applying the morphological tree, these differences were less apparent although fossorial species still showed slower, and arboreal species higher rates as compared to the rest of the taxa, either by analyzing humerus size or shape (**Table 4**).

By using *search.conv*, we tested the convergence in humerus shape between species living on tree branches although ascribed to different categories (intermediate and arboreal). *search.conv* returned a non-significant angle of 98.253° (p value = 0.867) between the species under the two states, the same applied when the angle was tested per unit time (p value = 0.099; **Table 5A**). A strong evidence for convergence appears within the strictly arboreal species, that is the *Bradypus* and *Choloepus* clades (θ_{real} = 0.235, $p\theta_{real}$ = 0.010; ($\theta_{real+\theta ace}$)/time = 0.383, $p(\theta_{real+\theta ace})$/time = 0.001; **Table 5B** and **Figures 5B,D**). Morphological convergence was additionally found for species evolving in the "fossorial" category (mean angle among fossorial species = 68.148°; p angle state = 0.002, **Table 5A** and **Figure 5C**). This notion is confirmed when the time distance between species is accounted for (θ_{time} = 0.786, $p\theta_{time}$ = 0.001, **Table 5A**).

overfitRR returned 0% of significant simulations when convergence between the arboreal and intermediate states is tested for both phylogenies. This is in agreement with *search.conv* results.

For the issue of convergence between *Bradypus* and *Choloepus* *overfitRR* returned 100% (for both θ_{real} and $\theta_{real+\theta ace}$)/time) instances of significance by using molecular tree. When the same analysis is performed by using morphological tree, *overfitRR* returned 71% for θ_{real} and 74% for $\theta_{real+\theta ace}$)/time instance of significant convergence.

For the issue of convergence between fossorial species, *overfitRR* returned 100% ($p.\theta_{state}$) and 99% ($p.\theta_{time}$) of significant p values when molecular tree is used. The same figures for the morphological tree were 100% ($p.\theta_{state}$) and 98% ($p.\theta_{time}$).

DISCUSSION

The taxonomic and phenotypic diversity of extant Xenarthrans represents only a small fraction of their past variations. Perhaps unsurprisingly, giant extinct glyptodonts (*Doedicurus*, *Glyptodon*, and their allies) experienced a shift toward a slow rate of size evolution, in keeping with their uniformly large body size. This stands true irrespective of whether molecular or morphological trees are used. In contrast, a significant positive shift in the rate of humerus size evolution appears in Euphractinae plus *Chlamyrophus* by using the morphological tree only, with *Eutatus* placed outside the clade of Glyptodontinae plus Euphractinae (**Figure 4B**). This probably related with a decrease in size of Euphractinae plus *Chlamyrophus* in contrast with the plesiomorphic condition of *Eutatus*, whose estimated body size is supposed to range between 36.8 and 71.7 kg (Vizcaíno and Bargo, 2003). On the contrary, extant Euphractine plus *Chlamyrophus* are only 2 kg in body size on average.

We found no significant instance of shape evolutionary shifts pertaining to the Xenarthran trees, meaning that major shape differences were channelled through phylogeny as further supported by GMM results. Phylomorphospace showed a neat separation between the two clades Cingulata and Pilosa along PC2 (**Figure 2**).

However, the humerus changed significantly relative to locomotory styles. The rate of shape evolution in fossorial

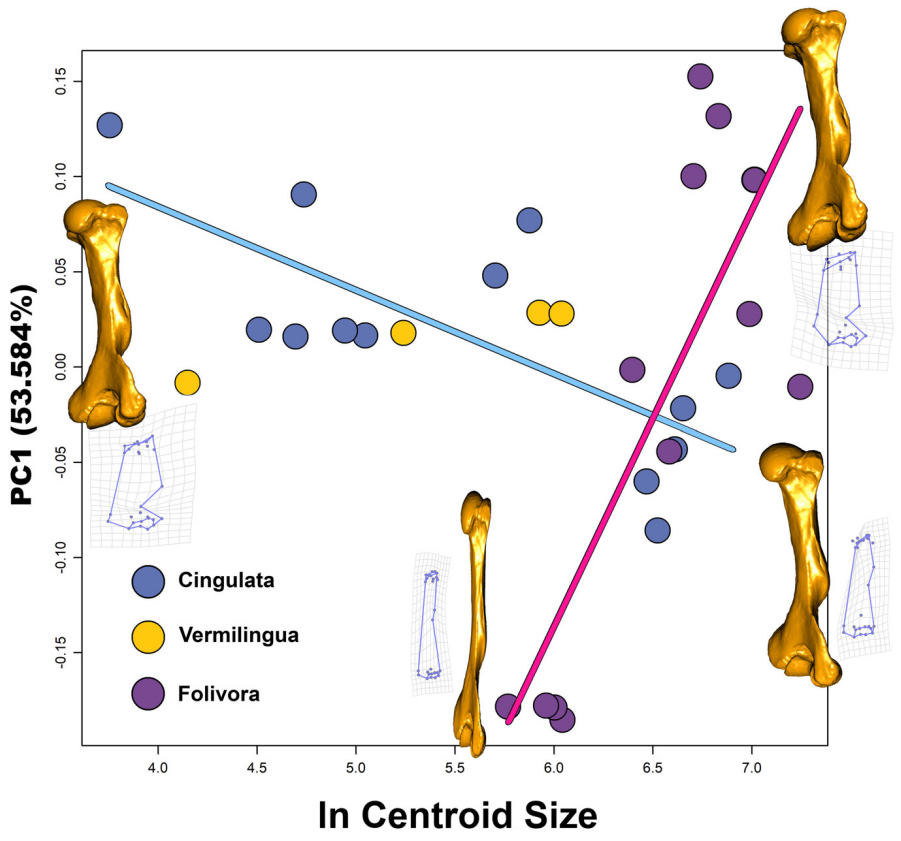

FIGURE 3 | Ln Centroid Size vs. PC1 scatter plot. Regression for Cingulata is represented by the light blue line. Regression for Folivora is represented by the pink line. At the extreme of PC1 for both groups are present the grids showing shape deformations and warping models (by using as reference *T. littoralis*).

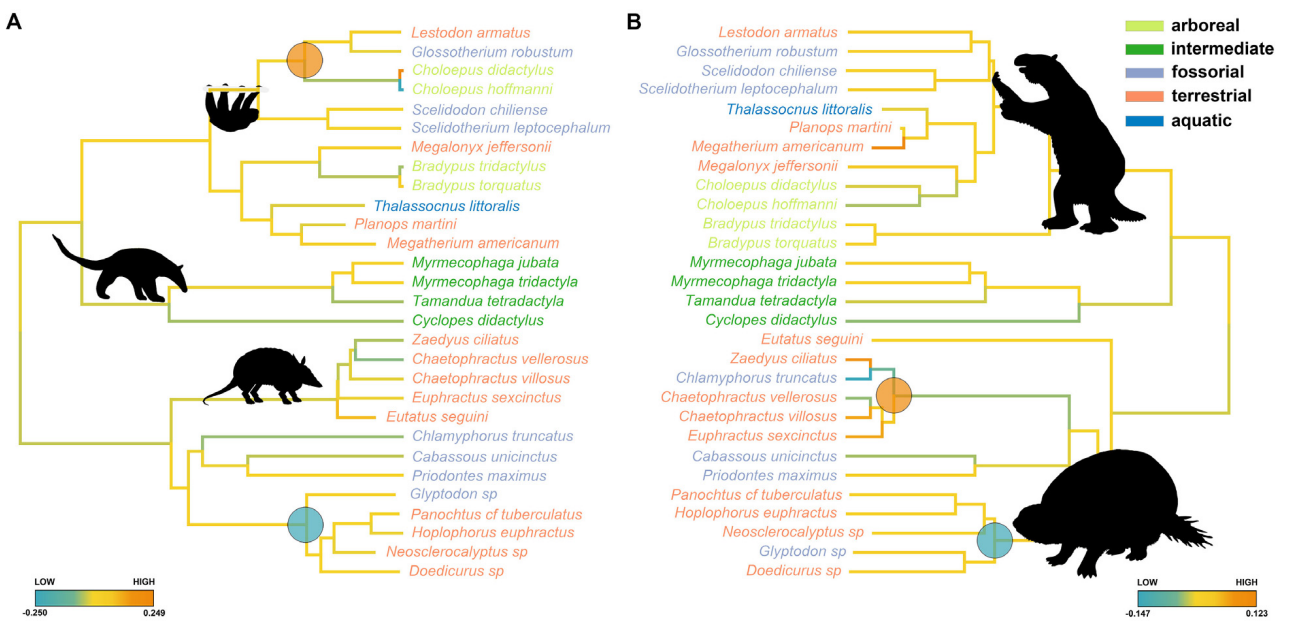

FIGURE 4 | Evolutionary rates (color coded) for the Xenarthra humerus size along the molecular **(A)** and morphological **(B)** tree. Species names are coded according to locomotor categories. Large dots at nodes represent clade shifting (blue = low, orange = high).

TABLE 4 | *search.shift* results for size showing shift in evolutionary rate.

	Molecular tree				Morphological tree			
	Size		Shape		Size		Shape	
	Rate difference	*p* values	Rate difference	*p* values	Rate difference	*p* values	Rate difference	*p* values
arboreal – aquatic	0.134	**0.002**	11.99	**<0.001**	−0.001	0.372	−1.457	0.158
fossorial – aquatic	0.004	0.367	0.045	0.311	0.017	0.636	−2.604	**0.049**
intermediate – aquatic	0.017	0.543	0.725	0.476	0.003	0.403	−3.021	**0.041**
terrestrial – aquatic	0.014	0.464	1.159	0.469	0.017	0.595	−1.107	0.179
fossorial – arboreal	−0.129	**0.003**	−11.945	**0.001**	0.018	0.777	−1.148	0.166
intermediate – arboreal	−0.117	**0.005**	−11.265	**0.001**	0.004	0.528	−1.564	0.127
terrestrial – arboreal	−0.12	**0.004**	−10.832	**0.001**	0.018	0.811	0.349	0.601
intermediate – fossorial	0.012	0.673	0.68	0.604	−0.015	0.247	−0.416	0.421
terrestrial – fossorial	0.009	0.565	1.114	0.702	0.000	0.481	1.497	0.969
terrestrial – intermediate	−0.003	0.373	0.433	0.501	0.015	0.762	1.913	**0.015**
terrestrial	−0.026	0.162	−2.04	0.081	0.009	0.758	1.151	0.957
fossorial	−0.031	0.086	−2.952	**0.008**	0.007	0.691	−1.136	0.054
intermediate	−0.013	0.473	−1.808	0.286	−0.011	0.319	−1.482	**0.045**
aquatic	−0.029	0.425	−2.366	0.188	−0.015	0.251	0.332	0.742
arboreal	0.123	**0.001**	11.259	**<0.001**	−0.013	0.492	1.805	0.918

Rate difference is computed as the average rate for all species evolving under the same state minus the average for each other state (for group comparison) or the rest of the tree (for the single state). p values is assessed by means of randomization.

Xenarthrans is significantly smaller than in other species. Such fossorial habitus characterizes most Cingulata and is possibly plesiomorphic to the group (Vizcaíno and Milne, 2002; Milne et al., 2009; Marshall, 2018), although it is surprisingly present among giant ground sloths like *Glossotherium* (Bargo et al., 2000; Vizcaíno et al., 2001; de Oliveira and Santos, 2018).

Conversely, arboreal species evolved at faster rates than in any other Xenarthra. Tree sloths were noted for their highly derived and convergent morphologies, canalizing change from a plesiomorphic, fossorial condition (Nyakatura, 2011; Nyakatura and Fischer, 2011), although it must be emphasized that scansorial species (which were not included in the analyses here) were present since the Miocene (Pujos et al., 2012; Toledo et al., 2017).

Overall, our results suggest that the acquisition of arboreal and fossorial lifestyles are loaded with great functional demands, leading to constrained, little variable morphologies (fossorial) or to significant changes in shape toward a particular configuration (from the ancestral conditions) to match a demanding lifestyle (arboreal sloths). These challenging adaptations present ideal cases to test convergence. We provided this test for both fossorial species and tree sloths, separately, and confirmed they do represent significant instances of morphological convergence (**Figure 5**). The same applies if phylogenetic uncertainty is accounted for. The results further support the observation that phylogenetic signal in humerus shape is as much high as for humerus size (Vizcaíno et al., 1999; Vizcaíno and Bargo, 2003), but also suggest that tree-living is the room for morphological change among Xenarthran taxa.

Limb proportions in fossil *Eutatus* were similar to extant Euphractine (Vizcaíno and Bargo, 2003). These species present limbs specialized in building borrows rather than in gathering food (Vizcaíno and Bargo, 2003). Thus, the high size evolutionary rates can be related with more robust humerii specialized for digging. It was demonstrated that Miocene glyptodonts weighed about 100 kg, but Pleistocene species may have weighed up to 1 ton (Vizcaíno et al., 2010; Milne et al., 2012). Our results indicate that the lowest evolutionary rate in humerus size occurs in *Panoctus*, *Doedicurus*, *Neosclerocalyptus*, and *Hoplophorus* suggesting humerus size in these taxa was linked to their large but uniform body size.

Xenarthra originated in South America about 62.5 million years ago (Presslee et al., 2019). During the Great Biotic Interchange in late Pliocene (Marshall et al., 1979; Webb, 2006)

TABLE 5 | Convergence results.

(A) *search.conv* results under "state" condition

state	θ_{state}	$p.\theta_{state}$	θ_{time}	$p.\theta_{time}$
Arboreal – intermediate	98.253	0.867	0.945	0.099
Fossorial	68.148	**0.002**	0.786	**0.001**

(B) *search.conv* results under "automatic" condition

node	θ_{real}	$p\ \theta_{real}$	$(\theta_{real+\theta ace})$/time	$p(\theta_{real+\theta ace})$/time
Bradypus – Choloepus	0.235	**0.01**	0.383	**0.001**

(A) Results as returned by search.conv. θ_{state}: mean angle between species within a within a single state; $p.\theta_{state}$: p value computed for θ_{state}. (B) Results as returned by search.conv for clade subtending Bradypus and Choloepus.θ_{real}: the mean angle between Bradypus and Choloepus divided by the time distance; p θ_{real}: the p-value computed for θ_{real}; $(\theta_{real+\theta ace})$/time: the mean theta angle between Bradypus and Choloepus plus the angle between aces, divided by the time distance; $p(\theta_{real+\theta ace})$/time: the p-value computed for $(\theta_{real+\theta ace})$/time. Significant p values (<0.05) are highlighted in bold.

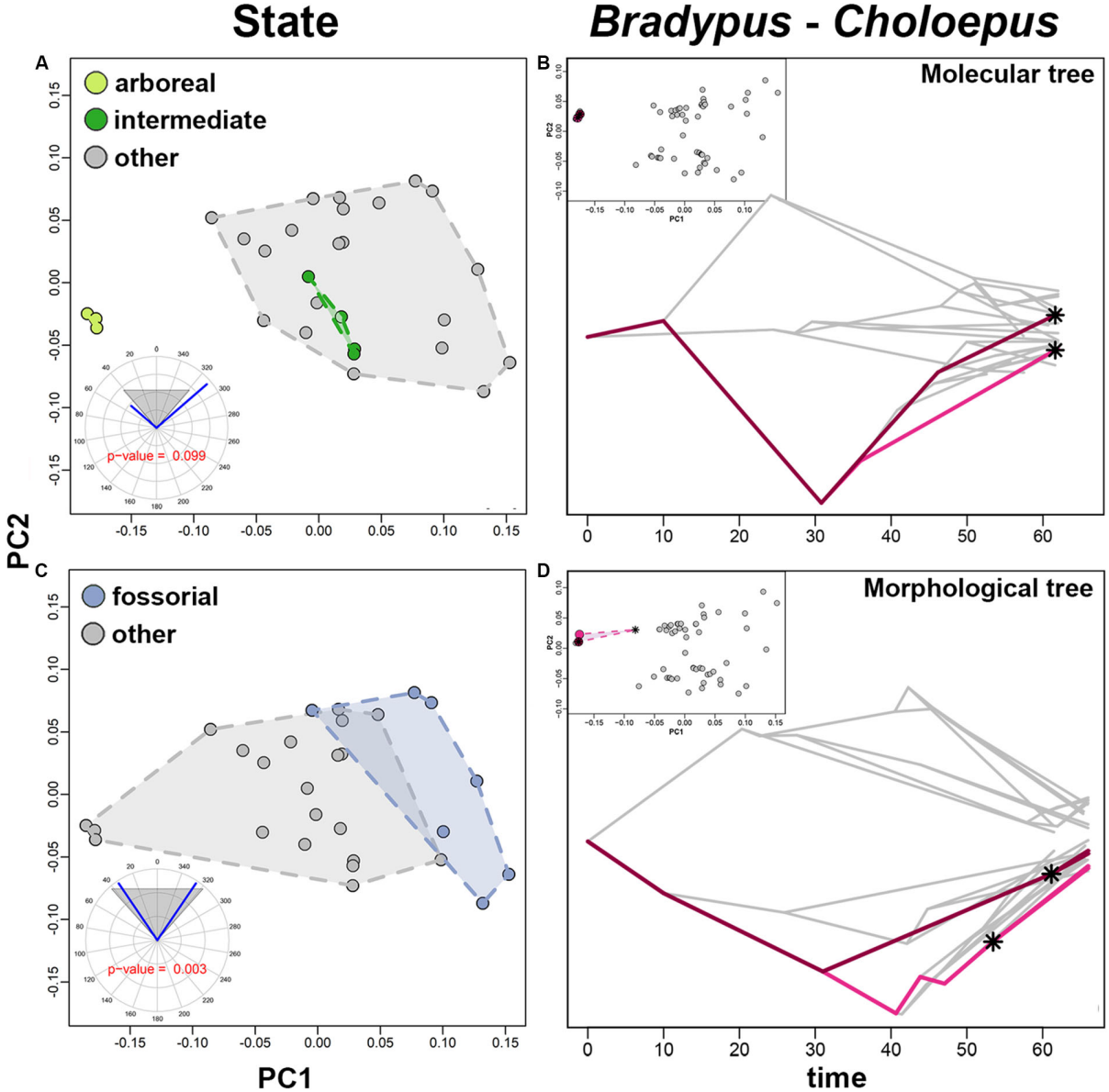

FIGURE 5 | (A,C) PC1 vs. PC2 scatter plot. Convex hulls are colored according to different states. Circular plots represent the mean angle between states, the gray area is the random angle range. **(B,D)** Traitgram plot with colored branched representing convergent clade. PC1 vs. PC2 scatter plot are produced, convergent clades are color coded. In both, traitgram and PC1 vs. PC2 scatter plot asterisks represent the ancestral phenotypes of the individual clades.

several species migrated to the North (Bocherens et al., 2017). Studies of fossil species have demonstrated that none of the known fossil sloths had arboreal lifestyle (White, 2010; Nyakatura, 2011). The last common ancestor of sloths probably was terrestrial or semi-arboreal (White, 2010; Nyakatura, 2012). Indeed, fossil sloths appear morphologically closer to extant Vermilingua (i.e., *Tamandua* and *Myrmecophaga,* herein classified as "intermediate") rather than to extant tree sloths (Toledo et al., 2012). We did not find instance of convergence among intermediate and arboreal species (**Figure 5**). This supports the idea that modern tree sloths acquired the suspensory habitus secondarily, which explains their higher shape evolutionary rates as compared to the humerii of species ascribed to different locomotor categories. Similarly, the long branch separating the extant tree sloth genera (Presslee et al., 2019) are suggestive of secondary adaptation. Extant sloths present a forelimb-dominated locomotion. *Bradypus* moves up to 10 m only using his forelimbs, and *Choloepus* hind limbs lost their primarily propulsive elements (Mendel, 1985; Nyakatura et al., 2010).

Similarly, since digging kinematics is one of the most demanding behaviors the mammalian skeleton could be designed for Sansalone et al. (2019), the pervasive call for convergence

to a functionally optimal design linked to digging was expected (Sansalone et al., 2020).

One obvious caveat we urge to consider is that, although nearly one-half of the species we considered in our tree are extinct, the history of Xenarthra cautions against giving too much faith to phylogenetic analyses using a tree devoid or otherwise scarce in terms of fossil species representation. The inclusion of fossil phenotypes is, and must carefully be, considered in trait evolution inference, especially when major patterns such as morphological convergence are sought after.

DATA AVAILABILITY STATEMENT

The datasets for this study are included in the **Supplementary Material**.

AUTHOR CONTRIBUTIONS

CS, PR, and CM conceived the project. CS and CM prepared samples and conducted the data analyses. All the authors discussed the results and wrote the manuscript.

FUNDING

CS was supported for this study by LJMU Ph.D. studentship fund.

ACKNOWLEDGMENTS

The authors are grateful to Alessandro Marques de Oliveira for sharing 3D models of Xenarthra humerii. More in details we acknowledge museum curators that hosted previous data collection in London (NHM, Roberto Portela Miguez, Pip Brewer), and Paris (MNHN, Guillaume Billet). Silvia Castiglione helped us to prepare an updated version of *overfitRR* explicitly tailored to work with small trees. The editor AH and the two reviewers equally helped us to improve this presented manuscript.

SUPPLEMENTARY MATERIAL

The Supplementary Material for this article can be found online at: https://www.frontiersin.org/articles/10.3389/fevo.2020.00139/full#supplementary-material

REFERENCES

Adams, D. C. (2014). Quantifying and comparing phylogenetic evolutionary rates for shape and other high-dimensional phenotypic data. *Syst. Biol.* 63, 166–177. doi: 10.1093/sysbio/syt105

Adams, D. C., Collyer, M. L., and Kaliontzopoulou, A. (2019). *Geomorph: Software for Geometric Morphometric Analyses. R Package Version* 3.1.0. Available at: https://cran.r-project.org/package=geomorph (accessed September 3, 2019).

Adams, D. C., Rohlf, F. J., and Slice, D. E. (2004). Geometric morphometrics: ten years of progress following the "revolution". *Ital. J. Zool.* 71, 5–16. doi: 10.1080/11250000409356545

Adams, D. C., Rohlf, F. J., and Slice, D. E. (2013). A field comes of age: geometric morphometrics in the 21st century. *Hystrix* 24, 7–14. doi: 10.4404/hystrix-24.1-6283

Amson, E., Arnold, P., van Heteren, A. H., Canoville, A., and Nyakatura, J. A. (2017). Trabecular architecture in the forelimb epiphyses of extant xenarthrans (Mammalia). *Front. Zool.* 1:52. doi: 10.1186/s12983-017-0241-x

Amson, E., and Nyakatura, J. A. (2017). The postcranial musculoskeletal system of xenarthrans: insights from over two centuries of research and future directions. *J. Mamm. Evol.* 25, 459–484. doi: 10.1007/s10914-017-9408-7

Arnold, S. J. (2015). Constraints on phenotypic evolution. *Am. Nat.* 140, S85–S107. doi: 10.1086/285398

Bargo, M. S. (2003). Biomechanics and palaeobiology of the Xenarthra: the state of the art. *Sencken Biol.* 1, 41–50.

Bargo, M. S., and Nyakatura, J. A. (2018). Morphology and evolution of the xenarthra: an introduction. *J. Mamm. Evol.* 4, 445–447. doi: 10.1007/s10914-017-9419-4

Bargo, M. S., and Vizcaíno, S. F. (2008). Paleobiology of pleistocene ground sloths (Xenarthra, Tardigrada): biomechanics, morphogeometry and ecomorphology applied to the masticatory apparatus. *Ameghiniana* 1, 175–196.

Bargo, M. S., Vizcaíno, S. F., Archuby, F. M., and Blanco, R. E. (2000). Limb bone proportions, strength and digging in some Lujanian (Late Pleistocene-Early Holocene) mylodontid ground sloths (Mammalia, Xenarthra). *J. Vertebr. Paleontol.* 3, 601–610.

Bertram, J. E. A., and Biewener, A. A. (1992). Allometry and curvature in the long bones of quadrupedal mammals. *J. Zool.* 226, 455–467. doi: 10.1111/j.1469-7998.1992.tb07492.x

Billet, G., Hautier, L., de Muizon, C., and Valentin, X. (2011). Oldest cingulate skulls provide congruence between morphological and molecular scenarios of armadillo evolution. *Proc. R. Soc. Lond.* 1719, 2791–2797. doi: 10.1098/rspb.2010.2443

Billet, G., Hautier, L., and Lebrun, R. (2015). Morphological diversity of the bony labyrinth (inner ear) in extant xenarthrans and its relation to phylogeny. *J. Mammal.* 4, 658–672.

Bocherens, H., Cotte, M., Bonini, R. A., Straccia, P., Scian, D., Soibelzon, L., et al. (2017). Isotopic insight on paleodiet of extinct Pleistocene megafaunal Xenarthrans from Argentina. *Gondwana Res.* 48, 7–14. doi: 10.1016/j.gr.2017.04.003

Boscaini, A., Gaudin, T. J., Mamani Quispe, B., Münch, P., Antoine, P. O., and Pujos, F. (2019). New well-preserved craniodental remains of Simomylodon uccasamamensis (Xenarthra: Mylodontidae) from the Pliocene of the Bolivian Altiplano: phylogenetic, chronostratigraphic and palaeobiogeographical implications. *Zool. J. Linn. Soc.* 2, 459–486. doi: 10.1093/zoolinnean/zly075

Botton-Divet, L., Cornette, R., Houssaye, A., Fabre, A. C., and Herrel, A. (2017). Swimming and running: a study of the convergence in long bone morphology among semi-aquatic mustelids (Carnivora: Mustelidae). *Biol. J. Linn. Soc.* 121, 38–49. doi: 10.1093/biolinnean/blw027

Brakefield, P. M. (2006). Evo-devo and constraints on selection. *Trends Ecol. Evol.* 21, 362–368. doi: 10.1016/j.tree.2006.05.001

Castiglione, S., Serio, C., Tamagnini, D., Melchionna, M., Mondanaro, Di Febbraro, et al. (2019). A new, fast method to search for morphological convergence with shape data. *PLoS ONE* 14:226949. doi: 10.1371/journal.pone.0226949

Castiglione, S., Tesone, G., Piccolo, M., Melchionna, M., Mondanaro, A., Serio, C., et al. (2018). A new method for testing evolutionary rate variation and shifts in phenotypic evolution. *Methods Ecol. Evol.* 9, 974–983. doi: 10.1111/2041-210X.12954

Chiarello, A. G. (2008). "Sloth ecology. An overview of field studies," in *The Biology of the Xenarthra*, eds S. F. Vizcaíno, and W. J. Loughry (Gainesville: University Press of Florida), 269–280.

Cohen, B. L. (2018). Match and mismatch of morphological and molecular phylogenies: causes, implications, and new light on cladistics. *Zool. J. Linn. Soc.* 2, 516–527. doi: 10.1093/zoolinnean/zly004

De Iuliis, G., Bargo, M. S., and Vizcaíno, S. F. (2001). Variation in skull morphology and mastication in the fossil giant armadillos *Pampatherium* spp. and allied genera (Mammalia: Xenarthra: Pampatheriidae), with comments on their systematics and distribution. *J. Vertebr. Paleontol.* 4, 743–754.

de Oliveira, A. M., and Santos, C. M. D. (2018). Functional morphology and paleoecology of Pilosa (Xenarthra, Mammalia) based on a two-dimensional geometric Morphometrics study of the Humerus. *J. Morphol.* 279, 1455–1467. doi: 10.1002/jmor.20882

Delsuc, F., Kuch, M., Gibb, G. C., Karpinski, E., Hackenberger, D., Szpak, P., et al. (2019). Ancient mitogenomes reveal the evolutionary history and biogeography of sloths. *Curr. Biol.* 12, 2031–2042. doi: 10.1016/j.cub.2019.05.043

Delsuc, F., Vizcaíno, S. F., and Douzery, E. J. (2004). Influence of tertiary paleoenvironmental changes on the diversification of South American mammals: a relaxed molecular clock study within xenarthrans. *BMC Evol. Biol.* 1:11. doi: 10.1186/1471-2148-4-11

Egi, N. (2001). Body mass estimates in extinct mammals from limb bone dimensions: the case of North American hyaenodontids. *Palaeontology* 44, 497–528. doi: 10.1111/1475-4983.00189

Elton, S. (2002). A reappraisal of the locomotion and habitat preference of Theropithecus oswaldi. *Folia Primatol.* 73, 252–280. doi: 10.1159/000067457

Elton, S., Jansson, A. U., Meloro, C., Louys, J., Plummer, T., and Bishop, L. C. (2016). Exploring morphological generality in the Old World monkey postcranium using an ecomorphological framework. *J. Anat.* 228, 534–560. doi: 10.1111/joa.12428

Engelmann, G. F. (1985). "The phylogeny of the Xenarthra," in *The Evolution and Ecology of Armadillos, Sloths, and Vermilinguas*, ed. G. G. Montgomery (Washington, D.C: Smithsonian Institution Press), 51–64.

Falkingham, P. L. (2012). Acquisition of high resolution three-dimensional models using free, open-source, photogrammetric software. *Palaeontol. Electron.* 15, 1–15. doi: 10.26879/264

Fariña, R. A., and Vizcaíno, S. F. (1997). Allometry of the bones of living and extinct armadillos (*Xenarthra*, *Dasypoda*). *Zeitschrift für Saugetierkunde* 62, 65–70.

Fariña, R. A., Vizcaíno, S., and Storch, G. (2003). "Morphological studies in fossil and extant Xenarthra-(Mammalia)," in *Senckenbergiana Biologica, Band 83 Heft 1*, eds R. A. Fariña, S. Vizcaíno, and G. Storch (Stuttgart: Schweizerbart and Borntraeger science publishers).

Fau, M., Cornette, R., and Houssaye, A. (2016). Photogrammetry for 3D digitizing bones of mounted skeletons: potential and limits. *Cr. Palevol.* 15, 968–977. doi: 10.1016/j.crpv.2016.08.003

Felsenstein, J. (1985). Phylogenies and the comparative method. *Am. Nat.* 125, 1–15. doi: 10.1086/284325

Fernicola, J. C., Rinderknecht, A., Jones, W., Vizcaíno, S. F., and Porpino, K. (2017). A new species of neoglyptatelus (Mammalia, Xenarthra, Cingulata) from the Late Miocene of Uruguay provides new insights on the evolution of the dorsal armor in cingulates. *Ameghiniana* 3, 233–252. doi: 10.5710/AMGH.02.12.2017.3150

Figueirido, B., Pérez-Claros, J. A., Hunt, R. M., and Palmqvist, P. (2011). Body mass estimation in amphicyonid carnivoran mammals: a multiple regression approach from the skull and skeleton. *Acta Palaeontol. Pol.* 56, 225–247. doi: 10.4202/app.2010.0005

Finarelli, J. A., and Flynn, J. J. (2006). Ancestral state reconstruction of body size in the Caniformia (Carnivora, mammalia): the effects of incorporating data from the fossil record. *Syst. Biol.* 55, 301–313. doi: 10.1080/10635150500541698

Gaudin, T., and Wible, J. R. (2006). "The phylogeny of living and extinct armadillos (Mammalia, Xenarthra, Cingulata): a craniodental analysis," in *Amniote Paleobiology: Perspectives on the Evolution of Mammals, Birds, and Reptiles*, eds M. T. Carrano, T. Gaudin, R. W. Blob, and J. R. Wible (Chicago: University of Chicago Press), 153–198.

Giacomini, G., Scaravelli, D., Herrel, A., Veneziano, A., Russo, D., Brown, R. P., et al. (2019). 3D photogrammetry of bat skulls: perspectives for macro-evolutionary analyses. *Evol. Biol.* 46, 249–259. doi: 10.1007/s11692-019-09478-6

Gibb, G. C., Condamine, F. L., Kuch, M., Enk, J., Moraes-Barros, N., Superina, M., et al. (2016). Shotgun mitogenomics provides a reference phylogenetic framework and timescale for living xenarthrans. *Mol. Biol. Evol.* 33, 621–642. doi: 10.1093/molbev/msv250

Gingerich, P. D. (1990). Prediction of body mass in mammalian species from long bone lengths and diameters. *Contrib. Mus. Paleonotol. Univ. Mich.* 28, 79–92.

Goswami, A., Milne, N., and Wroe, S. (2011). Biting through constraints: cranial morphology, disparity and convergence across living and fossil carnivorous mammals. *Proc. R. Soc. B-Bio. Sci.* 1713, 1831–1839. doi: 10.1098/rspb.2010.2031

Gould, S. J. (1989). A developmental constraint in cerion, with comments of the definition and interpretation of constraint in evolution. *Evolution* 43:516. doi: 10.1111/j.1558-5646.1989.tb04249.x

Harmon, L. J., Kolbe, J. J., Cheverud, J. M., and Losos, J. B. (2005). Convergence and the multidimensional niche. *Evolution* 59, 409–421. doi: 10.1111/j.0014-3820.2005.tb00999.x

Herrera, C. M., Powell, J. E., Esteban, G. I., and del Papa, C. (2017). A new eocene dasypodid with caniniforms (Mammalia, Xenarthra, Cingulata) from northwest Argentina. *J. Mamm. Evol.* 3, 275–288. doi: 10.1007/s10914-016-9345-x

Hildebrand, M. (1985). "Digging of quadrupeds," in *Functional Vertebrate Morphology*, ed. M. Hildebrand (Cambridge: Cambridge University Press), 89–109.

Kley, N. J., and Kearney, M. (2007). "Adaptations for digging and burrowing," in *Fins into Limbs: Evolution*, ed. B. K. Hall (Chicago: University of Chicago Press), 284–309.

Klingenberg, C. P. (2016). Size, shape, and form: concepts of allometry in geometric morphometrics. *Dev. Genes Evol.* 226, 113–137. doi: 10.1007/s00427-016-0539-2

Losos, J. B. (2011). Convergence, adaptation, and constraint. *Evolution* 65, 1827–1840. doi: 10.1111/j.1558-5646.2011.01289.x

Mahler, D. L., Revell, L. J., Glor, R. E., and Losos, J. B. (2010). Ecological opportunity and the rate of morphological evolution in the diversification of greater Antillean Anoles. *Evolution* 64, 2731–2745. doi: 10.1111/j.1558-5646.2010.01026.x

Marshall, L. G., Butler, R. F., Drake, R. E., Curtis, G. H., and Tedford, R. H. (1979). Calibration of the great american interchange. *Science* 204, 272–279. doi: 10.1126/science.204.4390.272

Marshall, S. K. (2018). *Comparative Morphology of the Forelimb Digging Apparatus in Armadillos (Xenarthra: Cingulata, Dasypodidae)* Dissertation., Youngstown State University, Ohio.

Melchionna, M., Mondanaro, A., Serio, C., Castiglione, S., Di Febbraro, M., Rook, L., et al. (2020). Macroevolutionary trends of brain mass in Primates. *Biol. J. Linn. Soc.* 1, 14–25. doi: 10.1093/biolinnean/blz161

Meloro, C., Cáceres, N. C., Carotenuto, F., Sponchiado, J., Melo, G. L., Passaro, F., et al. (2015a). Chewing on the trees: constraints and adaptation in the evolution of the primate mandible. *Evolution* 69, 1690–1700. doi: 10.1111/evo.12694

Meloro, C., Clauss, M., and Raia, P. (2015b). Ecomorphology of carnivora challenges convergent evolution. *Org. Divers. Evol.* 15, 711–720. doi: 10.1007/s13127-015-0227-5

Meloro, C., Elton, S., Louys, J., Bishop, L. C., and Ditchfield, P. (2013). Cats in the forest: predicting habitat adaptations from humerus morphometry in extant and fossil Felidae (Carnivora). *Paleobiology* 39, 323–344. doi: 10.1666/12001

Meloro, C., and Raia, P. (2010). Cats and dogs down the tree: the tempo and mode of evolution in the lower carnassial of fossil and living carnivora. *Evol. Biol.* 37, 177–186. doi: 10.1007/s11692-010-9094-3

Meloro, C., Raia, P., Piras, P., Barbera, C., and O'Higgins, P. (2008). The shape of the mandibular corpus in large fissiped carnivores: allometry, function and phylogeny. *Zool. J Linn. Soc.* 154, 832–845. doi: 10.1111/j.1096-3642.2008.00429.x

Meloro, C., and Slater, G. J. (2012). Covariation in the skull modules of cats: the challenge of growing saber-like canines. *J. Vertebr. Paleontol.* 32, 677–685. doi: 10.1080/02724634.2012.649328

Mendel, F. C. (1985). Use of hands and feet of three-toed sloths (Bradypus variegatus) during climbing and terrestrial locomotion. *J. Mammal.* 66, 359–366. doi: 10.2307/1381249

Mielke, F., Amson, E., and Nyakatura, J. A. (2018). Morpho-functional analysis using procrustes superimposition by static reference. *Evol. Biol.* 4, 449–461. doi: 10.1007/s11692-018-9456-9

Milne, N., Toledo, N., and Vizcaíno, S. F. (2012). Allometric and group differences in the xenarthran femur. *J. Mamm. Evol.* 19, 199–208. doi: 10.1007/s10914-011-9171-0

Milne, N., Vizcaíno, S. F., and Fernicola, J. C. (2009). A 3D geometric morphometric analysis of digging ability in the extant and fossil cingulate humerus. *J. Zool.* 278, 48–56. doi: 10.1111/j.1469-7998.2008.00548.x

Monteiro, L. R., and Abe, A. S. (1999). Functional and historical determinants of shape in the scapula of xenarthran mammals: evolution of a complex morphological structure. *J. Morphol.* 241, 251–263. doi: 10.1002/(SICI)1097-4687(199909)241:3<251::AID-JMOR7>3.0.CO;2-7

Montgomery, G. G. (1985). "Impact of vermilinguas (Cyclopes, Tamandua: Xenarthra = Edentata) on arboreal ant populations," in *Ecology and Evolution of Sloths, Anteaters and Armadillos (Mammalia, Xenarthra = Edentata)*, ed. G. G. Montgomery (Washington, D.C: Smithsonian Institution Press), 351–363.

Nyakatura, J. A. (2011). The convergent evolution of suspensory posture and locomotion in tree sloths. *J. Mamm. Evol.* 19, 225–234. doi: 10.1007/s10914-011-9174-x

Nyakatura, J. A. (2012). The convergent evolution of suspensory posture and locomotion in tree sloths. *J. Mamm. Evol.* 3, 225–234. doi: 10.1007/s10914-011-9174-x

Nyakatura, J. A., and Fischer, M. S. (2011). Functional morphology of the muscular sling at the pectoral girdle in tree sloths: convergent morphological solutions to new functional demands? *J. Anat.* 219, 360–374. doi: 10.1111/j.1469-7580.2011.01394.x

Nyakatura, J. A., Petrovitch, A., and Fischer, M. S. (2010). Limb kinematics during locomotion in the twotoed sloth (Choloepus didactylus, Xenarthra) and its implications for the evolution of the sloth locomotor apparatus. *Zoology* 113, 221–234.

Piras, P., Sansalone, G., Teresi, L., Kotsakis, T., Colangelo, P., and Loy, A. (2012). Testing convergent and parallel adaptations in talpids humeral mechanical performance by means of geometric morphometrics and finite element analysis. *J. Morphol.* 273, 696–711. doi: 10.1002/jmor.20015

Polly, P. D. (2007). "Limbs in mammalian evolution," in *Fins into Limbs: Evolution*, ed. B. K. Hall (Chicago: University of Chicago Press), 245–268.

Presslee, S., Slater, G. J., Pujos, F., Forasiepi, A. M., Fischer, R., Molloy, K., et al. (2019). Palaeoproteomics resolves sloth relationships. *Nat. Ecol. Evol.* 3, 1121–1130. doi: 10.1038/s41559-019-0909-z

Prothero, D. R. (2016). *The Princeton Field Guide to Prehistoric Mammals*, Vol. 112. Princeton, NJ: Princeton University Press.

Pujos, F., Gaudin, T. J., De Iuliis, G., and Cartelle, C. (2012). Recent advances on variability, morpho-functional adaptations, dental terminology, and evolution of sloths. *J. Mamm. Evol.* 19, 159–169. doi: 10.1007/s10914-012-9189-y

Raia, P., Carotenuto, F., Meloro, C., Piras, P., and Pushkina, D. (2010). The shape of contention: adaptation, history, and contingency in ungulate mandibles. *Evolution* 64, 1489–1503. doi: 10.1111/j.1558-5646.2009.00921.x

Raia, P., Carotenuto, F., Passaro, F., Piras, P., Fulgione, D., Werdelin, L., et al. (2013). Rapid action in the palaeogene, the relationship between phenotypic and taxonomic diversification in Coenozoic mammals. *Proc. Biol. Sci.* 280, 20122244–20122244. doi: 10.1098/rspb.2012.2244

Raia, P., Castiglione, S., Serio, C., Mondanaro, A., Melchionna, M., Di Febbraro, M., et al. (2020). *RRphylo: Phylogenetic Ridge Regression Methods for Comparative Studies. R package version* 2.4.4. Available online at: https://rdrr.io/cran/RRphylo/ (accessed September 3, 2019).

Rohlf, F. J., and Slice, D. (1990). Extensions of the procrustes method for the optimal superimposition of landmarks. *Syst. Biol.* 39, 40–59. doi: 10.2307/2992207

Sansalone, G., Castiglione, S., Raia, P., Archer, M., Dickson, B., Hand, S., et al. (2020). Decoupling functional and morphological convergence, the study case of fossorial mammalia. *Front. Earth Sci.* 8:112. doi: 10.3389/feart.2020.00112

Sansalone, G., Colangelo, P., Loy, A., Raia, P., Wroe, S., and Piras, P. (2019). Impact of transition to a subterranean lifestyle on morphological disparity and integration in talpid moles (Mammalia, Talpidae). *BMC Evol. Biol.* 19:179. doi: 10.1186/s12862-019-1506-0

Serio, C., Castiglione, S., Tesone, G., Piccolo, M., Melchionna, M., Mondanaro, A., et al. (2019). Macroevolution of toothed whales exceptional relative brain size. *Evol. Biol.* 4, 332–342. doi: 10.1007/s11692-019-09485-7

Shingleton, A. W., Frankino, W. A., Flatt, T., Nijhout, H. F., and Emlen, D. J. (2007). Size and shape: the developmental regulation of static allometry in insects. *BioEssays* 29, 536–548. doi: 10.1002/bies.20584

Simpson, G. G. (1980). *Splendid Isolation: The Curious History of South American Mammals*, Vol. 275. New Haven: Yale University Press.

Smaers, J. B., Mongle, C. S., and Kandler, A. (2016). A multiple variance Brownian motion framework for estimating variable rates and inferring ancestral states. *Biol. J. Linn. Soc.* 118, 78–94. doi: 10.1111/bij.12765

Speed, M. P., and Arbuckle, K. (2016). Quantification provides a conceptual basis for convergent evolution. *Biol. Rev.* 92, 815–829. doi: 10.1111/brv.12257

Springer, M. S., Murphy, W. J., Eizirik, E., and O'Brien, S. J. (2003). Placental mammal diversification and the Cretaceous-Tertiary boundary. *Proc. Natl. Acad. Sci. U.S.A.* 100, 1056–1061. doi: 10.1073/pnas.0334222100

Toledo, N., Bargo, M. S., Cassini, G. H., and Vizcaíno, S. F. (2012). The forelimb of early miocene sloths (Mammalia, Xenarthra, Folivora): morphometrics and functional implications for substrate preferences. *J. Mamm. Evol.* 19, 185–198. doi: 10.1007/s10914-012-9185-2

Toledo, N., Bargo, M. S., and Vizcaíno, S. F. (2015). Muscular reconstruction and functional morphology of the hind limb of santacrucian (Early Miocene) sloths (Xenarthra, Folivora) of Patagonia. *Anat. Rec.* 5, 842–864. doi: 10.1002/ar.23114

Toledo, N., Bargo, M. S., Vizcaíno, S. F., De Iuliis, G., and Pujos, F. (2017). Evolution of body size in anteaters and sloths (Xenarthra, Pilosa): phylogeny, metabolism, diet and substrate preferences. *Earth Environ. Sci. Trans R. Soc. Edinb.* 106, 289–301. doi: 10.1017/S1755691016000177

Varela, L., Tambusso, P. S., McDonald, H. G., and Fariña, R. A. (2019). Phylogeny, macroevolutionary trends and historical biogeography of sloths: insights from a Bayesian morphological clock analysis. *Syst. Biol.* 2, 204–218. doi: 10.1093/sysbio/syy058

Vizcaíno, S. F., Bargo, M. S., and Cassini, G. H. (2006). Dental occlusal surface area in relation to body mass, food habits and other biological features in fossil xenarthrans. *Ameghiniana* 1, 11–26.

Vizcaíno, S. F., Bargo, M. S., and Fariña, R. A. (2008). "Form, function, and paleobiology in xenarthrans," in *The Biology of the Xenarthra*, eds S. F. Vizcaíno, and W. J. WJ Loughry (Gainesville: University Press of Florida), 86–99.

Vizcaíno, S. F., and Bargo, S. M. (2003). Limb reconstruction of Eutatus seguini(Mammalia: Xenarthra: Dasypodidae), Paleobiological implications. *Ameghiniana* 40, 89–101.

Vizcaíno, S. F., Blanco, R. E., Bender, J. B., and Milne, N. (2010). Proportions and function of the limbs of glyptodonts (Mammalia, Xenarthra). *Lethaia* 44, 93–101. doi: 10.1111/j.1502-3931.2010.00228.x

Vizcaíno, S. F., De Iuliis, G., and Bargo, M. S. (1998). Skull shape, masticatory apparatus, and diet of Vassallia and Holmesina (Mammalia: Xenarthra: Pampatheriidae): when anatomy constrains destiny. *J. Mamm. Evol.* 4, 291–322. doi: 10.1023/A:1020500127041

Vizcaíno, S. F., Farina, R. A., and Mazzetta, G. V. (1999). Ulnar dimensions and fossoriality in armadillos. *Acta Theriol.* 44, 309–320.

Vizcaíno, S. F., and Milne, N. (2002). Structure and function in armadillo limbs (Mammalia: Xenarthra: Dasypodidae). *J. Zool.* 1, 117–127. doi: 10.1017/S0952836902000717

Vizcaíno, S. F., Zárate, M., Bargo, M. S., and Dondas, A. (2001). Pleistocene burrows in the Mar del Plata area [Argentina] and their probable builders. *Acta Palaeontol Pol.* 46, 289–301.

Voje, K. L., Hansen, T. F., Egset, C. K., Bolstad, G. H., and Pélabon, C. (2014). Allometric constraints and the evolution of allometry. *Evolution* 68, 866–885. doi: 10.1111/evo.12312

Walmsley, A., Elton, S., Louys, J., Bishop, L. C., and Meloro, C. (2012). Humeral epiphyseal shape in the Felidae: the influence of phylogeny, allometry, and locomotion. *J. Morphol.* 273, 1424–1438. doi: 10.1002/jmor.20084

Webb, S. D. (2006). The great american biotic interchange: patterns and processes1. *Ann. Missouri Bot. Gard.* 93, 245–257.

White, J. L. (2010). Indicators of locomotor habits in xenarthrans: evidence for locomotor heterogeneity among fossil sloths. *J. Vertebr. Paleontol.* 13, 230–242. doi: 10.1080/02724634.1993.10011502

Wroe, S., and Milne, N. (2007). Convergence and remarkably consistent constraint in the evolution of carnivore skull shape. *Evolution* 5, 1251–1260. doi: 10.1111/j.1558-5646.2007.00101.x

Zelditch, M. L., Swiderski, D. L., and Sheets, H. D. (2012). *Geometric Morphometrics for Biologists*. Cambridge, MA: Academic Press.

Conflict of Interest: The authors declare that the research was conducted in the absence of any commercial or financial relationships that could be construed as a potential conflict of interest.

frontiers in Earth Science

ORIGINAL RESEARCH
published: 29 May 2020
doi: 10.3389/feart.2020.00160

The Tail of the Late Jurassic Sauropod *Giraffatitan brancai*: Digital Reconstruction of Its Epaxial and Hypaxial Musculature, and Implications for Tail Biomechanics

Verónica Díez Díaz[1,2], Oliver E. Demuth[3,4], Daniela Schwarz[1] and Heinrich Mallison[5,6]*

[1] Museum für Naturkunde Leibniz-Institut für Evolutions- und Biodiversitätsforschung, Berlin, Germany, [2] Humboldt Universität zu Berlin, Berlin, Germany, [3] Structure and Motion Laboratory, Royal Veterinary College, Hatfield, United Kingdom, [4] School of Earth Sciences, University of Bristol, Bristol, United Kingdom, [5] Center of Natural History (CeNak), University of Hamburg, Hamburg, Germany, [6] Palaeo3D, Pöttmes, Germany

OPEN ACCESS

Edited by:
Pasquale Raia, University of Naples Federico II, Italy

Reviewed by:
Peter Lewis Falkingham, Liverpool John Moores University, United Kingdom
Ryan T. Tucker, Stellenbosch University, South Africa

***Correspondence:**
Verónica Díez Díaz
diezdiaz.veronica@gmail.com

Specialty section:
This article was submitted to Paleontology, a section of the journal Frontiers in Earth Science

Received: *31 January 2020*
Accepted: *29 April 2020*
Published: *29 May 2020*

Citation:
Díez Díaz V, Demuth OE, Schwarz D and Mallison H (2020) The Tail of the Late Jurassic Sauropod Giraffatitan brancai: Digital Reconstruction of Its Epaxial and Hypaxial Musculature, and Implications for Tail Biomechanics. Front. Earth Sci. 8:160. doi: 10.3389/feart.2020.00160

Dinosaur locomotion and biomechanics, especially of their pelvic girdles and hindlimbs, have been analyzed in numerous studies. However, detailed volumetric musculoskeletal models of their tails are rarely developed. Here, we present the first detailed three-dimensional volumetric reconstruction of the caudal epaxial and hypaxial musculature of the Late Jurassic sauropod *Giraffatitan brancai*, and highlight the importance and necessity of 3D modeling in musculoskeletal reconstructions. The tail of this basal macronarian is relatively short compared to diplodocids and other coexisting macronarians. The center of mass lies well in front of the hindlimbs, which support only ca. half the body weight. Still, our reconstruction suggests a total weight for the entire tail of ca. 2500 kg. We conclude that the hypaxial and tail-related hindlimb muscles (most specifically the *M. caudofemoralis longus* and its counterpart the *M. ilioischiocaudalis*) in *Giraffatitan* were well developed and robustly built, compensating for the shorter length of the *M. caufodemoralis longus*, the main hindlimb retractor muscle, in comparison with other sauropods. Our methodology allows a better-constrained reconstruction of muscle volumes and masses in extinct taxa, and thus force and weight distributions throughout the tail, than non-volumetric approaches.

Keywords: sauropoda, Tendaguru, *Giraffatitan*, volumetric musculoskeletal modeling, tail

INTRODUCTION

Reconstructions of the musculoskeletal system of dinosaurs have been inferred from the anatomical comparison of and the inference of homological structures in closely related or osteologically similar animals (e.g., Dilkes, 1999; Carrano and Hutchinson, 2002) based on the extant phylogenetic bracket (EPB) (Bryant and Russell, 1992; Witmer, 1995, 1997). Key examples for this are the highly esteemed and classical publications of Romer (e.g., Romer, 1923), which rely on thorough studies of the anatomy of living taxa. In the case of dinosaurs, numerous publications (e.g., Dilkes, 1999; Carrano and Hutchinson, 2002; Hutchinson, 2002; Organ, 2006; Schwarz-Wings, 2009; Allen, 2010) have analyzed the muscles of the limbs and the axial skeleton of living archosaurs (i.e., crocodilians

and birds), and extrapolated this information to infer it on to the preserved osteological remains of extinct taxa.

Musculature and ligaments often leave characteristic traces (= osteological correlates, Witmer, 1995) on the bone surface of all vertebrates. Where such osteological correlates for muscles are present on the vertebrae in both sauropods and crocodilians, these muscles can be reconstructed as level II inference (Witmer, 1995, 1997). However, variation in the soft tissue configuration and uncertainties in the interpretation of osteological correlates demand a cautious approach in reconstructing soft tissue anatomy of extinct taxa (Bryant and Russell, 1992; Witmer, 1995; Carrano and Hutchinson, 2002). Sauropod vertebrae expose a complex surface pattern of laminae, fossa, ridges, bulges and rugosities, which are associated with pneumatic structures and attachment sites of muscles, tendons and ligaments (Wedel et al., 2000; Wedel, 2003a,b, 2009; O'Connor, 2006; Schwarz-Wings, 2009). Unambiguous pneumatic structures can be distinguished from correlates for muscles and ligaments by the presence of pneumatic foramina that penetrate deeply into the bone (O'Connor, 2006).

Over the last few years, vertebrate paleontology took advantage of novel techniques and software (Cunningham et al., 2014; Sutton et al., 2014). Digitization methodologies (e.g., CT scanning and photogrammetry, see Mallison and Wings, 2014; Fahlke and Autenrieth, 2016) and Computer-Aided-Design (CAD) tools made it possible to capture the morphology of the bones upon which three-dimensional reconstructions of the musculoskeletal system of extinct animals could be improved. The spatial organization of muscle groups can be assessed in 3D and thus intersections of individual muscles prevented. These three-dimensional reconstruction methods have overwhelmingly focused on cranial and especially adductor musculature (Lautenschlager, 2013; Sharp, 2014; Button et al., 2016; Gignacand Erickson, 2017), while the axial musculature received little attention. The myological reconstruction of the dinosaur tail in particular is a complex task, as it consists of ten individual muscles, partly subdivided into multiple heads. Previous studies on dinosaur tail musculature have primarily focused on the *M. caudofemoralis longus* (CFL) (e.g., Mallison, 2011; Persons and Currie, 2011, 2012; Persons et al., 2014), because of its locomotive importance as the main hindlimb retractor muscle. However, none has attempted to reconstruct the complete musculoskeletal system of the tail. Here we present the reconstructed caudal anatomy of *Giraffatitan brancai* based on the comparison of the caudal vertebral anatomy, which has previously been described in great detail (e.g., Janensch, 1914, 1950a, 1961; Paul, 1988; Taylor, 2009), and muscle attachments with those of extant crocodilians.

The axial skeleton of *Giraffatitan* has been described extensively (Janensch, 1950a), and a reconstruction was also suggested for the mounted skeleton (Janensch, 1950b). Modern anatomical knowledge was later used to establish a new mount of the skeleton, on display at the Museum für Naturkunde Berlin (MfN) since 2007 (Remes et al., 2011). In the first mount and descriptions, Janensch (1950b) suggested an anteriorly ascending posed dorsal column, induced by the long forelimbs and high anterior trunk, and accordingly a matching tilted position of the sacrum. The lack of keystoning in the anterior caudal vertebrae convinced Janensch (1950b) that the anterior tail of *Giraffatitan* extended from the hips in a straight, thus caudally descending line, in contrast to the tails of other sauropods, which emerged from the hips horizontally. This posture led to the tail contacting the ground much further anteriorly in relation to its overall length than in the other species Janensch (1950b) mentioned: *Dicraeosaurus hansemanni*, *Diplodocus carnegii* and *Camarasaurus lentus*. During a general renovation of the Berlin dinosaur exhibition hall (between 2005 and 2007), the mounted skeleton was rebuilt. The new mount differs from the old mount in several key characteristics (Remes et al., 2011):

- Improvements to the models of the presacral vertebrae and head,
- The posture of the neck, the shape of the torso,
- The orientation of the pectoral girdle and forelimbs, and
- The posture of the tail, still emerging from the hip caudally descending, but curving slightly dorsally to remain well clear of the ground.

Here, we digitally reconstruct the tail of this sauropod. We applied photogrammetric 3D digitization and 3D modeling tools in combination with information provided by dissections of extant crocodilians (*Alligator mississippiensis*) (**Supplementary Figure S1**) and an Extant Phylogenetic Bracket (EPB; Witmer, 1995) approach by comparing the anatomy of the caudal vertebrae and muscles of *Giraffatitan* with that of extant crocodilians. The other side of the bracket, birds, shows a strongly reduced caudal musculoskeletal system, which is adapted for novel functions in flight and display (e.g., Gatesy and Dial, 1996; O'Connor et al., 2013). Bird tails are much shorter, with fewer vertebrae, of which up to half are co-ossified into the pygostyle. Just anterior to the pygostyle, there is a maximum of six mobile vertebrae present, depending on the species (Gatesy and Dial, 1996). Furthermore, changes between the thoracic and caudal epaxial musculature are hypothesized to coincide with the evolution of the synsacrum (a structure highly involved in the flight, together with the notarium, see Organ, 2006). For example, caudal epaxial muscles were decoupled from their locomotor function on the evolutionary line to birds (Gatesy and Dial, 1996), and several muscles were lost (e.g., *Mm. interspinales* and *M. multifidus*). In addition, due to the absence of chevrons, the attachments of the tail depressor muscles shifted to the transverse processes, among further modifications (Pittman et al., 2013). The absence of chevrons and the truncation of the bird tail also relate to a reduction of the hypaxial *M. caudofemoralis* in birds, but also in maniraptoran theropods, as hypothesized from the lack of a clearly distinguishable fourth trochanter (Gatesy, 1991a; Rashid et al., 2014). In addition, the origin of the *M. caudofemoralis longus* in birds, where present, is on the pygostyle (e.g., Gatesy, 1991a). These changes on the skeleton and muscle modifications, especially the ones related to the hypaxial musculature, led to a decoupling of the locomotor structures from each other (Gatesy and Dial, 1996; Dececchi and Larsson, 2013), therefore in extant birds the reduced tail muscles have lost their propulsion function and connection

to the hindlimbs. This leaves only extant crocodilians as a model for the configuration and architecture of the caudal musculature for sauropod dinosaurs. Modern crocodilians can be used to infer the set of epaxial and hypaxial tail muscles present in sauropod dinosaurs, especially given the similarities in the osteological correlates (see below). The musculoskeletal system of the crocodilian tail has been described in detail by many researchers (e.g., Hair, 1868; Romer, 1923; Frey, 1982a,b, 1988; Frey et al., 1989; Cong et al., 1998; Hutchinson and Gatesy, 2000; Wilhite, 2003; Allen et al., 2014). We focused on these publications for the reconstruction of the tail muscular anatomy of *Giraffatitan brancai*. We follow the homologization of different epaxial and hypaxial muscle groups in archosaurs by Tsuihiji (2005, 2007).

In addition, crocodilians are the sole living large reptiles that can walk with the belly and most of the tail being held off the ground. They lift their tail from the ground during high walk (distal half of tail sometimes on the ground, proximal half lifted up) and gallop (tail lifted completely), although this is not employed over long distances (see e.g., Cott, 1961; Webb and Gans, 1972; Zug, 1974; Gatesy, 1991b; Hutchinson et al., 2019). This makes them the closest available analog to sauropod dinosaurs.

Institutional abbreviations: MB.R. Museum für Naturkunde Berlin, Berlin, Germany.

MATERIALS AND METHODS

Material

The lectotype of *Giraffatitan brancai* (Taylor, 2009, 2011) is the partial skeleton SI (MB.R.2180), and the paralectotype is SII (MB.R.2181). The mounted skeleton in the exhibition of the Museum für Naturkunde (**Figure 1**) is a composite reconstruction, consisting mostly of MB.R.2181 (SII), and including elements of MB.R.2180 (SI), duplicates of some bones, and plaster reconstructions of the missing parts (Janensch, 1950b; Remes et al., 2011). However, neither SI nor SII included caudal vertebrae, even though other skeletal remains of *Giraffatitan* were found in the same quarry "S" in the Tendaguru area. Therefore, Janensch used the vertebrae from quarry "no," MB.R.5000, for the mount (Janensch, 1950b).

In total, three caudal series are known from the Tendaguru area for *Giraffatitan brancai*: MB.R.5000 (from quarry "no"), MB.R.2921 (from quarry "Aa") and MB.R.3736 (from quarry "D").

Giraffatitan brancai had ca. 50–60 caudal vertebrae.

- The longest caudal series recovered has 50 caudal vertebrae (MB.R.5000). It consists of the second to fifty-first caudal vertebrae (Janensch, 1950a). As Janensch (1950a) states, these caudal vertebrae were found "not articulated, with the exception of a few at the end, but altogether relatively in sequence."
- Series MB.R.3736 consists of 29 caudal vertebrae. The first 23 caudal vertebrae (from the second to the twenty-fourth of the series) were found in articulation, and the rest (from the twenty-sixth to the thirty-second, missing the thirty-first) were found associated (Janensch, 1950a). No chevrons were found next to this caudal series.
- Series MB.R.2921 consists of the first 18 caudal vertebrae (MB.R.2921.1-18) and fourteen of their chevrons (MB.R.2921.19-32), found in an articulated sequence behind the last sacral vertebra (Janensch, 1950a).

Janensch (1950a,b) mentioned severe taphonomic damage to series "no" (MB.R.5000), including shrinking of many centra. Additionally, there are some anatomical differences between MB.R.5000 and the other two caudal series, in particular concerning the presence of pneumatic features (Wedel and Taylor, 2013). Series MB.R.5000 was therefore used only for comparative purposes for this study, especially considering that access to it on the mount is difficult. Series MB.R.2921 and MB.R.3736 resemble each other in osteology, and were therefore primarily used for this study. For the analysis of the anatomical features both these caudal series were studied, but only MB.R.2921 (the better preserved series) was used for the three-dimensional reconstruction of the musculoskeletal system. Especially information on the neural arches and the epaxial musculature could be more confidently obtained in the caudal series MB.R.2921 and its elements are overall more complete than those of MB.R.3736.

Series MB.R.2921 shows some obvious damage: the left transverse processes of caudal vertebrae 1–3, 5–7, and 9 are missing, as is the right transverse processes of caudal vertebra 4, while those of caudal vertebrae 3 and 5 are damaged. The left prezygapophyses of all vertebrae within the entire series are well preserved, but the right prezygapophysis is missing in caudal vertebra 3. The postzygapophyses are all preserved but for the right one in caudal vertebra 2.

The damage in series MB.R.3736 is far more extensive. Only a small number of caudal vertebrae preserve zygapophyses, and most neural arches and spines as well as transverse processes are missing or badly damaged. The centra, in contrast, are mostly well preserved.

One partial sacrum was found in the same quarry "Aa," as were the caudal series MB.R.2921 (Janensch, 1950a, fig. 74). However, this sacrum could not be re-located in the collections of the MfN, and it must be assumed that the original fossil was lost during WWII. A simplified cast of it exists in the skeletal mount. For the development of the three-dimensional musculoskeletal model we used this sacrum cast MB.R.5003, as well as the right femur MB.R.5016 (quarry number "Ni"), right tibia MB.R.2181.84 (quarry number "SII") and right fibula MB.R.2181.85 (quarry number "SII") on display, adjusting their size to match the caudal series.

Methods

The fossils were digitized via photogrammetry, following the protocols of Mallison and Wings (2014), and the updated version of Mallison et al. (2017). A digital SLR camera (Canon EOS 70D with Canon 10–18 mm f4.5-5.6 lens) was used with a LED ring light. Images were processed in Agisoft

FIGURE 1 | The current mount (on display since 2007) of the Late Jurassic sauropod *Giraffatitan brancai* (foreground) at the main hall of the Museum für Naturkunde (Berlin, Germany). Photograph by Antje Dittmann (MfN).

PhotoScan Professional v.1.4.0[1], in order to obtain three-dimensional models of each bone. High-quality polygon mesh files were created (approximately 5 million polygons and 250 MB as binary STL files each) for curatorial and museological purposes, but also lower resolution color-free STL files (50.000 polygons) for the musculoskeletal modeling and biomechanical analysis presented here.

Several chevrons were poorly preserved, some with missing parts, e.g., the distal part of the blade, or one of the rami (MB.R.2921.19-20, 24, 29-30, 31). These elements were digitally restored in zBrush 4R7 (Pixologic)[2], either by mirroring the preserved ramus, or by scaling and superimposing the distal part of the blade of adjacent chevrons. The two missing chevrons, 1 and 12, were entirely created digitally. Chevrons MB.R.2921.19 (the second) and MB.R.2921.29 (the thirteenth) were used as proxy models and scaled to fit into the sequence, but also to the articular facets of their corresponding caudal vertebrae.

All 3D models were imported into Rhinoceros 5.0 (McNeel Associates)[3] and articulated in the osteological neutral pose (ONP, after Stevens and Parrish, 1999, 2005a,b; Mallison, 2010a,b) following the protocol described by Mallison (2010a,b): individual vertebrae were articulated in pairs to minimize the impact of preconceived ideas (e.g., overall downward position of the tail, as in the former reconstruction of the mounted skeleton of *Giraffatitan*). Additionally five cartilaginous neutral poses (CNP, after Taylor, 2014) were assessed to test the influence of the intervertebral cartilage on the muscle volume.

As previously commented, we only can rely for a 50% EPB level I inference when reconstructing most of the muscles in terms of insertions and passages, as we only have one part of the bracket (i.e., crocodilians). However, the general presence of the reconstructed muscles for tail and femur are present also in birds in most cases (e.g., the suite of epaxial muscles – at least until the pygostyle –, and the *M. caudofemoralis longus*), so a level II inference would only apply to the *M. ilioischiocaudalis*. Besides, and as already mentioned, those bones present in birds too (i.e., femur, sacrum and first two caudal vertebrae) are very strongly modified in extant taxa, as are the muscles because of their locomotionary differences. Morphologically, the sacrum and femur of sauropods are more similar to crocodilians than to birds, helping to confirm this level II inference.

The three-dimensional models of the musculature were created in the software package Autodesk Maya[4]. We used a polygon-based modeling approach, similar to the box modeling approach by Rahman and Lautenschlager (2017), to build each muscle individually from the origin to the insertion, on the

[1]http://www.agisoft.com

[2]http://pixologic.com/features

[3]www.rhino3d.com

[4]https://www.autodesk.com/products/maya/overview

basis of osteological correlates identified by study of the physical and digital specimen. This allowed us greater control over the flow of the muscle shape than in a NURBS-based approach (e.g., Persons and Currie, 2011; Persons et al., 2014). Finely segmented muscles, e.g., the transversospinalis group, were simplified into a single body.

Bone volumes were calculated with Rhinoceros 5.0, and muscle volumes with Maya. For the muscle mass we use the density value proposed by Méndez and Keys (1960) for mammalian muscles ($d = 1.06 \times 10^3$ kg/m^3), which is similar to the measurements obtained by Hutchinson et al. (2015) for the hindlimb muscles of an ostrich (*Struthio camelus*).

For the calculation of bone mass the following factors were taken into consideration. Most caudal vertebrae of *Giraffatitan* have small pneumatic fossa indicating a small amount of pneumatisation. Overall, the pattern of pneumatisation in *Giraffatitan* caudal vertebrae is variable and irregular (Wedel and Taylor, 2013). As the caudal vertebral centra have a high volume to surface ratio, we estimate their cortical portion to be rather smaller than in girdle bones, ribs, or complexly shaped presacral vertebrae, and the trabecular and marrow portion to be accordingly larger. The volumetric bone density is typically close to 2×10^3 kg/m^3 for long bones (e.g., Mohiuddin, 2013; Fletcher et al., 2018) and somewhat lower for marrow-rich bones, due to the lower density of marrow of ca. 1×10^3 kg/m^3. We here chose 1.5×10^3 kg/m^3 for overall bone volumetric density, expecting the amount of pneumaticity to be the main driver von average density variation in the tail of *Giraffatitan*.

RESULTS

Osteologically Neutral Pose (ONP)

For exact alignment we found the reduced size files with 50.000 polygons insufficiently detailed. We therefore worked with the higher-resolution files with five million polygons.

Initially, we used the prezygapophyses and postzygapophyses as proxy for assessing the correct articulation between vertebrae, assuming that given full zygapophyseal overlap and – as far as possible – sub-parallel centra faces, the distance between vertebral bodies probably reflects the approximate intervertebral cartilage volume (Christian and Preuschoft, 1996; Christian and Dzemski, 2007).

Articulating the zygapophyses of series MB.R.2129 with full overlap (**Figure 2E**) resulted in a nearly straight line of vertebrae, but tilted some of the centra around their vertical and longitudinal axes (**Figures 2A,B**). Also, a slight but noticeable asymmetry and "twisting" around various axes of most neural arches, including the postzygapophyses, induced a slight sigmoidal curve, initially to the left, then to the right. The deformations also caused a long-axis rotation in parts of the series, tilting the neural spines of caudal vertebrae 3 through 8 noticeably to the left (**Figure 2B**). Additionally, due to slight taphonomic deformation of some zygapophyses, we could not completely avoid small intersections between zygapophyses (e.g., between caudal vertebrae 17 and 18) or larger, unrealistic gaps in the zygapophyseal joints.

We therefore reassembled the series MB.R.2129 based on centra faces to create a more life-like, less taphonomy-influenced reconstruction (**Figure 2C**), with higher lateral symmetry, which we used for the 3D reconstruction of the musculature. This second articulation consequently suffers from some additional, massive intersection between zygapophyses. While the anterior rim of the first caudal vertebral centrum is markedly concave in lateral view, the posterior rim is flat in lateral view. In all other vertebrae, both the anterior and posterior rims of the centra are mostly flat in lateral view, allowing a straightforward assembly of the tail based on the centra faces. Therefore, we were able to create this centra-based articulation without any uncertainty with regards to the angles between the vertebrae.

The chevrons were positioned into the existing articulated caudal vertebral series by matching their anterior and posterior articular facets with the orientation of the ventral articulation surfaces of each centrum. A short space was retained between the chevron and the vertebra, representing the volume of the articular cartilage. We found that the centra faces could be retained in practically parallel orientation with the chevrons added.

Overall, series MB.R.2129 shows a slight curvature in lateral view, lifting the posterior end by ca. one full centrum height of caudal vertebra 18 compared to the trend of the first three vertebrae. Repeated "playing" with the bone trios (two vertebrae and their chevron) to optimize alignment tended to increase rather than decrease the curvature.

In the skeletal reconstruction of the MB.R.3736 series a slight sigmoidal shape is created by centra-only alignment in the long axis of the tail in lateral view, between the fifteenth and eighteenth vertebrae, and the terminal section bends slightly ventrally (**Figure 2D**).

Cartilaginous Neutral Poses (CNPs) (Figure 3)

Several previous studies analyzed the ONP of the neck of sauropods and the effect of the intervertebral cartilage (e.g., Taylor and Wedel, 2013a; Taylor, 2014; Vidal et al., 2020a and references therein), but there is scant published data on the effects of intervertebral cartilage within the tail. As stated by Taylor and Wedel (2013a) the thickness of the articular cartilage between the centra of adjacent vertebrae affects posture. In this work we also assess how this cartilage thickness affects the mass, volume, and extension of the musculature (see below). However, for extinct taxa we can only make assumptions about the cartilage that existed in life. For that, five CNPs (Taylor, 2014) with different cartilage thicknesses (2.5, 5, 10, 15, and 20%) were assessed. Cartilage thicknesses percentages were chosen after the calculations of Taylor and Wedel (2013a) and Taylor (2014) for the cervical vertebrae of several extant animals and sauropod taxa, as data on caudal series is no available yet. Cartilage thicknesses were calculated as percentages of the centrum lengths (**Supplementary Table S1**).

Intervertebral cartilage volumes were added to the previous ONP. Taylor (2014) quantified the angle of extension at intervertebral joints when different cartilage thicknesses were included. This extension occurs because the thin zygapophyseal

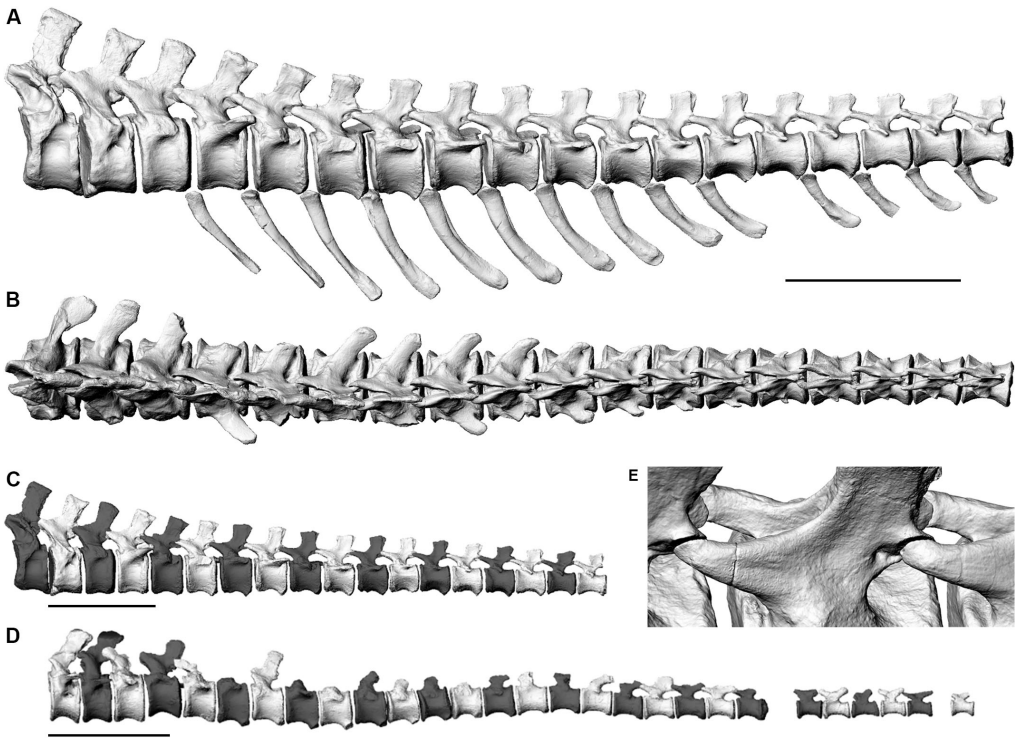

FIGURE 2 | Left lateral views **(A,C,D)** and dorsal view **(B)** of the three-dimensional skeletal reconstructions of two caudal vertebral series of the Late Jurassic sauropod *Giraffatitan brancai*. **(A–C)**. MB.R.2921 **(D)** MB.R.3736. **(A,B)** show alignment based on best fit of zygapophyses and sub-parallel centra, **(C,D)** show alignment based on centra faces. **(E)** Oblique close-up of the sets of zygapopyseal pairs (C 7–8 and C 8–9) from articulation in panels **(A,B)** aligned for best fit. Only the preserved remains have been illustrated here.

cartilage has no or negligible effect on the angle of extension between vertebrae, while the thick intervertebral one does: the angle of elevation at an intervertebral joint is increased when cartilage is included. This is true for opisthocoelous and procoelous vertebrae, but in the caudal series MB.R.2129 of *Giraffatitan* this dorsal or ventral extension is not present when different cartilage thicknesses are included, as these caudal vertebrae do not present condyles. Similar poses are obtained for the ONP and all the CNPs. However, it is important to state that in CNP 15% the zygapophyses start disarticulating from ca. seventeenth caudal onward, and in CNP 20% from the twelfth. An improved and more accurate model could be created by articulating the zygapophyses and thickening the base of the cartilage, resulting in a dorsal extension of the tail from this section. However, the cartilage volume is already thick at CNP 20%, and by increasing it in its base probably would lead to disarticulation of the chevrons too. Together with other results (see below) we do not consider this CNP 20% model as a possibility for a living animal. In the other CNPs the zygapophyses appear articulated, but a dorsal extension of the tail section that is not preserved could not be ruled out, as also seen in the CNP 15%. Besides, in the CNP 2.5 and 5% the caudal vertebrae are spaced very tightly, thus limiting movement of the tail, and furthermore making it impossible to correctly articulate the chevrons. Only the CNP 10% and 15% are therefore deemed possible for this caudal series.

Several sauropod caudal series have been found articulated or closely associated. Although it is uncertain linking the intervertebral spaces found in these articulated remains with the cartilage volume present in the living animal, we have checked them looking for hypothetical connections with our model. For example, the titanosaurian taxa *Oversosaurus* (Coria et al., 2013) and *Dreadgnothus* (Lacovara et al., 2014) preserved the first 20 caudal vertebrae articulated. Some measurements were made using the published material (figures, and a 3D model for the *Dreadgnothus* caudal series), and some interesting data were obtained: for *Overosaurus* intervertebral spaces of 26 to 28% the centrum length were calculated, while for *Dreadgnothus* the values changed along the series, being larger in the anterior section (ca. 40 to 44%) and decreasing through the series (20 to 22%). One specimen (DFMMh/FV 100) of the camarasauromorph *Europasaurus* presents an articulated caudal series of 13 vertebrae (Carballido and Sander, 2014). It was not possible to take accurate measurements as most of the vertebrae, although articulated, were displaced, but an intervertebral space of ca. 17–18% was calculated. The brachiosaurid *Padillasaurus* preserved the first eight caudal vertebrae in articulation (Carballido et al., 2015). The calculated intervertebral spaces were between 26 and 28%. However, this specimen presents a dorsal extension, so the calculated cartilage thicknesses are probably not comparable to the ones of the living animal. This dorsal extension of the tail is present in

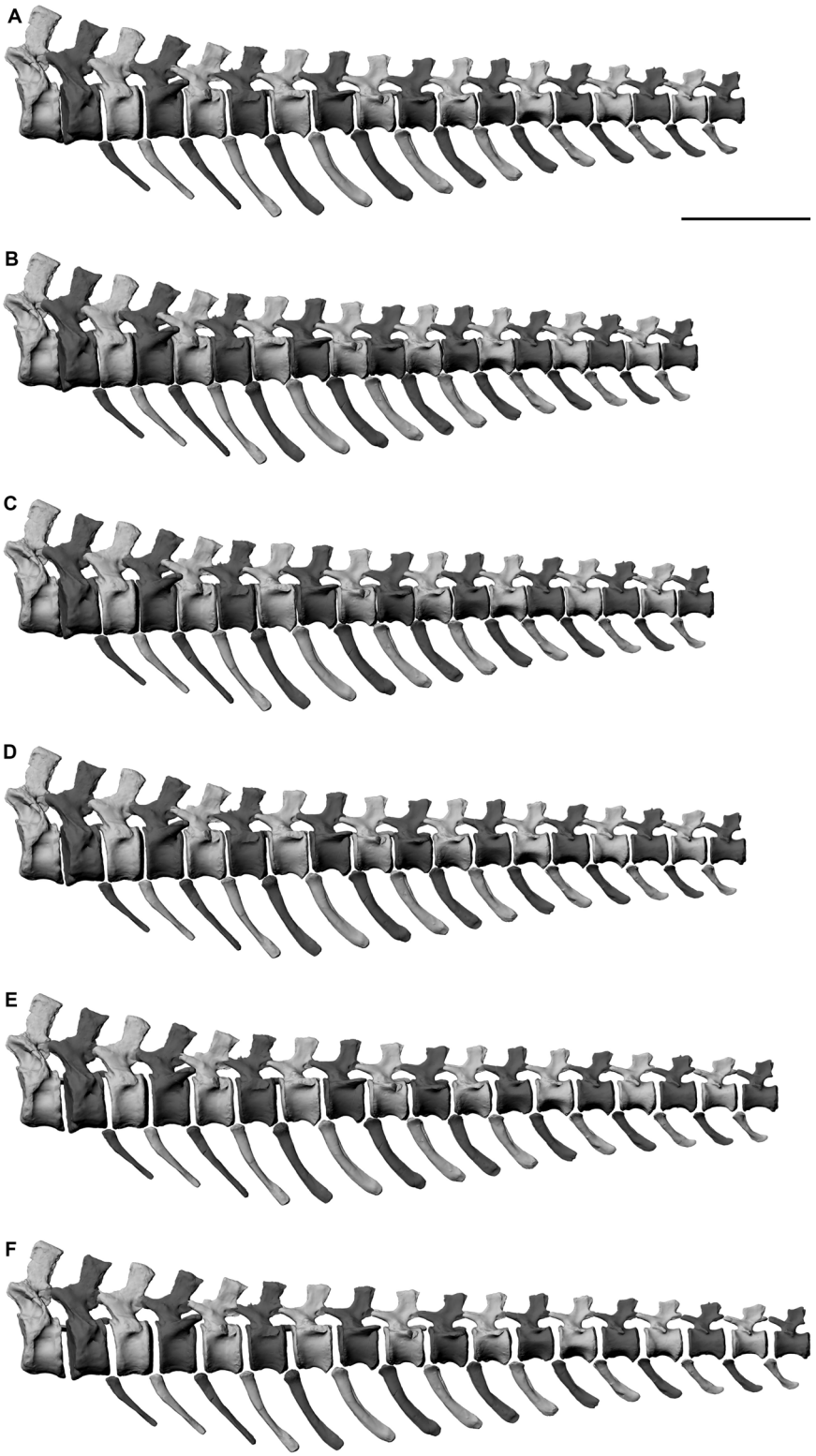

FIGURE 3 | Comparison between the **(A)** ONP, **(B)** CNP at 2.5%, **(C)** CNP at 5%, **(D)** CNP at 10%, **(E)** CNP at 15%, and **(F)** CNP at 20%. Scale = 50 cm.

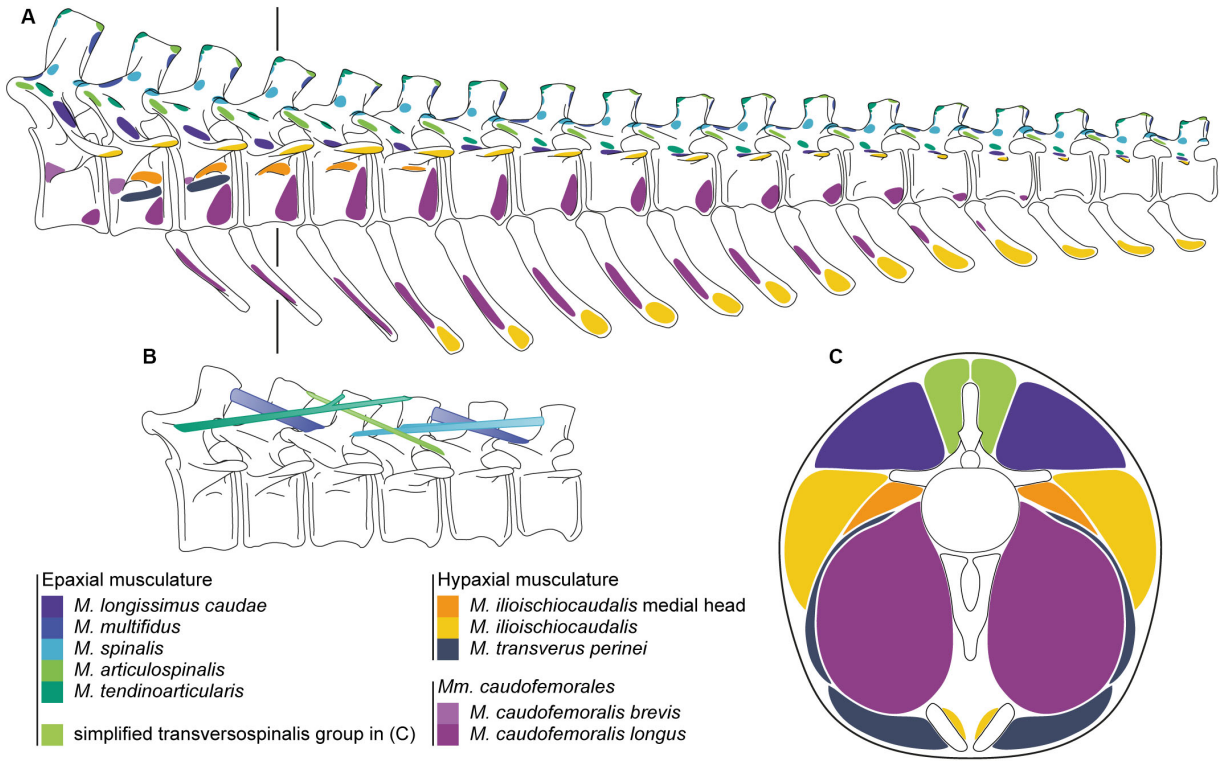

FIGURE 4 | (A) Origins and insertions of the caudal musculature of the Late Jurassic sauropod *Giraffatitan brancai*. **(B)** Simplified muscle paths of the transversospinalis group of the epaxial musculature. **(C)** Cross-section of the tail at the fourth caudal vertebrae showing the lateral extent of the tail musculature. The line in A indicates the location of the cross-section through the musculature. Paired ventral elements represent the ischia.

other sauropod caudal series, as *Camarasaurus* (Gilmore, 1925) or *Spinophorosaurus* (Remes et al., 2009). As already seen, numerous taphonomical factors need to be taken into account, so we cannot use these values with fidelity. Besides, they also indicate that cartilage thickness could highly vary through the caudal series, but also depend on the taxon. In addition, the articulation type between vertebrae (i.e., procoely, opisthocoely, etc.) probably affected this thickness too. A recent work on the caudal biomechanics of the titanosaur *Aeolosaurus maximus* suggests a cartilage thickness between 5 and 10% for the anterior section of the tail (Vidal et al., 2020b). More detailed work on these sauropod articulated caudal series needs to be undertaken to approach more accurately this issue.

Muscle Marks and Musculature Reconstruction

The caudal vertebrae and chevrons of *Giraffatitan* presents numerous osteological correlates related to the origins and insertions of the muscles and ligaments of the tail (**Figure 4** and **Supplementary Figure S1**). The inferred sets of epaxial and hypaxial muscles, together with the relevant hindlimb musculature for the correct reconstruction of the tail musculature (which are directly in or close to contact and/or restrict the volume of the tail musculature) are detailed in **Supplementary Table S2**.

Neural Arches

The lateral faces of the neural spines are slightly concave and show longitudinal (apicoventrally directed) rugosities, parallel to each other. At the apical edge of the neural spine both anterior and posterior processus – with different development stages depending on the position in the series – can be seen in form of the distal tips of both the prespinal and postspinal laminae. From caudal vertebra 3 on, the middle part of the tip of the neural spine is thickened, developing an apical prominence (slightly posteriorly displaced) from the fourth vertebra on. From caudal vertebra 8 on, this bulge shows sharp posterior edges in dorsoventral orientation on the lateral faces of the neural spines. In addition, three spurs are present in the neural spine laminae: two on the base of the spinoprezygapophyseal laminae, and one in the postspinal lamina. The spike present on the postspinal lamina appears in the caudal vertebrae 5, 6, 8–11, and 14. However, this feature could have been present in all caudal vertebrae with a distinct postspinal lamina. The prominences of the spinoprezygapophyseal laminae appear in the caudal vertebrae 2, 3, 5–7, although they were probably present from the first caudal vertebrae to the seventh. These osteological features correspond to the attachment of deep epaxial muscles (mediodistally) and *M. multifidus* (medially), and both the *M. spinalis* and *M. articulospinalis* (laterally). The *M. multifidus* originates from the distal posterior tip of the neural spine*M. articulospinalis* from the distal posterior tip.

Zygapophyses

The zygapophyses serve as attachment areas for the epaxial muscles including the *M. spinalis* (zygapophyseal joint capsule) and *M. articulospinalis* (lateral rugosity on the prezygapophyses). The *M. multifidus* inserts in a spur or rugosity on the spinoprezygaposeal lamina of the second next vertebra (from the first to the seventh vertebrae), or in the subtle dorsal rugosity on the prezygapophyses from the eighth vertebra onward. The *M. articulospinalis* inserts on a lateral rugosity of the prezygapophysis two vertebrae further down the tail. The development of the mentioned attachment structures also depend on the position in caudal series, being steadily reduced distally.

Vertebral Centra

Although the prezygodiapophyseal lamina is not well developed, an oblique bulge and rugosity can be seen between the prezygapophysis and the transverse process, which is interpreted as the osteological correlate for the insertion of the *M. tendinoarticularis*.

The transverse process is an important osteological correlate for both the epaxial and hypaxial muscles. Its distal tip is an insertion for the hypaxial musculature (dorsal aspect of the *M. ilioischiocaudalis*). A bulge and rugosity at the junction between the transverse process and the centrum (proximal tail) and longitudinal ridge (13th vertebra onward) acts as attachment for the bounding septum (Grenzseptum) between the lateral epaxial musculature (*M. tendinoarticularis* and *M. longissimus caudae*) and is further the insertion for the *M. longissimus caudae*. Transverse processes are present in all the caudal vertebrae of MB.R.2921, becoming smaller and rounder distally. In MB.R.3736 the transverse processes disappear by caudal vertebra 25 in the series. As they disappear, the mentioned longitudinal ridge persists close to the junction between the neural arch and the centrum, delineating the insertion of both the *M. longissimus caudae* (dorsally) and the *M. ilioischiocaudalis* (ventrally).

The major part of the *M. caudofemoralis brevis* originates from the medial surface of the postacetabular process of ilium and the ventral aspect of the last sacral rib. From there, the muscle extents distally and also attaches anterolaterally on the centra of caudal vertebrae 1 to 3.

The first two caudal centra of MB.R.2921 show a lateral concavity below the transverse processes, which we interpret as a space for cryptic diverticula (see below). However, between these depressions and the transverse process in caudal vertebra 2 there is a shallow shelf, there are subtle bumps on caudal vertebra 3 to 5 at this position, which we regard to be the attachment site of the medial head of the *M. ilioischiocaudalis* (see **Supplementary Figure S2**). Ventral to the lateral depression in caudal vertebra 2 and approximately at the same position on caudal vertebra 3 there is a faint ridge, which serves as the origin for the *M. transversus perinei*. The muscle extends laterally, wrapping around the *M. caudofemoralis longus* and the ischial ramus of the *M. ilioischiocaudalis* to insert on the distal lateral ischium and on the aponeurosis surrounding the cloaca.

The ventral half of the centrum is convex in the anteriormost nine vertebrae, and then becomes gradually more concave (just below the transverse process). In these anterior vertebrae the distal lateral surface of the centrum serves as attachment for the *M. caudofemoralis longus*. Caudal 11 (right side) and caudal 12 shows the first occurrence of a lateral broadening of the centrum at half its height, forming an incipient ridge, of which there is no trace in the previous vertebrae. This ridge gradually moves ventrally in the next three vertebrae on both sides, separating two lateral surfaces, and merging into the ventrolateral border of the centrum. We interpret this weakly developed ridge as the caudal limit of the *M. caudofemoralis longus*, constricting the muscle into a narrow tip well separated from the transverse processes, unlike the dorsally directed tapering seen in extant crocodiles. After the fourteenth caudal the ridge merges into the ventrolateral edge of the centrum; accordingly, the ventrolateral surface disappear entirely, indicating that the *M. caudofemoralis longus* does not extend distally beyond this point.

Chevrons

The lateral surfaces of the chevrons and their general morphology are important osteological correlates for the hypaxial musculature and their development. In the lateral surface of the chevrons, more dorsally located in the anterior ones, a weak oblique rugosity appears, for the insertion of the *M. caudofemoralis longus*. On the distal tip, in its lateral aspect, another rugosity, for the insertion of the ventral part of the *M. ilioischiocaudalis*, is apparent. The morphology of the distal blade of the chevrons changes along the series: the first three chevrons have a more acute distal blade, while the next ones have a more rounded and transversally compressed distal third. From the twelfth chevron (thirteenth caudal vertebra) onward, this distal third of the blade becomes more posteriorly directed. These differences in morphology reflect a change in the insertions and development of both *M. caudofemoralis longus* and *M. ilioischiocaudalis*.

Sizes, Masses and Volumes

From the addition of all individual bone and muscle masses (**Table 1** and **Supplementary Tables S3, S4**) we here suggest hypothetical weights for the preserved caudal series MB.R.2921, depending on the ONP and CNPs.

ONP

The caudal series MB.R.2921 presents a total length (from the first caudal vertebra to the last) of 280.82 cm when articulated in ONP. All the caudal bones (vertebrae and chevrons) weighted 106.92 kg (1775.67 kg with the pelvis and sacrum), and all the muscle (right and left) groups 950.07 kg. So the preserved caudal series MB.R.2921 of *Giraffatitan* approximately weighted 1056.99 kg in total (2725.74 kg with the pelvis and sacrum). The total volume of the caudal series is 967.57 liters (2080.07 liters with the pelvis and sacrum). It is important to keep in mind that not all the vertebrae were completely preserved (e.g., some of them were missing parts of the transverse processes), and some epaxial muscles have been simplified, but this should not affect the volume.

TABLE 1 | Comparison of the calculated volumes (l) and masses (kg) for each reconstructed muscle group of the caudal series MB.R.2921 of the Late Jurassic sauropod from Tanzania *Giraffatitan* in CNP and CNPs.

		ONP	CNP_2.5%	CNP_5%	CNP_10%	CNP_15%	CNP_20%
Volume (l)							
Muscle	TSP	22.669	20.802	21.312	22.325	23.340	24.354
	LC	76.924	70.681	72.407	75.853	79.303	82.750
	IIC	121.276	114.303	117.115	122.738	128.359	133.982
	IICmed	10.139	9.235	9.451	9.885	10.319	10.753
	CFB	36.952	35.003	35.406	36.213	37.018	37.825
	CFL	170.262	156.311	159.894	167.583	175.097	182.611
	TRPR	9.923	8.972	9.210	9.684	10.159	10.633
	Total	448.144	415.307	424.795	444.281	463.595	482.908
Mass (Kg)							
Muscle	TSP	24.029	22.050	22.591	23.665	24.740	25.815
	LC	81.539	74.922	76.751	80.404	84.061	87.715
	IIC	128.553	121.161	124.142	130.102	136.061	142.021
	IICmed	10.747	9.789	10.018	10.478	10.938	11.398
	CFB	39.169	37.103	37.530	38.386	39.239	40.095
	CFL	180.477	165.690	169.488	177.638	185.603	193.568
	TRPR	10.518	9.510	9.763	10.265	10.769	11.271
	Total	475.032	440.225	450.283	470.938	491.411	511.882

The muscle volumes were calculated with the software Maya. The muscle masses were calculated using the density value proposed by Méndez and Keys (1960) for mammalian muscles ($d = 1.06 \times 10^3$ kg l/m^3). CFB, m. caudofemoralis brevis; CFL, m. caudofermoralis longus; IIC, m. ilioischiocaudalis; IICmed, m. ilioischiocaudalis medial head; LC, m. longissimus caudae; TRPR, m. transversus perinei; TSP, Transversospinalis group. See ***Supplementary Figure S4*** *for the individual segments.*

CNPs

The calculated lengths (from the first caudal vertebra to the last) and masses for the caudal series MB.R.2921 when articulated in the five CNPs are detailed in **Table 2**.

A length difference of 44.76 cm is calculated from the lowest to the highest length values. With our model we suggest that the chosen intervertebral cartilage volume could affect between 14.5 and 17% the total length of the tail. A muscular mass difference of 143.32 kg can be stated between the CNP with the lowest cartilage thickness value (2.5%) and the model with the highest value (20%). With our current model we can hypothesize that the chosen cartilage thickness could affect the total mass of the reconstructed muscles between ca.12 and 14% (ca. 5% when we also take into account the mass of the pelvis and sacrum). The increase of the muscle volumes and masses is proportional to the increase in cartilage thickness ($r^2 = 1$, p-value $< 5.00E-07$) for each muscle individually and all combined (see **Supplementary Table S3**).

TABLE 2 | Total lengths (cm) and masses (kg) calculated for the caudal series MB.R.2921 of the Late Jurassic sauropod from Tanzania *Giraffatitan* in CNP and CNPs.

	Total length	Mass (w/o pelvis)	Mass (w/pelvis)
ONP	280.82	1056.99	2725.74
CNP_2.5%	262.15	987.37	2656.12
CNP_5%	268.55	1007.49	2676.24
CNP_10%	281.34	1048.8	2717.55
CNP_15%	294.12	1089.74	2758.5
CNP_20%	306.91	1130.69	2799.43

DISCUSSION

ONP and CNPs

In light of the steep position of the tail base on the mounted skeleton, a slight upward turn in the distal part of the anterior tail section as suggested for MB.R.2129 is not surprising, seeing how it is required to keep a full tail of ca. 50 vertebrae from dragging on the ground. Overall, the good fit of the alignment with subparallel centra faces and an overall rather straight long axis matches other sauropods and in fact most dinosaurs well (Upchurch et al., 2004). We therefore find no indication that the strong anterior uptilt of the hip of *Giraffatitan* in any major way influenced the overall biomechanical organization of the tail. The total lack of keystoning, already mentioned in relation to overall tail articulation by Janensch (1950a,b) is a marked contrast to e.g., the basal sauropodomorph *Plateosaurus*, in which the addition of chevrons to the digital mount forced a wedge-shaped gap between the caudal vertebral centra that induced a straight tail axis (Mallison, 2010a). Without the chevrons, i.e., with parallel centra faces, the tail of *Plateosaurus* would show a significant ventral curvature (Wellnhofer, 1993; Moser, 2003). In *Giraffatitan*, the distance between chevron and vertebra, caused by the articulation process described, is consistent throughout the tail. N.B.: The articulation in the 3D model is noticeably tighter than on the mounted skeleton, where the support rod for the tail runs between centra and chevrons, making an anatomically correct articulation impossible.

A curvature similar to that seen in MB.R.3736 is also discernible in the hypothetical caudal vertebral series of the titanosaurian sauropod *Lirainosaurus* (Vidal and Díez Díaz, 2017).

However, MB.R.3736 is noticeably straighter, probably because of the articulation morphology between the caudal vertebrae. *Lirainosaurus* has highly procoelous caudal vertebrae, with anterior and posterior articular surfaces highly inclined (*keystoned* centra, see Vidal and Díez Díaz, 2017, fig. 6B).

When comparing the calculated values for the ONP and the CNPs, it can be observed that the most similar lengths and masses are obtained for the ONP and the CNP with an intervertebral cartilage thickness of 10% of the centrum length.

Taylor (2009) calculated a volume of 1520 liters (∼1216 kg, although bone and muscle densities cannot be separated from these calculations) for the tail of *Giraffatitan*, after a modified reconstruction of Paul (1988). Most of the mass of the tail was probably located at its base, where the largest parts of the muscles are placed together with the heaviest bones. It is therefore reasonable to suggest that in *Giraffatitan* at least half of the weight of the tail would have been placed in the first 20 caudal vertebrae. When following our reconstruction and results, the tail of *Giraffatitan* could have weighted ca. 2500 kg (not including the pelvis and sacrum), doubling Taylor's calculations.

Reconstruction of the *Mm. caudofemorales*

The development of the *Mm. caudofemorales*, especially the *M. caudofemoralis longus,* has always been a major issue when reconstructing the tails of extinct animals. The general morphology of the *Mm. caudofemorales* (as well as their origins and insertions) seems to be highly conservative within crocodilians (see e.g., Gatesy, 1991a; Ibiricu et al., 2014). Previous studies suggested that in crocodilians the *M. caudofemoralis longus* originates from the sides of the centrum and ventral surface of the transverse processes of caudal vertebrae 3–15 (Romer, 1923; Galton, 1969). However, Wilhite (2003) confirmed that this muscle additionally originates from the lateral surface of the first 13 chevrons, but only runs along the underside of the transverse processes, from which it is separated by a layer of connective tissue and, in well-fed individuals, by a layer of fat. Therefore, chevron morphology may be indicative of the size, shape, and extent of *M. caudofemoralis longus* in fossil archosaurs. This hypothesis is also followed by Otero and Vizcaíno (2006, 2008). The development and morphology of the transverse processes and the lateral and ventral surfaces of the centra are therefore important indicators for the size, shape and extent of *M. caudofemoralis longus* in sauropod dinosaurs. Several previous studies highlight the importance of the lateroventral surfaces of the anterior caudal centra for the origin and development of the *Mm. caudofemorales* in titanosaurian sauropods (Borsuk-Bialynicka, 1977; Salgado and García, 2002; Salgado et al., 2005), and Gallina and Otero (2009) suggest that the development of the *M. caudofemoralis brevis* and *M. caudofemoralis longus* occurs in relation with the anterior caudal transverse processes morphological variation along the tail. Several osteological correlates are indicative of the development and extent of the *M. caudofemoralis longus* in *Giraffatitan*:

The transverse processes disappear by caudal 25 in MB.R.3736. However, the absence of transverse processes cannot be used for determining the distal end of the *M. caudofemoralis longus*. Persons and Currie, 2011 found that the process expands beyond the distal end of the *M. caudofemoralis longus* in some squamates. In *Alligator mississippiensis* the *M. caudofemoralis longus* ends at the fourteenth caudal vertebra, the first one without transverse processes (Frey, 1988; Mallison, 2019).

- The ventrolateral surfaces of the centra appear from the third to the fourteenth caudal in MR.2921.
- The dorsolateral rugosity is present from chevrons 4 to 11 (caudal vertebrae fifth to twelfth).

Therefore, we inferred the extent of the *M. caudofemoralis longus* from the first caudal vertebra onward and not beyond the fifteenth caudal vertebra in *Giraffatitan*. While the maximal extent of the *M. caudofemoralis longus* is important for volume calculation (and thus maximal force estimates) the bulk of the muscle is located in the anterior region, thus the influence of a slightly longer or shorter muscle (±1 vertebra) are only minor on the total volume. However, a correct reconstruction of *M. transversus perinei* is more important for an accurate estimate of hip joint moments than an exact determination of the taper point of *M. caudofemoralis longus*. The *M. transversus perinei* acts as a lateral constraint on the *M. caudofemoralis longus*. If no *M. transversus perinei* is reconstructed, there is a high risk of overestimation of the *M. caudofemoralis longus* volume at is base, where even minimal changes to the lateral extent induce large volume changes, and accordingly a misestimation of its overall power.

In basal saurischians (e.g., *Eoraptor* and *Guaibasaurus*) and non-avian theropods the *M. caudofemoralis brevis* originates from the brevis fossa, a transitional structure located on the ventromedial surface of the ilium (Carrano and Hutchinson, 2002; Holtz and Omólska, 2004; Langer, 2004; Makovicky and Norell, 2004; Makovicky et al., 2004; Norell and Makovicky, 2004; Omólska et al., 2004; Tykoski and Rowe, 2004). However, in sauropods the origin of the *M. caudofemoralis brevis* is somewhat ambiguous, as they lack a brevis shelf and fossa (Upchurch et al., 2004), similar to the condition in extant crocodilians. In *Giraffatitan* a concave surface appears medially in the postacetabular process, below the last sacral rib and in the junction with the ilium. This surface is inferred as the origin of the *M. caudofemoralis brevis*, in combination with the anterior lateral surface of the centra of caudal vertebra 1 to 3.

The *Mm. caudofemorales* insert on the fourth trochanter of the femur. In sauropods the trochanter appears as a longitudinal ridge, without any differential sites for the insertion of both *M. caudofemoralis longus* and *brevis*. Otero and Vizcaíno (2008) went as far as suggesting a common tendon for both muscles. In the case of *Giraffatitan* the trochanteric ridge is well-developed; therefore, we modeled the insertion of each muscle separately, the *M. caudofemoralis longus* medially and the *M. caudofemoralis brevis* posterolaterally located to the fourth trochanter. In extant crocodiles the insertion is often highly complex, with the tendon of the longus portion wrapping around the very short tendon of the brevis portion, and often inserting into it (Allen, 2015; HM, 2017). However, this complexity leaves no trace on

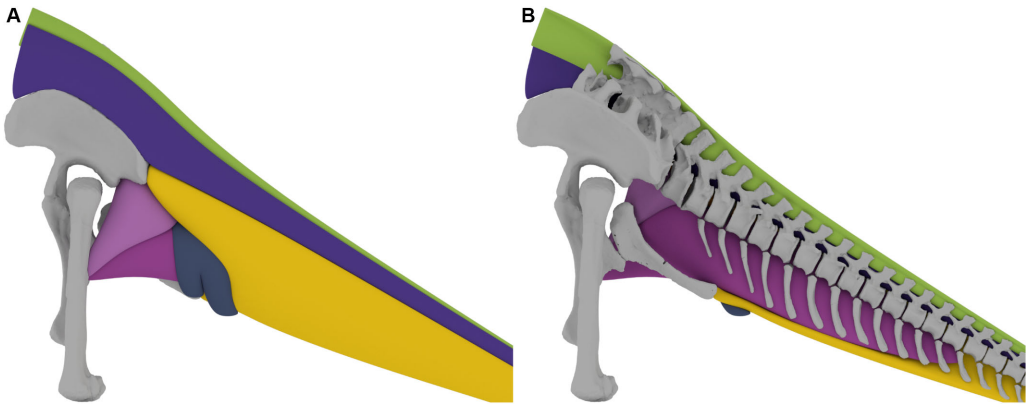

FIGURE 5 | (A) 3D tail muscle reconstruction of the Late Jurassic sauropod *Giraffatitan brancai*. **(B)** Sagittal section of the tail musculature, showing the dorsal and ventral extent of the musculature in relation to the vertebrae.

the bone, so that the exact paths and interactions cannot be reconstructed reliably.

Extent of the Caudal Musculature (Figures 5, 6)

The three-dimensional approach enabled the inference of the size and the spatial arrangement of the musculature. Individual muscles are not only constrained by their origins and insertions, but also by the neighboring musculature. It is therefore insufficient to model only the tail muscles. Consequently the nearby limb musculature was also modeled and taken into account. Nevertheless, some uncertainties regarding the development and proportions, lengths and volumes of the caudal musculature remain. In particular the ventral, lateral and dorsal extensions of the muscles are difficult to reconstruct, e.g., Persons (2009), Persons and Currie (2011), and Mallison (2011) demonstrated that the soft tissues in the tails of crocodilians and many squamates extend significantly beyond the bones dorsally and especially ventrally and laterally. Previous studies on caudal musculature in dinosaurs have predominantly used the extent of the bones as the extension for their soft tissue reconstructions (Carpenter et al., 2005, fig. 17.5; Arbour, 2009, fig. 9; Hutchinson et al., 2011, fig. 5), however, this minimal extension does not appear in any living animal. Persons (2009) correctly pointed out that the lateral width of the transverse processes is often a poor indicator of the lateral extent of *M. caudofemoralis longus* across a wide range of reptiles. Lacertilians such as the leopard gecko (*Eublepharis macularius*), the tokay gecko (*Gekko gecko*) and the green anole (*Anolis carolinensis*) possess tail muscles that extend beyond the bones (Ritzman et al., 2012; Gilbert et al., 2013, fig. 1.B; Sanggaard et al., 2012, fig.2.C, SI Movie_S2). In these lizards, and in the crocodilian *Alligator mississippiensis* (see Frey, 1988; Mallison, 2011) the hypaxial muscles are greatly expanded ventrally and laterally.

The lateral extent of the ventral muscles, the *M. caudofemoralis longus* and the *M. ilioischiocaudalis*, in the mid-tail region of *Giraffatitan* was determined in comparison with the extant crocodilian *Alligator mississippiensis* and in analyzing the general trajectory of these muscles. As muscles are normally not arbitrarily constrained in width by other soft-tissue, it was assumed that they follow a straight line from the origin to the insertion and not in a concave trajectory. In the proximal region the *M. caudofemoralis longus* is constrained in all directions. Medially it is confined by the muscles originating on the ischium, namely the *Mm. adductores femores* and the *M. flexor tibialis internus 3*. The *Mm. adductores femores* originate on the obturator plate and the middle ischial shaft, for *M. adductor femoralis 1* and *M. adductor femoralis 2*, respectively. They run down medially on the hindlimb and insert on the posterior surface of the femur distal to the fourth trochanter. The *Mm. adductores femores* are laterally covered by the *M. flexor tibialis internus 3*, which originates on a shallow depression on the proximal lateral ischium and inserts on the proximal tibia, and runs between the *Mm. adductores femores* and the *M. caudofemoralis longus*, thus limiting the latter medially. Dorsally and laterally the *M. caudofemoralis brevis* wraps around the *M. caudofemoralis longus*, and thus limits the extent in these directions. The *M. caudofemoralis longus* is further constrained laterally by the *M. flexor tibialis externus*, which spans from the postacetabulur process of the ilium to the proximal tibia and restricts both *M. caudofemoralis longus* and *M. caudofemoralis brevis*. Ventrally the *M. caudofemoralis longus* is constrained by the *M. ilioischiocaudalis* and the *M. transversus perinei*, as both encompass *M. caudofemoralis longus* and insert on the distal ischium, thus preventing a ventral extent below the distal tip of the ischium, see **Figure 5**.

In *Alligator mississippiensis*, the *M. tendinoarticularis* is only mildly developed in the tail base, corresponding to an increase in cross section of *M. longissimus caudae* (Frey, 1988). Because of the lack of osteological correlates for the contact between the two muscles any reconstruction must remain speculative, and this relative thinning of the *M. tendinoarticularis* compared to *M. longissimus caudae* has not been represented in previous muscle volume modeling attempts (e.g., Arbour, 2009; Persons, 2009; Persons and Currie, 2011; Persons et al., 2014). However, in the caudal series of *Giraffatitan*, the lateral oblique bulge between the prezygapophysis and the transverse

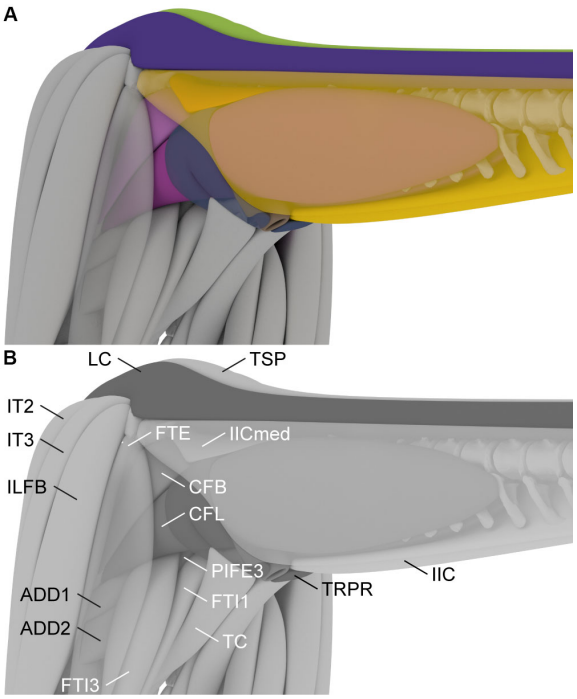

FIGURE 6 | 3D reconstruction of the tail and hindlimb musculature of the Late Jurassic sauropod *Giraffatitan brancai* used to constrain the extent of the *Mm. caudofemorales* muscles. The *m. ilioischiocaudalis* and *m. flexor tibialis externus* are semi-transparent to show the underlying musculature. In color **(A)** and labeled **(B)**. ADD1, *m. adductor femoris 1*; ADD2, *m. adductor femoris 2*; CFB, *m. caudofemoralis brevis*; CFL, *m. caudofemoralis longus*; FTE, *m. flexor tibialis externus*; FTI1, *m. flexor tibialis internus 1*; FTI3, *m. flexor tibialis 3*; IIC, *m. ilioischiocaudalis*; IICmed, *m. ilioischiocaudalis* medial head; IT2, *m. iliotibialis 2*; IT3, *m. iliotibialis 3*; ILFB, *m. iliofibularis*; LC, *m. longissimus caudae*; TC, *m. truncocaudalis*; TRPR, *m. transversus perinei*; TSP, Transversospinalis group.

process (the inferred osteological correlate for the insertion of the *M. tendinoarticularis*) becomes more prominent from the seventh vertebra onward (**Supplementary Figure S3**), disappearing again in the seventeenth caudal vertebra, which formed the basis for the reconstruction and proportions of both the *M. tendinoarticularis* and the *M. longissimus caudae*, confirming that the *M. tendinoarticularis* was less developed at the base of the tail. However, the tendons and fascicles of the epaxial musculature are highly intertwined and thus muscle divisions are not easily distinguishable (e.g., Frey et al., 1989; Tsuihiji, 2005; Organ, 2006; Schwarz-Wings et al., 2009). In our model we simplified the epaxial musculature by only modeling two elements: one gathering all the dorsomedial muscles (the deep musculature, the *M. multifidus,* and the Transversospinalis group), and the lateral *M. longissimus caudae*. However, for biomechanical analyses, and considering all the osteological correlates, individual musculo-tendon units are easier to create and model.

As indicated above, the lateral, ventral and dorsal extent of the tail is difficult to estimate in extinct animals. The base of the tail is laterally delimited for three main muscles: dorsally by the *M. longissimus caudae*, and ventrally by the dorsal ramus of the *M. ilioischiocaudalis* and the lateral expansion of the *M. caudofemoralis brevis*. Anatomically, and in terms of volume, the *M. longissimus caudae* (epaxial), the *M. caudofemoralis* group and the *M. ilioischiocaudalis* (hypaxial) seem to be the most important muscles of the base of the tail. Then, from the fifth caudal vertebra, when both rami of the *M. ilioischiocaudalis* meet and totally enclose the *M. caudofemoralis longus*, all the muscular groups occupy similar volumes.

Internal Structure of Epaxial Muscles

While we propose that the suite of epaxial and hypaxial tail muscles of *Giraffatitan*, including the *Mm. caudofemorales*, are generally comparable in terms of its general extensions, origins and insertions to crocodilians, here are some key differences between extant archosaurs and our inference for the tail musculature in *Giraffatitan*. Extant crocodilians possess a very specialized internal muscle architecture (e.g., Frey, 1988; Salisbury and Frey, 2001). Whereas the medial epaxial muscles, in particular *M. multifidus*, *M. spinalis*, and *M. articulospinalis*, form a system of counter-running (criss-crossing) tendons, the lateral epaxial muscles *M. tendinoarticularis* and in particular *M. longissimus* form large myoseptal sheets and cones. The tendons of the epaxial muscles are connected firmly not only to the vertebrae, but also to the osteoderms. The close association between the myosepts and tendons of the epaxial muscles in crocodilians is important as it forms a part of their bracing system (Salisbury and Frey, 2001). Besides, in contrast to extant birds and sauropods, extant and fossil crocodilians do not possess postcranial skeletal pneumaticity (e.g., Gower, 2001).

Additionally, birds also have a highly modified internal muscular construction, and thus their anatomy cannot simply be extrapolated onto non-avian dinosaurs. In birds, the presacral epaxial muscles form muscles slips that attach only to small areas of the bone (e.g., Boas, 1929; Zweers et al., 1987; Vanden Berge and Zweers, 1993). In combination with that, extant bird skeletons are highly pneumatic, which means that the vertebrae are interspersed by a large number of pneumatic diverticula that occupy parts of the vertebral surface and additionally resolve the vertebral surface to create pneumatic foramina (Gier, 1952; Duncker, 1971; Hogg, 1984a; Witmer, 1997; O'Connor, 2004), and muscle attachment areas are generally small.

For sauropod dinosaurs, a similar slip-like internal muscular architecture of the epaxial muscles as in extant birds has been hypothesized, based on the presence of unambiguous osteological correlates at the presacral vertebrae (see Wedel and Sanders, 2002; Taylor and Wedel, 2013b). Another similarity to birds is the presence of vertebral pneumaticity at least in the presacral vertebral column of most neosauropods (Wedel, 2003a,b, 2009); and additionally saltasaurine titanosaurs possess pneumatic sacral and anterior caudal vertebrae (Cerda et al., 2012; Zurriaguz and Cerda, 2017).

These similarities and differences need to be kept in mind when reconstructing the internal structure of musculature of non-avian dinosaurs. However, our model is a simplification, and

the reconstruction of the detailed internal muscle architecture is beyond the scope of this study.

Caudal Skeletal Pneumaticity and Its Influence on the Musculoskeletal System

Caudal pneumaticity is widely present in Neosauropoda, like the camellate internal tissue of titanosaurs. More basal titanosauriforms, as *Lusotitan* (Mannion et al., 2013; Mocho et al., 2017) and *Giraffatitan* (Wedel and Taylor, 2013), also present caudal pneumatic features, as lateral fossa and foramina. This caudal skeletal pneumaticity is also present in other sauropods, like *Apatosaurus*, *Barosaurus*, *Diplodocus*, *Tastavinsaurus,* and *Tornieria* (McIntosh, 2005; Remes, 2006; Royo-Torres, 2009; Mannion et al., 2013) [for more neosauropods with caudal skeletal pneumaticity see **Table 1** of Wedel and Taylor (2013)]. When diagnosing a fossa as pneumatic, is useful to check other pneumatic features on the same bone (Wedel, 2005; O'Connor, 2006), but also observe the presence of pneumatic foramina and subfossa within the fossa (Wilson, 1999; Yates et al., 2012). However, the interaction between air sacs and muscle development has not been studied in detail.

Caudal pneumaticity has been previously described in the three caudal series of *Giraffatitan* (Wedel and Taylor, 2013). This work describes with high detail all the pneumatic structures, so here we will only address the main features that could be useful for the musculoskeletal reconstruction of the tail of *Giraffatitan*.

MB.R.5000 caudal series presents the most complex pattern of pneumatization within Dinosauria (see Wedel and Taylor, 2013, fig. 8), but, as previously stated, MB.R.5000 could not be analyzed in our study. However, these characters are very useful when identifying and describing the ones present in the other caudal series from *Giraffatitan*. Several hypotheses were made related to the different extension of caudal pneumatization between MB.R.5000 and the other 2 caudal series referred to *Giraffatitan* (see Wedel and Taylor, 2013, and references herein). We followed the hypothesis of intraspecific variation, and used the pneumatic features of the series MB.R. 2921 and 3736 for our reconstruction. We confirmed Wedel and Taylor (2013) observation, that small pneumatic fossa are present on both sides of the centrum, below the transverse processes, in the second caudal of the series MB.R.2921 and MB.R.3736, whereas the rest of the caudal vertebrae of the series is apneumatic. These pneumatic diverticula (cryptic diverticula) also appear on extant birds and pterosaurs, and do not leave any diagnostic skeletal traces. The posterior dorsal vertebrae, synsacrum, pelvic girdle and hindlimb of birds are pneumatized by diverticula of the abdominal air sacs (Cover, 1953; King, 1966, 1975; Duncker, 1971; Hogg, 1984a,b; Bezuidenhout et al., 1999; O'Connor and Claessens, 2005; O'Connor, 2006). In the case of *Giraffatitan*, the caudal vertebral diverticula most plausibly originated from abdominal air sacs too, as also hypothesized by Wedel et al. (2000) and Wedel (2009) for the pneumatization of postdorsal vertebrae in non-avian dinosaurs.

In extant birds pneumatic diverticula have different ways of distribution, they pass along under the skin, in between the muscles, and among the viscera, and only a few of them leave traces on the skeleton (Duncker, 1971). However, these intermuscular diverticula are highly difficult to assess in extinct species. Although we have evidence of pneumatic features in the proximal part of the caudal series of *Giraffatitan* we have not included reconstructions of the caudal pneumatic diverticula, as they do not have a huge impact on the final extension of the muscular system.

Functions of the Caudal Muscle Systems

Epaxial Musculature

This complex of muscles has its major importance in the stabilization of all the vertebral column and equally in the flexion of parts of the vertebral column (Alexander, 1985; Salisbury and Frey, 2001; Henderson, 2004; Schwarz-Wings, 2009). Especially, the deep musculature and the *M. multifidus* help in this stabilization and, by synchronous contraction, in the dorsal bending of the tail, by connecting the apical edges of the neural spines. Lateral flexion of the tail is achieved by synchronous ipsilateral contraction of the *M. transversospinalis* Group, the *M. longissimus caudae* and/or the *M. ilioischiocaudalis*).

Hypaxial Musculature

The *M. caudofemoralis longus* (together with the *M. caudofemoralis brevis*) is the main hindlimb retractor in diapsids. It adducts and longitudinally rotates the femur (e.g., Gatesy, 1991a). The *M. caudofemoralis longus* is correlated with the *M. ilioischiocaudalis*: while the former is contracted, the *M. ilioischiocaudalis* (together with the epaxial *M. transversospinalis* Group and the *M. longissimus caudae*) help to stabilize the tail base to prevent unwanted movement of the tail by the *M. caudofemoralis longus*. *M. transversus perinei* wraps the *M. caudofemoralis longus* and thereby has a direct effect by limiting its maximum cross-section, which then has the effect of specifying more precisely the moment arm of this muscle. Additional quantitative biomechanical studies are needed to test this hypothesis.

CONCLUSION

We created a detailed three-dimensional musculoskeletal reconstruction of approximately the anterior half of the tail of the Late Jurassic sauropod *Giraffatitan brancai*, based on comparative anatomy, primarily with crocodilians, and digital techniques, such as photogrammetry and an innovative three-dimensional modeling approach. Using this reconstruction we were able to calculate the mass of the individual elements and hypothesize a total mass of ca. 2500 kg for the complete tail. We further suggest, based on our assessment of the musculoskeletal reconstruction, that *Giraffatitan* had a powerful tail that assisted in its stabilization, and propulsion, but also as counterweight for the presacral part of the body. The suite of hypaxial and epaxial muscles fulfills an important role in stabilizing the tail and hold it over the ground by synchronous bilateral contraction to optimize the moment arms for the main hindlimb retractor muscles, the *M. caudofemoralis longus*. Although *Giraffatitan* had a short tail

(compared to other concurrent taxa, e.g., diplodocids and other coexisting macronarians), it was well-developed and robust.

Additionally, we were able to confirm that Janensch (1950b) was right in his original assessment of the tail posture, and the current mount at the Museum für Naturkunde, after the remounting in 2007 when the skeleton was mounted adapting the resting posture of the animal based on the current knowledge on the anatomy and biomechanics of sauropods (Remes et al., 2011), is correct.

Intervertebral cartilage thickness is difficult to assess in extinct taxa. In this work we have observed that similar values for tail length and muscle masses and volumes are calculated for the MB.R.2129 caudal series of *Giraffatitan* both in ONP and in CNP with a cartilage thickness of 10%. Taylor (2014) also suggested 10% as best estimate for cartilage thickness for the neck of *Diplodocus* and *Apatosaurus*. And as previously stated by Christian and Preuschoft (1996) and Christian and Dzemski (2007), the zygapophyseal articulation overall probably reflects the intervertebral cartilage volume, which as seen could be ca. 10% of the centrum length. We agree with Taylor (2014), and suggest using a cartilage thickness between 10 and 15% when reconstructing sauropod axial series.

The methodology applied in this study helps us to better comprehend the biomechanical and detailed anatomical aspects of a reconstructed musculoskeletal system of an extinct animal and, in addition, to estimate the volume and mass more accurately.

DATA AVAILABILITY STATEMENT

All created 3D models and derived files of this study are stored under CC-BY-NC license and are freely available under the following DOI link: http://coll.mfn-berlin.de/data/10.7479/xm1h-5806. Further inquiries can be directed to the corresponding author.

AUTHOR CONTRIBUTIONS

VD, DS, and HM conceived and designed the study. VD and HM digitized the specimens. VD and OD performed the data analyses. OD performed the 3D modeling and prepared the figures. All authors contributed to the interpretation of the data, writing of the manuscript, read and approved the submitted version.

FUNDING

This study was supported by the Alexander von Humboldt Stiftung provided for VD.

ACKNOWLEDGMENTS

Mathew J. Wedel (Western University of Health Sciences in Pomona, California) provided useful help and comments on the postcranial skeletal pneumaticity. We would also like to thank the editor PR and the two reviewers PF and RT, who improved this work with their comments and suggestions.

SUPPLEMENTARY MATERIAL

The Supplementary Material for this article can be found online at: https://www.frontiersin.org/articles/10.3389/feart.2020.00160/full#supplementary-material

REFERENCES

Alexander, R. M. (1985). Mechanics of posture and gait of some large dinosaurs. *Zool. J. Linn. Soc. Lond.* 83, 1–25.

Allen, V., Molnar, J., Parker, W., Pollard, A., Nolan, G., and Hutchinson, J. R. (2014). Comparative architectural properties of limb muscles in Crocodylidae and Alligatoridae and their relevance to divergent use of asymmetrical gaits in extant Crocodylia. *J. Anat.* 225, 569–582. doi: 10.1111/joa.12245

Allen, V. R. (2010). *The Evolution of the Avian Hindlimb Conformation and Locomotor Function*. Ph.D. thesis, The Royal Veterinary College, London.

Arbour, V. M. (2009). Estimating impact forces of tail club strikes by ankylosaurid dinosaurs. *PLoS One* 4:e6738. doi: 10.1371/journal.pone.0006738

Bezuidenhout, A. J., Groenewald, H. B., and Soley, J. T. (1999). An anatomical study of the respiratory air sacs in ostriches. *Onderstepoort J. Vet. Res.* 66, 317–325.

Boas, J. E. V. (1929). *Biologisch-Anatomische Studien Über den Hals der Vögel. D. Kgl. Danske Vidensk. Selsk. skrifter: Naturvidensk. og Mathem. Afd*, Vol. 9. Copenhagen: Høst & Søn, 122.

Borsuk-Bialynicka, M. (1977). A new camarasaurid sauropod *Opisthocoelicaudia skarzynskii*, gen. n. sp. n. from the Upper Cretaceous of Mongolia. *Palaeontol. Polon.* 37, 45–64.

Bryant, H. N., and Russell, A. P. (1992). The role of phylogenetic analysis in the inference of unpreserved attributes of extinct taxa. *Philos. Trans. R. Soc. Lond. B* 337, 405–418.

Button, D. J., Barrett, P. M., and Rayfield, E. J. (2016). Comparative cranial myology and biomechanics of *Plateosaurus* and *Camarasaurus* and evolution of the sauropod feeding apparatus. *Palaeontology* 59, 887–913.

Carballido, J. L., Pol, D., Parra Ruge, M. L., Padilla Bernal, S., Páramo-Fonseca, M., and Etayo-Serna, F. (2015). A new early cretaceous brachiosaurid (Dinosauria, Neosauropoda) from northwestern Gondwana (Villa de Leiva, Colombia). *J. Vertebr. Paleontol.* 35:e980505. doi: 10.1080/02724634.2015.980505

Carballido, J. L., and Sander, P. M. (2014). Postcranial axial skeleton of *Europasaurus holgeri* (Dinosauria, Sauropoda) from the Upper Jurassic of Germany: implications for sauropod ontogeny and phylogenetic relationships of basal Macronaria. *J. Syst. Palaeontol.* 12, 335–387.

Carpenter, K., Sanders, F., McWhinney, L. A., and Wood, L. (2005). "Evidence for predator-prey relationships. Examples for *Allosaurus* and *Stegosaurus*," in *The Carnivorous Dinosaurs*, ed. K. Carpenter (Bloomington, IN: Indiana University Press), 325–350.

Carrano, M. T., and Hutchinson, J. R. (2002). Pelvic and hindlimb musculature of *Tyrannosaurus rex* (Dinosauria: Theropoda). *J. Morphol.* 253, 207–228. doi: 10.1002/jmor.10018

Cerda, I. A., Salgado, L., and Powell, J. E. (2012). Extreme postcranial pneumaticity in sauropod dinosaurs from South America. *Paläontol. Z.* 86, 441–449.

Christian, A., and Dzemski, G. (2007). Reconstruction of the cervical skeleton posture of *Brachiosaurus brancai* Janensch, 1914 by an analysis of the intervertebral stress along the neck and a comparison with the results of different approaches. *Fossil Record* 10, 38–49.

Christian, A., and Preuschoft, H. (1996). Deducing the body posture of extinct large vertebrates from the shape of the vertebral column. *Palaeontology* 39, 801–812.

Cong, L., Hou, L., Wu, X., and Hou, J. (1998). *The Gross Anatomy of Alligator Sinensis* Fauvel. Beijing: Forestry Publishing House.

Coria, R., Filippi, L. S., Chiappe, L. M., García, R., and Arcucci, A. B. (2013). *Overosaurus paradasorum* gen. et sp. nov., a new sauropod dinosaur (Titanosauria: Lithostrotia) from the late cretaceous of Neuquén, Patagonia, Argentina. *Zootaxa* 3683, 357–376. doi: 10.11646/zootaxa.3683.4.2

Cott, H. B. (1961). Scientific results of an inquiry into the ecology and economic status of the Nile crocodile (*Crocodylus niloticus*) in Uganda and northern Rhodesia. *Trans. Zool. Soc. Lond.* 229, 211–236.

Cover, M. S. (1953). Gross and microscopic anatomy of the respiratory system of the turkey. III. The air sacs. *Am. J. Vet. Res.* 14, 239–245.

Cunningham, J. A., Rahman, I. A., Lautenschlager, S., Rayfield, E. J., and Donoghue, P. C. J. (2014). A virtual world of paleontology. *Trends Ecol. Evol.* 29, 347–357. doi: 10.1016/j.tree.2014.04.004

Dececchi, T. A., and Larsson, H. C. (2013). Body and limb size dissociation at the origin of birds: uncoupling allometric constraints across a macroevolutionary transition. *Evolution* 67, 2741–2752. doi: 10.1111/evo.12150

Dilkes, D. (1999). Appendicular myology of the hadrosaurian dinosaur *Maiasaura peeblesorum* from the Late Cretaceous (Campanian) of Montana. *Earth Environ. Sci. Trans. R. Soc.* 90, 87–125.

Duncker, H.-R. (1971). The lung air sac system of birds. *Adv. Anat. Embryol. Cell Biol.* 45, 1–171. doi: 10.1017/S1464793106007111

Fahlke, J. M., and Autenrieth, M. P. (2016). photogrammetry vs. Micro-CT scanning for 3D surface generation of a typical vertebrate fossil – a case study. *J. Paleontol. Tech.* 14, 1–18.

Fletcher, J. W. A., Williams, S., Whitehouse, M. R., Gill, H. S., and Preatoni, E. (2018). Juvenile bovine bone is an appropriate surrogate for normal and reduced density human bone in biomechanical testing: a validation study. *Sci. Rep.* 8:10181. doi: 10.1038/s41598-018-28155-w

Frey, E. (1982a). Der Bau des Bewegungsapparates der Krokodile und seine Funktion bei der aquatischen Fortbewegung. Diploma thesis, University of Tübingen: Facultät Biologie, p. 204.

Frey, E. (1982b). Ecology, locomotion, and tail muscle anatomy of crocodiles. *Neues Jahrb. Geol. Paläontol. Abh.* 164, 194–199.

Frey, E. (1988). Anatomie des Körperstammes von *Alligator mississippiensis* Daudin (Anatomy of the body stem of *Alligator mississippiensis* Daudin). *Stuttg. Beitr. Nat. Ser. A* 424, 1–106.

Frey, E., Riess, J., and Tarsitano, S. F. (1989). The axial tail musculature of recent crocodiles and its phyletic implications. *Am. Zool.* 29, 857–862.

Gallina, P. A., and Otero, A. (2009). Anterior caudal transverse processes in sauropod dinosaurs: morphological, phylogenetic and functional aspects. *Ameghiniana* 46, 165–176.

Galton, P. M. (1969). The pelvic musculature of the dinosaur *Hypsilophodon* (Reptilia: Ornithischia). *Postilla* 131:64.

Gatesy, S. M. (1991a). Caudofemoral musculature and the evolution of theropod locomotion. *Paleobiology* 16, 170–186. doi: 10.1371/journal.pone.0025763

Gatesy, S. M. (1991b). Hind limb movements of the American alligator (*Alligator mississippiensis*) and postural grades. *J. Zool. Lond.* 224, 577–588.

Gatesy, S. M., and Dial, K. P. (1996). From frond to fan: *Archaeopteryx* and the evolution of short-tailed birds. *Evolution* 50, 2037–2048. doi: 10.1111/j.1558-5646.1996.tb03590.x

Gier, H. T. (1952). The air sacs of the loon. *Auk* 69, 40–49.

Gignac, P. M. and Erickson, G. M. (2017). The Biomechanics Behind Extreme Osteophagy in *Tyrannosaurus rex*. *Sci. Rep.* 7:2012. doi: 10.1038/s41598-017-02161-w

Gilbert, E. A. B., Payne, S. L., and Vickaryous, M. K. (2013). The anatomy and histology of caudal autotomy and regeneration in lizards. *Physiol. Biochem. Zool* 86, 631–644. doi: 10.1086/673889

Gilmore, C. (1925). A nearly complete articulated skeleton of *Camarasaurus*, a saurischian dinosaur from the Dinosaur National Monument. *Mem. Carnegie Mus.* 10, 347–384.

Gower, D. J. (2001). Possible postcranial pneumaticity in the last common ancestor of birds and crocodilians: evidence from *Erythrosuchus* and other Mesozoic archosaurs. *Naturwissenschaften* 88, 119–122. doi: 10.1007/s001140100206

Hair, P. (1868). On the arrangement of the muscular fibers of the alligator. *J. Anat.* 2, 26–41.

Henderson, D. M. (2004). Axial stress as a growth constraint in the vertebrae of sauropod dinosaurs. *J. Morphol.* 260, 297.

Hogg, D. A. (1984a). The development of pneumatisation in the skeleton of the adult domestic fowl. *J. Anat.* 139, 105–113.

Hogg, D. A. (1984b). The distribution of pneumatisation in the skeleton of the adult domestic fowl. *J. Anat.* 138, 617–629.

Holtz, T. R. Jr., and Omólska, H. (2004). "Saurischia," in *The Dinosauria*, 2nd Edn, eds D. B. Weishampel, P. Dodson, and H. Osmólska (Berkeley, CA: University of California Press), 21–24.

Hutchinson, J. R. (2002). The evolution of hindlimb tendons and muscles on the line to crown-group birds. *Comp. Biochem. Physiol. Part Mol. Integr. Physiol.* 133, 1051–1086. doi: 10.1016/s1095-6433(02)00158-7

Hutchinson, J. R., Bates, K. T., Molnar, J., Allen, V., and Makovicky, P. J. (2011). A computational analysis of limb and body dimensions in *Tyrannosaurus rex* with implications for locomotion, ontogeny, and growth. *PLoS One* 6:e26037. doi: 10.1371/journal.pone.0026037

Hutchinson, J. R., Felkler, D., Houston, K., Chang, Y. M., Brueggen, J., Kledzik, D., et al. (2019). Divergent evolution of terrestrial locomotor abilities in extant Crocodylia. *Sci. Rep.* 9:19302. doi: 10.1038/s41598-019-55768-6

Hutchinson, J. R., and Gatesy, S. M. (2000). Adductors, abductors, and the evolution of archosaur locomotion. *Paleobiology* 26, 734–751.

Hutchinson, J. R., Rankin, J. W., Rubenson, J., Rosenbluth, K. H., Siston, R. A., and Delp, S. L. (2015). Musculoskeletal modelling of an ostrich (*Struthio camelus*) pelvic limb: influence of limb orientation on muscular capacity during locomotion. *PeerJ* 3:e1001. doi: 10.7717/peerj.1001

Ibiricu, L. M., Lamanna, M. C., and Lacovara, K. J. (2014). The influence of caudofemoral musculature on the Titanosaurian (Saurischia: Sauropoda) tail skeleton: morphological and phylogenetic implications. *Hist. Biol.* 26, 454–471.

Janensch, W. (1914). Übersicht über die wirbeltierfauna der tendaguruschichten, nebst einer kurzen charakterisierung der neu aufgeführten arten von Sauropoden. *Archiv. Biontol.* 3, 81–110.

Janensch, W. (1950a). Die Wirbelsaule von *Brachiosaurus brancai*. *Palaeontographica* 3(Suppl. 7), 27–93.

Janensch, W. (1950b). Die Skelettrekonstruktion von *Brachiosaurus brancai*. *Palaeontographica* 3(Suppl. 7), 95–102.

Janensch, W. (1961). Die Gliedmaßen und Gliedmaßengürtel der Sauropoden der Tendaguru-Schichten. *Palaeontographica* 3(Suppl. 7), 177–235.

King, A. S. (1966). Structural and functional aspects of the avian lungs and air sacs. *Int. Rev. Gen. Exp. Zool.* 2, 171–267.

King, A. S. (1975). "Aves respiratory system," in *Sisson and Grossman's the Anatomy of the Domestic Animals*, 5th Edn, Vol. 2, ed. R. Getty (Philadelphia, PA: Saunders), 1883–1918.

Lacovara, K. J., Lamanna, M. C., Ibiricu, L. M., Poole, J. C., Schroeter, E. R., Ullmann, P. V., et al. (2014). A gigantic, exceptionally complete titanosaurian sauropod dinosaur from Southern Patagonia, Argentina. *Sci. Rep.* 4:6196. doi: 10.1038/srep06196

Langer, M. C. (2004). "Basal saurischia," in *The Dinosauria*, 2nd Edn, eds D. B. Weishampel, P. Dodson, and H. Osmólska (Berkeley, CA: University of California Press), 25–46.

Lautenschlager, S. (2013). Cranial myology and bite force performance of *Erlikosaurus andrewsi*: a novel approach for digital muscle reconstructions. *J. Anat.* 222, 260–272. doi: 10.1111/joa.12000

Makovicky, P. J., Kobayashi, Y., and Currie, P. J. (2004). "Therizinosauroidea," in *The Dinosauria*, 2nd Edn, eds D. B. Weishampel, P. Dodson, and H. Osmólska (Berkeley, CA: University of California Press), 151–164.

Makovicky, P. J., and Norell, M. A. (2004). "Troodontidae," in *The Dinosauria*, 2nd Edn, eds D. B. Weishampel, P. Dodson, and H. Osmólska (Berkeley, CA: University of California Press), 184–195.

Mallison, H. (2010a). The digital *Plateosaurus* I: body mass, mass distribution and posture assessed using CAD and CAE on a digitally mounted complete skeleton. *Palaeontol. Electron.* 2, 1–26.

Mallison, H. (2010b). The digital *Plateosaurus* II: an assessment of the range of motion of the limbs and vertebral column and of previous reconstructions using a digital skeletal mount. *Acta Palaeontol. Polon.* 55, 433–458.

Mallison, H. (2011). Defense capabilities of *Kentrosaurus aethiopicus* Hennig, 1915. *Palaeontol. Electron.* 14, 1–25.

Mallison, H., Belvedere, M., and Díez Díaz, V. (2017). *3D Imaging Handbook: Photogrammetry Digitization techniques for the SYNTHESYS Project*. Available online at: http://biowikifarm.net/v-mfn/3d-handbook/Photogrammetry_MfN (accessed, 2017).

Mallison, H., and Wings, O. (2014). Photogrammetry in paleontology–a practical guide. *J. Paleontol. Tech.* 12, 1–31.

Mannion, P. D., Upchurch, P., Barnes, R. N., and Mateus, O. (2013). Osteology of the late Jurassic Portuguese sauropod dinosaur *Lusotitan atalaiensis* (Macronaria) and the evolutionary history of basal titanosauriforms. *Zool. J. Linn. Soc.* 168, 98–206.

McIntosh, J. S. (2005). "The genus *Barosaurus* marsh (Sauropoda, Diplodocidae)," in *Thunderlizards. The Sauropodomorph Dinosaurs*, eds V. Tidwell and K. Carpenter (Bloomington, IN: Indiana University Press), 38–77.

Méndez, J., and Keys, A. (1960). Density and composition of mammalian muscle. *Metabolism* 9, 184–188.

Mocho, P., Royo-Torres, R., Malafaia, E., Escaso, F., and Ortega, F. (2017). First occurrences of non-neosauropod eusauropod procoelous caudal vertebrae in the Portuguese Upper Jurassic record. *Geobios* 50, 23–36.

Mohiuddin, S. (2013). Change in bone density as a function of water content. *World J. Med. Sci.* 8, 48–51.

Moser, M. (2003). *Plateosaurus engelhardti* Meyer, 1837 (Dinosauria: Sauropodomorpha) aus dem Feuerletten (Mittelkeuper; Obertrias) von Bayern. *Zittel. Reihe B Abh. Bayer. Staatssammlung Paläontol. Geol.* 24, 3–186.

Norell, M. A., and Makovicky, P. J. (2004). "Dromaeosauridae," in *The Dinosauria*, 2nd Edn, eds D. B. Weishampel, P. Dodson, and H. Osmólska (Berkeley, CA: University of California Press), 196–209.

O'Connor, J., Wang, X., Sullivan, C., Zheng, X., Tubaro, P., Zhang, X., et al. (2013). Unique caudal plumage of *Jeholornis* and complex tail evolution in early birds. *Proc. Natl. Acad. Sci. U.S.A.* 110, 17404–17408. doi: 10.1073/pnas.1316979110

O'Connor, P., and Claessens, L. P. A. M. (2005). Basic avian pulmonary design and flowthrough ventilation in non-avian theropod dinosaurs. *Nature* 436, 253–256. doi: 10.1038/nature03716

O'Connor, P. M. (2004). Pulmonary pneumaticity in the postcranial skeleton of extant Aves: a case study examining Anseriformes. *J. Morphol.* 261, 141–161. doi: 10.1002/jmor.10190

O'Connor, P. M. (2006). Postcranial pneumaticity: an evaluation of soft-tissue influences on the postcranial skeleton and the reconstruction of pulmonary anatomy in archosaurs. *J. Morphol.* 267, 1199–1226. doi: 10.1002/jmor.10470

Omólska, H., Currie, P. J., and Barsbold, R. (2004). "Oviraptorosauria," in *The Dinosauria*, 2nd Edn, eds D. B. Weishampel, P. Dodson, and H. Osmólska (Berkeley, CA: University of California Press), 165–183.

Organ, C. L. (2006). Thoracic epaxial muscles in living archosaurs and ornithopod dinosaurs. *Anat. Rec.* 288A, 782–793. doi: 10.1002/ar.a.20341

Otero, A., and Vizcaíno, S. F. (2006). "Hindlimb musculature of *Neuquensaurus australis* Lydekker (Sauropoda, Titanosauria)," in *Proceedings of the 9th Congreso Argentino de Paleontología y Bioestratigrafía*, (Córdoba: Academia Nacional de Ciencias, Resúmenes), 135.

Otero, A., and Vizcaíno, S. F. (2008). Hindlimb musculature and function of *Neuquensaurus australis* Lydekker (Sauropoda: Titanosauria). *Ameghiniana* 45, 333–348.

Paul, G. S. (1988). The brachiosaur giants of the Morrison and Tendaguru with a description of a new subgenus, *Giraffatitan*, and a comparison of the world's largest dinosaurs. *Hunteria* 2, 1–14.

Persons, W. (2009). Theropod tail muscle reconstruction and assessment of the locomotive contributions of the *M. caudofemoralis*. *J. Vertebr. Paleontol.* 3:164A.

Persons, W., and Currie, P. J. (2011). The tail of *Tyrannosaurus*: reassessing the size and locomotive importance of the *M. caudofemoralis* in non-avian theropods. *Anat. Rec.* 294, 119–131. doi: 10.1002/ar.21290

Persons, W., Currie, P. J., and Norell, M. A. (2014). Oviraptorosaur tail forms and functions. *Acta Palaeontol. Polon.* 59, 553–567.

Persons, W. S., and Currie, P. J. (2012). Dragon tails: convergent caudal morphology in winged archosaurs. *Acta Geol. Sin.* 86, 1402–1412.

Pittman, M., Gatesy, S. M., Upchurch, P., Goswami, A., and Hutchinson, J. R. (2013). Shake a tail feather: the evolution of the theropod tail into a stiff aerodynamic surface. *PLoS One* 8:e63115. doi: 10.1371/journal.pone.0063115

Rahman, I. M., and Lautenschlager, S. (2017). Applications of three-dimensional box modelling to paleontological functional analysis. *Paleontol. Soc. Pap.* 22, 119–132.

Rashid, D. J., Chapman, S. C., Larsson, H. C. E., Organ, C. L., Bebin, A.-G., Merzdorf, C. S., et al. (2014). From dinosaurs to birds: a tail of evolution. *EvoDevo J.* 5:25. doi: 10.1186/2041-9139-5-25

Remes, K. (2006). Revision of the Tendaguru sauropod dinosaur *Tornieria Africana* (Fraas) and its relevance for sauropod paleobiogeography. *J. Vertebr. Paleontol.* 26, 651–669.

Remes, K., Ortega, F., Fierro, I., Joger, U., Kosma, R., Marín Ferrer, J. M., et al. (2009). A new basal sauropod dinosaur from the middle jurassic of niger and the early evolution of sauropoda. *PLoS One* 4:e6924. doi: 10.1371/journal.pone.0006924

Remes, K., Unwin, D. M., Klein, N., Heinrich, W.-D., and Hampe, O. (2011). "Skeletal reconstruction of *Brachiosaurus brancai* in the Museum für Naturkunde, Berlin: summarizing 70 years of sauropod research," in *Biology of the Sauropod Dinosaurs. Understanding the Life of Giants 305-316*, eds N. Klein, K. Remes, C. T. Gee, and P. M. Sander (Bloomington, IN: Indiana University Press).

Ritzman, T. B., Stroik, L. K., Julik, E., Hutschins, E. D., Lasku, E., Denardo, D. F., et al. (2012). The gross anatomy of the original and regenerated tail in the green anole (*Anolis carolinensis*). *Anat. Rec.* 295, 1596–1608. doi: 10.1002/ar.22524

Romer, A. S. (1923). Crocodilian pelvic muscles and their avian and reptilian homologues. *Bull. Am. Mus. Nat. His.* 48, 533–552.

Royo-Torres, R. (2009). El saurópodo de Peñarroya de Tastavins. *Monogr. Turol.* 6, 1–548.

Salgado, L., Apesteguía, S., and Heredia, S. E. (2005). A new specimen of *Neuquensaurus australis*, a late cretaceous saltasaurinae titanosaur from North Patagonia. *J. Vertebr. Paleontol.* 25, 623–634.

Salgado, L., and García, R. (2002). Variación morfológica en la secuencia de vértebras caudales de algunos saurópodos titanosaurios. *Rev. Esp. Paleontol.* 17, 211–216.

Salisbury, S. W., and Frey, E. (2001). "The kinematics of aquatic locomotion in *Osteolaemus tetraspis* Cope," in *Crocodilian Biology and Evolution*, eds G. C. F. Grigg, F. Seebacher, and C. E. Franklin (Chipping Norton, NSW: Surrey Beatty & Sons), 165–179.

Sanggaard, K. W., Danielsen, C. C., Wogensen, L., Vinding, M. S., Rydtoft, L. M., Mortensen, M. B., et al. (2012). Unique structural features facilitate lizard tail autotomy. *PLoS One* 7:e51803. doi: 10.1371/journal.pone.0051803

Schwarz-Wings, D. (2009). Reconstruction of the thoracic epaxial musculature of diplodocid and dicraeosaurid sauropods. *J. Vertebr. Paleontol.* 29, 517–534.

Schwarz-Wings, D., Frey, E., and Martin, T. (2009). Reconstruction of the bracing system of the trunk and tail in hyposaurine dryosaurids (Crocodylomorpha; Mesoeucrocodylia). *J. Vertebr. Paleontol.* 29, 453–472.

Sharp, A. (2014). Three dimensional digital reconstruction of the jaw adductor musculature of the extinct marsupial giant *Diprotodon optatum*. *PeerJ* 2:e514. doi: 10.7717/peerj.514

Stevens, K. A., and Parrish, J. M. (1999). Neck posture and feeding habits of two Jurassic sauropod dinosaurs. *Science* 284, 798–800. doi: 10.1126/science.284.5415.798

Stevens, K. A., and Parrish, M. J. (2005a). "Digital reconstructions of sauropod dinosaurs and implications for feeding," in *The Sauropods: Evolution and Paleobiology*, eds J. A. Wilson and K. Curry Rogers (Berkeley, CA: University of California Press), 178–200.

Stevens, K. A., and Parrish, M. J. (2005b). "Neck posture, dentition and feeding strategies in Jurassic sauropod dinosaurs," in *Thunder Lizards: The Sauropodomorph Dinosaurs*, eds V. Tidwell and K. Carpenter (Bloomington, IN: Indiana University Press), 212–232.

Sutton, M. D., Rahman, I. A., and Garwood, R. J. (2014). *Techniques for Virtual Palaeontology*. Chichester: John Wiley & Sons, 208.

Taylor, M. P. (2009). A re-evaluation of *Brachiosaurus altithorax* Riggs 1903 (Dinosauria, Sauropoda) and its generic separation from *Giraffatitan brancai* (Janensch, 1914). *J. Vertebr. Palaeontol.* 29, 787–806.

Taylor, M. P. (2011). Correction: a re-evaluation of *Brachiosaurus altithorax* Riggs 1903 (Dinosauria, Sauropoda) and its generic separation from *Giraffatitan brancai* (Janensch, 1914). *J. Vertebr. Palaeontol.* 31:727.

Taylor, M. P. (2014). Quantifying the effect of intervertebral cartilage on neutral posture in the necks of sauropod dinosaurs. *PeerJ* 2:e712. doi: 10.7717/peerj.712

Taylor, M. P., and Wedel, M. J. (2013a). The effect of intervertebral cartilage on neutral posture and range of motion in the necks of sauropod dinosaurs. *PLoS One* 8:e78214. doi: 10.1371/journal.pone.0078214

Taylor, M. P., and Wedel, M. J. (2013b). Why sauropods had long necks; and why giraffes have short necks. *PeerJ* 1:e36. doi: 10.7717/peerj.36

Tsuihiji, T. (2005). Homologies of the *transversospinalis* muscles in the anterior presacral region of Sauria (Crown Diapsida). *J. Morphol.* 268, 986–1020. doi: 10.1002/jmor.10294

Tsuihiji, T. (2007). Homologies of the *longissimus*, *iliocostalis*, and hypaxial muscles in the anterior presacral region of extant diapsida. *J. Morphol.* 263, 151–178. doi: 10.1002/jmor.10565

Tykoski, R. S., and Rowe, T. (2004). "Ceratosauria," in *The Dinosauria*, 2nd Edn, eds D. B. Weishampel, P. Dodson, and H. Osmólska (Berkeley, CA: University of California Press), 47–70.

Upchurch, P., Barrett, P., and Dodson, P. (2004). "Sauropoda," in *The Dinosauria*, 2nd Edn, eds D. B. Weishampel, P. Dodson, and H. Osmólska (Berkeley, CA: University of California Press), 259–324.

Vanden Berge, J. C., and Zweers, G. A. (1993). "Myologia," in *Handbook of Avian Anatomy: Nomina Anatomica Avium*, eds J. J. Baumel, A. S. King, J. E. Breazile, H. E. Evans, and J. C. Vanden Berge (Cambridge, MA: Nuttal Ornithological Club), 189–247.

Vidal, D., and Díez Díaz, V. (2017). Reconstructing hypothetical sauropod tails by means of 3D digitization: *Lirainosaurus astibiae* as case study. *J. Iber. Geol.* 43, 293–305.

Vidal, D., Mocho, P., Páramo, A., Sanz, J. L., and Ortega, F. (2020a). Ontogenetic similarities between giraffe and sauropod neck osteological mobility. *PLoS One* 15:e0227537. doi: 10.1371/journal.pone.0227537

Vidal, L. S., Gomes da Costa Pereira, P. V. L., Tavares, S., Brusatte, S. L., Paglarelli, L., and dos Anjos Candeiro, C. R. (2020b). Investigating the enigmatic Aeolosaurini clade: the caudal biomechanics of *Aeolosaurus maximus* (Aeolosaurini/Sauropoda) using the neutral pose method and the first case of protonic tail condition in Sauropoda. *His. Biol.* 1–21. doi: 10.1080/08912963.2020.1745791

Webb, G. J. W., and Gans, C. (1972). Galloping in *Crocodylus johnstoni* – a reflection of terrestrial activity? *Rec. Aust. Mus.* 34, 607–618.

Wedel, M. J. (2003a). The evolution of vertebral pneumaticity in sauropod dinosaurs. *J. Vertebr. Paleontol.* 23, 344–357.

Wedel, M. J. (2003b). Vertebral pneumaticity, air sacs, and the physiology of sauropod dinosaurs. *Paleobiology* 29, 243–255.

Wedel, M. J. (2005). "Postcranial skeletal pneumaticity in sauropods and its implications for mass estimates," in *The Sauropods: Evolution and Paleobiology*, eds J. A. Wilson and K. Curry-Rogers (Berkeley, CA: University of California Press), 201–228.

Wedel, M. J. (2009). Evidence for Bird-like air sacs in saurischian dinosaurs. *J. Exp. Zool.* 311, 611–628. doi: 10.1002/jez.513

Wedel, M. J., Cifelli, R. I., and Sanders, R. K. (2000). Osteology, paleobiology, and relationships of the sauropod dinosaur *Sauroposeidon*. *Acta Palaeontol. Polon.* 45, 343–388.

Wedel, M. J., and Sanders, K. (2002). Osteological correlated of cervical musculature in Aves and Sauropoda (Dinosauria: Saurischia) with comments on the cervical ribs of *Apatosaurus*. *PaleoBios* 22, 1–6.

Wedel, M. J., and Taylor, M. P. (2013). Caudal pneumaticity and pneumatic hiatuses in the Sauropod Dinosaurs *Giraffatitan* and *Apatosaurus*. *PLoS One* 8:e78213. doi: 10.1371/journal.pone.0078213

Wellnhofer, P. (1993). Prosauropod dinosaurs from the Feuerletten (Middle Norian) of Ellingen near Weissenburg in Bavaria. *Rev. Paléobiol. Spéc. Vol.* 7, 263–271.

Wilhite, R. (2003). *Biomechanical Reconstruction of the Appendicular Skeleton in Three North American Jurassic Sauropods*. Ph.D. dissertation. Louisiana State University, Baton Rouge.

Wilson, J. A. (1999). A nomenclature for vertebral laminae in sauropods and other saurischian dinosaurs. *J. Vertebr. Paleontol.* 19, 639–653. doi: 10.1371/journal.pone.0017114

Witmer, L. M. (1995). "The extant phylogenetic bracket and the importance of reconstructing soft tissues in fossils," in *Functional Morphology in Vertebrate Paleontology*, ed. J. J. Thomason (Cambridge: Cambridge University Press), 19–33.

Witmer, L. M. (1997). The evolution of the antorbital cavity in archosaurs: a study in soft-tissue reconstruction in the fossil record with analysis of the function of pneumaticity. *J. Vertebr. Paleontol. Mem.* 3, 1–73.

Yates, A. M., Wedel, M. J., and Bonnan, M. F. (2012). The early evolution of postcranial skeletal pneumaticity in sauropodomorph dinosaurs. *Acta Palaeontol. Polon.* 57, 85–100. doi: 10.1111/j.1469-185X.2011.00190.x

Zug, G. R. (1974). Crocodilian galloping: an unique gait for reptiles. *Copeia* 2, 550–552.

Zurriaguz, V. I., and Cerda, I. A. (2017). Caudal pneumaticity in derived titanosaurs (Dinosauria: Sauropoda). *Cretac. Res.* 73, 14–24.

Zweers, G. A., Vanden Berge, J. C., and Koppendraier, R. (1987). Avian cranio-cervical systems. Part I: anatomy of the cervical column in the chicken (*Gallus gallus* L.). *Acta Morphol. Neerl. Scand.* 25, 131–155.

Conflict of Interest: HM owns company Palaeo3D. He performed all work on this manuscript in his function as an associate researcher with CeNak Hamburg.

The remaining authors declare that the research was conducted in the absence of any commercial or financial relationships that could be construed as a potential conflict of interest.

frontiers in Earth Science

ORIGINAL RESEARCH
published: 12 June 2020
doi: 10.3389/feart.2020.00176

Allometric and Phylogenetic Aspects of Stapes Morphology in Ruminantia (Mammalia, Artiodactyla)

Bastien Mennecart[1], Coraline Guignard[1], Laura Dziomber[2], Georg Schulz[3,4], Bert Müller[3] and Loïc Costeur[1]*

[1] Naturhistorisches Museum Basel, Basel, Switzerland, [2] Institute of Plant Sciences and Oeschger Centre for Climate Change Research, University of Bern, Bern, Switzerland, [3] Biomaterial Science Center, University of Basel, Allschwil, Switzerland, [4] Department of Biomedical Engineering, Micro- and Nanotomography Core Facility, University of Basel, Allschwil, Switzerland

The stapes is the smallest bone of the mammalian skeleton. Being the innermost middle ear ossicle, it is in contact with the inner ear and is directly responsible for sound transmission into it. Today, Ruminantia are one of the most diversified groups of large mammals with more than 200 species. However, their stapes has been very little studied. Here we investigate the shape of 66 stapes from 44 species of extant and extinct Ruminantia, including intra-individual and intra-specific observations, based on 3D tomographic data. Shape differences and similarities are quantitatively discussed thanks to 3D geometric morphometrics. The overall size of the stapes scales with a negative allometry in comparison to body mass. Moreover, the overall shape of the stapes informs about phylogeny. A trend is observed from a concave posterior crus with an enlarged stapes capitulum in Antilocapridae to a relatively straight posterior crus with a little reduced stapes capitulum in Cervidae, Bovidae being intermediate. In addition, the stapes of Antilocapridae is relatively trapezoid in lateral view; that of Cervidae is more triangular in lateral view; and that of Bovidae is relatively rectangular in lateral view. The stapedial footplate shape also gives phylogenetic information. The Tragulidae stapedial footplate is antero-posteriorly asymmetrical. The stapedial footplate is ovoid in stem Pecora. It is asymmetrical in Bovidae, while it is more symmetrical in Cervidae. This is in agreement with previous studies on the ruminant bony labyrinth showing that the oval window, the counterpart of the stapedial footplate on the inner ear, bears a strong phylogenetic signal already distinguishable in early Miocene ruminants.

Keywords: geometric morphometrics, ear region, systematics, middle ear ossicles, micro computed tomography

OPEN ACCESS

Edited by:
Pasquale Raia,
University of Naples Federico II, Italy

Reviewed by:
Saverio Bartolini Lucenti,
University of Florence, Italy
Antonio Profico,
Sapienza University of Rome, Italy

****Correspondence:***
Bastien Mennecart
mennecartbastien@gmail.com

Specialty section:
This article was submitted to Paleontology, a section of the journal Frontiers in Earth Science

Received: *18 December 2019*
Accepted: *06 May 2020*
Published: *12 June 2020*

Citation:
Mennecart B, Guignard C, Dziomber L, Schulz G, Müller B and Costeur L (2020) Allometric and Phylogenetic Aspects of Stapes Morphology in Ruminantia (Mammalia, Artiodactyla). Front. Earth Sci. 8:176. doi: 10.3389/feart.2020.00176

INTRODUCTION

The middle ear bones (ossicles) compose a chain of three bones (stapes, incus, and malleus) forming a complex structure only present in mammals. These bones play a central role in air-borne sound transmission from the outer environment to the inner ear (Merchant et al., 1996). The evolution of the incus and the malleus from the "reptilian grade" jaw bones to the smallest bones of the mammalian skeleton has been intensively studied (e.g., Rich et al., 2005; Luo, 2007; Meng et al., 2011; Maier and Ruf, 2016a,b). Their morphology and size are often associated to hearing sensitivity (Fleischer, 1978; Rosowski and Graybeal, 1991; Stoessel et al., 2016a; Bernardi and Couette, 2017).

However, only a few recent studies (except for Primates and aquatic mammals) focused on intraspecific variability or searched for phylogenetic characters potentially borne by this structure (e.g., Maier and Ruf, 2016b; Orliac and Billet, 2016; Bastl et al., 2017). The stapes is directly in contact with the inner ear through the stapedial fenestra or oval window. This bone can be well-preserved in fossil specimens where it can be found "fallen in a dead ear" as put by Orliac and Billet (2016). The stapes morphology is quite conservative among placental mammals (Fleischer, 1978). Nevertheless, the three dimensional (3D) structure of this bone is complex and can barely be described based on 2D images only (Stoessel et al., 2016b).

Ruminantia, hereafter also referred to as "ruminants," are one of the most diverse clades of large mammals, with more than 200 extant species living from the boreal tundra (e.g., reindeer) to the tropical forest (e.g., mouse deer), and the high mountains (e.g., Himalayan tahr; Nowak, 1999). Their social behavior ranges from solitary to gregarious. This diversity in ruminant ecology makes them a perfect case study for the investigation of ossicle ecomorphology. However, except for Fleischer (1973) and Maier and Ruf (2016b), there is almost no new data on the morphology of ruminant ossicles since Hyrtl (1845), Doran (1878), and Wilkie (1925, 1936). Costeur et al. (2016) described the ossification timing and the morphology of the ossicles in a mid-gestation cow fetus. The stapedial footplate does not reach its adult size at this stage contrary to the inner ear and its oval window articulating with the stapes (Costeur et al., 2016, 2017).

Here we describe the morphology of ruminant stapes covering all extant families and several fossil examples spanning 25 million years of ruminant evolution. Specific statistical analyses on the stapes shapes are performed in order to assess the impact of evolutionary allometry and phylogenetic inheritance on the morphology of this poorly studied middle-ear ossicle.

MATERIALS AND METHODS

Material

Sixty-six stapes from 44 species of ruminants were reconstructed from micro computed tomography data. The dataset includes Tragulidae (two extant species and one fossil from the early Miocene), stem Pecora (3 species from the latest Oligocene to early Miocene), and crown Pecora: Antilocapridae (3 species from the Pleistocene to recent), Bovidae (21 extant species), Cervidae (12 species from the early Miocene to recent), Giraffidae (1 extant species), and Moschidae (1 extant species; see **Table 1**). The bones from extant species are extracted from dry specimens of the Naturhistorisches Museum Basel (NMB, Switzerland). The fossil specimens exclusively came from Eurasia and America and are stored in Swiss, German, British, and American institutions (**Table 1**). To observe the intra-individual variability of the bone, the left and right stapes of the Bovidae *Aepyceros melampus* (NMB 9017), *Bubalus depressicornis* (NMB 3269), *Redunca fulvorufola* (NMB 15091), and *Gazella gazella* (NMB 11029); of the Cervidae *Elaphodus cephalophus* (NMB 2067) and *Muntiacus muntjak* (NMB C.2408); and of the Tragulidae *Hyemoschus aquaticus* (NMB 2692) and *Tragulus kanchil* (NMB 2131, NMB 2988, and NMB 3795) were reconstructed and compared. Similarly, insights into intraspecific variability is given through limited samples for the fossil Cervidae *Dicrocerus elegans* (2 specimens) and *Procervulus praelucidens* (2 specimens) and the fossil Pecora *Dremotherium feignouxi* (2 specimens) and quantified in the fossil Antilocapridae *Capromeryx arizonensis* (3 specimens), as well as 8 Tragulidae *Tragulus kanchil*.

Institutional Abbreviations

AMNH: American Museum of Natural History, New York (United States); MHNT: Muséum d'histoire naturelle de Toulouse (France); NHMUK: Natural History Museum of United Kingdom, London (United Kingdom); NMB: Naturhistorisches Museum Basel (Switzerland); and UF: Florida Museum of Natural History – University of Florida in Gainesville (United States).

Measurements and Nomenclature

The body mass and bony labyrinth length of the extant ruminants are adapted from Nowak (1999), and Wilson (2005) for the duikers (*Cephalophus dorsalis* and *Cephalophus zebra*). The stapes anatomical nomenclature is given on **Figure 1**.

CT-Scanning and Reconstruction

The specimens were scanned using high resolution hard X-ray computed tomography using nanotom® m (phoenix|x-ray, GE Sensing & Inspection Technologies GmbH, Wunstorf, Germany). Pixel resolution varies between 15 and 60 μm. During each aquisition 1440 equiangular radiographs were taken over 360° using an accelerating voltage of 90 kV and a beam current of 200 μA for recent material and 180 kV with a beam current of 30 μA for fossils. Segmentation of the stapes was done with AVIZO®9.0 Lite software (Visualization Sciences Group).

Morphometrics Analyses

The main objectives of this article are to characterize the allometry (both in size and shape) and the phylogenetical aspects of the stapes morphology in ruminants.

To quantify size allometry, resulting statistics based on linear measurements were performed with the PAST 4.0 software (Hammer et al., 2001). The correlation interface of the univariate analyses allows testing the relationship between the stapes (volume), the body mass (volume), the bony labyrinth (length), and different stapes parts (surface) using Linear r (Pearson) and p(uncorr) parameters based on decimal logarithm of the values (**Supplementary Data S2**). The weight (W) and length (L) relationships are $W = a \times L^{\alpha}$ or $\log(W) = \log(a) + \alpha \times \log(L)$ (Shingleton, 2010; Karachle et al., 2012). "α" is the slope of the correlation. In an isometric context, "α" is the coefficient balancing the dimensions of the equation (Karachle et al., 2012). Its isometrical values depends on the dimension of the compared data (length vs volume or mass, α = 3/1 when isometric; surface vs volume, α = 3/2 when isometric). When α > isometric value, there is a positive allometry of the first independent variable in comparison to the second dependent one. When α < isometric value, there is a negative allometry of the first variable in comparison to the second one (Shingleton, 2010).

TABLE 1 | List of studied specimens.

Family	Sub-family	Species	Inventory number	Age (Ma)
"stem Pecora"	–	*Parablastomeryx gilchristensis*	UF265266	19–17.5
	–	*Dremotherium feignouxi*	NMBMA5885	21
	–	*Dremotherium feignouxi*	NMBMA5886	21
	–	*Amphitragulus feningrei*	NMBcod632	24
Antilocapridae	Antilopinae	*Antilocapra americana*	NMBC1618	0
		Capromeryx arizonensis	UF402857*	2
		Capromeryx arizonensis	UF402858	2
		Capromeryx arizonensis	UF402859*	2
		Stockoceros onusrosagris	AMNHFAM 42553*	1.8–0.01
Giraffidae	–	*Giraffa camelopardis*	NMB2197	0
Cervidae	Cervinae	*Procervulus praelucidens*	MHNT.PAL. 2015.02385	16.5
		Procervulus praelucidens	MHNT.PAL.2015 .0226114*	16.5
		Dicrocerus elegans	NMBSan1001	15
		Dicrocerus elegans	NMBSan1003	15
		Elaphodus cephalophus	NMB2067.1	0
		Elaphodus cephalophus	NMB2067.2*	0
		Muntiacus muntjiak	NMBC2408.1	0
		Muntiacus muntjiak	NMBC2408.2*	0
		Rusa timorensis	NMB3657	0
		Rusa unicolor	NMB9597*	0
		Cervus nippon	NMB6106	0
	Capreolinae	*Hydropotes inermis*	NMB9892*	0
		Mazama americana	NHM.UK. PVOR.18701*	0
		Odocoileus sp.	UF402856*	2
		Mazama gouazoubira	NMB6672	0
		Ozotoceros bezoarticus	NMB2312*	0
		Pudu puda	NMBC2209	0
Moschidae	–	*Moschus moschiferus*	NMB8874	0
Bovidae	Bovinae	*Tragelaphus sciptus*	NMBC3568	0
		Bubalus depressicornis	NMB3269	0
		Bubalus depressicornis	NMB3269*	0
		Tetracerus quadricornis	NMB10472*	0
		Boselaphus tragocamelus	NMB10258	0
	Antilopinae	*Neotragus moschatus*	NMBC2122	0
		Aepyceros melampus	NMB9017.1	0
		Aepyceros melampus	NMB9017.2*	0
		Gazella gazella	NMB11029.1	0
		Gazella gazella	NMB11029.2*	0
		Gazella subgutturosa	NMB2497	0
		Eudorcas albonotata	NMB6414	0
		Redunca fulvorufula	NMB15091.1	0
		Redunca fulvorufula	NMB15091.2*	0
		Damaliscus pygargus	NMBC1948*	0
		Connochaetes gnou	NMB7591	0
		Ovis aries	NMB9037	0
		Rupicapra pyrenaica	NMBC1830*	0
		Ammotragus lervia	NMB2084*	0
		Capra hircus	NMB6920	0
		Ovibos moschatus	NMB11175	0
		Oreotragus oreotragus	NMBC4228*	0
		Oreotragus oreotragus	NMB8401*	0
		Cephalophus dorsalis	NMB15928	0
		Cephalophus zebra	NMBC2784	0
Tragulidae	–	*Dorcatherium crassum*	MHNT.PAL. 2015.02707*	16.5
		Hyemoschus aquaticus	NMB2692.1	0
		Hyemoschus aquaticus	NMB2692.2*	0
		Tragulus kanchil	NMB2131.1	0
		Tragulus kanchil	NMB2131.2	0
		Tragulus kanchil	NMB2988.1	0
		Tragulus kanchil	NMB2988.2	0
		Tragulus kanchil	NMB3791	0
		Tragulus kanchil	NMB3795.1	0
		Tragulus kanchil	NMB3795.2	0
		Tragulus kanchil	NMB3797	0
		Tragulus kanchil	NMB3806	0
		Tragulus kanchil	NMBC3802	0
		Tragulus kanchil	NMBC3735*	0

*Specimen with * have been mirrored for the analysis.*

Digitization of the stapes was performed using Landmark Editor 3.6 software (Wiley, 2006). In addition to the landmarks proposed in Stoessel et al. (2016b), we have landmarked the shape of the stapes capitulum (*capitulum stapedis*), the anterior crus (*crus anterius stapedis*), and the posterior crus (*crus anterius stapedis*; **Figure 1**). Eight landmarks of type 2 identify the maximum length of the stapes capitulum and the stapedial footplate (*basis stapedis*) and the maximum height of both intercrural foramens (**Figure 1**). Curves (each containing 10 equidistant semi landmarks) are placed on the stapes: two curves surrounding the stapedial footplate, two curves surrounding each intercrural foramen, one curve on each crus (anterior and posterior on their medial part), two curves surrounding the stapes capitulum.

We tested the correlation between the shape of the stapes and its size using a regression of the shape on the centroid size as defined by Klingenberg (2016) as "the square root of the sum of squared distances of all the landmarks of an object from their centroid [center of gravity, whose location is obtained by averaging the x and y (and z) coordinates of all landmarks]."

The correlation between two shape modules of the stapes has been tested using the modularity implementation of MorphoJ 1.06d software (Klingenberg, 2011). Morphological modules are parts whose components covary strongly, but which are relatively independent of other modules (e.g., Klingenberg, 2008). We have chosen to separate two modules. We have defined as a first module both crurae stapedis since they have a similar embryologic origin. The second module is the remaining set of landmarks. 1.000.000 random partitions have been considered using (**1**) the original dataset, (**2**) the dataset without allometrical signal, and (**3**) the dataset without allometrical signal pooled by family as explained afterward.

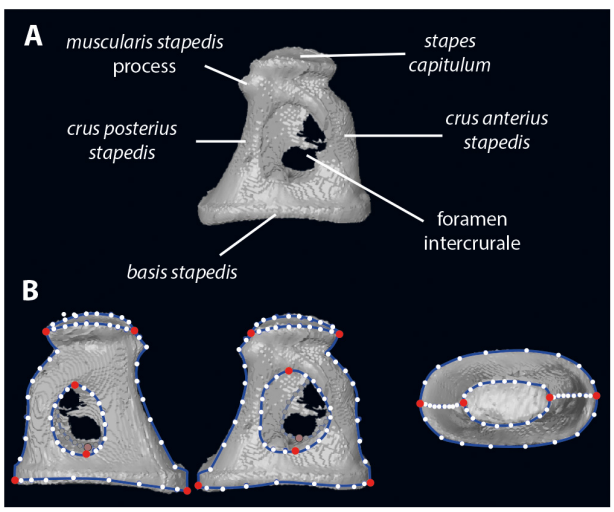

FIGURE 1 | Stapes morphology (based on *Hydropotes inermis* NMB 9892). **(A)** anatomical nomenclature; **(B)** landmark set (in red landmarks of type 2 and white semilandmarks on blue curves). 3D specimen is in **Supplementary Data S1**.

Shape variation in stapes morphology (disparity and similarity) was studied using a geometric morphometrics approach implemented in MorphoJ and R. To explore the phylogenetical relevance of this structure, we have created three datasets to characterize the shape of the stapes using (**1**) the original dataset (with allometrical signal), (**2**) a dataset without allometrical signal not pooled by family (since a significant correlation between the shape of the stapes and its size exists, p-values = 0.0018, see section "Phylogenetic signal", and **Supplementary Data S3**), and (**3**) a dataset without allometrical signal pooled by family (since a significant correlation between the size of the stapes and its phylogeny exists, p-values = 0.0235, see section "Phylogenetic signal", and **Supplementary Data S3**). As mentioned by Klingenberg (2016): "Pooled within-group (here the families) regression uses the shape and size deviations of each specimen from the shape and size averages of the group to which that specimen belongs (here the families), not the grand mean, to compute variances and covariances (. . .). Equivalently, pooled within-group regression can be explained as a two-step procedure where the differences among group averages are first removed by centering the shape and size data by group and then an ordinary regression is carried out on these centered data." Working on residual values allows an exploration of the dataset with non-allometric variation (Klingenberg, 2016) and to focus here on phylogenetical parameters.

The principal component analysis (PCA) is used on the three datasets (**1** original dataset, **2** dataset without allometrical signal, and **3** dataset without allometrical signal pooled by family) to visualize the overall shape variation among specimens. A permutation test (randomized rounds: 10.000; Klingenberg and Gidaszewski, 2010) based on the phylogenetic tree (**Supplementary Data S4**) is performed to test the presence or absence of a phylogenetic signal in the three datasets. Klingenberg and Gidaszewski (2010) defined that "The empirical p-value for the test is the proportion of permuted data sets in which the sum of squared changes is shorter or equal to the value obtained for the original data." Marriott (1979) and Edgington (1987) suggested that 1.000 permutations are a reasonable minimum for a test at 5% level of significance, while 5.000 are a reasonable minimum at the 1% level (Tzeng and Yeh, 1999). The phylogenetic tree was manually created using Mesquite 3.04 software (Maddison and Maddison, 2010) combining tree hypothesis published by Janis et al. (1998), Hassanin et al. (2012), Mennecart (2012), and Mennecart et al. (2019). Time calibration was provided by Bibi (2013) and Mennecart et al. (2017). Since it is difficult to observe the "geographical" proximity of two individuals within a polymorphospace including more than 4 dimensions, a hierarchical analysis using the cluster analysis option of the PAST 4.0 software (Hammer et al., 2001) has been performed (**Supplementary Data S2**). This allows observing graphically, along a tree, shape distances between specimens. Using the Euclidean similarity value option of PAST considering that the Procrustes coordinates, the Euclidean distances can directly be assimilated to Procrustes distances.

To characterize the phylogenetical differences of the stapes among the different ruminant families, standardized discriminant analyses have been performed.

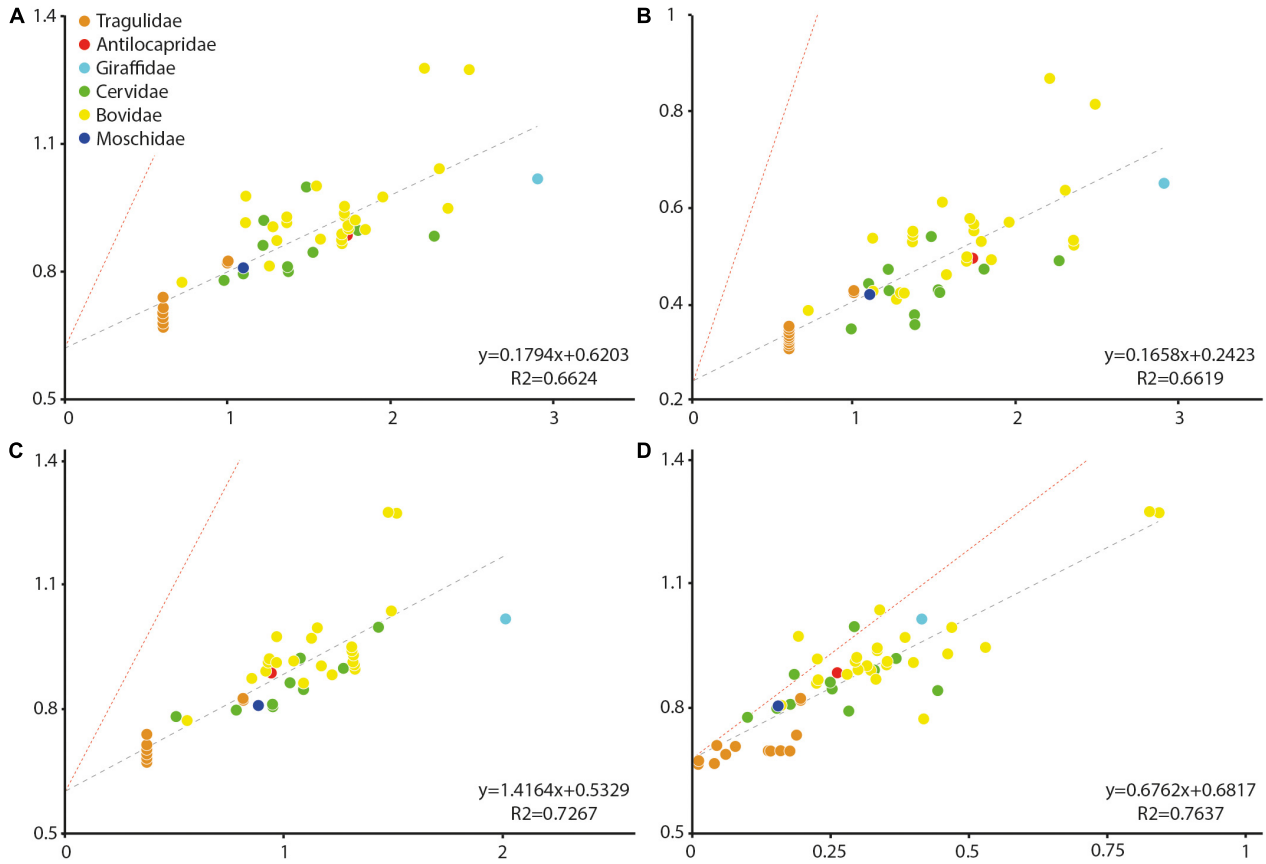

FIGURE 2 | Size allometry of the stapes structures in comparison to body mass in living ruminants, to other stapes structures, and to bony labyrinth length. **(A)** body mass against stapes centroid size; **(B)** body mass against the stapedial footplate centroid size; **(C)** bony labyrinth length against stapes centroid size; and **(D)** intercrural foramen centroid size against stapes centroid size. All values are in log. Antilocapridae red; Bovidae, yellow; Cervidae, green; Tragulidae, orange; Giraffidae, and light blue; Moschidae, dark blue. Red line corresponds to isometry.

A between-group PCA (bg-PCA) has been performed based on the three above mentioned datasets using the package *Morpho* (Schlager, 2017) in R (R Core Team, 2005) with the function "groupPCA." Contrary to the following Canonical Variate Analysis (CVA), a bg-PCA observes the variance between groups (here the well-defined ruminant families Tragulidae, Cervidae, Bovidae, and Antilocapridae and the stem Pecora) without standardizing the within groups-variance (Renaud et al., 2015). It gives less pressure on the shape similarities within group. Moschidae and Giraffidae have been excluded of the analyses since only one specimen (*Moschus moschiferus* and *Giraffa camelopardis*, respectively) possesses a well-preserved stapes. All supporting data of the bg-PCA (script and supporting information) can be found in **Supplementary Data S5**. Recent studies have cautioned the use of bg-PCA in high dimensional datasets (e.g., Cardini et al., 2019) but as reminded by Cardini et al. (2019) the common feature of correlated data in geometric morphometrics helps to circumvent this problem.

Additionally, the CVA was applied on the three above mentioned datasets to maximize the separation of the between-group means relative to the variation within groups ratio according to the specified chosen grouping variable (Renaud et al., 2015). CVA and bg-PCA provides complementary information (Mitteroecker and Bookstein, 2011; Renaud et al., 2015). Nevertheless, due the high degree of freedom in our analysis, CVA can be found in **Supplementary Data S6** as a comparative dataset (**Supplementary Data S3** presenting the results and 6 including figure and supporting information).

All statistical reports are shown in the **Supplementary Data S2, S3, S5**.

RESULTS

Allometric Signal

Stapes centroid size and stapedial footplate centroid size (in decimal logarithm of the values) are correlated with body mass (R^2 = 0.6624, p-value < 0.0001 and R^2 = 0.6619, p-value < 0.0001, respectively). A strong negative allometry is observed between these elements and body mass (α = 0.1794 and α = 0.1658, respectively, a isometry values being 1 and 1.5, respectively, **Figure 2**) indicating that larger species have relatively small stapes and smaller species have relatively large ones. The scaling relationship between the stapes centroid

size and its bony labyrinth length is positively allometric (α = 1.4164, a isometry values being 0.333) with a clear correlation (R^2 = 0.7267, p-value < 0.0001). The intercrural foramen centroid size and the stapes centroid size are correlated (R^2 = 0.7637, p-value < 0.0001). The intercrural foramen centroid size possesses a negative allometry in comparison to the stapes centroid size (α = 0.6762, a isometry values being 1.5) indicating that the intercrural foramen grows slower than the stapes (**Figure 2**).

To study the covariation between the shape and size, regressions of the shape (Procrustes coordinates) on the centroid size have been performed, both un-pooling and pooling the dataset by families. The not pooled dataset gives a statistically significant result (p-value = 0.0018, **Supplementary Data S3**) indicating a correlation between the size and the shape of the stapes (**Figure 3**). The effect size is nonetheless small, being R-squared at 0.037. Similar statistical results are observed when pooling the dataset by family (p-value = 0.0037 and a shape prediction at 3.46%). The main shape deformations observed in both analyses are the size of the intercrural foramens relative to the stapes size and the relative size of the stapedial footplate. In small forms, the two intercrural foramens are of similar size and relatively small (1/2 to 2/3 of the height of the stapes in the not pooled analysis and 1/2 for both intercrural foramens in the pooled analysis). Their stapedial footplate is more than twice as long as the stapes capitulum and relatively symmetrical. In large forms (*Ovibos moschatus* and *Connochaetes gnou*), one intercrural foramen remains relatively small and the second one almost entirely occupies the space between the stapes capitulum and the footplate, extending antero-posteriorly almost reaching the crura stapedis. Their stapedial footplate is smaller than twice the stapes capitulum length, the capitulum being wider in the pooled data (**Figure 3B**). The shape differences between the two analyses are mainly located on the shape of the stapedial footplate. While in the not pooled result the stapedial footplate is very asymmetrical with one side being flattened, in the pooled data, the stapedial footplate is only slightly asymmetrical. The two largest stapes of the dataset belong to Bovidae and all the smallest stapes belong to Tragulidae. A significant correlation between the size of the stapes and its phylogeny exists considering the unpooled dataset, (p-values = 0.0235, section "Phylogenetic signal", **Supplementary Data S3**). This informs that bovids do possess an asymmetrical stapedial footplate that is phylogenetically relevant.

Modularity

The determination of the different modules based on the three datasets containing the entire stapes (original data and after correction of the size effect without pooling and pooled by family) leads to similar results. The minimal RV coefficient calculated among the 1.000.000 partitions evaluated is 0.461519 for the original dataset, 0.467736 for the dataset with correction of the size effect, and 0.482582 for the dataset with correction of the size effect pooled within families. In each case, the two modules are "capitulum + stapedial footplate + crura stapedis" and "intercrural foramens" as in the original hypothesis (**Figure 3C**). There is no alternative partition with an RV coefficient smaller or equal to the value for the hypothesis (proportion is equal to 0.000). It is interesting to note that the crurae stapedis have a similar embryologic origin, forming at the end a hollow structure. The rest of the structure is made of bone: the capitulum and the stapedial footplate are the most massive bone portion of the stapes. These relatively flattened sections receive and transmit pressure perpendicular to their surface thanks to the crura stapedis.

PCA

Very little morphological variation is observed between the left and right stapes of a same individual. Observing the hierarchical analysis result, most of the left stapes cluster with their right counterpart (see hierarchical analysis in **Supplementary Data S2**). Similarly, a very weak intraspecific variability is observed. Most of the *Tragulus kanchil* cluster together associated to the other Tragulidae *Hyaemoschus aquaticus* (**Supplementary Data S2**). Similarly, the two duiker species (*Cephalophus dorsalis,* and *Cephalophus zebra*) cluster together (**Supplementary Data S2**) indicating that the entire shape of the stapes may provide phylogenetical information.

The shape disparity and the morphospace of the studied samples are very similar in all the three datasets (**1** original dataset, **2** dataset without allometrical signal (not pooled by family), and **3** dataset without allometrical signal pooled by family), the PC2 axis being mirrored in the results without size effect in comparison to original dataset (**Figure 4**). The changes mostly concern the position of the two large stapes (*Ovibos moschatus* and *Connochaetes gnou*). Considering the original dataset, the dataset without allometrical signal, and the dataset without allometrical signal pooled by family, the maximum of variance along PC1 (13.75, 13.87, and 13.86% of the variance, respectively) goes from a massive and short stapes in the negative values to a slender and elongated one in the positive values. The stapes capitulum and the stapedial footplate are enlarged with short crura stapedis in PC1 negative values. Their intercrural foramens are relatively rounded and central. The stapedial footplate is ovoid to slightly elongate. The stapes capitulum and the stapedial footplate are short with elongated crura stapedis in positive PC1 values. Their intercrural foramens are ovoid and the space between the intercrural foramens and the anterior crus is narrow. The stapedial footplate is ovoid and short. PC2 explains 9.14, 9.21, and 10.20% of the variance of the original dataset, the dataset without allometrical signal, and of the dataset without allometrical signal pooled by family, respectively. In the negative PC2 values based on the original dataset, the intercrural foramens are a little closer to the stapedial footplate, but the general shape is very similar to the consensus shape (**Figure 4**). Considering the PC2 positive values based on the original dataset, the height of the stapes is similar to the consensus but the latter is a little narrower. The intercrural foramens are very elongated and closer to the posterior crus. The negative and positive PC2 shape variations are inverted in the datasets without allometrical signal (not pooled and pooled by family) in comparison to the original dataset. The shape of the stapedial footplate is different along the PC2 axis between

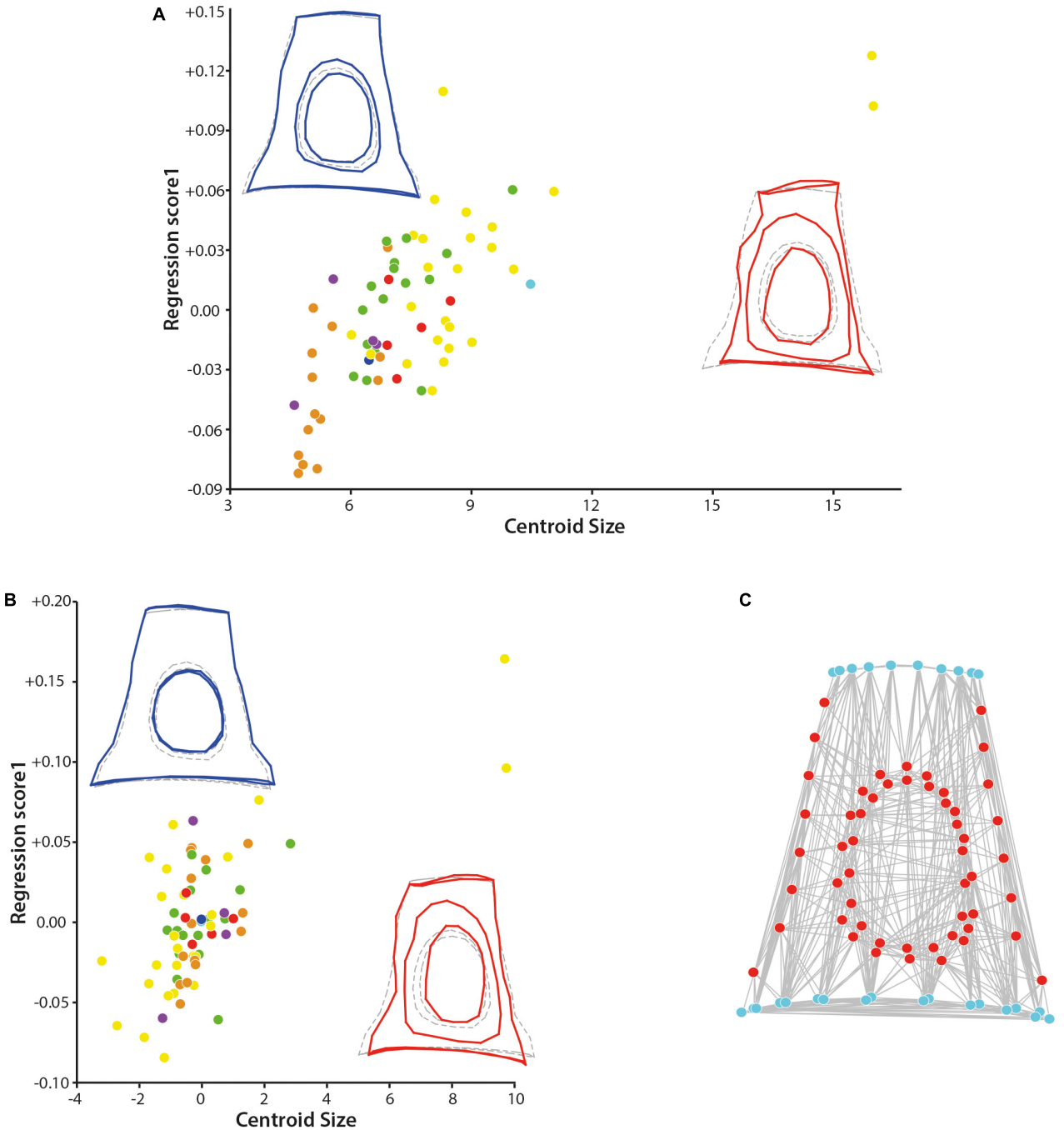

FIGURE 3 | Results of the regression on the centroid size and of the modularity test. **(A)** Regression of the shape of the stapes on the centroid size and **(B)** regression of the shape of the stapes on the centroid size pooled within families. **(C)** Result of the modularity test (similar to the original hypothesis) on the original 3D landmarks dataset, the stapes with size correction dataset, and the stapes with size correction pooled within families (all three analyses give similar result, graph shows the first result, the two others are not shown). Stem Pecora violet; Antilocapridae red; Bovidae, yellow; Cervidae, green; Tragulidae, orange; Giraffidae, and light blue; Moschidae, dark blue. Statistical results are available in **Supplementary Data S3**.

pooled data on one side and the original dataset and the not pooled ones on the other side (PC2 shape variation of the original data being mirrored in comparison to the not pooled one). The negative values of PC2 in the pooled dataset show a drop-like shape of the surface area of the stapedial footplate. Considering the not pooled data negative PC2 values (positive ones for the original data), the stapes is ovoid and more symmetrical. On the other end of PC2 axis, the stapedial footplate is ovoid and more asymmetrical in all three datasets. However, the asymmetry is more marked from the original dataset to the dataset after size

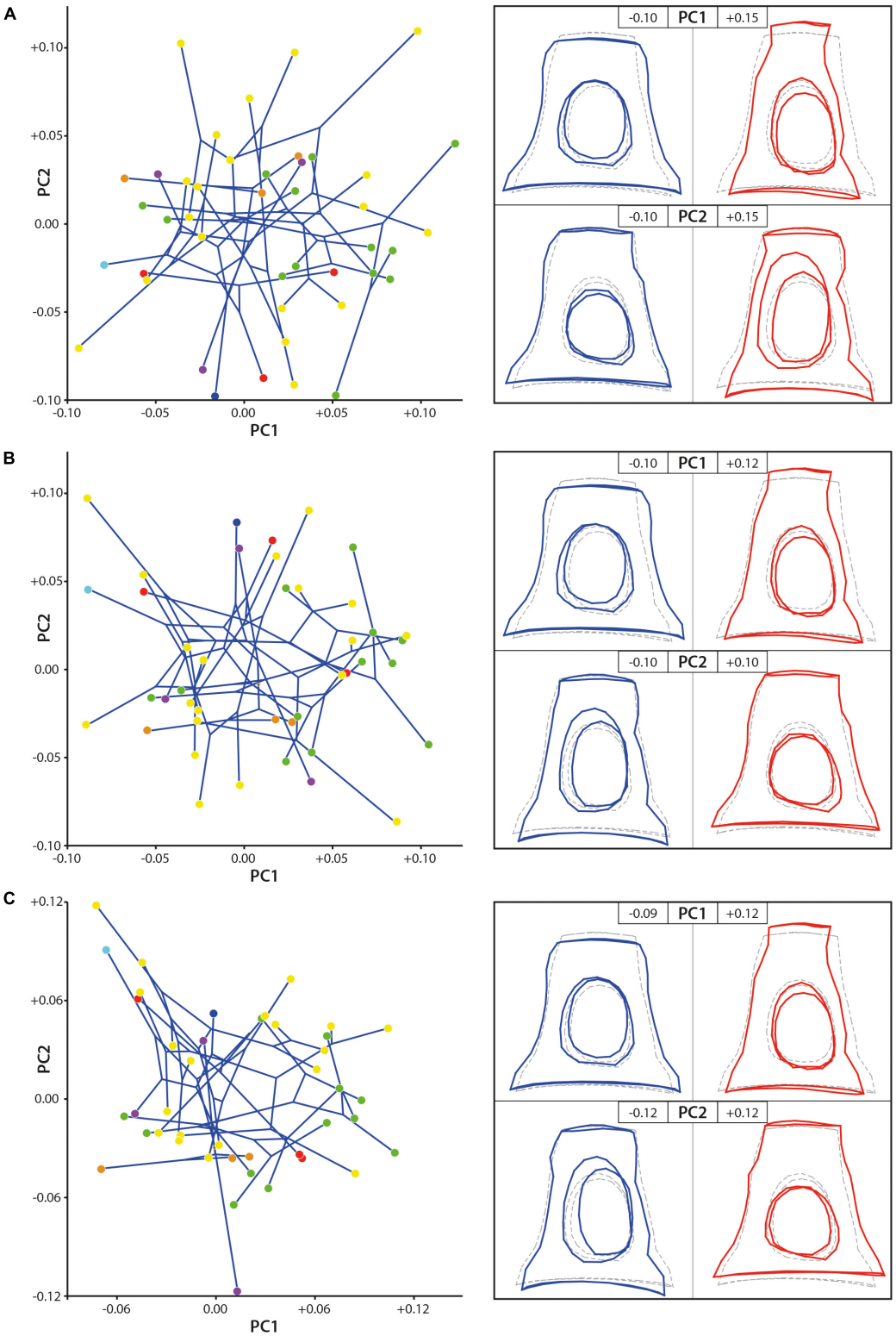

FIGURE 4 | Geometric morphometric PCA results. **(A)** stapes based on the original 3D landmarks coordinates (dataset 1; PC1 = 13.75%, PC2 = 9.14%), **(B)** dataset without allometrical signal not pooled by family (dataset 2; PC1 = 13.87%, PC2 = 9.21%), and **(C)** dataset without allometrical signal pooled by family (dataset 3; PC1 = 13.86%, PC2 = 10.20%). The morphological modifications along the axes (PC) are materialized by the hypothetical stapes shape associated to extreme values. Stem Pecora violet; Antilocapridae red; Bovidae, yellow; Cervidae, green; Tragulidae, orange; Giraffidae, and light blue; Moschidae, dark blue. Statistical results are available in **Supplementary Data S3**.

correction and pooled by family, the dataset after size correction being intermediate.

Phylogenetic Signal

No clear phylomorphospace can be directly observed using the two first PCs only (**Figure 4**). Nevertheless, the *p*-value resulting from the permutation test, testing the phylogenetic signal on the plotting area of the shape variation, is significant considering the original dataset and the dataset of the stapes after size effect correction without pooling by family (*p*-value = 0.0031 and *p*-value = 0.0029, respectively, **Supplementary Data S3**). It is highly significant when testing the phylogenetic signal on the datasets after size effect correction and pooled by family (*p*-value = 0.0008). It indicates that we can reject the null hypothesis of an overall shape variation (with and without size effect) across the tips of the tree which is not different from random rather than being phylogenetically structured. It means that the overall shape of the stapes is phylogenetically informative. The *p*-value resulting from the permutation test testing the phylogenetic signal on the centroid size of the stapes original dataset is also significant (*p*-value = 0.0235). It means that the size of the stapes is related to its phylogeny. Indeed, the two largest specimens from the dataset are Bovidae and the smallest specimens are Tragulidae.

bg-PCA

Bg-PC1 explains 45.51, 45.44, and 47.16% of shape variation associated to the predefined groups (families) for both (**1**) the original dataset (with allometrical signal), (**2**) the dataset without allometrical signal not pooled by family (since a significant correlation between the shape of the stapes and its size exists, and (**3**) the dataset without allometrical signal pooled by family, respectively (**Figure 5**). Bg-PC2 explains 23.66, 23.12, and 23.86% of the three datasets, respectively (**Figure 5**). Clear morphospaces for the different clades can be defined based on the shape of the stapes. Even if some overlap exists, notably between the Bovidae and the Cervidae, clear trends can be observed. The general repartition observed along the bg-PC based on the original dataset and dataset without allometrical signal pooled by family are almost similar with a better segregation of the families in the last analysis (**Figures 5A,C**). Indeed, while the Bovidae mostly plot in the positive values of bg-PC1, the Cervidae are mostly in the negative values in both cases. In these two analyses, the Antilocapridae are among the most negative values along bg-PC1. In all the analyses, the Tragulidae are located around 0 on bg-PC1. A clear separation between Tragulina and Pecora occurs along bg-PC2 of the original dataset and the dataset without allometrical signal pooled by family, the Tragulina being located in the most negative values. Considering the dataset without allometrical signal not pooled by family (dataset 2), the separation between the Bovidae and the Cervidae along bg-PC1 and between the Tragulidae and the Bovidae along bg-PC2 are not clear. It confirms that part of the allometry, deleted in this dataset, provide phylogenetical information. Nevertheless, the mean shape of the different families is relatively similar considering the three datasets.

The stapes of the Tragulidae are distinct being massive with a relatively elongated stapedial footplate and a little elongated stapes capitulum. The crura are relatively parallel and do not directly reach the edge of the stapedial footplate forming a strong angle. The stapedial footplate has a tear shape being antero-posteriorly asymmetrical. The Antilocapridae possess a concave crus stapedis and a shorter posterior crus than the anterior crus with an enlarged stapes capitulum, giving a trapezoidal lateral shape to the bone. The stapedial footplate is very enlarged, ovoid and slightly asymmetrical. The stapedial footplate is also ovoid in stem Pecora. In Cervidae, the crura stapedis are of similar length and straightness with a slightly reduced stapes capitulum. Their stapedial footplate is ovoid and narrow. The Bovidae have a relatively rectangular stapes in lateral view due to relatively straight crura stapedis and an enlarged stapes capitulum. The stapedial footplate is laterally asymmetrical.

Significant and similar results are observed considering the CVA confirming the results observed with the bg-PCA (**Supplementary Data S6**).

DISCUSSION

Allometry in the Stapes

Allometry is one of the main causes known to polarize morphological variation and constrain phenotypic evolution (e.g., Sansalone et al., 2017). Sense organs have been shown to scale negatively with body mass in mammals (Sánchez-Villagra, 2012; Costeur et al., 2019), which has possibly allowed them to evolve very sophisticated hearing capacities. A negative ontogenetic growth allometry is known for the middle ear ossicles including the stapes throughout the deep time evolution of mammals (Luo, 2011). A similar negative allometry at the evolutionary level of species was preliminary observed in a range of extant and extinct mammals (Orliac and Billet, 2016). We show here that the centroid sizes of the stapes and stapedial footplate are correlated with body mass in ruminants with a strong negative allometry (α = 0.1794 and α = 0.1658, respectively). Similar slopes have already been observed using the height of the stapes and the length, width, and the area of the stapedial footplate of large terrestrial mammals as variables against body mass (Fleischer, 1973; Nummela, 1995; Mason, 2001; Orliac and Billet, 2016). The relationship may be different in small size mammals, being more isometric (Nummela, 1995; Mason, 2001). Differences are also observed depending of the ecology of the animal. Subterranean and aquatic mammals, where the acoustic environment is different from the surface, possess a significantly enlarged area of the stapedial footplate in comparison to body mass (Nummela, 1995; Mason, 2001).

A negative allometry of size is observed between the centroid size of the stapes and the centroid size of the stapedial footplate (R^2 = 0.9267, *p*-value < 0.0001, α = 0.8901, a isometry values being 1.5, and see **Supplementary Data S2**). An isometric variation of the height of the stapes and the width of the stapedial footplate has been observed in Orliac

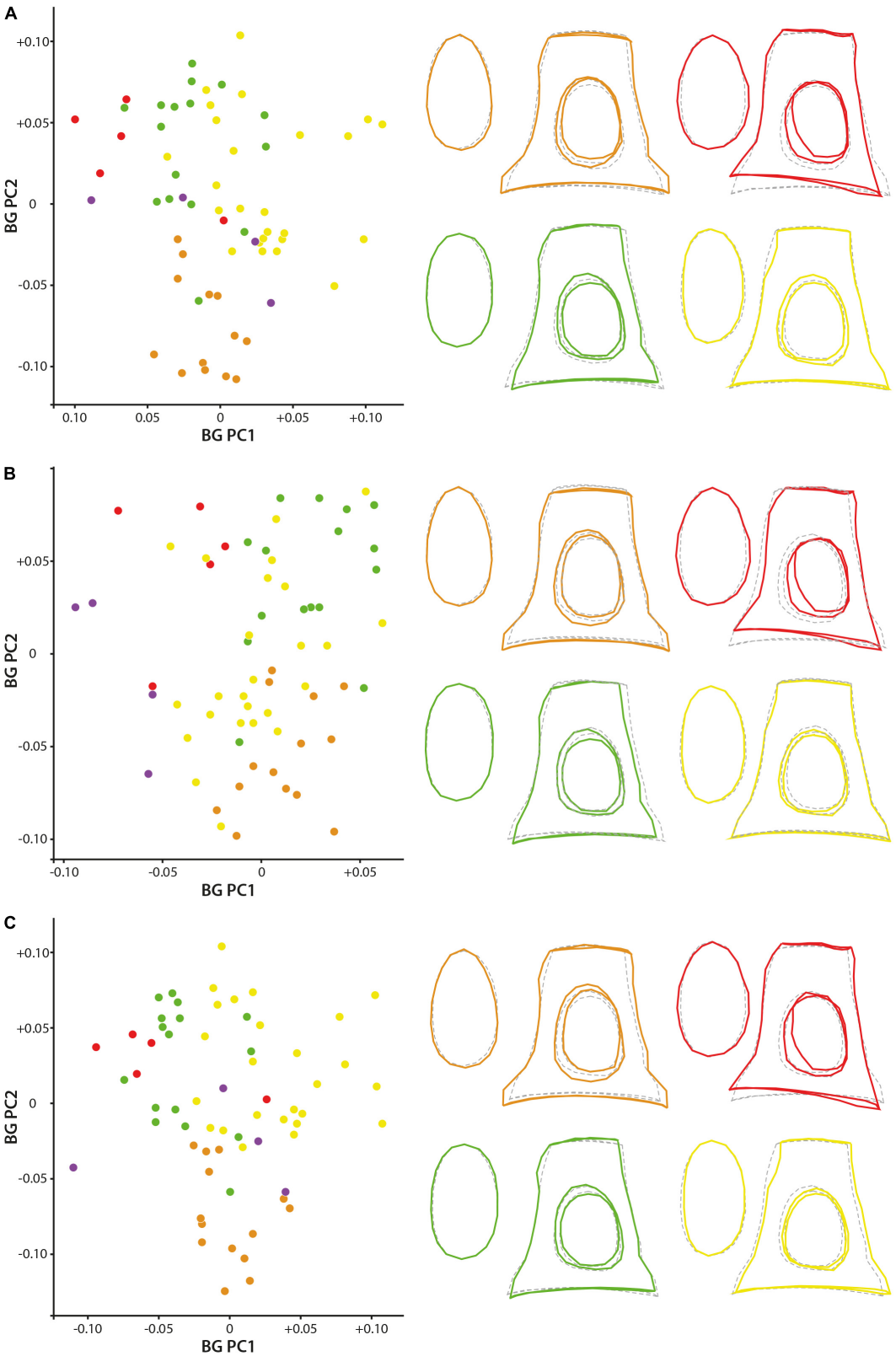

FIGURE 5 | Geometric morphometric bg-PCA results. **(A)** stapes based on the original 3D landmarks coordinates (dataset 1; PC1 = 45.5%, PC2 = 23.7%), **(B)** dataset without allometrical signal not pooled by family (dataset 2; PC1 = 45.4%, PC2 = 23.1%), and **(C)** dataset without allometrical signal pooled by family (dataset 3; PC1 = 47.2%, PC2 = 23.9%). The mean shape of the Antilocapridae is red, of the Bovidae is yellow, of the Cervidae is green, and of the Tragulidae is orange.

and Billet (2016). The shape of the stapedial footplate may explain such differences. Smaller species of our datatset have a more rounded stapedial footplate while the large ones have more ovoid shapes inducing a smaller relative area. The bony labyrinth shows a negative ontogenetic allometric growth relative to the petrosal bone, to skull length, and to body mass (Billet et al., 2015; Costeur et al., 2017, 2019). It has been demonstrated in ruminants (Mennecart and Costeur, 2016; Costeur et al., 2017) and other placental mammals (e.g., Thean et al., 2017) that bony labyrinth ossification is achieved long before birth, around mid-gestation. The size and weight of the stapes is probably limited by physiological and physical constrains. Nummela (1995) proposed that mammalian tympanic membrane may possess an upper size range to prevent from breakage. Since all the auditory region is highly constrained, this likely imposes an upper size limit to the ossicles in terrestrial mammals (Nummela, 1995), although this hypothesis should be further tested.

The stapedial footplate, the *crura stapedis,* and the *stapes capitulum* form a module. They are subject to similar orientations of strength constrains. The module formed by "intercrural foramens" shows a maximum of covariation. Diamond (1989) hypothesized that "the negative allometry of the stapes imposes an upper limit on the size an animal can reach and still retain a fully developed stapedial artery system" since "with increasing body size, the diameter of the intercrural foramen increases much more slowly than the mass of tissue supplied by the stapedial artery." The intercrural foramens, which are penetrated by the stapedial artery, show a negative allometry in comparison to the stapes centroid size and a clear shape allometry of these structures. It is not clear how long the stapedial artery persists in Ruminantia, it was clearly identified in bovine fetuses (Erdogan and Kilinc, 2012) but its pattern of regression after embryonic stages remains unknown in the group.

Phylogenetic Signal on the Stapes Morphology

The ear region possesses a strong phylogenetic signal (e.g., Schmelze et al., 2005; Quam et al., 2014; Mennecart and Costeur, 2016; Mennecart et al., 2016, 2017; Stoessel et al., 2016a,b; Bastl et al., 2017; Kerber and Sánchez-Villagra, 2018). Stoessel et al. (2016b) noticed that the human stapes differs from the other hominids by its height, a distinct stapedial head, and a specific kidney shape of the footplate, even if the other ossicles may be more phylogenetically informative (Stoessel et al., 2016b). Schmelze et al. (2005) also observed that the ossicles characters help structure the marsupial tree. In particular the stapedial footplate (bullate, flat, or concave), the stapedial ratio, and the overall stapes shape (Schmelze et al., 2005) are phylogenetically informative within the marsupial clade. The marsupial families, and even the Macropodinae subfamily, can be separated based on the association of these three characters only. Orliac and Billet (2016) found that the shape of the stapedial footplate is probably not influenced by allometry. They also suggested that "footplate shape may be examined in order to detect phylogenetically significant

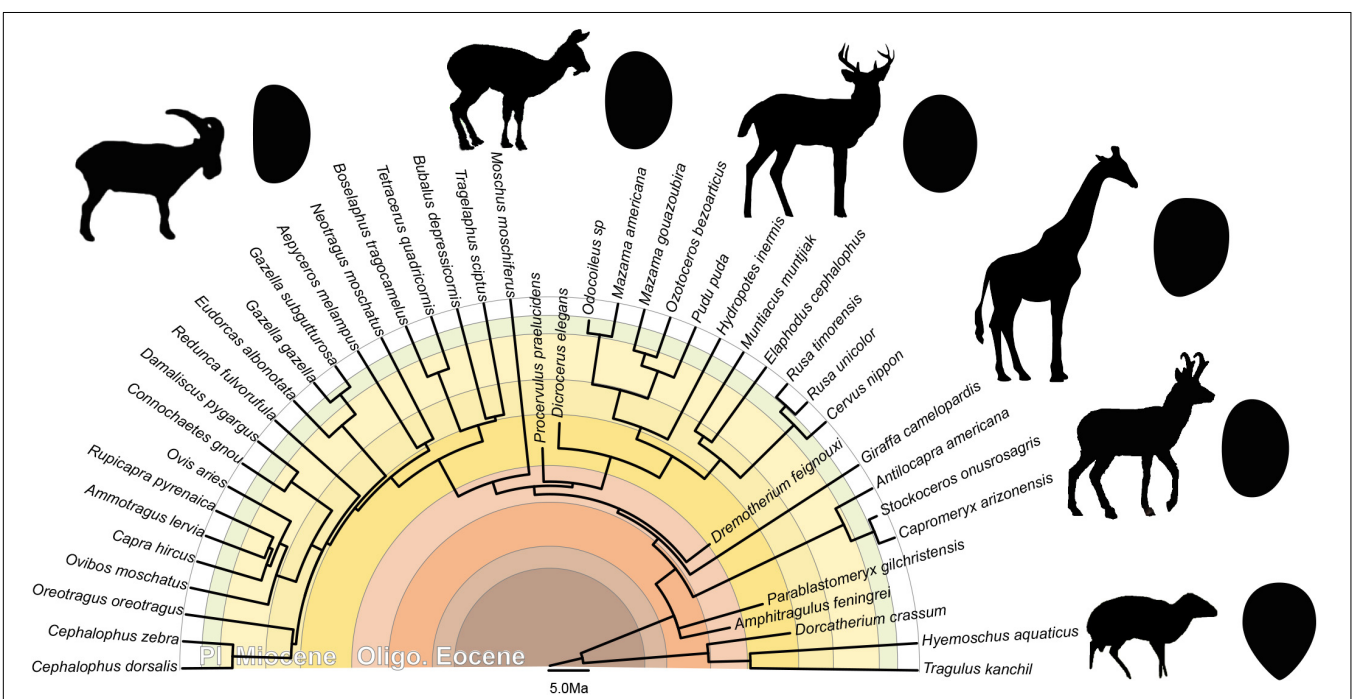

FIGURE 6 | Phylogeny of the studied ruminants with associated general stapedial footplate morphology. Topography of the tree based on (Janis et al., 1998; Hassanin et al., 2012; Mennecart, 2012; and Mennecart et al., 2019; calibration of the Cervidae nodes based on Mennecart et al., 2017; calibration of the Bovidae nodes based on Bibi, 2013). Oligo.: Oligocene; Pl.: Pliocene.

differences between artiodactyl groups (. . .) an elongated stapedial footplate (high footplate ratio) may for example constitute a synapomorphy of the clade Suoidea" (Orliac and Billet, 2016). Mennecart et al. (2017) already proposed that the shape of the stapedial fenestra (the inner ear counterpart of the stapedial footplate) is phylogenetically informative. They noted significant differences within the different Cervidae sub-families. In all considered Cervidae, the stapedial fenestra is ovoid (Mennecart et al., 2017), like the stapedial footplate in the present analysis. However, while the stapedial fenestra is massive in Procervulinae and Dicrocerinae (stem Cervidae), that of Cervinae (crown Cervidae) is elongated (Mennecart et al., 2017). The Capreolinae (crown Cervidae) have an intermediate shape. We here confirm that the stapedial footplate is phylogenetically informative, allowing a distinction between ruminant families. The *p*-values resulting from the permutation test, testing the phylogenetic signal on the plotting area of the shape variation, are significant considering the shape of the stapes with and without size correction (p-value = 0.0031, p-value = 0.0029, and p-value = 0.0008). Shape differences can be observed especially on the stapedial footplate outline (**Figure 6**). The stapedial footplate of Tragulidae has a tear shape being antero-posteriorly asymmetrical. The Cervidae have a symmetrical ovoid stapedial footplate. In Bovidae, the stapedial footplate is laterally asymmetrical. This asymmetry is more marked in larger specimens. These shape differences are already observed in early Miocene representatives making it a good character for family distinction along the ruminant deep time evolution.

CONCLUSION

This first large scale analysis of the ruminant stapes confirms that this bone grows with a negative allometry, as already observed in other mammal groups, i.e., it is relatively larger in smaller species than it is in larger species. This result is in accordance with ontogenetic and evolutionary studies that investigated the growth of sense organs, and in particular of the middle ear bones and bony labyrinth. This result may confirm the role of the middle ear on the evolution of large sizes in mammals since the stapes accommodates a passage for an arterial branch at least in embryonic ontogenetic stages. Regression of the stapedial artery before birth is known in various groups of mammals, especially in primates, but remains largely unknown in ruminants. More work involving dissections may help provide more information on the evolution of sizes in mammals in combination to presence, absence, or regression of the stapedial artery and its impact on the shape of the intercrural foramen. Ideally developmental works in various mammal groups would be essential to model stapedial growth at a large scale. Very much is known in some groups (i.e., primates or some rodents) but virtually nothing in others, such as in Ruminantia. Likewise, investigating the shape of the stapes and of its intracrural foramen in mammals across their evolutionary history, and not only like here within a relatively young clade, may provide information on the evolution of this regression through time. How critical this regression is in terms of hearing abilities is still unknown, although a functional advantage of not having an arterial branch passing through the stapes may be evident in limiting noise (from blood in the artery) transmission to the inner ear. Some mammals are known to keep the stapedial artery through life and this persistence still does not find functional or adaptive explanations.

Our results on the growth and modularity of parts of the stapes highlight under what constraints this critical bone grows and how integrated the ear region in mammals is when stapes shape analysis is compared to the other structures of the ear, i.e., the bony labyrinth, the other ossicles, or the tympanic membrane. Recent evidence has shown that the stapedial fenestra on the bony labyrinth presented a phylogenetic signal, the shape of its counterpart on the stapes, the stapedial footplate, is significant for family determination within Ruminantia, as demonstrated here. Its shape can indeed distinguish families for taxa already known in the early Miocene, when pecoran ruminants started their radiation. Our results confirm recent studies on the stapes itself in other groups of mammals showing that not only the region of the inner ear (bony labyrinth and petrosal bone) is a critical source of phylogenetic data but also that all aspects of the middle ear may provide information. The stapes is small and often falls into the cavity of the inner ear within the petrosal bone. It is therefore often preserved even in long extinct taxa. Its small size makes it a very easy bone to reconstruct from CT-generated data. It is consequently worth looking for in fossil mammal skulls. Although the stapes has been the focus of attention in anatomy for more than 150 years, its morphology in extant mammals is only starting to be investigated on a large taxonomical scale and museum's specimens constitute a great and easily accessible source of data for this bone and for the ear region in general. Our study focused on ruminants highlights the evolutionary and phylogenetic interest of the smallest bone of the mammalian skeleton and provides morphological characters of phylogenetic relevance for future works.

DATA AVAILABILITY STATEMENT

All datasets generated for this study are included in the article/**Supplementary Material**.

AUTHOR CONTRIBUTIONS

BaM and LC designed the study. GS and BeM scanned the specimens. BaM and CG reconstructed the stapes. BaM and LD performed the analyses. All the authors agreed with the manuscript.

FUNDING

This work was supported by the Swiss National Science Foundation (SNF projects 178853, 159854, and 133802).

ACKNOWLEDGMENTS

All our gratitude goes to all the curators and colleagues who provided access to their collection and allowed to scan the specimens. We would like to thank Pip Brewer (Natural History Museum of United Kingdom, London, United Kingdom); Jin Meng, Judith Galkin, Alana Gishlicm and Morgan Hill (American Museum of Natural History, New York, United States); Richard C. Hulbert and Jonathan Bloch (University of Florida, Gainesville, United States); and Yves Laurent and Francis Duranthon (Muséum d'Histoire Naturelle de Toulouse, France). Financial support of the Swiss National Science Foundation is especially acknowledged for financing projects on the ear region (SNF projects 178853 and 159854) the financial support in the frame of the R'equip initiative (133802). BaM warmly thanks Soledad De Esteban-Trivagno (Transmitting Science and ICP), Chris Klingenberg (University of Manchester), and Melissa Tallman (Grand Valley State University) for their precious help in geometric morphometrics through the Transmitting Science program. We would also like to thank the reviewers Paolo Piras, Saverio Bartolini Lucenti, and Antonio Profico for their helpful comments and the editor Pasquale Raia and Luca Pandolfi for inviting us in this special issue.

SUPPLEMENTARY MATERIAL

The Supplementary Material for this article can be found online at: https://www.frontiersin.org/articles/10.3389/feart.2020.00176/full#supplementary-material

DATA S1 | 3D stapes of *Hydropotes inermis* NMB9892.

DATA S2 | Additional figures and measurements.

DATA S3 | Geometric morphometric results for MorphoJ.

DATA S4 | Nexus file of the phylogenetic tree.

DATA S5 | Geometric morphometric results for R.

DATA S6 | Figure and description of the CVA.

REFERENCES

Bastl, K., Nagel, D., and Solé, F. (2017). Incus facet morphology in carnivorous mammals from different ecosystems: taxonomy vs. habitat. C. R. *Palevol* 16, 284–302. doi: 10.1016/j.crpv.2016.11.008

Bernardi, M., and Couette, S. (2017). Eocene paleoecology of *Adapis parisiensis* (Primate. Adapidae): from inner ear to life style. *Anat. Rec.* 300, 1576–1588. doi: 10.1002/ar.23609

Bibi, F. (2013). A multi-calibrated mitochondrial phylogeny of extant Bovidae (Artiodactyla. Ruminantia) and the importance of the fossil record to systematics. *BMC Evol. Biol.* 13:166. doi: 10.1186/1471-2148-13-166

Billet, G., Muizon, C., Schellhorn, R., Ruf, I., Ladevèze, S., and Bergqvist, L. (2015). Petrosal and inner ear anatomy and allometry amongst specimens referred to Litopterna (Placentalia). *Zool. J. Linn. Soc.* 173, 956–987. doi: 10.1111/zoj.12219

Cardini, A., O'Higgins, P., and Rohlf, F. J. (2019). Seeing distinct groups where there are none: spurious patterns from between-group PCA. *Evol. Biol.* 46, 303–316. doi: 10.1007/s11692-019-09487-5

Costeur, L., Mennecart, B., Schulz, G., and Müller, B. (2017). Prenatal growth stages show the development of the ruminant bony labyrinth and petrosal bone. *J. Anat.* 230, 347–353. doi: 10.1111/joa.12549

Costeur, L., Mennecart, B., Müller, B., and Schulz, G. (2019). Observations on the scaling relationship between bony labyrinth, skull size and body mass in ruminants. *Proc. SPIE* 11113:1111313. doi: 10.1117/12.2530702

Costeur, L., Mennecart, B., Schulz, G., and Müller, B. (2016). Middle ear bones of a mid-gestation ruminant foetus extracted from X-ray computed tomography. *Proc. SPIE* 9967:99671Q.

Diamond, M. K. (1989). Coarctation of the stapedial artery: an unusual adaptive response to competing functional demands in the middle ear of some Eutherians. *J. Morphol.* 200, 71–86. doi: 10.1002/jmor.1052000109

Doran, A. H. G. (1878). Morphology of the mammalian ossicula auditus. *Trans. Linn. Soc. Lond.* 1, 371–497. doi: 10.1111/j.1096-3642.1878.tb00663.x

Edgington, E. S. (1987). *Randomization Tests*. New York, NY: Marcel Dekker.

Erdogan, S., and Kilinc, M. (2012). Gross anatomy and arterial vascularization of the tympanic cavity and osseous labyrinth in mid- gestational bovine fetuses. *Anat. Rec.* 293, 2083–2093. doi: 10.1002/ar.21269

Fleischer, G. (1973). Studien am skelett des gehörorgans der säugetiere, einschliesslich des menschen. *Säugetierkd. Mitt.* 21, 131–239.

Fleischer, G. (1978). Evolutionary principles of the mammalian middle ear. *Adv. Anat. Embryol. Cel.* 55, 5–70.

Hammer, Ø, Harper, D. A. T., and Ryan, P. D. (2001). PAST: paleontological statistics software package for education and data analysis. *Palaeontol. Electron.* 4:9.

Hassanin, A., Delsuc, F., Ropiquet, A., Hammer, C., van Vuuren, J. B., Matthee, C., et al. (2012). Pattern and timing of diversification of *Cetartiodactyla* (Mammalia. Laurasiatheria), as revealed by a comprehensive analysis of mitochondrial genomes. *C. R. Biologies* 335, 32–50. doi: 10.1016/j.crvi.2011.11.002

Hyrtl, J. (1845). *Verleichende-anatomische Untersuchungen über das innere Gehörorgan des Menschen und der Säugethiere*. Prague: Friedrich Ehrlich.

Janis, C. M., Scott, K. M., and Jacobs, L. L. (1998). *Evolution of Tertiary Mammals of North America*. New York, NY: Cambridge University Press.

Karachle, P. K., Stergiou, K. I., and Wahl, C. (2012). "4. Morphometrics and allometry in fishes," in *Morphometrics*, (Christina Wahl: IntechOpen), 65–86. doi: 10.5772/34529

Kerber, L., and Sánchez-Villagra, M. R. (2018). Morphology of the middle ear ossicles in the rodent perimys (Neoepiblemidae) and a comprehensive anatomical and morphometric study of the phylogenetic transformations of these structures in *Caviomorphs*. *J. Mamm. Evol.* 26, 407–422. doi: 10.1007/s10914-017-9422-9429

Klingenberg, C. P. (2008). Morphological integration and developmental modularity. *Annu. Rev. Ecol. Evol. Syst.* 39, 115–132. doi: 10.1146/annurev.ecolsys.37.091305.110054

Klingenberg, C. P. (2011). MorphoJ: an integrated software package for geometric morphometrics. *Mol. Ecol. Resour.* 11, 353–357. doi: 10.1111/j.1755-0998.2010.02924.x

Klingenberg, C. P. (2016). Size, shape, and form: concepts of allometry in geometric morphometrics. *Dev. Genes Evol.* 226, 113–137. doi: 10.1007/s00427-016-0539-532

Klingenberg, C. P., and Gidaszewski, N. A. (2010). Testing and quantifying phylogenetic signals and homoplasy in morphometric data. *Syst. Biol.* 59, 245–261. doi: 10.1093/sysbio/syp106

Luo, Z. X. (2007). Transformation and diversification in early mammal evolution. *Nature* 450, 1011–1019. doi: 10.1038/nature06277

Luo, Z. X. (2011). Developmental patterns in Mesozoic evolution of mammal ears. *Annu. Rev. Ecol. Evol. Syst.* 42, 355–380. doi: 10.1146/annurev-ecolsys-032511-142302

Maddison, W. P., and Maddison, D. R. (2010). *Mesquite: a Modular System for Evolutionary Analysis. Version 3.04*.

Maier, W., and Ruf, I. (2016a). Evolution of the mammalian middle ear: a historical review. *J. Anat.* 228, 270–283. doi: 10.1111/joa.12379

Maier, W., and Ruf, I. (2016b). The anterior process of the malleus in *Cetartiodactyla*. *J. Anat.* 228, 313–323. doi: 10.1111/joa.12393

Marriott, F. H. C. (1979). Barnard's monte carlo tests: how many simulations? *Appl. Stat.* 28, 75–77.

Mason, M. J. (2001). Middle ear structures in fossorial mammals: a comparison with non-fossorial species. *J. Zool.* 255, 467–486. doi: 10.1017/s0952836901001558

Meng, J., Yuanqing, W., and Chuankui, L. (2011). Transitional mammalian middle ear from a new Cretaceous Jehol eutriconodontan. *Nature* 472, 181–185. doi: 10.1038/nature09921

Mennecart, B. (2012). The Ruminantia (Mammalia. *Cetartiodactyla*) from the oligocene to the early Miocene of Western Europe: systematics, palaeoecology and palaeobiogeography. *Geofocus* 32, 1–263.

Mennecart, B., and Costeur, L. (2016). A *Dorcatherium* (Mammalia, Ruminantia, middle Miocene) petrosal bone and the tragulid ear region. *J. Vert. Paleontol.* 36:e1211665. doi: 10.1080/02724634.2016.1211665

Mennecart, B., DeMiguel, D., Bibi, F., Rössner, G. E., Métais, G., Neenan, J. M., et al. (2017). Bony labyrinth morphology clarifies the origin and evolution of deer. *Sci. Rep.* 7:13176. doi: 10.1038/s41598-017-12848-12849

Mennecart, B., Rössner, G. E., Métais, G., DeMiguel, D., Schulz, G., Müller, B., et al. (2016). The petrosal and bony labyrinth of Early to Middle Miocene European deer (Mammalia. Cervidae) reveal their phylogeny. *J. Morphol.* 277, 1329–1338. doi: 10.1002/jmor.20579

Mennecart, B., Zoboli, D., Costeur, L., and Pillola, G. L. (2019). On the systematic position of the oldest insular ruminant *Sardomeryx oschiriensis* (Mammalia. Ruminantia) and the early evolution of the Giraffomorpha. *J. Syst. Palaeontol.* 17, 1–14. doi: 10.1080/14772019.2018.1472145

Merchant, S. N., Ravicz, M. E., and Rosowski, J. J. (1996). Acoustic input impedance of the stapes and cochlea in human temporal bones. *Hear. Res.* 97, 30–45. doi: 10.1016/s0378-5955(96)80005-0

Mitteroecker, P., and Bookstein, F. (2011). Linear discrimination, ordination, and the visualization of selection gradients in modern morphometrics. *Evol. Biol.* 38, 100–114. doi: 10.1007/s11692-011-9109-8

Nowak, R. M. (1999). *Walker's mammals of the world, 6th edition*. Baltimore, MD: The John Hopkins University Press.

Nummela, S. (1995). Scaling of the mammalian middle ear. *Hear. Res.* 85, 18–30. doi: 10.1016/0378-5955(95)00030-8

Orliac, M. J., and Billet, G. (2016). Fallen in a dead ear: intralabyrinthine preservation of stapes in fossil artiodactyls. *Palaeovertebrata* 40:e3. doi: 10.18563/pv.40.1.e3

Quam, R. M., Coleman, M. N., and Martinez, I. (2014). Evolution of the auditory ossicles in extant hominids: metric variation in African apes and humans. *J. Anat.* 225, 167–196. doi: 10.1111/joa.12197

R Core Team (2005). *R: A language and environment for statistical computing*. Vienna: R Foundation for Statistical Computing.

Renaud, S., Dufour, A.-B., Hardouin, E. A., Ledevin, R., and Auffray, C. (2015). Once upon multivariate analyses : when they tell several stories about biological evolution. *PLoS one* 10:e0132801. doi: 10.1371/journal.pone.0132801

Rich, T. H., Hopson, J. A., Musser, A. M., Flannery, T. F., and Vickers-Rich, P. (2005). Independent origins of middle ear bones in monotremes and therians. *Science* 307, 910–914. doi: 10.1126/science.1105717

Rosowski, J. J., and Graybeal, A. (1991). What did *Morganucodon* hear? *Zool. J. Linn. Soc.* 101, 131–168. doi: 10.1111/j.1096-3642.1991.tb00890.x

Sánchez-Villagra, M. R. (2012). *Embryos in deep time: the rock record of biological development. Berkeley and*. Los Angeles, CA: University of California Press.

Sansalone, G., Colangelo, P., Kotsakis, T., Loy, A., Castiglia, R., Bannikova, A. A., et al. (2017). influence of evolutionary allometry on rates of morphological evolution and disparity in strictly subterranean moles (Talpinae. Talpidae, Lipotyphla,Mammalia). *J. Mammal.* 25, 1–14. doi: 10.1007/s10914-016-9370-9379

Schlager, S. (2017). "Morpho and Rvcg – Shape analysis in R," in *Statistical Shape and Deformation Analysis*, eds G. Zheng, S. Li, and G. Szekely (Cambridge, MA: Academic Press), 217–256. doi: 10.1016/b978-0-12-810493-4.00011-0

Schmelze, T., Nummela, S., and Sánchez-Villagra, M. R. (2005). Phylogenetic transformations of the ear ossicles in marsupial mammals, with special reference to Diprotodontians: a character analysis. *Ann. Carnegie Mus.* 74, 189–200.

Shingleton, A. (2010). Allometry: the study of biological scaling. *Nat. Educ. Knowled.* 3:2.

Stoessel, A., David, R., Gunz, P., Schmidt, T., Spoor, F., and Hublin, J.-J. (2016a). Morphology and function of neandertal and modern human ear ossicles. *Proc. Natl Acad. U S A.* 112, 11498–11494. doi: 10.1073/pnas.1605881113

Stoessel, A., Gunz, P., David, R., and Spoor, F. (2016b). Comparative anatomy of the middle ear ossicles of extant hominids – introducing a geometric morphometric protocol. *J. Hum. Evol.* 91, 1–25. doi: 10.1016/j.jhevol.2015.10.013

Thean, T., Kardjilov, N., and Asher, R. (2017). Inner ear development in cetaceans. *J. Anat.* 230, 249–261. doi: 10.1111/joa.12548

Tzeng, T. D., and Yeh, S. Y. (1999). Permutation tests for difference between two multivariate allometric patterns. *Zool. Stud.* 38, 10–18.

Wiley, D. (2006). *Landmark Editor 3.6. (Institute for Data Analysis and Visualization*. Davis, CA: University of California.

Wilkie, H. C. (1925). The ossicula auditûs of the sheep (Ovis aries). *J. Comp. Pathol.* 38, 298–301. doi: 10.1016/s0368-1742(25)80051-1

Wilkie, H. C. (1936). The auditory organ of the ox (Bos taurus). *Proc. Zool. Soc. Lond.* 106, 985–1009. doi: 10.1111/j.1469-7998.1936.tb06299.x

Wilson, V. J. (2005). *Duikers of Africa (Masters of the African forest floor)*. Pretoria: Zimbi book.

Conflict of Interest: The authors declare that the research was conducted in the absence of any commercial or financial relationships that could be construed as a potential conflict of interest.

frontiers in Earth Science

ORIGINAL RESEARCH
published: 26 June 2020
doi: 10.3389/feart.2020.00247

Target Deformation of the *Equus stenonis* Holotype Skull: A Virtual Reconstruction

Omar Cirilli[1,2], Marina Melchionna[3], Carmela Serio[4], Raymond L. Bernor[5,6], Maia Bukhsianidze[7], David Lordkipanidze[7], Lorenzo Rook[2], Antonio Profico[8] and Pasquale Raia[3]*

[1] Dottorato di Ricerca in Scienze della Terra, Università degli Studi di Pisa, Pisa, Italy, [2] Paleo[Fab]Lab, Dipartimento di Scienze della Terra, Università degli Studi di Firenze, Firenze, Italy, [3] Dipartimento di Scienze della Terra, dell'Ambiente e delle Risorse, Università degli Studi di Napoli Federico II, Naples, Italy, [4] Research Centre in Evolutionary Anthropology and Palaeoecology, School of Biological and Environmental Sciences, Liverpool John Moores University, Liverpool, United Kingdom, [5] Laboratory of Evolutionary Biology, Department of Anatomy, College of Medicine, Howard University, Washington, DC, United States, [6] Human Origins Program, Department of Anthropology, National Museum of Natural History, Smithsonian Institution, Washington, DC, United States, [7] Georgian National Museum, Tbilisi, Georgia, [8] PalaeoHub, Department of Archaeology, University of York, Heslington, United Kingdom

OPEN ACCESS

Edited by:
K. Christopher Beard, University of Kansas, United States

Reviewed by:
Julie Winchester, Duke University, United States
Maria Teresa Alberdi, Museo Nacional de Ciencias Naturales (MNCN), Spain

***Correspondence:**
Omar Cirilli
omar.cirilli@phd.unipi.it;
omar.cirilli@yahoo.com

Specialty section:
This article was submitted to Paleontology, a section of the journal Frontiers in Earth Science

Received: *19 December 2019*
Accepted: *05 June 2020*
Published: *26 June 2020*

Citation:
Cirilli O, Melchionna M, Serio C, Bernor RL, Bukhsianidze M, Lordkipanidze D, Rook L, Profico A and Raia P (2020) Target Deformation of the Equus stenonis Holotype Skull: A Virtual Reconstruction. Front. Earth Sci. 8:247. doi: 10.3389/feart.2020.00247

Equus stenonis is one of the most prevalent European Pleistocene fossil horses. It is believed to be the possible ancestor of all Old World Early Pleistocene *Equus*, extant zebras and asses, and as such provides insights into *Equus* evolution and its biogeography and paleoecology. The *Equus stenonis* holotype skull (IGF560) was first described by Igino Cocchi in 1867, from the Early Pleistocene locality of Terranuova (Upper Valdarno basin, Italy). IGF560 is a nearly complete, although medio-laterally crushed and badly compressed skull. Here we provide the first application of a new virtual reconstruction protocol, termed Target Deformation, to the *Equus stenonis* holotype. The protocol extends beyond classic retrodeformation by using target specimens as a guide for the virtual reconstruction. The targets used as a reference are two fragmentary, yet well-preserved *E. stenonis* skulls, coming from Olivola (Italy; IGF11023) and Dmanisi (Georgia; Dm 5/154.3/4.A4.5), both Early Pleistocene in age. These two specimens do not display any major deformation, but preserve different, only slightly overlapping portions of the skull. The virtual reconstruction protocol we carried out has shown its feasibility, by producing two 3D models whose final morphology is perfectly congruent with the natural variability of a comparative sample of *E. stenonis* specimens. This study shows the potential of using even broken or otherwise fragmentary specimens to guide retrodeformation in badly distorted and damaged specimens. The application of Target Deformation will allow us to increase the availability of comparative specimens in studies of fossil species morphology and evolution, as well as to the study of taphonomic processes.

Keywords: *Equus stenonis*, target deformation, virtual reconstruction, 3D, equidae

INTRODUCTION

A number of taphonomic processes are known to alter the physical preservation of fossil remains. As a consequence, fossils usually become badly deformed (e.g., losing biological symmetry, being compressed or bent) or incomplete (Shipman, 1981; Lyman, 1994; Schlager et al., 2018). The lack of this valuable information worsens the already fragmentary fossil record, which limits the opportunity to study fossil remains with the same analytical power that is typical for neontological samples. Therefore, paleontologists have to face the classic challenge to take the best out of specimens which show significant deformations, miss anatomical parts, or both. Remains of fossil horses provide no exception. Although moderately frequent in the fossil record, horses are mostly represented (and studied) by post-cranial elements, which by virtue of their stocky built (in the case of long bones) and low aspect ratio (in the case of legs distal elements) are much less deformed (or broken) than either mandibles or skulls. The latter are elongated and full of complex intracranial and extracranial cavities in horses, which makes their complete, undistorted preservation potential exceedingly low (Budras et al., 2009).

Herein, we present a new virtual reconstruction protocol, termed Target Deformation, which takes advantage of recent progress in digital restoration of fossil specimens, including retrodeformation (Schlager et al., 2018), digital alignment of disarticulated portions (DTA, Profico et al., 2019b), and 3D thin plate spline transformation (tps3d) (Bookstein, 1989; Schlager et al., 2018) to provide the virtual reconstruction of badly deformed, partially incomplete cranial material by using target fossil remains of the same species. We demonstrate here that our procedure is viable even by using very incomplete target remains, which are common in the fossil record and cannot be used by themselves in comparative analyses.

Our case study is the *Equus stenonis* holotype skull (IGF560, **Figure 1**), originating from the Early Pleistocene locality of Terranuova (Tuscany, Italy), is a 1.8 Ma locality in the Upper Valdarno Basin, which is housed in the Natural History Museum (Geology and Paleontology Section) of the University of Florence. We applied Target Deformation to the *E. stenonis* holotype by using two different targets, an incomplete *E. stenonis* skull (Dm 5/154.3/4.A4.5; **Figure 2**) originating from Dmanisi, Georgia, and another partial skull (IGF11023; **Figure 3**) retrieved from the fossil locality of Olivola, Italy. Both target skulls are lacking large portions of their crania. Importantly, the Dmanisi specimen has a nicely undeformed mid-cranial vault entirely lacking the muzzle. In contrast, the Olivola skull neurocranium is missing most of the cranial vault, while preserving the muzzle.

The virtual reconstruction carried out herein has demonstrated the feasibility of this method, by the production of two 3D models whose final morphology is fully congruent with a comparative sample of *E. stenonis* specimens from other localities in Europe. Eventually, by reflecting the right side of the 3D *E. stenonis* holotype model, we produced a fully symmetrical, vivid representation of the original skull shape in the *Equus stenonis* holotype specimen.

Equus stenonis

Equus stenonis Cocchi, 1867 (**Figure 1**) is the most common Early Pleistocene European fossil horse. It occurs in Spanish, French, Italian, Bulgarian, Romanian, and Greek Early Pleistocene localities (Alberdi et al., 1998; Athanassiou, 2001; Azzaroli, 2003; Alberdi and Palombo, 2013; Bernor et al., 2019; Boulbes and van Asperen, 2019), and in the Georgian locality of Dmanisi (Vekua, 1995) even if its chronological range still remains undefined. Nomade et al. (2014), assigned a new 2.4 Ma age to the French locality of Saint Vallier, yielding *Equus stenonis vireti* Prat (1964) which therefore represents the oldest evidence of this species in Europe. *Equus stenonis* last occurrence is more debatable, although the horse's presence at Farneta/Pirro Nord Faunal Units (FU), in Italy, correlated to circa 1.5–1.3 Ma, possibly represents the species last appearance being replaced shortly thereafter by *Equus suessenbornesis* (Alberdi and Palombo, 2013; Palombo and Alberdi, 2017).

The *Equus stenonis* holotype is a skull with associated mandible (IGF560), discovered by the Italian paleontologist Igino Cocchi in the 1867 near Terranuova (Arezzo, Tuscany), a 1.8 Ma fossil locality in the Upper Valdarno basin in Central Italy, belonging to the Olivola/Tasso Faunal Unit (FU). The skull is housed in the Natural History Museum in Florence. Cocchi named the species, without any description. A preliminary

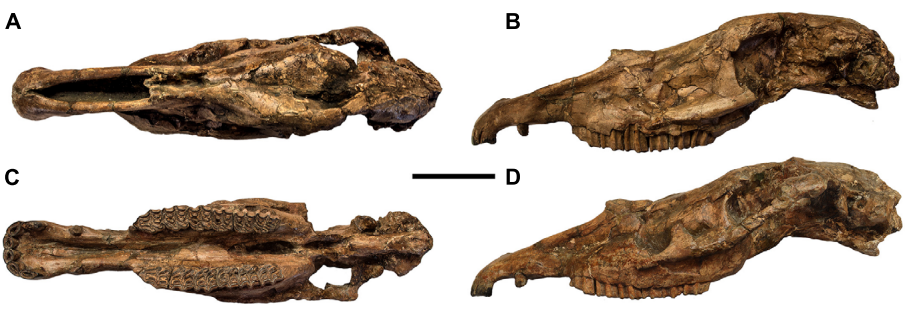

FIGURE 1 | *Equus stenonis* IGF560 holotype, housed in the Geological and Paleontological section of the Natural History Museum of Florence. **(A)** Dorsal view; **(B)** lateral view, left side; **(C)** ventral view; **(D)** lateral view, right side reflected. Scale bar 10 cm.

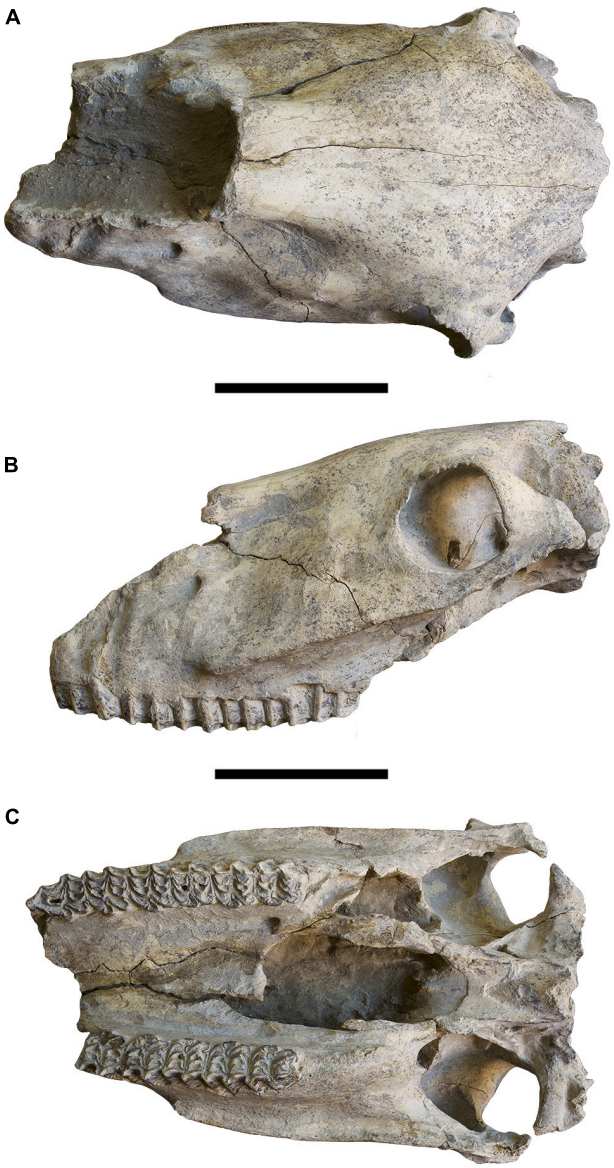

FIGURE 2 | *Equus stenonis* Dm 5/154.3/4.A4.5, from the Georgian locality of Dmanisi. **(A)** Cranial view; **(B)** lateral view, left side; **(C)** ventral view. Scale bar 10 cm.

description was later given by Forsyth Major (1885) and, in more detail, by Azzaroli (1964). De Giuli (1972) wrote a comprehensive review of the anatomical features of the *E. stenonis* sample from Olivola. *Equus stenonis* was discussed in several papers during the last few years, focusing on its biogeographic dispersion and its phylogenetic position within the stenonine horse group (Alberdi et al., 1998; Forsten, 1999; Athanassiou, 2001; Azzaroli, 2003; Alberdi and Palombo, 2013; Palombo et al., 2017; Boulbes and van Asperen, 2019). Recently, Bernor et al. (2019) provided an updated description of the holotype, demonstrating its relationships with the Old World *Equus* and extant zebras and its possible relationship with the North American *Equus simplicidens*.

Equus stenonis Holotype Skull IGF560

The *Equus stenonis* holotype is an almost complete, medio-laterally deformed skull, lacking its left zygomatic arch. The skull has an elongated snout with a large canine, indicating that it is an adult male. The nasal bones are retracted to the level of P3 mesostyle. The snout is elongate with an arcuate incisor arcade. The maxillary cheek teeth are inclusive of dP^1-M^3. The M^3 is worn, dP^1 is (remarkably) still in place although with advanced wearing. The maxillary cheek teeth have the following features: dP^1 is small and rounded; P^2 has a short anterostyle; all cheek teeth have a short protocone linked to the protoloph; pli caballins are single on all cheek teeth; fossettes are well developed on P^2-P^4 and M^2, lesser developed on M^1 and M^3; hypoglyph is moderately deep on P^2-M^2 and not expressed on M^3.

In ventral view, the palatine processes of the muzzle are medio-laterally compressed, but the muzzle breadth between the posterior I^3 borders is well preserved. The palate is highly compressed, and the left upper teeth row is rotated counterclockwise to the internal side and slightly sheared in its antero-posterior sagittal plane. The choanae are heavily distorted and medio-laterally compressed, even if the vomer and the basisphenoid bones are preserved. The ventral occipital bones are damaged, yet the paracondylar processes within the occipital condyles and the foramen magnum are preserved.

In lateral view, the preorbital fossa is faintly delimited as a depression on the postero-superior maxilla level, and the facial maxillary crest is strongly developed on both sides. The zygomatic bone is preserved on the right side only. The orbits are preserved on the right side, while only the anterior ridge of the left orbit is present. The skull shows significant damage in the lateral maxillary region and the area of the paranasal sinuses, being more evident on the right side with respect to the nasal bones. The rostral process is not preserved.

In dorsal view, the temporal bones are preserved on both sides, although compressed medio-laterally. The right frontal bone above the orbital process. On the left side the frontal bone is strongly compressed with concomitant plastic deformation of the frontal sinuses and a shear compression along the sagittal plane. The maxillary and premaxillary bones (the muzzle) are well preserved, although the latter shows a slight counterclockwise rotation on the left side, as it is apparent in the positioning of the left P^2-M^3 cheek teeth row.

Equus stenonis Dm 5/154.3/4.A4.5, Dmanisi

The Dmanisi *Equus stenonis* fossil specimen Dm 5/154.3/4.A4.5 (**Figure 2**) was used as a retrodeformation target. The skull is lacking the muzzle and the occipital bones, although the cranial vault is complete and undeformed. The skull shows the typical *E. stenonis* occlusal maxillary cheek tooth pattern, including presence of short, squared protocones connected to the protoloph, which is a characteristic of the *E. stenonis* holotype.

In ventral view, the maxillary cheek tooth rows are nearly complete (only the right P^2 is missing) and the teeth show a medium stage of wear. The palate and the choanae are well preserved, the pterygoid bones are lacking, but the anterior border of the vomer is preserved. The two mandibular fossa of the zygomatic process are preserved.

In lateral view, the skull does not display any deformation. The preorbital fossa is small but clearly visible, and dorsally placed on both sides. The infraorbital foramen is preserved on the left side, the two facial maxillary crests are strongly developed from the zygomatic process up to P^4/M^1 vertical border in both sides and are clearly distinguishable from the orbital processes. The two maxillae do not show any deformation in correspondence to the paranasal sinus.

In dorsal view, the occipital bones are missing, and the frontal bones do not show any deformation in correspondence to the frontal sinuses. The supraorbital foramina are preserved. The nasal bones are broken but preserved up to the level of the preorbital fossa.

Equus stenonis IGF11023, Olivola

The *Equus stenonis* specimen from Olivola (**Figure 3**) is our second target skull. The skull is incomplete having preserved its muzzle and palatal regions. The skull, although damaged on the lateral and dorsal surfaces, does not show any sign of deformation in ventral view. The palatine process is preserved in the premaxilla with all the upper incisors *in situ*, except for the right I1. The palate is not deformed although the choanae are missing. The two maxillary tooth rows are well preserved, the teeth are in a middle stage-of-wear. The protocone displays the typical *E. stenonis* morphology. In lateral view, the two facial maxillary crests are well developed up to the P^4/M^1 boundary on both sides. The zygomatic processes are not preserved, the left orbital process is present. The skull shows a slight deformation in proximity to the paranasal sinuses.

FIGURE 3 | *Equus stenonis* IGF11023, from the Early Pleistocene locality of Olivola. **(A)** Ventral view; **(B)** lateral view, left side. Scale bar 10 cm.

MATERIALS AND METHODS

3D *Equus stenonis* Digital Models

The *Equus stenonis* 3D digital meshes used in the analysis, the holotype skull IGF560 and the two target specimens Dm 5/154.3/4.A4.5 and IGF 11023, were acquired using the structural light 3D Scanner Artec Eva and Artec Space Spider[1]. The accuracy of the Artec Eva is up to 0.1 mm, with a resolution of 0.5 mm. It is capable of capturing the object's texture with a 1.3 megapixel resolution, with a 3D reconstruction rate for real time fusion of up to 16 frames per second, and a data acquisition speed of 2 million points for each second of recording. It works with a flash bulb (not a laser) 3D light source. Artec Eva is designed to digitally acquire objects larger than 10 cm. Artec Space Spider has a the 3D point accuracy of up to 0.05 mm, with a 3D resolution of 0.1 mm. It is capable of capturing the object texture with a 1.3 megapixel resolution, with a 3D reconstruction rate for real time fusion up to 7.5 frames per second, and a data acquisition speed of 1 million points each second of recording. It works with blue LED 3D light source. The optimal object size to be acquired under Artec Space Spider is > 5 cm.

Due to different target specifications, we used both scanners to build the IGF560, Dm 5/154.3/4.A4.5 and IGF 11023 3D meshes. Each skull was scanned with Artec Eva obtaining 6 partial scans (3 for dorsal view and 3 for ventral view), to acquire the external surface geometry. The upper teeth row and the incisor teeth have been scanned with Artec Space Spider (2 scans for each upper incisor row and the incisive arch, along the labial and lingual sides). Through the definition of morphological landmarks, the 12 digital scans obtained with the two light structured scanners have been aligned and the mesh created by using Artec Studio 14 software[2]. The 3D models have been exported in the .obj format.

Equus stenonis Target Deformation Protocol

Digital reconstruction techniques are becoming very popular in paleontology, as they represent a powerful tool to analyze disarticulated and damaged fossil remains, and even to reconstruct missing parts (Benazzi et al., 2014; Cunningham et al., 2014; Profico et al., 2019a).

Here we designed a workflow that sequentially combines different analytical tools and algorithms to obtain a virtual restoration of the *Equus stenonis* holotype skull (IGF560) by using target specimens as a guide (all meshes have been decimated to 500,000 triangles).

The procedure includes three steps:

1. Perform the retrodeformation of the *Equus stenonis* holotype (IGF560) by using a bilateral landmark configuration.
2. Align the target specimens (the Georgian Dm 5/154.3/4.A4.5 and IGF11023 from Olivola) to each other in order to calculate a mean target shape.

[1]www.artec3d.com

[2]www.artec3d.com/3d-software/artec-studio

3. Warp the retrodeformed holotype onto the mean target shape.

Retrodeformation aims to remove asymmetric alterations due to taphonomic processes by applying a set of corresponding bilateral landmarks. An effective retrodeformation protocol was recently implemented by Schlager et al. (2018) and is available in the R software environment as embedded in the Morpho R package (Schlager, 2017). Despite traditional approaches (Ogihara et al., 2006; Gunz et al., 2009; Ghosh et al., 2010), this algorithm computes a non-linear symmetrization method detecting multiple local affine deformations reducing the interpolation performed by TPS (Bookstein, 1989). This protocol works with bilateral landmarks. For each pair of landmarks, their centroid is computed. The algorithm works by minimizing the stretch required to orthogonalize each local frame. The retrodeformation algorithm is embedded in the *retroDeformMesh()* function of the Morpho package (Schlager, 2017). The function uses a triangular mesh representing a digital model of the holotype, a set of bilateral landmarks to be placed directly on it, and a two-column matrix defining the left and right landmark indices. We used the IGF560 3D mesh as the initial surface with a set of 60 bilateral landmarks (**Figure 4**). The landmarks are listed in **Supplementary Table S1**. All landmarks were manually sampled using the Amira software (ver. 5.4.5 thermofisher.com/amira-avizo). The 60 bilateral landmarks describe the entire morphology of IGF560. We avoid the use of surface semi-landmarks because the specimen IGF560 exhibits cracks and other damage on its surface. The aim of the retrodeformation procedure is to restore the original symmetry of IGF560. At the end of the process we obtained the retrodeformed version, IGF560R, of the original holotype IGF560 (**Figure 5A**).

The second step involved the alignment of the two target specimens (Dmanisi Dm 5/154.3/4.A4.5 and Olivola specimen IGF11023) and the calculation of a mean shape which can be used as a guide for further deformation (**Figure 5B**). The alignment of the two specimens was performed by applying the Digital Tool for Alignment (DTA), recently developed by Profico et al. (2019a) in the R environment (R Core Team, 2013) and embedded in the Arothron package (Profico et al., 2020). DTA uses the shape information contained in a reference sample (or in a reference specimen) to find the best alignment fit for disarticulated regions of a damaged specimen. To achieve this, the DTA algorithm includes first a generalized Procrustes Analysis

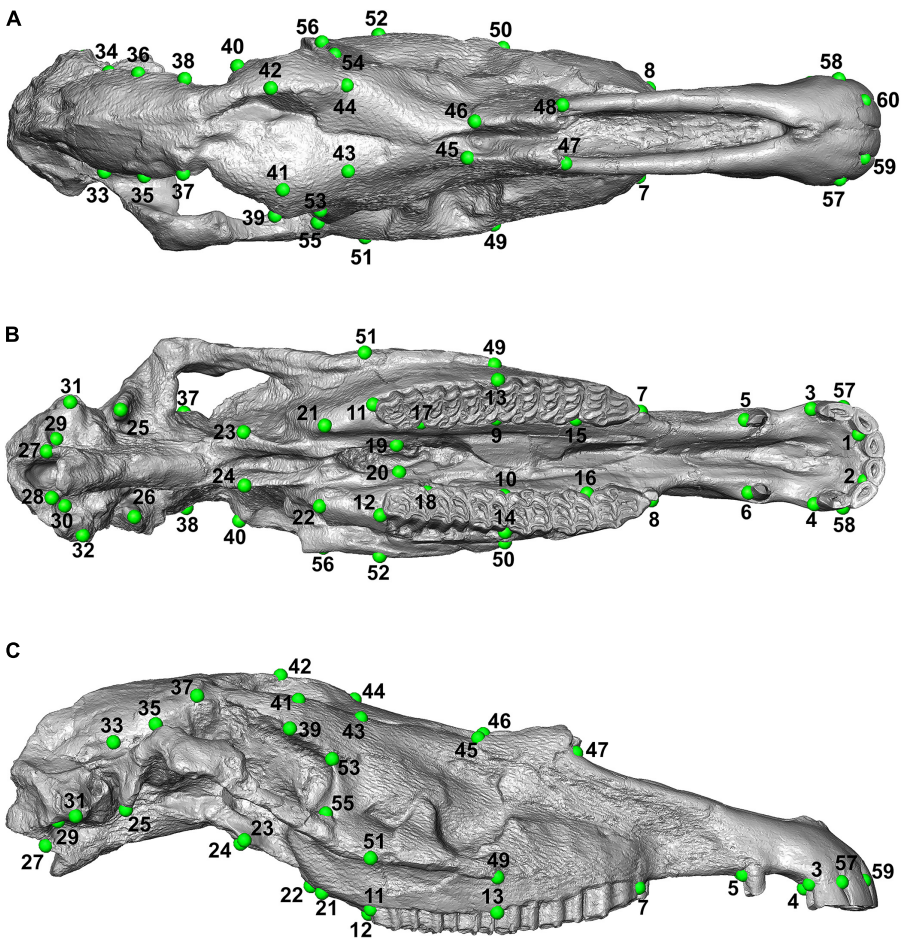

FIGURE 4 | Landmark configuration used on IGF560. **(A)** Dorsal view; **(B)** ventral view; **(C)** lateral view.

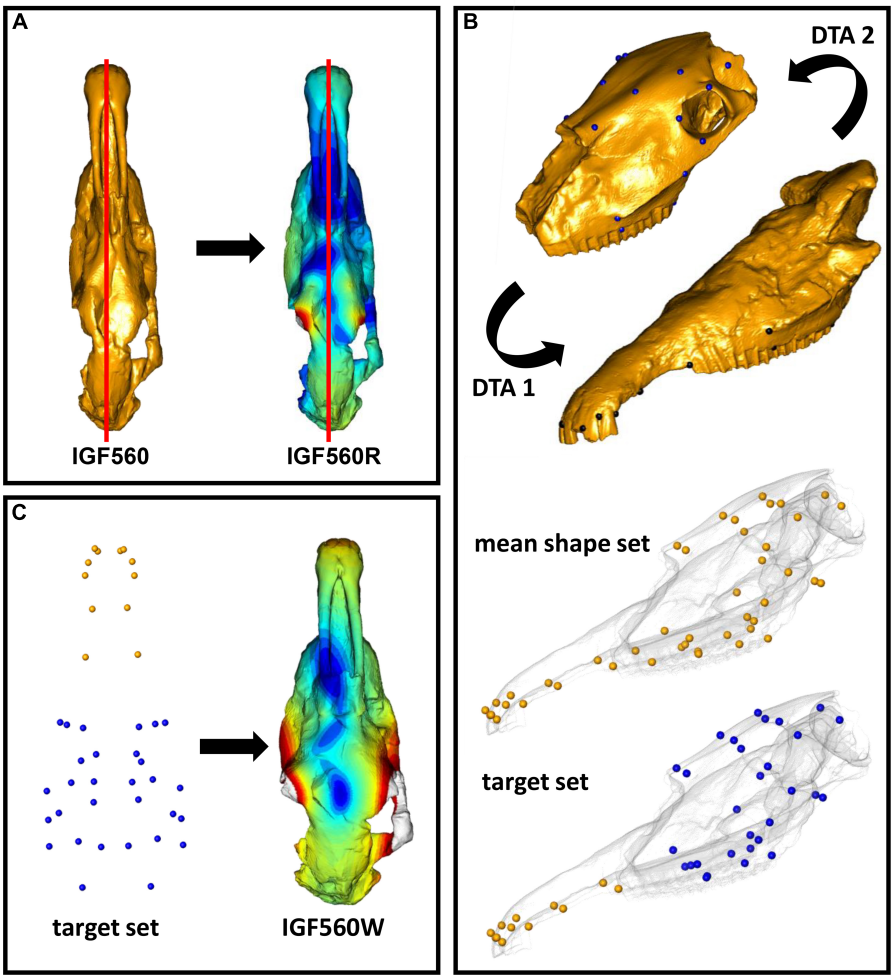

FIGURE 5 | Fossil restoration process explained step by step. **(A)** The IGF560 specimen is symmetrized by using *retroDeformMesh()* to obtain IGF560R. **(B)** IGF11023 is first oriented on Dm5 (DTA 1), then Dm5 is oriented on IGF11023 (DTA 2). A mean shape between the first aligned set and the second is computed. The target set is built by using the Dm5 landmark set and the landmarks of the mean shape set belonging to the snout. **(C)** IGF560R is warped via thin plate spline transformation based on the target configuration.

between the reference and target models. The quantification of the morphological distances between the aligned configuration and the reference model dataset allows us to choose the best reference model, identified in the alignment with the least morphological distance. In this case study, we performed two inverse DTAs (Dm5/154.3/4.A4.5 vs. IGF11023 and IGF11023 vs. Dm5/154.3/4.A4.5), by considering the two target specimens as if they were individually undeformed portions belonging to a single, disarticulated skull. We used a set of 30 bilateral landmarks for Dm 5/154.3/4.A4.5 and 24 bilateral landmarks for IGF11023 (**Figure 5B** and **Supplementary Table S1**). All landmarks were manually sampled with Amira software. Once we obtained two different aligned sets, we computed the mean shape.

Eventually, the third step consisted of warping IGF560R on the mean shape obtained by using the two targets. As we know that the Dm 5/154.3/4.A4.5 specimen is mostly undeformed, we decided to build the target set for the final warping by keeping all the landmarks originally sampled on Dm 5/154.3/4.A4.5 and embedding all the extra landmarks coordinates from the mean shape set. The warping process was performed through the Morpho function *tps3d()* (Schlager, 2017), which deforms a set of coordinates or a mesh via thin plate spline transformation based on a reference and a target configuration. This step produced the retrodeformed and warped-to-targets mesh IGF560W (**Figure 5C**).

We further applied 3D reflection to IGF560R to obtain a perfectly symmetrical model with two zygomatic arches. This produces a symmetrical rendering of IGF560 which we refer to as IGF560R-S. We repeated the warping process on IGF560R-S, producing the virtual reconstruction IGF560W-S. The goal of the mirroring process is to compare the simple restoration procedure, as accomplished in IGF560R, to a more stretched application, where the starting digital model is forced to be symmetrical.

In order to compare the restoration model results, we used the Morpho function *meshDist()* (Schlager, 2017) to

compute the surface mesh distances between all the virtual models sharing the same mesh, that is all the pairwise comparisons between IGF560, IGF560R, IGF560W and their symmetrical equivalents IGF560R-S and IGF560W-S. The surface distances were computed as the differences between homologous vertex coordinates of two meshes, which can be retrieved by the Morpho function *vert2points()* (Schlager, 2017).

In addition, to visualize the local deformation between the original and the retrodeformed model we used the function *localmeshDist()* (Profico et al., 2020). The *localmeshDist* returns a 3D color map showing the local deformation in terms of area reduction or expansion. In this way, it is possible to visualize which areas during the target deformation procedure were either reduced or expanded.

Finally, we performed a Principal Component Analysis (PCA) by comparing biometric distances taken on the virtual specimens to equivalent measurements taken on several skulls of fossil and extant species to evaluate the goodness of the Target Deformation procedure.

TARGET DEFORMATION RESULTS

The Target Deformation results on the *Equus stenonis* holotype are shown in **Figure 6**. **Figures 6A–D** represent IGF560, IGF560R, IGF560W, respectively, with the color scale bar obtained from the *meshDist()* and *localmeshDist()* function to evaluate the morphological distance between the three target deformation versions of IGF560 (**Table 1**).

Compared to IGF560, IGF560R displays a maximal deformation of 12 mm in correspondence to the frontal bones above the orbital processes and the temporal bones, where the brain case has been rendered symmetrical on the right side. The left maxillary and premaxillary process, within the P^2-M^3 cheek teeth row, show a higher value of distance, due to the slight rotation on the left side of the original holotype. In ventral view, IGF560R renders the two upper teeth rows completely parallel. The palatine processes of the muzzle still remain medio-laterally compressed, even if the anterior breadth of the muzzle within the incisor arch (left I^3 – right I^3) displays a slight rotation on the right side. The palate exhibits a medium deformation between the two upper teeth rows, more evident on the left side.

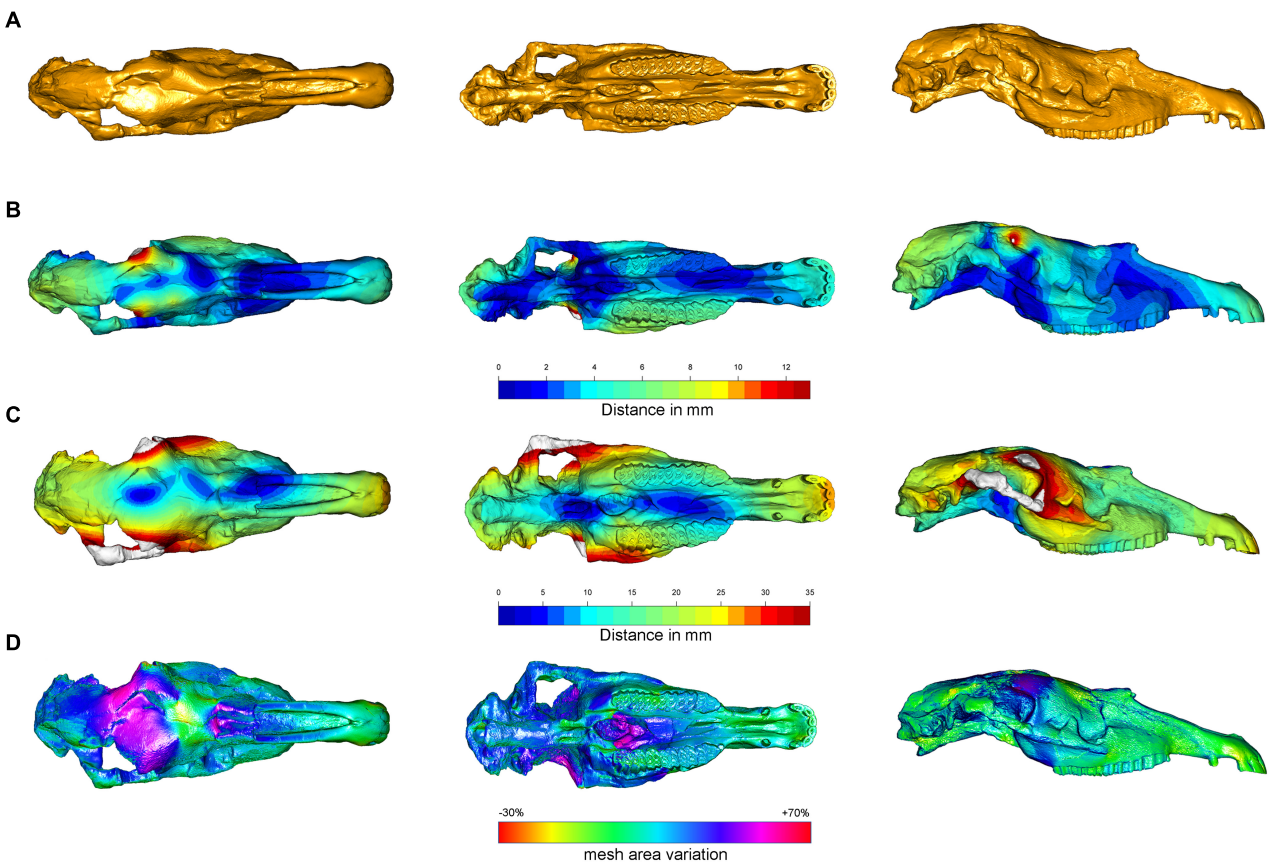

FIGURE 6 | Comparison of the 3D models obtained with the Target Deformation. **(A)** Represent IGF560. Color gradient (from blue to red) indicates the increase in mesh vertex displacement in millimeters in IGF560R **(B)** and IGF560W **(C)**. Panel **(D)** shows the mesh triangles area variation in terms of contraction (red/yellow) and expansion (blue/purple).

TABLE 1 | Surface mesh pairwise distances in terms of maximum (lower triangle) and absolute mean values (upper triangle) between IGF560, IGF560R, IGF560W, and their symmetrical equivalents IGF560R-S and IGF560W-S.

	Original model				Specular model	
	IGF560	**IGF560R**	**IGF560W**		**IGF560R-S**	**IGF560W-S**
IGF560	–	3.732	18.262	IGF560R-S	–	17.549
IGF560R	17.188	–	17.574	IGF560W-S	46.554	–
IGF560W	53.986	46.352	–			

Figure 6C renders a 3D model, IGF560, rendered by applying the DTA and tps3d protocols. Here, the power of Target Deformation becomes evident. This specimen exhibits an strong deformation on the right zygomatic arch, on both lateral facial crests behind the maxilla level and the orbits. The maximum distortion reached on this model is of 35 mm, as represented by the red areas. The temporal and occipital bones show the homologous deformation target, within a deformation average from 15 mm from the sagittal plane of the skull to 25 mm on both lateral sides. In ventral view, the best evidence of the Target Deformation is provided on the palate and the palatine process of the muzzle. The maximum palate distance between P^4 and M^1 is up to 28 mm, and between the posterior border of I^3 (see M13–M14–M15 in **Table 2**). It is remarkable that the two upper cheek teeth rows and maxilla processes behind the M^3 have not been broadened, and the upper teeth occlusal morphology has not been deformed. The choanae show the analogous deformation on both sides, within the sphenoid, the two paracondylar processes and occipital condyle. In ventral and lateral views, the muzzle and the nasal processes have been slightly elongated and widened, even if the final breadth of the palatine process does not diverge significantly from the holotype. This demonstrates that the maximum medio-lateral deformation has been reached in the central and posterior areas of the skull, whereas the muzzle has not been involved with the same stress deformation.

Supplementary Figure S1 illustrates the IGF560R-S model. To obtain this model, the right side of *Equus stenonis* Holotype has been reflected, to get a perfectly symmetrical skull with two zygomatic arches. In IGF560R-S, the damage on the left side of the holotype has been altered by restoring the left zygomatic arch. The Target Deformation performed on IGF560R-S has yielded IGF560W-S (**Supplementary Figure S1**). The results on this model are quite similar to IGF560W, with the most deformed areas represented from the two zygomatic arches, both lateral facial crests behind the maxilla level and the orbits. In ventral view, both sides of the skull exhibit a homologous level of deformation at the posterior borders of the I^3, in the palatine process and the palate and on the basal occipital region with sphenoid, the two paracondylar processes and occipital condyle. Greater deformation occurs on the upper incisors, probably due to a slight elongation of the muzzle. Deformation in the same area is also evident on IGF560W. No landmarks have been selected on the zygomatic arch (**Figure 4**), due to its absence on the left side of the holotype and also due to the incomplete preservation of both sides on the skull from Dmanisi. However, the results are in accordance with skull retrodeformation, even if slightly overestimated (see M19 in **Table 2**). Definitely, a set of control landmarks on the zygomatic arch and processes would have given a better result for this area of the skull.

TABLE 2 | Measurements of IGF560, IGF560W, IGF560R-S, and IGF560W-S. Measurements follow Eisenmann et al. (1988) and Bernor et al. (1997).

Specimen	IGF 560 Holotype	IGF 560W	IGF 560R-S	IGF 560W-S
M1	152.7	156.7	152.7	156.9
M2	122.6	128.8	120.8	130.3
M3	132.3	131.7	128.7	132.8
M4	148.1	145.9	152.5	147.6
M5	272.6	277.4	278.3	277.9
M6	540.8	550.3	537.8	550.9
M7	99.1	101.9	98.9	101.9
M8	82.5	81.9	81.7	81.6
M9	178.2	180.8	175.2	180.8
M10	97.5		90.3	
M11	17.8	34.3	19.2	31.9
M12	18.9	38.7	28.8	38.9
M13	50.9	78.8	51.8	78.6
M14	32.9	40.9	36.1	42.1
M15	62.8	69.9	64.3	68.7
M16	79.4	78.7	79.5	76.3
M17	171.8	165.7	168.3	165.4
M18	108.2	200.2	117.3	201.3
M19			160.4	234.6
M20			64.4	87.8
M21	89.2	105.5	98.3	107.1
M22	40.1		34.4	35.4
M23	407.5	439.8	406.7	436.5
M24	187.3	204.3	184.1	210.9
M25	114.8	115.3	117.6	115.8
M26	112.2	113.4	112.2	113.6
M27	12.8	12.3	11.9	12.3
M28	64.1	70.2	68.5	69.6
M29	45.6	53.4	47.1	54.8
M30	220.1	233.7	217.2	233.7
M31	166.6	165.9	163.1	169.4
M32	54.2	53.3	52.9	53.3
M33	75.5	77.9	73.1	77.8
M34	80.3	83.1	80.3	83.3
M35	28.4	28.1	28.4	28.4
M36	63.9	61.9	63.4	62.5
M37	65.6	60.7	65.6	61.3
M38	108.3	110.7	108.3	110.9

The blue areas recognizable in dorsal view on IGF560W and IGF560W-S can be interpreted as the results of the original vector stress deformation to which IGF560 has been exposed. Indeed, these areas are located on the most damaged dorsal and ventral area of the skull and, in IGF560W, follow the deformation of the left side of the skull on the central region of the neurocranium.

In **Figure 6D** we reported the mesh area variations between IGF560 and IGF560W computed by using the function *localmeshDist*. Cold and warm color palettes indicate respectively local expansion and reduction in the final virtual reconstruction (i.e., IGF560W) compared to the original model (i.e., IGF560). The target deformation procedure leads to a great expansion of the neurocranium, which is laterally compressed and broken in the original specimen, and a moderate expansion of the ventral aspect of the right zygomatic arch. The choanae and the sphenoidal region show an analogous expansion on both sides. Only the upper portion of the frontal bone resulted in a contraction. The remaining anatomical regions of the IGF560 do not result in local differences.

MORPHOMETRIC ANALYSIS

We evaluated the Target Deformation performance by undertaking a PCA on the IGF560W and IGF560W-S models in addition to a set of fossil and extant *Equus* specimens. The skull measurements we used follow the standards published by Eisenmann et al. (1988) and Bernor et al. (1997). The comparison sample includes *Equus simplicidens* (Hagerman Horse Quarry, Idaho, United States, 3.3 Ma; Rook et al., 2019), *Equus eisenmannae* (Longdan, Linxia Basin, Gansu Province, China, 2.55 Ma; Wang and Deng, 2011; Rook et al., 2019), *Equus huanghoensis* (China, Early Pleistocene; Li et al., 2016; Sun and Deng, 2019), *Equus sanmeniensis* (China, Early Pleistocene; Sun and Deng, 2019), *Equus* sp. from Senèze (Senèze, France, 2.1 Ma; Nomade et al., 2014; Eisenmann, 2017), *Equus stenonis vireti* (Saint Vallier, France, 2.4 Ma; Nomade et al., 2014), *Equus koobiforensis* (Koobi Fora, Kenya, 1.9 Ma; Rook et al., 2019), and extant *Equus grevyi*. The IGF560 holotype has not been included in this sample due its severe medio-lateral deformation.

We have chosen the most distinctive skull measurements to evaluate whether IGF 560W and IGF 560W_S effectively place close to other *E. stenonis* specimens: M1 = basal length of the muzzle; M3 = vomerine length; M4 = post vomerine length: from the middle of the vomerine notch to basion; M6 = total basal length of the skull; M7 = upper premolar row length (P^2–P^4); M8 = upper molar row length (M^1–M^3); M9 = upper cheek tooth row length (P^2–M^3); M15 = muzzle width, between the posterior sides to distal limits of the I^3; M18 = frontal breadth behind the orbits; M23 = anterior ocular line: from the prosthion to the most external point of the orbital process; M30 = length of the naso-incisival notch: from the prosthion to the back of the narial opening; M31 = cheek length: from the back of the narial opening to the most anterior point of the orbit. The complete dataset used in the PCA is reported in **Supplementary Table S2**.

In **Figure 7** we reported the PCA plot showing the morphological similarities of IGF560W and IGF560W-S as compared to the comparative sample. The loadings of the PCA are reported in **Supplementary Figure S2**, whereas the PCA component values are shown in **Table 3**. The PC1 and PC2 explain the 59.4% of the total variance (PC1 = 36.89%; PC2 = 22.51%). PC1 mostly clusters specimens by the measurement M6 and M23 (total linear length) from negative to positive values. PC2 separates species by the M3 and M31 variables at positive values, and M4 and M30 at negative values. The two models obtained with the new Target Deformation protocol, IGF560W and IGF560W-S, are positioned closed to the *E. stenonis vireti* sample from Saint Vallier and the *Equus* sp. from the Early Pleistocene of Senèze. These results allow us to confirm the performance of the Target Deformation, where the two IGF560W and IGF560W-S 3D models can be considered as coherent and trustworthy with the skull morphology of the European *E. stenonis* samples form Saint Vallier and Senèze. Only these two localities have provided complete slightly deformed or undeformed skulls, which can be considered in a multivariate analysis including several skull measurements.

DISCUSSION AND CONCLUSION

The new virtual reconstruction protocol, which includes recent implementations in digital restoration of fossil specimens as retrodeformation (Schlager et al., 2018), a digital tool for alignment (DTA, Profico et al., 2019b), and 3D thin plate spline transformation (tps3d) (Schlager, 2017), has been applied on a case study utilizing one of the most important type specimens in the evolution of Old World *Equus* during the Pleistocene, the *Equus stenonis* from the Upper Valdarno Basin, Italy. We have demonstrated that this 3D virtual reconstruction protocol is capable of virtually restoring a severely crushed specimen by using partially complete skull specimens, such as the fragmentary *E. stenonis* skulls from Olivola and Dmanisi. Fossil horses are often deformed in their skull, due to their long and slender morphology and the presence of several pneumatized paranasal sinuses which occur within the skull. Through Target Deformation, the original shape of the skulls can be restored in a detail that allows performing morphologic, morphometric and phylogenetic analyses.

The Target Deformation study undertaken on the *E. stenonis* holotype IGF560 has produced the 3D model IGF560W which has revealed a skull morphology congruent with other specimens ascribed to the same species. This reconstruction is further supported by a multivariate analysis of cranial measurements. Our results indicate that the new 3D meshes IGF560W and IGF560W-S have a skull whose shape falls within the intraspecific variability of the European *Equus stenonis* from the Early Pleistocene of Saint Vallier and Senèze.

One potential caveat is that Target Deformation cannot provide shapes outside the range of the target specimens, potentially replicating their measurements. However, we argue that by producing intermediate shapes using separate specimens via DTA, Target Deformation does not produce measurement pseudoreplication, provided the original specimens are not themselves part of the analysis. In our case, neither the

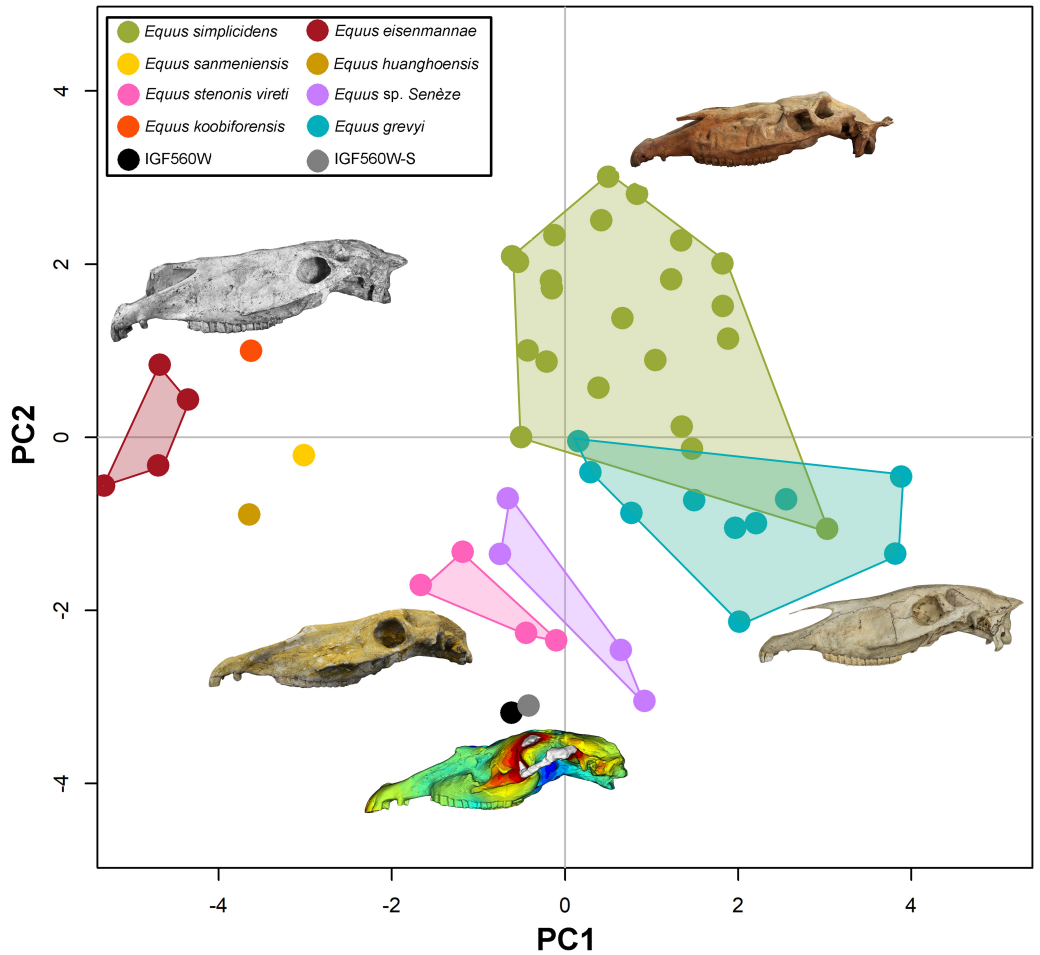

FIGURE 7 | Principal component analysis, comparing IGF560W and IGF560W-S with a set North American and Eurasian Plio-Pleistocene *Equus* and with the extant *Equus grevyi*.

TABLE 3 | PCA components values.

Importance of components	**PC1**	**PC2**	**PC3**	**PC4**	**PC5**	**PC6**
Standard deviation	2.1040	1.6434	1.2623	0.98985	0.91467	0.68406
Proportion of variance	0.3689	0.2251	0.1328	0.08165	0.06972	0.03899
Cumulative proportion	0.3689	0.594	0.7268	0.80843	0.87814	0.91714
Importance of components	**PC7**	**PC8**	**PC9**	**PC10**	**PC11**	**PC12**
Standard deviation	0.53857	0.48271	0.4559	0.36043	0.32237	0.17198
Proportion of variance	0.02417	0.01942	0.01732	0.01083	0.00866	0.00246
Cumulative proportion	0.94131	0.96073	0.97805	0.98887	0.99754	1.00000

incomplete Dmanisi and Olivola skulls, nor the mediolaterally compressed and partially broken IGF560 could serve the goal to perform a comparative analysis of *Equus* skull shape variation. Nevertheless, as reported in the PCA, the new 3D models obtained with the Target Deformation protocol, IGF560W and IGF560W-S, can be included in a morphometric multivariate analysis in order to increase the *E. stenonis* fossil skull representatives. This means target deformation promises to increase the statistical power of comparative analyses and could improve the digital restoration process. Although not specifically tested here, we argue that by sizing up deformation directly from the original specimens, Target Deformation can be a viable tool to study the impact of taphonomic distortion on fossil preservation.

The virtual restoration protocol presented here can be undertaken on any other 3D species model involving either

vertebrate or invertebrate fossils. Target Deformation could provide substantial improvement for examining and reporting damaged fossil specimens.

DATA AVAILABILITY STATEMENT

All datasets generated for this study are included in the article/**Supplementary Material**.

AUTHOR CONTRIBUTIONS

OC, MM, LR, and PR conceived the study. OC, MM, AP, and CS performed the analyses. All authors contributed to the article and approved the submitted version.

FUNDING

OC and LR acknowledged the Italian Ministry of Foreign Affairs (MAECI, DGSP-VI) and the Italian Embassy in Georgia, for the support to the Georgian-Italian Dmanisi collaborative project. MB acknowledged the Shota Rustaveli Georgian Science Foundation (Grant No. FR-18-27262). RB wishes to acknowledge research funding by NSF EAR grants 8806645, 0125009, 1113175, 1558586; DBI grant 1759882 for the Futres database. This is Futres publication number 10.

ACKNOWLEDGMENTS

We are thankful to Elisabetta Cioppi and Luca Bellucci for providing access to the fossil horse collection at the Geological and Paleontological section of the Natural History Museum in Florence. OC thanks Didier Berthet (Natural History Museum in Lyon), Emmanuel Robert (Universitè Claude Bernard-1, Lyon) and the Smithsonian Museum Support Centre for the study of fossil and extant horses. Paleo[Fab]Lab thanks TBNET SOLUZIONI 3D (Arezzo) for their support and kind availability.

SUPPLEMENTARY MATERIAL

The Supplementary Material for this article can be found online at: https://www.frontiersin.org/articles/10.3389/feart.2020.00247/full#supplementary-material

The external Supplementary Material for reproduction of the Target Deformation protocol (code and example data) are available on Zenodo: doi: 10.5281/zenodo.3895217.

FIGURE S1 | IGF560R-S **(A)** and IGF560W-S **(B)** comparison by *meshdist()*; color gradient (from blue to red) indicates the increase in mesh vertex displacement in millimeters.

FIGURE S2 | Principal component analysis loadings.

TABLE S1 | List of the selected landmarks on *Equus stenonis* IGF560 3D model.

TABLE S2 | Raw data used in the principal component analysis.

REFERENCES

Alberdi, M. T., and Palombo, M. R. (2013). The late early to early middle pleistocene stenonoid horses from Italy. *Quat. Int.* 288, 25–44. doi: 10.1016/j.quaint.2011.12.005

Alberdi, M. T., Ortiz Jaureguizar, E., and Prado, J. L. (1998). A quantitative review of European stenonoid horses. *J. of Paleontol.* 72, 371–387. doi: 10.1017/S0022336000036350

Athanassiou, A. (2001). New data on the *Equus stenonis* Cocchi, 1867 from the late pliocene locality of Sésklo (Thessaly. Greece). *Geodiversitas* 23, 439–469.

Azzaroli, A. (1964). The two villafranchian horses of the upper valdarno. *Palaeontogr. Ital.* 59, 1–12.

Azzaroli, A. (2003). Phylogeny of the genus *Equus* L. *Palaeontogr. Ital.* 84, 11–16.

Benazzi, S., Gruppioni, G., Strait, D. S., and Hublin, J. J. (2014). Virtual reconstruction of KNM-ER 1813 *Homo habilis* cranium. *Am. J. Phys. Anthropol.* 153, 154–160. doi: 10.1002/ajpa.22376

Bernor, R. L., Cirilli, O., Jukar, A. M., Potts, R., Buskianidze, M., and Rook, L. (2019). Evolution of Early *Equus* in Italy, georgia, the Indian subcontinent, East Africa, and the Origins of African Zebras. *Front. Ecol. Evol.* 7:166. doi: 10.3389/fevo.2019.00166

Bernor, R. L., Tobien, H., Hayek, L. A. C., and Mittmann, H. W. (1997). *Hippotherium primigenium* (*Equidae*, *Mammalia*) from the late Miocene of Höwenegg (Hegau, Germany). *Andrias* 10, 1–230.

Bookstein, F. L. (1989). Principal warps: thin-plate splines and the decomposition of deformations. *IEEE Trans. Pattern Anal. Mach. Intell.* 11, 567–585. doi: 10.1109/34.24792

Boulbes, N., and van Asperen, E. N. (2019). Biostratigraphy and Palaeoecology of European *Equus*. *Front. Ecol.Evol.* 7:301. doi: 10.3389/fevo.2019.00301

Budras, K. D., Sack, W. O., and Röck, S. (2009). *Anatomy of the Horse*. Hannover: Schlutersche Verkagsgesellscheft mbH & Co. KG.

Cocchi, I. (1867). L'uomo fossile dell'Italia Centrale (The fossil man in central Italy). *Memorie della Società Italiana Scienze Naturali* 2, 1–180.

Cunningham, J. A., Rahman, I. A., Lautenschlager, S., Rayfield, E. J., and Donoghue, P. C. (2014). A virtual world of paleontology. *Trends Ecol. Evol.* 29, 347–357. doi: 10.1016/j.tree.2014.04.004

De Giuli, C. (1972). On the type form of *Equus stenonis* Cocchi. *Palaeontogr. Ital.* 68, 35–49.

Eisenmann, V. (2017). *The Senèze equids*. Available online at: https://vera-eisenmann.com/the-seneze-equids-text (accessed December 5, 2020).

Eisenmann, V., Alberdi, M. T., De Giuli, C., and Staesche, U. (1988). "Studying Fossil Horses. Volume I – Methodology," in *Proceeding of the Collected papers after the New York International Hipparion Conference*, eds M. O. Woodburne and P. Y. Sondaar (Leiden: Brill), 1–71.

Forsten, A. (1999). A review of *Equus stenonis* Cocchi (*Perissodactyla*, *Equidae*) and related forms. *Quat. Sci. Rev.* 18, 1373–1408. doi: 10.1016/S0277-3791(98)00073-70

Forsyth Major, C. J. (1885). On the mammalian fauna of the Val d'Arno. *Quart. J. Geol. Soc. London* 41, 1–8. doi: 10.1144/GSL.JGS.1885.041.01-04.2

Ghosh, D., Amenta, N., and Kazhdan, M. (2010). *Closed form Blending of Local Symmetries*. Hoboken, NJ: Wiley Online Library, 1681–1688.

Gunz, P., Mitteroecker, P., Neubauer, S., Weber, G. W., and Bookstein, F. L. (2009). Principles for the virtual reconstruction of hominin crania. *J. Hum. Evol.* 57, 48–62. doi: 10.1016/j.jhevol.2009.04.004

Li, Y., Zhang, Y., Sun, B., Ao, H., and Xue, X. (2016). New fossils of the early pleistocene *Equus huanghoensis* (*Equidae*, *Perissodactyla*) from nihewan in hebei province of China. *Sci. China Earth Sci.* 59, 83–94. doi: 10.1007/s11430-015-5138-y

Lyman, R. L. (1994). *Vertebrate Taphonomy*. Cambridge: Cambridge University Press.

Nomade, S., Pastre, J. F., Guillou, H., Faure, M., Guérin, C., Delson, E., et al. (2014). Ar-40/Ar-39 constraints on some french landmark late pleistocene to early pleistocene large mammalian paleofaunas: paleoenviromental and paleoecological implications. *Quat. Geochronol.* 21, 2–15. doi: 10.1016/j.quageo.2012.12.006

Ogihara, N., Nakatsukasa, M., Nakano, Y., and Ishida, H. (2006). Computerized restoration of nonhomogeneous deformation of a fossil cranium based on bilateral symmetry. *Am. J. Phys. Anthropol.* 130, 1–9. doi: 10.1002/ajpa.20332

Palombo, M. R., Alberdi, M. T., Bellucci, L., and Sardella, R. (2017). An intriguing middle-sized horse from coste san giacomo (Anagni Basin, central Italy). *Q. Res.* 87, 347–362. doi: 10.1017/qua.2017.6

Palombo, M. R., and Alberdi, M. T. (2017). Light and shadows in the evolution of South European stenonoid horses. *Fossil. Imprint* 73, 115–140. doi: 10.2478/if-2017-0006

Prat, F. (1964). Contribution a la classification des equidés villafranchiens. *Procès Verbaux de la Socíété Linnéenne de Bordeaux* 101, 14–32.

Profico, A., Bellucci, L., Buzi, C., Di Vincenzo, F., Micarelli, I., Strani, F., et al. (2019a). Virtual anthropology and its application in cultural heritage studies. *Stud. Conserv.* 64, 323–336. doi: 10.1080/00393630.2018.1507705

Profico, A., Buzi, C., Davis, C., Melchionna, M., Veneziano, A., Raia, P., et al. (2019b). A new tool for digital alignment in virtual anthropology. *Anat. Rec.* 302, 1104–1115. doi: 10.1002/ar.24077

Profico, A., Buzi, C., Melchionna, M., Piras, P., Raia, P., and Veneziano, A. (2020). *Arothron: Geometric Morphometrics Analysis and Virtual Anthropology. R package version 1.1.1*.

R Core Team (2013). *R: A Language and Environment for Statistical Computing*. Vienna: R Core Team.

Rook, L., Bernor, R. L., Avilla, L. D., Cirilli, O., Flynn, L., Jukar, A. M., et al. (2019). Mammal biochronology (Land mammal ages) around the world from the late miocene to middle pleistocene and major events in horse evolutionary history. *Front. Ecol. Evol.* 7:278. doi: 10.3389/fevo.2019.00278

Schlager, S. (2017). "Morpho and Rvcg - shape analysis in R," in *Statistical Shape and Deformation Analysis*, eds G. Zheng, S. Li, and G. Szekely (Cambridge: Academic Press), 217–256. doi: 10.1016/b978-0-12-810493-4.00011-0

Schlager, S., Profico, A., Di Vincenzo, F., and Manzi, G. (2018). Retrodeformation of fossil specimens based in 3D bilateral semi-landmarks: implementation in the R package "Morpho". *PLoS One* 13:e0194073. doi: 10.1371/journal.pone.0194073

Shipman, P. (1981). *Life History of a Fossil and Introduction to Taphonomy and Paleoecology*. Cambridge: Harvard University Press.

Sun, B., and Deng, T. (2019). The *Equus* datum and the early radiation of *Equus* in China. *Front. Ecol. Evol.* 7:429. doi: 10.3389/fevo.2019.00429

Vekua, A. (1995). Die wirbeltierfauna des villafranchian von dmanisi und ihre biostratigraphisce bedeutung. *Jb. Röm. Ger. ZentMus. Mainz* 42, 77–180.

Wang, S.-Q., and Deng, T. (2011). Some evolutionary trends of *Equus eisenmannae* (Mammalia, Perissodactyla) in the stratigraphic sequence of Longdan, China, in comparison to modern *Equus*. *J. Vertebr. Paleontol.* 31, 1356–1365. doi: 10.1080/02724634.2011.611203

Conflict of Interest: The authors declare that the research was conducted in the absence of any commercial or financial relationships that could be construed as a potential conflict of interest.

frontiers in Earth Science

ORIGINAL RESEARCH
published: 14 July 2020
doi: 10.3389/feart.2020.00273

From Smart Apes to Human Brain Boxes. A Uniquely Derived Brain Shape in Late Hominins Clade

Marina Melchionna[1], Antonio Profico[2], Silvia Castiglione[1], Gabriele Sansalone[3], Carmela Serio[4], Alessandro Mondanaro[5], Mirko Di Febbraro[6], Lorenzo Rook[5], Luca Pandolfi[5], Fabio Di Vincenzo[7], Giorgio Manzi[7] and Pasquale Raia[1]*

[1] *Dipartimento di Scienze della Terra, dell'Ambiente e delle Risorse, Università degli Studi di Napoli Federico II, Naples, Italy,* [2] *PalaeoHub, Department of Archaeology, University of York, Heslington, United Kingdom,* [3] *Function, Evolution and Anatomy Research Lab, Zoology Division, School of Environmental and Rural Science, University of New England, Armidale, NSW, Australia,* [4] *Research Centre in Evolutionary Anthropology and Palaeoecology, School of Biological and Environmental Sciences, Liverpool John Moores University, Liverpool, United Kingdom,* [5] *Department of Earth Sciences, University of Florence, Florence, Italy,* [6] *Dipartimento di Bioscienze e Territorio, University of Molise, Pesche, Italy,* [7] *Department of Environmental Biology, Sapienza University of Rome, Rome, Italy*

OPEN ACCESS

Edited by:
Mary Teresa Silcox, University of Toronto Scarborough, Canada

Reviewed by:
Antoine Balzeau, Centre National de la Recherche Scientifique (CNRS), France
Emmanuel Paul Gilissen, Royal Museum for Central Africa, Belgium

***Correspondence:**
Antonio Profico
antonio.profico@york.ac.uk

Specialty section:
This article was submitted to Paleontology, a section of the journal Frontiers in Earth Science

Received: *20 December 2019*
Accepted: *16 June 2020*
Published: *14 July 2020*

Citation:
Melchionna M, Profico A, Castiglione S, Sansalone G, Serio C, Mondanaro A, Di Febbraro M, Rook L, Pandolfi L, Di Vincenzo F, Manzi G and Raia P (2020) From Smart Apes to Human Brain Boxes. A Uniquely Derived Brain Shape in Late Hominins Clade. Front. Earth Sci. 8:273. doi: 10.3389/feart.2020.00273

Modern humans have larger and more globular brains when compared to other primates. Such anatomical features are further reflected in the possession of a moderately asymmetrical brain with the two hemispheres apparently rotated counterclockwise and slid anteroposteriorly on one another, in what is traditionally described as the Yakovlevian torque. Developmental disturbance in human brain asymmetry, or lack thereof, has been linked to several cognitive disorders including schizophrenia and depression. More importantly, the presence of the Yakovlevian torque is often advocated as the exterior manifestation of our unparalleled cognitive abilities. Consequently, studies of brain size and asymmetry in our own lineage indirectly address the question of what, and when, made us humans, trying to trace the emergence of brain asymmetry and expansion of cortical areas back in our *Homo* antecedents. Here, we tackle this same issue by studying the evolution of human brain size, shape, and asymmetry on a phylogenetic tree including 19 apes and *Homo* species, inclusive of our fellow ancestors. We found that a significant positive shift in the rate of brain shape evolution pertains to the clade including modern humans, Neanderthals, and *Homo heidelbergensis*. Although the Yakovlevian torque is well evident in these species and levels of brain asymmetry are correlated to changes in brain shape, further early *Homo* species possess the torque. Even though a strong allometric component is present in hominoid brain shape variability, this component seems unrelated to asymmetry and to the rate shift we recorded. These results suggest that changes in brain size and asymmetry were not the sole factors behind the fast evolution of brain shape in the most recent *Homo* species. The emergence of handedness and early manifestations of cultural modernity in the archeological record nicely coincide with the same three species sharing the largest and most rapidly evolving brains among all hominoids.

Keywords: endocast, brain volume, asymmetry, primates, human evolution, *Homo neanderthalensis*, *Homo heidelbergensis*

INTRODUCTION

The evolution of the human brain is one of the most intensely investigated topics in anthropology. Most studies on the subject matter focus on the achievement of our outstanding brain size (Rilling, 2006); fewer more focus on brain shape, which is intrinsically hard to study given it takes producing skull endocasts of our ancestors that come short in numbers and are not always easily accessible (Holloway, 2018). Recent developments in virtual anthropology (Weber, 2014) are now making fossil human endocasts a less rare commodity (Bruner et al., 2018), so that we are gaining scientific knowledge on our brain evolution at an unprecedented rate (Falk et al., 2000; Zollikofer and De León, 2013). Paralleling such increasing availability of brain endocasts, phylogenetic comparative methods offer ever better opportunities to study the rate and direction of phenotypic evolution, allowing the inclusion of fossil forms in studies of trait evolution. This is a key addition as the inclusion of fossils to extant-species phylogenies provides better understanding of the tempo and mode of evolution (Slater et al., 2012; Puttick, 2016; Schnitzler et al., 2017).

Recent studies on endocranial volume (i.e., the best proxy for brain size) in hominins invariably point to the presence of phenotypic leaps coinciding with the appearance of *Homo* (Du et al., 2018), although several lines of evidence indicate that not all *Homo* species belong to this "unusually big-brained" class of species, the latter being restricted to *Homo heidelbergensis*, *Homo neanderthalensis*, and *Homo sapiens* (Ruff et al., 1997; Rightmire, 2004; Profico et al., 2017; Diniz-Filho et al., 2019). These studies point to a non-gradual process of brain increase along the hominin lineage, probably prompted by the causal association between speciation and brain size (Du et al., 2018; Melchionna et al., 2019; Rocatti and Perez, 2019; Sansalone et al., 2020). These recent findings are slowly superseding earlier reports describing a pattern of gradual brain size increase in hominins (e.g., Lee and Wolpoff, 2016).

Our understanding of the evolution of brain shape in the human lineage might be experiencing a reverse trend. Despite logical enthusiasm around early findings illustrating an exquisitely human brain shape and level of brain asymmetry (Holloway, 1981; Holloway and De La Coste-Lareymondie, 1982), it has been later noted that the typical brain shape in *H. sapiens*, which is characterized by a strong left-occipital right-frontal asymmetry known as the Yakovlevian torque (Toga and Thompson, 2003) or occipital bending (LeMay, 1976; Holloway and De La Coste-Lareymondie, 1982; Chance and Crow, 2007; Balzeau et al., 2013), is present to a degree in both fossil human species and great apes (Gannon et al., 1998; Balzeau and Gilissen, 2010; Frayer et al., 2016; Neubauer et al., 2020). This casts doubt on the link between brain asymmetry and properly human cognitive abilities and still suggests that the evolution of human brain shape is best viewed as a gradual process toward exaggerated asymmetry and large size (Balzeau and Gilissen, 2010; Corballis, 2010; Gomez-Robles et al., 2013; Neubauer et al., 2018). However, the observation by Xiang et al. (2019) that torque magnitude is independent of brain size variation within *H. sapiens* and repeated findings that brain asymmetry is more variable in humans than in apes (Balzeau et al., 2012a; Neubauer et al., 2020) challenge this view and point to either a punctuational evolutionary event (Crow, 1993; Hou et al., 2019; Xiang et al., 2019) or a shift in the rate of evolution adding variability in humans (Balzeau et al., 2012a; Neubauer et al., 2020).

Here, we used 3D geometric morphometrics to study brain size and shape evolution in Hominoidea using 123 cranial endocasts belonging to 19 different extant and fossil species, including *Australopithecus africanus*, *Homo ergaster*, *Homo erectus*, *H. heidelbergensis*, and *H. neanderthalensis*. We built a phylogenetic tree for the species in the study sample and applied a phylogenetic comparative method especially thought to work with phylogenetic hypotheses including paleontological data. We computed the rate of brain shape evolution and searched for possible rate shifts, and how they correlate to levels of brain asymmetry. We eventually tested whether there is a significant allometric component in brain shape variation.

MATERIALS AND METHODS

Endocasts, Volumes, and Landmark Configuration

We included 123 skull digital models of both extinct and extant species in the analysis. The fossil specimens are Sts 5 (*A. africanus*); KNM-ER 3733 and KNM-ER 3883 (*H. ergaster*); Ngandong 7, Ngandong 12, Sambungmacan 3, Zhoukoudian DI, and Zhoukoudian LIII (*H. erectus*); Kabwe 1, Petralona, and Atapuerca 4 (*H. heidelbergensis*); Saccopastore 1, La Chapelle-aux-Saints, and La Quina 5 (*H. neanderthalensis*); and Abri Pataud, Chancelade 1, Cro-Magnon 1, Mladeè 1, and Skhul V (anatomically modern humans). We also included endocasts of 10 modern *H. sapiens*, 10 *Pan troglodytes*, 10 *Gorilla beringei*, 10 *Gorilla gorilla*, six *Pongo abelii*, eight *Hylobates agilis*, nine *Hydrophis klossi*, 10 *Hylobates lar*, 10 *Hylobates muelleri*, four *Hoolock hoolock*, five *Hylobates pileatus*, eight *Symphalangus syndactylus*, two *Nomascus concolor*, and two *Nomascus leucogenys*. To produce the digital endocasts, we used the CT scans of crania belonging to living species from the Smithsonian Institute and the Digital Morphology Museum, Kupri[1], repositories. We first reconstructed the cranial surfaces by using the software Amira® (version 5.4.5, Visualization Sciences Group, ©2013[2]). Endocasts were obtained within the R software environment by using the *endomaker* function (Profico et al., 2020). The function works by reproducing the inner surface of the cranial cavity. It is based on an automatic reconstruction procedure named AST-3D (Profico et al., 2018). The procedure consists in reproducing the inner surface starting from multiple points of view (POVs) manually placed inside the cavity. The advantage of *endomaker* is that it performs the AST-3D algorithm automatically on brain case, without placing POVs. The function further computes the endocranial volume (i.e., the actual volume of the digital endocast) calling the *volendo* function of the

[1]http://dmm.pri.kyoto-u.ac.jp/dmm/WebGallery/index.html
[2]https://www.fei.com/software/amira-for-life-sciences/

Arothron R package. *volendo* calculates the 3D space occupied by the digital endocast discretized into voxels, identifying the voxels inside the mesh as those included within a concave-hull containing the mesh of the endocast and then computing the sum of inner voxels.

We extracted the cranial endocasts of Sts 5, Petralona, Saccopastore 1, Ngandong 7, Ngandong 12, KNM-ER-3733, and KNM-ER-3883 by using the Arothron R package (**Figure 1**). The other hominin fossil specimens are either manually segmented 3D models or laser-scanned physical casts (details are reported in **Supplementary Table S1**).

To register endocast shapes, we manually collected from each specimen 16 landmarks by using Amira (**Supplementary Table S2**). Then, 1000 bilateral semilandmarks (500 on each side) were automatically placed and slid in the R software environment by using the Morpho R package (Schlager, 2017) (**Figure 2**).

Some fossil specimens may suffer distortion by the taphonomic process, including missing portions. We did not include deformed specimens as they miss the relevant phenotypic information. However, in order to maximize sample size, we applied shape mirroring some specimens but nonetheless excluded them from the analysis of brain asymmetry as the mirroring erases such information. In particular, Kabwe I, La Quina 5, and KNM-ER 3883 are incomplete. In Kabwe I, small portions of the right occipital and parietal lobe are missing. A portion of the left cerebellum is missing in KNM-ER 3883. La Quina 5 lacks the entire base and a portion of the left frontoparietal lobe. Whenever we were not able to sample specific landmarks due to missing parts, the configurations were fixed by using the Morpho function *fixLMmirror*, estimating missing landmarks from their bilateral counterparts. This procedure is based on the reflecting and relabeling technique (Gunz et al., 2009). More specifically, the landmark configuration is mirrored, left and right landmarks are relabeled, and the missing data are imputed by deforming the mirrored version to the original one (Schlager, 2017). The same procedure was applied on the semilandmark sets after the sliding step. As this technique involves mirroring, the hominin specimens Kabwe I, La Quina 5, and KNM-ER 3883 were excluded from the asymmetry analysis.

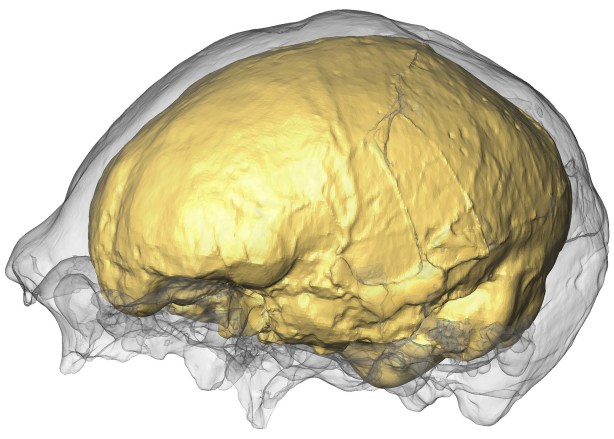

FIGURE 1 | Ngandong 7 skull (gray) and its endocast produced with the function *endomaker*.

Procrustes Analysis and RRphylo

We computed the mean landmark configuration per species. To this aim, we first performed a preliminary alignment of the specimens via Generalized Procrustes Analysis (GPA) (Gower, 1975) using the function *procGPA* in Morpho (Schlager, 2017). Subsequently, we computed the mean shape configuration per species.

To analyze the differences in brain shape among different species, we performed a Procrustes superimposition and a principal component analysis (PCA) on the vectorized landmark sets through the Morpho function *procSym*. This function returns both aligned coordinates and scores from the PCA.

In order to analyze the rate of brain shape evolution, we computed the phylogenetic tree for the species under analysis by using the phylogenetic hypotheses implemented in Meloro et al. (2015) and Melchionna et al. (2019). To search for evolutionary shifts in brain shape, we applied the *RRphylo* function in the R package RRphylo (Raia et al., 2020). The function relies on ridge regression to compute phenotypic evolutionary rates for each branch of the phylogeny and to estimate ancestral phenotypes with either univariate or multivariate data (Castiglione et al., 2018). In the present framework, we used all the principal component (PC) scores retrieved from the PCA pooled by species as phenotypic data, along with the Hominidae tree including the 19 analyzed species as the phylogeny (see **Supplementary Material**). Individual clades within the phylogeny were tested for the presence of rate shifts in brain shape evolution by applying the function *search.shift*. This function locates nodes subtending to clades possessing significantly higher/lower absolute phenotypic rate values by using a two-tailed permutation test (Castiglione et al., 2018). Since brain shape variations might possess a strong allometric component (Aristide et al., 2016), and brain asymmetry (see below) might represent an important source of brain shape variation, we performed the analysis by using once the endocranial volume and once the mean asymmetry per species as predictors. This is currently implemented in the multiple regression version of *RRphylo* (Melchionna et al., 2019; Serio et al., 2019). The analysis without endocranial volume taken as a prediction (pure shape) is presented as part of the **Supplementary Material**.

We analyzed the evolution of brain size using the mean endocranial volume per species as the phenotype and scanned the phylogeny and data seeking after significant shifts in the endocranial volume. The same procedure was applied to brain asymmetry. Eventually, to assess the presence of allometry in the brain shape data, we regressed brain shape against the mean endocranial volumes by means of generalized phylogenetic least squares regression (multivariate PGLS). We applied two different PGLS models. The first implements classic PGLS by using the *procD.gls* function in geomorph (Adams et al., 2019). The second rescales the tree branch lengths according to the multivariate rate variation across the tree branches as calculated by *RRphylo* before running *procD.gls*. These implementations are available in the function *PGLS_fossil* in the RRphylo package.

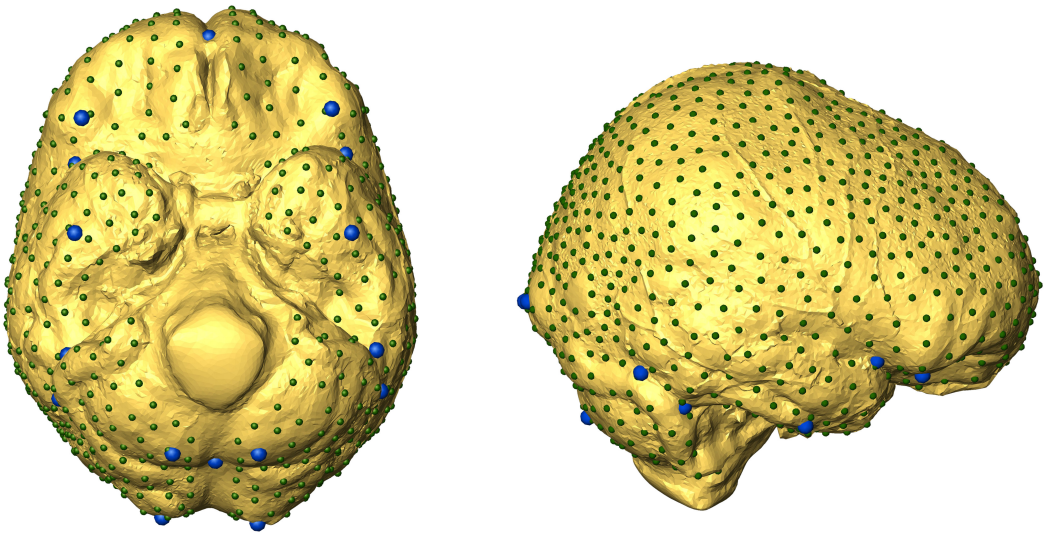

FIGURE 2 | Landmark configurations used in the present work. Fixed landmarks (in blue) were manually defined. Semilandmarks are shown smaller and in dark green.

Measuring Asymmetry in Cranial Endocasts

Bilateral endocast asymmetry was assessed by comparing the brain morphology on the right and left sides. We used the same landmark and semilandmark configurations shown in Section "Endocasts, Volumes, and Landmarks Configuration." In order to record differences in shape between the two halves of the endocast, we defined a set of 1000 semilandmarks, sampling 500 homologous points on each side. We built a symmetric reference for semilandmark placing and sliding procedures. In this way, the slid semilandmarks can be used as a proxy to calculate the difference in shape between right and left sides in all the specimens composing the sample.

After the sliding procedure, we applied the following procedure to each bilateral semilandmark configuration:

i. Calculation of the rotation matrix to mirror, scale, and align (ordinary Procrustes analysis step) the left side into the right side and *vice versa* following Klingenberg et al. (2002) (**Figure 3**);
ii. Definition of a matrix of differences between the symmetric semilandmark configuration and the original one;
iii. Definition of a matrix of difference between right and mirrored left sides and *vice versa*.

At the end of this process, we obtained two suitable matrices to analyze the asymmetry of the cranial endocasts. We explored the relation between asymmetry and shape by applying a partial least squares (PLS). We defined as first block the endocast shape and as second block the matrix of asymmetry calculated on each specimen. The endocast shape consists in the semilandmark configurations after the GPA analysis (scaling included). We perform also a PLS on a less dense semilandmark configuration (50 semilandmarks on each side).

RESULTS

The PCA results are shown in **Figure 4** (PC1 vs PC2). On the PC1 (which explains 35.93% of the total variance), the overall shape goes from flattened endocasts (PC1 positive values) to more globular shapes with a rounded and expanded frontoparietal region. The occipital lobes become markedly asymmetric at PC1 negative values. Along the PC1, there is a separation between the most recent species of *Homo* (*H. heidelbergensis*, *H. neanderthalensis*, and *H. sapiens*) and the other hominids. Positive values of PC2 correspond to a brain shape that narrows in the temporal area (which is typical of the *Australopithecus* brain morphology), whereas at negative values of the PC2, the brain endocast flattens dorsoventrally.

Brain volume (per unit mass) shows a negative rate shift coinciding with the genus *Hylobates* ($p_{\text{two-tailed}} < 0.001$; **Supplementary Figure S1**). Interestingly, brain shape asymmetry shows a positive rate shift regarding the species of the genus *Homo* ($p_{\text{two-tailed}} = 0.979$; **Figure 5**, right). When the average brain volume is considered as a predictor in *RRphylo*, there is a positive and significant rate shift in brain shape evolution for the clade including *H. heidelbergensis*, *H. neanderthalensis*, and *H. sapiens* ($p_{\text{two-tailed}} = 0.999$; **Figure 5**, left) and a negative and significant rate shift for the Hylobatidae clade ($p_{\text{two-tailed}} < 0.001$; **Figure 5**, left). When brain asymmetry is considered as a predictor in *RRphylo*, the results do not change; there is a positive and significant rate shift in brain shape evolution for the clade including *H. heidelbergensis*, *H. neanderthalensis*, and *H. sapiens* ($p_{\text{two-tailed}} = 0.999$) and a negative and significant rate shift for the Hylobatidae clade

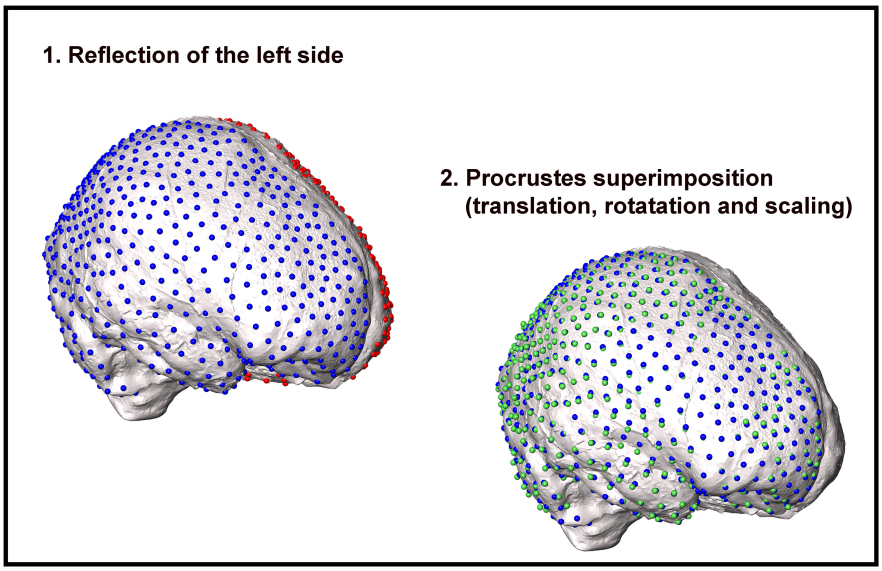

FIGURE 3 | Workflow illustrating the procedure to compute bilateral asymmetry in cranial endocasts. First, the semilandmark configuration of one side (red spheres on the left side) is reflected on the other hemisphere (green spheres). Second, the mirrored semilandmark configuration is scaled to the centroid size of the right side (blue spheres). Third, the configurations are superimposed and rotated around the common centroid to achieve the best fit between the corresponding semilandmarks. For graphical purposes, the procedure is shown on one side only.

($p_{\text{two-tailed}} < 0.001$). Eventually, the same two rate shifts still apply when shape is analyzed on its own, ignoring the allometric component.

We found a positive allometric scaling between the brain shape and the endocast volume, either using the Brownian motion ($p = 0.001$) or allowing the evolutionary rates to change across the tree with *RRphylo* ($p = 0.001$).

The PLS performed between endocast shape and asymmetry highlights a significant correlation between the two blocks. The correlation coefficient related to the first axis is equal to 0.56, and the *p*-value is equal to 0.010 as assessed by a permutation test ($N = 1000$). The correlation coefficient of the second axis is equal to 0.45, and the *p*-value is equal to 0.001 (see **Supplementary Figure S2**). On the first PLS axis, *Homo erectus* and Middle to Late Pleistocene humans (i.e., *H. neanderthalensis*, *H. heidelbergensis*, and *H. sapiens*) are located at negative values of both axes (shape and asymmetry, **Figure 6**). The Hylobatidae are found at positive values of blocks 1 and 2. The first axis of covariation (PLS1, block 1) explains 14.23% of the total variance of the endocast shape. The shape variations related to the genus *Homo* show as in this group of species that the left hemisphere is larger (see **Figure 6** and **Supplementary Figure S3**) with an expansion of the right parietal lobe.

On the second axis of the PLS (see **Supplementary Figure S2**), the morphology associated at positive values highlights the right hemisphere extending anteriorly, according to the classical Yakovlevian torque pattern. At negative values of both axes, the endocast morphology shows a distortion along the midsagittal profile with a greater asymmetry in the superior parietal region and in the anterior portion of the frontal lobe. By reducing the number of semilandmarks on each hemisphere from 500 to 50, we observe the same pattern of shape variations in the PLS analysis (see **Supplementary Figures S6, S7**).

DISCUSSION

Humans are often noted for their exceptional brain size and extremely developed cognitive abilities. It has long been noted that our brain is strongly asymmetric, with evident differences between the left and right sides (Leuret and Gratiolet, 1839). The left cerebral hemisphere often extends posteriorly beyond the right, and the latter extends beyond the left frontally, originating the so-called *petalia* (Galaburda et al., 1978; Toga and Thompson, 2003; Balzeau and Gilissen, 2010). This asymmetric structure is often described as the Yakovlevian torque (Yakovlev and Rakic, 1966). The torque is more than a mere distortion of the bilateral symmetry of the brain. Several studies have indicated that a significant relationship exists between brain asymmetry and the lateralization of cognitive functions such as handedness and linguistic processing. In modern humans, the right frontal (RF) protrusion and left occipital (LO) protrusion are statistically correlated with right-handedness in 85–90% of individuals (Cashmore et al., 2008; Häberling and Corballis, 2016), whereas the reverse pattern is associated to some degree with left-handedness and ambidexterity (Cashmore et al., 2008; Grimaud-Herve and Lordkipanidze, 2010). Lateralization is further observed in hemispheric language dominance. Approximately 95% of right-handed individuals have left-hemispheric dominance for language (Rasmussen and Milner, 1977; Pujol et al., 1999; Szaflarski et al., 2002). A strong variation in the degree of Yakovlevian torque is associated with several functional disorders

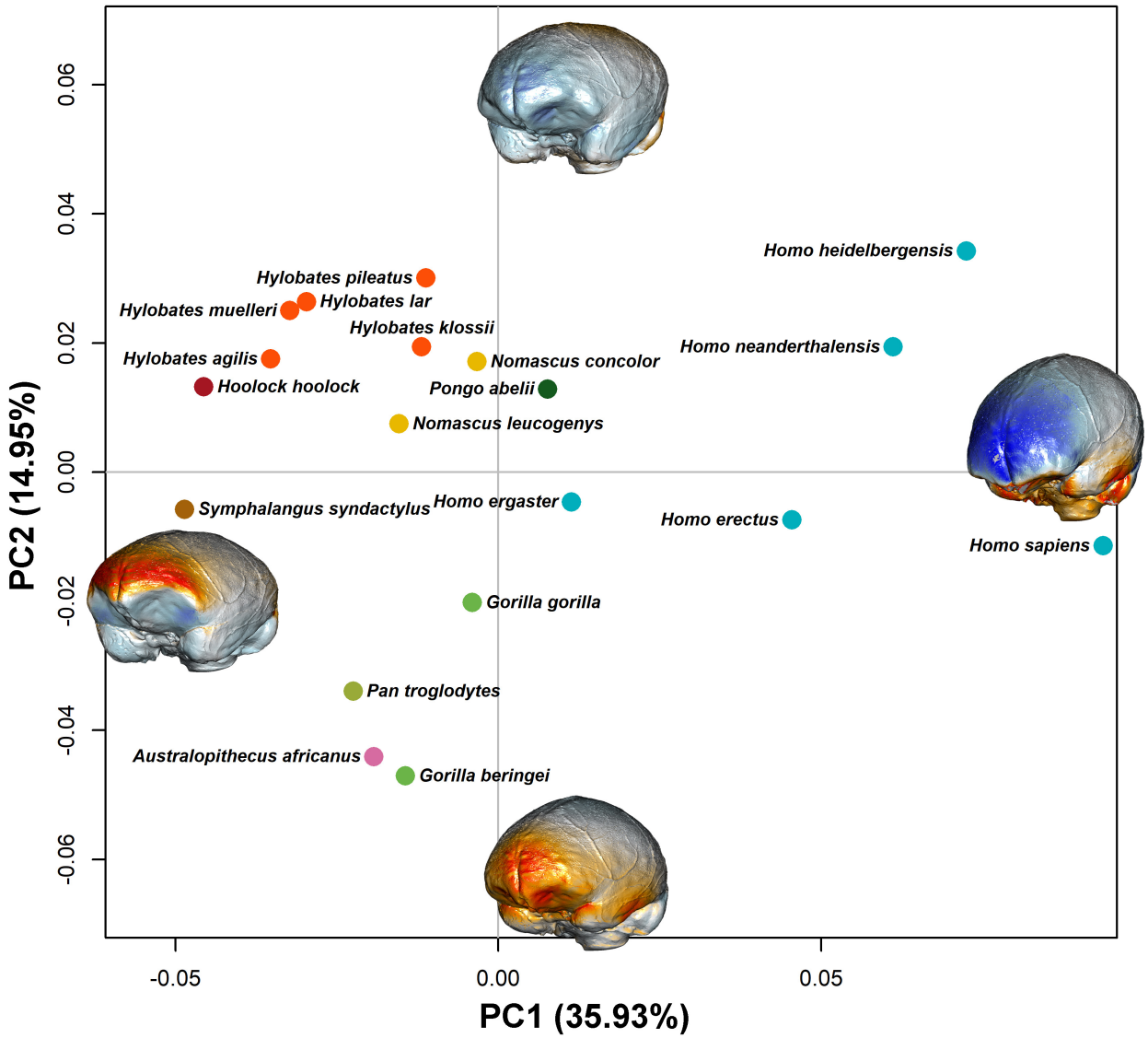

FIGURE 4 | PC1 and PC2 scores are shown. Species represents the mean shape configuration between samples after alignment. They are colored by genus. The endocasts represent the shape at the extreme of the PC axis (endocasts are not in scale). Blue tones represent expansion from the consensus shape, and orange/red tones represent contraction. The two PCs explain, respectively, 35.93 and 14.95% of the total variation.

like depression and schizophrenia (Mackay et al., 2010; Maller et al., 2015; Liu et al., 2016). In schizophrenia, in particular, cerebral asymmetry is reduced, and language processing is less lateralized than in non-schizophrenic subjects (Sommer et al., 2001). This evidence testifies to the intimate connection between the pattern of structural brain asymmetry and lateralization in the development of higher cognitive abilities (Walker, 1980; Gevins et al., 1983; Lefebvre et al., 2004).

Brains of non-human anthropoids are also functionally lateralized to a degree (Holloway, 1981; Cantalupo and Hopkins, 2001; Wu et al., 2006; Falk, 2007; Hofman and Falk, 2012; Gomez-Robles et al., 2013; Hopkins et al., 2015; Poza-Rey et al., 2017). Hylobatids possibly show higher frequency of left- than right-handers (Morino et al., 2017). The great apes present specific patterns of hemispheric asymmetry, which is less frequent than in humans and rarely involves both the frontal and the occipital lobes. Some scholars (Prieur et al., 2016, 2019; Marie et al., 2018) noted the presence of a low-frequency right-handedness bias in bimanual tasks in chimpanzees and gorillas (Hopkins et al., 2019). Although several studies (McGrew and Marchant, 2001; Mosquera et al., 2007; Harrison and Nystrom, 2008) indicate that great apes do not display any hand preference at the population level (Fitch and Braccini, 2013; Uomini, 2015), some groups can have a majority of left-handers (Cashmore et al., 2008; Uomini, 2009; Chapelain et al., 2011), chimpanzee groups were reported to be predominantly right-handed (Hopkins et al., 2004), and even in monkeys, handedness is related to hemispheric specialization (Margiotoudi et al., 2019).

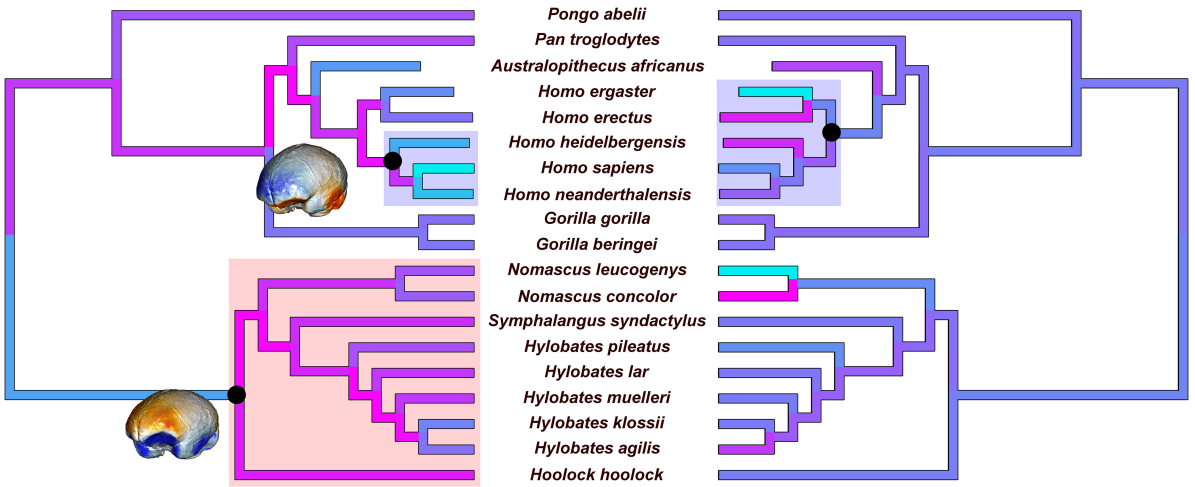

FIGURE 5 | Results of the evolutionary rate analysis of brain shape when mean volume per species is used as a predictor (left). The reconstruction of the endocast shape of the common ancestors is provided (endocasts are not in scale) for the tree root and for the common ancestor of modern *Homo* species. Results of the rate analysis of the average asymmetry values are shown on the right side. Evolutionary rates are scaled for the branches of the tree from higher (cyan) to lower (magenta) values. Clades that show significantly higher and lower rates are highlighted with blue and red rectangles, respectively.

With so much emphasis on brain asymmetry and its relationship to cognition, it is unsurprising that profound effort has been devoted to studying fossil endocasts so as to reveal the evolution of brain asymmetry in hominids and non-human apes. Different studies now point in the direction that a clearly asymmetrical brain pertains to modern human species, whereas the status of australopiths and early *Homo* is much less obvious (Tobias, 1987; Rightmire, 2004; Wu et al., 2006). Brain asymmetry is documented in Paleolithic *H. sapiens*, in *H. neanderthalensis* (albeit the endocast of La Chapelle-aux-Saints has a reversed RO/LF petalia pattern), and in Middle Pleistocene *H. heidelbergensis* (Holloway et al., 2004). A reversed RO/LF petalia pattern has been described in *Homo floresiensis* (Falk et al., 2005) as well in KNM-ER 1813, in some specimens of *H. erectus* from Asia (Sangiran 2, Sangiran 10, Sangiran 17, and Ckn.L.2) and in D2280 from Dmanisi, while D2282 is described as possessing an RF/LO pattern (Grimaud-Herve and Lordkipanidze, 2010) like four of the five endocasts of *H. erectus* from Ngandong (Poza-Rey et al., 2017). A human-like pattern is also described in *Homo rudolfensis* KNM-ER 1470 (Holloway, 1983) and *H. ergaster* KNM-ER 3733, KNM-ER 3883, and KNM-WT 15000 (Holloway et al., 2004). Small RF/LO petalias have been described for *A. africanus*, *Paranthropus boisei*, and *Paranthropus aethiopicus* (Holloway et al., 2004), while the *Homo habilis* specimens from Olduvai usually lack RF/LO petalias (Tobias, 1987; Holloway et al., 2004, but see Frayer et al., 2016). Despite this wealth of data apparently suggesting a continuous development of brain asymmetry throughout human evolution, the precise quantification of the magnitude of the asymmetry and its evolutionary significance in terms of cognitive abilities remain elusive (Balzeau et al., 2020). Furthermore, given the 3D geometric complexity of the torque, its recognition on endocranial casts by using traditional linear measurements as in these studies is often prone to a consistent degree of uncertainty. Our analysis based on 3D geometric morphometrics overcomes this limitation and offers the first integrated glimpse on the rates of evolutionary change of brain shape in the different branches of the Hominoidea. Although the allometric component of brain shape change is strong, the pattern is not linear. Rates of the shape change are distinctly lower for Hylobatidae and distinctly higher for the clade including *H. heidelbergensis*, *H. neanderthalensis*, and *H. sapiens*. The early *Homo* (*H. erectus* + *H. ergaster*) and *Australopithecus*, conversely, are in line with the apes (**Figures 4**, **6**), although early *Homo* show the same level of asymmetry as later species in the genus, resulting in a significant rate shift in the asymmetry level coinciding with the genus (**Figure 5**, right). This means that the relative expansion of brain size in Middle to Late Pleistocene *Homo* is accompanied by a major reorganization in the brain morphology that goes beyond sheer allometric effects and asymmetry and possibly keeps changing in *H. sapiens* (Bastir et al., 2008; Neubauer et al., 2018; Weaver and Gunz, 2018; Gunz et al., 2019) and *H. neanderthalensis* (Balzeau et al., 2012b; Mounier et al., 2016).

The pattern of low evolutionary rates in hylobatids is consistent with their evolutionary history and ecologies. The origin of Hylobatidae is placed at 21.8 Ma, and the radiation of the clade occurred between 6.4 and 8.0 Ma (Israfil et al., 2011). Israfil et al. (2011) suggest that such rapid radiation could be paired with biogeographic factors as the population dispersal and variations in the density of the forestal habitat (vicariant speciation). The low degree of body size differentiation and relatively minor ecological diversity when compared to great apes might be responsible for the apparently slow rate of brain shape evolution in this group.

Along the human lineage, the shifts in evolutionary rate in brain size evolution (Du et al., 2018; Diniz-Filho et al., 2019) and increased rates of brain shape evolution (this study) coincide, thus suggesting that brain evolution followed a distinctive path

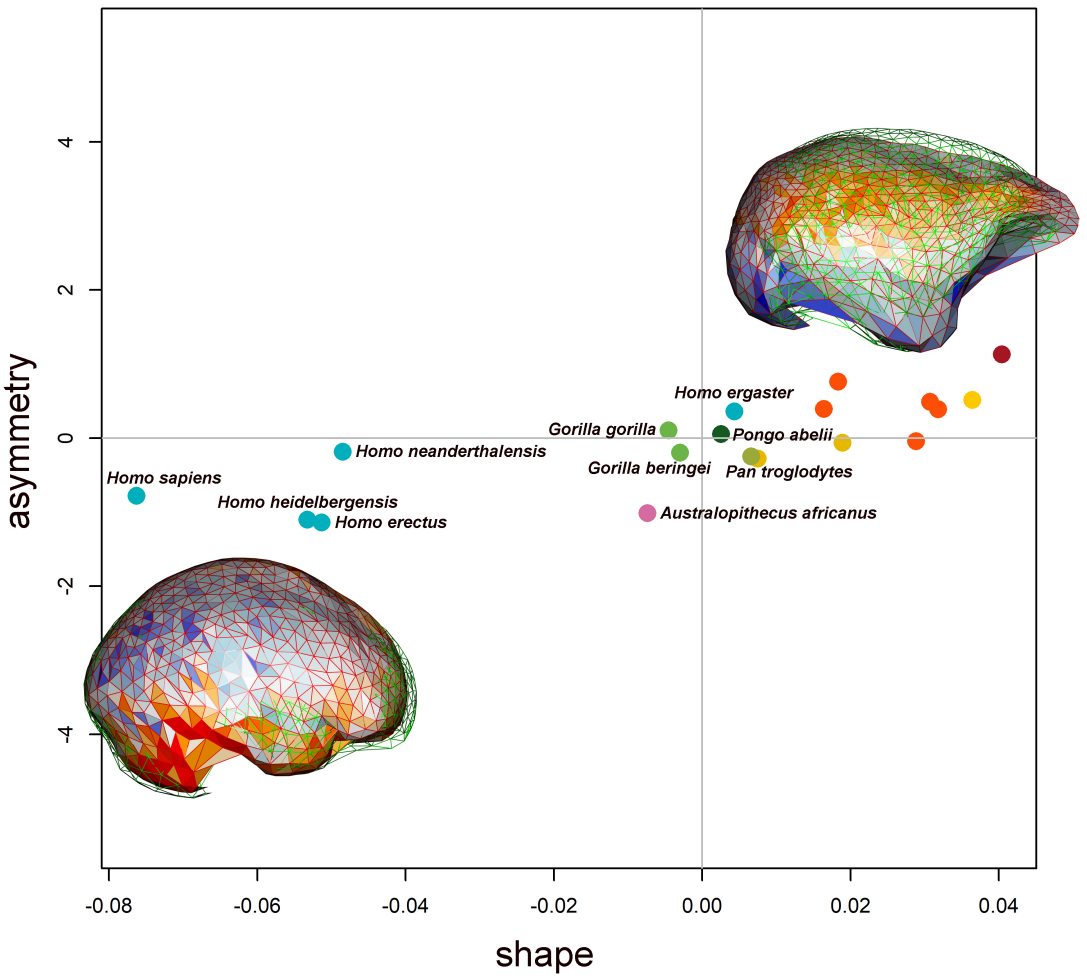

FIGURE 6 | Biplot showing the first axis of the PLS. On the *x*-axis is the endocast shape, and on the *y*-axis is the endocast asymmetry. The species are reported with the same dot colors reported in **Figure 4**. The shape variations related to both shape and asymmetry are reported at the extreme of the *x*- and *y*-axes. The displacement between the right (wireframe in red) and left (wireframe in green) sides is shown overlapped to the colored mesh, indicating the local deformation. Warm and cold colors indicate, respectively, which regions are more contracted and expanded in the right side compared with the left one.

joining *H. heidelbergensis*, *H. neanderthalensis*, and *H. sapiens*. This is entirely consistent with the archeological record of human behavior. Numerous studies on the anterior dentition in *H. heidelbergensis*, Neanderthals, and Paleolithic modern humans show a predominant right-hand frequency (> 90%), similar to the pattern for living humans attributed to right-handers (de Castro et al., 1988; Lozano et al., 2009; Frayer et al., 2012; Poza-Rey et al., 2017). Studies of experimental production of lithic stone tools demonstrate that brain lateralization is involved in the production of late Acheulean tools or when participants watch Acheulean tool production, but not when participants make or watch others making Oldowan tools (Stout, 2011; Stout and Khreisheh, 2015). Uomini and Meyer (2013) suggested that the same areas for stone tool manufacture, of the Acheulean in particular, are lateralized and located on the left side in brain areas also involved in language processing and social learning.

It is intriguing that the birth of symbolic culture, marked by the use of pigments and personal ornamentation, traces back to the Middle Stone Age with Acheulean tradition at some 300 ka and is itself consistent with human fossil specimens belonging to the species *H. heidelbergensis* (Henshilwood et al., 2002; d'Errico, 2003; d'Errico and Henshilwood, 2007; Manzi, 2016) and *H. neanderthalensis* (Zilhão et al., 2010). It must be noted, though, that the indication for symbolic culture in species other than *H. sapiens* is controversial to say the least (Mcbrearty and Brooks, 2000; White et al., 2019).

Here, we demonstrate that the pace of brain shape evolution shifted since the appearance of the common ancestor to *H. heidelbergensis*, *H. neanderthalensis*, and *H. sapiens*. Although these species share a large brain, levels of brain asymmetry were comparatively large in earlier *Homo* species, and allometric effects cannot entirely account for the shift toward the faster rate of brain shape evolution in the Middle to Late human species. Remarkably, the rate shift coincides with archeological evidence for the emergence of symbolic culture.

DATA AVAILABILITY STATEMENT

All datasets generated for this study are included in the article/**Supplementary Material**.

AUTHOR CONTRIBUTIONS

PR, MM, and AP conceived the study. MM, AP, SC, and CS performed the analyses. All authors contributed to the article and approved the submitted version.

ACKNOWLEDGMENTS

We are grateful to Costantino Buzi, Chiara Iacuzzo, and Maria Modafferi for sharing some of their own work on fossil endocasts with us.

SUPPLEMENTARY MATERIAL

The Supplementary Material for this article can be found online at: https://www.frontiersin.org/articles/10.3389/feart.2020.00273/full#supplementary-material

This file includes:

The phylogenetic tree used in the analyses in Newick format.

FIGURE S1 | Results of the evolutionary rate analysis on the average volumes.

FIGURE S2 | Biplot showing the second axis of the PLS.

FIGURE S3 | Variation in centroid size between right and left hemisphere within the genus *Homo*.

FIGURE S4 | Variation in centroid size between right and left hemisphere in great apes (*Homo* excluded) plus *Australopithecus africanus*.

FIGURE S5 | Variation in centroid size between right and left hemisphere in lesser apes.

FIGURE S6 | Biplot showing the first axis of the PLS using a subset of 100 semilandmarks (50 on each side).

FIGURE S7 | Biplot showing the second axis of the PLS using a subset of 100 semilandmarks (50 on each side).

TABLE S1 | List of materials used in this study.

TABLE S2 | Definition of landmarks acquired on each endocast.

DATA.rda: an RData file containing the phylogenetic tree, the landmark and semilandmark sets used in the analyses of the endocast shape (123 specimens), the semilandmark sets used in the asymmetry analyses (120 specimens), the vector of the corresponding ECV values and a mesh containing the triangulated semilandmark configuration.

script.R: The annotated script used to replicate the analyses reported in this study. The supplementary material is available on Melchionna et al. (2020). From smart apes to human brain boxes. A uniquely derived brain shape in late hominins clade: supplementary material. *Zenodo*: doi: 10.5281/zenodo.3931032.

REFERENCES

Adams, D. C., Collyer, M., Kaliontzopoulou, A., and Sherratt, E. (2019). *geomorph: Software for Geometric Morphometric Analyses. R Package Version 3.1.0*. Available online at: https://cran.r-project.org/package=geomorph

Aristide, L., Dos Reis, S. F., Machado, A. C., Lima, I., Lopes, R. T., and Perez, S. I. (2016). Brain shape convergence in the adaptive radiation of new world monkeys. *Proc. Natl. Acad. Sci. U.S.A.* 113, 2158–2163. doi: 10.1073/pnas.1514473113

Balzeau, A., Ball-Albessard, L., and Kubicka, A. M. (2020). Variation and correlations in departures from symmetry of brain torque, humeral morphology and handedness in an archaeological sample of *Homo sapiens*. *Symmetry* 12:432. doi: 10.3390/sym12030432

Balzeau, A., and Gilissen, E. (2010). Endocranial shape asymmetries in *Pan paniscus*, *Pan troglodytes* and *Gorilla gorilla* assessed via skull based landmark analysis. *J. Hum. Evol.* 59, 54–69. doi: 10.1016/j.jhevol.2010.03.013

Balzeau, A., Gilissen, E., and Grimaud-Hervé, D. (2012a). Shared pattern of endocranial shape asymmetries among great apes, anatomically modern humans, and fossil hominins. *PLoS One* 7:e29581. doi: 10.1371/journal.pone.0029581

Balzeau, A., Holloway, R. L., and Grimaud-Hervé, D. (2012b). Variations and asymmetries in regional brain surface in the genus Homo. *J. Hum. Evol.* 62, 696–706. doi: 10.1016/j.jhevol.2012.03.007

Balzeau, A., Grimaud-Hervé, D., Détroit, F., Holloway, R. L., Combès, B., and Prima, S. (2013). First description of the Cro-Magnon 1 endocast and study of brain variation and evolution in anatomically modern *Homo sapiens*. *Bull. Mem. Soc. Anthropol. Paris* 25, 1–18. doi: 10.1007/s13219-012-0069-z

Bastir, M., Rosas, A., Lieberman, D. E., and O'Higgins, P. (2008). Middle cranial fossa anatomy and the origin of modern humans. *Anat. Rec.* 291, 130–140. doi: 10.1002/ar.20636

Bruner, E., Ogihara, N., and Tanabe, H. C. (2018). *Digital Endocasts*. Cham: Springer.

Cantalupo, C., and Hopkins, W. D. (2001). Asymmetric broca's area in great apes. *Nature* 414, 505–505. doi: 10.1038/35107134

Cashmore, L., Uomini, N., and Chapelain, A. (2008). The evolution of handedness in humans and great apes: a review and current issues. *J. Anthropol. Sci.* 86, 1–30. doi: 10.1007/s10764-010-9484-5

Castiglione, S., Tesone, G., Piccolo, M., Melchionna, M., Mondanaro, A., Serio, C., et al. (2018). A new method for testing evolutionary rate variation and shifts in phenotypic evolution. *Met. Ecol. Evol.* 9, 974–983. doi: 10.1111/2041-210X.12954

Chance, S. A., and Crow, T. J. (2007). Distinctively human: cerebral lateralisation and language in *Homo sapiens*. *J. Anthropol. Sci.* 85, 83–100.

Chapelain, A. S., Hogervorst, E., Mbonzo, P., and Hopkins, W. D. (2011). Hand preferences for bimanual coordination in 77 Bonobos (*Pan paniscus*): replication and extension. *Int. J. Primatol.* 32, 491–510.

Corballis, M. C. (2010). "Handedness and cerebral asymmetry: an evolutionary perspective," in *Two Halves of the Brain: Information Processing in the Cerebral Hemispheres*, eds K. Hugdahl and R. Westerhausen (Cambridge, MA: The MIT press), 65–88. doi: 10.7551/mitpress/9780262014137.003.0063

Crow, T. J. (1993). Sexual selection, machiavellian intelligence, and the origins of psychosis. *Lancet* 342, 594–598. doi: 10.1016/0140-6736(93)91415-i

de Castro, J. B., Bromage, T. G., and Jalvo, Y. F. (1988). Buccal striations on fossil human anterior teeth: evidence of handedness in the middle and early Upper Pleistocene. *J. Hum. Evol.* 17, 403–412. doi: 10.1016/0047-2484(88)90029-2

d'Errico, F. (2003). The invisible frontier. A multiple species model for the origin of behavioral modernity. *Evol. Anthropol.* 12, 188–202. doi: 10.1002/evan.10113

d'Errico, F., and Henshilwood, C. S. (2007). Additional evidence for bone technology in the southern African Middle Stone Age. *J. Hum. Evol.* 52, 142–163. doi: 10.1016/j.jhevol.2006.08.003

Diniz-Filho, J. A. F., Jardim, L., Mondanaro, A., and Raia, P. (2019). Multiple components of phylogenetic non-stationarity in the evolution of brain size in fossil hominins. *Evol. Biol.* 46, 47–59. doi: 10.1007/s11692-019-09471-z

Du, A., Zipkin, A. M., Hatala, K. G., Renner, E., Baker, J. L., Bianchi, S., et al. (2018). Pattern and process in hominin brain size evolution are scale-dependent. *Proc. R. Soc. B* 285:20172738. doi: 10.1098/rspb.2017.2738

Falk, D. (2007). The evolution of Broca's area. *IBRO Hist. Neurosci.* 15, 2513–2518.

Falk, D., Hildebolt, C., Smith, K., Morwood, M. J., Sutikna, T., Brown, P., et al. (2005). The brain of LB1, *Homo floresiensis*. *Science* 308, 242–245. doi: 10.1126/science.1109727

Falk, D., Redmond, J. C. Jr., Guyer, J., Conroy, C., Recheis, W., Weber, G. W., et al. (2000). Early hominid brain evolution: a new look at old endocasts. *J. Hum. Evol.* 38, 695–717. doi: 10.1006/jhev.1999.0378

Fitch, W. T., and Braccini, S. N. (2013). Primate laterality and the biology and evolution of human handedness: a review and synthesis. *Ann. N. Y. Acad. Sci.* 1288, 70–85. doi: 10.1111/nyas.12071

Frayer, D. W., Clarke, R. J., Fiore, I., Blumenschine, R. J., Pérez-Pérez, A., Martinez, L. M., et al. (2016). OH-65: the earliest evidence for right-handedness in the fossil record. *J. Hum. Evol.* 100, 65–72. doi: 10.1016/j.jhevol.2016.07.002

Frayer, D. W., Lozano, M., Bermúdez de Castro, J. M., Carbonell, E., Arsuaga, J. L., Radovčić, J., et al. (2012). More than 500,000 years of right-handedness in Europe. *Laterality* 17, 51–69. doi: 10.1080/1357650X.2010.529451

Galaburda, A. M., LeMay, M., Kemper, T. L., and Geschwind, N. (1978). Right-left asymmetrics in the brain. *Science* 199, 852–856. doi: 10.1126/science.341314

Gannon, P. J., Holloway, R. L., Broadfield, D. C., and Braun, A. R. (1998). Asymmetry of chimpanzee planum temporale: humanlike pattern of wernicke's brain language area homolog. *Science* 279, 220–222. doi: 10.1126/science.279.5348.220

Gevins, A. S., Schaffer, R. E., Doyle, J. C., Cutillo, B. A., Tannehill, R. S., and Bressler, S. L. (1983). Shadows of thought: shifting lateralization of human brain electrical patterns during brief visuomotor task. *Science* 220, 97–99. doi: 10.1126/science.6828886

Gomez-Robles, A., Hopkins, W. D., and Sherwood, C. C. (2013). Increased morphological asymmetry, evolvability and plasticity in human brain evolution. *Proc. R. Soc. B* 280, 20130575–20130575. doi: 10.1098/rspb.2013.0575

Gower, J. C. (1975). Generalized procrustes analysis. *Psychometrika* 40, 33–51. doi: 10.1007/BF02291478

Grimaud-Herve, D., and Lordkipanidze, D. (2010). "The fossil hominid's brain of dmanisi: D 2280 and D 2282," in *The Human Brain Evolving: Paleoneurological Studies in Honor of Ralph L. Holloway*, eds K. Schick and N. Toth (Gosport, IN: Stone Age Institute Press), 59–82.

Gunz, P., Mitteroecker, P., Neubauer, S., Weber, G. W., and Bookstein, F. L. (2009). Principles for the virtual reconstruction of hominin crania. *J. Hum. Evol.* 57, 48–62. doi: 10.1016/j.jhevol.2009.04.004

Gunz, P., Tilot, A. K., Wittfeld, K., Teumer, A., Shapland, C. Y., van Erp, T. G. M., et al. (2019). Neandertal introgression sheds light on modern human endocranial globularity. *Curr. Biol.* 29, 120–127. doi: 10.1016/j.cub.2018.10.065

Häberling, I. S., and Corballis, M. C. (2016). Cerebellar asymmetry, cortical asymmetry and handedness: two independent networks. *Laterality* 21, 397–414. doi: 10.1080/1357650X.2015.1110161

Harrison, R. M., and Nystrom, P. (2008). Handedness in captive bonobos (*Pan paniscus*). *Folia Primatol.* 79, 253–268. doi: 10.1159/000113539

Henshilwood, C. S., d'Errico, F., Yates, R., Jacobs, Z., Tribolo, C., Duller, G. A. T., et al. (2002). Emergence of modern human behavior: middle stone age engravings from South Africa. *Science* 295, 1278–1280. doi: 10.1126/science.1067575

Hofman, A., and Falk, D. (2012). *Evolution of the Primate Brain: From Neuron To Behavior*, Vol. 195. Amsterdam: Elsevier.

Holloway, R. L. (1981). Volumetric and asymmetry determinations on recent hominid endocasts: spy I and II, Djebel Ihroud I, and the salè *Homo erectus* specimens, with some notes on neandertal brain size. *Am. J. Phys. Anthropol.* 55, 385–393. doi: 10.1002/ajpa.1330550312

Holloway, R. L. (1983). Human paleontological evidence relevant to language behavior. *Hum. Neurobiol.* 2, 105–114.

Holloway, R. L. (2018). "On the making of endocasts: the new and the old in paleoneurology," in *Digital Endocasts*, eds E. Bruner, N. Ogihara, and H. C. Tanabe (Cham: Springer), 1–8. doi: 10.1007/978-4-431-56582-6_1

Holloway, R. L., and De La Coste-Lareymondie, M. C. (1982). Brain endocast asymmetry in pongids and hominids: some preliminary findings on the paleontology of cerebral dominance. *Am. J. Phys. Anthropol.* 58, 101–110. doi: 10.1002/ajpa.1330580111

Holloway, R. L., Yuan, M. S., and Broadfield, D. C. (2004). *The Human Fossil Record: Brain Endocasts: the Paleoneurological Evidence*. New York, NY: John Wiley & Sons Publishers.

Hopkins, W. D., Mareno, M. C., and Schapiro, S. J. (2019). Further evidence of a left hemisphere specialization and genetic basis for tool use skill in chimpanzees (*Pan troglodytes*): reproducibility in two genetically isolated populations of apes. *J. Comp. Psychol.* 133, 512–519. doi: 10.1037/com0000183

Hopkins, W. D., Misiura, M., Pope, S. M., and Latash, E. M. (2015). Behavioral and brain asymmetries in primates: a preliminary evaluation of two evolutionary hypotheses. *Ann. N. Y. Acad. Sci.* 1359, 65–83. doi: 10.1111/nyas.12936

Hopkins, W. D., Wesley, M. J., Izard, M. K., Hook, M., and Schapiro, S. J. (2004). Chimpanzees (*Pan troglodytes*) are predominantly right-handed: replication in three populations of apes. *Behav. Neurosci.* 118:659. doi: 10.1037/0735-7044.118.3.659

Hou, L., Xiang, L., Crow, T. J., Leroy, F., Rivière, D., Mangin, J.-F., et al. (2019). Measurement of sylvian fissure asymmetry and occipital bending in humans and *Pan troglodytes*. *Neuroimage* 184, 855–870. doi: 10.1016/j.neuroimage.2018.08.045

Israfil, H., Zehr, S. M., Mootnick, A. R., Ruvolo, M., and Steiper, M. E. (2011). Unresolved molecular phylogenies of gibbons and siamangs (family: hylobatidae) based on mitochondrial, Y-linked, and X-linked loci indicate a rapid Miocene radiation or sudden vicariance event. *Mol. Phyl. Evol* 58, 447–455. doi: 10.1016/j.ympev.2010.11.005

Klingenberg, C. P., Barluenga, M., and Meyer, A. (2002). Shape analysis of symmetric structures: quantifying variation among individuals and asymmetry. *Evolution* 56, 1909–1920. doi: 10.1111/j.0014-3820.2002.tb00117.x

Lee, S.-H., and Wolpoff, M. H. (2016). The pattern of evolution in pleistocene human brain size. *Paleobiology* 29, 186–196. doi: 10.1017/S0094837300018054

Lefebvre, L., Reader, S. M., and Sol, D. (2004). Brains, innovations and evolution in birds and primates. *Brain Behav. Evol.* 63, 233–246. doi: 10.1159/000076784

LeMay, M. (1976). Morphological cerebral asymmetries of modern man, fossil man, and nonhuman primate. *Ann. N. Y. Acad. Sci.* 280, 349–366. doi: 10.1111/j.1749-6632.1976.tb25499.x

Leuret, F., and Gratiolet, P.-L. (1839). *Anatomie Comparée Du Système Nerveux: Considéré Dans Ses Rapports Avec L'intelligence*. Paris: J.-B. Bailliere.

Liu, W., Mao, Y., Wei, D., Yang, J., Du, X., Xie, P., et al. (2016). Structural asymmetry of dorsolateral prefrontal cortex correlates with depressive symptoms: evidence from healthy individuals and patients with major depressive disorder. *Neurosci. Bull.* 32, 217–226. doi: 10.1007/s12264-016-0025-x

Lozano, M., Mosquera, M., De Castro, J. M. B., Arsuaga, J. L., and Carbonell, E. (2009). Right handedness of *Homo heidelbergensis* from sima de los huesos (Atapuerca, Spain) 500,000 years ago. *Evol. Hum. Behav.* 30, 369–376. doi: 10.1016/j.evolhumbehav.2009.03.001

Mackay, C. E., Roddick, E., Barrick, T. R., Lloyd, A. J., Roberts, N., Crow, T. J., et al. (2010). Sex dependence of brain size and shape in bipolar disorder: an exploratory study. *Bipolar Disord.* 12, 306–311. doi: 10.1111/j.1399-5618.2010.00804.x

Maller, J. J., Anderson, R., Thomson, R. H., Rosenfeld, J. V., Daskalakis, Z. J., and Fitzgerald, P. B. (2015). Occipital bending (Yakovlevian torque) in bipolar depression. *Psychiatry Res. Neuroimag.* 231, 8–14. doi: 10.1016/j.pscychresns.2014.11.008

Manzi, G. (2016). Humans of the middle pleistocene: the controversial calvarium from Ceprano (Italy) and its significance for the origin and variability of *Homo heidelbergensis*. *Quat. Int.* 411, 254–261. doi: 10.1016/j.quaint.2015.12.047

Margiotoudi, K., Marie, D., Claidière, N., Coulon, O., Roth, M., Nazarian, B., et al. (2019). Handedness in monkeys reflects hemispheric specialization within the central sulcus. An in vivo MRI study in right-and left-handed olive baboons. *Cortex* 118, 203–211. doi: 10.1016/j.cortex.2019.01.001

Marie, D., Roth, M., Lacoste, R., Nazarian, B., Bertello, A., Anton, J., et al. (2018). Left brain asymmetry of the planum temporale in a nonhominid primate: redefining the origin of brain specialization for language. *Cereb. Cortex* 28, 1808–1815. doi: 10.1093/cercor/bhx096

Mcbrearty, S., and Brooks, A. S. (2000). The revolution that wasn't: a new interpretation of the origin of modern human behavior. *J. Hum. Evol.* 39, 453–563. doi: 10.1006/jhev.2000.0435

McGrew, W. C., and Marchant, L. F. (2001). Ethological study of manual laterality in the chimpanzees of the mahale mountains, Tanzania. *Behaviour* 138, 329–358. doi: 10.1163/15685390152032497

Melchionna, M., Mondanaro, A., Serio, C., Castiglione, S., Di Febbraro, M., Rook, L., et al. (2019). Macroevolutionary trends of brain mass in primates. *Biol. J. Linn. Soc.* 129, 14–25. doi: 10.1093/biolinnean/blz161

Melchionna, M., Profico, A., Serio, C., and Raia, P. (2020). *From Smart Apes To Human Brain Boxes. A Uniquely Derived Brain Shape In Late Hominins Clade: Supplementary Material*. London: Zenodo.

Meloro, C., Cáceres, N. C., Carotenuto, F., Sponchiado, J., Melo, G. L., Passaro, F., et al. (2015). Chewing on the trees: constraints and adaptation in the evolution of the primate mandible. *Evolution* 69, 1690–1700. doi: 10.1111/evo.12694

Morino, L., Uchikoshi, M., Bercovitch, F., Hopkins, W. D., and Matsuzawa, T. (2017). Tube task hand preference in captive hylobatids. *Primates* 58, 403–412. doi: 10.1007/s10329-017-0605-z

Mosquera, M., Llorente, M., Riba, D., Estebaranz, F., González-Brao, M., Lorenzo, C., et al. (2007). Ethological study of manual laterality in naturalistic housed chimpanzees (*Pan troglodytes*) from the mona foundation sanctuary (Girona, Spain). *Laterality* 12, 19–30. doi: 10.1080/13576500600886754

Mounier, A., Balzeau, A., Caparros, M., and Grimaud-Hervé, D. (2016). Brain, calvarium, cladistics: a new approach to an old question, who are modern humans and Neandertals? *J. Hum. Evol.* 92, 22–36. doi: 10.1016/j.jhevol.2015.12.006

Neubauer, S., Gunz, P., Scott, N. A., Hublin, J.-J., and Mitteroecker, P. (2020). Evolution of brain lateralization: a shared hominid pattern of endocranial asymmetry is much more variable in humans than in great apes. *Sci. Adv.* 6:eaax9935. doi: 10.1126/sciadv.aax9935

Neubauer, S., Hublin, J.-J., and Gunz, P. (2018). The evolution of modern human brain shape. *Sci. Adv.* 4:eaao5961. doi: 10.1126/sciadv.aao5961

Poza-Rey, E. M., Lozano, M., and Arsuaga, J.-L. (2017). Brain asymmetries and handedness in the specimens from the sima de los huesos site (Atapuerca, Spain). *Quat. Int.* 433, 32–44. doi: 10.1016/j.quaint.2015.10.004

Prieur, J., Lemasson, A., Barbu, S., and Blois-Heulin, C. (2019). History, development and current advances concerning the evolutionary roots of human right-handedness and language: brain lateralisation and manual laterality in non-human primates. *Ethology* 125, 1–28. doi: 10.1111/eth.12827

Prieur, J., Pika, S., Barbu, S., and Blois-Heulin, C. (2016). Gorillas are right-handed for their most frequent intraspecific gestures. *Anim. Behav.* 118, 165–170. doi: 10.1016/j.anbehav.2016.06.008

Profico, A., Buzi, C., Melchionna, M., Veneziano, A., and Raia, P. (2020). Endomaker, a new algorithm for fully automatic extraction of cranial endocasts and the calculation of their volumes. *Am. J. Phys. Anthropol.* 172:43. doi: 10.1002/ajpa.24043

Profico, A., Piras, P., Buzi, C., Di Vincenzo, F., Lattarini, F., Melchionna, M., et al. (2017). The evolution of cranial base and face in cercopithecoidea and hominoidea: modularity and morphological integration. *Am. J. Primatol.* 79:e22721. doi: 10.1002/ajp.22721

Profico, A., Schlager, S., Valoriani, V., Buzi, C., Melchionna, M., Veneziano, A., et al. (2018). Reproducing the internal and external anatomy of fossil bones: two new automatic digital tools. *Am. J. Phys. Anthropol.* 16:499. doi: 10.1002/ajpa.23493

Pujol, J., Deus, J., Losilla, J. M., and Capdevila, A. (1999). Cerebral lateralization of language in normal left-handed people studied by functional MRI. *Neurology* 52, 1038–1038. doi: 10.1212/WNL.52.5.1038

Puttick, M. N. (2016). Partially incorrect fossil data augment analyses of discrete trait evolution in living species. *Biol. Lett.* 12:20160392. doi: 10.1098/rsbl.2016.0392

Raia, P., Castiglione, S., Serio, C., Mondanaro, A., Melchionna, M., Di Febbraro, M., et al. (2020). *RRphylo: Phylogenetic Ridge Regression Methods for Comparative Studies. R Package Version 2.3.0*.

Rasmussen, T., and Milner, B. (1977). The role of early left-brain injury in determining lateralization of cerebral speech functions. *Ann. N. Y. Acad. Sci.* 299, 355–369. doi: 10.1111/j.1749-6632.1977.tb41921.x

Rightmire, G. P. (2004). Brain size and encephalization in early to mid-pleistocenehomo. *Am. J. Phys. Anthropol.* 124, 109–123. doi: 10.1002/ajpa.10346

Rilling, J. K. (2006). Human and nonhuman primate brains: are they allometrically scaled versions of the same design? *Evol. Anthropol.* 15, 65–77. doi: 10.1002/evan.20095

Rocatti, G., and Perez, S. I. (2019). The evolutionary radiation of hominids: a phylogenetic comparative study. *Sci. Rep.* 9:15267. doi: 10.1038/s41598-019-51685-w

Ruff, C. B., Trinkaus, E., and Holliday, T. W. (1997). Body mass and encephalization in pleistocene homo. *Nature* 387:173. doi: 10.1038/387173a0

Sansalone, G., Allen, K., Ledogar, J. A., Ledogar, S., Mitchell, D. R., Profico, A., et al. (2020). Variation in the strength of allometry drives rates of evolution in primate brain shape. *Proc. R. Soc. B* 20200807. doi: 10.1098/rspb.2020.0807

Schlager, S. (2017). "Morpho and Rvcg - shape analysis in R," in *Statistical Shape and Deformation Analysis*, eds G. Zheng, S. Li, and G. Szekely (Cambridge, MA: Academic Press), 217–256. doi: 10.1016/b978-0-12-810493-4.00011-0

Schnitzler, J., Theis, C., Polly, P. D., and Eronen, J. T. (2017). Fossils matter - understanding modes and rates of trait evolution in musteloidea (Carnivora). *Evol. Ecol. Res.* 18, 187–200.

Serio, C., Castiglione, S., Tesone, G., Piccolo, M., Melchionna, M., Mondanaro, A., et al. (2019). macroevolution of toothed whales exceptional relative brain size. *Evol. Biol.* 46, 332–342. doi: 10.1007/s11692-019-09485-7

Slater, G. J., Harmon, L. J., and Alfaro, M. E. (2012). Integrating fossils with molecular phylogenies improves inference of trait evolution. *Evolution* 66, 3931–3944. doi: 10.1111/j.1558-5646.2012.01723.x

Sommer, I. E. C., Ramsey, N. F., and Kahn, R. S. (2001). Language lateralization in schizophrenia, an fMRI study. *Schizophr. Res.* 52, 57–67. doi: 10.1016/S0920-9964(00)00180-8

Stout, D. (2011). Stone toolmaking and the evolution of human culture and cognition. *Philos. Trans. R. Soc. B* 366, 1050–1059. doi: 10.1098/rstb.2010.0369

Stout, D., and Khreisheh, N. (2015). Skill learning and human brain evolution: an experimental approach. *Camb. Archaeol. J.* 25, 867–875. doi: 10.1017/S0959774315000359

Szaflarski, J. P., Binder, J. R., Possing, E. T., McKiernan, K. A., Ward, B. D., and Hammeke, T. A. (2002). Language lateralization in left-handed and ambidextrous people: fMRI data. *Neurology* 59, 238–244. doi: 10.1212/WNL.59.2.238

Tobias, P. V. (1987). The brain of *Homo habilis*: a new level of organization in cerebral evolution. *J. Hum. Evol.* 16, 741–761. doi: 10.1016/0047-2484(87)90022-4

Toga, A. W., and Thompson, P. M. (2003). Mapping brain asymmetry. *Nat. Rev. Neurosci.* 4, 37–48. doi: 10.1038/nrn1009

Uomini, N. T. (2009). The prehistory of handedness: archaeological data and comparative ethology. *J. Hum. Evol.* 57, 411–419. doi: 10.1016/j.jhevol.2009.02.012

Uomini, N. T. (2015). "Paleoneurology and behaviour," in *Human Paleoneurology*, ed. E. Bruner (Cham: Springer), 121–143. doi: 10.1007/978-3-319-08500-5_6

Uomini, N. T., and Meyer, G. F. (2013). Shared brain lateralization patterns in language and acheulean stone tool production: a functional transcranial doppler ultrasound study. *PLoS One* 8:e72693. doi: 10.1371/journal.pone.0072693

Walker, S. F. (1980). Lateralization of functions in the vertebrate brain: a review. *Br. J. Psychol.* 71, 329–367. doi: 10.1111/j.2044-8295.1980.tb01750.x

Weaver, T. D., and Gunz, P. (2018). Using geometric morphometric visualizations of directional selection gradients to investigate morphological differentiation. *Evolution* 72, 838–850. doi: 10.1111/evo.13460

Weber, G. W. (2014). Virtual anthropology. *Am. J. Phys. Anthropol.* 156, 22–42. doi: 10.1002/ajpa.22658

White, R., Bosinski, G., Bourrillon, R., Clottes, J., Conkey, M. W., Rodriguez, S. C., et al. (2019). Still no archaeological evidence that Neanderthals created Iberian cave art. *J. Hum. Evol.* 17:102640. doi: 10.1016/j.jhevol.2019.102640

Wu, X., Schepartz, L. A., Falk, D., and Liu, W. (2006). Endocranial cast of Hexian *Homo erectus* from South China. *Am. J. Phys. Anthropol.* 130, 445–454. doi: 10.1002/ajpa.20378

Xiang, L., Crow, T., and Roberts, N. (2019). Cerebral torque is human specific and unrelated to brain size. *Brain Struct. Funct.* 224, 1141–1150. doi: 10.1007/s00429-018-01818-0

Yakovlev, P. I., and Rakic, P. (1966). Patterns of decussation of bulbar pyramids and distribution of pyramidal tracts on two sides of the spinal cord. *Trans. Am. Neurol. Assoc.* 91, 366–367.

Zilhão, J., Angelucci, D. E., Badal-García, E., d'Errico, F., Daniel, F., Dayet, L., et al. (2010). Symbolic use of marine shells and mineral pigments by Iberian Neandertals. *Proc. Natl. Acad. Sci. U.S.A.* 107, 1023–1028. doi: 10.1073/pnas.0914088107

Zollikofer, C. P. E., and De León, M. S. P. (2013). Pandora's growing box: inferring the evolution and development of hominin brains from endocasts. *Evol. Anthropol.* 22, 20–33. doi: 10.1002/evan.21333

Conflict of Interest: The authors declare that the research was conducted in the absence of any commercial or financial relationships that could be construed as a potential conflict of interest.

frontiers in Earth Science

ORIGINAL RESEARCH
published: 24 July 2020
doi: 10.3389/feart.2020.00248

Upper Paleozoic to Lower Mesozoic Tetrapod Ichnology Revisited: Photogrammetry and Relative Depth Pattern Inferences on Functional Prevalence of Autopodia

Eudald Mujal[1,2†], Lorenzo Marchetti[3†], Rainer R. Schoch[1†] and Josep Fortuny[2†]*

[1] Staatliches Museum für Naturkunde Stuttgart, Stuttgart, Germany, [2] Institut Català de Paleontologia Miquel Crusafont, Cerdanyola del Vallès, Spain, [3] Urweltmuseum GEOSKOP/Burg Lichtenberg (Pfalz), Tallichtenberg, Germany

In recent years photogrammetry has become an essential tool in the study of tetrapod footprints. Morphological analyses of footprints are interpretative; thus, researchers should use as much information as possible in order to eventually provide an objective conclusion. In this regard, photogrammetry is an extremely helpful tool to avoid potential biases and to better present ichnological data. We review the use of this technique in several Permian and Triassic tetrapod ichnological studies, with considerations on (1) ichnotaxonomy, (2) track-trackmaker correlation, (3) locomotion and/or behavior, (4) substrate induced effects, and (5) preservation of the fossil record and heritage. Furthermore, based on the available three-dimensional (3D) data on Permian and Triassic material, we present a first qualitative interpretation of relative depth patterns and the related functional prevalence (most deeply impressed area) within footprints. We identified three main groups: (1) anamniote, captorhinomorph/parareptile tracks (medial-median functional prevalence), (2) diapsid tracks (median functional prevalence), and (3) synapsid tracks (median-lateral functional prevalence). The use of 3D photogrammetric models brings new light to the tetrapod footprint record, helping to better understand tetrapod communities throughout the late Paleozoic (and the end-Guadalupian and end-Permian extinctions) and the tetrapod recovery during the early Mesozoic.

Keywords: photogrammetry, tetrapod ichnology, ichnotaxonomy, locomotion, preservation, Permian, Triassic

OPEN ACCESS

Edited by:
Martin Daniel Ezcurra, Museo Argentino de Ciencias Naturales Bernardino Rivadavia, Argentina

Reviewed by:
Silvina De Valais, CONICET Research Institute in Paleobiology and Geology (IIPG), Argentina
Steven W. Salisbury, The University of Queensland, Australia
Verónica Krapovickas, Consejo Nacional de Investigaciones Científicas y Técnicas (CONICET), Argentina

***Correspondence:**
Josep Fortuny
josep.fortuny@icp.cat

†ORCID:
Eudald Mujal
orcid.org/0000-0002-6310-323X
Lorenzo Marchetti
orcid.org/0000-0002-1047-7887
Rainer R. Schoch
orcid.org/0000-0002-0312-2877
Josep Fortuny
orcid.org/0000-0003-4282-1619

Specialty section:
This article was submitted to Paleontology, a section of the journal Frontiers in Earth Science

Received: *20 December 2019*
Accepted: *05 June 2020*
Published: *24 July 2020*

Citation:
Mujal E, Marchetti L, Schoch RR and Fortuny J (2020) Upper Paleozoic to Lower Mesozoic Tetrapod Ichnology Revisited: Photogrammetry and Relative Depth Pattern Inferences on Functional Prevalence of Autopodia. Front. Earth Sci. 8:248. doi: 10.3389/feart.2020.00248

INTRODUCTION

Tetrapod footprints are abundant vertebrate remains in upper Paleozoic to lower Mesozoic terrestrial successions (Klein and Lucas, 2010; Lucas, 2019). Their study facilitates the reconstruction of past ecosystems, especially where skeletal remains are absent, scattered, or poorly preserved. Tetrapod tracks of late Carboniferous to Middle Triassic age have been intensively studied since the 19th century, and especially during the 20th century, with the publication of an extensive literature that includes research articles, books, and monographies (among many other publications: Kaup, 1835; Geinitz, 1861, 1863; Curioni, 1870; Geinitz and Deichmüller, 1882; Pabst, 1895, 1908; Marsh, 1894; Maidwell, 1911; Nopcsa, 1923; Gilmore, 1927; Moodie, 1929, 1930;

Abel, 1935; Peabody, 1948; Heyler and Lessertisseur, 1963; Haubold, 1970, 1971a,b; Gand, 1987). These works often include morphological analyses, usually comprising (1) a graphic interpretation (mostly represented by line and shadow drawings) of footprints and (2) a quantification of the track and trackway proportions by measuring different features (for measurement standards: Haubold, 1971b; Leonardi, 1987). Such analyses form the basis of ichnotaxonomy that follows the rules of the International Code of Zoological Nomenclature (ICZN; International Commission on Zoological Nomenclature, 1999). Based on these morphological analyses, hundreds of ichnotaxa (grouped in ichnogenera and ichnospecies, and sometimes in ichnofamilies as well) have been erected. Nevertheless, in several studies the conditions of the original substrate (e.g., composition, granulometry, original moisture, rheology) where footprints were impressed and the behavior of the trackmakers have not been fully considered, though such factors are the main constraints (together with the autopodia anatomy) of the final track morphology (Falkingham, 2014; Gatesy and Falkingham, 2017; Belvedere et al., 2018; Marchetti et al., 2019a). Therefore, several ichnotaxa have been erected on the basis of extramorphological features, which represent variations not due to the foot anatomy (Peabody, 1948; Haubold, 1996). This has resulted in an oversplitting of ichnotaxa and also, in particular cases, in an oversimplification (McKeever and Haubold, 1996; Marchetti et al., 2019c,d). This is why footprints useful for ichnotaxonomy need to be selected by means of morphological preservation, which is the preservation of features derived from the foot anatomy (Marchetti et al., 2019a).

At the end of the 20th century, new techniques to create 3D digital models started to be applied in tetrapod ichnology, revolutionizing this field. These techniques allowed a better understanding of the processes of footprint formation, and thus of producers' locomotion, by creating virtual 3D models of this mechanism (e.g., Gatesy et al., 1999; Falkingham and Gatesy, 2014). 3D digital modeling rapidly expanded in dinosaur ichnology by digitizing actual fossil footprints in order to provide more objective interpretations and measurements (e.g., Leonardi and Mietto, 2000; Bates et al., 2008a,b, 2010; Petti et al., 2008). However, 3D modeling has not been widely used in the study of Permian and Triassic tetrapod ichnofossils, with few exceptions including 3D models, mostly used as complementary representations of footprints (e.g., de Klerk, 2002; Petti et al., 2009). In the beginning, the use of 3D techniques, often based on laser scanning, was very limited, especially due to the cost and limited portability of the scanners; however, this completely changed with the rapid advances of photogrammetric techniques (Matthews, 2008; Remondino et al., 2010; Falkingham, 2012; Mallison and Wings, 2014; Falkingham et al., 2018). In fact, because of its low cost and efficiency, photogrammetry rapidly spread out in ichnological studies, especially in dinosaur ichnology. The introduction of 3D models brought more objectivity to the analyses of a given morphology. Several studies focused in the best procedure to obtain the raw data for 3D photogrammetric models (i.e., digital photos), as well as in the methodologies to create models and/or how they should be studied and presented in scientific articles (e.g., Matthews, 2008; Petti et al., 2008; Falkingham, 2012; Mallison and Wings, 2014; Belvedere et al., 2018; Falkingham et al., 2018). Historical photogrammetry, in which 3D digital models are created from scans of analog photographs taken before photogrammetry even existed (e.g., Falkingham et al., 2014; Lallensack et al., 2015), is now also being used. Only recently, several works dealing with tetrapod footprints from the Permian and Triassic (and, to a lesser degree, the upper Carboniferous) used photogrammetry to better interpret the morphology of the tetrapod footprints and locomotion (e.g., Mujal et al., 2015, 2016b, 2017a; Marchetti et al., 2017a, 2019c,d; Citton et al., 2018; Lagnaoui et al., 2019; Mujal and Marchetti, 2020; Mujal and Schoch, 2020; and references therein).

The study between non-avian dinosaur ichnology and Permian–Triassic tetrapod ichnology is slightly different, though they both follow the same conventions and use the same methodologies to correctly interpret the footprint morphology. In fact, non-dinosaur tetrapod footprints are generally smaller in comparison with most dinosaur footprints and show a higher degree of complexity, whereas dinosaur tracks (with some exceptions related to small-sized dinosaur ichnotaxa) show more complex depth patterns and thus difficulties to trace footprint outlines (e.g., Lallensack, 2019). In this work, we review different ichnofossil records in which photogrammetry was used, ranging from the lower Permian (Cisuralian) to the Middle Triassic. We review previously published works on tetrapod ichnology including 3D models. In addition, in order to provide a wider overview and for further comparisons, we also create new 3D models of some tracks and ichnotaxa, from which photogrammetric studies have not been carried out. We synthesize examples with the aim to demonstrate how photogrammetry helped in the ichnological analyses, not only for newly uncovered fossils but also in ichnotaxonomic revisions. We identify up to five fields in which photogrammetry is of great use: (1) ichnotaxonomy, (2) track-trackmaker correlations, (3) locomotor and/or behavioral considerations, (4) substrate induced effects, (5) preservation of the fossil record and heritage. Moreover, for the first time, we discuss the footprint relative depth patterns of the most important upper Carboniferous, Permian, and Triassic tetrapod groups using 3D digital models and compare them to the phylogenies of these groups.

MATERIALS AND METHODS

Elaboration of 3D Photogrammetric Models

Photogrammetry plays a prominent role in tetrapod ichnological analyses and is essential in some cases (e.g., in the identification of the true shape of footprints when other techniques fail). Furthermore, a single 3D model can be used for different purposes. Photogrammetry provides important information in ichnotaxonomy, in track-trackmaker correlations, in elucidating the locomotion of the producers, in the reconstruction of taphonomic processes and of paleoenvironmental settings, as well as in the digital preservation of this heritage.

Herein, we provide a brief resume of how we created 3D photogrammetric models. Noteworthy, the majority of the examples reviewed in this work are uncollected specimens. In this case, the photographs for the 3D models were obtained during fieldwork, so the data collection was usually constrained by the natural light conditions. The following work flow is modified from Mujal (2017).

Overall, photogrammetry relies on obtaining digital 3D models of an object. The photogrammetric models are built from photos of the specimens (**Figure 1**). For detailed explanations on the procedures of photo acquisition, we refer to Matthews (2008), Falkingham (2012), and Mallison and Wings (2014). In the examples presented here, these procedures were set according to the (field) conditions of each specimen. First of all, the track-bearing surface must be cleaned. Then, centimetric and/or millimetric scales, as well as white paper squares with specific black geometric forms (being easily recognizable by the modeling software), are placed around the footprint or trackway to be modeled (**Figure 1A**). Afterward light conditions are evaluated, as specimens must not have too much shadow nor too many bright zones during the photo acquisition. If necessary, a (weak) shadow is projected over the entire specimen to be modeled in order to obtain homogeneous light conditions. Once light conditions are suitable, photographs can be taken in these ways: (1) photos of the specimen from all its perspectives and angles, i.e., moving along a cupola- or umbrella-like form around the specimen while photographing (**Figure 1B**), and/or (2) photos orthogonal to the surface, covering the entire area to be modeled and taking into account that two consecutive photos must overlap at least one third (**Figure 1C**). On average, 30 photos per footprint/pes-manus couple were taken, but this number varies according to the size and complexity of each specimen (e.g., some models are built up with 50, 60, and 70 photos, or in specific cases, such as whole trackways, with more than 200 photos). The use of camera tripods is recommended, although in most cases (for specimens in the field) they cannot be used due to the location of the samples. Different digital cameras were used, all being characterized by having at least 8.1 Megapixel of resolution. The cameras we used are Sony DSC-T200, device standard lens 35–175 mm F3.5–F4.4; Sony DSC-H50, device standard lens 31–465 mm F2.7–F4.5; Panasonic DMC-FZ18, device standard lens 28–504 mm F2.8–F4.2; Canon PowerShot SX410 IS, device standard lens 4.3–172 mm F.3.5–F6.3; Canon EOS 70D, lenses 18–135 mm and 10–18 mm; focal lengths are usually of 4, 5, or 6 mm. Once the photos were obtained, they were processed by a workstation, with recommended minimum requirements: i7 processor (or equivalent-updated) with minimum 32GB RAM and graphic card GeForce RTX 2060 equivalent or updated. Photos were taken (in JPG format) without any size reduction in different software, most of which are freely available:

(1.1) Visual SfM (open access; v.0.5.22 to v.0.5.25[1]): Generation of the dense point cloud on which the 3D model is based (**Figures 1B,C**).

(1.2) Agisoft Photoscan (standard version 1.1.4[2]): Generation of the dense point cloud and the triangular mesh, and application of the original texture (i.e., color) of the specimen.

(2) MeshLab (open access; v.1.3.2 and v.2016.12[3]): (1) generation of the triangular mesh based on the dense point cloud; (2) application of the original texture (i.e., color) of the specimen; (3) cleaning (removing) of the generated odd points; (4) aligning, scaling, and orientation of the 3D model (**Figure 1D**). Note that the two first steps are unnecessary if Agisoft Photoscan is used.

(3) ParaView (open access; v.3.98.1 to v.4.1.0[4]): Generation of the depth map by using a color scale and application of the contours (**Figure 1E**). In order to provide a homogeneous view of the whole track sample, in this work we have used the "Rainbow Desaturated" filter for the elevation map. Otherwise, the number of contours is set according to the complexity of each specimen; the number of lines in each model generally varies between 30 and 60.

Depth Pattern Analysis

We conducted a qualitative analysis aiming to identify and classify depth patterns among tetrapod ichnotaxa from the upper Carboniferous to the Middle Triassic (see section "Relative Depth Patterns on Permian to Triassic Tetrapod Footprints" below). The database includes new data and a review of the published 3D data (de Klerk, 2002; Mujal et al., 2015, 2016a,b, 2017a,b, 2018b; Citton et al., 2016, 2018, 2019a,b, 2020; Meade et al., 2016; Milàn et al., 2016; Marchetti et al., 2017a,b, 2018a,b, 2019b,c,d; Francischini et al., 2018, 2020; Lagnaoui et al., 2019; Marchetti, 2019; Cavin and Piuz, 2020; Cisneros et al., 2020; Farman and Bell, 2020; Mujal and Marchetti, 2020; Mujal and Schoch, 2020; Reolid et al., 2020). Note that the number of tracks and localities from the upper Carboniferous is notably lower than those from the lower Permian. Nevertheless, most of the upper Carboniferous ichnotaxa are also present in the lower Permian (Lucas, 2019, and references therein).

In order to avoid misinterpretations, here we define the functional prevalence of footprints as the part of the footprint that is more deeply impressed than the other parts of the same footprint. This character must be consistent along a trackway and/or between tracks assigned to the same ichnotaxon, and under different substrate (as well as different paleoenvironments) and locomotory conditions.

The relative depth patterns of footprints are independent from all the ichnotaphonomic effects as defined by Marchetti et al. (2019a). Therefore, it should be related to the functional anatomy of the trackmakers' postcranial skeleton (or, more specifically, autopodia). Medial, median, and lateral refer to the inner, middle, and outer parts, respectively, of a footprint as defined by Leonardi (1987). To characterize the track-bearing substrate (e.g., mudstone, sandstone, limestone), we evaluated composition, granulometry, and sedimentary structures. Such information, when available (e.g., some tracks are currently only documented by artificial casts), was integrated with data from the

[1] www.ccwu.me/vsfm/

[2] www.agisoft.com

[3] meshlab.sourceforge.net

[4] www.paraview.org

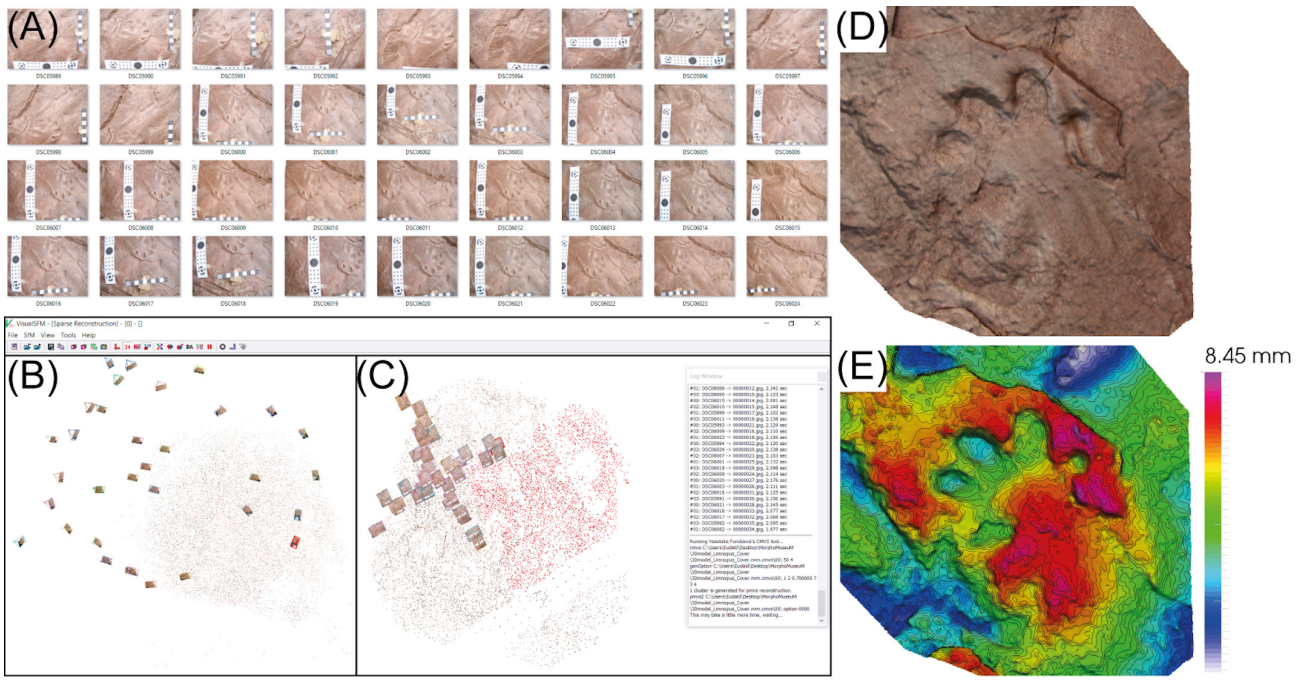

FIGURE 1 | Photogrammetry workflow (from Mujal, 2017). **(A)** Set of photos to generate the 3D model with different centimetric scales. **(B,C)** Relative position of the photos as seen in Visual SfM software; photos were obtained changing the perspective in each one **(B)** and moving the camera laterally **(C)**. **(D)** 3D model with the original texture of the specimen as prepared with MeshLab. **(E)** Depth color map and contours of the 3D model as prepared with ParaView. **(A,C–E)** Correspond to the same modeling process. The example used is a right manus-pes couple of *Limnopus* isp. from the Pyrenean Basin (corresponding mold and replica are IPS82608).

geological successions that yielded the studied specimens. For the sake of clarity, and as further explained in section "Relative Depth Patterns on Permian to Triassic Tetrapod Footprints" below, the substrate features, if not relevant for the analysis, are not specified nor discussed.

Tetrapod Ichnoassociations From the Lower Permian to the Middle Triassic

Here, we list the localities yielding the tetrapod ichnofossil record (for which 3D photogrammetric models were created) reviewed in section "Results and Discussion" below; further details on such localities are found in the **Supplementary Data S1**. The label of each analyzed specimen is mentioned through the present work and/or in the corresponding figure caption (see also institutional abbreviations below). For further specimen numbers we also refer the reader to the publications herein cited.

- Pyrenean Basin (northeastern Iberian Peninsula):
    - Artinskian (Cisuralian) ichnoassociations from the Lower Red Units (time-equivalent to the Peranera Formation) (see Gisbert, 1981; Voigt and Haubold, 2015; Mujal et al., 2016a, 2018a) analyzed by Mujal et al. (2016b), who included 3D models.
    - Guadalupian–Lopingian ichnoassociation from the Upper Red Unit analyzed by Mujal et al. (2017b), who included 3D models.
    - Lower–Middle Triassic ichnoassociations from the Buntsandstein facies unit analyzed by Mujal et al. (2016a, 2017a), who included 3D models.
- Catalan Basin (northeastern Iberian Peninsula): Middle Triassic ichnoassociations from the Buntsandstein facies (early–middle Anisian; Fortuny et al., 2011, who did not include 3D models) and middle Muschelkalk facies (late Anisian–middle Ladinian; Mujal et al., 2015, 2018b, who included 3D models).
- Lodève Basin (southern France; for units datations see Michel et al., 2015):
    - Asselian (Cisuralian) trackways of *Ichniotherium cottae* from the Usclas Saint Privat or the Tuillières-Loiras formations (previously studied by Heyler and Lessertisseur, 1963; recently reanalyzed by Mujal and Marchetti, 2020, who included 3D models).
    - Artinskian (Cisuralian) ichnoassociations from the Rabejac Formation (e.g., Gand, 1987; Heyler and Gand, 2000; Gand and Durand, 2006, who did not include 3D models).
    - Guadalupian tracks of *Merifontichnus* from the La Lieude Formation (e.g., Gand et al., 2000, who did not include 3D models).
    - Middle Triassic archosauromorph tracks from red-bed deposits (e.g., Demathieu, 1985;

Dematheieu and Demathieu, 2004; Gand et al., 2007, and references therein, who did not include 3D models).

- Orobic Basin (northern Italy): Kungurian (Cisuralian) trackway of *Amphisauropus kablikae* from the Pizzo del Diavolo Formation of the Orobic Basin (see Marchetti et al., 2015; Marchetti, 2016) analyzed by Marchetti et al. (2017a), who included 3D models.
- Hessian Basin (Germany): Lopingian ichnoassociations from eolian units of the Cornberg Formation (see Schmidt, 1959) analyzed by Marchetti et al. (2019c), who included 3D models.
- Central European Basin (Germany): Ladinian (Middle Triassic) tracks from the base of the Antrhakonitbank at the Vellberg *Fossil-Lagerstätte*, Lower Keuper (Erfurt Formation; see Schoch and Seegis, 2016) analyzed by Mujal and Schoch (2020), who included 3D models.
- Lochmaben and Dumfries basins (Scotland, United Kingdom): Lopingian ichnoassociations from eolian units of the Cornockle and Locharbriggs formations (see Anonymous, 1828; Jardine, 1853; McKeever and Haubold, 1996) analyzed by Marchetti et al. (2019c), who included 3D models.
- Arizona (United States): Kungurian (Cisuralian) ichnoassociations from the eolian units of the De Chelly and Coconino formations (see Gilmore, 1927; Haubold et al., 1995a) analyzed by Marchetti et al. (2019b), who included 3D models.
- Karoo Basin (South Africa): Guadalupian to Lower Triassic ichnoassociations from continental fluvial units of the Abrahamskraal, Teekloof, and Balfour formations (see Smith and Botha-Brink, 2014; Klein et al., 2015) analyzed by Marchetti et al. (2019d), who included 3D models.

Institutional Abbreviations

AM, Albany Museum, Grahamstown (Makhanda, as of 4 October 2018), South Africa.
DUMFM, Dumfries Museum and Camera Obscura, Dumfries, Scotland, United Kingdom.
EMVG, 'Casa del Tempo', Ecomuseo della Val Gerola, Sondrio, Lombardy, Italy.
IPS, Institut Català de Paleontologia Miquel Crusafont, Sabadell, Catalonia, Spain.
MF-LOD, Lodève collection at Musée Fleury, Lodève, France.
MNA, Museum of Northern Arizona, Flagstaff, AZ, United States.
MNHN.F.LOD, Lodève collection at Muséum National d'Histoire Naturelle, Paris, France.
NHMUK PV, British Museum of Natural History, London, United Kingdom.
NMK, Museum of Natural History in the Ottoneum, Kassel, Germany.
RAM, Raymond M. Alf Museum of Paleontology, Claremont, CA, United States.
RMS, National Museum of Scotland, Edinburgh, Scotland, United Kingdom.
SMNS, Staatliches Museum für Naturkunde Stuttgart, Stuttgart, Germany.
UCMP, University of California, Berkeley, CA, United States.
UG, Faculty of Geoscience and Geography, Göttingen University, Göttingen, Germany.
UGKU, Urweltmuseum GEOSKOP/Burg Lichtenberg (Pfalz), Tallichtenberg, Germany.
UM-LOD, Lodève collection at Université de Montpellier, Montpellier, France.
USNM, Smithsonian – National Museum of Natural History, Washington, DC, United States.
YPM, Yale Peabody Museum of Natural History, New Haven, CT, United States.

RESULTS AND DISCUSSION

Herein, we present a review of research on tetrapod tracks involving 3D photogrammetric models. Taken together, the analyzed examples cover both a long age interval (Cisuralian to Middle Triassic) and a wide range of substrates and paleoenvironments (eolian, fluvial, lacustrine, and coastal settings). Subsequently, we provide a first analysis based on the relative depth pattern of tetrapod footprints, suggesting a link with the functional prevalence of autopodia.

Photogrammetry: A Toolkit for Ichnologists

Following we identify different ichnological fields in which photogrammetry is useful, independently from the analyzed ichnotaxon, age, substrate, and paleoenvironment.

Ichnotaxonomy

Tetrapod ichnotaxonomy is primarily based on the morphology of footprints (distinguishing manual and pedal impressions for quadruped trackmakers) and, to a lesser extent, on the trackway pattern. In ideal conditions, the footprint morphology and the trackway pattern are considered to reflect anatomical traits of the trackmaker (e.g., Olsen, 1995; Carrano and Wilson, 2001; Belvedere et al., 2018; Marchetti et al., 2019a). In fact, each ichnotaxon could be potentially correlated with a specific trackmaker group, often at family or higher level groups (Falcon-Lang et al., 2010).

Anatomy-consistent morphology is the very base of ichnotaxonomy (e.g., Baird, 1957; Haubold et al., 1995b; Haubold, 1996; Marchetti et al., 2019a). Autopodial anatomy is recorded during the trackmaker's locomotion, i.e., footprints record a dynamic behavior. Therefore, before doing ichnotaxonomical inferences, the process of autopodia impression in the sediment should be understood (e.g., Gatesy et al., 1999; Falkingham and Gatesy, 2014; Gatesy and Falkingham, 2017; Mujal and Schoch, 2020). In addition, the effects of the substrate conditions at the time of impression should be considered (see also section "Relative Depth Patterns on Permian to Triassic Tetrapod Footprints" below), because they can alter significantly the morphological traits linked to anatomy (Falkingham, 2014). Moreover, a number of other effects occurring after the track recording, such as trace fossil

and sedimentary structure superimpositions and the sediment erosion, should be correctly interpreted (e.g., Marty et al., 2009). Nonetheless, as shown in section "Relative Depth Patterns on Permian to Triassic Tetrapod Footprints" below, we observe that 3D models help to identify the anatomy-related ichnotaxa morphology through the analysis of shape and relative depth patterns of imprints, even if the track morphologies are apparently different due to different substrates. Therefore, 3D models help in comparing track morphologies useful for ichnotaxonomy, thus avoiding oversplitting or overlumping of ichnotaxa that would have no faunistic and hence no evolutionary, biomechanic, biostratigraphic, and paleobiogeographic meaning (e.g., Marchetti et al., 2019a,d; Mujal and Marchetti, 2020).

3D models help to identify important anatomy-consistent features of both new and already known ichnotaxa that may remain unseen to the naked eye. Indeed, this is the case of several ichnotaxa (including different morphologies and sizes) from previously published specimens. Herein we review and summarize examples from some of our studies (see section "Tetrapod Ichnoassociations from the Lower Permian to the Middle Triassic" above and **Supplementary Data S1**) showing the use of 3D photogrammetric models in recognizing relevant ichnotaxonomic features:

- The complete shape of pedal impressions in MNHN.F.LOD83 from the Cisuralian of southern France re-analyzed by Mujal and Marchetti (2020) was identified through the study of the 3D model that these authors carried out (**Figure 2A**). Impressions of pedal digits IV and V (roman numbers and red arrows in **Figure 2A**) are unclear when observed in the original specimen, but a consistent depth pattern was observed in the false color depth maps. The 3D model also facilitated the identification of two trackways, which were also unclear from the previous analysis by Heyler and Lessertisseur (1963). The actual length of several digit impressions, as well as the shape of sole and palm impressions, is masked by the presence of digit scratches and other irregularities of the surface; nevertheless, the false color maps allowed for the discrimination of all these features. Because of the correct recognition of these features, Mujal and Marchetti (2020) assigned the tracks of MNHN.F.LOD83 to *Ichniotherium cottae*, being the first unambiguous report of this ichnogenus from the French Lodève Basin.
- In some *Limnopus* isp. specimens (some of the originals were not collected; e.g., mold and replica IPS82608), from the Artinskian of the Catalan Pyrenees studied by Mujal et al. (2016b), the actual shape of the tracks (including also diagnostic features of the ichnogenus, such as the number of digit impressions and their relative length and proportions) was inferred from the false color depth maps, which also revealed the presence of deformed pedal impressions (**Figure 2B**).
- The tracks referred to cf. *Varanopus* (original not collected; mold and replica IPS82607) by Mujal et al. (2016b) (**Figure 2C**) are notably deformed (most probably due to an originally water-saturated substrate), and the digit impressions were recognized only after the study of the false color depth maps. The 3D model that Mujal et al. (2016b) published better illustrates the orientation of the footprints, allowing observation of the trackway arrangement and thus providing correct measurement of the trackway parameters. In the same way, some digital impressions (e.g., from the pedal track in Mujal et al., 2016a; **Figure 2C**) were only recognized through the study of the 3D model, because their relief is relatively low. All these features are diagnostic of *Varanopus*; nonetheless, given the relatively poor preservation of the tracks, an open nomenclature was preferred by Mujal et al. (2016b), which we follow here.
- The *Hyloidichnus* isp. specimens (not collected) studied by Mujal et al. (2016b) could only be identified after analyzing the 3D model of a manus-pes set (**Figure 2D**). The impression of pedal digit IV was first identified in the false color depth map provided by Mujal et al. (2016b): such impression is partially masked (overprinted) by rain drop impressions and flow ripples. In fact, it is a very shallow impression that could not be distinguished on photographs due to the light conditions. After this first identification, further tracks from the same surface and stratigraphically close levels (not collected) were also classified as *Hyloidichnus* isp. by Mujal et al. (2016b).
- The type material of *Laoporus* (YPM 2143, 2144, USNM V 8422) from the Kungurian Coconino Fm. of the United States was recently re-analyzed by Marchetti et al. (2019d), who concluded that the supposed diagnostic features of this ichnogenus (subequal pes and manus with digit impressions of subequal length) were actually due to the locomotion on sandy inclined planes (dune foreset surfaces). The 3D model created by Marchetti et al. (2019d) allowed to identify both the generally deeper, parallel, and sub-equal digit drag traces and the actual digit imprints, which are generally shorter, shallower, and with a different orientation (arrows in **Figure 2E**). Therefore, the inferred digit impressions of *Laoporus* are actually digit drag traces parallel to the slope and they actually represent the digit sliding during locomotion. Therefore, this ichnogenus is considered a *nomen dubium* and this material is assigned to cf. *Varanopus* isp. based on anatomy-consistent features, i.e., the actual length of digit impressions and their relative proportions (for further details, see Marchetti et al., 2019d) (**Figure 2E**).
- The holotype of *Chelichnus duncani* (DUMFM 5) from the Lopingian of Scotland, United Kingdom, was re-analyzed with the aid of photogrammetry by Marchetti et al. (2019c). The 3D model shows a ridge between the digit tip and the digit base impressions. This was an important feature for the assignment of this material to cf. *Dicynodontipus* and for its attribution to therapsid tracks. *C. duncani* is considered a *nomen dubium* due to its incompleteness, especially as regards the pes imprints.
- The study of the false color depth maps on 3D models was central for the ichnotaxonomic revision of

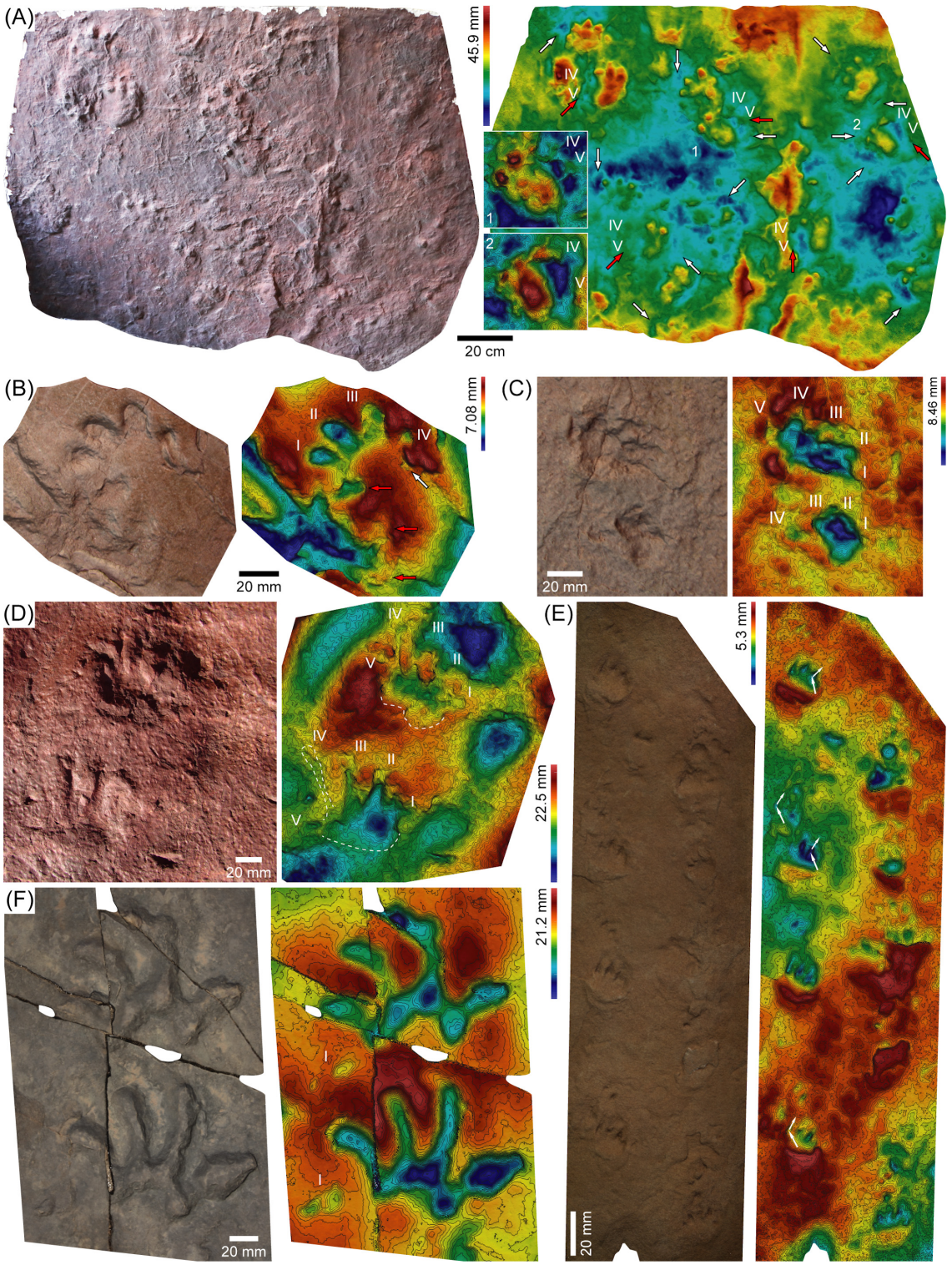

FIGURE 2 | 3D models [except **(A,D)**, which include a photo instead] and corresponding depth maps of Cisuralian **(A–E)** and Lopingian **(F)** ichnotaxa. **(A)** Tracks and trackways of *Ichniotherium cottae* (MNHN.F.LOD83), Lodève Basin; arrows indicate expulsion rims (white) and pedal digit V impressions (red); 1 and 2 indicate detailed 3D models of pes tracks showing digits IV and V. **(B)** Right manus-pes couple of *Limnopus* isp. (mold and replica IPS82608), Pyrenean Basin; arrows indicate parts of the pes track (red) and a hole on the substrate that apparently looked like a digit impression (white). **(C)** Left manus-pes couple of cf. *Varanopus* (mold and replica IPS82607), Pyrenean Basin. **(D)** Left manus-pes couple of *Hyloidichnus* isp., Pyrenean Basin. **(E)** Trackway in upslope progression of cf. *Varanopus* (YPM 2143), Coconino Formation; arrows indicate sliding and true orientation of digit impressions. **(F)** Right manus-pes couple of *Karoopes gansfonteinensis* (GF-TR 1), Karoo Basin.

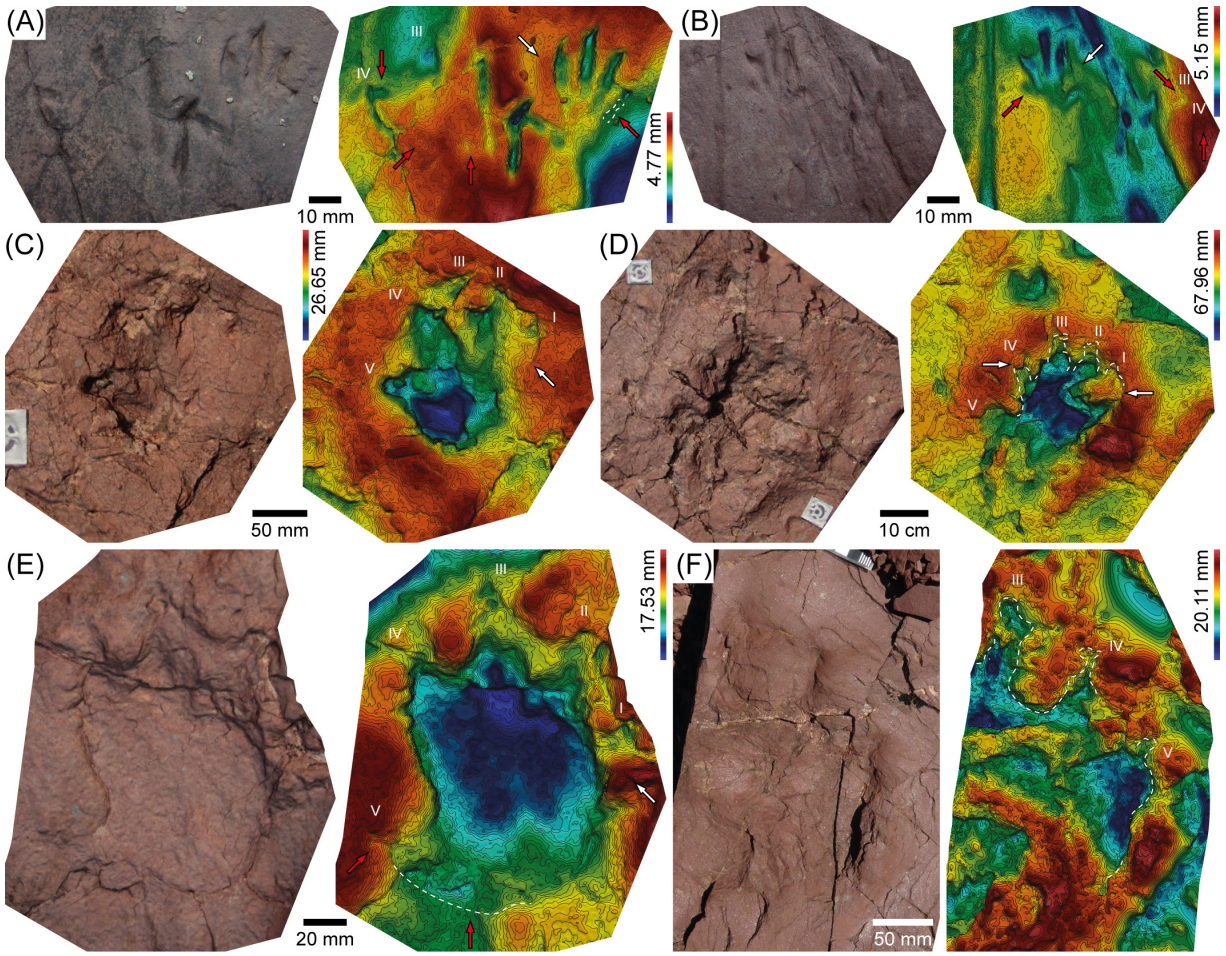

FIGURE 3 | 3D models [except **(F)**, which includes a photo instead] and corresponding depth maps of Lower–Middle Triassic archosauromorph tracks from the Pyrenean Basin. **(A,B)** Left **(A)** and right **(B)** manus-pes couples of *Prorotodactylus mesaxonichnus*. **(C,D)** Manus **(C)** and pes **(D)** tracks of a left couple of Chirotheriidae indet. (similar to *Protochirotherium*; mold and replica IPS82616). **(E)** Chirotheriidae indet. left track similar to *Protochirotherium*. **(F)** Large partial right pes track of Chirotheriidae indet. Arrows indicate anatomical (red) and sedimentary (e.g., digits collapse) (white) features; see text for discussion.

the Guadalupian–Lower Triassic tetrapod tracks from South Africa (Marchetti et al., 2019d). This is true especially for the erection of the ichnotaxon *Karoopes gansfonteinensis*, which is characterized by tracks more deeply impressed laterally (e.g., GF-TR 1, 2, 3, SAM-NN 3) (**Figure 2F**). This is an important feature different from some morphologically similar captorhinomorph tracks such as *Hyloidichnus* and *Merifontichnus*. The same is observed in material assigned to cf. *Capitosauroides* isp. (GF-TR 9, GFTS 1, SAM-PK-K 7878a, b). Because of the deeper lateral impression of these tracks, an assignment to *Batrachichnus* or *Limnopus* (anamniote ichnogenera) could be discarded by Marchetti et al. (2019d), although the overall morphology is quite similar, especially in incomplete imprints. Therefore, as we further discuss in section "Relative Depth Patterns on Permian to Triassic Tetrapod Footprints" below, the relative depth pattern allows the clear distinction of *Karoopes* and *Capitosauroides* from captorhinomorph and anamniote ichnotaxa, which are instead more deeply impressed medially.

- Several anatomical traits of *Prorotodactylus mesaxonichnus* from the Lower–Middle Triassic of the Catalan Pyrenees described by Mujal et al. (2017a), including impressions of pedal digits IV and V, as well as the proximal impression of pedal digit III, were first recognized in 3D models (red arrows in **Figures 3A,B**). This allowed the measurement of the actual length of the digit impressions and of the digit divarication. In addition, the equivalent depth patterns observed in specimens with an apparently different morphology (e.g., **Figures 3A,B**) allowed to assign this material to the same ichnotaxon.
- The large archosauromorph tracks from the Lower–Middle Triassic of the Catalan Pyrenees described by Mujal et al. (2017a) were identified as Chirotheriidae footprints resembling *Protochirotherium* through the analysis of the 3D models. Several digit impressions are partially collapsed (white arrows in **Figures 3C–E**), and some parts of the

impressed surface are missing due to natural erosion (**Figures 3C–E**); in one case a pes track preserves only three digit impressions (**Figure 3F**). Nonetheless, the false color maps allowed Mujal et al. (2017a) a correct interpretation of the digits outline and their relative position, showing the typical morphology of chirotheriid ichnotaxa.

Generally, despite different types of preservation and even in different (or slightly different) trackway parameters, examining the whole set of 3D models we observe a consistent ("homogeneous") relative depth pattern within tracks of a single ichnotaxon, even if impressed in different substrates. This is because the tracks assigned to an anatomy-based ichnotaxon are impressed by the same type of trackmakers, which probably had autopodia with analog structure and morphology (e.g., Voigt et al., 2007; Marchetti et al., 2017a; Mujal et al., 2017a; Mujal and Schoch, 2020).

According to the recommendations by Belvedere et al. (2018) and Falkingham et al. (2018), 3D models, when possible, should be used in the definition of ichnotaxa, being tools to recognize ichnotaxobases (see also Bertling et al., 2006). When depth patterns are considered in ichnotaxonomy (i.e., contributing in ichnotaxobases), the use of 3D models is recommended. Henceforth, a further consideration must be raised: several holotypes of tetrapod ichnotaxa, from different geological periods correspond to tracks and trackways that were documented but not collected. In these cases, high fidelity molds and replicas were created instead. Here the question regarding such type material is highlighted. According to the ICZN rules (International Commission on Zoological Nomenclature, 1999), a holotype must correspond to an original fossil stored in an adequate repository (museum, research institute, university, etc.) for its safe keeping. However, this is not always feasible (especially in the case of trace fossils), and in most cases, the uncollected type material remains unprotected, and sooner or later will be lost due to erosion (Lucas and Harris, 2020).

Molds and casts of holotype specimens (i.e., "plastotypes") are stored in institutions, but they can eventually deteriorate (as it could also occur with original specimens) as the life time of the mold/cast material is limited and suffers degradation through time (see also section "Preservation and Heritage" below). In this case further molds from the original fossil should be created through time, but the preparation of new molds from the first cast would easily imply a loss of fidelity with respect to the original fossil. As already suggested by Adams et al. (2010) [being further supported by Mallison and Wings (2014), as well as by Belvedere et al. (2018), and Lucas and Harris (2020)], we support the use of digital (3D) models as type material, i.e., digitypes (see further discussion on physical replicas by Lucas and Harris, 2020). 3D models have great advantages in the study, as well as in their sharing and repository. A recent study has partially applied such solution: Lockley et al. (2019) erected a new ichnotaxon of Pleistocene marine turtle tracks, the holotype of which remains in the field; the authors created a 3D model of the holotype trackway and printed part of it in order to appropriately store it in fossil collections, even if possibly the lifetime of the replica material is also limited.

Track-Trackmaker Correlation

The analysis of relative depth patterns of footprints is strictly linked to morphofunctional features of the possible trackmakers (see section "Relative Depth Patterns on Permian to Triassic Tetrapod Footprints" below), which can be inferred from the analysis of articulated and complete appendicular skeletons. In addition, the whole set of movements performed by the trackmaker's limbs (and, potentially, by the whole body of the trackmaker) can also be elucidated by the study of depth patterns (e.g., Gatesy et al., 1999; Falkingham and Gatesy, 2014; Gatesy and Falkingham, 2017; Marchetti et al., 2017a; Mujal et al., 2017a; Mujal and Schoch, 2020). Therefore, a thorough study of these features is of fundamental importance for the track-trackmaker correlations. Following, different case-studies discussions are presented based on above considerations:

- The large tracks of *Ichniotherium cottae* preserved in MNHN.F.LOD83 (**Figure 2A**) are attributed to large basal diadectomorph reptiliomorphs, being different from those of smaller specimens of *I. cottae* and of *I. sphaerodactylum* (Mujal and Marchetti, 2020), which were produced by more derived taxa of the group (Voigt et al., 2007). In fact, the comparison of 3D photogrammetric models of different specimens (see Figure 5 by Mujal and Marchetti, 2020) showed that the large French *I. cottae* tracks display a more deeply impressed medial area, whereas smaller *Ichniotherium* tracks are more deeply impressed in their median part (Mujal and Marchetti, 2020). In this case, the differences in the relative depth of tracks, together with the relative position (rotation) of each track respect to the trackway midline, are a key feature to distinguish the most probable trackmakers. Therefore, when trackways are not available, 3D models of isolated tracks may still provide information for the track-trackmaker correlation (see also Mujal and Schoch, 2020).
- The ichnogenus *Amphisauropus* shows tracks more deeply impressed in their medial part, as suggested by Voigt (2005) and Avanzini et al. (2008). The 3D model of the *Amphisauropus kablikae* trackway (EMVG 2), from the Kungurian of the Italian Southern Alps and created by Marchetti et al. (2017a), confirms this hypothesis. According to the analysis by Marchetti et al. (2017a) of the false color depth maps (**Figure 4A**), the most deeply impressed area is placed at the base of digits I and II, where it is possible to observe a large circular pad impression (see red arrows and zoom inset in **Figure 4A**). This is exactly the same area that is subject to the stronger strain within the tarsus and carpus of the seymouriamorph *Seymouria sanjuanensis*. Therefore, this constituted an important feature for the correlation of *Amphisauropus* to the seymouriamorph group (Marchetti et al., 2017a). Of note, a similar medial functional prevalence, with digits I and II and their

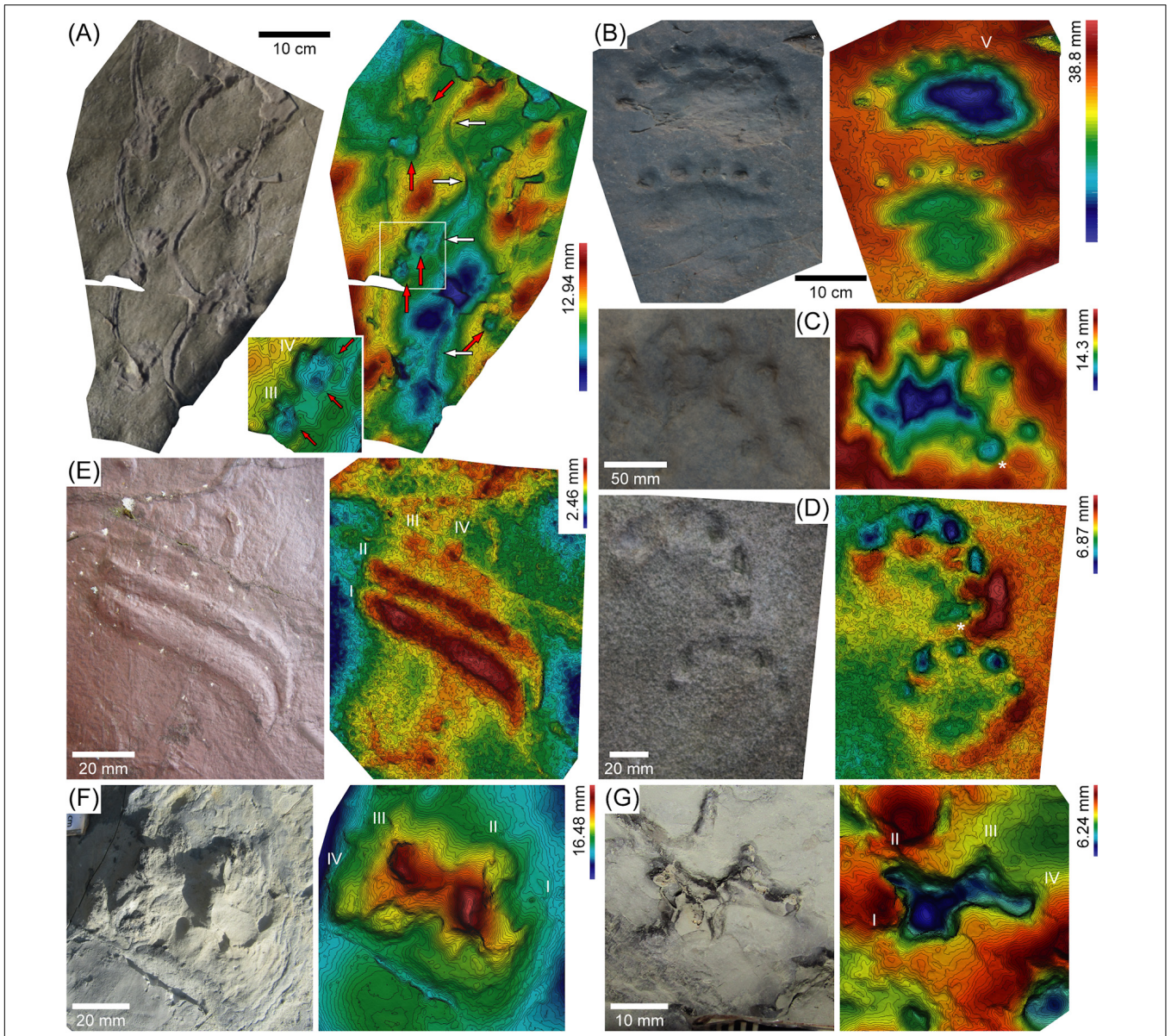

FIGURE 4 | 3D models [except **(E,F,G)**, which include photos instead] and corresponding depth maps of Cisuralian **(A,E)**, Lopingian **(B,C,D)**, and Ladinian (Middle Triassic) **(F,G)** ichnotaxa. **(A)** Trackway of *Amphisauropus kablikae* (EMVG 2), Orobic Basin; arrows indicate the deepest parts of tracks (red) and the steepest parts of the tail impression (white); zoom of one of the manus-pes couples (white square) showing the deeper medial side of tracks. **(B)** Right manus-pes couple of *Brontopus giganteus* (KW-TR 1), Karoo Basin. **(C)** Left manus track of *Dolomitipes accordii* (BE 3), Karoo Basin. **(D)** Left manus-pes couple of *Dolomitipes* isp. (UG-NN 1), Hessian Basin. Asterisks (*) in **(C,D)** indicate equivalent anatomical part. **(E)** Left manus track of *Characichnos* isp. produced by a *Limnopus*-trackmaker, Pyrenean Basin. **(F,G)** Right manus tracks of an indeterminate ichnotaxon attributed to capitosaur stereospondyl trackmakers by Mujal and Schoch (2020); **(F)** is a track natural cast not recovered and **(G)** is preserved in SMNS 97003.

bases being much deeper than the rest of the footprint, is also observed in 3D models of temnospondyl tracks (Mujal et al., 2016a) (**Figure 2B**).

- The identification of footprint depth patterns was central in the track-trackmaker correlation of the Guadalupian–Lower Triassic therapsid tracks from South Africa carried out by Marchetti et al. (2019d). The very broad and more deeply impressed lateral part of the palm of the ichnogenus *Brontopus* (KW-TR 1; **Figure 4B**) suggests that trackmakers were dinocephalian therapsids, which have a broad metacarpal V. The more deeply impressed manus compared to pes imprints helped in the attribution of the ichnogenus *Dolomitipes* (BE-TR 1, AM 5744/5) (**Figures 4C,D**) to dicynodont therapsids, which are characterized by a marked postural dichotomy. The more deeply impressed lateral side of footprints helped Marchetti et al. (2019d) in the attribution of the ichnotaxa *Karoopes* (GF-TR1, 2, 3, SAM-NN 3) (**Figure 2F**) and

Capitosauroides (GF-TR 9, GFTS 1, SAM-PK-K 7878a, b) to therapsid synapsids.

- In the tetrapod ichnoassemblages from the Lower–Middle Triassic of Port del Cantó and Tossal de Pollerini ichnosites (Pyrenean Basin), Mujal et al. (2017a) observed a similar depth pattern between different ichnotaxa: the posterior (proximal) part of digit I impression displays an elevated relief (**Figure 3**). This is related to the collapse of the footprint wall in its side (white arrows in **Figure 3C–E**). In other cases, this area is less impressed (red arrows in **Figures 3A,B**). Such features could be linked to the nature of the footprint producers, all of which are considered to be archosauromorphs (Mujal et al., 2017a). Alternatively, this could be the result of a similar gait of the trackmakers under similar substrate conditions. In any case, the impressions of digits II, III, and IV from both manus and pes tracks are usually the deepest (though exceptions exist: e.g., Mujal et al., 2017a), denoting a trend toward a tridactyl functional prevalence of autopodia. This is the case of chirotheriid ichnotaxa, as well as of other archosauromorph tracks, such as *Prorotodactylus*, *Rotodactylus,* and *Rhynchosauroides* (the later also referred to lepidosauromorph trackmakers) (Mujal et al., 2015, 2017a, 2018b).

Locomotion and Behavior

Differential depths within a track, as well as subtle differences in steepness of impressions, are often indicative of the functional prevalence and progression direction of the trackmakers (**Figures 4**, **5**). Footprints and trackways may record the whole set of limb movements (or at least partially) (e.g., Gatesy and Falkingham, 2017; Mujal and Schoch, 2020). In these cases, 3D models help to elucidate the timeline of footprints impression.

The 3D model of the *Amphisauropus kablikae* trackway in EMVG 2 was used in the identification of the locomotion pattern by Marchetti et al. (2017a) (**Figure 4A**): the tail impression displays different steepness of the lateral margins along the trackway (white arrows in **Figure 4A**). This, combined with the relative position of the tail impression respect to the tracks, indicates the direction of movement of the tail and the body of the trackmaker during locomotion. Moreover, the continuous digit drag traces indicate the precise position of the limbs during the entire step cycle. The 3D model provided additional clues to Marchetti et al. (2017a) on the digits that were closer to the substrate while lifted and thus generated deeper drag traces. It should be taken into account that the observed depth patterns and different steepness along the trackway are small, often indiscernible to the naked eye.

The Permian tetrapod footprints from eolian paleoenvironments were commonly preserved on the foreset dune surfaces (e.g., Gilmore, 1926, 1927; Schmidt, 1959; McKeever and Haubold, 1996). Since these surfaces were inclined and the sand was likely dry at the time of impression (as indicated by the sand avalanches and expulsion rims; the sand was probably dampened shortly after the impression or in the first phases of burial, allowing the preservation of tracks; Marchetti et al., 2019b; for further details on track preservation, see Mancuso et al., 2016, and references therein), the tetrapod locomotion could be difficult, and it was influenced by the force of gravity not perpendicular to the trampled surface. This caused asymmetric trackway pattern, footprint morphology, and footprint depth in trackways not perpendicular to the slope, which were caused by the trackmaker trying to oppose the force of gravity. While these effects are long known (e.g., Leonardi, 1987; Fornós et al., 2002; Hunt and Lucas, 2005; Loope, 2006; Krapovickas et al., 2015), only recently have they been thoroughly interpreted with the aid of the 3D models (Marchetti et al., 2019b,c). The most accurate tool to evaluate these asymmetries is certainly the study of false color depth maps and contours from 3D models. Commonly, the downslope side of the asymmetric trackway is more deeply impressed and shows higher expulsion rims. This was observed by Marchetti et al. (2019b,c) in several specimens, including trackways of *Amphisauropus* (MNA-V 3442A; **Figure 5D**), *Ichniotherium* (UCMP 42945), cf. *Tambachichnium* (USNM-V 11502), *Dolomitipes* (UG-NN 1; **Figure 4D**), and *Pachypes* (DUMFM-NN 2).

In all the 3D models of *Prorotodactylus mesaxonichnus* manus tracks from the Lower–Middle Triassic of the Catalan Pyrenees created by Mujal et al. (2017a), a broad and relatively high expulsion rim between the impressions of digits IV and V is observed (white arrow in **Figures 3A,B**). This feature, clearly visible in the false color maps (but often unseen at naked eye), indicates that the forelimbs applied a postero-lateral pressure during the taking off phase (Mujal et al., 2017a). Hence, the manus was slightly rotated outwards and/or the trackmaker performed a lateral movement of the trunk (as also suggested by the sinuous tail impressions of some trackways; Mujal et al., 2017a).

The ichnogenus *Characichnos* is interpreted as the trace fossil of swimming tetrapods. *Characichnos* generally consists of digit drag traces on the substrate, therefore, not fully representing the anatomy of the trackmaker's autopodia (except for number of digits and width) but rather its behavior. In fact, *Characichnos* tracks are associated with different ichnotaxa and are attributed to very different trackmakers, in a very long stratigraphic interval (e.g., Thomson and Droser, 2015; Vila et al., 2015; Mujal et al., 2016a). Nevertheless, in some cases *Characichnos* may show features similar to the associated ichntoaxa, possibly due to specific morphofunctional characteristics of the trackmaker. This was observed by Mujal et al. (2016b), who performed 3D models of *Characichnos* isp. (although not figured there) associated with *Limnopus* isp. tracks (mold and replica IPS82604) from the Artinskian of the Catalan Pyrenees. The 3D models reveal the same depth pattern in trace fossils assigned to both ichnogenera. In some cases, only impressions of digits I and II are preserved as scratches, and the false color depth map revealed that these scratches are associated with two digit tip imprints corresponding to digits III and IV (**Figure 4E**). This trait enhanced the correlation between the two track morphologies (*Limnopus* and *Characichnos*, walking and swimming tracks, respectively; see Mujal et al., 2016a). This provides additional support to the interpreted medial functional prevalence of the trackmakers' forelimbs, with digits I and II more deeply impressed (or in this case, producing deeper drag traces) than digits III and IV

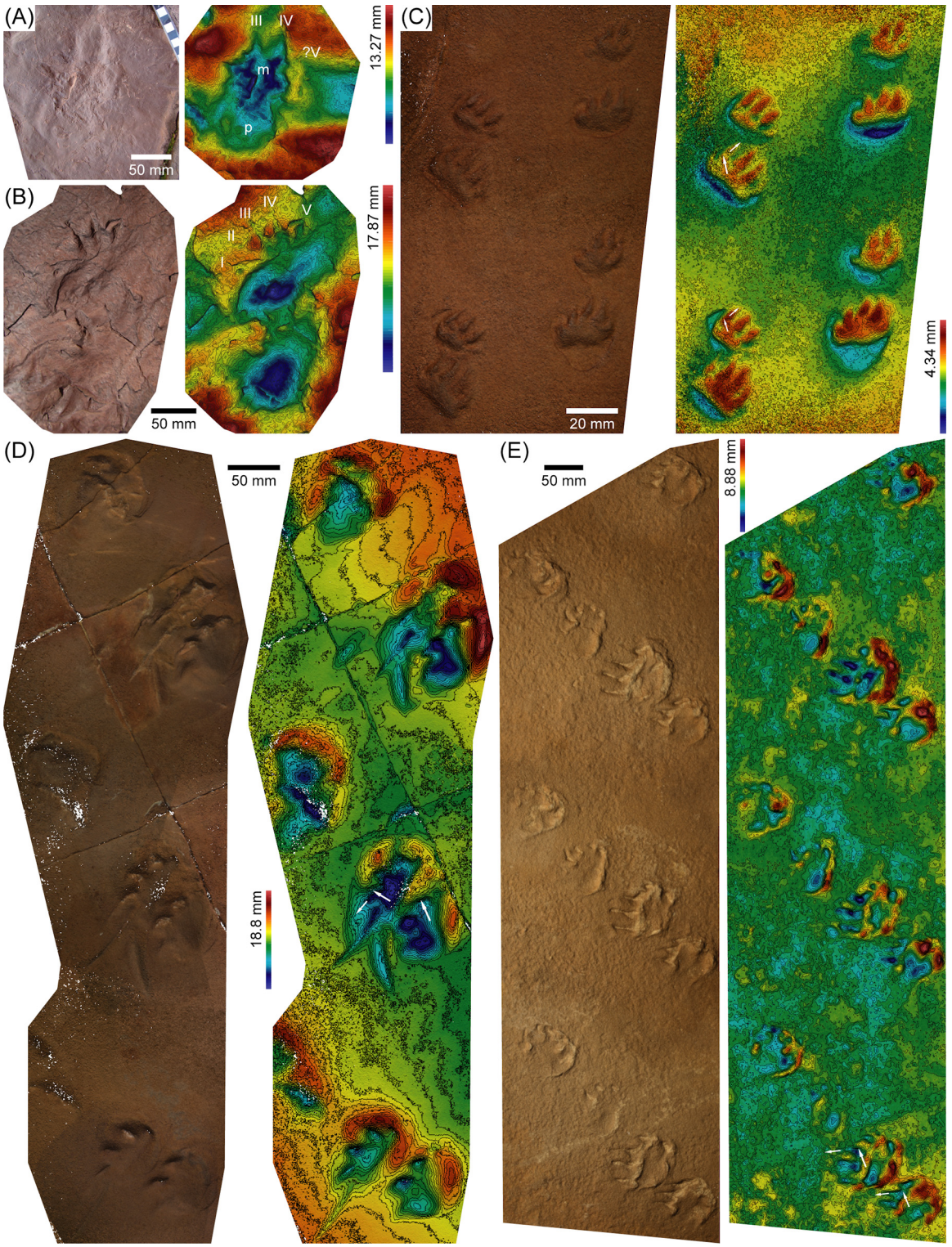

FIGURE 5 | 3D models [except **(A)**, which includes a photo instead] and corresponding depth maps of Cisuralian **(A–D)** and Lopingian **(E)** ichnotaxa. **(A,B)** Right manus-pes couples of *Dimetropus leisnerianus*, Pyrenean Basin; note that tracks in **(A)** are partially eroded. **(C)** Trackway in upslope progression of *Varanopus curvidactylus* (MNA-V 3327), Coconino Formation. **(D)** Trackway in downslope progression of *Amphisauropus* isp. (MNA-V 3442A), De Chelly Formation. **(E)** Trackway in upslope progression with significant lateral component of *Dolomitipes* isp. (NMK-PAL 183), Hessian Basin. Arrows in **(C–E)** indicate sliding and true orientation of digit impressions.

(see section "Relative Depth Patterns on Permian to Triassic Tetrapod Footprints" below).

The set of tracks from the Ladinian of southern Germany, referred to temnospondyls producers by Mujal and Schoch (2020), could not be assigned to a specific ichnotaxon due to the paucity and preservation of the material. Nevertheless, the 3D models of footprints revealed a consistent depth pattern within footprints of apparently different shape due to their different size and preservation mode (**Figures 4F,G**). This allowed Mujal and Schoch (2020) to decipher a consistent locomotor pattern of the trackmakers (interpreted as a bottom-walking locomotion in subaqueous conditions), hence implying that they most probably correspond to the same trackmaker group.

Substrate Induced Effects

The 3D model of MNHN.F.LOD83 from the Asselian of Lodève, southern France (Mujal and Marchetti, 2020), reveals the presence of shallow and relatively wide expulsion rims around most of the tracks (white arrows in **Figure 2A**). Such structures remain difficult to identify by the naked eye due to their low relief: they were not reported by Heyler and Lessertisseur (1963), and Mujal and Marchetti (2020) noticed them only after the analysis of the 3D models. The identification of expulsion rims allowed for better inference of the substrate conditions, despite tracks preserved as plaster casts and the original substrate is lost. The expulsion rims, together with the relative depth patterns of the tracks, denote a peculiar fact: those from the pes tracks are higher (in this case, deeper, as they are casts) than those of the manus tracks, whereas manus tracks are much better impressed than pes tracks. This indicates an impression of the hindlimbs relatively stronger than of the forelimbs (but more focalized to a part of the autopodia in the case of the hindlimbs; see further discussion in Mujal and Marchetti, 2020).

A manus-pes set of *Dimetropus leisnerianus* from the Artinskian of the Catalan Pyrenees (not collected) was strongly eroded (smoothed) by the water flow probably soon after the impression of the footprints (Mujal et al., 2016a) (**Figure 5A**). Indeed, in the field, tracks were identified as shallow irregular impressions within a surface featured by unidirectional flow ripples. The identification of such impressions as *D. leisnerianus* was possible thanks to the 3D model: the false color depth map shows the depth pattern that characterizes this ichnospecies, with a broad and rounded sole impression and relatively thin digit impressions; the same can be observed in other manus-pes couples found by Mujal et al. (2016b) within the same stratigraphic succession (**Figure 5B**).

The morphology of Permian tracks from eolian paleoenvironments was strongly influenced by the substrate (Marchetti et al., 2019b,c). This is because the track-bearing surfaces were foreset dune surfaces; thus, they were relatively dry sand slopes that caused difficulty in trackmaker progression and very common digit sliding and sand avalanches. These digit drag traces were generally parallel to the slope and were generated when the trackmaker's foot slid downslope with respect to the touch-down position. This was observed in trackways directed parallel, perpendicular, and transverse to the slope and masks the original orientation and morphology of the digits, causing problems in ichnotaxonomy (Marchetti et al., 2019b,c; Francischini et al., 2020). In order to correctly interpret this substrate-induced effect and recognize the actual digit impressions, the analysis of the 3D models is very helpful. Some notable examples of this are observed for trackways of *Amphisauropus*, *Varanopus,* and *Dolomitipes* with different orientations compared to the slope studied by Marchetti et al. (2019b,c) (RAM-NN 1, UCMP V 42944, MNA-V 3327, MNA-V 3442A, NMK-PAL 183, YPM 2143) (**Figures 2E**, **5C–E**).

Preservation and Heritage

Collecting and/or excavating tetrapod footprints (and especially complete trackways) is often difficult or impossible. Therefore, an alternative solution in order to preserve the fossil record must be found. Traditionally, the use of molds and replicas of tracks and complete trackways has fulfilled this necessity (e.g., Heyler and Lessertisseur, 1963; Gand et al., 2000; Mujal et al., 2016a,b, 2017a; Marchetti et al., 2019d; Lucas and Harris, 2020). However, such molds and casts usually do not preserve the whole record of a site but a small part of it and even if adequately stored, can be deteriorated, depending on the lifetime of the mold/cast material nature, even becoming useless, as all material has a lifetime before degradation (mostly being of silicone, gypsum, acrylic resin, etc.).

The preservation of the tetrapod ichnofossil record may present some difficulties that should be considered. This is commonly due to difficult access to the localities (either because they are in private properties or due to orographic characteristics, i.e., remote areas) that may lead to the loss of specimens due to erosion and weathering. This problem has been faced by several of our works, in which photogrammetry has been a useful tool to overcome the impossibility to collect/cast/move specimens (e.g., Mujal et al., 2016a,b, 2017a,b; Marchetti et al., 2019b,d; Mujal and Marchetti, 2020):

- Manipulation of large casts can be harmful for their preservation, as they can be damaged during analysis. Nevertheless, 3D photogrammetric models facilitate the analysis, as tracks can be (virtually) moved and observed in different perspectives. This was indeed the case of MNHN.F.LOD83 (see Mujal and Marchetti, 2020).
- Photogrammetry is advantageous through time: previous non-optimal photogrammetric results may become useful thanks to newer versions of software. In fact, herein we have re-run a model using the same photos of a *Limnopus* isp. manus-pes set (IPS73724) and results show that the new 3D model is more detailed than the previous one (which due to its poor resolution was discarded by Mujal et al., 2016a) and also ichnologically informative (**Figure 6A**).
- Creation of molds (and replicas) can be impossible due to difficult access to localities (e.g., remote areas only accessible by foot, crossing creeks and relatively dense forests) and to the situation of the track-bearing surfaces (in high slopes, being even vertically exposed), as is the case of Catalan Pyrenees localities. In the case of relatively small tracks (e.g., 2–5 cm long), molds may still be possible to create (e.g., Mujal et al., 2016b,a, 2017a), although those

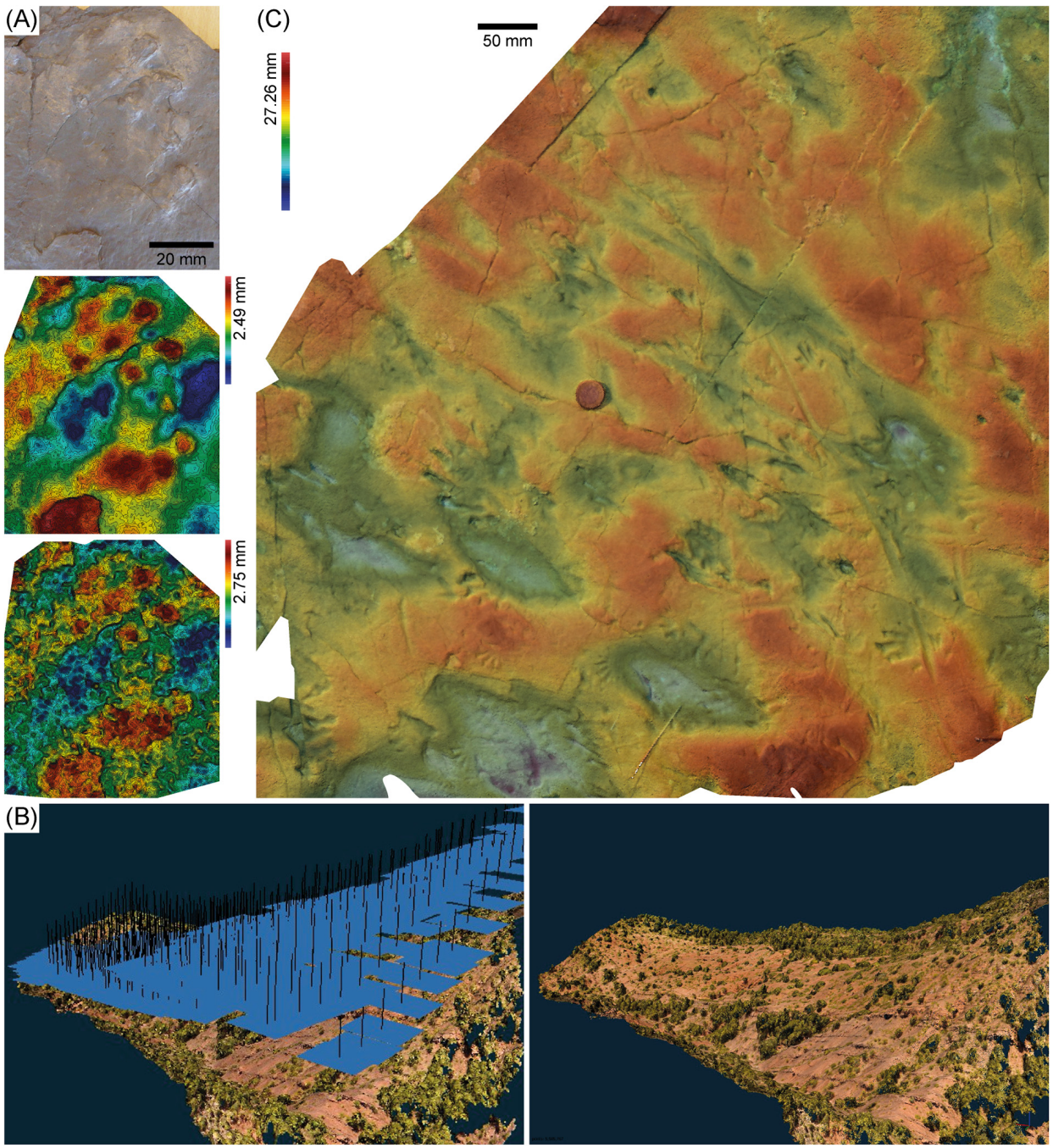

FIGURE 6 | (A) Photo (top) and depth maps of the 3D models (new, middle; old, bottom) of a right manus-pes couple of *Limnopus* isp. (IPS73724), Pyrenean Basin, Cisuralian; note that the surface is much smoothed in the new model, allowing better elucidation of footprint features. **(B)** Captures of the 3D model obtained with drone of the Coll de Terrers outcrop, Pyrenean Basin, Guadalupian–Lopingian; left image contains the position of each photo. **(C)** 3D model with the depth map superimposed on transparency of a large surface containing abundant *Prorotodactylus mesaxonichnus* tracks, including the trackway paratype (mold and replica IPS93867), Pyrenean Basin, Early–Middle Triassic.

of relatively large trampled surfaces are often of difficult transport and are easily damaged, implying further careful lab work (EM and JF, pers. obs. 2016). Therefore, 3D photogrammetry is the optimal tool for the preservation of such record. Recently, during fieldtrips to Tossal de Pollerini and Coll de Terrers sites (Mujal et al., 2017a,b) an unnamed aerial vehicle was used to take photos for the creation of high-resolution 3D photogrammetric models of: (1) the whole outcrops (**Figure 6B**) (for similar documentation of tracksites, see Citton et al., 2017;

Romilio et al., 2017; Petti et al., 2018) and (2) relatively large (∼2–5 m^2) track-bearing surfaces (with sets of around 100 photos per surface) (**Figure 6C**). Besides providing new ichnological and sedimentological data (currently under analysis), these new models constitute a digital repository of this paleontological heritage.

- The most important Guadalupian–Lower Triassic tetrapod ichnosites from South Africa (Marchetti et al., 2019d) are surfaces left in place on private property. This is potentially harmful for the preservation of this heritage because of erosion and weathering while the tracksite remains unprotected. This is the case of Klein Waterval and Bethel sites, which are located in canyons/rills and covered by sediment at the time of field work (LM, pers. obs. 2018). Some latex casts of portions of these surfaces are preserved in repositories, but their quality is often not adequate for a new study. Therefore, the creation of 3D photogrammetric models of the most important trackways and surfaces from all these localities, as Marchetti et al. (2019d) did, is the ideal way to preserve such heritage for the scientific community (for further discussion see also Reolid et al., 2020).

Relative Depth Patterns on Permian to Triassic Tetrapod Footprints

Herein we present and discuss the relative depth patterns of tetrapod tracks and their implications for the functional prevalence of autopodia in a phylogenetic framework.

Substrates and Paleoenvironments

The localities of the herein reviewed tetrapod footprints encompass a wide range of substrates and paleoenvironments (see section "Tetrapod Ichnoassociations from the Lower Permian to the Middle Triassic" above and **Supplementary Data S1**). Most of the localities belong to siliciclastic successions commonly including red-beds, but also dark mudstones. Such successions usually represent alluvial, fluvial, and lacustrine paleoenvironments. Besides, a few of them represent coastal (e.g., sabkhas and tidal flats) and eolian paleoenvironments. In a few cases, the track-bearing substrate is a carbonate mudstone, usually of microbial origin, in coastal or restricted marine settings.

More specifically, the substrate preserving footprints, either in concave epirelief or convex hyporelief (or both, if part and counterpart strata/slabs are found) includes: (1) mudstones (claystones and siltstones), either massive or laminated; (2) sandstones, ranging from very fine-grained to coarse-grained, either massive or with parallel lamination and/or flow and wave ripples; (3) fine-grained and well-sorted (eolian) sandstones with large-scale cross lamination, wind ripples, and sand avalanches; (4) fine grained limestones (i.e., carbonate mudstones), either massive or laminated. Footprint surfaces are either flat or undulated; other structures, such as desiccation cracks, raindrops and wrinkles, as well as other vertebrate and/or invertebrate trace fossils, may also be present. In many cases, other trace fossils and structures cross, overprint, and/or mask the analyzed tetrapod footprints. In such cases, 3D models help to elucidate the sequence of events and, as a result, to correctly identify the footprint outline (see Marchetti et al., 2013; Mujal et al., 2015).

Although paleoenvironmental settings (and paleoclimatic conditions) constrain the distribution of tetrapod ichnotaxa (e.g., Mujal et al., 2016a), we observe that the same ichnotaxon can be present in a relatively wide range of substrates (e.g., Mujal et al., 2018a). Also, the absolute depth of footprints from the same ichnotaxon (or even along the same trackway) can vary consistently on different substrates, from very deep, to intermediate, and to very shallow. Nevertheless, all the diagnostic (anatomical) features of ichnotaxa (e.g., digit number, morphology and relative length, palm/sole impression shape and size, relative depth within a footprint) do not vary, even if their recognition relies on the effects caused by substrate rheology and behavior (see Gatesy and Falkingham, 2017; Mujal et al., 2018a; Marchetti et al., 2019a). The whole set of 3D photogrammetric models (i.e., both reviewed from previous publications and newly presented, see **Figures 2–7**) show a consistent relative depth pattern within pes and manus imprints of each ichnotaxon, independently from the absolute depth of each footprint. Therefore, the original substrate conditions (rheology) and environmental settings do not play a major role in the relative depth pattern (i.e., the diagnostic 3D features) observed within tracks of the same ichnotaxon, whereas their absolute depth may vary consistently (see also discussion in Mujal et al., 2018a).

Our qualitative interpretation of footprint relative depth patterns allows us to identify the functional prevalence of the autopodia, which results from specific morphofunctional features of the trackmaker, thus further linking the ichnotaxa to the potential trackmakers (see section "Relative Footprint Depth Patterns and Functional Prevalence of Autopodia" below). 3D models elucidate potentially biased observations related to the absolute depth of footprints: false color depth maps help to minimize the differences between shallowly and deeply impressed tracks of the same ichnotaxon (e.g., see Figures 5H,I of Mujal and Marchetti, 2020). As highlighted in the introduction of the present work, there is a major difference between upper Carboniferous to Triassic tetrapod ichnology and non-avian dinosaur ichnology. For instance, a deeply impressed theropod dinosaur track may show four digit impressions, whereas a shallow one would be just tridactyl, which could eventually lead to oversplitting and misinterpretation of ichnogenera (for a thorough study of such case, see Razzolini et al., 2014). On the contrary, within upper Carboniferous, Permian, and Triassic tetrapod tracks the anatomy-related morphological features are the same in deep and shallow imprints (only very shallow tracks may show less digit and/or palm/sole impressions) and/or in imprints impressed on mudstones, siltstones, carbonates, and dune sandstones. In fact, in different substrates or substrate rheological properties the relative depth pattern of tracks assigned to the same ichnotaxon is generally constant (especially if trackmakers maintain the same locomotion; e.g., Mujal et al., 2018a; Marchetti, 2019; Mujal and Schoch, 2020). Even on originally inclined surfaces, which caused additional asymmetries to the footprint depth, the relative depth pattern within footprints of the same ichnotaxon is still recognizable

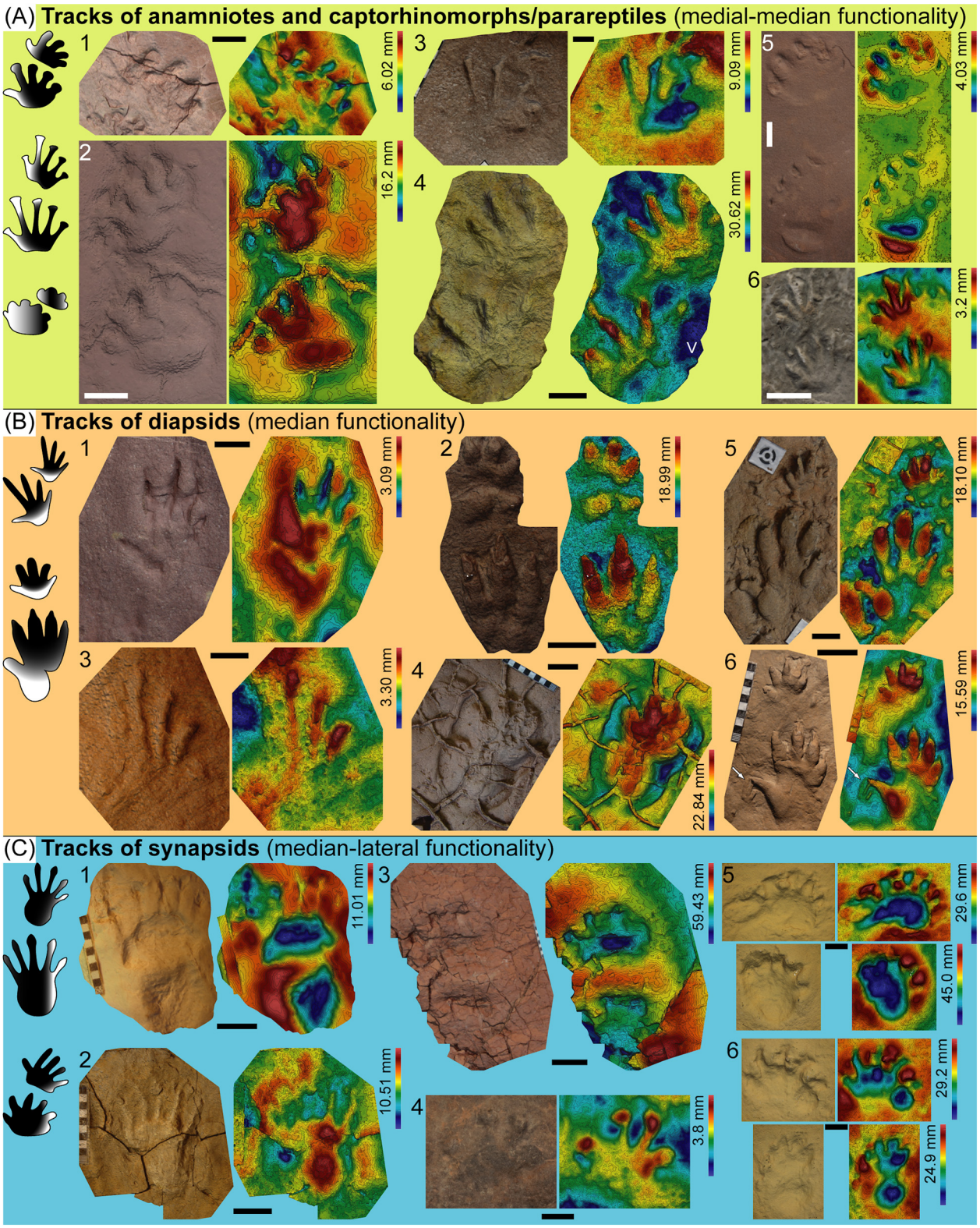

FIGURE 7 | Depth patterns among Cisuralian to Middle Triassic tetrapod ichnotaxa shown by selected 3D models and corresponding depth maps. In the left part of each section, schematic unscaled left manus-pes couples showing the parts with functional prevalence (black areas) of each group are depicted. **(A) 1** left couple (partial pes track) of *Limnopus* isp. (mold and replica IPS82606), Pyrenean Basin, Cisuralian; **2** left couple of *Ichniotherium sphaerodactylum* (UGKU 130), Tambach

(Continued)

FIGURE 7 | Continued
Formation (Germany), Cisuralian; **3** left couple (partial manus track) of *Hyloidichnus* isp. (MF-LOD 2001.1447.1), Lodève Basin, Cisuralian; **4** left couple of *Merifontichnus thalerius* (UM-LOD 16), Lodève Basin, Guadalupian; **5** right couple of *Pachypes loxodactylus* (DUMFM-NN 2), Dumfries Basin, Lopingian; **6** left couple of *Procolophonichnium nopcsai* (NHUMK R3173), Karoo Basin, Early Triassic. **(B) 1** left manus track of *Prorotodactylus mesaxonichnus* (mold and replica IPS93869), Pyrenean Basin, Early–Middle Triassic; **2** left couple (partial pes track) of *Chirotherium barthii* (mold and replica IPS17899), Catalan Basin (Buntsandstein), Middle Triassic; **3** right pes track of *Rhynchosauroides* isp. (IPS73720), Catalan Basin (middle Muschelkalk), Middle Triassic; **4** right pes track of *Isochirotherium* isp. (IPS81873), Catalan Basin (middle Muschelkalk), Middle Triassic; **5, 6** left couples of *Chirotherium barthii* (MF-LOD 2001.1438.1 and MF-LOD 2001.1437.1, respectively), and right pes track of *Rotodactylus* isp. (arrow in **6**), Lodève Basin, Middle Triassic. **(C) 1** and **2** pes tracks of *Dimetropus leisnerianus* (**1**, right imprint, MNHN.F.LOD59; **2**, left imprint –undertrack–, UM-LOD 260), Lodève Basin, Cisuralian; **3** right couple of a *Dicynodontipus*-like morphotype, Pyrenean Basin, Lopingian; **4** left pes of cf. *Capitosauroides* (SAM-PT-K 7870), Karoo Basin, Lopingian; **5** right couple of *Dolomitipes icelsi* (AS-TR Q), Karoo Basin, Lopingian; **6** left couple of *Dolomitipes accordii* (AS-TR 2), Karoo Basin, Lopingian. Scale bars represent 10 mm [in **1** and **3** of **(B)**], 20 mm [in **1**, **3**, **5,** and **6** of **(A)**, and **4** of **(C)**], 50 mm [in **2** and **4** of **(A)**, **2**, **4**, **5,** and **6** of **(B)**, and **1** and **2** of **(C)**] and 10 cm [in **3**, **5,** and **6** of **(C)**].

(e.g., Marchetti et al., 2019b). In fact, ichnotaxonomy is based on footprint outline morphology and relative depth patterns of the impressions (i.e., anatomical features of autopodia) (Voigt, 2005). Hence, relative depth patterns are recognizable in any substrate. In this sense, only footprints with substantial extramorphological variations (that completely mask/overprint anatomical features; see Peabody, 1948; Haubold, 1996) are excluded from such analyses (see section "Substrate Induced Effects" above).

Relative Footprint Depth Patterns and Functional Prevalence of Autopodia

As a whole, we preliminary identify three main groups of upper Carboniferous–Middle Triassic ichnotaxa (selected, representative specimens are shown in **Figure 7**) characterized by a different functional prevalence:

1) Anamniote and captorhinomorph/parareptile tracks: medial-median functional prevalence (**Figures 2A–E**, **4A,E–G**, **5C,D**, **6A**, **7A**).
2) Diapsid tracks: median functional prevalence (**Figures 3**, **6C**, **7B**).
3) Synapsid tracks: median-lateral functional prevalence (**Figures 2F**, **3B–D**, **5A,B,E**, **7C**).

The first group of tracks (**Figure 7A**) includes ichnogenera produced by temnospondyl and lepospondyl amphibians (*Batrachichnus*, *Limnopus*, *Matthewichnus*), seymouriamorphs (*Amphisauropus*), diadectomorphs (*Ichniotherium*), and captorhinomorph/parareptiles (*Erpetopus*, *Hyloidichnus*, *Merifontichnus*, *Notolacerta*, *Procolophonichnium*, *Pachypes*, *Varanopus*). The medial (inner) part of these tracks (usually digits I and II, and the corresponding portion of the palm/sole) are generally the most deeply impressed parts. Depth patterns may vary between manus and pes tracks, the medial-lateral decrease in relief is usually more evident in the pes tracks. Besides, the trackways are often broad, with relatively low pace angulations (with the only exception of some captorhinomorph/parareptile tracks such as *Erpetopus* and *Varanopus*, which show also relatively high pace angulation and primary pes-manus overstep).

The second group of tracks (**Figure 7B**) includes ichnogenera produced by diapsid reptiles, being archosauromorph tracks the most representative group. It includes ichnogenera from the Chirotheriidae ichnofamily (e.g., *Brachychirotherium*, *Chirotherium*, *Isochirotherium*, *Parachirotherium*, *Protochirotherium*, *Sphingopus*, *Synaptichnium*), dinosauromorph tracks (e.g., *Atreipus*, *Eubrontes*, *Evazoum*, *Grallator*), relatively small-sized non-chirotheriid ichnotaxa such as *Dromopus*, *Prorotodactylus*, *Rotodactylus,* and *Rhynchosauroides*, as well as larger non-chirotheriid ichnotaxa such as *Apatopus* and *Paradoxichnium*. Of note, the *Rhynchosauroides* trackmakers may correspond to archosauromorphs or lepidosauromorphs, hence broadly corresponding to neodiapsid reptiles. Interestingly, also the varanopid ichnogenus *Tambachichnium* belongs to this group. Recently, varanopids have been interpreted as diapsids instead of synapsids (Laurin and Piñeiro, 2018; Ford and Benson, 2020; but see discussion in MacDougall et al., 2018). Based on the present analysis of relative depth patterns, different options could explain why varanopids are found within the group of diapsid tracks: (1) perhaps they reflect a very basal position of varanopids within synapsids; (2) a functional/convergent signal rather than a phylogenetic signal for this group. However, the latter option seems unfeasible as, in general terms, functional prevalence is correlated with phylogenetical signal. The first option is herein preferred; nonetheless, it should be remarked that the present analysis of depth patterns is preliminary, including only one ichnotaxon (*Tambachichnium*) correlated to varanopids, not precluding that further sampling could reveal differences across varanopid evolution.

Tracks of the second group are most commonly produced by autopodia with semidigitigrade to semiplantigrade postures, and digits II, III, and IV are usually the deepest, being in many cases the only impressed parts of the autopodia. Noteworthy, some chirotheriid tracks also display a relatively deep impression of the proximal pad of pedal digit V, being similar to that of digits II, III, and IV (see 5 and 6 in **Figure 7B**). Trackways are usually narrow, though most of the *Dromopus* and *Rhynchosauroides* specimens and some *Prorotodactylus* specimens display relatively low pace angulations (Mujal et al., 2017a). In the small-sized ichnotaxa, a certain degree of overstepping of the pes respect to the manus impressions is common, ranging from a slight lateral position of the pes respect to the manus to a complete overstepping of the pes, being positioned to the anterolateral side of the manus tracks. Generally, the tracks of this group show a trend toward a tridactyl functionality that can be mesaxonic (e.g., *Chirotherium*, *Isochirotherium*, *Parachirotherium*, *Sphingopus*, *Atreipus*), as observed in ornithopod and theropod dinosaur tracks (e.g., Castanera et al., 2013; Lallensack, 2019), or ectaxonic

(e.g., *Dromopus*, *Rhynchosauroides*, *Rotodactylus*), as observed in most modern diapsids.

The third group of tracks (**Figure 7C**) is attributed to the synapsid group (i.e., including therapsids), with the exception of varanopid synapsid tracks (i.e., *Tambachichnium*; see discussion above). This group of tracks includes ichnogenera from the Pennsylvanian–Cisuralian (e.g., *Dimetropus*), the Guadalupian (e.g., *Brontopus*), the Lopingian (e.g., *Capitosauroides*, *Dicynodontipus*, *Dolomitipes*, *Karoopes*), and the Triassic (e.g., *Capitosauroides*, *Dicynodontipus*, *Pentasauropus*, *Therapsipus*) (see also Figure 9 by Marchetti et al., 2019d). These tracks often show a more deeply impressed digit IV, or in some cases even digit V, as well as the parts of palm/sole impressions proximal to digits IV and V. In addition, these tracks are generally suggestive of trackmakers with a plantigrade posture, with relatively broad sole and palm impressions and short digit imprints. Complete overstep of pes respect to manus tracks is uncommon and only observed in the ichnotaxa *Dicynodontipus* and *Karoopes*.

The relative depth patterns of footprints become more significant when mapped onto a cladogram of tetrapods (**Figure 8**). Although the discussion on the phylogeny at the amniote and reptile origin is currently debated (e.g., Laurin and Piñeiro, 2017, 2018; MacDougall et al., 2018; Ford and Benson, 2020), the three groups that we identify are very wide. We plotted our groups on two cladograms based on MacDougall et al. (2018) (see **Figure 8A**) and Ford and Benson (2020) (see **Figure 8B**), both of which including a possible new position of the varanopid group, being out of Synapsida. Group 1 apparently forms the primitive condition of upper Carboniferous to Middle Triassic tetrapods, as it occurs in both the putative lissamphibian stem-group (temnospondyls) as well as amniote stem lineages (e.g., seymouriamorphs and diadectomorphs), which are at the base of both cladograms represented (**Figure 8**). Interestingly, group 1 does not only encompass anamniotes and stem amniotes, but also extends to parareptiles and captorhinids, which form successive sister taxa of diapsid reptiles (Reisz et al., 2011; MacDougall et al., 2018) (**Figure 8A**). This suggests that the depth pattern of group 2 (diapsid tracks) derived from the depth pattern of group 1 (probably from captorhinomorphs), independently from the evolution of the synapsid footprint depth pattern (group 3), which forms a separate modification from the basal tetrapod footprint depth pattern (**Figure 8**). Further studies should focus on the question why the pattern of group 1 is so widespread across early tetrapods and what this means in functional and locomotory terms.

Some recent studies nested the parareptiles within diapsids (Ford and Benson, 2020). This would imply a separation of group 1 in two sub-groups: (1) anamniotes, stem amniotes, and captorhinids and (2) parareptiles (**Figure 8B**). A possible explanation for this is a morphological reversal between group 2 (Diapsida) and group 1 (Parareptilia) to the ancestral depth pattern condition. However, this would represent a less parsimonious chain of events. All in all, based on available interpretations of early amniotes, we concur in general terms with the interpretation of MacDougall et al. (2018).

The present work is the first step to (1) create a general framework to analyze upper Paleozoic to Triassic tetrapod trace fossils and (2) evaluate how the three identified groups evolved through time and space. Of note, these analyses also have to consider the exceptions/differences observed within the groups, as well as differences between ecosystems (i.e., different paleoenvironments in which the footprints are preserved and the related biases, as not all the paleoenvironments are equally preserved in the fossil record). In addition, future studies of tetrapod tracks from any age interval and (ichno-) taxonomic group should also test this analysis. For instance, in a preliminary overview, we observed that dinosaur tracks from different lineages (see examples in Castanera et al., 2013; Salisbury et al., 2016; Lallensack et al., 2017) appear to fit with group 2, which encompasses diapsids. Furthermore, the identification of these groups, when possible, should be accompanied with additional data regarding the ichnotaxa considered, including general footprints' morphologies, relative proportions, and trackway parameters. In fact, depth patterns are considered ichnotaxobases (e.g., Voigt, 2005; Marchetti et al., 2017a). Also, such classification must be based on a representative sample, avoiding assumptions or interpretations derived from the study of a small number of specimens.

Of interest, despite the different types of substrates (even for the same ichnotaxon) and the wide age range of each of the three identified groups, a substantially consistent relative depth pattern of tracks is observed within the groups (**Figure 7**). Indeed, all these groups cross major biotic crises, such as the end-Guadalupian and end-Permian mass extinctions. This would indicate that the functional prevalence of each group is preserved and inherited despite environmental and climatic (catastrophic) changes. Henceforth, evidences of such events may be found in broader context analyses, including quantitative studies of the functional prevalence of autopodia, encompassing a relatively wide stratigraphic range.

A further question to explore is the relationship of these groups with the postcranial skeleton record of the supposed producers, which may help to identify the anatomic and functional reasons of these depth patterns. Also, it should be checked if the herein proposed groups of footprints according to their functional prevalence keep a relationship and/or present a correlation with the morphofunctional categories of temporal skull fenestra in amniotes (Wernerburg, 2019; Ford and Benson, 2020). Indeed, in a general point of view, a similar distribution of high-rank taxonomic groups exists between these two different grouping.

CONCLUSION

Photogrammetry has been proved to be an extremely useful tool in the study of upper Paleozoic and Triassic tetrapod ichnofossils. Nevertheless, this technique has not been commonly applied in this ichnological record, especially when compared with dinosaur footprints. Through the present work, we review and highlight the benefits of using photogrammetry. Indeed, it is proved that 3D models can be key elements in ichnotaxonomy. Footprint relative depth patterns, when appropriately compared with other

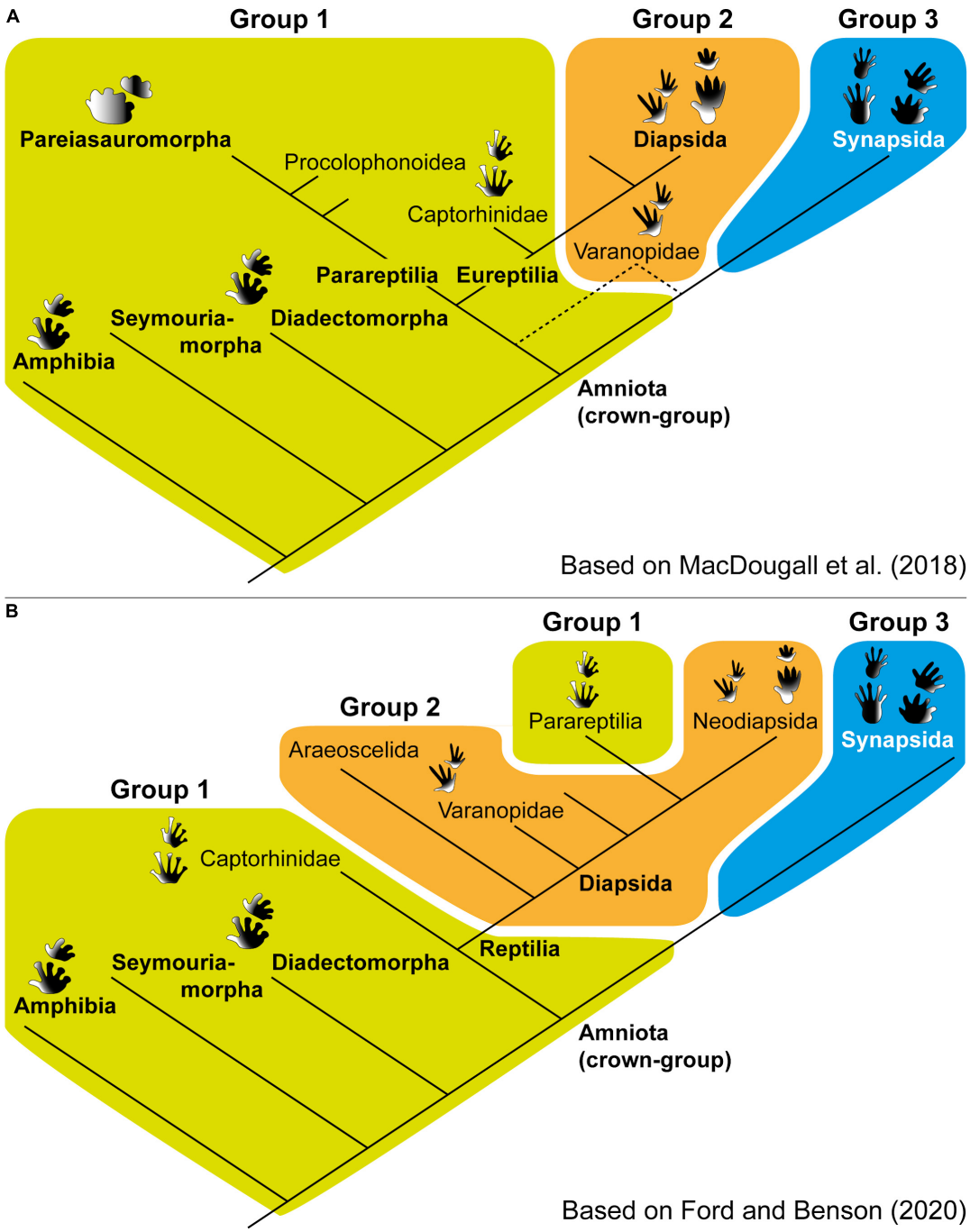

FIGURE 8 | Simplified cladograms of tetrapods showing the relationship of the three footprint groups of relative depth patterns. **(A)** Tree based on MacDougall et al. (2018); note the dashed lines of varanopids: the line from the reptile lineage was recovered by these authors, the line from the synapsid lineage corresponds to the classical interpretation (here preferred; see text for discussion). **(B)** Tree based on Ford and Benson (2020); note the split of group 1, implying a less parsimonious chain of events.

tracks and skeletal remains, refine the correlation of tracks with the potential trackmakers. False color depth maps also help to unravel the formation and superimposition of structures that can mask footprints. Such structures may result from both the locomotion of the same (or other) trackmakers and from sedimentary processes (e.g., ripples, collapse of the substrate in inclined surfaces), as well as from weathering of the footprints. Furthermore, 3D models are a suitable solution to preserve the ichnological record, especially when original specimens cannot be collected and thus are subjected to disappearance.

A review of the available 3D data of Permian and Triassic (and upper Carboniferous to a lesser degree) tetrapod footprints allowed us to preliminary identify three main groups of tracks linked to specific relative depth patterns derived from the functional prevalence of autopodia: (1) anamniote and captorhinomorph/parareptile tracks (medial-median functional prevalence); (2) diapsid tracks (median functional prevalence); and (3) synapsid tracks (median-lateral functional prevalence). This qualitative analysis shows a substantially consistent depth pattern within each group, despite being preserved in different substrates and corresponding to a wide stratigraphic interval. All in all, this indicates that 3D models may show features linked to the potential trackmakers that remain unseen by the naked eye.

DATA AVAILABILITY STATEMENT

All datasets generated for this study are included in the article/**Supplementary Material**.

AUTHOR CONTRIBUTIONS

JF, EM, LM, and RS contributed on the conception and design of the study and performed the ichnological analysis. EM and LM organized the database. EM wrote the first draft of the manuscript and prepared the figures, with comments from all authors. LM, RS, and JF wrote sections of the manuscript. All the authors contributed to manuscript revision, read, and approved the submitted version.

FUNDING

EM received funding from the SYNTHESYS Project http://www.synthesys.info/ (FR-TAF-3621 and FR-TAF-4808) which is financed by European Community Research Infrastructure Action under the FP7 "Capacities" Program; Secretaria d'Universitats i Recerca (Departament d'Economia, Generalitat de Catalunya; grant number 2013 CTP 00013); the Erasmus+ program of the Universitat Autònoma de Barcelona. LM was funded by the Alexander von Humboldt Foundation. JF was supported by the Spanish Agencia Estatal de Investigación and the European Regional Development Fund of the European Union (AEI/FEDER EU, project CGL2017-82654-P). JF is member of the consolidated research group 2017 SGR 86 GRC of the Generalitat de Catalunya. EM and JF are members of the project "Evolució dels ecosistemes durant la transició Paleozoic–Mesozoic a Catalunya" (ref. CLT009/18/00066), financially supported by the Departament de Cultura (Generalitat de Catalunya). This research received support from the CERCA program (ICP) from the Generalitat de Catalunya.

ACKNOWLEDGMENTS

We thank all curators and researchers for allowing access to specimens presented in this work, stored in their corresponding institutions, which include Muséum National d'Histoire Naturelle (Paris), Institut des Sciencies de l'Evolution de Montpellier (at Université de Montpellier, Montpellier), Musée Fleury (Lodève). We thank all the land owners who granted access to the specimens *in situ*. We especially thank Sergio Llácer (ICP) for the elaboration of several 3D models for this work. We also thank Rafel Matamales-Andreu (ICP) for the help in acquisition of photos and elaboration of 3D models from Erillcastell, and Jaume Balagué (Terra Dron) for the acquisition of aerial and close-range photos, and data processing from Erillcastell and Coll de Terrers. We acknowledge three reviewers who helped to substantially improve an earlier version of the manuscript, as well as Martin D. Ezcurra for editorial handling.

SUPPLEMENTARY MATERIAL

The Supplementary Material for this article can be found online at: https://www.frontiersin.org/articles/10.3389/feart.2020.00248/full#supplementary-material

DATA SHEET S1 | Reviewed localities.

REFERENCES

Abel, O. (1935). *Vorzeitliche Lebensspuren*. Jena: Fischer.

Adams, T. L., Strganac, C., Polcyn, M. J., and Jacobs, L. L. (2010). High resolution three-dimensional laser-scanning of the type specimen of Eubrontes (?) glenrosensis Shuler, 1935, from the Comanchean (Lower Cretaceous) of Texas: implications for digital archiving and preservation. *Palaeontol. Electron.* 13, 1–11.

Anonymous. (1828). Notice about Dumfriesshire footprints. *London Paris Obser.* 141, 93–94.

Avanzini, M., Neri, C., Nicosia, U., and Conti, M. A. (2008). A new Early Permian ichnocoenosis from the "Grupo vulcanico atesino" (Mt. Luco, Southern Alps, Italy). *Stud. Trent. Sci. Natl. Acta Geol.* 83, 231–236.

Baird, D. (1957). Triassic reptile footprint faunules from Mildford, New Jersey. *Bull. Mus. Comp. Zool.* 117, 449–520.

Bates, K. T., Manning, P. L., Margetts, L., and Sellers, W. I. (2010). Sensitivity analysis in evolutionary robotic simulation of bipedal dinosaur running. *J. Vert. Paleontol.* 30, 458–466. doi: 10.1080/02724630903409329

Bates, K. T., Manning, P. L., Vila, B., and Hodgetts, D. (2008a). Three-dimensional modelling and analysis of dinosaur trackways. *Palaeontology* 51, 999–1010. doi: 10.1111/j.1475-4983.2008.00789.x

Bates, K. T., Rarity, F., Manning, P. L., Hodgetts, D., Vila, B., Oms, O., et al. (2008b). High-resolution LiDAR and photogrammetric survey of the Fumanya dinosaur tracksites (Catalonia): implications for the conservation and interpretation of geological heritage sites. *J. Geol. Soc.*165, 115–127. doi: 10.1144/0016-76492007-033

Belvedere, M., Bennett, M. R., Marty, D., Budka, M., Reynolds, S. C., and Bakirov, R. (2018). Stat-tracks and mediotypes: powerful tools for modern ichnology based on 3D models. *PeerJ* 6:e4247. doi: 10.7717/peerj.4247

Bertling, M., Braddy, S. J., Bromley, R. G., Demathieu, G. R., Genise, J., Mikuláš, R., et al. (2006). Names for trace fossils: a uniform approach. *Lethaia* 39, 265–286. doi: 10.1080/00241160600787890

Carrano, M. T., and Wilson, J. A. (2001). Taxon distributions and the tetrapod track record. *Paleobiology* 27, 564–582. doi: 10.1666/0094-8373(2001)027<0564:tdattt>2.0.co;2

Castanera, D., Pascual, C., Razzolini, N. L., Vila, B., Barco, J. L., and Canudo, J. I. (2013). Discriminating between medium-sized tridactyl trackmakers: tracking ornithopod tracks in the base of the Cretaceous (Berriasian. Spain). *PLoS One* 8:e81830. doi: 10.1371/journal.pone.0081830

Cavin, L., and Piuz, A. (2020). A several-kilometer-long archosaur route in the triassic of the swiss alps. *Front. Earth Sci.* 8:4. doi: 10.3389/feart.2020.00004

Cisneros, J. C., Day, M. O., Groenewald, J., and Rubidge, B. S. (2020). Small footprints expand middle Permian amphibian diversity in the South African Karoo. *Palaios* 35, 1–11. doi: 10.2110/palo.2018.098

Citton, P., Carluccio, R., Nicolosi, I., and Nicosia, U. (2019a). Re-evaluation of Chelichnus tazelwürmi, a non mammalian therapsid-grade track from the Upper Permian Arenaria di Val Gardena. *Hist. Biol.* 31, 322–340. doi: 10.1080/08912963.2017.1370586

Citton, P., Ronchi, A., Maganuco, S., Caratelli, M., Nicosia, U., Sacchi, E., et al. (2019b). First tetrapod footprints from the Permian of Sardinia and their palaeontological and stratigraphical significance. *Geol. J.* 54, 2084–2098. doi: 10.1002/gj.3285

Citton, P., Díaz-Martínez, I., de Valais, S., and Cónsole-Gonella, C. (2018). Triassic pentadactyl tracks from the Los Menucos Group (Río Negro province, Patagonia Argentina): possible constraints on the autopodial posture of Gondwanan trackmakers. *PeerJ* 6:e5358. doi: 10.7717/peerj.5358

Citton, P., Nicolosi, I., Carluccio, R., and Nicosia, U. (2016). Unveiling trampling history through trackway interferences and track preservational features: a case study from the Bletterbach gorge (Redagno, Western Dolomites, Italy). *Palaeontol. Electron.* 19.2. 20A, 1–20. doi: 10.26879/611

Citton, P., Romano, M., Carluccio, R., D'Ajello Caracciolo, F., Nicolosi, I., Nicosia, U., et al. (2017). The first dinosaur tracksite from Abruzzi (Monte Cagno, Central Apennines, Italy. *Cretaceous Res.* 73, 47–59. doi: 10.1016/j.cretres.2017.01.002

Citton, P., Ronchi, A., Nicosia, U., Sacchi, E., Maganuco, S., Cipriani, A., et al. (2020). Tetrapod tracks from the Middle Triassic of NW Sardinia (Nurra region. Italy). *Italian J. Geosci.* 139, 309–320. doi: 10.3301/ijg.2020.07

Curioni, G. (1870). Osservazioni geologiche sulla Val Trompia. *Rend. Ist. Lomb. Sci. Lett. Arti Mem.* 3, 1–60.

de Klerk, W. J. (2002). A dicynodont trackway from the Cistecephalus assemblage zone in the Karoo, east of Graaff-Reinet. South Africa. *Palaeontol. Afr.* 91, 73–91.

Demathieu, G. (1985). Trace fossil assemblages in middle Triassic marginal marine deposits, Eastern border of the Massif Central, France. *SEPM Spec. Publ.* 35, 53–66. doi: 10.2110/pec.85.35.0053

Demathieu, G., and Demathieu, P. (2004). Chirotheria and other ichnotaxa of the European Triassic. *Ichnos* 11, 79–88. doi: 10.1080/10420940490444898

Falcon-Lang, H. J., Gibling, M. R., Benton, M. J., Miller, R. F., and Bashforth, A. R. (2010). Diverse tetrapod trackways in the Lower Pennsylvanian Tynemouth Creek Formation, near St. Martins, southern New Brunswick, Canada. *Palaeogeogr. Palaeoclimatol. Palaeoecol.* 296, 1–13. doi: 10.1016/j.palaeo.2010.06.020

Falkingham, P. L. (2012). Acquisition of high resolution three-dimensional models using free, open-source, photogrammetric software. *Palaeontol. Electron.* 15.1. 1T, 1–15.

Falkingham, P. L. (2014). Interpreting ecology and behaviour from the vertebrate fossil track record. *J. Zool.* 292, 222–228. doi: 10.1111/jzo.12110

Falkingham, P. L., Bates, K. T., Avanzini, M., Bennett, M., Brody, E. M., Breithaupt, B. H., et al. (2018). A standard protocol for documenting modern and fossil ichnological data. *Palaeontology* 61, 469–480. doi: 10.1111/pala.12373

Falkingham, P. L., Bates, K. T., and Farlow, J. O. (2014). Historical photogrammetry: Bird's Paluxy River dinosaur chase sequence digitally reconstructed as it was prior to excavation 70 years ago. *PLoS One* 9:e93247. doi: 10.1371/journal.pone.0093247

Falkingham, P. L., and Gatesy, S. M. (2014). The birth of a dinosaur footprint: subsurface 3D motion reconstruction and discrete element simulation reveal track ontogeny. *Proc. Natl. Acad. Sci. U.S.A.* 111, 18279–18284. doi: 10.1073/pnas.1416252111

Farman, R. M., and Bell, P. R. (2020). Australia's earliest tetrapod swimming traces from the Hawkesbury Sandstone (Middle Triassic) of the Sydney Basin. *J. Paleontol.* 13, 1–13. doi: 10.1017/jpa.2020.22

Ford, D. P., and Benson, R. B. J. (2020). The phylogeny of early amniotes and the affinities of Parareptilia and Varanopidae. *Nat. Ecol. Evol.* 4, 57–65. doi: 10.1038/s41559-019-1047-3

Fornós, J. J., Bromley, R. G., Clemmensen, L. B., and Rodriguez-Perea, A. (2002). Tracks and trackways of Myotragusbalearicus Bate (Artiodactyla, Caprinae) in Pleistocene aeolianites from Mallorca (Balearic Islands, Western Mediterranean). *Palaeogeogr. Palaeoclimatol. Palaeoecol.* 180, 277–313. doi: 10.1016/s0031-0182(01)00431-x

Fortuny, J., Bolet, A., Sellés, A. G., Cartanyà, J., and Galobart, À (2011). New insights on the Permian and Triassic vertebrates from the Iberian Peninsula with emphasis on the Pyrenean and Catalonian basins. *J. Iber. Geol.* 37, 65–86. doi: 10.5209/rev_JIGE.2011.v37.n1.5

Francischini, H., Dentzien-Dias, P., Lucas, S. G., and Schultz, C. L. (2018). Tetrapod tracks in Permo–Triassic eolian beds of southern Brazil (Paraná Basin). *PeerJ* 6:e4764. doi: 10.7717/peerj.4764

Francischini, H., Lucas, S. G., Voigt, S., Marchetti, L., Santucci, V. L., Knight, C. L., et al. (2020). On the presence of Ichniotherium in the Coconino Sandstone (Cisuralian) of the Grand Canyon and remarks on the occupation of deserts by non-amniote tetrapods. *Pal. Z.* 94, 207–225. doi: 10.1007/s12542-019-00450-5

Gand, G. (1987). *Les traces de Vertébrés tétrapodes du Permien français (paléontologie, stratigraphie, paléoenvironnements)*. Dissertation thesis, Université de Bourgogne, Dijon.

Gand, G., Demathieu, G., and Montenat, C. (2007). Les traces de pas d'amphibiens, de dinosaures et autres reptiles du Mésozoïque français: inventaire et interprétations. *Palaeovertebrata* 1- 4, 1–149.

Gand, G., and Durand, M. (2006). "Tetrapod footprint ichno-associations from French Permian basins. Comparisons with other Euramerican ichnofaunas," in *Non-Marine Permian Biostratigraphy and Biochronology*, eds S. G. Lucas, G. Cassinis, and J. W. Schneider (London: Geological Society of London Special Publication 265), 157–177. doi: 10.1144/gsl.sp.2006.265.01.07

Gand, G., Garric, J., Demathieu, G., and Ellenberger, P. (2000). La palichnofaune de vertébrés tétrapodes du Permien supérieur du Bassin de Lodève (Languedoc-France). *Palaeovertebrata* 29, 1–82.

Gatesy, S. M., and Falkingham, P. L. (2017). Neither bones nor feet: track morphological variation and 'preservation quality'. *J. Vert. Paleontol.* 37:e1314298. doi: 10.1080/02724634.2017.1314298

Gatesy, S. M., Middleton, K. M., Jenkins, F. A. Jr., and Shubin, N. H. (1999). Three-dimensional preservation of foot movements in Triassic theropod dinosaurs. *Nature* 399, 141–144. doi: 10.1038/20167

Geinitz, H. B. (1861). *Dyas oder die Zechsteinformation und des Rotliegende. Die Animalischen ueberreste der Dyas, vol. I*. Leipzig: William Engelmann.

Geinitz, H. B. (1863). Beiträge zur Kenntnis der organischen Überreste in der Dyas. *N. Jb. Min. Geol. Paläont.* 1863, 385–398.

Geinitz, H. B., and Deichmüller, J. V. (1882). Die Saurier der unteren Dyas von Sachsen. *Palaeontographica* 29, 1–4.

Gilmore, C. W. (1926). Fossil footprints from the Grand Canyon. *Smithson. Miscell. Coll.* 77, 1–41.

Gilmore, C. W. (1927). Fossil footprints from the Grand Canyon. II. *Smithson. Miscell. Coll.* 80, 1–78.

Gisbert, J. (1981). *Estudio geológico-petrológico del Estefaniense-Pérmico de la Sierra del Cadí (Pirineo de Lérida): Diagénesis y sedimentología*. Dissertation thesis, Universdad de Zaragoza, Zaragoza.

Haubold, H. (1970). Versuch der Revision der Amphibien-Fährten des Karbon und Perm. *Freib. Forsch. C* 260, 83–117.

Haubold, H. (1971a). Die Tetrapodenfährten des Buntsandsteins in der Deutschen Demokratischen Republik und in Westdeutschland und ihre Äquivalente in der gesamten Trias. *Paläntologische Abhandlungen A* 4, 395–548.

Haubold, H. (1971b). *Encyclopedia of Palaeoherpetology, Part 18: Ichnia amphibiorum et Reptiliorum fossilium*. Stuttgart: Gustav Fischer Verlag, 1–124.

Haubold, H. (1996). Ichnotaxonomie und Klassifikation von Tetrapodenfährten aus dem Perm. *Hallesch. Jahr. Geowiss. B* 18, 23–88.

Haubold, H., Hunt, A. P., Lucas, S. G., and Lockley, M. G. (1995a). Wolfcampian (early Permian) vertebrate tracksfrom Arizona and New Mexico. *N. M. Mus. Nat. Hist. Sci. Bull.* 6, 135–165.

Haubold, H., Lockley, M. G., Hunt, A. P., and Lucas, S. G. (1995b). Lacertoid footprints from Permian dune sandstones, Cornberg and De Chelly Sandstones. *N. M. Mus. Nat. Hist. Sci. Bull.* 6, 235–244.

Heyler, D., and Gand, G. (2000). Pistes et traces du Permien du sud de la France dans les collections du Muséum National d'Histoire Naturelle (Paris), première partie: les bassin de Lodève. *Bull. Soc. Hist. Nat. Autun.* 176, 7–50.

Heyler, D., and Lessertisseur, J. (1963). Piste de tétrapodes permiens dans la région de Lodève (Hérault). *Mém. Mus. Natl. Hist. Nat. Série C Sci. de la Terre* 11, 125–221.

Hunt, A. P., and Lucas, S. G. (2005). "Tetrapod Ichnofacies and their utility in the Paleozoic," in *Pennsylvanian Footprints in the Black Warrior Basin of Alabama*, eds R. J. Buta, A. K. Rindsberg, and D. Kopaska-Merkel (Alabama: Alabama Paleontological Society), 113–119.

International Commission on Zoological Nomenclature (1999). *International Code of Zoological Nomenclature*, 4th Edn. London: International Trust for Zoological Nomenclature.

Jardine, W. (1853). *The Ichnology of Annandale*. Edinburgh: The University of Edinburg.

Kaup, J. J. (1835). Über Tierfährten bei Hildburghausen. *N. Jb. Min. Geol. Pal.* 1835, 327–328.

Klein, H., and Lucas, S. G. (2010). Review of the tetrapod ichnofauna of the Moenkopi Formation/Group (Early–Middle Triassic) of the American Southwest. *N. M. Mus. Nat. Hist. Sci. Bull.* 50, 1–167.

Klein, H., Lucas, S. G., and Voigt, S. (2015). Revision of the ?Permian-Triassic tetrapod ichnogenus Procolophonichnium Nopcsa, 1923 with description of the new ichnospecies *P. lockleyi*. *Ichnos* 22, 155–176. doi: 10.1080/10420940.2015.1063490

Krapovickas, V., Marsicano, C. A., Mancuso, A. C., de la Fuente, M. S., and Ottone, E. G. (2015). Tetrapod and invertebrate trace fossils from aeolian deposits of the lower Permian of central-western Argentina. *Hist. Biol.* 27, 827–842. doi: 10.1080/08912963.2014.904857

Lagnaoui, A., Melchor, R. N., Bellosi, E. S., Villegas, P. M., Espinoza, N., and Umazano, A. M. (2019). Middle Triassic Pentasauropus-dominated ichnofauna from western Gondwana: Ichnotaxonomy, palaeoenvironment, biostratigraphy and palaeobiogeography. *Palaeoegeogr. Palaeoclim. Palaeoecol.* 524, 41–61. doi: 10.1016/j.palaeo.2019.03.020

Lallensack, J. N. (2019). Automatic generation of objective footprint outlines. *PeerJ* 7:e7203. doi: 10.7717/peerj.7203

Lallensack, J. N., Klein, H., Milàn, J., Wings, O., Mateus, O., and Clemmensen, L. B. (2017). Sauropodomorph dinosaur trackways from the Fleming Fjord Formation of East Greenland: evidence for Late Triassic sauropods. *Acta Palaeontol. Pol.* 62, 833–843.

Lallensack, J. N., Sander, P. M., Knötschke, N., and Wings, O. (2015). Dinosaur tracks from the Langenberg Quarry (Late Jurassic, Germany) reconstructed with historical photogrammetry: evidence for large theropods soon after insular dwarfism. *Palaeontol. Electron.* 18, 1–34.

Laurin, M., and Piñeiro, G. H. (2017). A reassessment of the taxonomic position of Mesosaurs, and a surprising phylogeny or early Amniotes. *Front. Earth Sci.* 5:88. doi: 10.3389/feart.2017.00088

Laurin, M., and Piñeiro, G. H. (2018). Response: commentary: a reassessment of the taxonomic position of Mesosaurs, and a surprising phylogeny or early Amniotes. *Front. Earth Sci.* 6:200. doi: 10.3389/feart.2018.00220

Leonardi, G. (1987). *Glossary and Manual of Tetrapod Palaeoichnology*. Brasilia: Departamento Nacional da Produção Mineral.

Leonardi, G., and Mietto, P. (2000). *Dinosauri in Italia: Le orme giurassiche dei Lavini di Marco (Trentino) e gli altri resti fossili italiani*. Pisa-Roma: Accademia Editoriale.

Lockley, M. G., Cawthra, H. C., De Vynck, J. C., Helm, C. W., McCrea, R. T., and Nel, R. (2019). New fossil sea turtle trackway morphotypes from the Pleistocene of South Africa highlight role of ichnology in turtle paleobiology. *Q. Res.* 92, 626–640. doi: 10.1017/qua.2019.40

Loope, D. B. (2006). Dry-season tracks in dinosaur-triggered grainflows. *Palaios* 21, 132–142. doi: 10.2110/palo.2005.p05-55

Lucas, S. G. (2019). An ichnological perspective on some major events of Paleozoic tetrapod evolution. *Boll. Soc. Paleont. It.* 58, 223–266.

Lucas, S. G., and Harris, J. D. (2020). The "plastotype problem" in ichnological taxonomy. *Ichnos* 27, 107–110. doi: 10.1080/10420940.2019.1688802

MacDougall, M. J., Modesto, S. P., Brocklehurst, N., Verrière, A., Reisz, R. R., and Fröbisch, J. (2018). Response: a reassessment of the taxonomic position of mesosaurs, and a surprising phylogeny of early Amniotes. *Front. Earth Sci.* 6:99. doi: 10.3389/feart.2018.00099

Maidwell, F. T. (1911). Notes on footprints from the Keuper of Runcorn Hill. *Proc. Liverpool Geol. Soc.* 11, 140–152.

Mallison, H., and Wings, O. (2014). Photogrammetry in paleontology – A practical guide. *J. Paleontol. Tech.* 12, 1–31.

Mancuso, A. C., Krapovickas, V., Marsicano, C., Benavente, C., Benedito, D., de la Fuente, M., et al. (2016). Tetrapod tracks taphonomy in eolian facies from the Permian of Argentina. *Palaios* 31, 374–388. doi: 10.2110/palo.2015.077

Marchetti, L. (2016). New occurrences of tetrapod ichnotaxa from the Permian Orobic Basin (Northern Italy) and critical discussion of the age of the ichnoassociation. *Papers Palaeontol.* 2, 363–386. doi: 10.1002/spp2.1045

Marchetti, L. (2019). Can undertracks show higher morphologic quality than surface tracks? Remarks on large amphibian tracks from the Early Permian of France. *J. Iber. Geol.* 45, 353–363. doi: 10.1007/s41513-018-0080-4

Marchetti, L., Belvedere, M., Voigt, S., Klein, H., Castanera, D., Díaz-Martínez, I., et al. (2019a). Defining the morphological quality of fossil footprints. Problems and principles of preservation in tetrapod ichnology with examples from the Palaeozoic to the present. *Earth Sci. Rev.* 193, 109–145. doi: 10.1016/j.earscirev.2019.04.008

Marchetti, L., Klein, H., Buchwitz, M., Ronchi, A., Smith, R. M., De Klerk, W. J., et al. (2019d). Permian-Triassic vertebrate footprints from South Africa: ichnotaxonomy, producers and biostratigraphy through two major faunal crises. *Gondw. Res.* 72, 139–168. doi: 10.1016/j.gr.2019.03.009

Marchetti, L., Voigt, S., and Lucas, S. G. (2019c). An anatomy-based study of the Lopingian eolian tracks of Germany and Scotland reveals the first evidence of the end-Guadalupian mass extinction at low paleolatitudes of Pangea. *Gondw. Res.* 73, 32–53. doi: 10.1016/j.gr.2019.03.013

Marchetti, L., Voigt, S., Lucas, S. G., Francischini, H., Dentzien-Dias, P., Sacchi, R., et al. (2019b). Tetrapod ichnotaxonomy in eolian paleoenvironments (Coconino and De Chelly formations, Arizona) and late Cisuralian (Permian) sauropsid radiation. *Earth Sci. Rev.* 190, 148–170. doi: 10.1016/j.earscirev.2018.12.011

Marchetti, L., Bernardi, M., and Avanzini, M. (2013). Some insights on well-preserved Amphisauropus and Erpetopus trackways from the Eastern Collio Basin (Trentino-Alto Adige NE Italy). *Boll. Soc. Paleont. It.* 52, 55–62.

Marchetti, L., Mujal, E., and Bernardi, M. (2017a). An unusual Amphisauropus trackway and its implication for understanding seymouriamorph locomotion. *Lethaia* 50, 162–174. doi: 10.1111/let.12184

Marchetti, L., Belvedere, M., and Mietto, P. (2017b). Lopingian tetrapod footprints from the Venetian Prealps, Italy: new discoveries in a largely incomplete panorama. *Acta Palaeontol. Pol.* 62, 801–817.

Marchetti, L., Petti, F. M., Bernardi, M., Citton, P., Rossi, R., and Schirolli, P. (2018a). On the first description of tetrapod footprints from Italy: re-analysis of the original specimen after 150 years. *Rend. Online Soc. Geol. It.* 44, 112–118. doi: 10.3301/rol.2018.16

Marchetti, L., Voigt, S., and Santi, G. (2018b). A rare occurrence of Permian tetrapod footprints: *Ichniotherium cottae* and *Ichniotherium sphaerodactylum* on the same stratigraphic surface. *Ichnos* 25, 106–118. doi: 10.1080/10420940.2017.1380005

Marchetti, L., Ronchi, A., Santi, G., and Voigt, S. (2015). The Gerola Valley site (Orobic Basin, Northern Italy): a key for understanding late Early Permian tetrapod ichnofaunas. *Palaeoegeogr. Palaeoclim. Palaeoecol.* 439, 97–116. doi: 10.1016/j.palaeo.2015.02.032

Marsh, O. C. (1894). Footprints of vertebrates in the Coal Measures of Kansas. *Am. J. Sci. Ser.* 3, 81–84. doi: 10.2475/ajs.s3-48.283.81

Marty, D., Strasser, A., and Meyer, C. A. (2009). Formation and taphonomy of human footprints in microbial mats of present-day tidal-flat environments: implications for the study of fossil footprints. *Ichnos* 16, 127–142. doi: 10.1080/10420940802471027

Matthews, N. A. (2008). *Aerial and Close-Range Photogrammetric Technology: Providing Resource Documentation, Interpretation, and Preservation. Technical Note 428*. Denver: U.S. Department of the Interior, Bureau of Land Management, National Operations Center.

McKeever, P. J., and Haubold, H. (1996). Reclassification of vertebrate trackways from the Permian of Scotland and related forms from Arizona and Germany. *J. Paleontol.* 70, 1011–1022. doi: 10.1017/s0022336000038713

Meade, L. E., Jones, A. S., and Butler, R. J. (2016). A revision of tetrapod footprints from the late Carboniferous of the West Midlands. UK. *PeerJ* 4:e2718. doi: 10.7717/peerj.2718

Michel, L. A., Tabor, N. J., Montañez, I. P., Schmitz, M. D., and Davydov, V. I. (2015). Chronostratigraphy and Paleoclimatology of the Lodève Basin, France: evidence for a pan-tropical aridification event across the Carboniferous–Permian boundary. *Palaeoegeogr. Palaeoclim. Palaeoecol.* 430, 118–131.doi: 10.1016/j.palaeo.2015.03.020

Milàn, J., Klein, H., Voigt, S., and Stemmerik, L., (2016). First record of tetrapod footprints from the Carboniferous Mesters Vig Formation in East Greenland. *Bull. Geol. Soc. Denmark* 64, 69–76.

Moodie, R. L. (1929). Vertebrate footprints from the red beds of Texas. *J. Geol.* 38, 548–565. doi: 10.1086/623755

Moodie, R. L. (1930). Vertebrate footprints from the Red Beds of Texas II. *Amer. J. Sci.* 97, 352–368. doi: 10.2475/ajs.s5-17.100.352

Mujal, E. (2017). *Registre sedimentari i icnològic del fini-Carbonífer, Permià i Triàsic continentals dels Pirineus Catalans: Evolució i crisis paleoambientals a l'equador de Pangea*. Dissertation thesis, Universitat Autònoma de Barcelona, Cerdanyola del Vallès.

Mujal, E., Fortuny, J., Bolet, A., Oms, O., and López, J. Á (2017a). An archosauromorph dominated ichnoassemblage in fluvial settings from the late early Triassic of the Catalan Pyrenees (NE Iberian Peninsula). *PLoS one* 12:e0174693. doi: 10.1371/journal.pone.0174693

Mujal, E., Fortuny, J., Pérez-Cano, J., Dinarès-Turell, J., Ibáñez-Insa, J., Oms, O., et al. (2017b). Integrated multi-stratigraphic study of the Coll de Terrers late Permian–early Triassic continental succession from the Catalan Pyrenees (NE Iberian Peninsula): a geologic reference record for equatorial Pangaea. *Glob. Planet. Chang.* 159, 46–60. doi: 10.1016/j.gloplacha.2017.10.004

Mujal, E., Gretter, N., Ronchi, A., López-Gómez, J., Falconnet, J., Diez, J. B., et al. (2016b). Constraining the Permian/Triassic transition in continental environments: stratigraphic and paleontological record from the Catalan Pyrenees (NE Iberian Peninsula). *Palaeogeogr. Palaeoclimatol. Palaeoecol.* 445, 18–37. doi: 10.1016/j.palaeo.2015.12.008

Mujal, E., Fortuny, J., Oms, O., Bolet, A., Galobart, À, and Anadón, P. (2016a). Palaeoenvironmental reconstruction and early Permian ichnoassemblage from the NE Iberian Peninsula (Pyrenean Basin). *Geol. Mag.* 153, 578–600. doi: 10.1017/s0016756815000576

Mujal, E., Fortuny, J., Rodríguez-Salgado, P., Diviu, M., Oms, O., and Galobart, À (2015). First footprints occurrence from the Muschelkalk detritical unit of the Catalan Basin: 3D analyses and palaeoichnological implications. *Span. J. Palaeontol.* 30, 97–108.

Mujal, E., Fortuny, J., Marmi, J., Dinarès-Turell, J., Bolet, A., and Oms, O. (2018b). Aridification across the Carboniferous–Permian transition in central equatorial Pangea: the Catalan Pyrenean succession (NE Iberian Peninsula). *Sediment. Geol.* 363, 48–68. doi: 10.1016/j.sedgeo.2017.11.005

Mujal, E., Iglesias, G., Oms, O., Fortuny, J., Bolet, A., and Méndez, J. M. (2018a). Rhynchosauroides footprint variability in a Muschelkalk detrital interval (late Anisian–middle Ladinian) from the Catalan Basin (NE Iberian Peninsula). *Ichnos* 25, 150–161. doi: 10.1080/10420940.2017.1337571

Mujal, E., and Marchetti, L. (2020). Ichniotherium tracks from the Permian of France, and their implications for understanding the locomotion and palaeobiogeography of large diadectomorphs. *Palaeogeogr. Palaeoclimatol. Palaeoecol.* 547:109698. doi: 10.1016/j.palaeo.2020.109698

Mujal, E., and Schoch, R. R. (2020). Middle Triassic (Ladinian) amphibian tracks from the Lower Keuper succession of southern Germany: implications for temnospondyl locomotion and track preservation. *Palaeogeogr. Palaeoclimatol. Palaeoecol.* 543:109625. doi: 10.1016/j.palaeo.2020.109625

Nopcsa, F. V. (1923). Die familien der reptilien. *Fortschritte Geol. Pal.* 2, 1–210.

Olsen, P. E. (1995). A new approach for recognizing track makers. *Geol. Soc. Am. Abst. Progr.* 27:72.

Pabst, W. (1895). Thierfährten aus dem Rothliegenden von Friedrichroda, Tambach und Kabarz in Thüringen. *Z. Dtsch. geol. Ges.* 47, 570–576.

Pabst, W. (1908). Die Tierfährten in dem Rotliegenden,Deutschlands'. *Nova Acta Leopold* 89, 315–481.

Peabody, F. E. (1948). Reptile and amphibian trackways from the Moenkopi Formation of Arizona and Utah. *Univ. California Publ. Bull. Dept. Geol. Sci.* 27, 295–468.

Petti, F. M., Avanzini, M., Belvedere, M., De Gasperi, M., Ferretti, P., Girardi, S., et al. (2008). Digital 3D modelling of dinosaur footprints by photogrammetry and laser scanning techniques: integrated approach at the Coste dell'Anglone tracksite (Lower Jurassic, Southern Alps, Northern Italy). *Stud. Trent. Sci. Nat., Acta Geol.* 83, 303–315.

Petti, F. M., Avanzini, M., Nicosia, U., Girardi, S., Bernardi, M., Ferretti, P., et al. (2009). Late Triassic (early-middle Carnian) chirotherian tracks from the Val Sabbia Sandstone (eastern Lombardy, Brescian Prealps, northern Italy). *Riv. It. Paleont. Strat.* 115, 277–290.

Petti, F. M., Petruzzelli, M., Conti, J., Spalluto, L., Conti, J., Wagensommer, A., et al. (2018). The use of aerial and close-range photogrammetry in the study of dinosaur tracksites: lower Cretaceous (upper Aptian/lower Albia) Molfetta ichnosite (Apulia, southern Italy). *Palaeontol. Electron.* 21, 1–18.

Razzolini, N. L., Vila, B., Castanera, D., Falkingham, P. L., Barco, J. L., Canudo, J. I., et al. (2014). Intra-trackway morphological variations due to substrate consistency: the El Frontal dinosaur tracksite (lower Cretaceous Spain). *PLoS One* 9:e93708. doi: 10.1371/journal.pone.0093708

Reisz, R. R., Modesto, S. P., and Scott, D. M. (2011). A new Early Permian reptile and its significance in early diapsid evolution. *Proc. R. Soc. B* 278, 3731–3737. doi: 10.1098/rspb.2011.0439

Remondino, F., Rizzi, A., Girardi, S., Petti, F. M., and Avanzini, M. (2010). 3D ichnology – Recovering digital 3D models of dinosaur footprints. *Photogrammetr. Record* 25, 266–282. doi: 10.1111/j.1477-9730.2010.00587.x

Reolid, J., Cardenal, F. J., Reolid, M., and Mata, E. (2020). 3D Imaging of southernmost Triassic archosaur footprints from Europe (Southern Spain) *J. Iberian Geol.* 46, 145–161. doi: 10.1007/s41513-020-00125-0

Romilio, A., Hacker, J. M., Zlot, R., Poropat, G., Bosse, M., and Salisbury, S. W. (2017). A multidisciplinary approach to digital mapping of dinosaurian tracksites in the Lower Cretaceous (Valanginian–Barremian) Broome Sandstone of the Dampier Peninsula. Western Australia. *PeerJ* 5:e3013. doi: 10.7717/peerj.3013

Salisbury, S. W., Romilio, A., Herne, M. C., Tucker, R. T., and Nair, J. P. (2016). The dinosaurian ichnofauna of the Lower Cretaceous (Valanginian–Barremian) Broome Sandstone of the Walmadany Area (James Price Point), Dampier Peninsula, Western Australia. *J. Vert. Paleontol.* 36, 1–152. doi: 10.1080/02724634.2016.1269539

Schmidt, H. (1959). Die Cornberger Fährten im Rahmen der Vierfüßler-Entwicklung. *Abh. Hess. Landesamt Bodenforsch.* 28, 1–137.

Schoch, R. R., and Seegis, D. (2016). A Middle Triassic palaeontological gold mine: the vertebrate deposits of Vellberg (Germany). *Palaeogeogr. Palaeoclimatol. Palaeoecol.* 459, 249–267. doi: 10.1016/j.palaeo.2016.07.002

Smith, R. M. H., and Botha-Brink, J. (2014). Anatomy of a mass extinction: sedimentological and taphonomic evidence for drought-induced die-offs at the Permo-Triassic boundary in the main Karoo Basin, South Africa. *Palaeogeogr. Palaeoclimatol. Palaeoecol.* 396, 99–118. doi: 10.1016/j.palaeo.2014.01.002

Thomson, T. J., and Droser, M. L. (2015). Swimming reptiles make their mark in the Early Triassic: delayed ecologic recovery increased the preservation potential of vertebrate swim tracks. *Geology* 43, 215–218. doi: 10.1130/g36332.1

Vila, B., Castanera, D., Marmi, J., Canudo, J. I, and Galobart, À (2015). Crocodile swim tracks from the latest Cretaceous of Europe. *Lethaia* 48, 256–266. doi: 10.1111/let.12103

Voigt, S. (2005). *Die Tetrapoden ichnofauna des kontinentalen Oberkarbon und Perm im Thüringer Wald - Ichnotaxonomie, Paläoökologie und Biostratigraphie*. Dissertation thesis, Martin-Luther-Universität Halle-Wittenberg, Göttingen.

Voigt, S., Berman, D. S., and Henrici, A. C. (2007). First well-established track-trackmaker association of Paleozoic tetrapods based on Ichniotherium trackways and diadectid skeletons from the Lower Permian of Germany. *J. Vert. Paleontol.* 27, 553–570. doi: 10.1671/0272-4634(2007)27[553:fwtaop]2.0.co;2

Voigt, S., and Haubold, H. (2015). Permian tetrapod footprints from the Spanish Pyrenees. *Palaeogeogr. Palaeoclimatol. Palaeoecol.* 417, 112–120. doi: 10.1016/j.palaeo.2014.10.038

Wernerburg, I. (2019). Morphofunctional categories and ontogenetic origin of temporal skull openings in amniotes. *Front. Earth Sci.* 7:13. doi: 10.3389/feart.2019.00013

Conflict of Interest: The authors declare that the research was conducted in the absence of any commercial or financial relationships that could be construed as a potential conflict of interest.

frontiers in Earth Science

ORIGINAL RESEARCH
published: 18 September 2020
doi: 10.3389/feart.2020.00345

Toward an "Ancient" Virtual World: Improvement Methods on X-ray CT Data Processing and Virtual Reconstruction of Fossil Skulls

Alejandro Pérez-Ramos and Borja Figueirido*

Departamento de Ecología y Geología, Facultad de Ciencias, Málaga, Spain

This article focuses on new virtual advances to solve technical problems usually encountered by paleontologists when using X-ray computed tomography (XCT), such as (i) the limited scanning envelope (i.e., field of view of CT systems/machines) to acquire data on large structures; (ii) the use in the same study of biological objects acquired with different types of computed tomography systems (medical and laboratory XCTs and laboratory high-resolution XμCT) and therefore different resolutions; and (iii) matrix removal within the fossil (e.g., cranial cavities, intratrabecular cavities, among other cavities). All these problems are very common in paleontology, and therefore, solving them is important to save effort and the time invested in data processing. In this article, we propose various solutions to tackle these issues, based on new technical advances focused on improving and processing the images obtained from XCT. Other aspects include image filtering and histogram calibration to remove background noise and artifacts. Such artifacts can result from dense mineral inclusion occurring during the fossilization process or derived from anthropogenic restoration of the sample. Accordingly, here, we provide a protocol to acquire data on samples with size that exceed the scanning envelope of the X-ray tomography machine, joining the parts with enough accuracy, and we propose the use of the interpolation "bicubic" method. Moreover, using this method, it is possible to use medical/laboratory XCT data together with XμCT data and therefore opening new ways to manipulate the acquired data within the image stack. Another advantage is the use of plugins for quantitative analysis, which require data with isometric voxels, such as the plugin BoneJ of the software ImageJ. We also deal with the problem of removing the exogenous material that usually fills the internal cavities of fossils by means of using filters based on edge detection by gradient. Applying this method, it is possible to segment the non-bony matrix parts more quickly and efficiently. All of this is exemplified using five fossil skulls belonging to the cave bear group (*Ursus spelaeus* sensu lato), an iconic fossil species from the Pleistocene of Eurasia.

Keywords: X-ray CT scan, thresholding, mirroring, image filtering, reslice, voxel size, bicubic interpolation, ImageJ

OPEN ACCESS

Edited by:
Josep Fortuny,
Institut Català de Paleontologia Miquel Crusafont, Spain

Reviewed by:
Jordi Marcé-Nogué,
University of Rovira i Virgili, Spain
Vincent Fernandez,
Natural History Museum, United Kingdom

****Correspondence:***
Alejandro Pérez-Ramos
pera@uma.es

Specialty section:
This article was submitted to Paleontology, a section of the journal Frontiers in Earth Science

Received: *08 February 2020*
Accepted: *27 July 2020*
Published: *18 September 2020*

Citation:
Pérez-Ramos A and Figueirido B (2020) Toward an "Ancient" Virtual World: Improvement Methods on X-ray CT Data Processing and Virtual Reconstruction of Fossil Skulls. Front. Earth Sci. 8:345. doi: 10.3389/feart.2020.00345

INTRODUCTION

The advent of personal computers and digital technology in the twentieth century has allowed the emergence of new digital tools useful in paleontological research, including new software for image analysis and computational analysis (Jablonski and Shubin, 2015; du Plessis and Broeckhoven, 2019). This "digital revolution" took place in the mid-2000s, when there was already performed research with X-ray computed tomography (XCT) data in the paleontological field (Cunningham et al., 2014; Sutton et al., 2014). This allowed the development of new, more economical, and sometimes freely accessible digital tools for virtual anatomic analysis, such as high-resolution XCT (laboratory XCT and XμCT), three-dimensional (3D) acquisition of surfaces through laser scanners, and new advanced software for image analysis in two and three dimensions.

The new digital tools have allowed surpassing the frontiers of knowledge in many fields, which have opened new horizons of research in many disciplines (du Plessis and Broeckhoven, 2019). In the case of paleontology, this "digital revolution" has substantially changed the way of analyzing the scientific material, generating new fields of research at different levels of analysis that were previously inaccessible (Racicot, 2017). For example, this is the case of histological studies in fossils with non-invasive techniques (i.e., virtual paleohistology; e.g., Sanchez et al., 2012), virtual reconstructions of distorted fossil specimens with lacking parts (i.e., retrodeformation techniques; e.g., Tallman et al., 2014), development of powerful biomechanical models (i.e., finite element analysis; e.g., Figueirido et al., 2014, 2018; Tseng et al., 2017; Pérez-Ramos et al., 2020), or the study of internal structures, non-accessible without using invasive techniques such as brain endocasts (i.e., paleoneurology; e.g., Cuff et al., 2016) or paranasal sinuses and turbinates (i.e., functional anatomy of internal structures; e.g., Curtis and Van Valkenburgh, 2014; Van Valkenburgh et al., 2014; Matthews and du Plessis, 2016). All these techniques undoubtedly lead to new avenues for future research in the paleobiology of extinct organisms.

Moreover, the new "virtual world" has significantly changed how scientists conceive the collections of living and fossil organisms. For example, nowadays, virtual free-access collections such as Morphomuseum[1], Phenome10K[2], or the pioneer Digimorph[3] are substantially increasing. Furthermore, such digital collections could be used to detect fossil fakes or to have a digital copy of the original specimen that can be adequately preserved against possible loss (Rahman et al., 2012).

All these virtual techniques are based on the 3D characterization of the object (e.g., skull, mandibles, or any other skeletal part preserved as a fossil or footprints and burrow casts) subject to analysis (Knaust, 2012; Kouraiss et al., 2019). This could be also done to digitize solely the external surface of the object (e.g., using laser scanning, modulated-light, structure-light surface scanning or photogrammetry) or to digitize both the external surface as well as the internal structures with XCT (Kouraiss et al., 2019) or synchrotron microtomography (SRμCT) (Sanchez et al., 2012; Davesne et al., 2019; Honkanen et al., 2020). Depending on the type of the object and the aim of the study, the resolution required will be different, and therefore, one type of tomography will be used. For those studies of large- or medium-sized specimens, the use of medical XCT system is appropriate. However, for other studies that require more level of resolution (e.g., those based on cranial sutures, roughness of muscle insertions, crown dental topology, or other tiny bone elements such as the anatomy of the trabeculae), the use of laboratory XCT system and XμCT system will be recommended. On the other hand, to study cellular elements such as osteocytes or other components of cellular size, the use of synchrotron (SRμCT) is recommended. However, these sources are still difficult to access because of competitiveness for access and large technological size, increasing also the costs of their use. On the other hand, the use of computed tomography of neutron sources (nCT) is recently having great acceptance in the scientific community, as it has a resolution comparable to that of a μCT. However, nCT has the same disadvantages as SRμCT relative to use, economic cost, and time. Moreover, as it is a very recent technique, with very few institutions having this technology, access to nCT is much more competitive than to μCT or SRμCT. Despite this, the advantages of using nCT are greater than their limitations. For example, its use does not disrupt organic matter preserved in fossils (DNA, RNA, or proteins) compared to SRuCT (Lakey, 2009; Immel et al., 2016), as nCTs are based on very low neutron energies with high penetration power due to their low interaction with matter (Tremsin et al., 2015). The other advantage is that it is possible to obtain high contrasts of internal structures in fossil samples – contrary to that of X-rays – especially to distinguish between mineralized tissues (fossil entity) and matrix. This is due to the great penetration capacity with very low neutron attenuation (Schwarz et al., 2005; Sutton, 2008; Schillinger et al., 2018; Zanolli et al., 2020).

Therefore, the use of both medical XCT and laboratory XCT is more common and easily accessible. However, the data obtained with nCT are complementary with the data obtained from XCT (Sutton, 2008; Mays et al., 2017; Zanolli et al., 2020). This increases the analytical capacity to visualize internal structures that only with X-rays are impossible to detect.

Several acquisition parameters must be considered to generate 3D virtual models from XCT, such as X-ray voltage and current, spatial resolution, image acquisition time, rotation steps, filters, and so on (Kak and Slaney, 1988; Zollikofer and Ponce de León, 2005; Endo and Frey, 2008; Naresh et al., 2020). Once the 3D object has been acquired, the resulting image stacks could be enhanced, eliminating the background noise and removing possible artifacts resulting from data acquisition. To do this, different algorithms and digital filters are implemented in the specific software of virtual reconstruction and image processing such as the free-access 3D Slicer v 4.9.0 (Kikinis et al., 2014) and ImageJ (Rueden et al., 2017). Afterward, the enhanced images should be segmented by thresholding of the gray-values histogram (Pertusa, 2010). This process is very sensitive and dependent on the material properties such as bone density and mineralization. Subsequently, the virtual model of the object is

[1]https://morphomuseum.com/

[2]https://www.phenome10k.org/

[3]http://digimorph.org/

generated and can be subject to different evolutionary studies using 3D geometric morphometrics (GMM) for ecomorphology (Drake, 2011), finite element analysis for biomechanics (Racicot, 2017; Tseng et al., 2017), or computational fluid dynamics to decipher the behavior of extinct animals in fluid environments (e.g., Rahman, 2017). In addition, such models can be printed out using rapid prototyping to have a physical replica of the object under study and therefore improving the anatomical understanding and opening the possibility of using these models for teaching or public engagement.

In this article, we perform different imaging processing techniques that are necessary when working with XCT data prior to developing any evolutionary study. In particular, we solve some typical problems usually encountered by paleontologists when using virtual techniques. We use five fossil skulls of cave bears (*Ursus spelaeus*) as study cases to illustrate our proposed analyses when working with fossil material of any kind. Our main objective is to provide new protocols of existing tools to solve the aforementioned problems, that is, (i) to eliminate artifacts typical of the use of XCT technology; (ii) to solve problems of data anisotropy, which is particularly important when comparing different types of XCT data, i.e., from medical XCT or laboratory XCT with XμCT; (iii) to improve segmentation and therefore to improve the virtually cleaning of those materials that usually encompass or fill the internal structures of fossils; (iv) to restore and replace lacking parts of fossils in order to provide an accurate anatomical reconstruction; and (v) to solve errors accumulated in previous processes by processing the mesh and quantifying the topological deviation resulting from previous restorations. To illustrate this, we use as an example five fossil skulls belonging to the cave bear, which were XCT scanned at different museums and institutions. The five skulls belong to different extinct Pleistocene species or subspecies of cave bears (*U. spelaeus* sensu lato): *U. spelaeus spelaeus*; *U. spelaeus ladinicus*; *U. spelaeus eremus;* and *Ursus ingressus* (**Table 1**; see **Supplementary Data**).

To illustrate this, we will use conventional software for 3D processing and analysis, which is described below. First, we use ImageJ[4] to (i) calibrate the images; (ii) eliminate the artifacts by filters; (iii) unify parts of image stacks; (iv) apply different methods for improving data interpolation; and (v) homogenize voxel size and reorient data. Second, we use both Avizo Lite[5] and Mimics[6] to restore and replace virtually possible lacking parts of the fossil skulls. Third, we use Geomagic Wrap[7] to process the virtual meshes by checking their topological optimization and mesh integrity.

In the following sections of the article, we explain all the steps to proceed with virtual models of fossil skulls, including the protocols to follow and the better software to use in each particular case.

X-RAY COMPUTED TOMOGRAPHY ACQUISITION

Although there are several types of scanning machines with different specific settings, here, we present only those that we used to digitize the skulls of cave bears, which are the most commonly used by paleontologists: (i) medical XCT systems, which are the cheapest due to its speed of acquisition (1–2 min). Their voltage and current range between 60 and 140 kV and 100 and 400 mA, respectively, but their resolution is low (1–0.2 mm), which could be a problem for analyses that require more accurate models (**Figure 1A**; **Table 1**, see **Supplementary Data**); and (ii) XμCT systems, which normally possess higher resolution than medical XCTs (10–1 μm) and a high-energy range commonly up to 225 kV(**Figure 1B**; **Table 1**, see **Supplementary Data**). However, the acquisition time is longer than the time required with medical XCT, and it can take several hours for fossils. The choice of one type of machine or another will depend on the size and density

[4]http://rsbweb.nih.gov/ij/

[5]www.vsg3d.com

[6]www.materialise.com

[7]www.3dsystems.com

TABLE 1 | XCT scan acquisition parameters of each skull belonging to the extinct bears used in this article as an example.

Species/serial number	kV	mA	Image matrix (pixels) (original)	Voxel size (X, Y, Z) mm (original)	Voxel size iso (X,Y,Z) mm (standardized)	Image matrix (pixels) (processed)	Voxel size post. (X, Y, Z) mm (processed)
Ursus spelaeus ladinicus PIUW-CU 703	130	0.33	1,491 × 1,139	0.150, 0.150, 0.150	0.150, 0.150, 0.150	1,024 × 1,024	0.150, 0.150, 0.150
Ursus spelaeus eremus PIUW-SW 483*	120	160	512 × 512	0.533, 0.533, 0.200	0.533, 0.533, 0.533	1,024 × 1,024	0.266, 0.266, 0.266
Ursus spelaeus spelaeus E-ZYX-1000*	120	160	512 × 512	0.750, 0.750, 0.365	0.750, 0.750, 0.750	1,024 × 1,024	0.375, 0.375, 0.375
Ursus ingressus PIUW3000/5/105*	120	160	512 × 512	0.611, 0.611, 0.200	0.611, 0.611, 0.611	1,024 × 1,024	0.305, 0.305, 0.305
Ursus spelaeus spp. unnumbered sp.	180	0.16	1,024 × 1,024	0.246, 0.246, 0.246,	0.246, 0.246, 0.246,	1,024 × 1,024	0.246, 0.246, 0.246,

kV, kilovolt; mA, milliampere. Note that the original conditions of acquisition have been standardized (isotropic voxel size) to the same conditions of analyses (processed). The specimens marked with one asterisk (*) were acquired using the medical XCT system. The specimens without asterisk were acquired with XμCT system (see ***Supplementary Data****).*

FIGURE 1 | Examples of acquisition machines used to scan our sample of cave bear skulls. **(A)** XCT machine, GE Medical Systems (Brivo CT385 Series) of the Clínicas Rincón, Málaga. **(B)** High-resolution μCT X8060 of the Vienna Micro-CT Lab (https://www.micro-ct.at/en/) at the Department of Evolutionary Anthropology (see **Supplementary Data**).

of the fossil sample, because there are technical limitations for each type of XCT machine. For a correct acquisition of the data, it is necessary to consider two fundamental variables of the X-ray source, voltage (kV) and current (mA) (Caldemeyer and Buckwalter, 1999; Calzado and Geleijns, 2010; Beck, 2012; Raman et al., 2013). The voltage indicates the energy of the emitted photons, which is linked to the power of penetration. The milliamps or microamps (intensity) are the number of photons emitted per second on a given surface area. For a large fossil sample obtained from a medical XCT, it is recommended to use the maximum power (120–140 kV) and an average intensity to reduce the contribution of a diffusion effect in recorded images called Compton scattering (Glover, 1982; Sabo-Napadensky and Amir, 2005; Johnson, 2012; Ravanfar-Haghighi et al., 2014). Two acquisitions of our sample were collected with a kV greater than 400: the skulls of *Ursus arctos* and of *Ursus maritimus*, using the laboratory XCT system of the University of Texas (see **Supplementary Data**). Although it may seem paradoxical to

see high values of kV for the artifacts produced by the effects mentioned above, this could be related to a very short and fast acquisition time. Together with a high current intensity (3 and 1.80 mA, respectively), the artifacts are avoided and hence obtaining a proper XCT data (**Table 1**; see **Supplementary Data**).

CT DATA PROCESSING FROM XCT

Image Stack Calibration

The two types of processes to object acquisition using XCT systems are based on 360° rotation. The first type is the detector that rotates with respect to the object (medical XCT systems), and the second is the object that rotates with respect to the detector (laboratory XCT systems and XμCT systems). This generates a series of stacked projections of lines that contain each set of detector readings per projection. The position of the object to the source-detector array traces a sinusoidal curve (Racicot, 2017). This is known as sinogram (Kak and Slaney, 1988; Racicot, 2017). These sinogram data can be useful to detect possible artifacts resulted from object acquisitions derived from scan movement. Such abnormalities should be corrected during the process of image "reconstruction," which is the mathematical process of converting sinograms to two-dimensional (2D) slice images (Racicot, 2017). It is worth to mention that this should not be confused with the process of 3D digital reconstruction from XCT slices.

In any acquisition from XCT systems, various artifacts may appear because of physical problems of the object, such as (i) a high density of the material, (ii) an excessive size of the object for the limits of the scanning envelope of the machine, and (iii) displacement of the object during the acquisition process or due to the inaccurate calibration of the machine (i.e., the parameters of acquisition used). Accordingly, the first step to follow is to review and to calibrate the images obtained to eliminate artifacts.

CT data are usually exported as 32-bit or 16-bit image stacks in TIFF (Tagged Image File Format) or DICOM (Digital Imaging and Communication On Medicine) formats. In our case, we calibrated the images with ImageJ v.1.50e[8] to eliminate the background noise (Pertusa, 2010; Bushberg et al., 2012; see **Figure 2A**). Therefore, the first step to follow is to calibrate the range of the histogram by selecting the regions of interest (ROIs). The procedure in ImageJ to perform this step is Image→Adjust→Brightness/Contrast. The calibration of the histogram must be done across different steps. The first step is obtaining a profile plot for the gray values across a transect in a convenient zone of the object, but crossing the sample at two different locations. To do this, the segment has to be selected in the submenu and to drag the transect over the image. The path in ImageJ is Analyze→Plot Profile. Accordingly, the range of gray values associated with bone and other structures such as the background noise is adequately observed (**Figure 2B**). Doing this, the range of values corresponding to the background noise is cropped in the histogram (**Figure 2C**). The cropping normally uses the background noise histogram value closest to the range of bone histogram value. **Figure 2B** shows two histogram profiles, each corresponding to a different transect. From the two histogram profiles, the value closest to the range of the bone values is selected, in this case, -28414, serving as a cutoff. To do this, one has to return to the set menu Image→Adjust→Brightness/Contrast, and in the submenu "Set," the minimum value of the right histogram (**Figure 2B**) has to be selected (-28414). Using this procedure, it is possible to obtain the left histogram (**Figure 2C**). The histogram is then cropped with the Apply menu, giving a new-cropped histogram (**Figure 2C** right). This process should be repeated until the histogram displays well-defined ranges for all the structures of the object.

The last step is to homogenize the histogram through a process named "normalization" (Pertusa, 2010; Pérez and Pascau, 2013; Burger and Burge, 2016) (**Figure 2D**). The normalization is easily performed following the path: Process→Enhance Contrast. In the pop-up window, the value 0.5% in saturated pixels could be specified, as well as the options for normalization in order to process all the slices and to use the stack of the histogram (Pertusa, 2010). One possibility is to use the automatic method of selection, but this method usually increases the actual gray values of the histogram (red line; **Figure 2D**) relative to the gray values obtained from the normalization method (blue line; **Figure 2D**). If the object does not present artifacts, the images should be converted from 16-bit to 8-bit (Image→Type→choose 8-bit). This reduces the size of the data, because 8-bit data are half the size of 16-bit data and therefore improving the speed of the subsequent analytical procedures. In contrast, if the objects present artifacts such as rings, different filters for image cleaning should be applied before converting the image from 16 to 8-bit (Pertusa, 2010; Racicot, 2017).

Once the background noise is removed, all images are converted to 8-bit and normalized to 0.5% of gray values. This is performed to standardize the gray values of the histogram. The standardized image stacks in TIFF formats are imported into specific software such as Avizo Lite[9], Materialize Mimics Innovation Suite[10], VG Studio[11], or other freely accessible software such as Dragonfly software[12] or 3D Slicer[13].

Image Stack Segmentation

To make an accurate segmentation, a correct calibration of the image stack should be done. The segmentation is a process to select and categorize parts of an image. Segmentation is usually performed by thresholding, which results in isolating voxels that correspond to a given range of gray values (Forsyth and Ponce, 2003; Gonzalez and Woods, 2008; Pertusa, 2010; Pérez and Pascau, 2013). In XCT data images, the voxel is the volumetric unit of the pixel in three dimensions and hence being the equivalent of the pixel in a 2D image (Pertusa, 2010; Pérez and Pascau, 2013). In this way, using

[8]http://rsbweb.nih.gov/ij/

[9]www.vsg3d.com

[10]www.materialise.com

[11]www.volumegraphics.com

[12]www.theobjects.com

[13]www.slicer-org

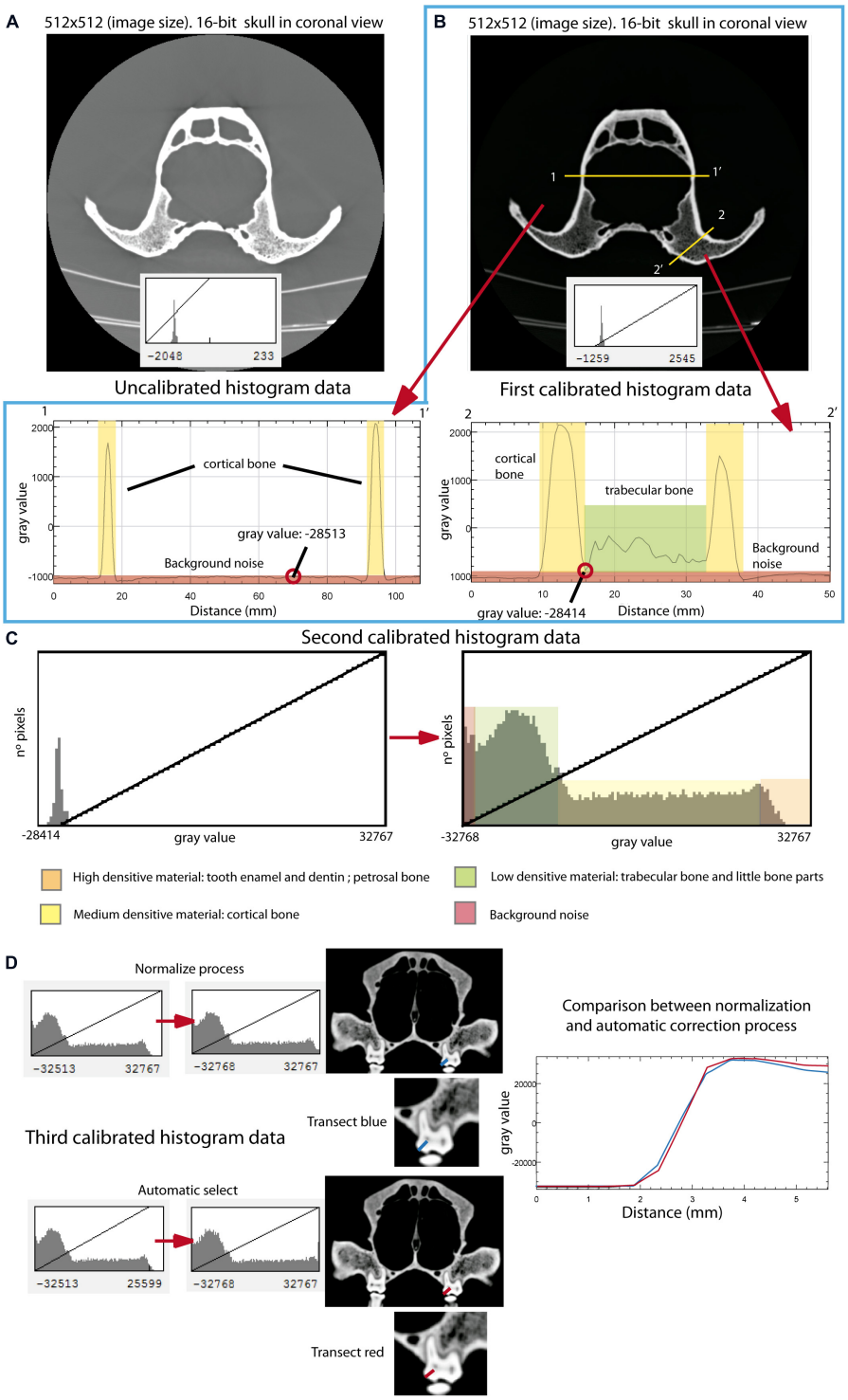

FIGURE 2 | Image cleaning and calibration process using the skull of *Ursus americanus* (VU261) as an example. **(A)** Original image stack obtained from the XCT scanning (upper) with no-calibrated histogram (lower) in coronal view. **(B)** First step for calibrating the histogram. Note that two different transects across the object are represented by a yellow line. The respective two plot profiles from these two transects are represented in this figure: the cortical bone represented in yellow areas and the trabecular bone represented in green areas. Note that in the first transect there is no trabecular bone. The red color in both plot profiles represents the background noise. **(C)** Histogram resulted from the process of calibration and cleaning obtained in the first step. The left graph is the original histogram of one image only, and the right graph is the resulting histogram after cropping the gray values in the left diagram corresponding to the background noise. **(D)** After repeating the same process as in **(B,C)**, the third step for histogram calibration is using the process of normalization (upper graphs) and the automatic selection method (bottom graphs). On the right side, there is a plot comparing both methods, plotting gray values on a transect when using normalization (blue line), and the automated selection method (red line).

segmentation tools, it is possible to separate the object of study from the background. The path for this process in ImageJ is Image→Adjust→Threshold, and in this pop-up window, one can choose the range of interest. In this pop-up window, check the selection method (preferable to choose "Default"), the background option (black or white), and the stack of images option (Pertusa, 2010; Pérez and Pascau, 2013). To begin the pathway using Avizo, one has to click on the imported object, and in the drop-down menu, it is possible to choose the option Image Segmentation→Multi-thresholding and validate by clicking on the "apply" green box. By clicking on the multislices icon (segmentation editor), it is possible to generate new-labeled materials with Avizo. Once the range of gray values is selected within the ROI, the binarization process is performed through the path: Process→Binary→Make binary, in ImageJ (Pertusa, 2010). The binarization is the conversion of the gray values of each voxel or pixel into zeros and ones, representing the background in black and the object of interest in white, respectively. In ImageJ, there is the option to indicate whether the background is dark or white. This process generates a layer resulting from this binarization in order to add more information of the same type (same structure or material) to that layer. 3D Slicer v 4.9.0 (Kikinis et al., 2014) and Dragonfly (Morin-Roy et al., 2014) are powerful free-access software to accomplish these tasks, although the latter has more options of segmentation. Proprietary software such as Avizo and Mimics has better powerful image filters. This power is based on the specific and optimized types of matrix algorithms that improve the functionality of the filter. However, in software like ImageJ, it is possible to import new plugins[14] or generate matrices (kernels) to adapt the filters to particular problems, i.e., the path is Process→Filters→Convolve (Pertusa, 2010). In our study case, we have used the filters of ImageJ to calibrate and remove artifacts from the image stack and Avizo Lite 9.2. (e.g., Yang et al., 2013), as well as Mimics (e.g., An et al., 2017) for its segmentation.

Using the protocol defined here, the cortical bone was segmented with a threshold histogram value range of 70–255 and added in one layer to generate the cranial model. The trabecular bone was segmented within a range of 40–70 and added to the same layer. It is recommendable to perform a general segmentation of the fossil and later including in this first segmented part of the structure the smaller parts such as the trabeculae. Doing this, it is possible to avoid an overestimation of the external surface segmentation of the fossil because of physical effects of the tomographic process (e.g., Compton effect).

For the teeth, we generated a separate layer, including the enamel, dentin, and pulp cavity (Pérez-Ramos et al., 2019, 2020; **Figure 3D**).

Image Cleaning Filters

Removing Image Artifacts

Once the stack of images is cleaned from background noises, there are still artifacts in the image, such as rings, beam hardening, and scattering (**Figure 3A**). These are generated for a highly dense material derived from preservational biases during fossilization or human-made materials during the physical restoration of the fossil (dense plaster, nails, or wire mesh) (Racicot, 2017). In these cases, the artifacts must be removed from the histogram before converting the image data to 8-bit. It is advisable to do this when the histogram is 16-bit because the range of the histogram is higher, and therefore, there are more possibilities to eliminate the artifacts accurately. Afterward, it is possible to proceed with converting the image data to 8-bit for faster image postprocessing. To remove all these effects, several image filters can be applied such as the "mean" and "sharp" filters available in ImageJ across the path: Process→Filters→ Mean and Process→Sharpen (Hsieh, 2009; Pertusa, 2010; Rueden et al., 2017). Whereas the "mean" filter removes the noise but blurs the image, the "sharp" one restores clearer edges between structures. Afterward, other mathematical operator processes can be applied to separate gradients of gray values, multiplying each pixel by certain values (1.25–1.5) in order to increase the contrast of the image stack (Process→Math→ Multiply). This result has to be usually subtracted to a gray value (100–200) (Process→Math→ Subtract). The process can be repeated by iteration until having the separation between the whitest and the darkest range. After each iteration, the histograms should be normalized to avoid calculation errors when applying the aforementioned filters: Process→Enhance Contrast at 0.5% (Maheswari and Radha, 2010; Maini and Aggarwal, 2010).

Removing Endocast Material

In those images with a low contrast between the object and the background, there are different contrast filters such "emphasis" that certainly helps to delimit the object margins. A Sobel edge detector compares an approximation of the image gradient to a threshold (Saif et al., 2016) and automatically decides if a pixel is part of a given margin (Shrivakshan and Chandrasekar, 2012; Sujatha and Sudha, 2015). A proper thresholding must be determined and computed, so the comparison generates useful results. An edge may be defined as the border between blocks of different colors or different gray levels (Qiu et al., 2012). With this method, in those cases where the fossils are filled with a stone matrix with a density and texture very similar to bone, we managed to separate and segment the actual fossil material accurately and quickly.

Mathematically, the edges are represented by first- and second-order derivatives. Among other edge detection operators (e.g., Banu et al., 2013), we used Canny's (1986) edge detection algorithm in our practical example of cave bears, which is an improved method of the Sobel operator, and it is considered a powerful method for edge detection (Shrivakshan and Chandrasekar, 2012; Saif et al., 2016). A second group of filters that detect edges are those that use a second-order derived expression of the image, usually the Laplacian or non-linear deferential expression. We used this filter in partial parts when edge detection was more complicated given the low gradient of neighboring pixels (**Figures 3B,C**). In our example of cave bears, we have used Avizo Lite 9.2 to perform this process. In this software, the tool is called "Watershed," which is within the option of segmentation

[14]https://imagej.nih.gov/ij/plugins/index.html#filters

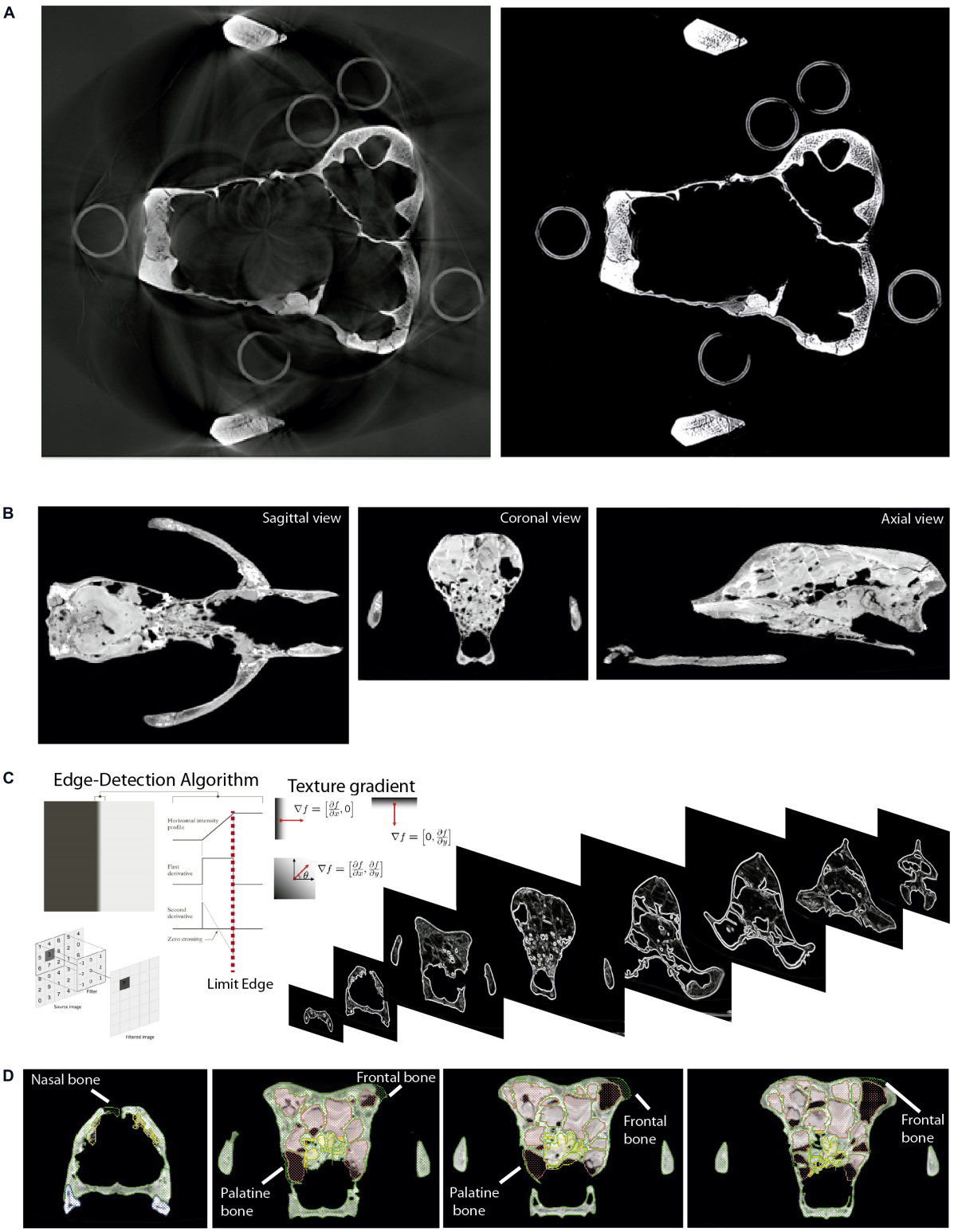

FIGURE 3 | Digital cleaning of the skull of *Ursus spelaeus* spp. as an example. **(A)** Removing artifact from the XμCT, showing on the left the original image stack, and on the right the image without ring-shaped artifacts after applying the "mean" and "sharp" filters. **(B)** Sagittal, coronal, and axial views of the skull filled with exogenous material. **(C)** Edge-detection process applied to delimit the exogenous material from real bone (ref. image: Forsyth and Ponce, 2003; Gonzalez and Woods, 2008). **(D)** Coronal views of different slices along the anteroposterior axis, showing the bone delimited through the gradient filtering and the reconstructed parts (nasal, frontal, and palatine bones).

editor. The process to follow is detailed and explained in Galibourg et al. (2017).

Unifying Parts of Image Stacks

A general problem when working with any type of XCT system is the scanning envelope of the machine used. Sometimes, this field of view is smaller than the size of the object that a XCT can scan, and therefore, a solution is to perform the scanning process in parts. The simplest case is when the object has the same orientation in all the acquisitions and therefore only changes the scanning envelope by an adjustment of the XCT detector or by moving the specimen. In this case, the process of unifying all image stacks is automatic using an algorithm named in ImageJ as "Concatenate" (Lu et al., 2009; Murtin et al., 2018). However, in cases where the object should be moved during the acquisition, the object (in our case, the skull of *U. spelaeus* spp.) is oriented differently in each acquisition (**Figure 4**). This is a problem to unify the image stacks. Different processes (described below) to fit all the images at the same orientation should be performed before using the "Concatenate" algorithm of ImageJ (Lu et al., 2009; Murtin et al., 2018). To do this, the reslice function of ImageJ was used, using the path: Image→Stacks→Reslice.

The process of unifying different parts of the same XμCT dataset was applied to the skull of *U. spelaeus* spp. (see **Supplementary Data** and **Table 1**), as its size exceeded the size of the acquisition window of the XμCT machine. To solve this problem, five acquisitions of the same skull were made in different regions (rostral, medial, caudal, right, and left zygomatic arches; **Figure 4**). Such parts were joined following the next procedure: (i) we performed all scans with a similar condition (voltage, current, and ideally magnification/voxel size); (ii) we did the tomographic reconstruction with the same parameters; (iii) we normalized the gray values of the dataset with identical parameters (Pertusa, 2010). In this way, all the specimens had a similar size (number of voxels in X, Y, and Z axes) and the same voxel size, which is the case of *U. spelaeus*. As the first step was to remove useless slices (without information of the object on them), it is essential to have the same dimension in the X and Y axes, but not in the Z axis. In our case (**Figure 4**), the conditions of the histogram, as well as the voxel and pixel sizes, were the same in all the specimens with the same image size (1,024 × 1,024 pixels) and isotropic voxel size of 0.2463 mm (same voxel size in 3 axes). The XμCT acquisition conditions are 180 kV and 0.16 mA (**Table 1**, and see in **Supplementary Data**). The XμCT dataset of the caudal part of the skull had 1,024 slices (**Figure 4A**) and from the slice 477 to the slice 1,024 had relevant information of the object (i.e., bone represented). For this reason, removing other slices with no information (e.g., empty spaces within the skull) reduces data size and eases the process. The XμCT dataset of the medial part of the skull had 1,024 slices (**Figure 4B**), and only the slices from 1 to 880 had relevant information of the object. From these subsets of slices, we used the stacking tool of ImageJ (Pertusa, 2010; Rueden et al., 2017) "Concatenate" to merge the two stacks of images corresponding to the medial and caudal datasets (Image→Stacks→Tools→Concatenate). The rostral part (**Figure 4C**) was misaligned with respect to the fused part (caudal–medial). To solve this problem, we positioned the two parts in the same view (coronal) using the reslice function and in the same slice to make the alignment between the frontal region and the next corresponding slice of the frontal block of image stacks. This process was repeated to fit and merge the lateral parts of both the right and left zygomatic arches (**Figures 4D,E**). To align each of the parts of the skulls, we displayed in the same window both parts using the reslice function. With the Rotate tool (Image→Transform–Rotate) and Translate (Image→Transform–Translate) within the menu, it is possible to check the grid lines option. To measure the position of alignment with the pattern image, we used the angle and line tools. To get the values of the measurement, we used the path Analyze→Measure. Using the "Rotate" and "Translate" tools, the adjacent part will be adjusted to the same position than the other one. This process will be carried out in all views using the reslice function (sagittal, coronal, and axial) to maximize the level of precision. This process should be repeated, depending on the number of parts to merge. Therefore, by concatenating all parts, the structures are aligned in all the views correctly. Once the five XμCT datasets were merged (**Figures 4F–I**), the general histogram of this new XμCT dataset was normalized to standardize the entire histogram as a whole and to convert the image stacks from 16- to 8-bit (**Figure 2D**). This process of unifying parts of image stacks was applied to the skull of *U. spelaeus* spp. to develop a previous study (Pérez-Ramos et al., 2019).

Interpolation Process

Before performing any comparative analysis based on voxels (e.g., histological analyses), some processing of XCT data is required in order to convert them to isotropic (Parsania and Virparia, 2016; Rajarapollu and Mankar, 2017). Therefore, the XCT datasets of all the skulls should be comparable, which explains why all of them should have the same voxel size and orientation. To do this, we used ImageJ (Maret et al., 2012; Rueden et al., 2017). While Avizo recognizes that voxel size is different, and it can compare datasets without any problem, having the same size and voxel size among specimens makes it easier and opens analytical possibilities with more software and plugins tools (e.g., BoneJ). Moreover, after doing this, in some cases, the profile and contrast of some small parts (e.g., connections among trabeculae) should be enhanced. To do this, we applied an interpolation method called "bicubic" (Van Hecke et al., 2010; Parsania and Virparia, 2016; Rajarapollu and Mankar, 2017), making the observation of smaller features easier. This method of interpolation was applied in our practical example of cave bears to (i) convert non-isotropic to isotropic voxels in order to standardize voxel size, (ii) increase voxel and pixel sizes resolution in order to have a higher contrast of the small structures at histological level, and (iii) reorient the sample in the dataset in order to have the same orientation. The procedure followed to execute these three points is outlined below:

(i) Converting non-isotropic to isotropic voxel. This method converts a non-isotropic voxel (see **Table 1**, voxel size "original"), only the specimens marked with one asterisk, into isotropic voxel (see **Table 1**, voxel size Iso "standardized"), which is an

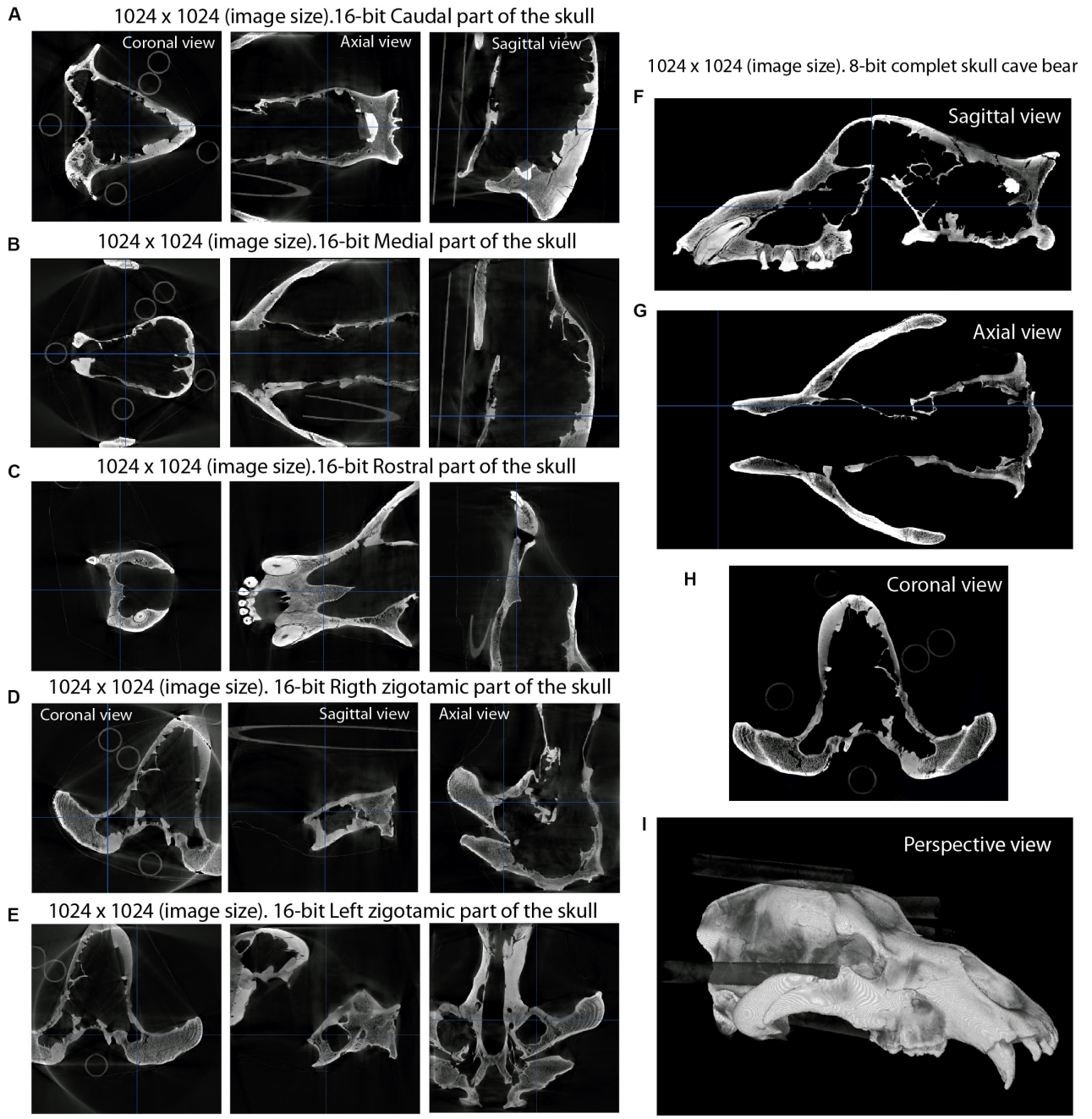

FIGURE 4 | Digital process of fitting different image stacks to the same orientation, using the reslice function in ImageJ (Rueden et al., 2017) on the cave bear skull (*U. spelaeus* spp.). **(A)** Image stack of the caudal part. **(B)** Image stack of the medial part. **(C)** Image stack of the frontal part. **(D)** Image stack of the right zygomatic arch. **(E)** Image stack of the left zygomatic arch. **(F–H)** Result of the concatenation and reslicing showing the skull in sagittal **(F)**, axial **(G)**, and coronal **(H)** views. **(I)** perspective view of the fitted object "3D rendering window."

anisotropic bicubic interpolation (**Figures 5A,B**). This process runs on each voxel and on the three axes. The process to perform such a conversion is to divide the value of voxel depth by the value of pixel width (Image→ Properties). The resulting value is used in the scale selection in ImageJ (Maret et al., 2012; Rueden et al., 2017). Finally, such value of the scale should be added to the Z axis (Image→Scale→choose option bicubic interpolation).

(ii) Increasing voxel and pixel sizes. In some studies performed here, an increment in voxel and pixel sizes of the medical XCT dataset and laboratory XCT dataset was applied to improve the contrast of small structures such as the trabeculae of cancellous bone. To perform this process, pixel size was increased in medical XCT datasets of 512 × 512 pixels to 1,024 × 1,024 pixels (see **Table 1**, image matrix "processed"), using this path

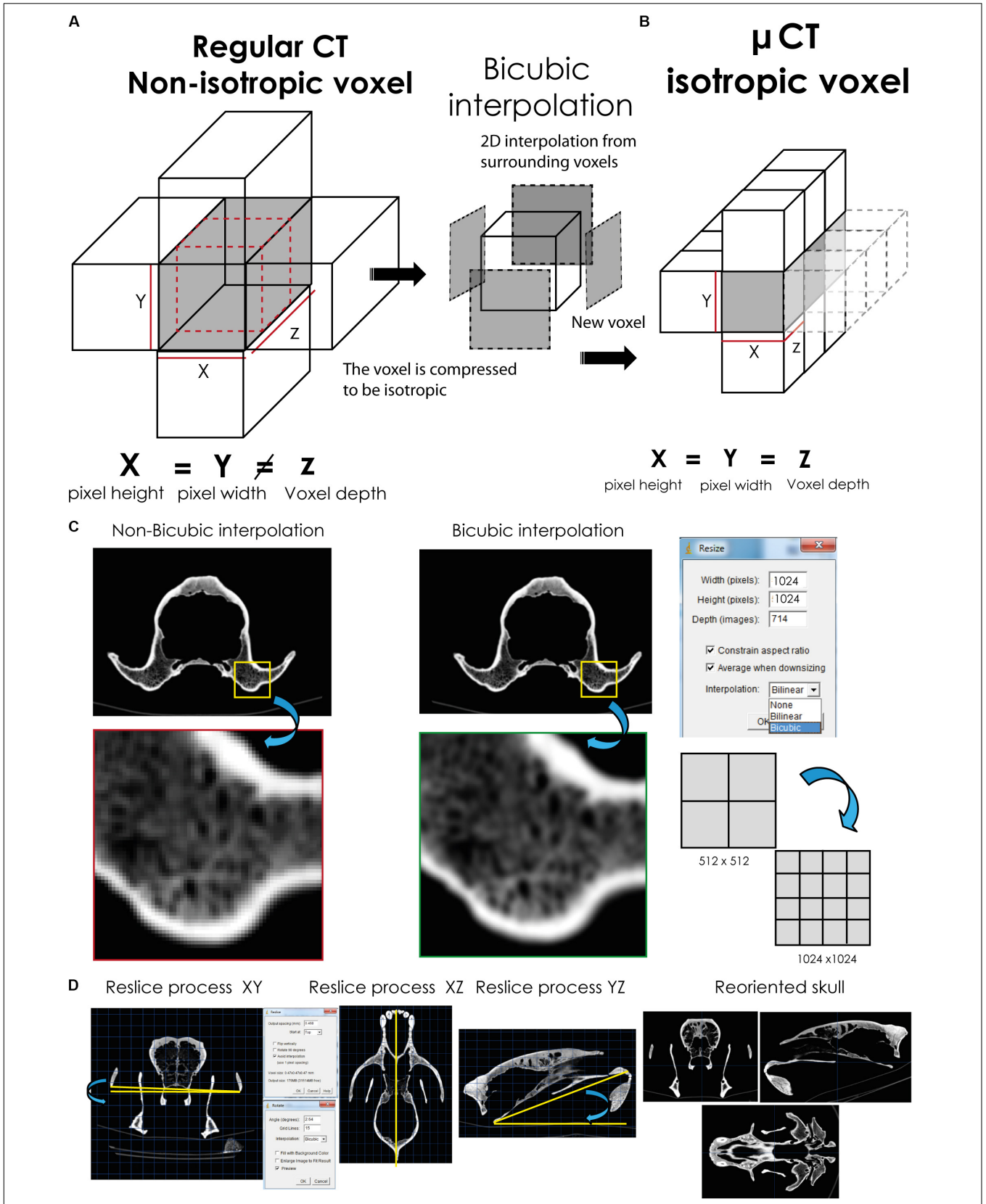

FIGURE 5 | Application of the bicubic interpolation to change the number of voxels in the three axes and to reorient the skull. The conversion from a non-isotropic voxel **(A)** to an isotropic one **(B)** is shown. **(C)** Increasing voxel size to improve the contrast of small structures. **(D)** Reorienting the XCT data.

Image→Adjust→Size (Resize). For increasing voxel size (see **Table 1**, voxel size "processed"), using the same pathway for converting non-isotropic to isotropic voxel. We performed these processes in ImageJ (Rueden et al., 2017) using the bicubic interpolation method (Maret et al., 2012; Parsania and Virparia, 2016; Camardella et al., 2017; Rajarapollu and Mankar, 2017; **Figure 5C**). Increasing first the pixel size and then the voxel size is recommended.

(iii) Reorienting the sample in the dataset. We aligned the specimens locating the prostion/basion at the same plane (**Figure 5D**). To do this, the reslice function of ImageJ (Rueden et al., 2017) was applied, using this path Image→Stacks→Reslice. The method only operates with image stacks with isotropic voxels. Therefore, the bicubic method is necessary to execute correctly this step. With the reslice function, we can move the orientation of the entire image stack, being in our case in dorsal, coronal, and sagittal views (**Figure 5D**). In each view, using the rotate tool (Image→Transform→Rotate) and translate tool (Image→Transform→Translate), we reorient the skull in the correct position (**Figure 5D**). To reorient the skull, the zygomatic arches are oriented to the same plane in coronal view (**Figure 5D**, left) and to know how many degrees the skull should be rotated. Afterward, this angle is measured with the angle tool in the submenu of ImageJ in sagittal, axial, and coronal views (**Figure 5D**, intermediate) to reorient the skull in order to have the prostion and basion into the same plane (**Figure 5D**, right). Within the rotate and translate tools menu, one must put the angles (angle tool) and the distance to move (line tool). To reorient each image in the same position, we activated the "grid lines" option and chose the "bicubic" interpolation option.

VIRTUAL RECONSTRUCTION OF FOSSIL SKULLS

This section describes the most common methods used for reconstructing the 3D models of fossil skulls following different sources (i.e., Zollikofer and Ponce de León, 2005; Abel et al., 2012; Cunningham et al., 2014; Sutton et al., 2014; Tallman et al., 2014; Lautenschlager, 2016; Mostakhdemin et al., 2016; Gunz et al., 2020). Moreover, for a correct anatomical reconstruction, one usually has to use different specific bibliographic sources on the anatomy of the group studied. In our case, we have followed Moore (1982) and Novacek (1993), and we have also relied on the anatomy of the skull of living bears, especially those species with a closer phylogenetic relationship with the cave bear (i.e., *U. arctos*, *Ursus americanus*, *Ursus maritimus*, and *Ursus thibetanus*).

We have used Avizo to generate the 3D models through segmentation, as explained in *Image Stack Segmentation*. We have also used this software to generate the dental models and cranial parts that will be later used during the mirroring (generating the specular model of the preserved part) to restore lacking parts in fossils. The two file formats used in our study are STL (stereolithography) and PLY (polygon file format). The first format is used for simple models, i.e., those that only contain mesh data without color or texture, and the second for models with a high number of triangles (high mesh resolution) with color and texture data. The mirroring process was generated with Geomagic, where the fragment used as a reference needed small anatomical improvements (e.g., bone microfractures). These mirrored models were imported in STL format into Mimics to display with red polylines the contours of these parts (**Figures 6–8**). In this study, Mimics has been used to reposition the elements more accurately with the path Reposition←CMF/Simulation. A great advantage of Mimics over other software is its ability to visualize within the display viewer of the XCT data the polylines in red (outline of mirrored objects) that mark the contour of the model to be reconstructed. The mirroring process (generate mirror or specular models) is executed within Mimics (path Mirror←CMF/Simulation) or later during the postprocessing, using 3D software for model viewer such as Blender or Geomagic. In our example, we have only used Geomagic with the path Mirror←Tools. The reconstruction of lacking parts with Mimics gives the most accurate results, Because we can generate the structures by segmentation following the pattern of red lines that mark the missing structure. We managed to generate an almost complete model in the same viewer of the XCT data generating a layer (green color in **Figures 6–9**). The reposition of the elements by isolated parts in other software, such as bone fragments that fit virtually into programs such as Blender[15], Geomagic, or Maya[16], can give small errors in anatomical and morphological geometric replacement.

MESH POSTPROCESSING

Once the 3D mesh model has been generated, several methods of postprocessing should be applied to improve it (Zollikofer and Ponce de León, 2005; Abel et al., 2012; Cunningham et al., 2014; Lautenschlager, 2016; Mostakhdemin et al., 2016; Racicot, 2017). The postprocessing methods refer to those processes that are applied on the mesh model to repair, optimize, or edit the mesh created from the layers (or masks) obtained from segmentation. The process to generate this mesh from a surface or plane with known coordinates is called tessellation (Botsch et al., 2006). In our case, we exported the meshes with the maximum numbers of triangles, and later these were simplified with a specialized software, such as 3D Slicer, MeshLab, 2020 freeware[17], or Geomagic Wrap. In this section, the mesh postprocessing and topological analyses have been carried out with Geomagic. The first step to follow was to export the surface models in PLY or STL format to more specific software to display models such as Geomagic or MeshLab. The first process of reducing the number of triangles must be applied, called decimation (Botsch et al., 2006). This process is explained in **Figure 10**, using the skull of *U. ingressus* as an example. In the case that some missing parts of the skulls were reconstructed, we verified if such reconstructions were anatomically correct by comparing the fossil skull with other models of modern bears.

The process of virtual restoration of fossil skulls and the subsequent simplification of the mesh can lead to topological

[15]https://www.blender.org/

[16]http://autodesk.com/maya

[17]http://MeshLab.sourceforge.net/

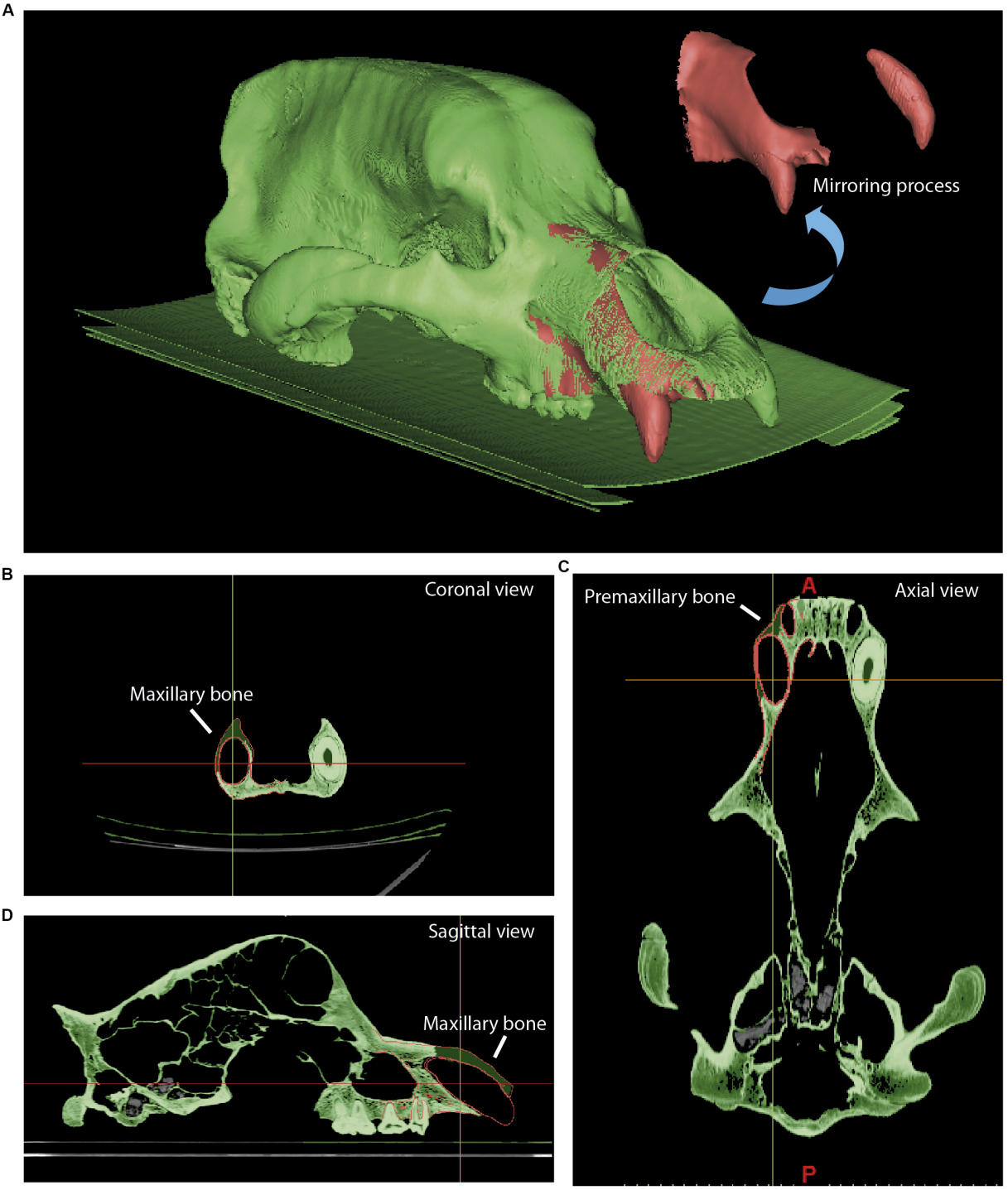

FIGURE 6 | Reconstruction of the skull using the mirroring process, illustrated with the digital rendering of *Ursus ingressus* (PIUW3000/5/105). **(A)** The 3D virtual model skull showing the mirrored partial bone skull and the canine (in red) with the original bone in green. In **(B–D)**, the orthogonal views showing original bone in green and the reconstructed bone highlighted by the red polyline are shown.

deviations relative to the original non-restored skull. In addition, simplifying the mesh can affect its integrity. In this section, we will apply two analytical processes using Geomagic to check the integrity (i) and the topological deviation (ii) of the model mesh. Below, both processes are explained in more detail:

(i) It is necessary to check the integrity of the mesh to discard any topological error (e.g., self-intersections, highly

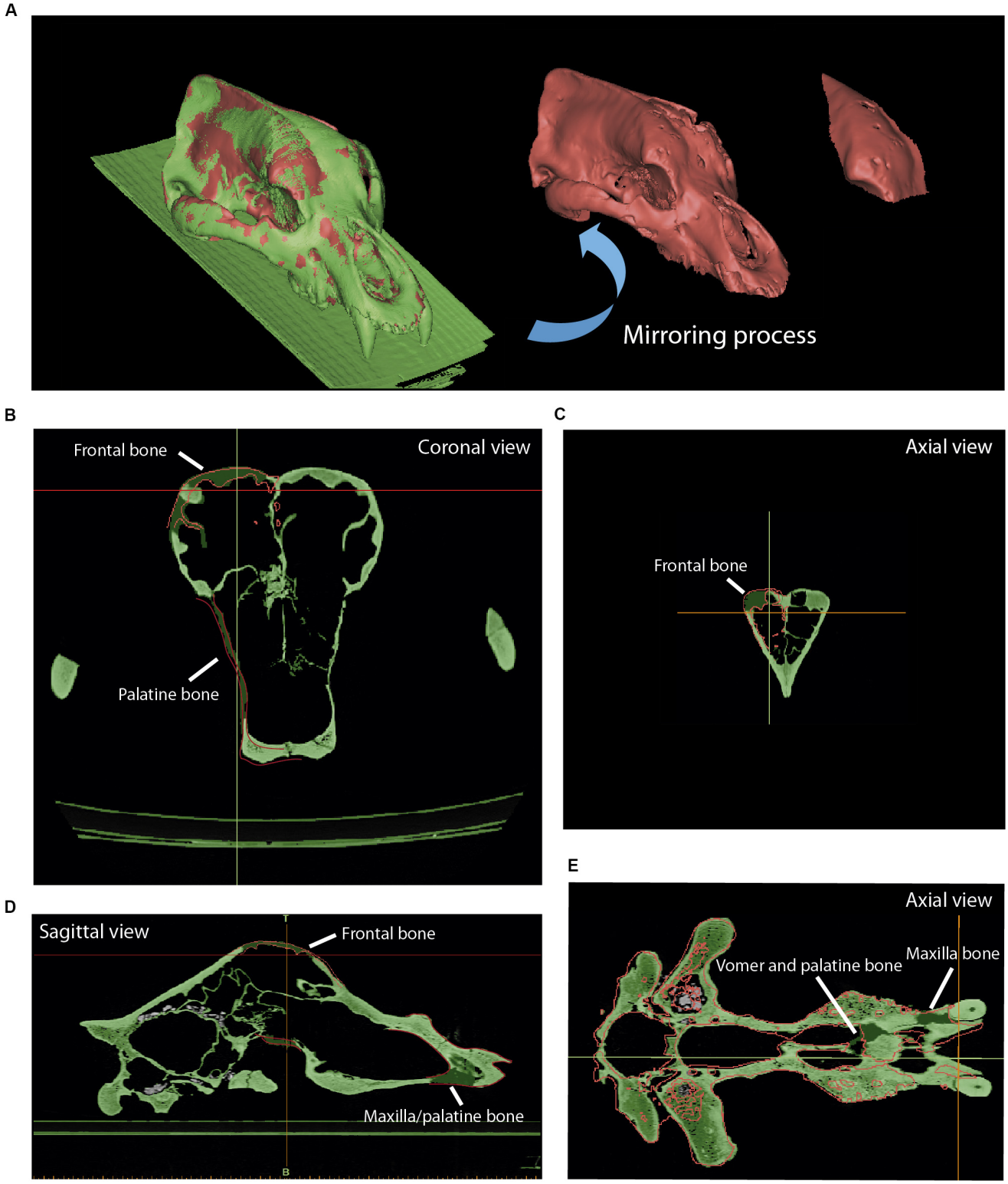

FIGURE 7 | Reconstruction of the skull of *Ursus spelaeus eremus* (PIUW-SW 483). **(A)** Three-dimensional models showing in red the mirrored parts of the frontal dome and in green the original bone. **(B)** Coronal view showing the red polyline to reconstruct the lacking parts of bone. **(C)** Axial view showing the red polyline to reconstruct the left portion of the frontal bone. **(D)** Sagittal view showing the reconstructed parts of the frontal, maxillary, and palatine bones. **(E)** Axial view showing the reconstructed bone parts of the vomer, palatine, and maxillary bones.

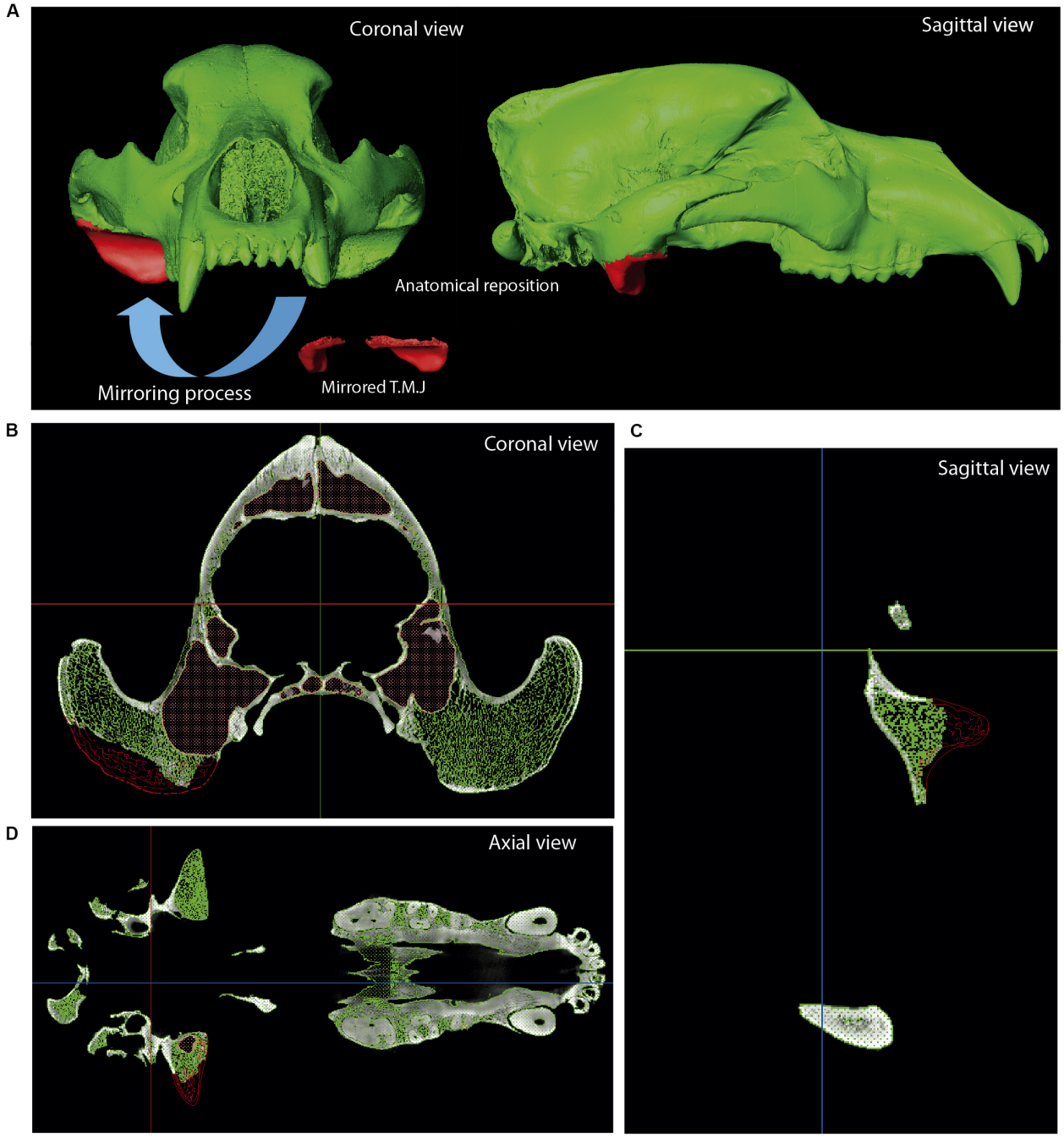

FIGURE 8 | Reconstruction of *Ursus spelaeus ladinicus* (PIUW-CU 703). **(A)** Coronal, sagittal, and perspective views of the 3D virtual models showing the red the polyline used to mirror the left TMJ. Actual bone in green. The lacking right TMJ is shown in sagittal **(B)**, coronal **(C)**, and axial views **(D)**. Abbreviation: TMJ, temporomandibular joint.

creased edges or spikes) or open spaces at some point on its surface (i.e., non-manifold edges, small holes or tunnels). To do this, an analytical processing of curvature map was applied. This analytical method was performed with Geomagic using the command: Curves→Draw→curvature map; in MeshLab, the tool is named "Quality mapper." **Figure 10A** shows a non-uniform mesh with artifacts. This is a consequence of the restoration process of lacking parts. We have named the mesh without removing these artifacts as "unprocessed mesh." The curvature map analysis filter was applied to check if the integrity of the mesh was correct (**Figures 10A**, **11A**, **12A,B**, left model), as it appears the mixed color patterns in the surfer model. We applied various smoothing processes to eliminate these artifacts from the mesh, controlling the degree of the effect of

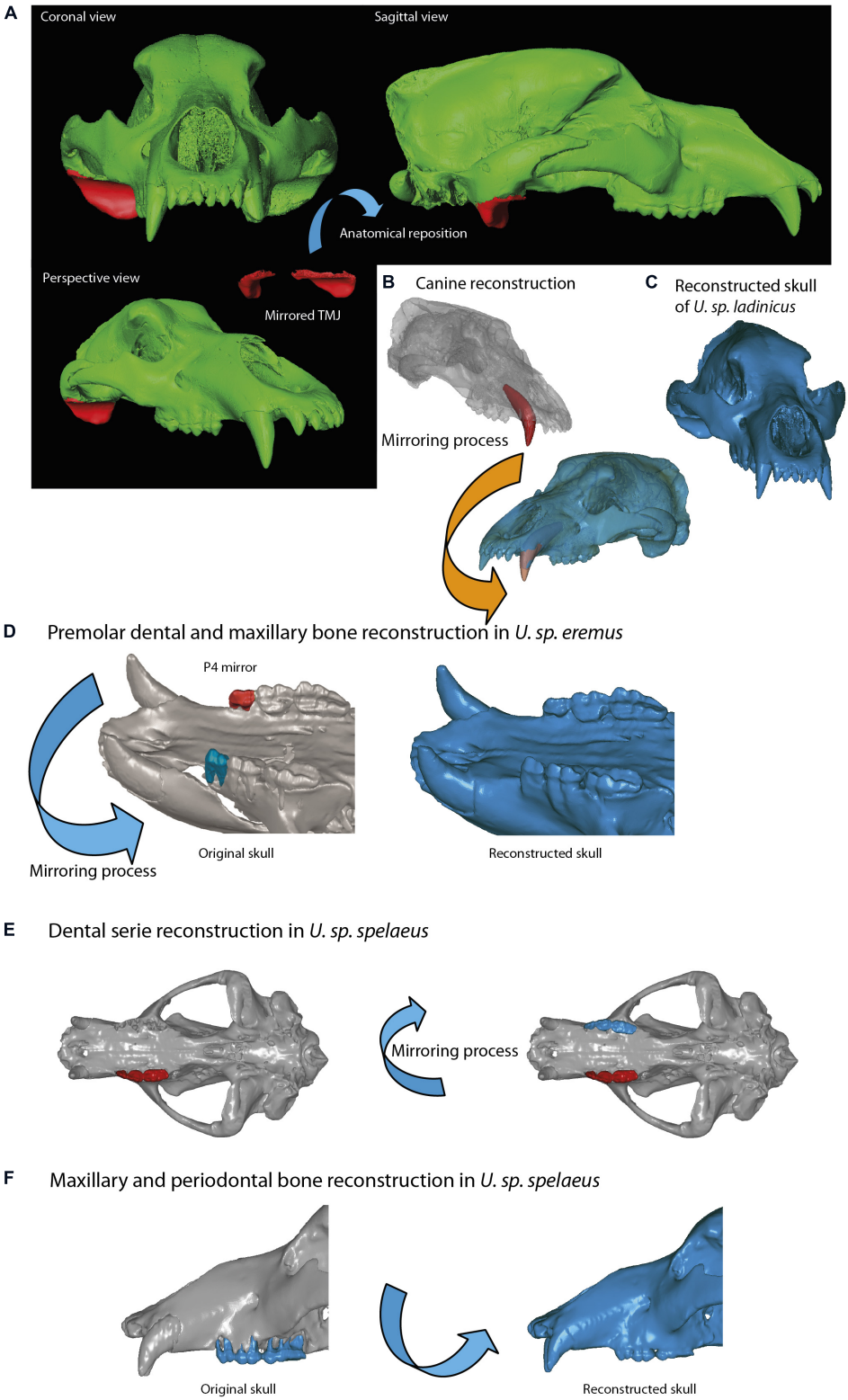

FIGURE 9 | Skull reconstruction with implantation of parts. **(A–C)** Skull of the *U. spelaeus ladinicus* (PIUW-CU 703); missing parts are restored by mirroring the contralateral part of the skull. **(A)** Restoration of the right TMJ. **(B)** Restoration of the left canine. Original bone in green, mirrored part used for restoration in red. **(D)** Reconstruction of the missing right P4 (blue), using a mirrored version of the existing left P4 (red) in *U.* sp. *eremus*. **(E)** Reconstruction of the missing left dental serie (blue), using a mirrored version of the existing right dental serie (red) in *U.* sp. *eremus*. **(F)** Comparison between the original skull of *U.* sp. *spelaeus* (in gray) and the final skull (in blue) with the periodontal region of the maxillary bone reconstructed.

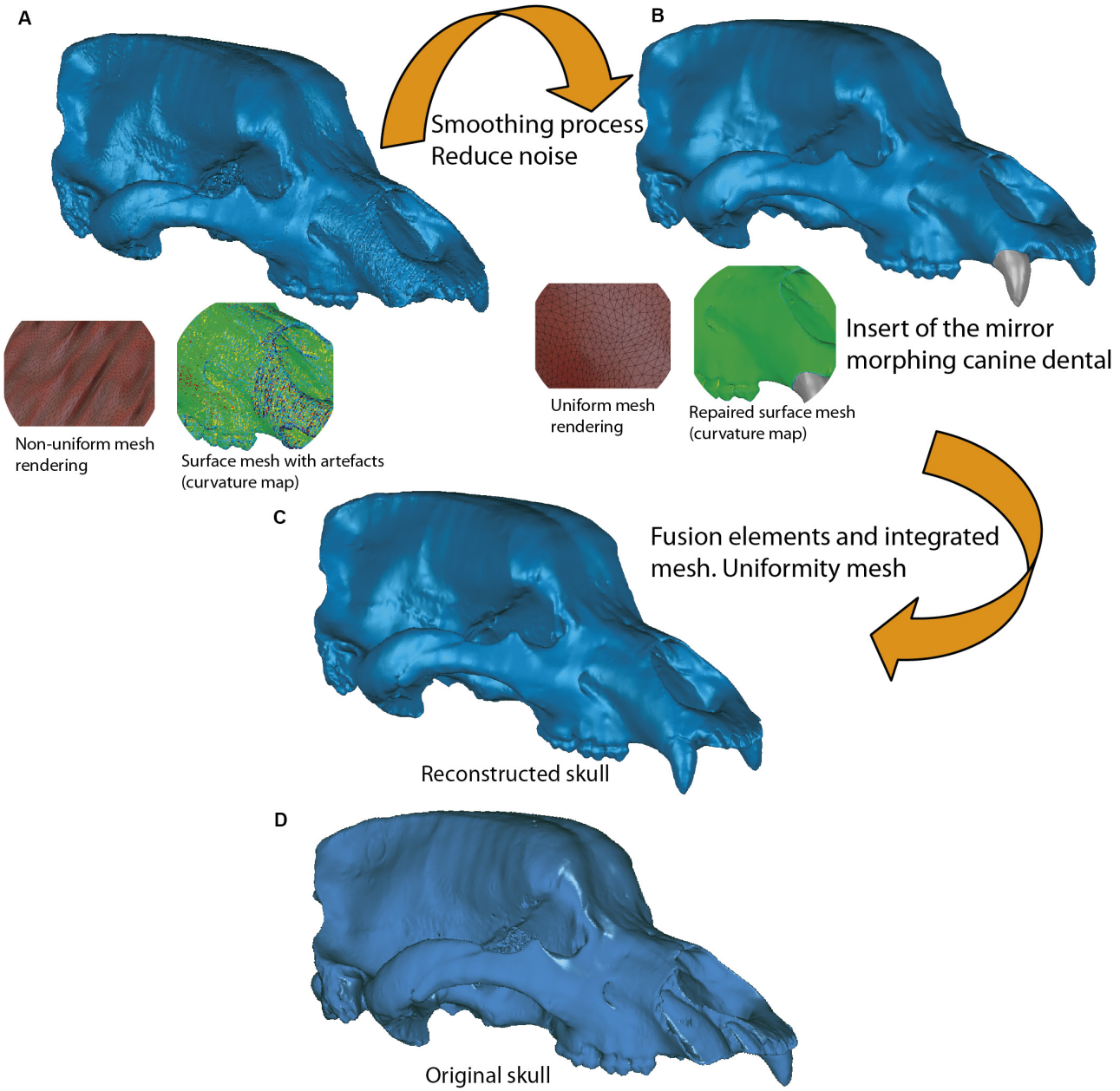

FIGURE 10 | Example of mesh tessellation and decimation using the dataset of *Ursus ingressus* (PIUW3000/5/105) as an example. **(A,B)** First step of mesh postprocessing and smoothing, based on the decimated density of mesh triangulation. **(B,C)** Second step of mesh postprocessing, consisting of the fusion and integration of different elements, being in this case the lacking teeth. **(C)** Final step of mesh postprocessing, consisting of noise deletion in the mesh by special tool, Uniformity mesh. **(D)** Original mesh of the skull before of the reconstruction process.

such process (Polygons→Reduce Noise). The option "Prismatic shapes aggressive," as well as the smoothness level as low, with iterations of about 2 or 4 should be selected (**Figure 10B**). At the end of this process, the "Quicksmooth" tool should be applied. This tool generates a uniform mesh. By applying these tools, artifacts on the mesh surface have been removed. The clean and uniform mesh has been named as a "processed mesh." To check if the "processed mesh" was correct (**Figures 10B,C**, **11B**, **12A,B**, right model), we applied the curvature map analysis filter. As the color pattern of the surfer model was regular green (**Figures 10B,C**), this indicates that the processed mesh was correct. Indeed, in the color pattern of the curvature map, cold colors are assigned to outside edges, green colors are assigned to the surfaces with little angle (i.e., all the ventral and dorsal faces of all triangles have the same orientation), and warm colors to the inside edges (**Figure 11C**). Once this first step of postprocessing of the mesh is correct, then the next step of mesh postprocessing (i.e., topological analysis) should be carried out.

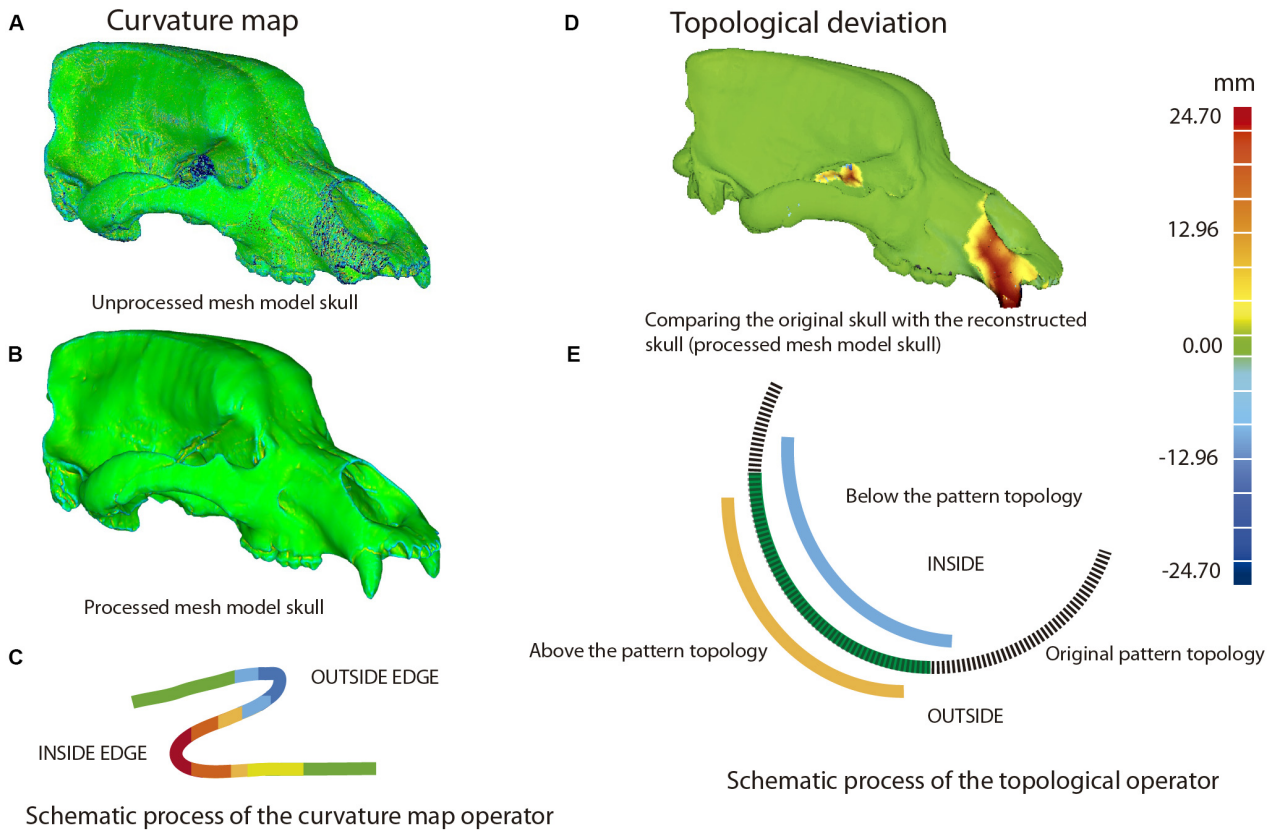

FIGURE 11 | Example of topological deviations using the dataset of *Ursus ingressus* (PIUW3000/5/105) as an example. **(A–C)** First postprocessing mesh, based on the curvature map, unprocessed mesh **(A)**, and processed mesh **(B)**. **(C)** Schematic process of the curvature map operator: outside edge, cold colors; inside edge, warm colors. **(D)** Second postprocessing mesh, consisting of topological deviations. The regions of warm colors correspond with the reconstructed bone parts. **(E)** Schematic process of the operator of topological deviation.

(ii) This analytical process quantifies the topological deviations between two mesh models. In our case, it helps us to quantify if the simplification of the mesh and cleaning of the artifacts have been very aggressive or poorly applied, generating significant deformations in the original topology of the model. This process is explained in **Figure 11**, using the skull of *U. ingressus* as an example. In the case of comparing the original skulls with the reconstructed ones, the information is obtained as a heat map, reflecting the topological arrangement of the added bone structures (**Figures 11D,E**). Therefore, those structures artificially added will have a positive deviation with warm colors, and those that have been removed or are below the topological profile of the original skull will have cold colors (**Figure 11E**). For such a comparison (**Figure 12D**), the reconstructed skull is chosen as the topological pattern against the original skull. For example, if the topology of the restored skull is above the surface pattern of the topology of the non-restored skull, the mesh color will be warm. In contrast, if the topology of the restored skull is below the surface pattern of the non-restored skull, the mesh color will be blue. Therefore, the topological information obtained is different from that in the first case (**Figure 12C**). This information is used to quantify the level of preservation of the element (skull, jaw, etc.) and its preservational condition. Another important aspect is to quantify the effect of repairing the skull and postprocessing the model mesh. For example, a high smoothing can cause various details to disappear, such as reliefs and roughness of the muscle insertions, loss of bone sutures. and loss of details of the dental topology, among others.

Across this section, we have highlighted several tools that can be used in automatic mode. We recommend using "mesh doctor" at the end of the mesh postprocessing to assess if there are artifacts in the mesh (small triangle intersections, spikes, or small holes). If the mesh has a very low number of triangles, we can use the "reintegration" tool, always setting the limits of the topology. The "uniformity" tool is useful to remove very aggressive triangles, and one has to select the aggressive prisms option with a medium number of iterations and a low effect level to remove them. With this procedure, we avoid large deviations of the mesh with the original topology.

Once all these processes have been performed, the resulting 3D mesh models are subject to any kind of evolutionary studies such as those based on ecomorphology or biomechanics. In the case of biomechanical studies, models should be imported into software such as Strand 7[18] (Tseng et al., 2017; Pérez-Ramos et al., 2020).

[18]http://www.strand7.com/

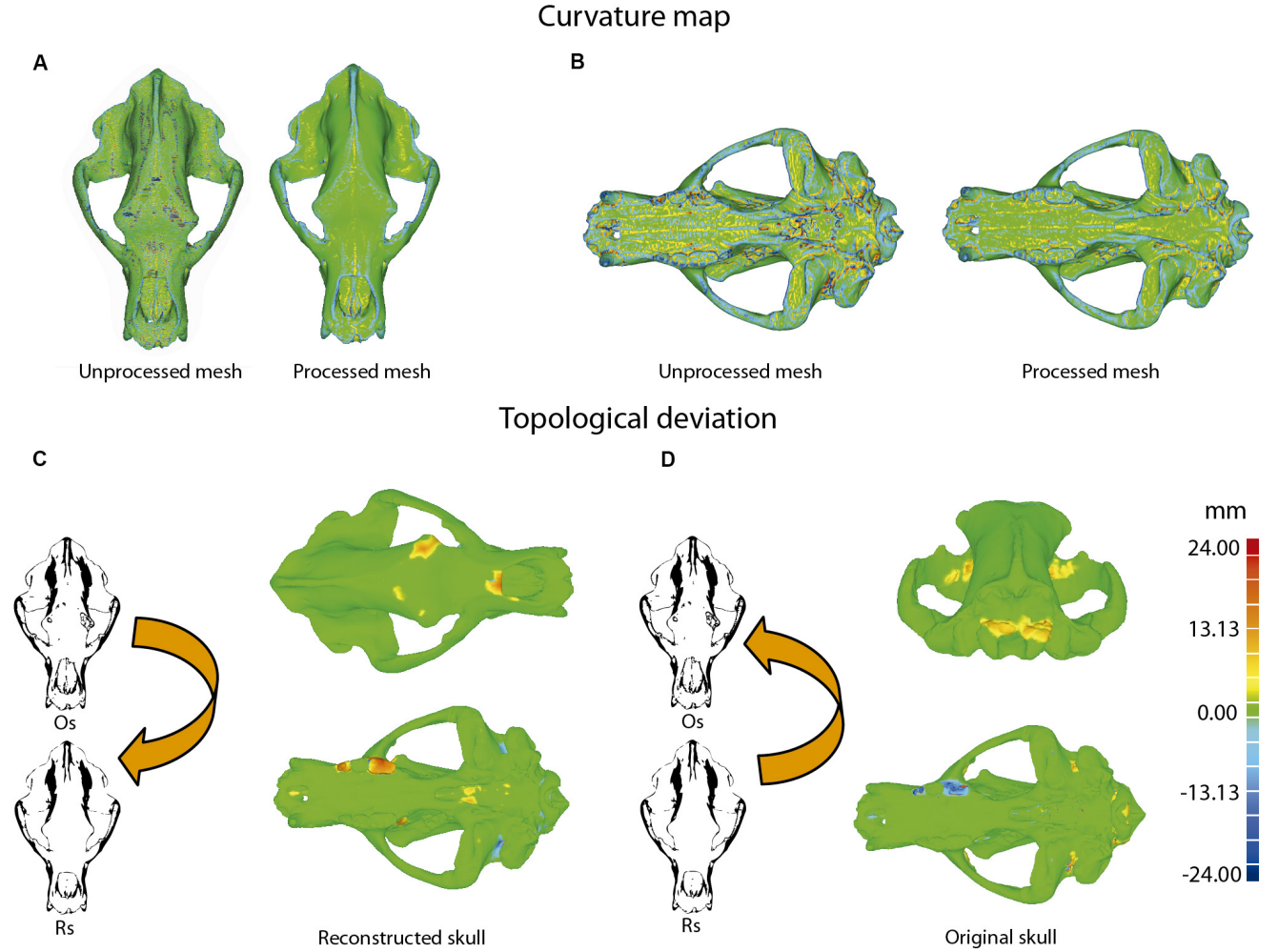

FIGURE 12 | Example of topological deviations using the dataset of *Ursus spelaeus spelaeus* (E-ZYX-1000). **(A,B)** First postprocessed mesh, consisting of curvature maps, in dorsal view **(A)** of the unprocessed mesh (left side), and the reconstructed skull (right side), and in ventral view **(B)** of the unprocessed mesh (left side) and the processed mesh reconstructed skull (right side). **(C,D)** Topological variation between the original (Os) and reconstructed (Rs) meshes using either the original skull as a reference **(C)** or the reconstructed one **(D)**. Note that parts added in the reconstructed skull appear in warm colors when the original skull is used as a reference but appear blue when the reconstructed skull is used as a reference. Os, original skull; Rs, reconstructed skull.

For studies of GMM, one can use other software to digitize the landmarks such as Stratovan Checkpoint Software (Stratovan Corporation, Davis, CA, United States) or the Geomorph (Adams and Otárola-Castillo, 2013; Adams et al., 2016) package of R (R Core Team, 2015).

CASE STUDY: CAVE BEAR SKULLS

Ursus ingressus Skull (PIUW3000/5/105)

The skull of *U. ingressus* was scanned using a medical XCT system (see **Table 1** and **Supplementary Data**). The optimal histogram range was chosen to create masks (different layers) for both bone and teeth, as explained in the process of segmentation. The 3D surface model created from that mask is represented in **Figure 6** in green, and the parts of bone that are lacking due to preservational reasons are represented in red. The right side of the skull is missing; the contralateral bones of the left side (in green) should be isolated, mirrored, and positioned to replace the missing part (in red), using Mimics. Once the mirrored bone parts were obtained in Geomagic (i.e., front part of the maxilla, premaxilla, nasal, palatine, some frontal parts, and foramina of the sphenoid; **Figures 6B–D**), they were fitted anatomically into the skull by means of polylines or contours in Mimics. Using these contours in red, we generated a bone mask (**Figures 6B–D**, in green) interpolating within the region bounded by the contours of the polylines. Finally, the lacking parts were reconstructed. This is the case of the mirrored canine that was "implanted" into the reconstructed alveolus (**Figure 6A**). This same virtual reconstruction was also carried out in other fossil skulls. Once the

anatomical restoration was finished, the model was exported to Geomagic (STL or PLY format) at high resolution (high number of mesh triangles). How to conduct this analysis is explained in further depth in section "Mesh Postprocessing."

Ursus spelaeus spelaeus Skull (E-ZYX-1000)

The skull of *U. spelaeus spelaeus* was acquired with a medical XCT system (see **Table 1** and **Supplementary Data**). Because of the specific preservational conditions (limestone matrix filling the internal cavities) of this skull, we applied edge detection filters to discern bone material from exogenous material. This process is explained in detail in *Removing Endocast Material*. The virtual restoration of this skull is represented in **Figures 3B–D**. For the process of virtual reconstruction, we used a gradient edge detection filter through the watershed tool, within the segmentation editor of Avizo Lite 9.2 or 3D Slicer 4.10. The reason to apply these edge detection gradients is that this skull was filled with several karstic particles, mainly carbonated material and clay sediments of different types of grain, occupying and filling internal spaces, such as paranasal structures, which should be removed. Thresholding the skull is problematic, as the range of gray values of the fossil and the karst overlap in the histogram. To do this, we used other methods that allowed distinguishing the exogenous materials from real bone (**Figures 3C,D**). The algorithm used for the edge detection gradient was based on the complex matrix operators of Sobel type. Therefore, we used a segmentation method by interpreting pixel values as altitudes, where a gray-level image can be seen as a topographic relief. The idea behind these algorithms is to compute the lines from this topographic image. This process converts the original images into 3D topographic border gradients (**Figure 3C**), which are used by the software as a guide to generate segmentation layers based on the initial conditions of signaling and layer marking. In other words, in the original project, some points in three views along the data will mark the different structures subject to separation in a rough way. This algorithm generates the masks of the structures completely delimited from the others (**Figure 3D**) when interpolating the border gradient data (**Figure 3C**) with the premarked signals. In **Figure 3D**, the green layer is referred to bone, the yellow layer refers to the karstic material within the skull, the red layer is referred to the paranasal cavities, and the blue layer is referred to teeth (only visible in frontal view). In the maxillodental reconstruction of this skull, the left dental series was very worn by the preservational processes, and therefore, it was reconstructed (**Figures 9E,F**) using the same procedure than for the skull of *U. ingressus*. To do this, the right dental series was chosen with very good preservation, and a mirror process was performed to obtain the left dental series (**Figure 9E**). The exact repositioning and positioning of teeth were performed following the same process than the one used for the skull of *U. ingressus*. The bone of the periodontal areas on the left side was partially restored in the segmentation process (**Figure 9F**), using the same procedure than in the skull of *U. ingressus* (**Figure 6**). Once the anatomical reconstruction was finished, the model was exported to Geomagic (STL or PLY format) in high-resolution (high number of mesh triangles). The applied analysis is explained in detail in "Mesh Postprocessing" section.

Ursus spelaeus eremus Skull (PIUW-SW 483)

The skull of *U. spelaeus eremus* was scanned with a medical XCT system (see **Table 1** and **Supplementary Data**). This skull needed a high degree of virtual restoration across different areas (**Figure 7**). The preserved parts of the bone shown in **Figure 7A** (in green) were mirrored in red (in Geomagic), and these parts were used to generate the reconstructed bone of the broken or lacking bone parts in Mimics (**Figures 7A–D**). In this case, the parts that were restored are the frontal, lateral palatine and vomer, and maxilla. To regenerate these broken parts, we used the multiple-slice edit tool of Mimics, through the red contour of the polyline that delimits the area, where we will generate the same skull bone layer (in green). For the virtual restoration of the fourth right premolar, we mirrored the left fourth premolar in Geomagic (**Figure 9D**), and it was "implanted" into its corresponding alveolus with Mimics (**Figure 9D**). The fourth premolar was precisely reconstructed in the alveolar cavity, adapting the shape, size, and orientation of such dental piece to the specific anatomical requirements. To execute this process, the "reposition" tool was used in the CMF/Simulation menu in Mimics. Once the skull was virtually reconstructed, it was postprocessed. This analysis is explained in detail in "Mesh Postprocessing" section.

Ursus spelaeus ladinicus Skull (PIUW-CU 703)

In the case of the skull of *U. spelaeus ladinicus*, it was acquired with a XμCT system (see **Table 1** and **Supplementary Data**). The virtual reconstruction of *U. spelaeus ladinicus* is shown in **Figure 8**. In this case, only the right temporomandibular joint (TMJ) and the left canine were virtually repaired in Mimics. For repairing the right TMJ, a preliminary step was performed to preselect the left TMJ. With this anatomical selection, we proceeded to mirror the structure (the command is CMF/Simulation→Mirror in Mimics) (**Figures 8A–D**). As this structure is essentially formed by trabecular bone with a high complexity of the trabeculae, it is unfeasible to generate a new layer of bone as performed in other fossils. Therefore, the easiest way to proceed here was to adapt the repositioned fragment and merge it later, through the command CMF/Simulation→Reposition and Merge in Mimics (**Figures 9A–D**). The left canine was precisely reconstructed in the alveolar cavity, adapting the shape, size, and orientation of such dental piece to the specific anatomical requirements with the same command reposition tool (**Figure 9B**). With this process, the skull of *U. spelaeus ladinicus* is fully repaired and reconstructed with the TMJ and the left canine (**Figure 9C**). Once the skull was virtually reconstructed, its mesh was postprocessed. The analysis is explained in detail in "Mesh Postprocessing" section.

CONCLUSION

The use of the new advances and improvements of computed tomography has brought a big step forward in the way of analyzing fossils. XCT provides internal information without applying invasive approaches, and we can apply different methods on these internal data that are essentially described in this article, such as (i) virtually repairing and cleaning the matrix in fossils through edge detection filters, which facilitate work and costs for the researcher; (ii) unify the different acquisitions of the same XCT dataset from very large study samples; (iii) remove artifacts from datasets with incorrect calibration of the XCT acquisition parameters or by preservational biases experienced during the process of fossilization; (iv) using medical and laboratory XCT data together by the bicubic interpolation method, which saves image processing time; (v) reposition of bone parts in fossils with high precision to perform anatomical comparisons and evolutionary analyses of any kind. Moreover, it is possible to evaluate mesh integrity of the models and the effects of such virtual processes on mesh geometry and topology. We have here described a complete protocol to process data in order to give solutions for the typical problems encountered by paleontologists and to obtain reliable meshes to be used in different analyses across different fields of research, such as ecomorphology (e.g., Drake, 2011; Figueirido et al., 2011, 2015; Figueirido, 2018; Pérez-Ramos et al., 2019), histology (e.g., Doube et al., 2010; Figueirido et al., 2018; Syahrom et al., 2018), comparative anatomy (e.g., Miyashita et al., 2011; Van Valkenburgh et al., 2014), and biomechanics (e.g., Wroe et al., 2013; Figueirido et al., 2014; Pérez-Ramos et al., 2020) or phenotypic evolution in general (e.g., Drake, 2011; Polly et al., 2016; Martín-Serra et al., 2019), information that could be later used in more holistic palaecological studies (e.g., Figueirido et al., 2012, 2019). In this work, the new protocols presented could be extrapolated to the dataset from nCT. Nowadays, the nCT is not as extensively used as CT with X-ray sources, at least in vertebrate paleontology. However, nCT is an alternative technique especially valid for those scenarios where X-rays fail to provide important internal anatomical detail given their limited penetration range in highly dense materials, (e.g., Zanolli et al., 2020) and when the preservation of fossilized organic material is required (e.g., Mays et al., 2017). Therefore, the continuous advance in new protocols and computational methods that are available in this virtual world will open new horizons for the study of ancient real worlds across the history of life.

DATA AVAILABILITY STATEMENT

The datasets generated for this study are available on request to the corresponding author.

AUTHOR CONTRIBUTIONS

AP-R analyzed the sample of cave bears. AP-R and BF wrote the manuscript. Both authors contributed to the article and approved the submitted version.

FUNDING

This article has been supported by projects CGL2015-68300P, CGL2017-92166-EXP, UMA18-FEDERJA188, and CGL-2016-78577-P.

ACKNOWLEDGMENTS

We are grateful to Lorenzo Rook, Pasquale Raia, and Josep Fortuny for inviting us to contribute to this volume. We are also especially grateful to Paul Palmqvist for his comments on an earlier version of this manuscript. We are specially grateful to Jordi Marcé-Nogué and Vincent Fernandez for their highly constructive review of our paper.

SUPPLEMENTARY MATERIAL

The Supplementary Material for this article can be found online at: https://www.frontiersin.org/articles/10.3389/feart.2020.00345/full#supplementary-material

REFERENCES

Abel, R. L., Laurini, C. R., and Richter, M. (2012). A palaeobiologist's guide to 'virtual' micro-CT preparation. *Palaeontol. Electron.* 15, 1–16. doi: 10.26879/284

Adams, D. C., Collyer, M., Kaliontzopoulou, A., and Sherratt, E. (2016). *Geomorph: Software for Geometric Morphometric Analyses*. Available online at: https://hdl.handle.net/1959.11/21330 (accessed April, 2019).

Adams, D. C., and Otárola-Castillo, E. (2013). geomorph: an R package for the collection and analysis of geometric morphometric shape data. *Methods Ecol. Evol.* 4, 393–399. doi: 10.1111/2041-210X.12035

An, G., Hong, L., Zhou, X. B., Yang, Q., Li, M. Q., and Tang, X. Y. (2017). Accuracy and efficiency of computer-aided anatomical analysis using 3D visualization software based on semi-automated and automated segmentations. *Ann. Anat. Anat. Anz.* 210, 76–83. doi: 10.1016/j.aanat.2016.11.009

Banu, S., Giduturi, A., and Sattar, S. A. (2013). Interactive image segmentation and edge detection of medical images. *Int. J. Adv. Comput. Res.* 3, 211–215.

Beck, M. S. (2012). *Process Tomography: Principles, Techniques and Applications*, 2nd Edn. Oxford: Butterworth-Heinemann.

Botsch, M., Pauly, M., Rossl, C., Bischoff, S., and Kobbelt, L. (2006). "Geometric modeling based on triangle meshes," in *Proceedings of the ACM SIGGRAPH Courses*, New York, NY. doi: 10.1145/1185657.1185839

Burger, W., and Burge, M. J. (2016). *Digital Image Processing: An Algorithmic Introduction Using Java*. London: Springer doi: 10.1007/978-1-4471-6684-9.

Bushberg, J. T., Seibert, J. A., Leidholdt, E. M. Jr., and Boone, J. M. (2012). *The Essential Physics of Medical Imaging*, 3rd Edn. Philadelphia, PA: LWW.

Caldemeyer, K. S., and Buckwalter, K. A. (1999). The basic principles of computed tomography and magnetic resonance imaging. *J. Am. Acad. Dermatol.* 41, 768–771. doi: 10.1016/S0190-9622(99)70015-0

Calzado, A., and Geleijns, J. (2010). Computed tomography. Evolution, technical principles and applications. *Rev. Fís. Med.* 11, 163–180.

Camardella, L. T., Breuning, H., and Vilella, O. D. V. (2017). Are there differences between comparison methods used to evaluate the accuracy and reliability of digital models? *Dental Press J. Orthod.* 22, 65–74. doi: 10.1590/2177-6709.22.1.065-074.oar

Canny, J. (1986). A computational approach to edge detection. *IEEE Trans. Pattern Anal. Mach. Intell.* 8, 679–698. doi: 10.1109/TPAMI.1986.4767851

Cuff, A. R., Stockey, C., and Goswami, A. (2016). Endocranial morphology of the extinct North American lion (*Panthera atrox*). *Brain Behav. Evol.* 88, 213–221. doi: 10.1159/000454705

Cunningham, J. A., Rahman, I. A., Lautenschlager, S., Rayfield, E. J., and Donoghue, P. C. (2014). A virtual world of paleontology. *Trends Ecol. Evol.* 29, 347–357. doi: 10.1016/j.tree.2014.04.004

Curtis, A. A., and Van Valkenburgh, B. (2014). Beyond the sniffer: frontal sinuses in Carnivora. *Anat. Rec.* 297, 2047–2064. doi: 10.1002/ar.23025

Davesne, D., Meunier, F. J., Schmitt, A. D., Friedman, M., Otero, O., and Benson, R. B. (2019). The phylogenetic origin and evolution of acellular bone in teleost fishes: insights into osteocyte function in bone metabolism. *Biol. Rev.* 94, 1338–1363. doi: 10.1111/brv.12505

Doube, M., Kłosowski, M. M., Arganda-Carreras, I., Cordelières, F. P., Dougherty, R. P., Jackson, J. S., et al. (2010). BoneJ: free and extensible bone image analysis in ImageJ. *Bone* 47, 1076–1079. doi: 10.1016/j.bone.2010.08.023

Drake, A. G. (2011). Dispelling dog dogma: an investigation of heterochrony in dogs using 3D geometric morphometric analysis of skull shape. *Evol. Dev.* 13, 204–213. doi: 10.1111/j.1525-142X.2011.00470.x

du Plessis, A., and Broeckhoven, C. (2019). Looking deep into nature: a review of micro-computed tomography in biomimicry. *Acta Biomater.* 85, 27–40. doi: 10.1016/j.actbio.2018.12.014

Endo, H., and Frey, R. (2008). *Anatomical Imaging: Towards a New Morphology*. Tokyo: Springer-Verlag doi: 10.1007/978-4-431-76933-0.

Figueirido, B. (2018). Phenotypic disparity of the elbow joint in domestic dogs and wild carnivores. *Evolution* 72, 1600–1613. doi: 10.1111/evo.13503

Figueirido, B., Janis, C. M., Pérez-Claros, J. A., De Renzi, M., and Palmqvist, P. (2012). Cenozoic climate change influences mammalian evolutionary dynamics. *Proc. Natl. Acad. Sci. U.S.A.* 109, 722–727. doi: 10.1073/pnas.1110246108

Figueirido, B., Lautenschlager, S., Pérez-Ramos, A., and Van Valkenburgh, B. (2018). Distinct predatory behaviors in scimitar-and dirk-toothed sabertooth cats. *Curr. Biol.* 28, 3260–3266. doi: 10.1016/j.cub.2018.08.012

Figueirido, B., MacLeod, N., Krieger, J., De Renzi, M., Pérez-Claros, J. A., and Palmqvist, P. (2011). Constraint and adaptation in the evolution of carnivoran skull shape. *Paleobiology* 37, 490–518. doi: 10.1666/09062.1

Figueirido, B., Martín-Serra, A., Tseng, Z. J., and Janis, C. M. (2015). Habitat changes and changing predatory habits in North American fossil canids. *Nat. Commun.* 6:7976. doi: 10.1038/ncomms8976

Figueirido, B., Palmqvist, P., Pérez-Claros, J. A., and Janis, C. M. (2019). Sixty-six million years along the road of mammalian ecomorphological specialization. *Proc. Natl. Acad. Sci. U.S.A.* 116, 12698–12703. doi: 10.1073/pnas.1821825116

Figueirido, B., Tseng, Z. J., Serrano-Alarcón, F. J., Martín-Serra, A., and Pastor, J. F. (2014). Three-dimensional computer simulations of feeding behaviour in red and giant pandas relate skull biomechanics with dietary niche partitioning. *Biol. Lett.* 10:20140196. doi: 10.1098/rsbl.2014.0196

Forsyth, D., and Ponce, J. (2003). *Computer Vision: A Modern Approach*, 2nd Edn. Upper Saddle River, NJ: Prentice Hall.

Galibourg, A., Dumoncel, J., Telmon, N., Calvet, A., Michetti, J., and Maret, D. (2017). Assessment of automatic segmentation of teeth using a watershed-based method. *Dentomaxillofac Rad.* 47:20170220. doi: 10.1259/dmfr.20170220

Glover, G. H. (1982). Compton scatter effects in CT reconstructions. *Med. Phys.* 9, 860–867. doi: 10.1118/1.595197

Gonzalez, R. C., and Woods, R. E. (2008). *Digital Image Processing*, 3rd Edn. Upper Saddle River, NJ: Prentice-Hall.

Gunz, P., Neubauer, S., Falk, D., Tafforeau, P., Le Cabec, A., Smith, T. M., et al. (2020). Australopithecus afarensis endocasts suggest ape-like brain organization and prolonged brain growth. *Sci. Adv.* 6:eaaz4729. doi: 10.1126/sciadv.aaz4729

Honkanen, M. K., Saukko, A. E., Turunen, M. J., Shaikh, R., Prakash, M., Lovric, G., et al. (2020). Synchrotron microCT reveals the potential of the dual contrast technique for quantitative assessment of human articular cartilage composition. *J. Orthop. Res.* 38, 563–573. doi: 10.1002/jor.24479

Hsieh, J. (2009). *Computed Tomography: Principles, Design, Artifacts, and Recent Advances*, 2nd Edn. Bellingham, WA: SPIE Press.

Immel, A., Le Cabec, A., Bonazzi, M., Herbig, A., Temming, H., Schuenemann, V. J., et al. (2016). Effect of X-ray irradiation on ancient DNA in sub-fossil bones – Guidelines for safe X-ray imaging. *Sci. Rep.* 6:32969. doi: 10.1038/srep32969

Jablonski, D., and Shubin, N. H. (2015). The future of the fossil record: Paleontology in the 21st century. *Proc. Natl. Acad. Sci. U.S.A.* 112, 4852–4858. doi: 10.1073/pnas.1505146112

Johnson, T. R. (2012). Dual-energy CT: general principles. *AJR Am. J. Roentgenol.* 199, S3–S8. doi: 10.2214/AJR.12.9116

Kak, A. C., and Slaney, M. (1988). *Principles of Computerized Tomographic Imaging*. New York, NY: IEEE Press.

Kikinis, R., Pieper, S. D., and Vosburgh, K. (2014). "3D Slicer: a platform for subject-specific image analysis, visualization, and clinical support," in *Intraoper. Imaging Image-Guided Therapy*, ed. F. Jolesz (New York, NY: Springer), 277–289. doi: 10.1007/978-1-4614-7657-3_19

Knaust, D. (2012). "Methodology and techniques," in *Developments in Sedimentology*, eds D. Knaust and R. G. Bromley (Amsterdam: Elsevier), 245–271 doi: 10.1016/B978-0-444-53813-0.00009-5.

Kouraiss, K., El Hariri, K., El Albani, A., Azizi, A., Mazurier, A., and Lefebvre, B. (2019). Digitization of Fossils from the Fezouata Biota (Lower Ordovician. *Geoheritage* 11, 1889–1901. doi: 10.1007/s12371-019-00403-z

Lakey, J. H. (2009). Neutrons for biologists: a beginner's guide, or why you should consider using neutrons. *J. R. Soc. Interface* 6, S567–S573. doi: 10.1098/rsif.2009.0156.focus

Lautenschlager, S. (2016). Reconstructing the past: methods and techniques for the digital restoration of fossils. *R. Soc. Open Sci.* 3:160342. doi: 10.1098/rsos.160342

Lu, J., Fiala, J. C., and Lichtman, J. W. (2009). Semi-automated reconstruction of neural processes from large numbers of fluorescence images. *PLoS One* 4:e5655. doi: 10.1371/journal.pone.0005655

Maheswari, D., and Radha, V. (2010). Noise removal in compound image using median filter. *Int. J. Comput. Sci. Eng.* 2, 1359–1362.

Maini, R., and Aggarwal, H. (2010). A comprehensive review of image enhancement techniques. *J. Comp.* 2, 8–13.

Maret, D., Telmon, N., Peters, O. A., Lepage, B., Treil, J., Inglèse, J. M., et al. (2012). Effect of voxel size on the accuracy of 3D reconstructions with cone beam CT. *Dentomaxillofac Rad.* 41, 649–655. doi: 10.1259/dmfr/81804525

Martín-Serra, A., Nanova, O., Varón-González, C., Ortega, G., and Figueirido, B. (2019). Phenotypic integration and modularity drives skull shape divergence in the Arctic fox (*Vulpes lagopus*) from the Commander Islands. *Biol. Lett.* 15:20190406. doi: 10.1098/rsbl.2019.0406

Matthews, T., and du Plessis, A. (2016). Using X-ray computed tomography analysis tools to compare the skeletal element morphology of fossil and modern frog (Anura) species. *Palaeontol. Electron.* 19, 1–46. doi: 10.26879/557

Mays, C., Bevitt, J., and Stilwell, J. (2017). Pushing the limits of neutron tomography in palaeontology: three-dimensional modelling of in situ resin within fossil plants. *Palaeontol. Electron.* 20, 1–12. doi: 10.26879/808

MeshLab (2020). Available online at: http://MeshLab.sourceforge.net/ (accessed April, 2019).

Miyashita, T., Arbour, V. M., Witmer, L. M., and Currie, P. J. (2011). The internal cranial morphology of an armoured dinosaur Euoplocephalus corroborated by X-ray computed tomographic reconstruction. *J. Anat.* 219, 661–675. doi: 10.1111/j.1469-7580.2011.01427.x

Moore, W. J. (1982). *The Mammalian Skull. Biological Structure and Function*. Cambridge: Cambridge University Press.

Morin-Roy, F., Kauffmann, C., Tang, A., Hadjadj, S., Thomas, O., Piché, N., et al. (2014). Impact of contrast injection and stent-graft implantation on reproducibility of volume measurements in semiautomated segmentation of abdominal aortic aneurysm on computed tomography. *Eur. Radiol.* 24, 1594–1601. doi: 10.1007/s00330-014-3175-0

Mostakhdemin, M., Amiri, I. S., and Syahrom, A. (2016). *Multi-Axial Fatigue of Trabecular Bone with Respect to Normal Walking*. Singapore: Springer doi: 10.1007/978-981-287-621-8.

Murtin, C., Frindel, C., Rousseau, D., and Ito, K. (2018). Image processing for precise three-dimensional registration and stitching of thick high-resolution

laser-scanning microscopy image stacks. *Comput. Biol. Med.* 92, 22–41. doi: 10.1016/j.compbiomed.2017.10.027

Naresh, K., Khan, K. A., Umer, R., and Cantwell, W. J. (2020). The use of X-ray computed tomography for design and process modeling of aerospace composites: A review. *Mater. Des.* 190:108553. doi: 10.1016/j.matdes.2020.108553

Novacek, M. J. (1993). "Patterns of diversity in the mammalian skull," in *The Skull, volume 2: Patterns of Structural and Systematic Diversity*, eds J. Hanken and B. K. Hall (Chicago, IL: University of Chicago Press), 438–545.

Parsania, P. S., and Virparia, P. V. (2016). A comparative analysis of image interpolation algorithms. *Int. J. Adv. Res. Comput. Commun. Eng.* 5, 29–34. doi: 10.17148/IJARCCE.2016.5107

Pérez, J. M. M., and Pascau, J. (2013). *Image Processing with ImageJ*. Birmingham: Packt Publishing Ltd.

Pérez-Ramos, A., Kupczik, K., Van Heteren, A. H., Rabeder, G., Grandal-D'Anglade, A., Pastor, F. J., et al. (2019). A three-dimensional analysis of tooth-root morphology in living bears and implications for feeding behaviour in the extinct cave bear. *Hist. Biol.* 31, 461–473. doi: 10.1080/08912963.2018.1525366

Pérez-Ramos, A., Tseng, Z. J., Grandal-D'Anglade, A., Rabeder, G., Pastor, F. J., and Figueirido, B. (2020). Biomechanical simulations reveal a trade-off between adaptation to glacial climate and dietary niche versatility in European cave bears. *Sci. Adv.* 6:eaay9462. doi: 10.1126/sciadv.aay9462

Pertusa, J. F. (2010). *Técnicas de Análisis de Imagen. Aplicaciones en Biología [Image Analysis Techniques. Applications in Biology]*, 2nd Edn. Valencia: Publicacions de la Universitat de València.

Polly, P. D., Stayton, C. T., Dumont, E. R., Pierce, S. E., Rayfield, E. J., and Angielczyk, K. D. (2016). Combining geometric morphometrics and finite element analysis with evolutionary modeling: towards a synthesis. *J. Vertebr. Paleontol.* 36:e1111225. doi: 10.1080/02724634.2016.1111225

Qiu, T., Yan, Y., and Lu, G. (2012). An autoadaptive edge detection algorithm for flame and fire image processing. *IEEE Trans. Instrum. Meas.* 61, 1486–1493. doi: 10.1109/TIM.2011.2175833

R Core Team (2015). *R: A Language and Environment for Statistical Computing*. Vienna: R Foundation for Statistical Computing.

Racicot, R. (2017). Fossil secrets revealed: X-ray CT scanning and applications in paleontology. *Paleontol. Soc. Pap.* 22, 21–38. doi: 10.1017/scs.2017.6

Rahman, I. A. (2017). Computational fluid dynamics as a tool for testing functional and ecological hypotheses in fossil taxa. *Palaeontology* 60, 451–459. doi: 10.1111/pala.12295

Rahman, I. A., Adcock, K., and Garwood, R. J. (2012). Virtual fossils: a new resource for science communication in paleontology. *Evol. Educ. Outreach.* 5, 635–641. doi: 10.1007/s12052-012-0458-2

Rajarapollu, P. R., and Mankar, V. R. (2017). Bicubic interpolation algorithm implementation for image appearance enhancement. *Int. J. Comput. Sci. Technol.* 8, 23–26.

Raman, S. P., Mahesh, M., Blasko, R. V., and Fishman, E. K. (2013). CT scan parameters and radiation dose: practical advice for radiologists. *J. Am. Coll. Radiol.* 10, 840–846. doi: 10.1016/j.jacr.2013.05.032

Ravanfar-Haghighi, R., Chatterjee, S., Kumar, P., and Chatterjee, V. (2014). Numerical analysis of the relationship between the photoelectric effect and energy of the X-ray Photons in CT. *Front. Biomed. Technol.* 1, 240–251.

Rueden, C. T., Schindelin, J., Hiner, M. C., DeZonia, B. E., Walter, A. E., Arena, E. T., et al. (2017). ImageJ2: ImageJ for the next generation of scientific image data. *BMC Bioinformatics* 18:529. doi: 10.1186/s12859-017-1934-z

Sabo-Napadensky, I., and Amir, O. (2005). Reduction of scattering artifact in multislice CT. *Proc. SPIE* 5745, 983–991. doi: 10.1117/12.594885

Saif, J. A., Hammad, M. H., and Alqubati, I. A. (2016). Gradient based image edge detection. *Int. J. Eng. Technol.* 8, 153–156. doi: 10.7763/ijet.2016.v6.876

Sanchez, S., Ahlberg, P. E., Trinajstic, K. M., Mirone, A., and Tafforeau, P. (2012). Three-dimensional synchrotron virtual paleohistology: a new insight into the world of fossil bone microstructures. *Microsc. Microanal.* 18, 1095–1105. doi: 10.1017/S1431927612001079

Schillinger, B., Beaudet, A., Fedrigo, A., Grazzi, F., Kullmer, O., and Laab, M. (2018). Neutron imaging in cultural heritage research at the FRM II Reactor of the Heinz Maier-Leibnitz Center. *J. Imaging* 4:22. doi: 10.3390/jimaging4010022

Schwarz, D., Vontobel, P., Lehmann, E. H., Meyer, C. A., and Bongartz, G. (2005). Neutron tomography of internal structures of vertebrate remains: a comparison with X-ray computed tomography. *Palaeontol. Electron.* 8:11.

Shrivakshan, G. T., and Chandrasekar, C. (2012). A comparison of various edge detection techniques used in image processing. *Int. J. Comput. Sci. Issues* 9, 269–276.

Sujatha, P., and Sudha, K. K. (2015). Performance analysis of different edge detection techniques for image segmentation. *Indian J. Sci. Technol.* 8, 1–6. doi10.17485/ijst/2015/v8i14/72946

Sutton, M. D. (2008). Tomographic techniques for the study of exceptionally preserved fossils. *Proc. R. Soc. B.* 275, 1587–1593. doi: 10.1098/rspb.2008.0263

Sutton, M. D., Rahman, I. A., and Garwood, R. J. (2014). *Techniques for Virtual Palaeontology*. London: John Wiley & Sons, Ltd doi: 10.1002/9781118591192.

Syahrom, A., bin Mohd Szali Januddi, M. A. F., Harun, M. N., and Öchsner, A. (2018). "3D Modeling of Cancellous Bone," in *Cancellous Bone*, eds A. Öchsner, F. M. Lucas, and H. Altenbach (Singapore: Springer), 43–56. doi: 10.1007/978-981-10-5472-3_5

Tallman, M., Amenta, N., Delson, E., Frost, S. R., Ghosh, D., Klukkert, Z. S., et al. (2014). Evaluation of a new method of fossil retrodeformation by algorithmic symmetrization: crania of papionins (Primates, Cercopithecidae) as a test case. *PLoS One* 9:e100833. doi: 10.1371/journal.pone.0100833

Tremsin, A. S., Morgano, M., Panzner, T., Lehmann, E., Filgers, U., Vallerga, J. V., et al. (2015). High resolution neutron imaging capabilities at BOA beamline at Paul Scherrer Institut. *Nucl. Instr. Methods Phys. Res. A* 784, 486–493. doi: 10.1016/j.nima.2014.09.026

Tseng, Z. J., Su, D. F., Wang, X., White, S. C., and Ji, X. (2017). Feeding capability in the extinct giant Siamogale melilutra and comparative mandibular biomechanics of living Lutrinae. *Sci. Rep.* 7:15225. doi: 10.1038/s41598-017-15391-9

Van Hecke, W., Leemans, A., De Backer, S., Jeurissen, B., Parizel, P. M., and Sijbers, J. (2010). Comparing isotropic and anisotropic smoothing for voxel-based DTI analyses: a simulation study. *Hum. Brain Mapp.* 31, 98–114. doi: 10.1002/hbm.20848

Van Valkenburgh, B., Pang, B., Bird, D., Curtis, A., Yee, K., Wysocki, C., et al. (2014). Respiratory and olfactory turbinals in feliform and caniform carnivorans: the influence of snout length. *Anat. Rec.* 297, 2065–2079. doi: 10.1002/ar.23026

Wroe, S., Chamoli, U., Parr, W. C., Clausen, P., Ridgely, R., and Witmer, L. (2013). Comparative biomechanical modeling of metatherian and placental saber-tooths: a different kind of bite for an extreme pouched predator. *PLoS One* 8:e66888. doi: 10.1371/journal.pone.0066888

Yang, Z. J., Ren, W. Y., Mostafavi, M., Mcdonald, S. A., and Marrow, T. J. (2013). "Characterisation of 3D fracture evolution in concrete using in-situ X-ray computed tomography testing and digital volume correlation," in *Proceedings of the 8th international conference on FraMCoS*, eds J. G. M. van Mier, G. Ruiz, C. Andrade, R. C. Yu, and X. X. Zhang (Toledo, OH: CIMNE), 236–242.

Zanolli, C., Schillinger, B., Kullmer, O., Schrenk, F., Kelley, J., Rössner, G. E., et al. (2020). When X-Rays Do Not Work. Characterizing the Internal Structure of Fossil Hominid Dentognathic Remains Using High-Resolution Neutron Microtomographic Imaging. *Front. Ecol. Evol.* 8:42. doi: 10.3389/fevo.2020.00042

Zollikofer, C. P., and Ponce de León, M. S. (2005). *Virtual Reconstruction: A Primer in Computer-Assisted Paleontology and Biomedicine*. Hoboken, NJ: Wiley-Interscience.

Conflict of Interest: The authors declare that the research was conducted in the absence of any commercial or financial relationships that could be construed as a potential conflict of interest.

Advantages of publishing in Frontiers

OPEN ACCESS
Articles are free to read for greatest visibility and readership

FAST PUBLICATION
Around 90 days from submission to decision

HIGH QUALITY PEER-REVIEW
Rigorous, collaborative, and constructive peer-review

TRANSPARENT PEER-REVIEW
Editors and reviewers acknowledged by name on published articles

Frontiers
Avenue du Tribunal-Fédéral 34
1005 Lausanne | Switzerland

Visit us: www.frontiersin.org
Contact us: info@frontiersin.org | +41 21 510 17 00

REPRODUCIBILITY OF RESEARCH
Support open data and methods to enhance research reproducibility

DIGITAL PUBLISHING
Articles designed for optimal readership across devices

FOLLOW US
@frontiersin

IMPACT METRICS
Advanced article metrics track visibility across digital media

EXTENSIVE PROMOTION
Marketing and promotion of impactful research

LOOP RESEARCH NETWORK
Our network increases your article's readership